P-592

NASA Conference Publication 2397

Langley Symposium on Aerodynamics

Volume I

(NASA-CP-2397) LANGLEY SYMPOSIUM ON AERODYNAMICS, VOLUME 1 (NASA) 592 p
CSCL 01B
N88-14926
--THRU--
N88-14956
Unclas
H1/01 0117224

(1+30)

Date for general release January 31, 1988

APR 1988
RECEIVED
NASA STI FACILITY
ACCESS DEPT.

Proceedings of a symposium held at
NASA Langley Research Center
Hampton, Virginia
April 23-25, 1985

NASA

NASA Conference Publication 2397

Langley Symposium on Aerodynamics

Volume I

Sharon H. Stack, *Compiler*
Langley Research Center
Hampton, Virginia

Proceedings of a symposium held at
NASA Langley Research Center
Hampton, Virginia
April 23-25, 1985

NASA
National Aeronautics
and Space Administration

Scientific and Technical
Information Branch

1985

PREFACE

This publication is a compilation of the papers presented at the Langley Symposium on Aerodynamics held on April 23-25, 1985, at NASA Langley Research Center, Hampton, Virginia. The purpose of this symposium was to present current work and results of the Langley Aeronautics Directorate covering the areas of computational fluid dynamics, viscous flows, airfoil aerodynamics, propulsion integration, test techniques, and low-speed, high-speed, and transonic aerodynamics.

The symposium was organized into the following seven sessions:

I. Theoretical Aerodynamics
II. Test Techniques
III. Fluid Physics
IV. Viscous Drag Reduction
V. Propulsion/Integration
VI. Flight Dynamics
VII. High Performance Vehicles

Sessions I to IV are printed in Volume I, which has a FEDD restriction. Sessions V to VII are printed in Volume II, which has an ITAR restriction. Papers are grouped by sessions in the order in which they were presented. An author index and a list of attendees are included at the end of each volume.

Robert E. Bower
Conference Chairman

PRECEDING PAGE BLANK NOT FILMED

PAGE ii INTENTIONALLY BLANK

CONTENTS

VOLUME I

PREFACE iii

1. OPENING REMARKS 1
   Robert E. Bower

SESSION I - THEORETICAL AERODYNAMICS
Chairman: Percy J. Bobbitt

2. COMPUTATIONAL FLUID DYNAMICS OVERVIEW .... 5 ✓S1
   Percy J. Bobbitt

3. FINITE-VOLUME SCHEME FOR TRANSONIC POTENTIAL FLOW ABOUT AIRFOILS AND BODIES IN AN ARBITRARILY SHAPED CHANNEL .... 25 ✓S2
   Jerry C. South, Jr., Michael L. Doria, and Lawrence L. Green

4. BREAKDOWN OF THE CONSERVATIVE POTENTIAL EQUATION .... 45 ✓S3
   M. D. Salas and C. R. Gumbert

5. APPLICATION OF A FULL POTENTIAL METHOD FOR ANALYSIS OF COMPLEX AIRCRAFT GEOMETRIES .... 73 ✓S4
   Kenneth M. Jones and Noel A. Talcott, Jr.

6. UPWIND RELAXATION ALGORITHMS FOR EULER/NAVIER-STOKES EQUATIONS .... 89 ✓S5
   J. L. Thomas, R. W. Walters, D. H. Rudy, and R. C. Swanson, Jr.

7. A MULTISTAGE TIME-STEPPING SCHEME FOR THE THIN-LAYER NAVIER-STOKES EQUATIONS .... 109 ✓S6
   R. C. Swanson, Jr., Eli Turkel, and V. N. Vatsa

8. NUMERICAL SIMULATION OF A CONTROLLED BOUNDARY LAYER .... 137 ✓S7
   Thomas A. Zang and M. Yousuff Hussaini

9. VISCOUS VORTEX FLOWS .... 153 ✓S8
   R. P. Weston, J. P. Chamberlain, C. H. Liu, and Peter-Michael Hartwich

10. A THEORY FOR THE CORE FLOW OF LEADING-EDGE VORTICES .... 169 ✓S9
    James M. Luckring

11. ANALYSIS AND PERFORMANCE PREDICTION OF SCRAMJET INLETS UTILIZING A THREE-DIMENSIONAL NAVIER-STOKES CODE .... 187 ✓S10
    Ajay Kumar and Carl A. Trexler

PRECEDING PAGE BLANK NOT FILMED

PAGE IV INTENTIONALLY BLANK

SESSION II - TEST TECHNIQUES
Chairman: Linwood W. McKinney

12. LOW-DISTURBANCE WIND TUNNELS .... 209 ✓ S11
I. E. Beckwith, Z. T. Applin, P. C. Stainback, and L. Maestrello

13. WIND TUNNEL WALL INTERFERENCE .... 225 ✓ S12
Perry A. Newman, Raymond E. Mineck, Richard W. Barnwell, and William B. Kemp, Jr.

14. STATUS OF MAGNETIC SUSPENSION TECHNOLOGY .... 261 ✓ S13
Richmond P. Boyden and Ping Tcheng

15. FLOW DIAGNOSTICS AND VISUALIZATION IN WIND TUNNELS AND FLIGHT .... 279 ✓ S14
P. C. Stainback, C. B. Johnson, B. J. Holmes, C. J. Obara, D. Carraway, J. F. Meyers, S. P. Wilkinson, W. C. Honaker, P. L. Lawing, R. R. Antcliff, O. Jarrett, Jr., R. C. Rogers, and J. P. Stack

16. PRELIMINARY CALIBRATION AND TEST RESULTS FROM THE NATIONAL TRANSONIC FACILITY .... 311 ✓ S15
Linwood W. McKinney and Dennis E. Fuller

SESSION III - FLUID PHYSICS
Chairman: Dennis M. Bushnell

17. BOUNDARY LAYER TRANSITION .... 333 ✓ S16
L. Maestrello, A. Bayliss, S. M. Mangalam, and M. R. Malik

18. WALL TURBULENCE CONTROL .... 347 ✓ S17
Stephen P. Wilkinson, A. Margrethe Lindemann, George B. Beeler, Catherine B. McGinley, Wesley L. Goodman, and R. Balasubramanian

19. SEPARATED FLOW .... 361 ✓ S18
W. L. Sellers III, R. E. Dunham, Jr., W. L. Goodman, F. G. Howard, R. J. Margason, D. H. Rudy, C. L. Rumsey, H. P. Stough III, and J. L. Thomas

20. VORTEX DYNAMICS .... 375 ✓ S19
George C. Greene, John E. Lamar, C. H. Liu, and L. R. Kubendran

SESSION IV - VISCOUS DRAG REDUCTION
Chairman: Jerry N. Hefner

21. OVERVIEW OF THE LANGLEY VISCOUS DRAG REDUCTION PROGRAM .... 393 ✓ S20
Jerry N. Hefner

22. ADVANCED NATURAL LAMINAR FLOW AIRFOIL WITH HIGH LIFT TO DRAG RATIO .... 401 ✓ S21
Jeffrey K. Viken, Werner Pfenninger, and Robert J. McGhee

23. COMPUTATIONAL DESIGN OF NATURAL LAMINAR FLOW WINGS FOR TRANSONIC TRANSPORT APPLICATION .... 415 ✓ S22
Edgar G. Waggoner, Richard L. Campbell, Pamela S. Phillips, and Jeffrey K. Viken

24. NATURAL LAMINAR FLOW NACELLE FOR TRANSPORT AIRCRAFT .... 445 ✓ S23
Milton Lamb, William K. Abeyounis, James C. Patterson, Jr., and Richard J. Re

25. FLIGHT RESEARCH ON NATURAL LAMINAR FLOW .... 461 ✓ S24
B. J. Holmes, C. C. Croom, E. C. Hastings, Jr., C. J. Obara, and C. P. van Dam

26. DESIGN AND EXPERIMENTAL EVALUATION OF A SWEPT SUPERCRITICAL LAMINAR FLOW CONTROL (LFC) AIRFOIL .... 475 ✓ S25
W. D. Harvey, C. D. Harris, C. W. Brooks, P. G. Clukey, and J. P. Stack

27. LAMINAR FLOW INTEGRATION - FLIGHT TESTS STATUS AND PLANS .... 485 ✓ S26
R. D. Wagner, D. F. Fisher, M. C. Fischer, D. W. Bartlett, and R. R. Meyer, Jr.

28. ROUGHNESS AND WAVINESS REQUIREMENTS FOR LAMINAR FLOW SURFACES .... 519 ✓ S27
Clifford J. Obara and Bruce J. Holmes

29. INSECT CONTAMINATION PROTECTION FOR LAMINAR FLOW SURFACES .... 539 ✓ S28
Cynthia C. Croom and Bruce J. Holmes

30. RIBLETS FOR AIRCRAFT SKIN-FRICTION REDUCTION .... 557 ✓ S29
Michael J. Walsh

31. AIRFOIL LARGE EDDY BREAKUP DEVICES FOR TURBULENT DRAG REDUCTION .... 573 ✓ S30
J. B. Anders

ATTENDEES .... 587 Omit

AUTHOR INDEX .... 599 Omit

VOLUME II*

SESSION V - PROPULSION/INTEGRATION
Chairman: Louis J. Williams

32. PROPULSION/AIRFRAME INTEGRATION - AN OVERVIEW 1
William P. Henderson

33. NOZZLE AFTERBODY INTEGRATION FOR HIGH-PERFORMANCE AIRCRAFT 15
Laurence D. Leavitt and James R. Burley II

34. AERODYNAMIC INTEGRATION FOR ADVANCED TURBOPROP AIRCRAFT 43
P. L. Coe, Jr., J. C. Patterson, Jr. and Dana Morris Dunham

35. ACOUSTICS FOR ADVANCED TURBOPROP AIRCRAFT 59
Patricia J. W. Block

36. PROPULSION AT HYPERSONIC SPEEDS: AN OVERVIEW 73
H. Lee Beach, Jr.

37. STATUS OF HYDROGEN-FUELED SCRAMJET ENGINE TESTS 83
R. Wayne Guy, S. Zane Pinckney, and Earl H. Andrews

SESSION VI - FLIGHT DYNAMICS
Chairman: Joseph L. Johnson, Jr.

38. RECENT STUDIES OF AERODYNAMIC EFFECTS ON HIGH ANGLE-OF-ATTACK FLIGHT DYNAMICS OF FIGHTER AIRCRAFT 95
Raymond D. Whipple, Jay M. Brandon, Mark A. Croom, and Luat T. Nguyen

39. ADVANCED HIGH ANGLE-OF-ATTACK CONTROL CONCEPTS FOR FIGHTER AIRCRAFT 121
Luat T. Nguyen, David E. Hahne, Daniel G. Murri, and Marilyn E. Ogburn

40. LEADING-EDGE DESIGN FOR IMPROVED SPIN RESISTANCE OF WINGS INCORPORATING CONVENTIONAL AND ADVANCED AIRFOILS 141
H. Paul Stough III, Frank L. Jordan, Jr., Daniel J. DiCarlo, and Kenneth F. Glover

---

*Contents of Volume II are included for convenience.

SESSION VII - HIGH-PERFORMANCE VEHICLES
Chairman: Roy V. Harris, Jr.

41. HIGH-PERFORMANCE VEHICLES: AN OVERVIEW 159
Roy V. Harris, Jr.

42. SUBSONIC/TRANSONIC DEVELOPMENT OF VORTEX FLAPS FOR FIGHTER AIRCRAFT 163
W. Elliott Schoonover, Jr., Neal T. Frink, James B. Hallissy, and Long P. Yip

43. STUDIES OF SEVERAL ADVANCED SUPERSONIC WING DESIGNS FOR SUBSONIC AND SUPERSONIC MANEUVER 179
W. J. Small, B. L. Shrout, G. D. Riebe, K. W. Hom, B. A. Campbell, H. W. Carlson, C. M. Darden, J. S. Jackson, and M. E. Johnson

44. FORWARD-SWEPT WING TECHNOLOGY FOR MANEUVERING AIRCRAFT 193
Michael J. Mann, Charles E. Mercer, and James B. Hallissy

45. POWERED AERODYNAMICS FOR ADVANCED STOL FIGHTER CONFIGURATIONS 207
J. W. Paulson, Jr., P. F. Quinto, D. W. Banks, G. T. Kemmerly, and G. M. Gatlin

46. NEW CONSIDERATIONS IN SUPERSONIC WING DESIGN 221
David S. Miller and Peter F. Covell

47. MULTI-BODY AIRCRAFT: OLD CONCEPT - NEW APPLICATION 235
Richard M. Wood, O. J. Rose, and S. Naomi McMillin

48. STORE CARRIAGE DRAG AND SEPARATION AT SUPERSONIC SPEEDS 251
Robert L. Stallings, Jr., Floyd J. Wilcox, Jr., A. B. Blair, Jr., and William J. Monta

49. SUMMARY OF THE LANGLEY HYPERSONIC MISSILE TASK TEAM STUDY 269
Patrick J. Johnston, Wallace C. Sawyer, and Don C. Marcum, Jr.

50. MACH 5 CRUISE AIRCRAFT RESEARCH 285
Joe D. Watts, Frank V. Olinger, John P. Weidner, Stuart K. Johnson, Bobby W. Sanders, and J. Wayne Keyes

ATTENDEES 305

AUTHOR INDEX 317

OPENING REMARKS

Robert E. Bower
NASA Langley Research Center
Hampton, Virginia

AERONAUTICS DIRECTORATE

Technical Areas

- **Basic Fluid Mechanics**
  - Computational Fluid Dynamics ①
  - Testing Techniques ②
  - Viscous Flows ③
  - Airfoils ④
- **Aerodynamics**
  - Subsonic ⑤
  - Transonic ⑥
  - High-Speed ⑦
- **Flight Dynamics** ⑧
- **Propulsion**
  - Propulsion Aerodynamics ⑨
  - Hypersonic Propulsion ⑩
- **Flight Environment** ⑪

AERONAUTICS DIRECTORATE

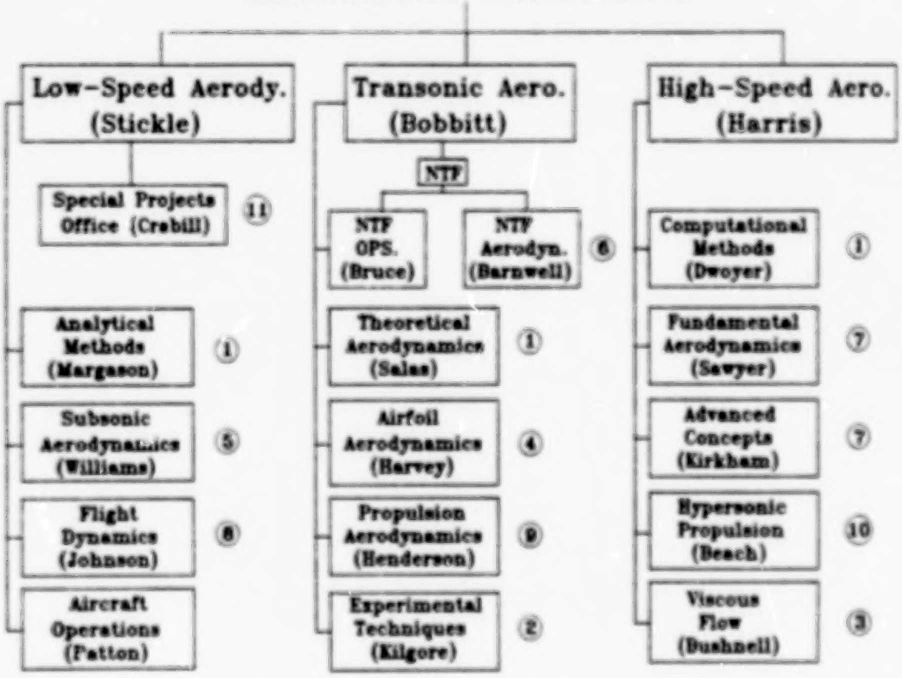
Low-Speed Aerody. (Stickle)
Special Projects Office (Crebill) ⑪
Analytical Methods (Margason) ①
Subsonic Aerodynamics (Williams) ⑤
Flight Dynamics (Johnson) ⑧
Aircraft Operations (Patton)
Transonic Aero. (Bobbitt)
NTF
NTF OPS. (Bruce)
NTF Aerodyn. (Barnwell) ⑥
Theoretical Aerodynamics (Salas) ①
Airfoil Aerodynamics (Harvey) ④
Propulsion Aerodynamics (Henderson) ⑨
Experimental Techniques (Kilgore) ②
High-Speed Aero. (Harris)
Computational Methods (Dwoyer) ①
Fundamental Aerodynamics (Sawyer) ⑦
Advanced Concepts (Kirkham) ⑦
Hypersonic Propulsion (Beach) ⑩
Viscous Flow (Bushnell) ③

FACILITIES

NEW:

① VPS-32 (Modified CYBER 205)
② 0.3-Meter Adaptive Wall Cryogenic Transonic Tunnel
② Magnetic Suspension and Balance Low-Speed Tunnel
③ Low-Disturbance Supersonic Wind Tunnel
⑥ National Transonic Facility
⑦ 20-Inch Supersonic Tunnel

IMPROVED FLOW QUALITY:

④ 8-Foot Transonic Pressure Tunnel
④ Low-Turbulence Pressure Tunnel
⑤ 4 x 7 Meter Low-Speed Tunnel

REHAB AND MODIFICATION:

⑦ Unitary Plan Supersonic Tunnel
③ ⑦ Gas Dynamics Laboratory
⑧ 30- by 60-Foot Low-Speed Tunnel
⑧ Spin Tunnel
⑨ 16-Foot Transonic Tunnel
⑩ 8-Foot High Temperature Structures Tunnel

SMALL, CHEAP-TO-OPERATE BASIC RESEARCH APPARATUS:

① ③ ④ ⑧

AERONAUTICS DIRECTORATE

MAJOR GOALS/THRUSTS

1. Develop & Apply Advanced COMPUTATIONAL FLUID DYNAMICS (VPS-32) to the Solution of Basic Aerodynamics & Propulsion Integration Problems Across the Speed Regime
2. Expand Efforts in TRANSONIC AERODYNAMICS to Include High Reynolds Number Studies in the NTF & Concepts for Interference-Free Testing
3. Increase Attention to BASIC FLUID MECHANICS Problems Including Vortex Control, Boundary-Layer Control, Turbulence, & Separation
4. Achieve Major Reductions in the VISCOUS DRAG of Aircraft & Missiles Across the Speed Regime
5. Attain an Improved Understanding of PROPULSION INTEGRATION Effects for Fighters & Advanced Turboprops
6. Establish & Demonstrate the Technology Base for Practical SCRAMJET Propulsion Systems
7. Attain an Improved Predictive Performance Capability of Vehicles Operating at Very HIGH ANGLES OF ATTACK Utilizing Propulsive Control
8. Increase Aerodynamic Research Applicable to Advanced, High-Speed MILITARY AIRCRAFT & MISSILES
9. Establish a FLIGHT ENVIRONMENT Data Base for the Improved Design Criteria & Safe Operation of Aircraft

LANGLEY SYMPOSIUM ON AERODYNAMICS

April 23-25, 1985

I. **Theoretical Aerodynamics**
- Code Development
- Verification Experiments
- Applications

II. **Test Techniques**
- NTF
- Interference-Free Concepts
- Ultra Quiet Tunnels
- Instrumentation

III. **Basic Fluid Mechanics**
- Transition
- Turbulence
- Separation
- Vortex Flows

IV. **Viscous Drag Reduction**
- NLF
- LFC/HLF
- Turbulence Drag

V. **Propulsion/Integration**
- Turbofans
- Advanced Turboprops
- Scramjets

VI. **Flight Dynamics**
- High Alpha
- Propulsion Control
- Spin Prevention

VII. **High Performance Vehicles**
- Supersonic Cruise
- Maneuverability
- Missile Store and Separation
- Hypersonics

D1

N88-14927

S1-34

117225

20P.

COMPUTATIONAL FLUID DYNAMICS OVERVIEW

Percy J. Bobbitt
Langley Research Center
Hampton, Virginia

[redacted] Computers and CFD

Our ability to treat more complex geometries with more complex or complete governing equations is governed by the speed and storage of our computers and the speed, or efficiency, of our solution algorithms. About a year ago, Langley's CYBER 203 was replaced by the VPS-32 with the potential for roughly an order of magnitude increase in memory and a slight increase in speed. Euler and Reynolds Averaged Navier-Stokes (RANS) solutions that can be expedited in approximately 10 minutes with this computer are depicted in the figure. Also, the capabilities of the NAS-HSP-1 (CRAY-2) and CRAY-1 are shown for reference. The A, AC, and LES symbols within the ovals indicate airfoil, complete-aircraft-configuration, and large-eddy-simulation calculations, respectively.

Clearly, we are at a point where the calculation of flows about complete aircraft (AC) using the Euler equations has become possible. (A recent AIAA paper by J. C. South, Jr.[1] indicates that the Euler boundary for complete aircraft (AC) calculation is on the optimistic side and that these types of calculations will probably require a NAS-like computer to achieve a 10-minute calculation time.) Two-dimensional as well as some three-dimensional flows can now be computed using the RANS equations. Storage is available for fairly complex geometries using RANS equations but computation time is excessive. The need for faster solution algorithms for those types of equations is clear. In the next few years, it is expected that computers with an order of magnitude increase in speed beyond the CRAY-2 will become available thus allowing "practical" RANS computations in a reasonably short time. With the present rate of growth of our computer technology, large eddy simulations of the flow about an airfoil will become possible in the early 1990's.

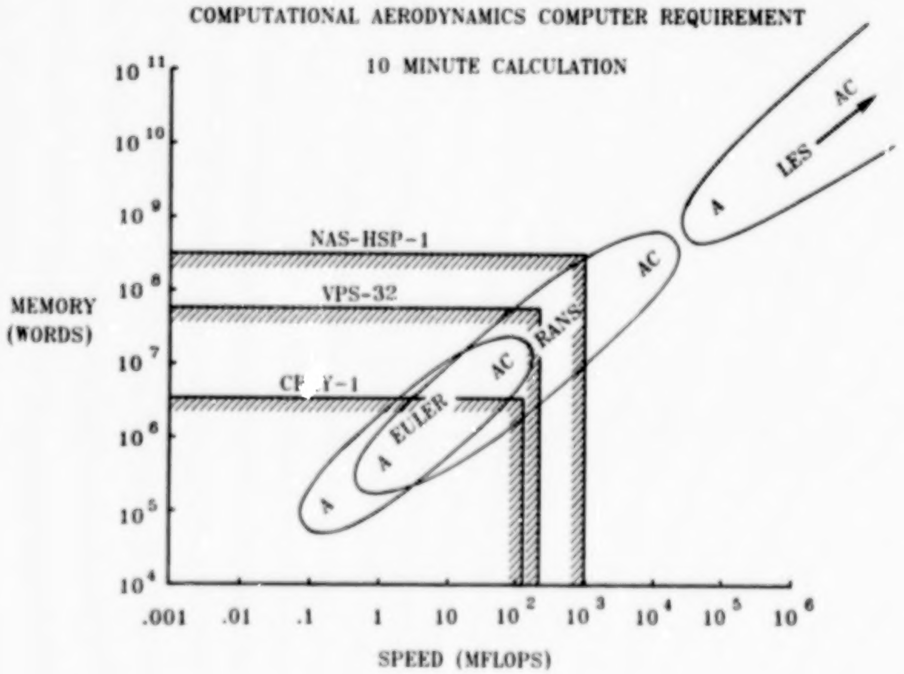

Potential Equation Research

A considerable amount of research is still being devoted to the various nonlinear forms of the potential equation. Included are activities aimed at improving the speed of computation, the ease of application to complex geometries, and the accuracy of the solutions. Many of the specific applications have necessitated significant improvements and modifications in existing codes. In some cases, a complete code development, including an appropriate grid system, was required such as that described in the first paper of the session by South et al. The second paper, by Salas and Gumbert, treats the nonuniqueness problem associated with the "conservative" formulation of the full potential equation and explains some of the large discrepancies encountered in the past between various airfoil codes. The application of a wing/body code due to V. J. Shankar to two supersonic fighter configurations is described in the paper by Jones and Talcott. Finally, one element of the analysis presented in the "vortex breakdown" paper by Luckring is based on the linear potential equation.

- MULTIGRID METHODS
- MASS FLUX BOUNDARY CONDITIONS
- WIND-TUNNEL FLOWS (+)
    - ASSESSMENT & CORRECTIONS
    - ADAPTIVE WALLS
- NONUNIQUENESS OF "CONSERVATIVE" EQUATION SOLUTIONS (+)
- WING/BODY APPLICATIONS (+) (•)
- VORTEX FLOWS (+)
- NOZZLE FLOWS
- PROPELLER SLIPSTREAM
- AIRFOIL DESIGN (•)

(+) PRESENTATION IN THEORETICAL AERODYNAMICS SECTIONS

(•) ILLUSTRATIVE RESULTS IN OVERVIEW

Euler Equation Research

It was noted in the discussion of our first figure that the VPS-32 computer has the capability of handling 3-D computations for the Euler as well as the RANS equations. The paper by Thomas et al. presents results from one such effort in which a second- or third-order accurate upwind scheme for the discretization of the convective and pressure derivatives (based on a technique developed by Van Leer) is used. A relaxation scheme for the unfactored, implicit, backward Euler time method is also applied. When treating RANS equations, central differencing has been used for the viscous terms. Results have been obtained for several 2-D problems for both the Euler and RANS equations; present activities are concentrated on extensions to 3-D.

Other theoretical research using the Euler equations includes wing/body, leading-edge vortex and transport-engine-nacelle flows. A code has also been developed to calculate the effects of a propeller slipstream on wing pressures. An example is shown later of an Euler wing/body calculation.

- FLUX SPLIT, UPWIND SCHEMES (+)
- WING-BODY APPLICATIONS (*)
- VORTEX FLOWS
- NACELLE FLOWS
- PROPELLER SLIPSTREAM

(+) PRESENTATION IN THEORETICAL AERODYNAMICS SECTIONS
(*) ILLUSTRATIVE RESULTS IN OVERVIEW

Navier-Stokes Equation Research

Computational fluid dynamics (CFD) research concerning the Navier-Stokes equations takes a variety of forms. The paper previously discussed by Thomas et al. presents an implicit upwind flux split scheme which leads to a diagonally dominant matrix structure, which allows large time steps to be taken in three-dimensional problems. In the paper by Swanson et al., a class of explicit multistage time-stepping schemes is used to construct a solution algorithm. Various methods are employed for accelerating convergence to steady state. Two-dimensional (airfoil) results have been obtained; three-dimensional programs are now being debugged.

Several codes have been written over the past few years which solve for the time-varying behavior of the viscous boundary-layer flow using the full Navier-Stokes equation. These solutions are normally referred to as numerical simulations. The paper by Zang and Hussaini presents the results of a numerical simulation of transitional flow and various methods for delaying transition. Another study of this type is given in a paper in the Fluid Physics Session by Maestrello et al.

Vortex flows are receiving a lot more attention in recent times from the CFD world. The paper by Weston et al. in this session presents results of several Navier-Stokes analyses in which the growth and decay of vortices over and behind a wing are simulated. Vortex breakdown or bursting is the subject of the Luckring paper. In his analysis, a viscous core and inviscid outer flow are matched to effect a consistent global solution.

In the last paper in this session, Kumar and Trexler treat the supersonic flow in a scramjet inlet utilizing the three-dimensional Navier-Stokes equations. Recent experimental results for two types of inlets are compared with predictions.

FLUX-SPLIT, UPWIND SCHEMES (+)

THIN LAYER NAVIER-STOKES - 2-D & 3-D (+)

TRANSITION SIMULATION - 2-D & 3-D (+)

VORTEX FLOWS (+)

SCRAMJET INLETS (+)

AFTERBODY/NOZZLE FLOWS (•)

(+) PRESENTATION IN THEORETICAL AERODYNAMICS SECTIONS
(•) ILLUSTRATIVE RESULTS IN OVERVIEW

Applied CFD and Validation Research

The papers given in the Theoretical Aerodynamics Session comprise a representative sample of the ongoing basic and applied CFD research programs. Time does not permit a synopsis of all of the research projects in progress; basic methodology investigations are particularly difficult to follow when "abbreviated". On the other hand, the flavor of a validation or applied activity can usually be imparted with just a few figures. Consequently the remainder of the overview will be aimed at giving a more complete picture of our broad-based applied CFD and validation programs. The applied CFD research has a number of goals including

- Code validation
- Increased understanding of flow physics
- Experiment definition
- Development of design procedures

The ATAT program, described below, and the other three activities chosen for review all have these goals but with varying emphasis.

Advanced Technology Airfoil Test (ATAT) Program

A cooperative program with the U. S. transport industry has just been concluded which was aimed at validating and improving airfoil design methodology at flight Reynolds numbers. An extensive series of correlation and advanced technology airfoils were tested in the Langley 0.3-Meter Transonic Cryogenic Tunnel; they are listed on the opposite figure. The design constraints were that the thickness ratio be 0.12, the c_ℓ be approximately 0.65 and the Mach number be 0.765. For the most part, the Korn-Garabedian code was employed by the participants, but some use was made of the Grumfoil code of R. Melnik. Criteria used for transition strips and sidewall suction were examined in several of the tests. Tunnel-wall interference corrections accounting for sidewall interference, top and bottom wall interference, or all four walls were also studied. Similar programs have been developed with industry for transport and fighter configurations with the NTF as a focus.

ADVANCED TECHNOLOGY AIRFOIL TEST (ATAT) PROGRAM

INDUSTRY

BCAC 1
BCAC 2
DAC
LAC 1
LAC 2
LAC 3

ADVANCED NASA

NASA SC(3)0712A
NASA SC(3)0712B

CORRELATION

NACA 0012
NACA 65-213
NASA SC(2)0510
NASA SC(2)0714

DFVLR CAST 10
DFVLR CAST 10, c/2

Comparison of Data With Grumfoil at Near Design Lift

The data shown in the figure below were obtained during the course of the ATAT program on the NASA SC(3)0712 airfoil. It was part of an investigation of the effects of sidewall bleed and the utility of various tunnel-wall correction techniques. Experimental results are for a normal tunnel Mach number of 0.76, a R_c of 6×10^6, and a c_ℓ of 0.56. The left-hand figure is a comparison of the data with the Grumfoil code run at the experimental c_ℓ and Mach number and shows that the theory yields too high a suction pressure level and a stronger shock on the top side than experiment. If the data are corrected for the sidewalls and the top and bottom walls (center plot), the corrected Mach number is lower and the geometric angle of attack (α_G) is slightly higher. The resulting pressures are in better agreement on the top with the bottom remaining essentially unchanged. Finally, if only the sidewall correction is applied, the agreement on both the top and bottom surfaces is improved over the four-wall-correction results. Clearly, the validation of airfoil design procedures requires a good understanding of tunnel-wall interference.

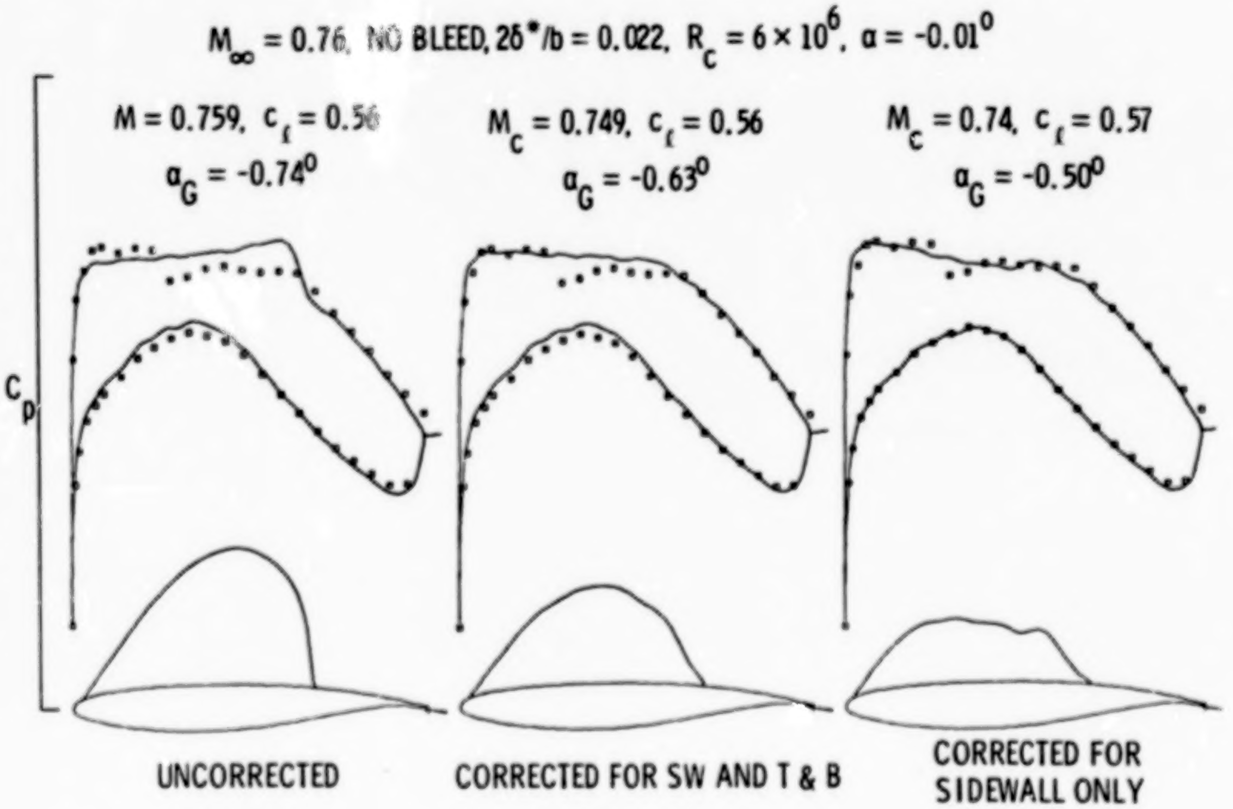

Comparison of Data With Grumfoil for a High-Lift Case

This is a plot similar to the previous one with the only differences being a higher Reynolds number (25×10^6) and a higher c_ℓ (≈ 0.93). The conclusion relative to the wall corrections is the same, i.e., the sidewall correction, by itself, provides the best agreement with experiment from the Langley 0.3-Meter Transonic Cryogenic Tunnel.

$M_\infty = 0.76$, NO BLEED, $2\delta^*/b = 0.018$, $R_c = 25 \times 10^6$, $\alpha = 2.03^\circ$

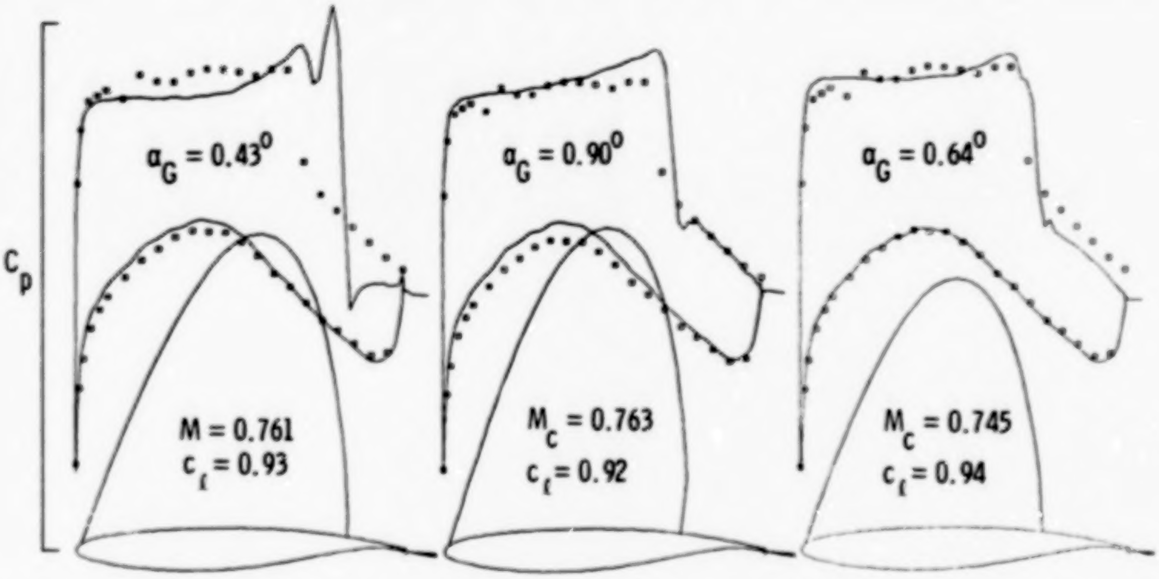

UNCORRECTED — CORRECTED FOR SW AND T & B — CORRECTED FOR SW ONLY

F-14 Variable Sweep Transition Flight Experiment

A number of transonic wing/body codes have been developed over the past half dozen years based on various forms of the nonlinear potential equation. One of the most accurate we have found is one developed by A. Jameson called FLO30. It has been mated by Craig Streett of the LaRC with a 3-D boundary layer routine based on the method of P. D. Smith to form the TAWFIVE code. In addition, he has "patched in" the strong trailing-edge interaction developed by R. Melnik of Grumman to provide a better accounting of the pressure variations normal to the surface and wake and the effects of wake curvature.

In the figure, the result of applying TAWFIVE code to the basic F-14 wing at two span stations is depicted. The agreement here is typical; many cases show even better agreement. More details of this application and others are given in a paper by Waggoner et al. in the Viscous Drag Reduction Session.

M = 0.70 α = 2.1° ALT = 25,000 FT.

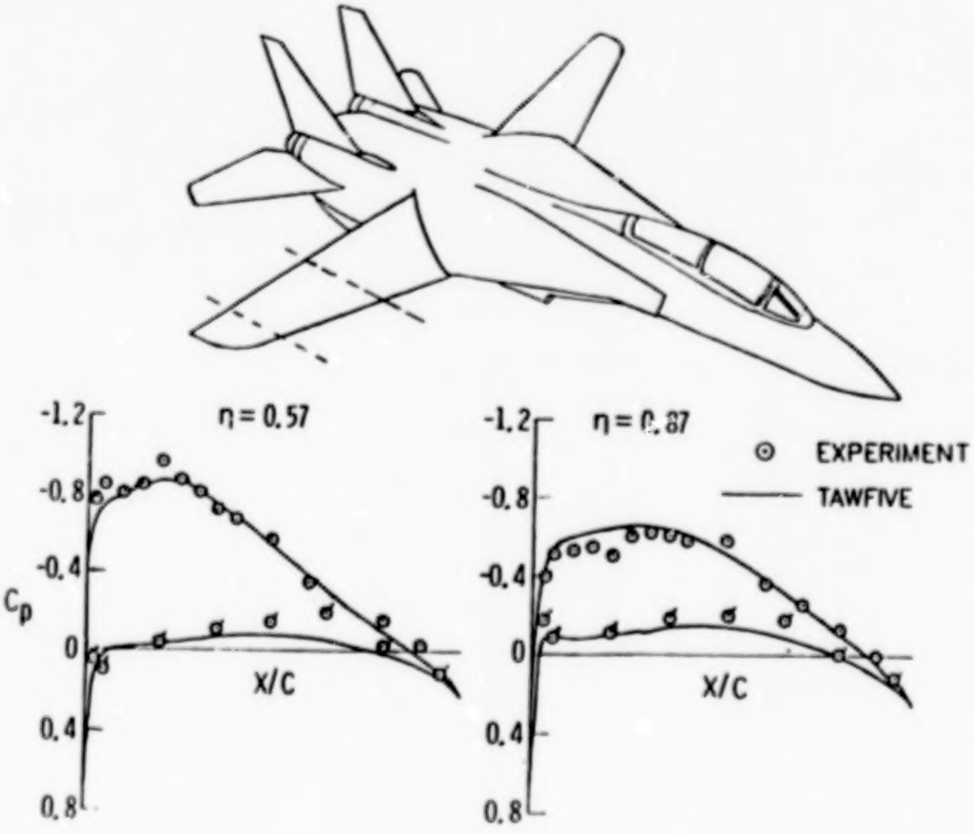

Euler Solutions for High-Speed Flow About Complex Three-Dimensional Configurations

High-speed flow about complex aerospace configurations has been simulated by numerically solving the Euler equations[2]. A finite-volume explicit scheme with Runge-Kutta time integration is employed to solve the three-dimensional compressible Euler equations. The incorporation of carefully chosen dissipative terms and convergence accelerations such as enthalpy damping and maximum time-stepping has rendered the method very efficient in solving high-speed flows involving strong shocks and local subsonic regions. Discretization of the computational space is achieved by an algebraic method developed for quasi-three-dimensional grid generation for blended wing-body geometries and other complex configurations. The method has proven its versatility as applied to realistic aircraft geometries. The software for both grid generation and flow simulation reside on the VPS-32 system.

A typical set of results is presented in the figure below on this page. The body-geometry investigated is a fighter-like configuration used for full potential flow computations at the Rockwell International Science Center. Surface pressure plots are presented for three cross-sectional planes located along the axis of the body. A comparison of the full potential and Euler solutions presented shows a reasonable degree of agreement between the pressure values predicted by the two methods.

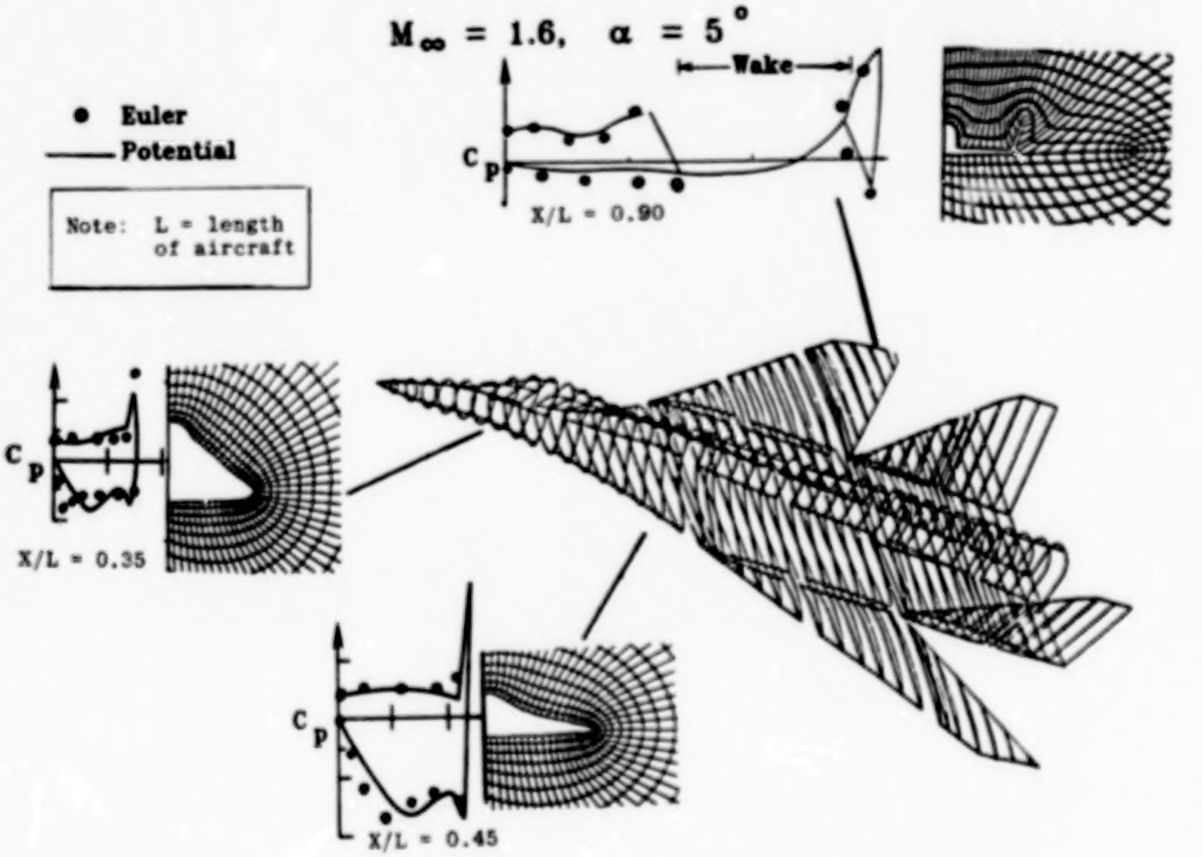

Navier-Stokes Results for Fully Deployed 2-D Thrust Reverser

A Navier-Stokes code has been developed by R. MacCormack at the University of Washington for solving the flow field in two-dimensional nozzles having up to three exhaust ports. The code solves the finite-volume form of the Navier-Stokes equations using MacCormack's explicit-implicit scheme combined with flux-vector splitting. Turbulence is modeled with the Baldwin-Lomax eddy viscosity model. The code has been applied to solving the flow in fully deployed thrust reverser ports such as that shown in the figure. The results are in good qualitative agreement with experiment for the limited cases calculated to date. A more detailed assessment of the accuracy of the computational model is under way.

NAVIER-STOKES RESULTS FOR FULLY-DEPLOYED 2-D THRUST REVERSER

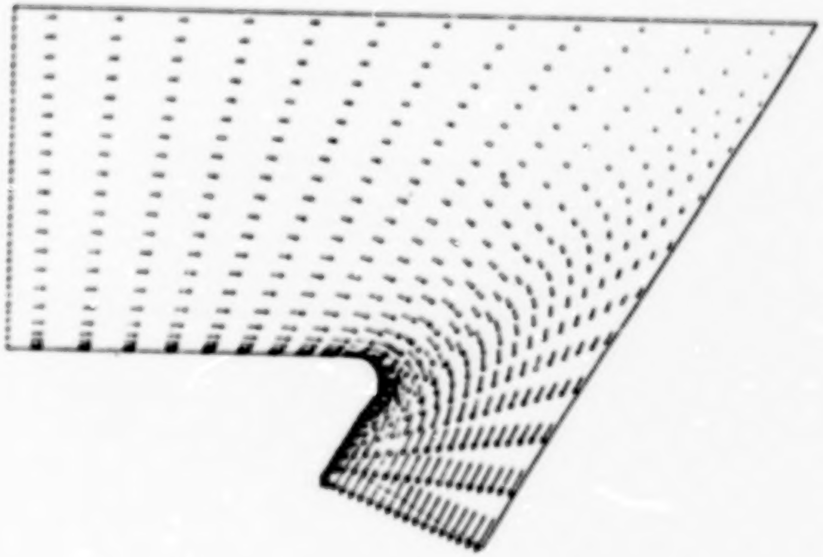

VELOCITY VECTORS

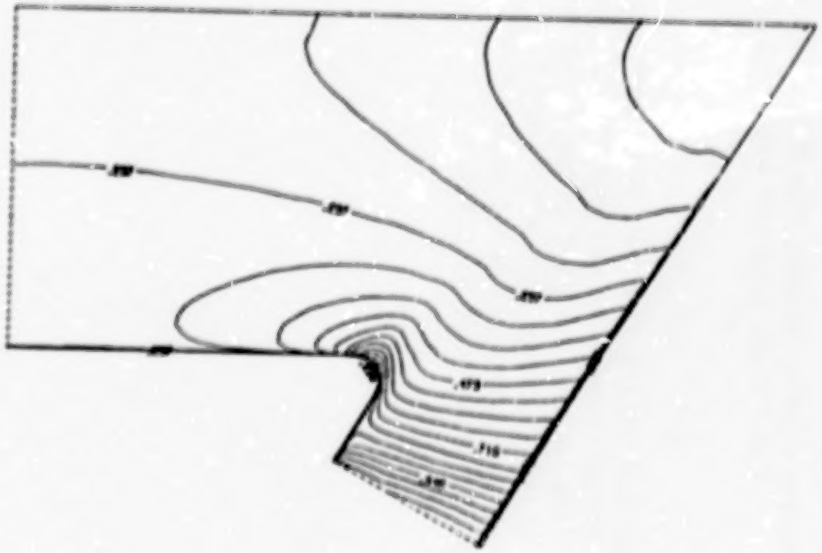

MACH NUMBER CONTOURS

Navier-Stokes Results for Partially Deployed 2-D Thrust Reverser With Vectoring

The MacCormack 2-D nozzle code has also been used to calculate flows in nozzles with both thrust reversing and vectoring. Results from several test problems show the flow in the reverser ports to be relatively insensitive to the degree of vectoring. Comparisons with recent experimental data for more realistic geometries are currently being made by Green and Wilmoth, NASA Langley, and Imlay, University of Washington.

NAVIER-STOKES RESULTS FOR PARTIALLY-DEPLOYED 2-D THRUST REVERSER W/VECTORING

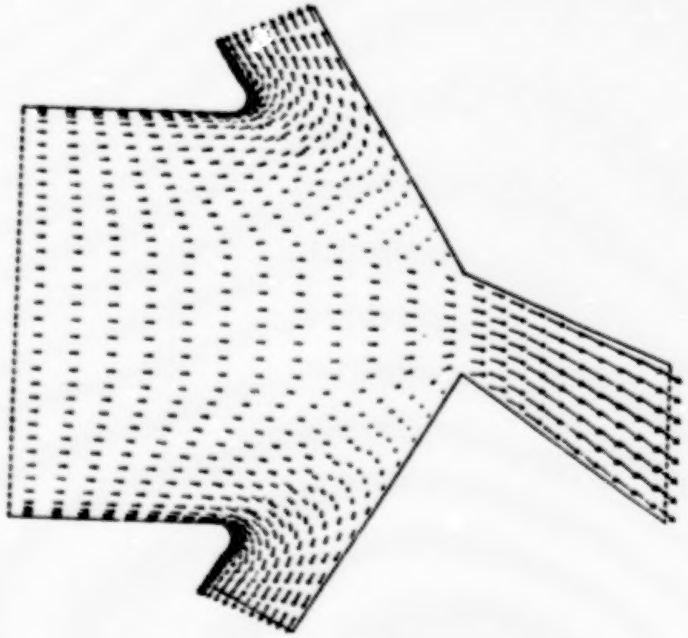

VELOCITY VECTORS

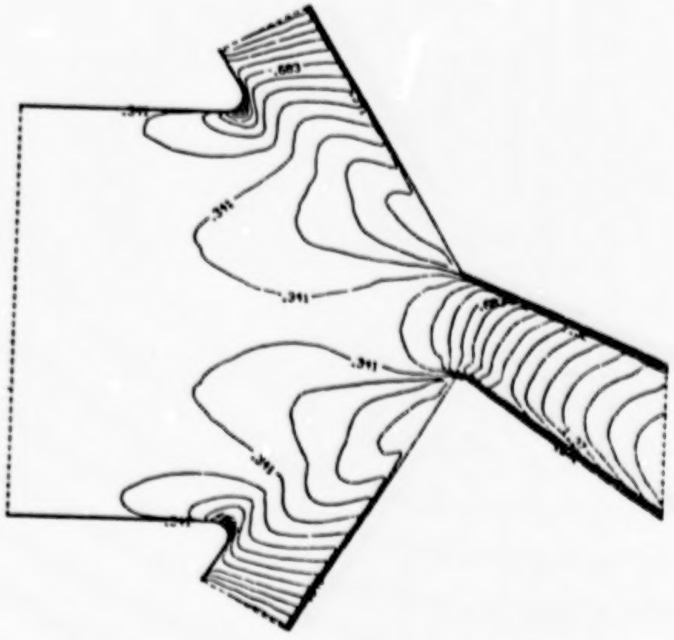

MACH NUMBER CONTOURS

Navier-Stokes Results for 2-D/C-D Nozzle

Comparisons of Navier-Stokes results (denoted by MACTRV) with experimental data of Re and Leavitt[3] for a 2-D/C-D nozzle have been recently obtained by Wilmoth. The agreement between wall pressures predicted by the 2-D code and experimental data along the centerplane wall is good over a wide range of nozzle pressure ratios. For the case shown (NPR = 2), good agreement is obtained over the entire nozzle length including the separated flow caused by nozzle overexpansion. These results give validity to the use of a 2-D approximation for rectangular nozzles with straight sidewalls.

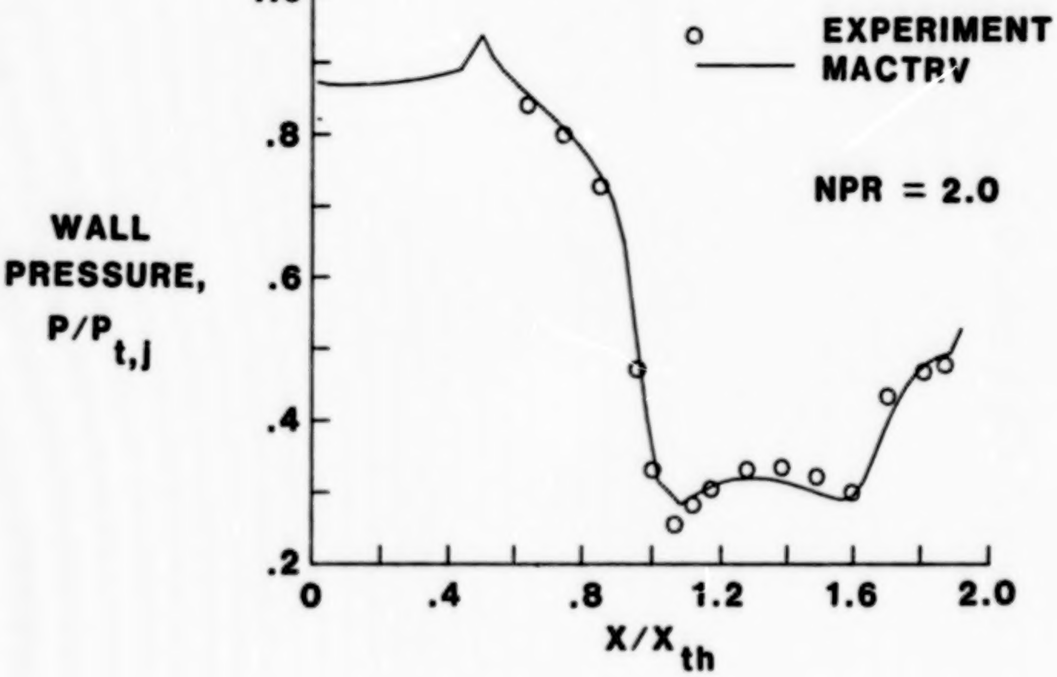

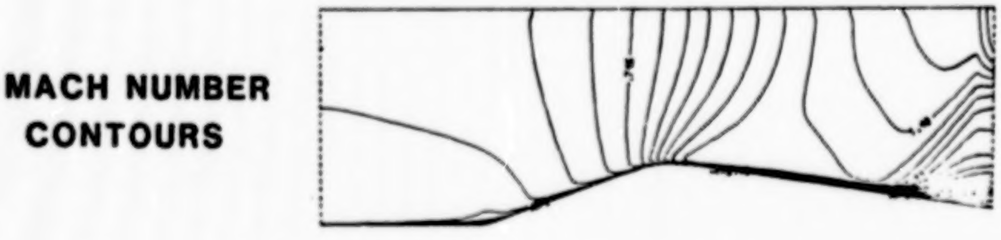

Navier-Stokes Results for 2-D/C-D Nozzle

Navier-Stokes predictions of 2-D/C-D nozzle performance parameters have also been made. For the case shown, both the discharge coefficient and thrust ratio agree with experiment to within 1 percent over a pressure ratio range of 2 to slightly over the design NPR. Use of the measured discharge coefficient to compute ideal thrust gives even better agreement for the thrust ratio. Similar studies for nozzles with thrust reversing and vectoring are planned.

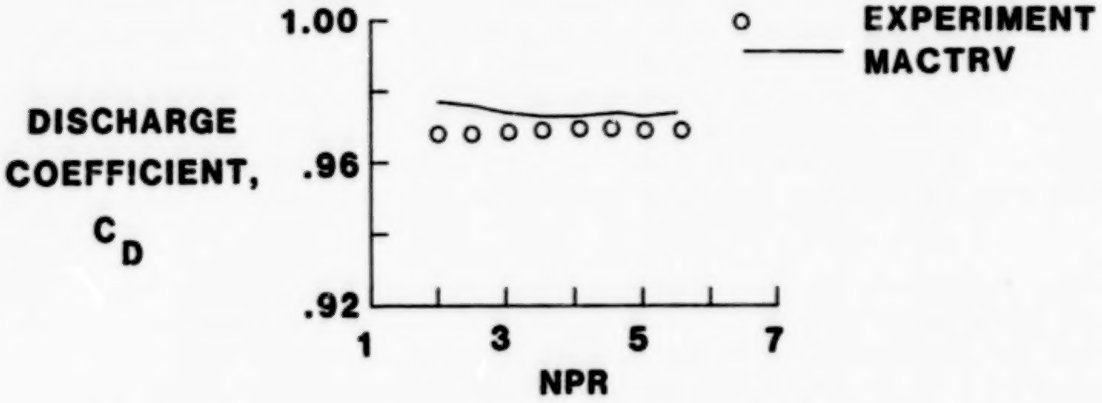

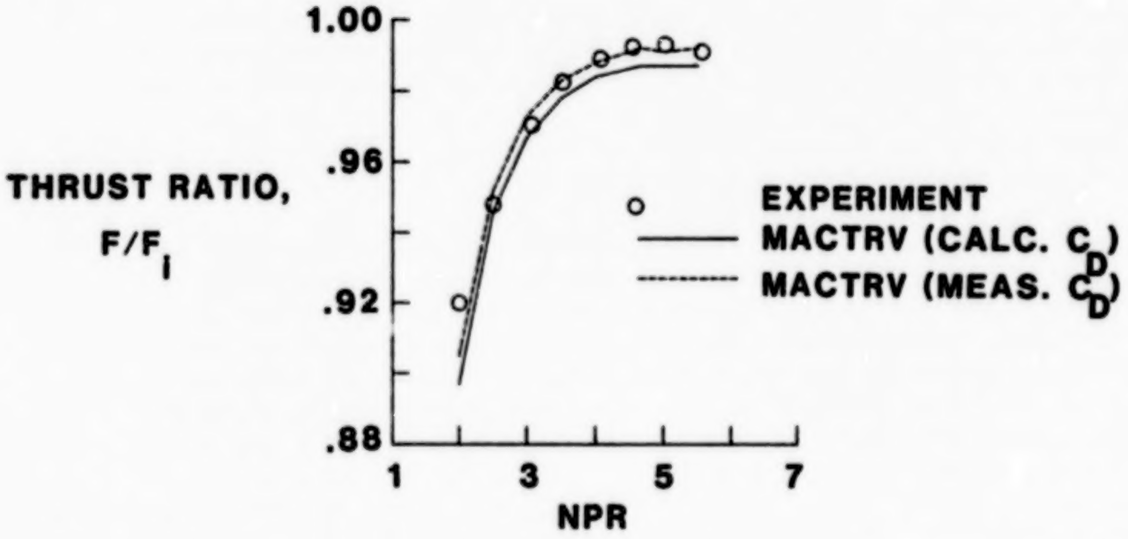

Concluding Observations

The bulleted items on the figure represent a collection of opinions about what is important and what are the areas that need more work. The first bullet derives from observing over several decades the way industry, as well as some individual applied-code researchers, operates. Rarely does one doing applied work want to pay the cost of obtaining the world's most precise answer. Indeed he doesn't need it very often. Codes able to give reliable trends will always have a place in research and design. Long-running, high-cost codes are most often used for "vernier" adjustments within the circle of final design space or for clarification of a particular flow phenomenon.

The uniqueness problem outlined in the paper by Salas and Gumbert may exist for governing equations other than full potential and for 3-D problems as well. Clearly it is necessary to be particularly careful when conservative formulations are used for flow fields with shocks. Difference schemes resulting in artificial viscosity which is significant in magnitude compared with the natural viscosity are another concern. Grid refinements will frequently reduce or illuminate the problem. Obviously, stable solution schemes which have little or no residual artificial viscosity are to be preferred.

Computing equipment, like the family budget, is immediately saturated following an increase in capacity. It is desirable then to increase the efficiency of our solution algorithms, so that more computing can be accomplished with a given system or, perhaps of equal importance, simply to reduce the cost of a given computation.

With the activation of computers which are capable of Navier-Stokes calculations including simulations, the amount of information computed and available (and sometimes required) is becoming mind boggling. More and more use of graphics in our debugging strategies and data analyses is clearly needed. Carpet plots and "isolines" will be in demand. In any case the large data bases created must be accessible in "real time" and at the work site.

The trend of our experimental research is toward more basic phenomena all the time. Hardly anyone is satisfied with simply measuring forces and moments. Surface pressure data, flow field velocity vectors of both the steady and unsteady variety, gas composition, and transition boundaries are just a few illustrations of the quantities which are now being measured to validate our theoretical predictions. If possible we make the measurement using nonintrusive techniques. The money and time required to carry out a comprehensive experiment are often measured in hundreds of thousands of dollars and years, respectively. Highly skilled researchers are required and are in short supply. We are much more in need of good diagnosticians than CFD practitioners, and there is certainly no surplus of the latter.

CONCLUDING OBSERVATIONS

- HIERARCHY OF CODES ALWAYS NEEDED
  - BOUNDARY LAYERS & TURBULENCE MODELS IMPORTANT FOR FORESEEABLE FUTURE
- UNIQUENESS & ARTIFICIAL VISCOSITY ARE STILL CONCERNS
- EFFICIENCY OF SOLUTION ALGORITHM IMPORTANT NO MATTER HOW FAST OUR COMPUTERS GET
- DATA DISPLAY & ANALYSIS BECOMING MORE OF A PROBLEM
- EXPERIMENTAL VALIDATION RESEARCH BECOMING MORE BASIC, DIFFICULT & COSTLY

References

1. South, J. C., Jr.: Recent Advances in Computational Transonic Aerodynamics. AIAA Paper 85-0366, January 1985.

2. Moitra, A.: Numerical Solution of the Euler Equations for High-Speed, Blended Wing-Body Configurations. AIAA Paper No. 85-0123, 1985.

3. Re, Richard J.; and Leavitt, Laurence D.: Static Internal Performance Including Thrust Vectoring and Reversing of Two-Dimensional Convergent-Divergent Nozzles. NASA TP-2253, 1984.

D2

N88-14928

S2-02
117226
19P.

FINITE-VOLUME SCHEME FOR TRANSONIC POTENTIAL FLOW ABOUT AIRFOILS AND BODIES IN AN ARBITRARILY SHAPED CHANNEL

Jerry C. South, Jr.
NASA Langley Research Center
Hampton, Virginia

Michael L. Doria
Valparaiso University
Valparaiso, Indiana

Lawrence L. Green
NASA Langley Research Center
Hampton, Virginia

[redacted]

ABSTRACT

A conservative finite-volume difference scheme is developed for the potential equation to solve transonic flow about airfoils and bodies in an arbitrarily shaped channel. The scheme employs a mesh which is a nearly conformal "O" mesh about the airfoil and nearly orthogonal at the channel walls. The mesh extends to infinity upstream and downstream, where the mapping is singular. Special procedures are required to treat the singularities at infinity, including computation of the metrics near those points. Channels with exit areas different from inlet areas are solved; a body with a sting mount is an example of such a case.

INTRODUCTION

This presentation describes a "Finite-Volume Scheme for Transonic Potential Flow About Airfoils and Bodies in an Arbitrarily Shaped Channel" by Jerry C. South, Jr.; Michael L. Doria; and Lawrence L. Green (ref. 1). The work was done primarily while Dr. Doria was working as an ASEE Research Fellow in the Theoretical Aerodynamics Branch. A 1982 AIAA paper by Doria and South (ref. 2) explains the basic formulation which is summarized here. This work focuses on several improvements which have made the scheme more useful and accurate.

GRID GENERATION

The grid generation procedure uses a sequence of Schwarz-Christoffel and shearing transformations, first proposed by Caughey (ref. 3), to map the physical airfoil-in-channel problem to a uniform rectangular computational domain. The mapping results in a nearly orthogonal "O"-type mesh extending from the airfoil surface to the tunnel wall. The mapping provides for grid point clustering near the airfoil and particularly at the leading and trailing edges. The grid generation procedure now accepts very general body and channel shapes (2-D or axisymmetric) which can be described either analytically or by input coordinates which are spline-fitted.

- Sequence of Schwarz-Christoffel and shearing transformations proposed by Caughey (ref. 3)
- Nearly orthogonal "O" - type mesh
- Clustering of grid points at L. E. and T. E.
- Accepts very general body and channel shapes

ORIGINAL PAGE IS
OF POOR QUALITY

GRID--NACA 4409 IN DIVERGING TUNNEL

This "O"-type grid for an NACA 4409 airfoil in a diverging tunnel demonstrates many of the grid generation procedure capabilities. The airfoil is cambered, at angle of attack, and offset from the tunnel centerline. Coordinates for the airfoil were input and spline-fitted. Also, the tunnel wall is rather arbitrarily shaped. One set of coordinate lines forms rings between the body surface and the tunnel wall. Another set of coordinate lines emanates from the body and terminates at the tunnel wall. One grid line emanates from the body but extends to upstream or downstream infinity, where the mapping is singular and special procedures are required. Grid points are clustered near the leading and trailing edges. The grid produced is twice as fine as that on which the flow problem is solved to allow for accurate metric calculation by central differences.

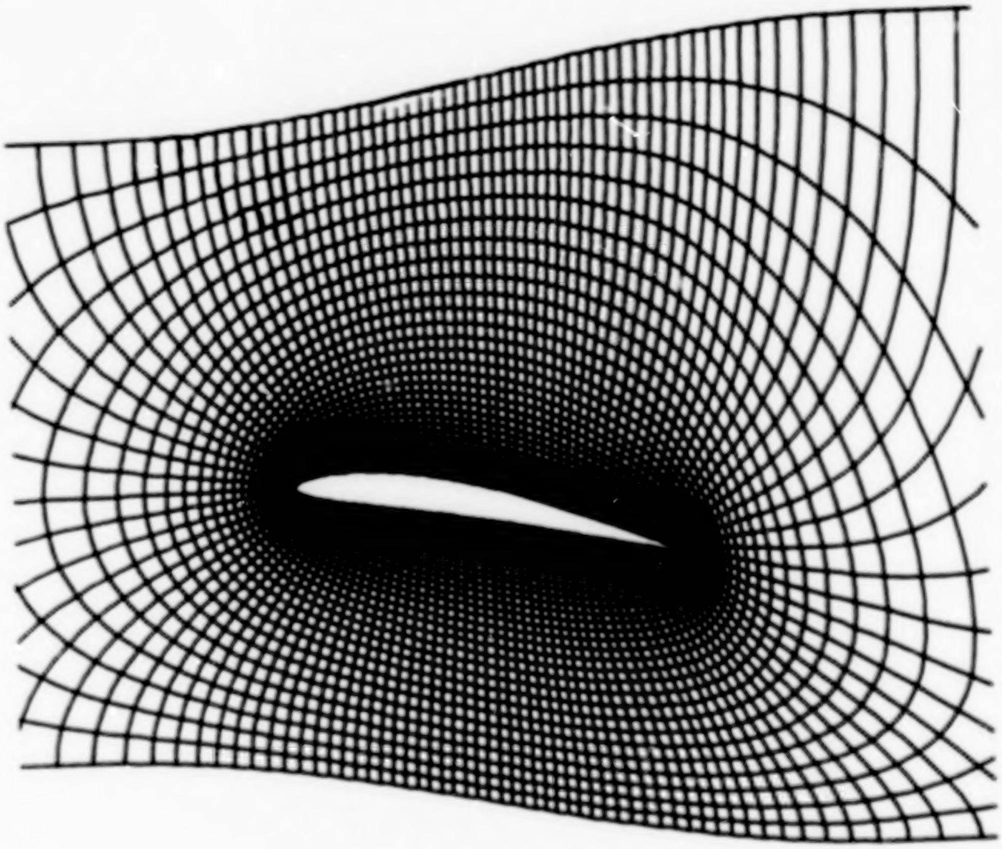

COMPUTATIONAL DOMAIN

This is a sketch of the computational domain for the airfoil-in-tunnel problem. The airfoil surface is mapped onto the X-axis. The tunnel wall is mapped into the line Y = 1, with the lower wall being on the left and upper wall on the right. Coordinate lines which form rings in the physical plane are mapped into lines of constant Y, and those coordinate lines radiating from the body in the physical plane are mapped into lines of constant X. The line in the physical plane extending to upstream infinity is mapped into the Y-axis and the line extending to downstream infinity is split between X = 1 and X = -1. A typical streamline starting at upstream infinity, passing over the airfoil and terminating at downstream infinity is shown. Cells A, B, C, and D each have as one corner a point in the physical plane at infinity where the mapping is singular and special procedures, described subsequently, are required.

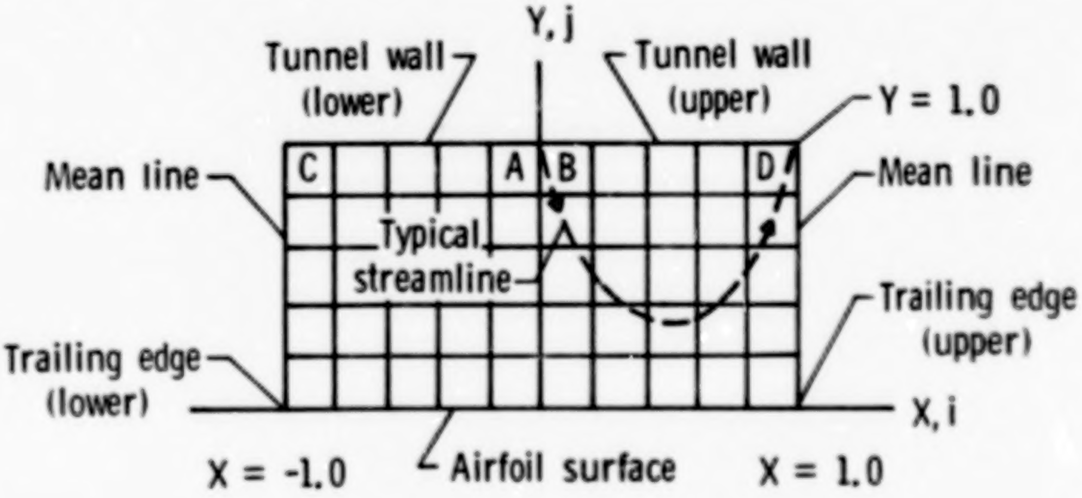
Y, j
Tunnel wall (lower)
Tunnel wall (upper)
Y = 1.0
Mean line
Mean line
C
A
B
D
Typical streamline
Trailing edge (upper)
Trailing edge (lower)
X, i
X = -1.0
Airfoil surface
X = 1.0

Cells A, B, C and D have singular points at corners

GOVERNING EQUATIONS IN CARTESIAN COORDINATES

The continuity equation is written in Cartesian coordinates for either planar 2-D flow if $\sigma = 0$ or axisymmetric flow if $\sigma = 1$. Assuming isentropic flow, the density is given as a function of the Mach number, M_∞; the total velocity, q; and the ratio of specific heats, γ. Assuming irrotationality, the streamwise and normal components of velocity are related to a disturbance potential, ϕ, by the expressions shown.

$$(y^\sigma \rho u)_x + (y^\sigma \rho v)_y = 0$$

$$\rho = \left[1 + .5(\gamma - 1) M_\infty^2 (1 - q^2)\right]^{1/(\gamma - 1)}$$

$$u = 1 + \Phi_x$$

$$v = \Phi_y$$

$$\sigma = \begin{cases} 0 \text{ for planar 2D} \\ 1 \text{ for axisymmetric} \end{cases}$$

COORDINATE TRANSFORMATION

For a generalized transformation between physical coordinates (x,y) and computational coordinates (X,Y), the metrics g_{11}, g_{12}, and g_{22} and the Jacobian are shown. In a perfectly orthogonal mapping, g_{12} would be zero. For the mapping considered here, g_{12} is several orders of magnitude smaller than g_{11} and g_{22}. The partial derivative x_Y in g_{22} will require special treatment near the singular points at infinity.

$$x = x(X,Y) \qquad y = y(X,Y)$$

$$g_{11} = (x_X)^2 + (y_X)^2$$

$$g_{12} = x_X x_Y + y_X y_Y$$

$$g_{22} = (x_Y)^2 + (y_Y)^2$$

$$J = x_X y_Y - x_Y y_X$$

GOVERNING EQUATIONS IN CURVILINEAR COORDINATES

The transformed governing equation and expressions for the contravariant velocity components in terms of the disturbance potential are shown. The component U is in the direction around the airfoil in the physical plane and V is in the direction normal to the airfoil surface and tunnel wall. Notice that U depends on g_{22} which requires special treatment near the singular points at infinity. Also, since the mapping is not orthogonal, g_{12} is not zero and U and V both depend on ϕ_X and ϕ_Y.

$$(y^{\sigma} \rho J U)_X + (y^{\sigma} \rho J V)_Y = 0$$

$$JU = y_Y + (g_{22} \Phi_X - g_{12} \Phi_Y)/J$$

$$JV = -y_X + (-g_{12} \Phi_X + g_{11} \Phi_Y)/J$$

FINITE DIFFERENCE EQUATIONS

The mass balance for a typical four-sided cell is shown, using compass-point notation (N, S, E, and W) to designate the cell faces. The retarded-density formulation is used to provide numerical stability in supersonic regions and to allow for shock capturing. In this formulation, the isentropic density, ρ, is replaced by a retarded density, $\bar{\rho}$, which is shifted upwind in the streamwise direction, ξ, if the local Mach number is greater than unity. The contravariant components of velocity are expressed in terms of the metrics and the disturbance potential; the resulting simultaneous equations for ϕ are solved iteratively by AF2, ZEBRA I, or VLOR.

Retarded density method

$$(y^\sigma \bar{\rho} JU)_E - (y^\sigma \bar{\rho} JU)_W + \alpha (y^\sigma \bar{\rho} JV)_N - \alpha (y^\sigma \bar{\rho} JV)_S = 0$$

$$\bar{\rho} = \rho - \mu \rho_\xi \Delta \xi$$

$\mu = f(M) = 0$ at subsonic points

$0 < \mu < 1$ at supersonic points

$$\alpha = \Delta X / \Delta Y$$

Express JU and JV in terms of Φ, g_{11}, g_{12} and g_{22}

solve for Φ using AF2, ZEBRA I or VLOR

ADDED MASS SOURCES/SINKS

Cells A, B, C, and D contain singularities at one corner and are actually five-sided cells in the physical domain since they extend to upstream or downstream infinity. The mass flowing across the fifth face of these cells has not been accounted for in writing the finite-difference equations, and it is necessary to include for these cells a source or sink term as shown in the mass balance equation. The form of these source or sink terms can be rigorously derived from the form of the singularity of the mapping at these points and must be included to calculate flows in channels where the inlet area is different from the exit area, such as diverging or converging tunnels.

$$S_A = -(\rho_{IN} u_{IN}) \left[(y_{ML})_{IN} - (y_{LW})_{IN} \right]$$

$$S_B = -(\rho_{IN} u_{IN}) \left[(y_{UW})_{IN} - (y_{ML})_{IN} \right]$$

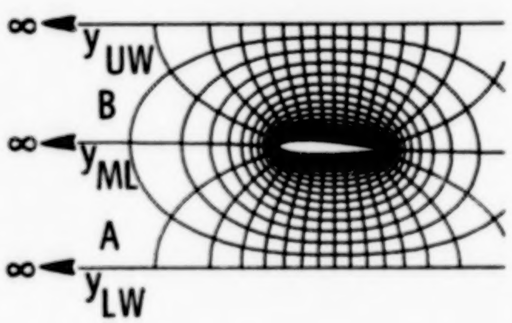

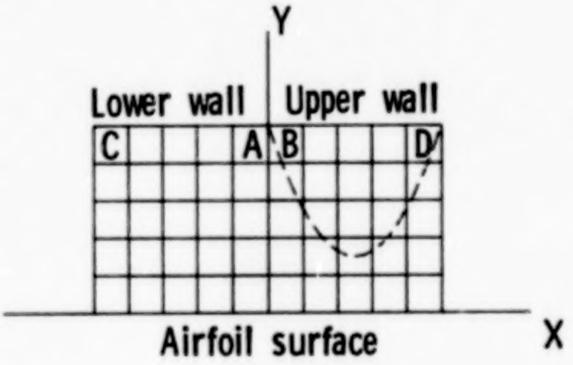

LOGARITHMIC DIFFERENCING OF METRICS

The mass flux across the face adjoining cells A and B (or equivalently, cells C and D) is not, in general, zero and should be calculated as part of the solution. This requires calculating the U contravariant velocity component through this face which implies evaluating g_{22} in the cell face. However, as the computational coordinate $Y \to 1$ along $X = 0$, the physical coordinate x behaves logarithmically in Y. Since the physical x becomes negatively infinite when $Y = 1$, that is, at the upstream singular point, central differencing to obtain x_Y along this face is impossible. Instead, the derivative is evaluated using the form shown, derived from the logarithmic behavior of x in Y along the coordinate line leading to the singularity. Without this modification, the solution could not be converged fully since the maximum residual would "hang up" at fairly large values in cells A, B, C, and D.

As $Y \longrightarrow 1$ along $X = 0$, $x = A \ln(1 - Y)$

$x(1) = -\infty$, central differencing impossible

instead use $(\delta x/\delta Y)_W = 2(x_W - x_{SW})/(\Delta Y \ \ln 2)$

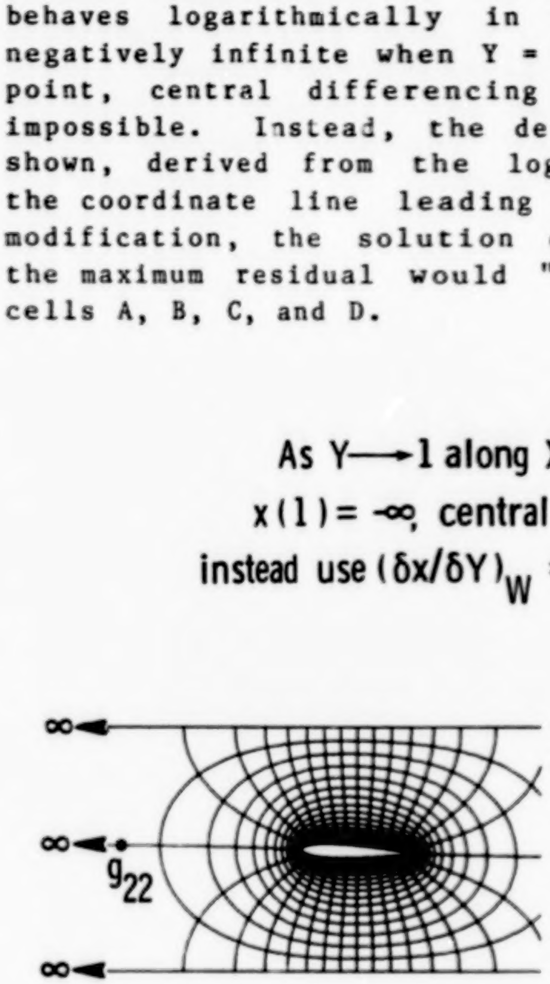

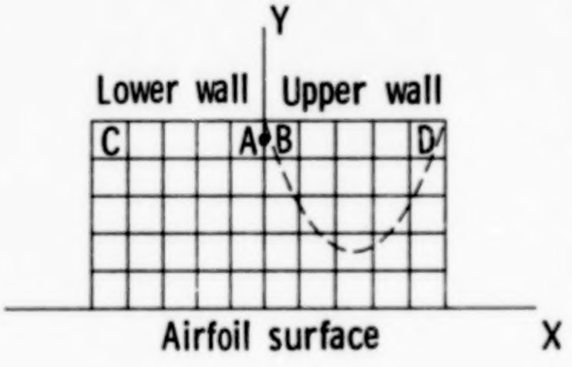

FREE-AIR BOUNDARY CONDITION

For cell faces along solid boundaries at the airfoil and tunnel walls, the mass flux is set to zero to enforce the boundary condition. This is equivalent to a Neumann or derivative boundary condition on ϕ. The far-field behavior in free air, however, is different from that found in a tunnel. Thus, an alternative, Dirichlet condition for ϕ in the outer ring has been included as an option; it properly simulates the far-field behavior in free air if applied sufficiently far away from the airfoil. The expression is derived from the disturbance potential for a compressible vortex. Use of this free-air boundary condition instead of the solid-wall boundary condition has the added benefit that the angle of attack can be changed without remapping the problem, as is necessary for in-tunnel cases.

$$\Phi_{I,JMAX-1} = \frac{\Gamma}{2\pi}\left[\pi - \tan^{-1}(\beta\tan\theta)\right]$$

$$\beta = \left[1 - (M_{\infty})^2\right]^{1/2}, \quad \theta = [0, 2\pi]$$

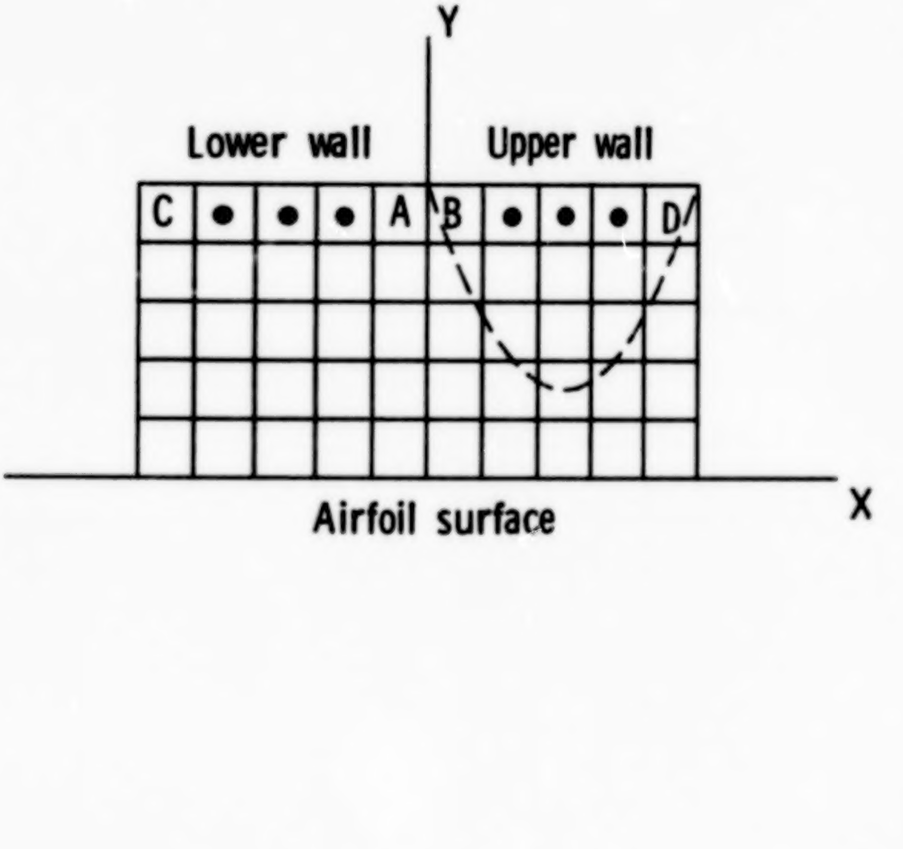

EXIT CONDITION FOR SUPERSONIC FLOW

The final improvement involves specifying the value for the disturbance potential in cells C and D, which is consistent with supersonic flow at the exit. In supersonic flow, all signals propagate downstream only. No influence can be felt upstream from a point farther downstream. To simulate this behavior at a supersonic exit, it is assumed that $\phi_{XX} = 0$. The potential in cells C and D is expressed in terms of those upwind on the same ring. This is substituted into the tridiagonal system and solved using the horizontal scheme ZEBRA I. Thus, the exit mass flux is allowed to adjust to conditions upstream of the exit. Anomalous Mach numbers appeared near the exit if this boundary condition was not used, although convergence was achieved.

$$\left(\Phi_{XX}\right)_{ij} = \left(\Phi_{i-1,j} - 2\Phi_{ij} + \Phi_{i+1,j}\right) / \Delta X^2$$

- Solve for Φ in cell D from $\Phi_{XX} = 0$
- Substitute into horizontal tridiagonal system

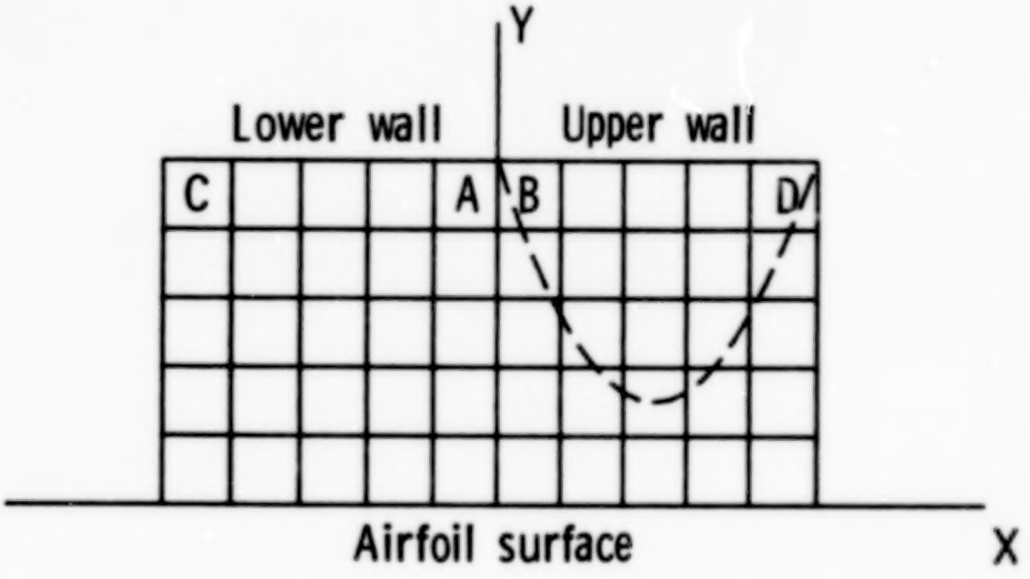

NACA 4409 IN DIVERGING TUNNEL

Computed constant Mach number contours around an NACA 4409 airfoil in a diverging tunnel for an upstream Mach number of 0.5 are shown. The airfoil is at 8 degrees angle of attack, has camber, and is offset from the tunnel centerline. There is a supersonic region around the upper surface leading edge and a strong shock at about 10 percent of the airfoil chord. Downstream of the divergence the flow has a Mach number lower than the inlet Mach number, as would be expected from continuity.

$M_\infty = 0.5, \ \alpha = 8°$

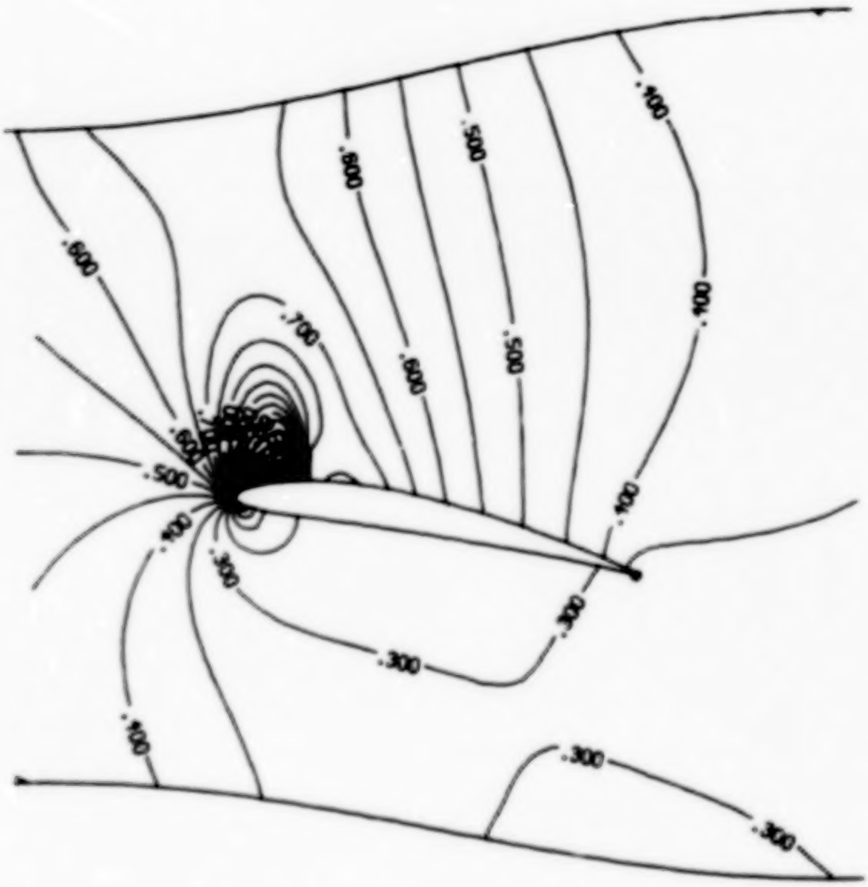

ELLIPSOID ON STING

Computed constant Mach number contours are shown for an axisymmetric case of an ellipsoid with a sting in a straight wall tunnel with supersonic flow at the inlet and exit. For the upstream Mach number of 1.15, a bow shock can be seen ahead of the ellipsoid with an embedded subsonic region between the bow shock and the body. Another subsonic region appears near the ellipsoid/sting junction. If either one of these subsonic regions, surrounded by supersonic flow, was large enough to intersect the wall, the problem would be ill-posed with the current boundary conditions and would eventually diverge. Typical of axisymmetric cases, only the upper half of the physical domain is computed.

$M_\infty = 1.15,\ H = 1$

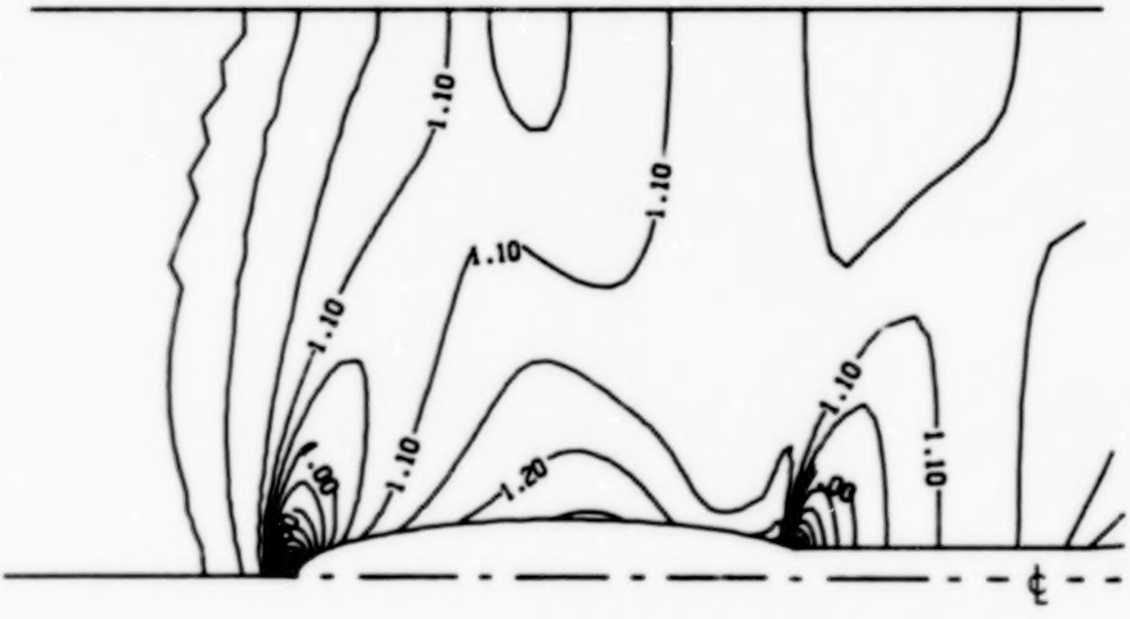

NLR 7301 IN FREE AIR

The computed constant Mach number contours and surface pressure coefficient for the NLR 7301 airfoil are shown. The upstream Mach number is 0.721 and the angle of attack is -0.194 degrees. The airfoil was designed in the hodograph plane to be shock free at these conditions; it is a quite sensitive flow to compute. The present solution shows a weak shock and a slightly underdeveloped supersonic region relative to the design. The calculated lift coefficient is 0.610 compared to the design of 0.595. It is interesting to note that the design point for this airfoil lies in the range of nonuniqueness for the conservative full-potential equation, as shown by Salas and Gumbert (ref. 4).

$M_\infty = 0.721, \alpha = -0.194°$

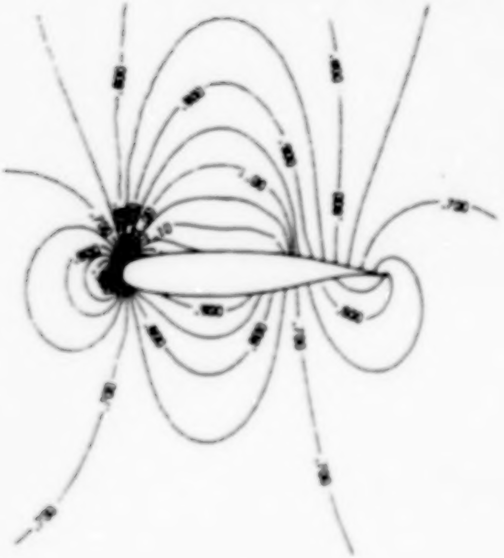

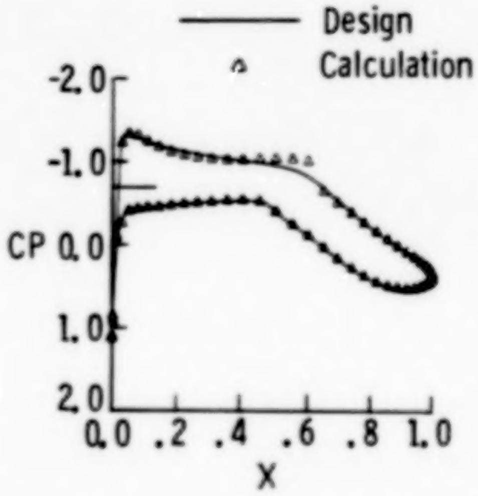

SUMMARY

A conservative finite-volume scheme for transonic potential flow around bodies in an arbitrarily shaped channel, including converging or diverging walls and stings, has been presented. The concept of logarithmic differencing to obtain metrics near singularities has been applied to correct a previous convergence problem. A free-air Dirichlet-type boundary condition has been added as an option. An extrapolation-type boundary condition for supersonic flow at the exit has been included. More details of these and other aspects of this procedure can be found in a 1982 AIAA paper (ref. 2) and in a 1985 paper from the 3rd Symposium on Numerical and Physical Aspects of Aerodynamic Flows (ref. 1).

- Conservative, finite-volume scheme for transonic potential flow
- Arbitrary body and channel shapes (converging/diverging tunnel, flared-sting)
- Logarithmic differencing (convergence)
- Free-air boundary condition
- Exit condition for supersonic flow

REFERENCES

1. South, Jerry C., Jr.; Doria, Michael L.; and Green, Lawrence L.: Finite-Volume Scheme for Transonic Potential Flow About Airfoils and Bodies in an Arbitrarily-Shaped Channel. Conf. Proc. 3rd Symposium on Numerical and Physical Aspects of Aerodynamic Flows, Long Beach, CA, Jan. 1985.

2. Doria, Michael L.; and South, Jerry C., Jr.: Transonic Potential Flow and Coordinate Generation for Bodies in a Wind Tunnel. AIAA Paper 82-0223, Jan. 1982.

3. Caughey, D. A.: A Systematic Procedure for Generating Useful Conformal Mappings - Application to Transonic Aerodynamics. Int. J. Num. Meth. in Engr., vol. 12, no. 11, 1978, pp. 1641-1657.

4. Salas, Manuel D.; and Gumbert, Clyde R.: Breakdown of the Conservative Potential Equation. AIAA Paper 85-0367, Jan. 1985.

N88-14929

D3

S3-02
117227
27P.

BREAKDOWN OF THE CONSERVATIVE POTENTIAL EQUATION

M. D. Salas and C. R. Gumbert
Langley Research Center
Hampton, Virginia

PRECEDING PAGE BLANK NOT FILMED

PAGE 44 INTENTIONALLY BLANK

[redacted]

MULTIPLE SOLUTIONS OF THE TRANSONIC POTENTIAL FLOW EQUATION

In 1981, John Steinhoff and Antony Jameson discovered that numerical codes based on the conservative full-potential equation could converge to more than one solution.[1] The case shown corresponds to a symmetrical Joukowski airfoil section at zero angle of attack and 0.832 free-stream Mach number. Two fully converged solutions were obtained by Steinhoff and Jameson, one symmetrical with zero lift and the other asymmetrical with a large positive lift.

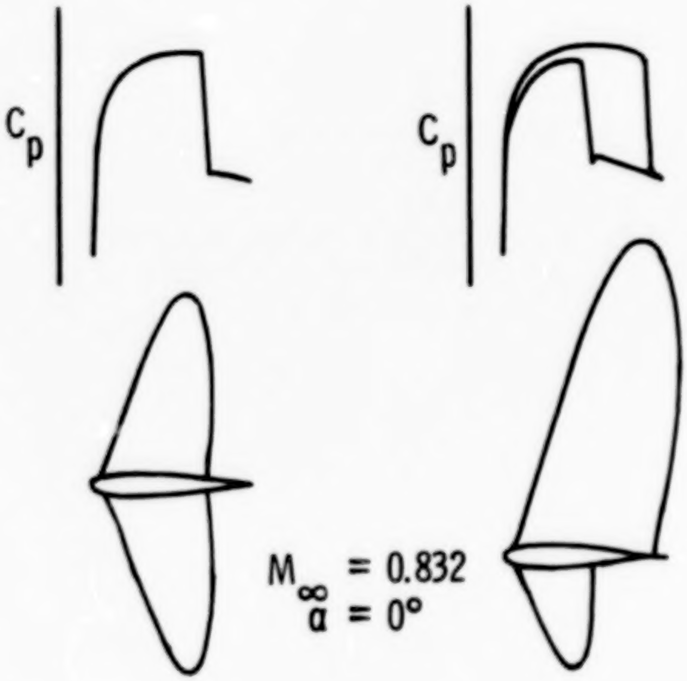

MULTIPLE SOLUTIONS OF THE TRANSONIC POTENTIAL FLOW EQUATION

The major findings reported by Steinhoff and Jameson[1] were the discovery of multiple solutions, usually occurring in narrow bands of M_∞ and α, and a hysteresis loop in the lift behavior. After many tests, they concluded that the problem existed at the differential level (i.e., not a numerical problem); that perhaps it was connected to a physical phenomenon such as buffet; and that, therefore, it could also be observed if the Euler or Navier-Stokes equations were used instead of the conservative potential equation.

Major Findings

- Multiple solutions
- Hysteresis loop
- Narrow bands of M_∞, α

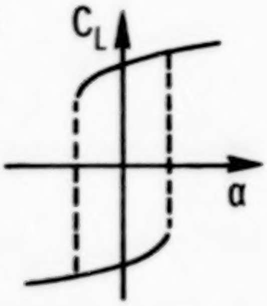

Conclusions

- Problem at differential level
- Possible physical significance
- Possible problem of Euler or Navier Stokes equations

A COMPARATIVE STUDY OF THE NONUNIQUENESS PROBLEM OF THE POTENTIAL EQUATION

To answer some of the issues raised by Steinhoff and Jameson, a study comparing the potential and Euler solutions was conducted in 1983.[2] The results of this work confirmed that the problem existed at the differential level. The hysteresis loop was found to be a result of the "folding back" nature of the lift curve exhibited by the conservative potential equation but not the Euler equations. In addition, it was found that the problem obeyed the transonic similarity law. It was conjectured that the nonuniqueness was associated with the isentropic shock jump conditions.

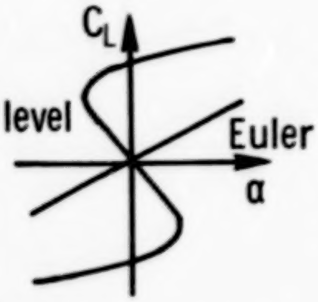

Major Findings

- Confirmed problem at differential level
- No hysteresis loop
- No problem with Euler equations
- Problem obeyed transonic similarity law

Conclusion

- Problem associated with shock jump conditions

PRESENT INVESTIGATION ADDRESSES THE FOLLOWING QUESTIONS

After these investigations, a number of issues remained to be answered. Since only a few airfoil shapes had been considered, it was not clear if the problem would appear for all airfoil shapes. Was it limited to narrow M_∞,α bands as originally proposed by Steinhoff and Jameson? Or did it occur throughout the M_∞,α plane? What was the cause of the problem?

- Is the problem universal?
- Where does it occur in M_∞, α plane?
- What is its cause?

AIRFOIL SECTIONS INVESTIGATED WITH A MULTIGRID CONSERVATIVE POTENTIAL CODE

To answer these questions an investigation was conducted for the five airfoil shapes shown in this figure. Two of these airfoils, the KORN 75-06-12 and the NLR-7301, are shockless supercritical airfoils at design conditions. For each airfoil, approximately 10 different free-stream Mach numbers were tested at approximately 20 different angles of attack using a conservative potential code. Overall, approximately 1,000 calculations were performed.

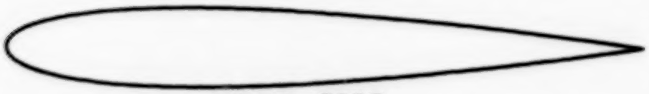

NACA 0012

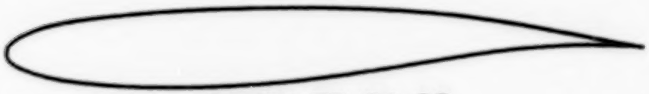

KORN 75-06-12

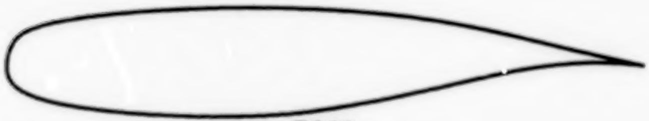

NLR -7301

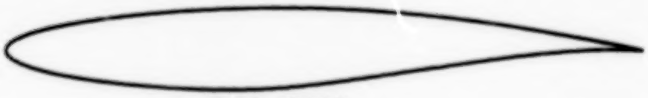

RAE 2822

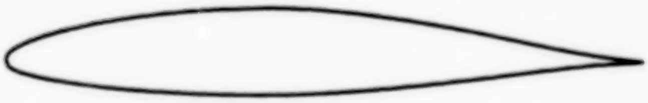

NACA 65-213

NACA 0012

Spline-fitted lift curves for an NACA 0012 airfoil section at various M_∞ obtained from a conservative potential code are shown on this figure.

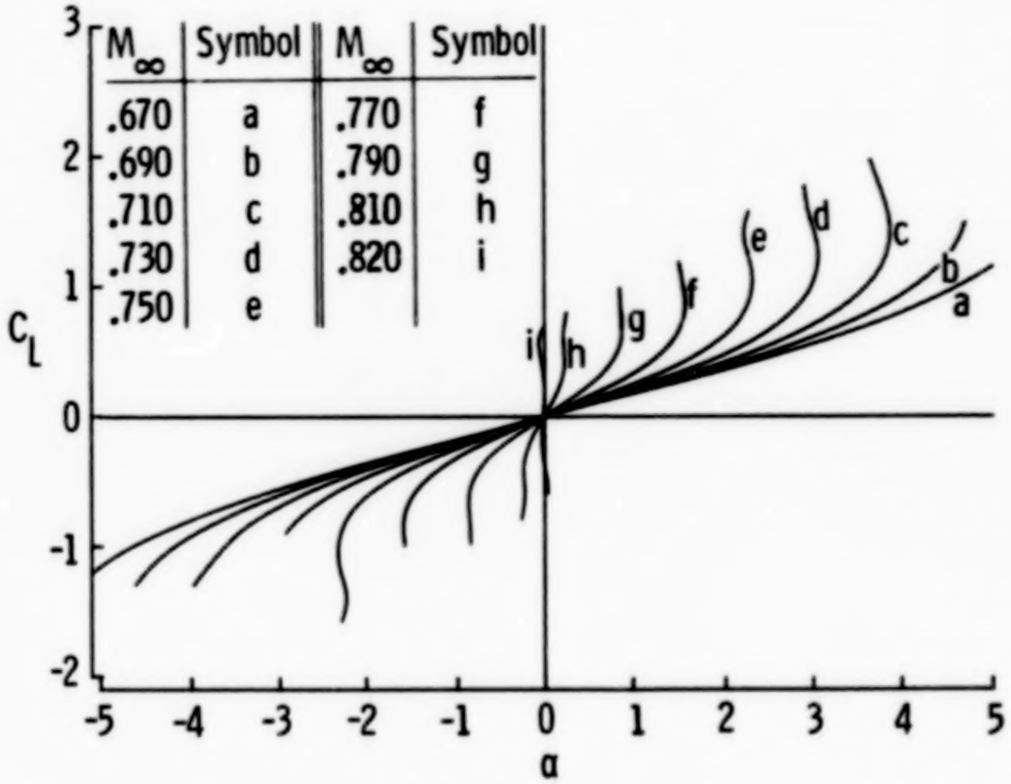

KORN 75-06-12

Spline-fitted lift curves for a KORN 75-06-12 airfoil section at various M_∞ obtained from a conservative potential code are shown on this figure.

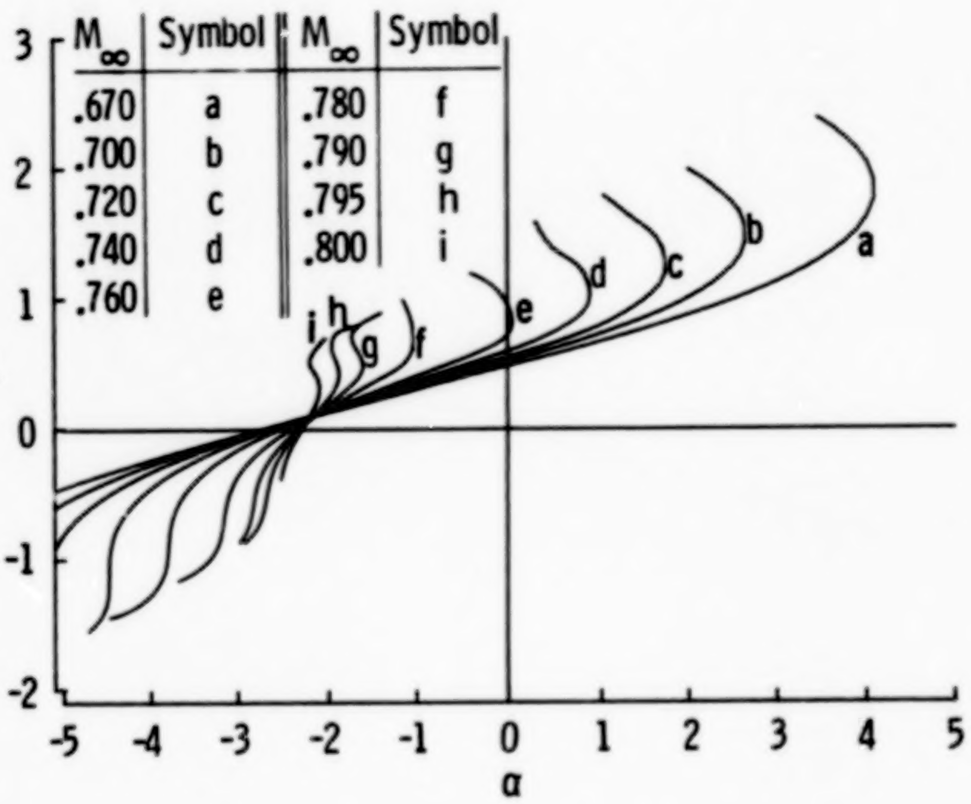

NLR-7301

Spline-fitted lift curves for an NLR-7301 airfoil section at various M_∞ obtained from a conservative potential code are shown on this figure.

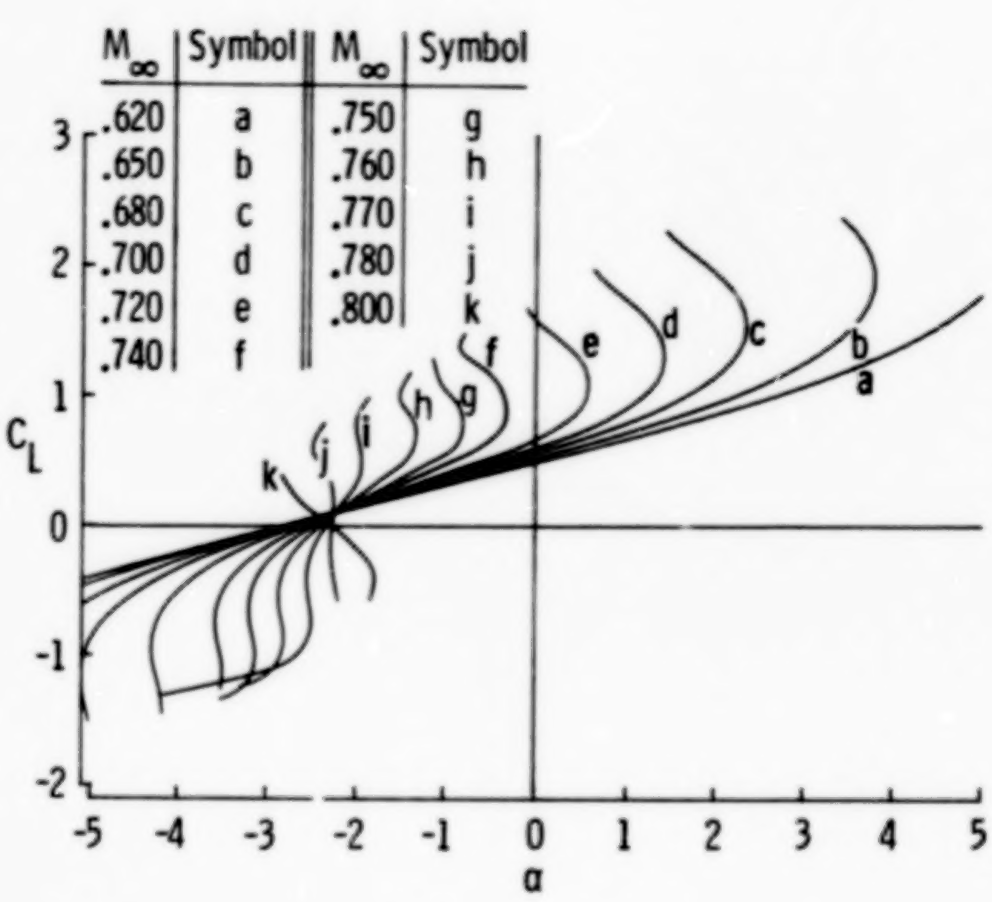

RAE 2822

Spline-fitted lift curves for an RAE 2822 airfoil section at various M_∞ obtained from a conservative potential code are shown on this figure.

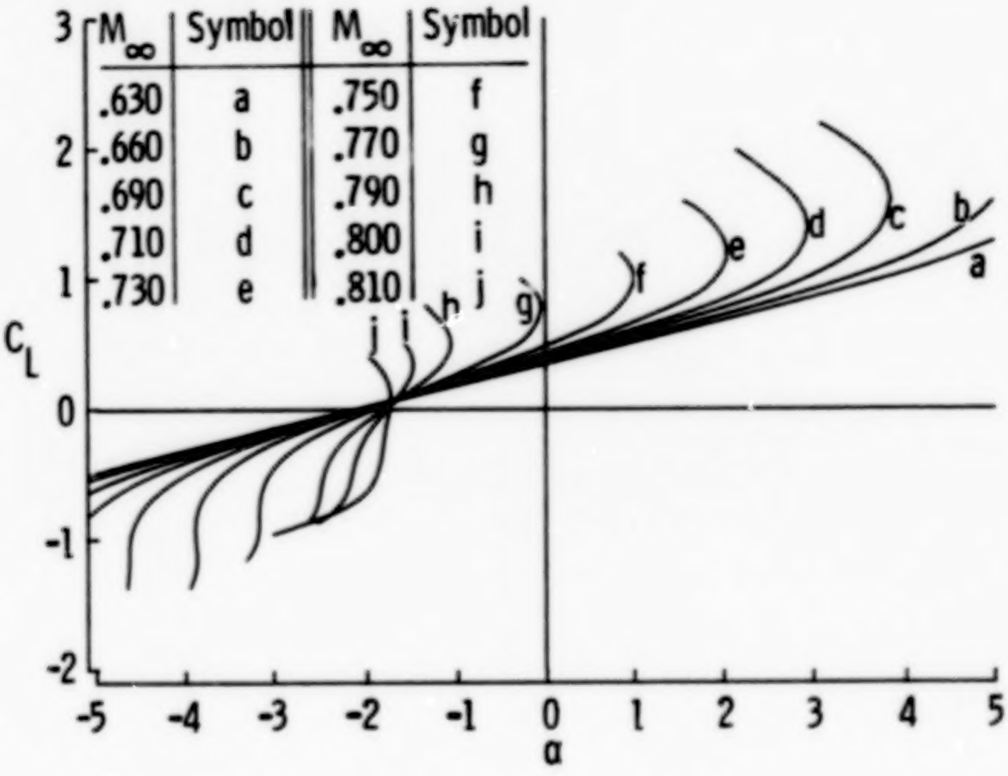

NACA 65-213

Spline-fitted lift curves for an NACA 65-213 airfoil section at various M_∞ obtained from a conservative potential code are shown on this figure.

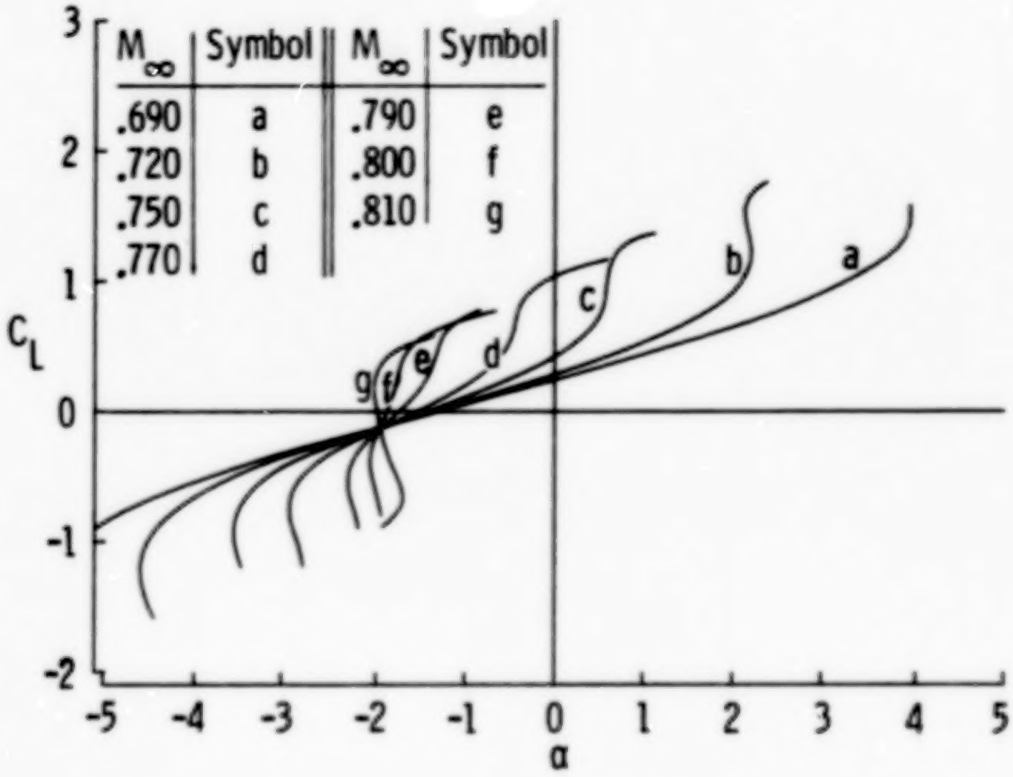

NACA 0012

Spline-fitted drag curves for an NACA 0012 airfoil section at various M_∞ obtained from a conservative potential code are shown on this figure.

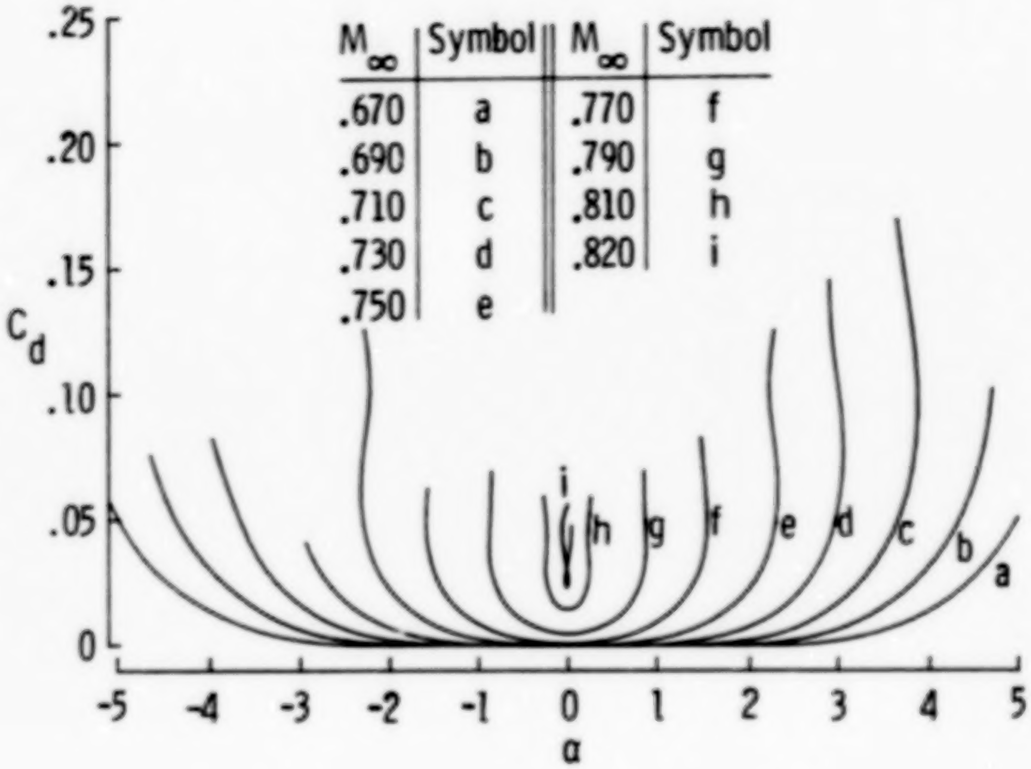

KORN 75-06-12

Spline-fitted drag curves for a KORN 75-06-12 airfoil section at various M_∞ obtained from a conservative potential code are shown on this figure.

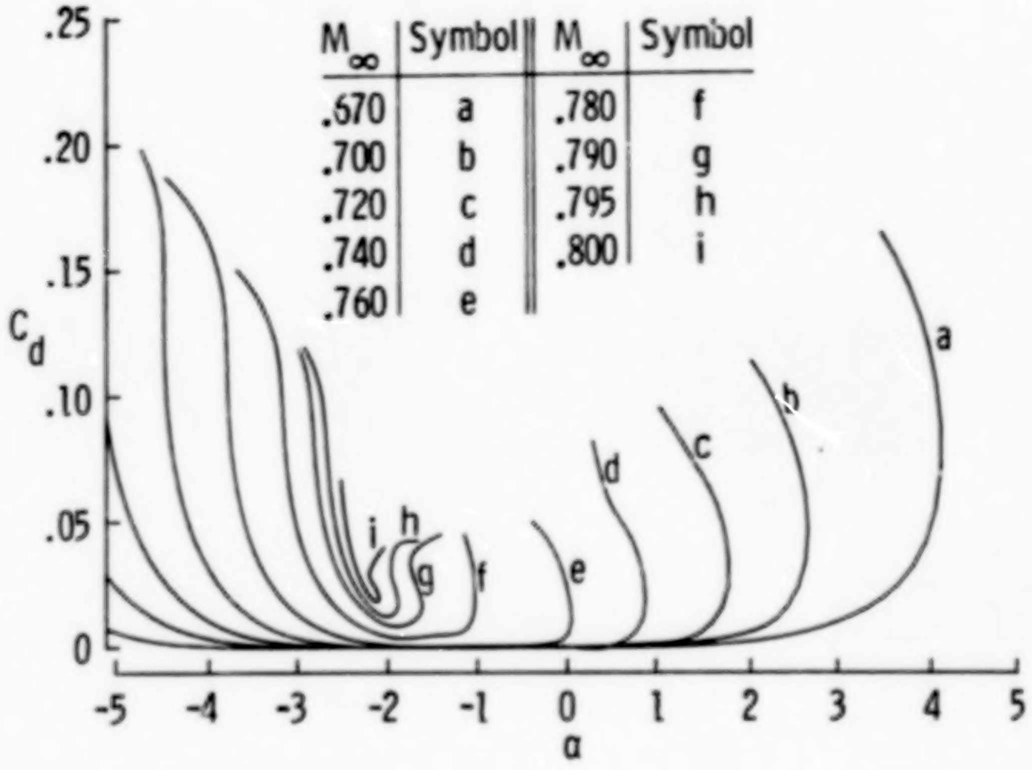

NLR-7301

Spline-fitted drag curves for an NLR-7301 airfoil section at various M_∞ obtained from a conservative potential code are shown on this figure.

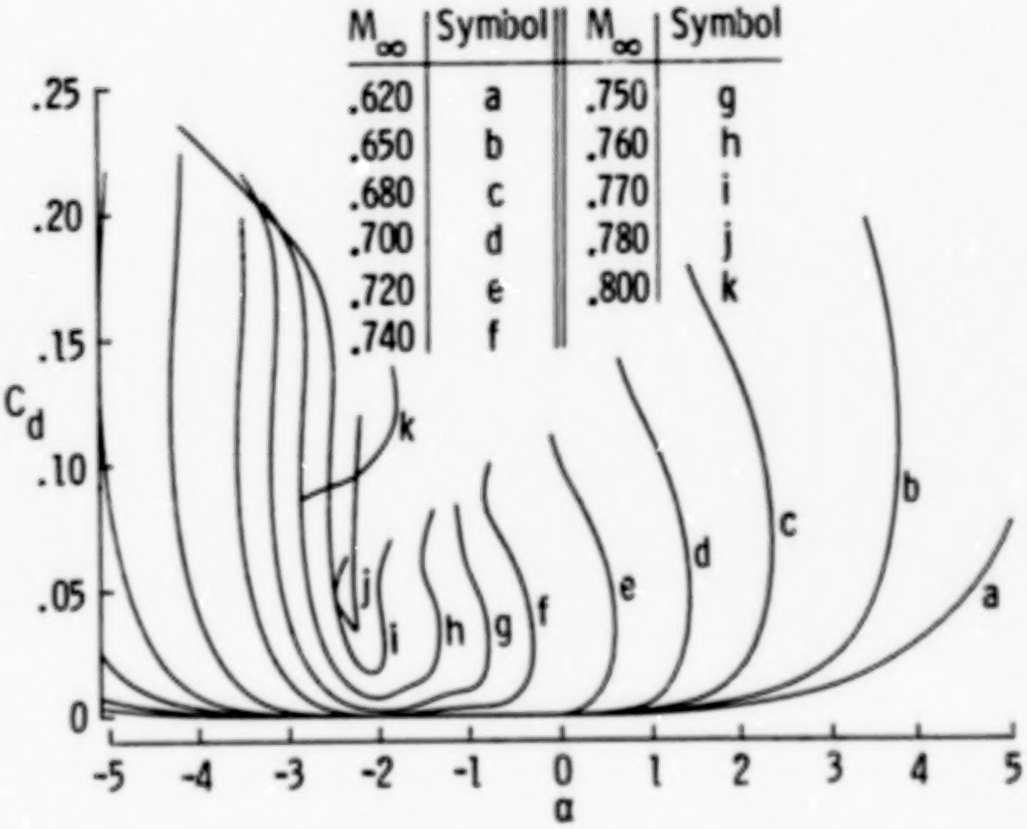

RAE 2822

Spline-fitted drag curves for an RAE 2822 airfoil section at various M_∞ obtained from a conservative potential code are shown on this figure.

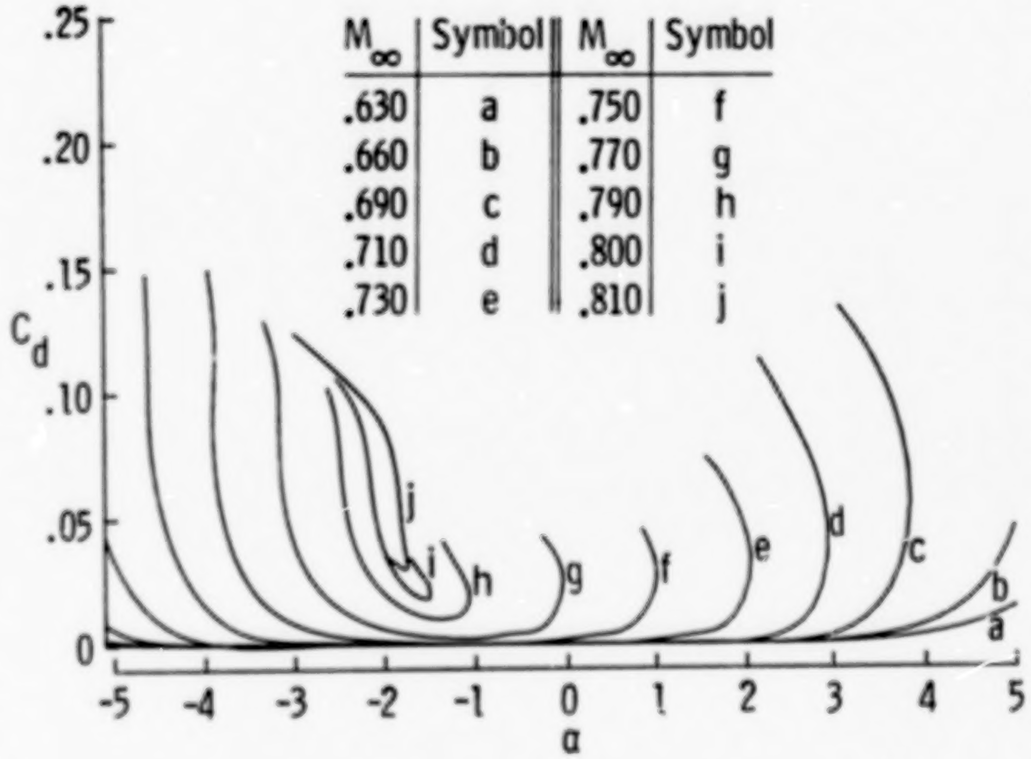

NACA 65-213

Spline-fitted drag curves for an NACA 65-213 airfoil section at various M_∞ obtained from a conservative potential code are shown on this figure.

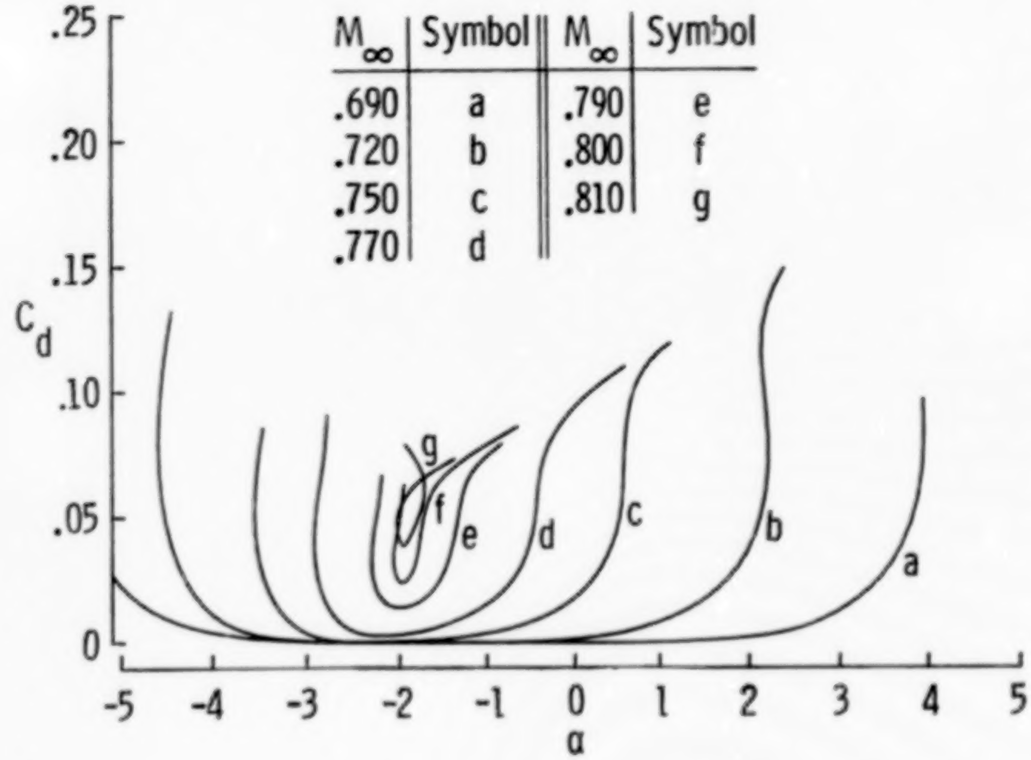

DETAILED LOOK AT NACA 0012

A comparison between the conservative potential results and Euler results shows a remarkable qualitative difference in the lift behavior. Results are shown for an NACA 0012 section, but the same trend is observed for the other airfoils tested.

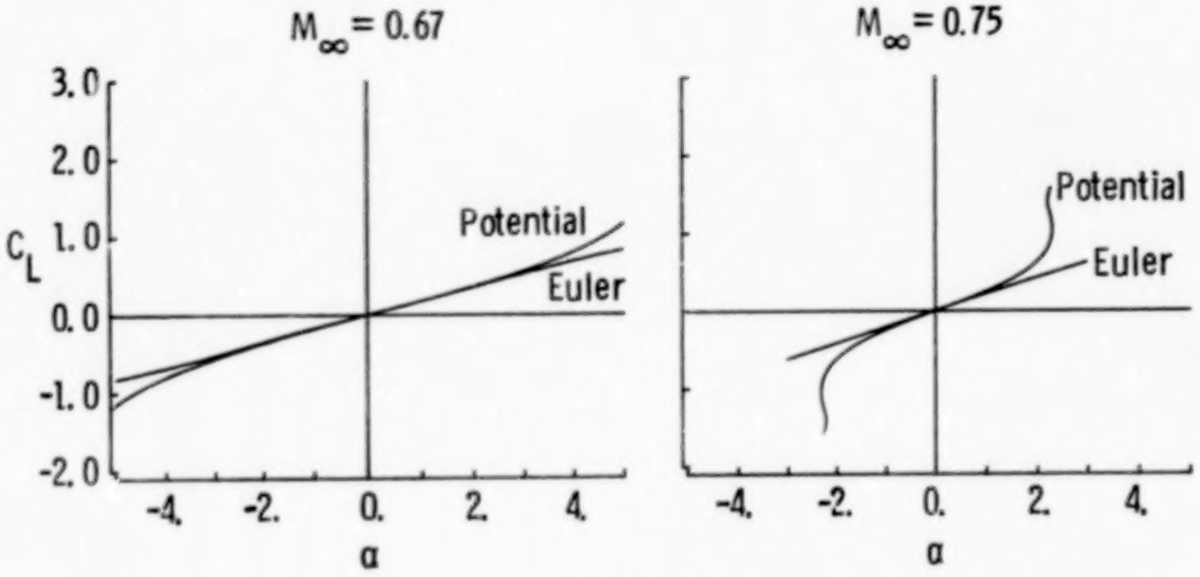

LIFT-CURVE SLOPE

An inspection of the angle made by the lift curve with the horizontal, plotted versus the lift coefficient, shows that outside of the Prandtl-Glauert region (linear) the potential and Euler behaviors follow opposite trends. If the point at which the two depart is examined, we find that it corresponds to the appearance of shock waves in the calculation (i.e., strong nonlinear behavior).

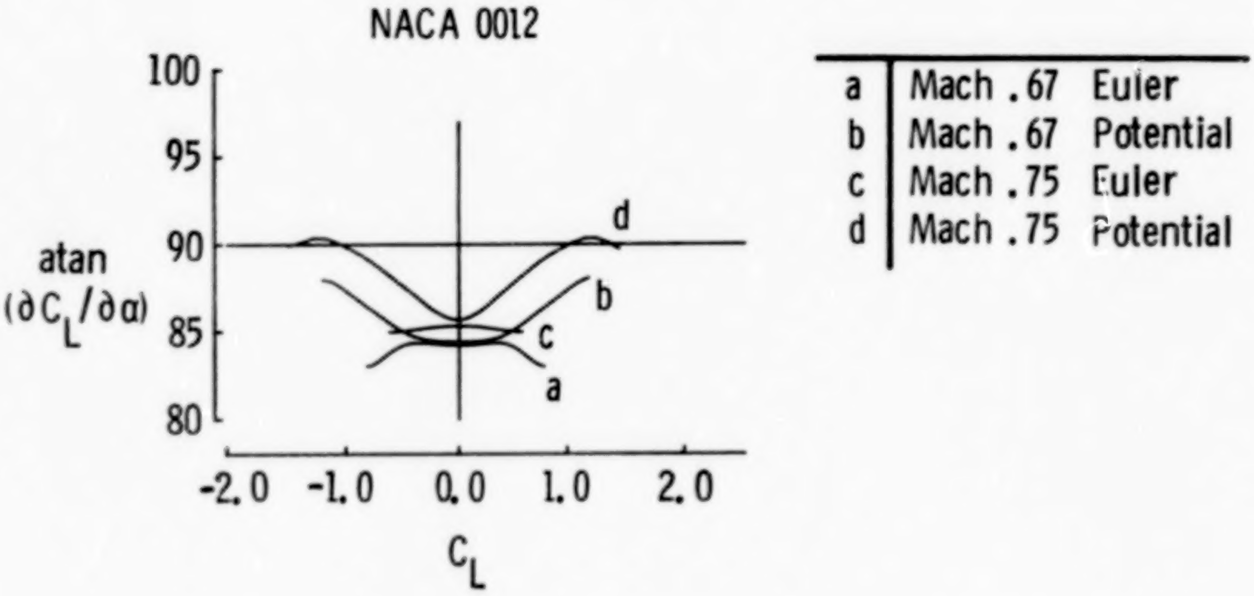

SKETCH OF LIFT-CURVE SLOPE MAIN FEATURES

The typical conservative potential behavior is shown in this figure. The potential and Euler solutions agree in the linear behavior region. Once a shock wave occurs, the lift predicted by the potential approximation increases like e^{α}. It is this behavior of the potential approximation which eventually leads to a "folding back" of the lift curve as its slope increases past 90°.

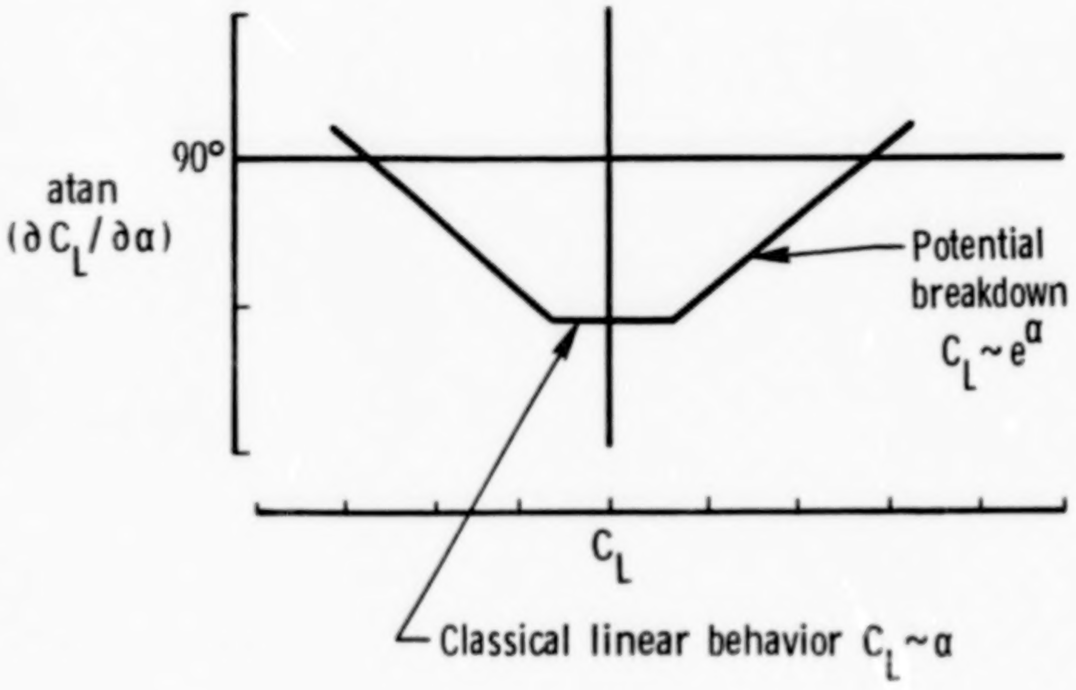
90°
atan $(\partial C_L/\partial\alpha)$
Potential breakdown $C_L \sim e^{\alpha}$
C_L
Classical linear behavior $C_L \sim \alpha$

NACA 0012

The angle made by the lift curve plotted as a function of C_L for the NACA 0012 airfoil as predicted by the conservative potential code is shown on this figure.

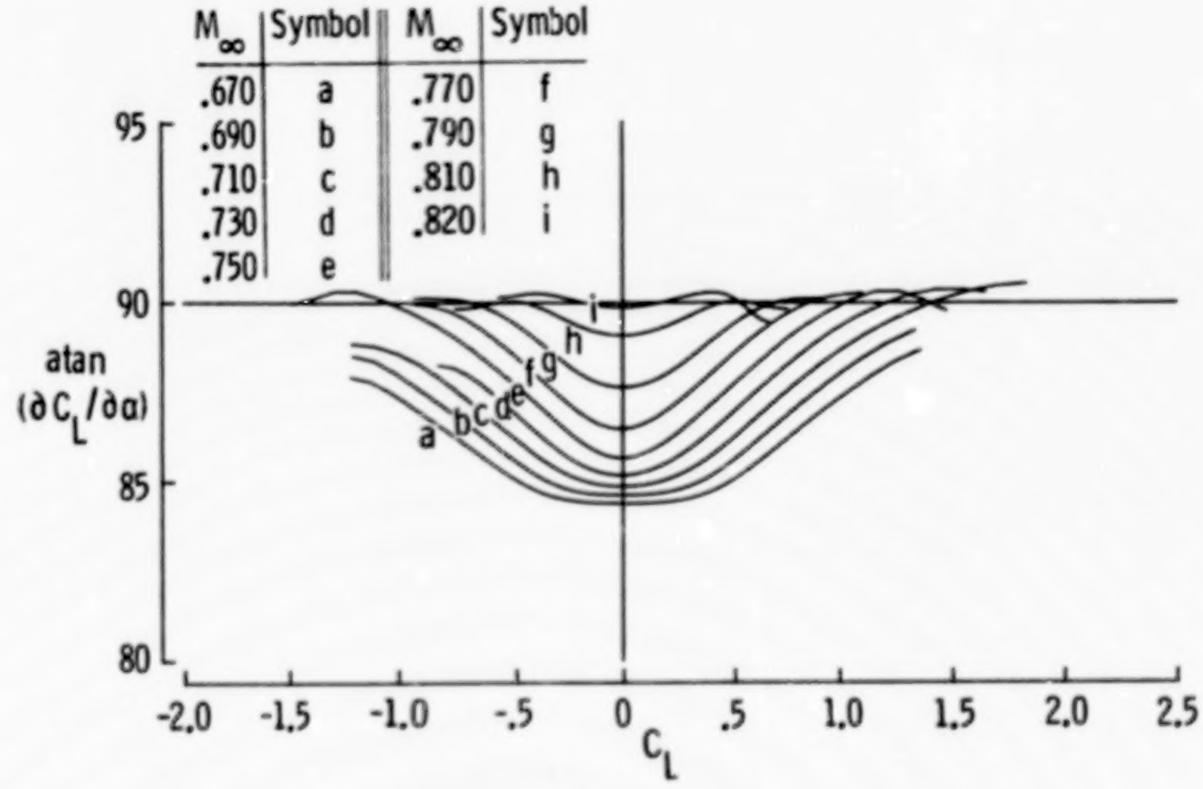

KORN 75-06-12

The angle made by the lift curve plotted as a function of C_L for the KORN 75-06-12 airfoil as predicted by the conservative potential code is shown on this figure.

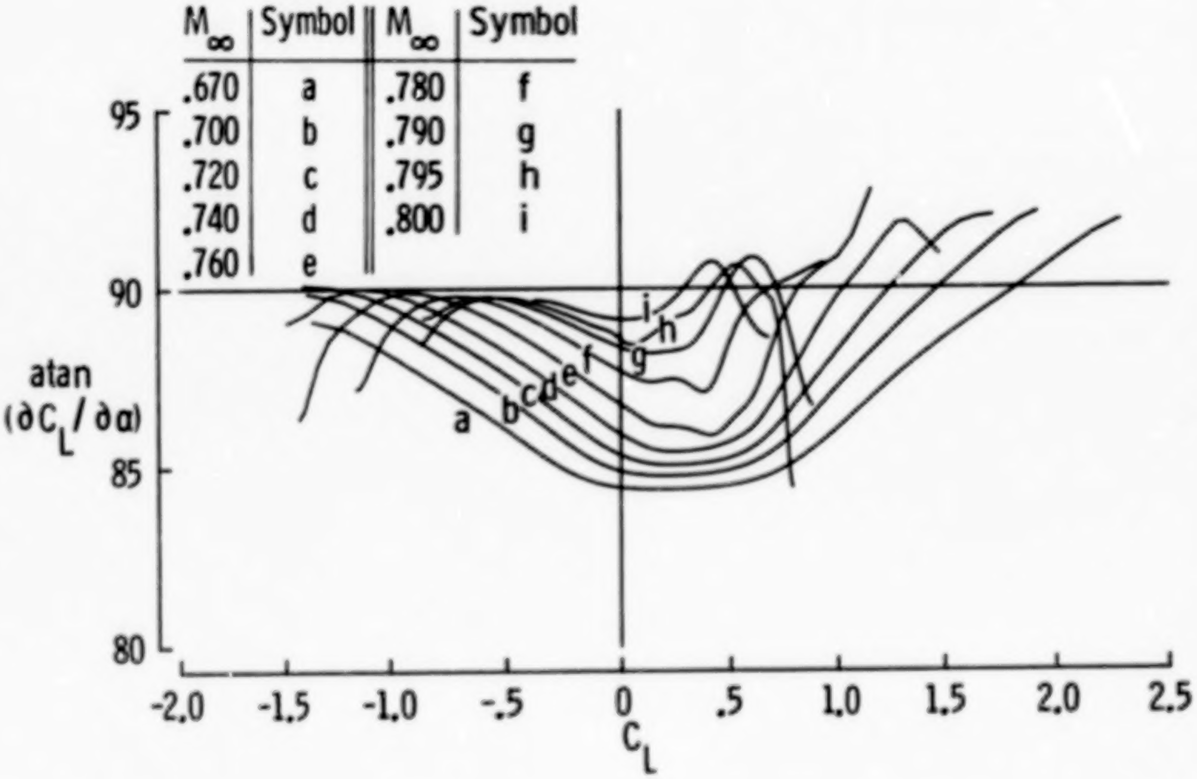

NLR-7301

The angle made by the lift curve plotted as a function of C_L for the NLR-7301 airfoil as predicted by the conservative potential code is shown on this figure.

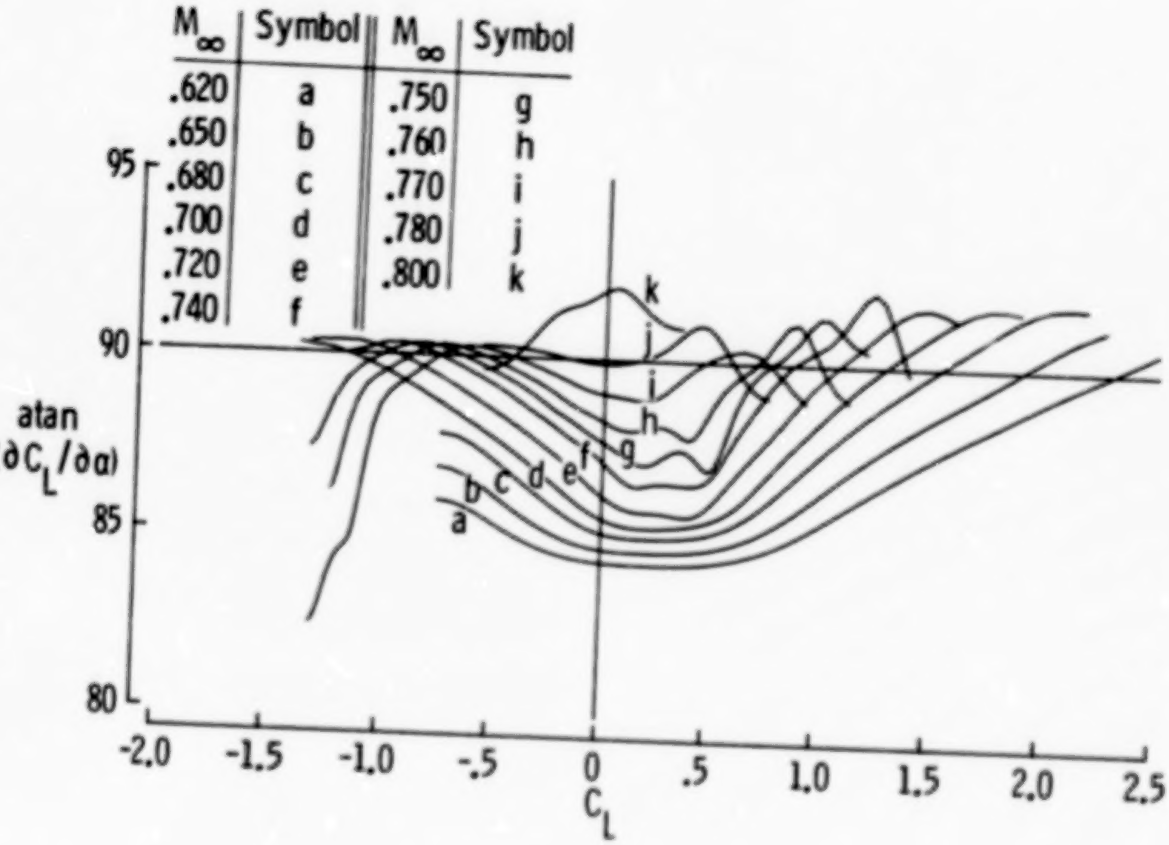

RAE 2822

The angle made by the lift curve plotted as a function of C_L for the RAE 2822 airfoil as predicted by the conservative potential code is shown on this figure.

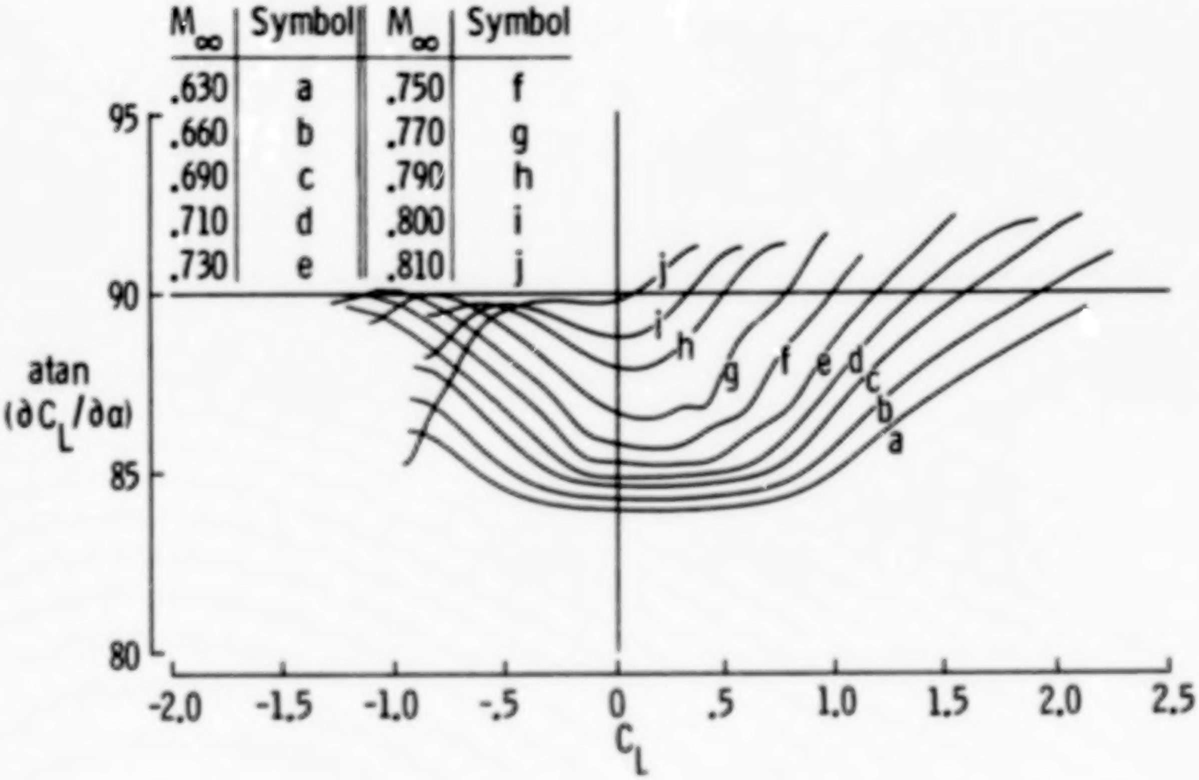

NACA 65-213

The angle made by the lift curve plotted as a function of C_L for the NACA 65-213 airfoil as predicted by the conservative potential code is shown on this figure.

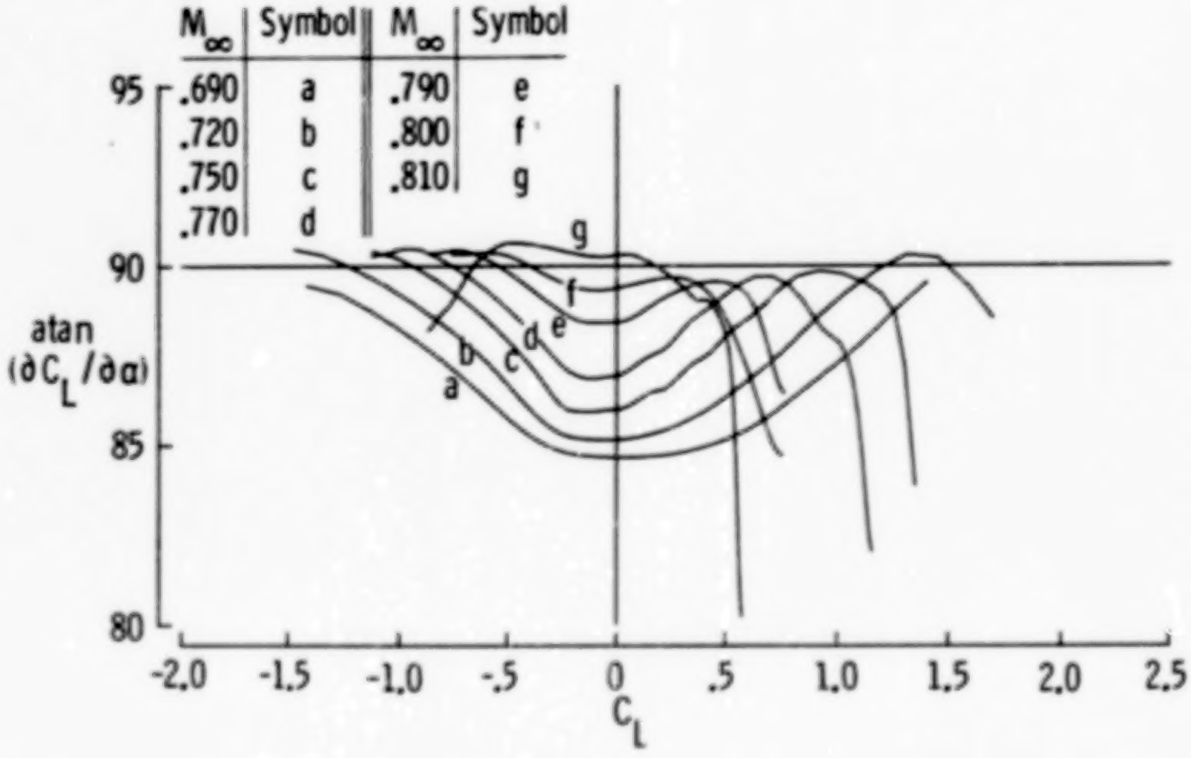

BREAKDOWN REGION IN M_∞,α PLANE

This figure shows where the potential approximation breaks down for each of the five airfoils tested. The shockless design points for the KORN 75-06-12 and NLR-7301 airfoils are also shown in the figure. Note that these design points are isolated shockless flows surrounded by flows with shocks.

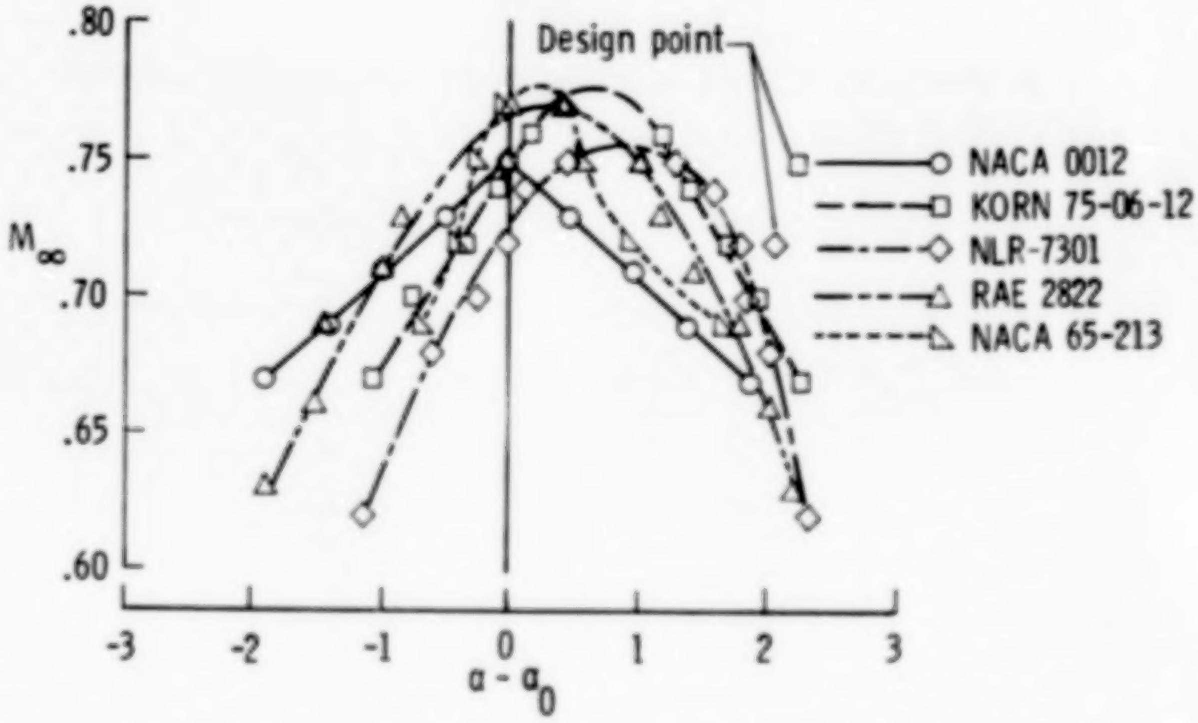

CONCLUSIONS

The breakdown of the conservative potential approximation occurs for all airfoils tested. It develops as soon as shock waves appear in the flow field. Since shock waves are not properly represented by the potential approximation, it is conjectured that the breakdown is due to the isentropic shock jump condition of the potential approximation.

- The problem appears universal for conservative potential formulation.
- It occurs as soon as shock waves are developed.
- It is conjectured that the problem is due to the isentropic shock jump condition.

REFERENCES

1. Steinhoff, J.; and Jameson, A.: Multiple Solutions of the Transonic Potential Flow Equation. AIAA Paper 81-1019, June 1981.

2. Salas, M. D.; Jameson, A.; and Melnik, R. E.: A Comparative Study of the Nonuniqueness Problem of the Potential Equation. AIAA Paper 83-1888, July 1983.

D4

N88-14930

S4-05
117228

APPLICATION OF A FULL POTENTIAL METHOD FOR ANALYSIS OF COMPLEX AIRCRAFT GEOMETRIES

Kenneth M. Jones and Noel A. Talcott, Jr.
NASA Langley Research Center
Hampton, Virginia

PRECEDING PAGE BLANK NOT FILMED

PAGE 72 INTENTIONALLY BLANK

[redacted]

PRESENT ANALYSIS TECHNIQUES

Currently, there are a wide variety of aerodynamic prediction techniques used for the analysis of supersonic flow over aircraft configurations. These methods range from techniques based on supersonic linear theory to nonlinear analysis methods based on the solution of the Euler or Navier-Stokes equations. Linearized methods are commonly used to analyze complex configurations but are frequently unable to provide accurate results in complex flow regions, particularly at high angle of attack and/or high supersonic Mach numbers, due to the restrictions of linearized theory. The more sophisticated Euler and Navier-Stokes solvers can provide accurate results even in complex flow regions but are not yet at a stage where they can be used as practical prediction techniques for complex aircraft designs. The development of efficient full potential solvers now permits accurate nonlinear aerodynamic analysis of supersonic flow over complex aircraft geometries.

- Linearized Analysis Methods
- Potential Flow Solvers
  - Inviscid
  - Irrotational
  - Isentropic
  - "Weak" Shocks
- Euler/Navier-Stokes Solvers
  - Inviscid/Viscous
  - Rotational
  - Non-Isentropic
  - Rankine-Hugoniot Shock

ORIGINAL PAGE IS
OF POOR QUALITY

SUPERSONIC FULL POTENTIAL ANALYSIS METHOD

The underlying philosophy in developing the method strives for ease of implementation while producing useful output for those working on current aerodynamic problems. Steps have been taken throughout the code development process to ensure geometric generality and ease of input necessary to execute the code. This led to the separation of the equation solution procedure and the gridding process. A body-fitted grid system is generated from the geometric definition of the configuration using a numerical grid generation subroutine. To ensure geometric generality, many other features have been incorporated into the code for analysis of complex aircraft shapes. Embedded subsonic regions, which often exist on aircraft at low supersonic Mach numbers, can now be analyzed using a relaxation technique built into the code. Wakes behind lifting surfaces and their effect on downstream lifting surfaces are accounted for in the solution. To assess a vehicle's performance at many flow conditions, the method allows analysis at angles of yaw and/or angle of attack.

Yaw and Angle of Attack

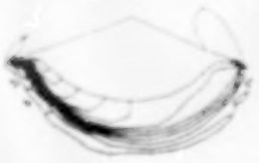

Wake Treatment

Advanced Fighter Concept

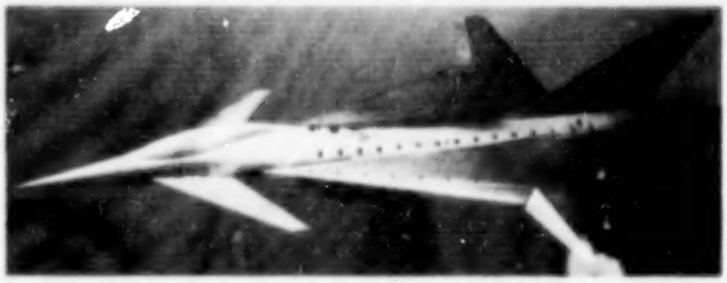

Numerical Grid Generation

Embedded Subsonic Regions

ORIGINAL PAGE IS
OF POOR QUALITY

ANALYZING A SUPERSONIC FIGHTER CONFIGURATION

Problem Areas

Many aircraft concepts are often difficult to analyze due to the geometric complexity of the configuration. Shown is a wire frame model of a Langley-developed fighter concept that has been analyzed with the full potential code. Before this configuration was analyzed, certain problem areas were identified and prompted the development of many of the enhancements discussed in the previous figure. At low supersonic Mach numbers the fuselage-canopy juncture region is an area where a subsonic pocket of flow may occur. Without the embedded subsonic flow option, a subsonic region of flow would terminate the solution process. Another area that must be addressed is configurations with multiple lifting surfaces and trailing wakes that influence downstream aircraft components. A recent modification enables the researcher to analyze configurations with wing-mounted and centerline-mounted nacelles.

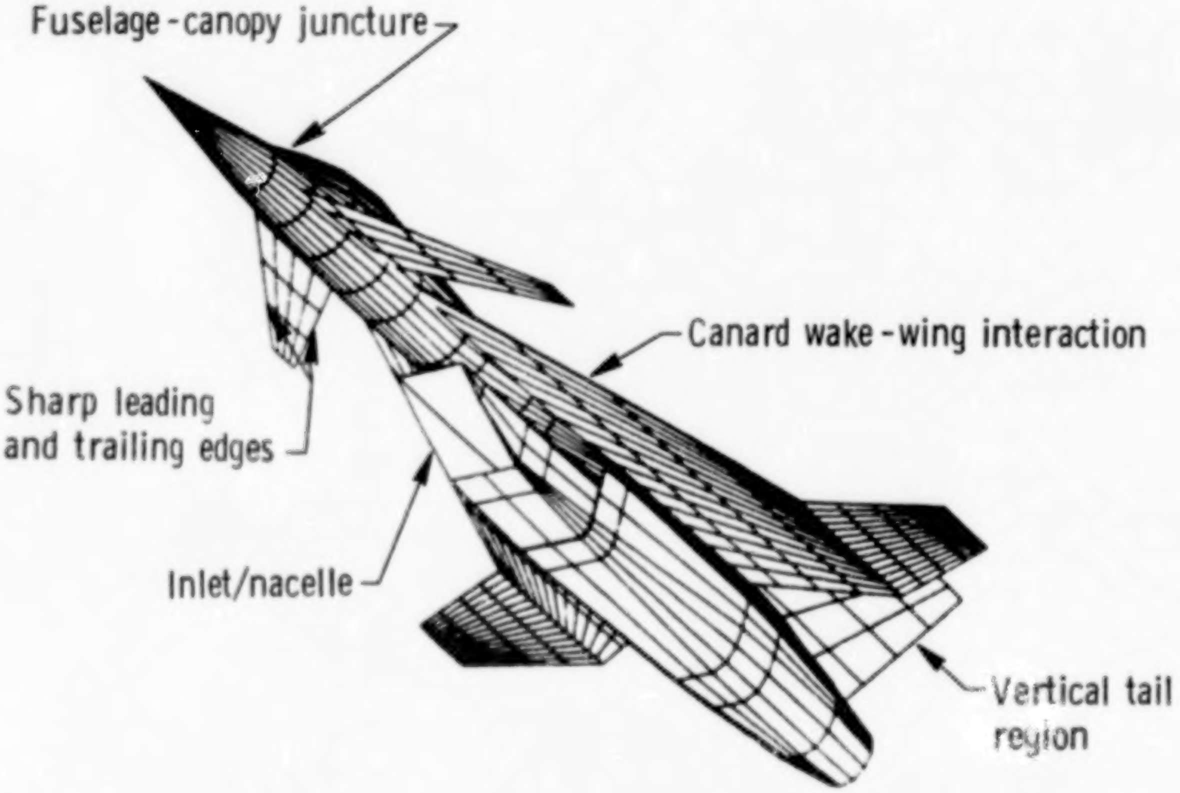
Fuselage-canopy juncture
Canard wake-wing interaction
Sharp leading and trailing edges
Inlet/nacelle
Vertical tail region

SUPERSONIC FIGHTER CONFIGURATION

Computational Grids

The separation of the gridding and the flow field analysis portion of the code allows verification of the grid system before proceeding with the solution. This has proven invaluable in detecting and correcting possible grid problems or errors in the geometric definition of the model. This figure shows four computational grids used in the analysis of the Langley fighter concept. They also illustrate the geometric complexity that can be accommodated with this code.

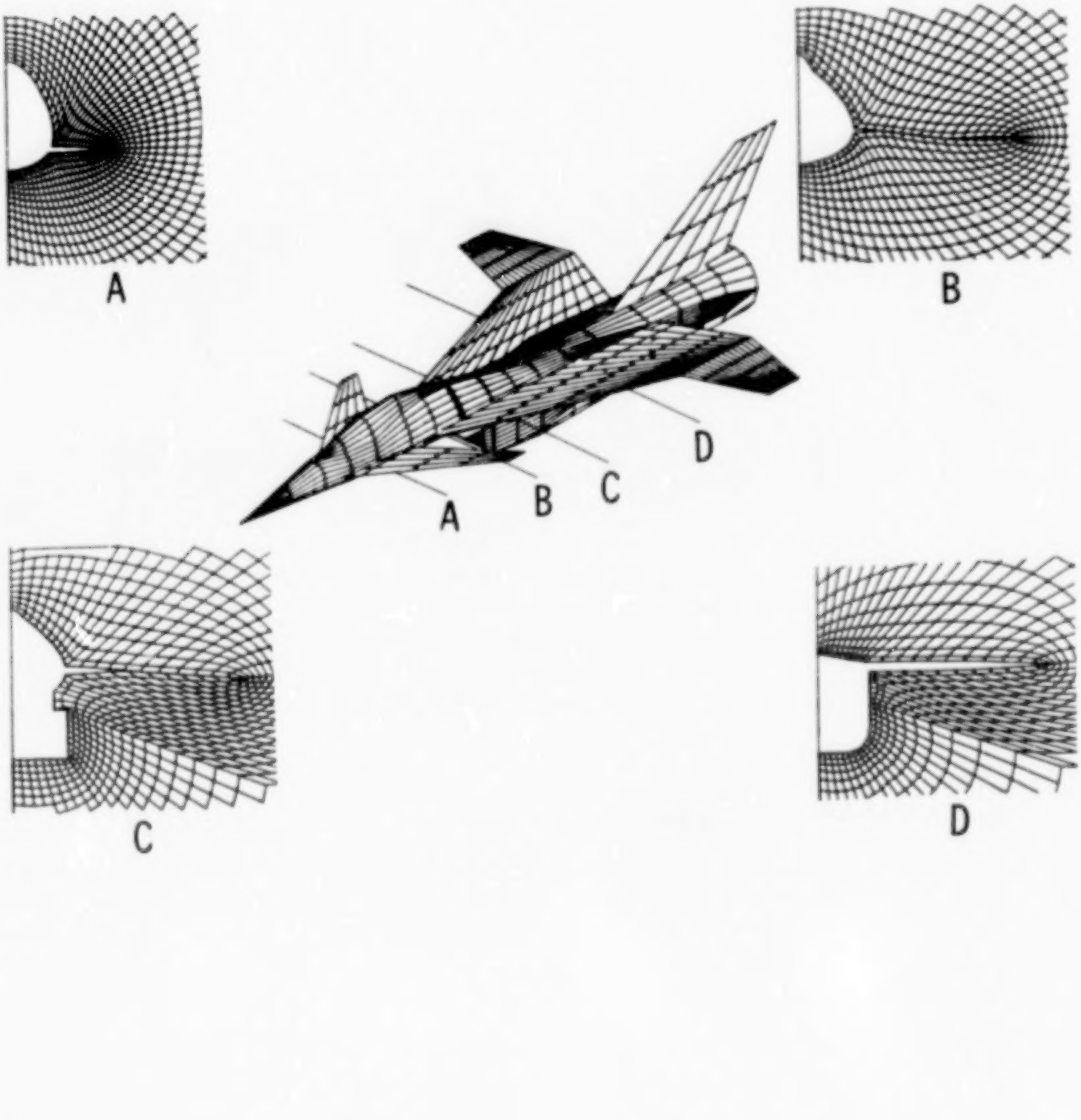

SUPERSONIC FIGHTER CONCEPT

Flow Field Solution

Results on the Langley supersonic fighter configuration at $M = 2$, $\alpha = 4^\circ$ are shown on this figure. These results are in the form of pressure contours in the flow field. Longitudinal pressure contours are plotted on the plane of symmetry. The major characteristics of the flow are evident in this view. Two cross-sectional pressure contour plots are shown on the right of the figure. Section A-A is at a forward location which includes the canard, and the canard shock off the sharp leading-edge is evident in the contour plot. The shock off the nacelle is evident in the contour plot at Section B-B, which is just downstream of the inlet face.

$M = 2$, $\alpha = 4^\circ$

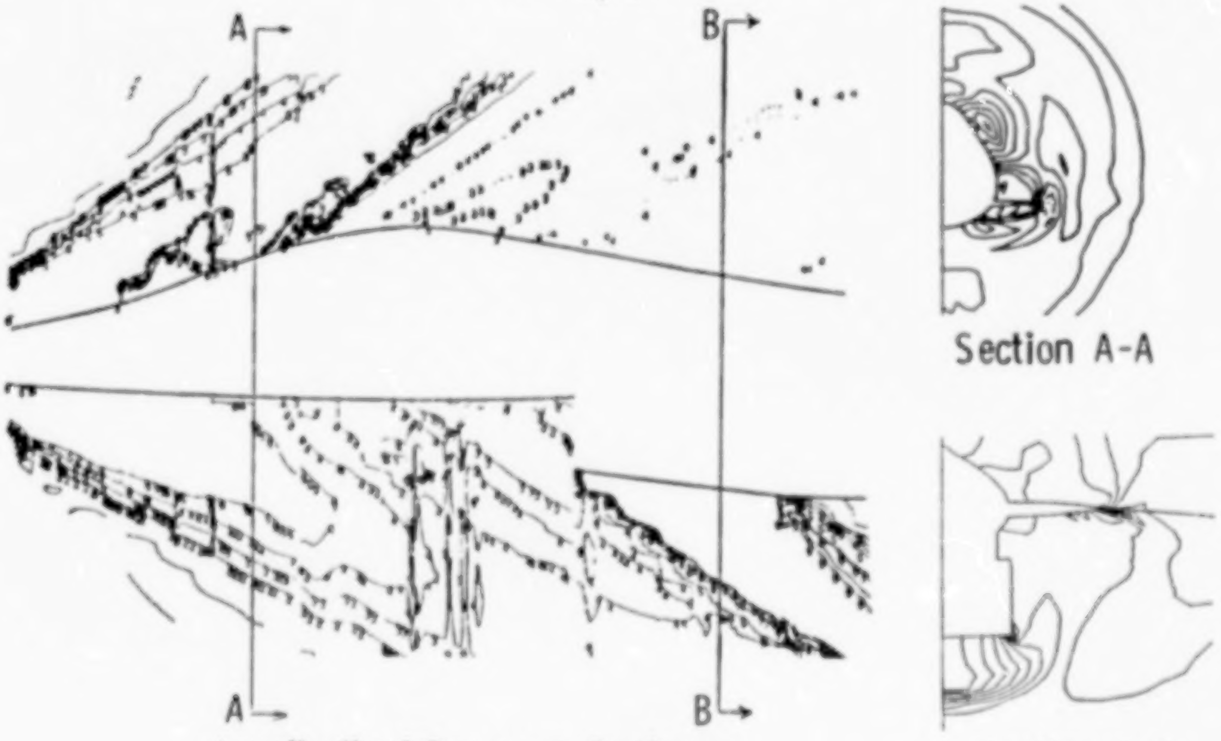

Longitudinal Pressure Contours

Section A-A

Section B-B

ORIGINAL PAGE IS
OF POOR QUALITY

SUPERSONIC FIGHTER CONCEPT

Schlieren Photograph $M = 2$, $\alpha = 4^{\circ}$

A comparison of the longitudinal pressure contours with a schlieren photograph is helpful in determining the quality of the full potential results. The pressure contours are in good agreement with the flow characteristics seen in the schlieren photograph.

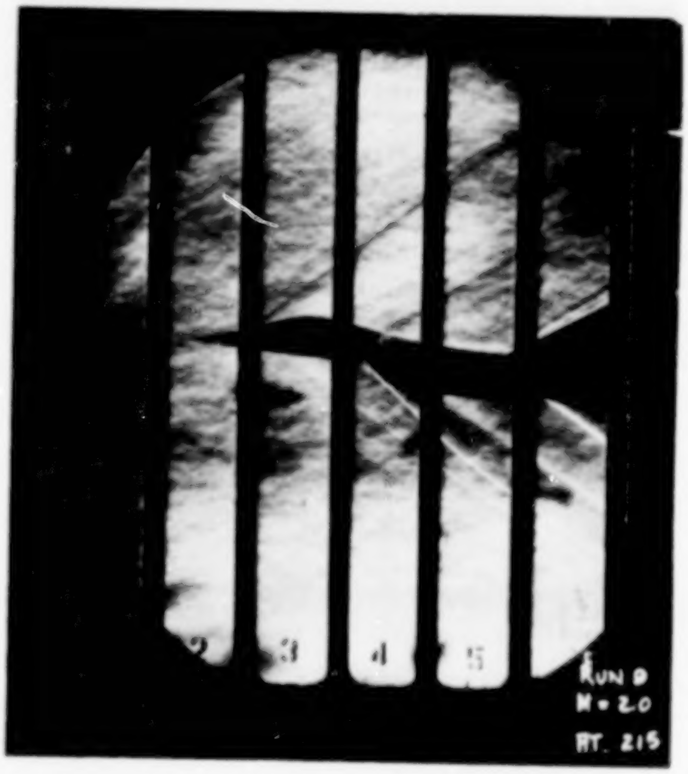

ORIGINAL PAGE IS
OF POOR QUALITY

ROCKWELL ADVANCED FIGHTER CONCEPT

The High-Speed Aerodynamics Division at NASA Langley and the Rockwell International Corporation are engaged in a cooperative effort to demonstrate the applicability of new nonlinear analysis/design techniques for advanced supersonic wing design. The effort was aimed at demonstrating the ability of a nonlinear analysis technique based on solution of the supersonic potential flow equations. The cooperative program included both the aerodynamic design and testing of several outboard wing panels for an advanced supersonic fighter concept. The aerodynamic design of the wing panels was a two step process. Standard linearized theory techniques were used to determine a design point(s) twist and camber distribution(s). This was followed by an assessment of the flow quality via the potential flow solver. If necessary the surface contours could be modified in an iterative fashion to prevent flow separation over the wing panels. The purpose of the experimental investigation was to determine the effect on supersonic aerodynamic characteristics of increasing wing sweep and provide a data base for code validation.

The wind tunnel model is shown installed in the Langley Unitary Plan Wind Tunnel and is a preliminary design version of a Rockwell fighter concept. Five outboard wing panel geometries were tested: a 48° leading-edge sweep baseline; a 55° leading-edge sweep wing with a camber distribution biased toward a maneuver lift coefficient for Mach 1.6; an uncambered 55° reference wing; and two redesigned 48° leading-edge sweep wing panels (multi-operating point wings - subsonic, transonic, supersonic). The redesigned 48° wings represented a low twist cruise wing (M = 1.5) and a high twist maneuver concept (M = 1.6). Testing was performed at Mach numbers of 1.5 to 2.5. Both longitudinal and lateral aerodynamic force characteristics were measured. Surface pressure data were obtained at Mach numbers of 1.5 to 1.8 for the 55° cambered wing and the 48° low and high twist wings.

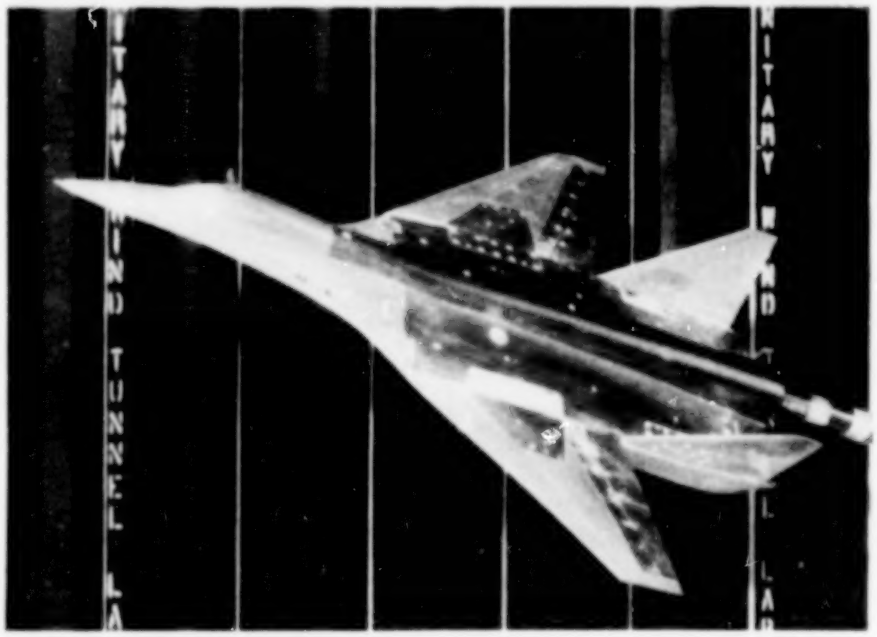

ROCKWELL ADVANCED FIGHTER CONCEPT

Cross Section and Grid at 65-Percent Body Station

As stated before, it is best to study representative computational grids on the configuration before proceeding with the flow field analysis. This figure is an example of a cross section and computational grid used in the analysis of the Rockwell fighter concept. Notice that the Rockwell fighter concept has a wing-mounted nacelle while the Langley fighter had a centerline-mounted nacelle.

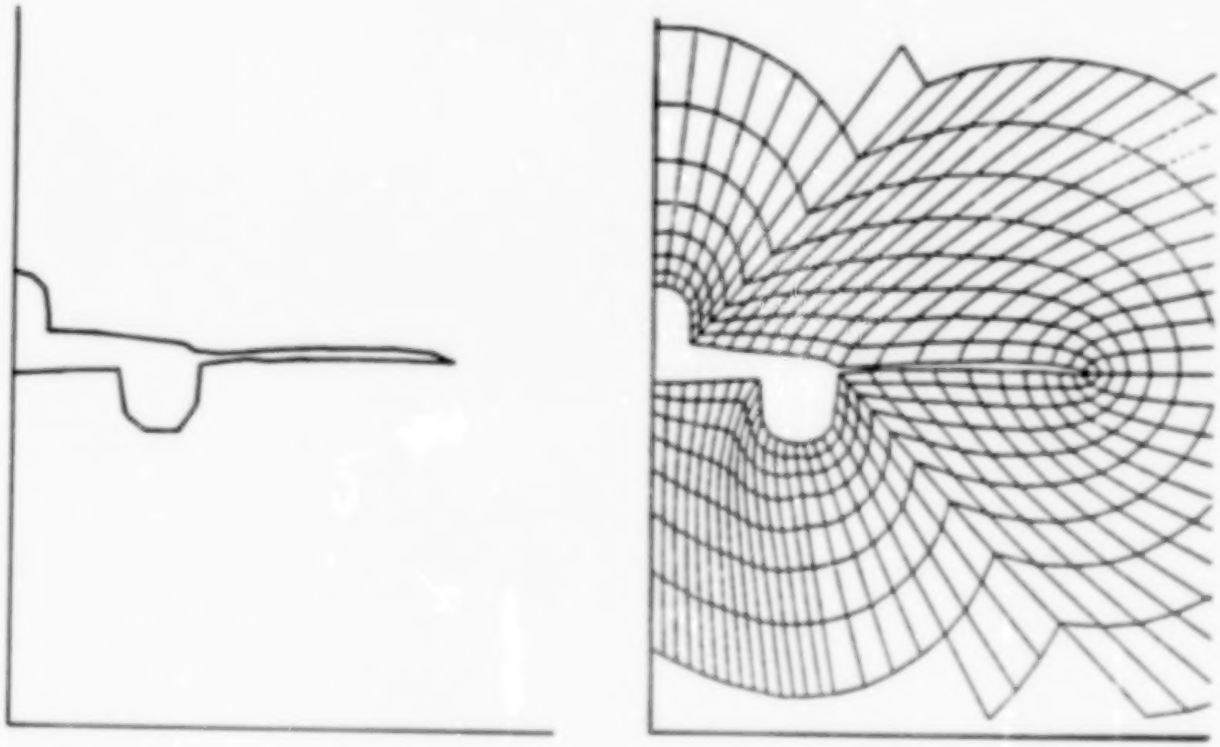

ROCKWELL ADVANCED FIGHTER CONCEPT

Pressure Contours and Crossflow Velocity Vectors

Results from the full potential analysis of a configuration can be presented in many ways. Pressure contours and crossflow velocity vector displays are useful to evaluate the flow structure about the configuration. The pressure contours and crossflow velocity vectors from the analysis of the Rockwell fighter concept at $M_\infty = 1.6$, $\alpha = 4.46^\circ$ are shown here. The circular shock below the wing of the fighter, which is caused by the nacelle, shows up well in the crossflow pressure contour plot.

$M_\infty = 1.6$, $\alpha = 4.46^\circ$

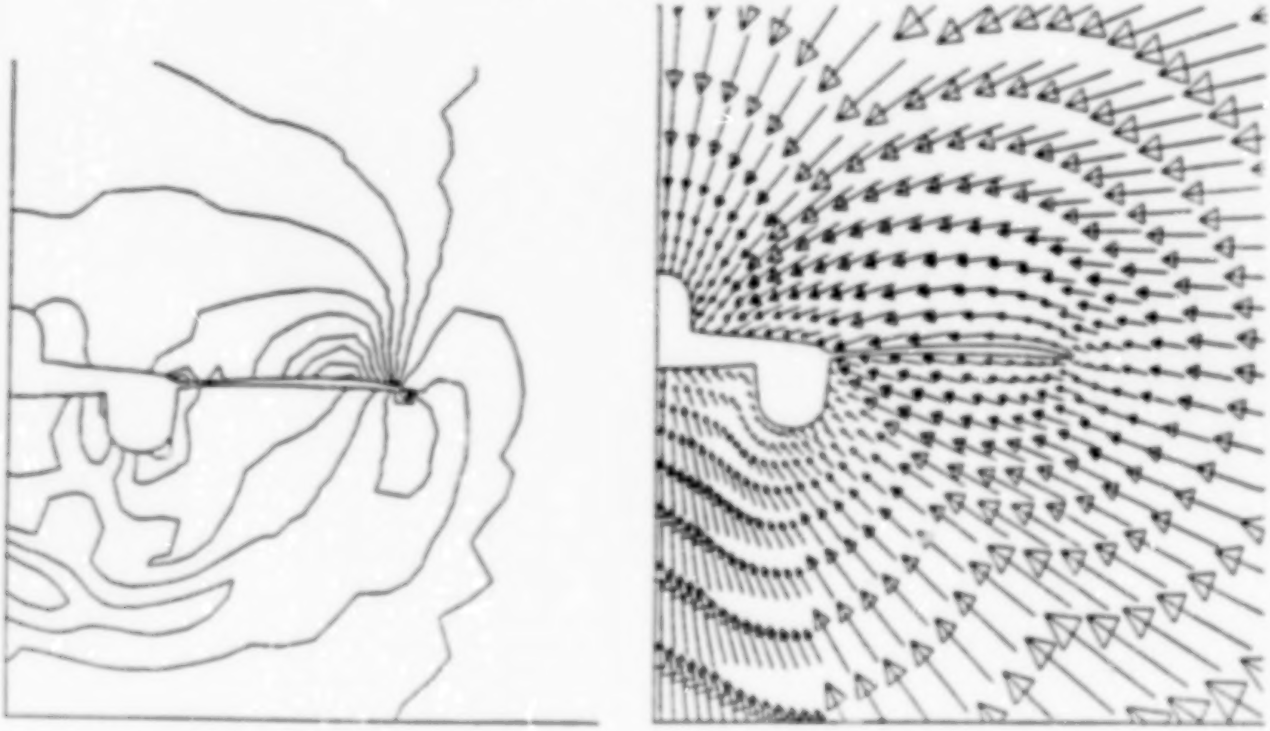

ROCKWELL FIGHTER CONFIGURATION

Upper Surface Pressure Distribution

The potential flow predictions and the measured surface pressure data for the twisted and cambered 55° sweep configuration at $M_\infty = 1.6$ (nacelle off) are shown in the figure. Upper surface pressure comparisons are made at four span stations. Again the agreement is quite good even near the leading edge. The comparisons are not quite as good at the leading edge for the two outboard span stations on the upper surface of the wing. This is a result of poor grid resolution near the outboard LE. To improve the results at these stations more grid points must be used near the leading edge as well as employing a smaller marching step size in this region of the calculation.

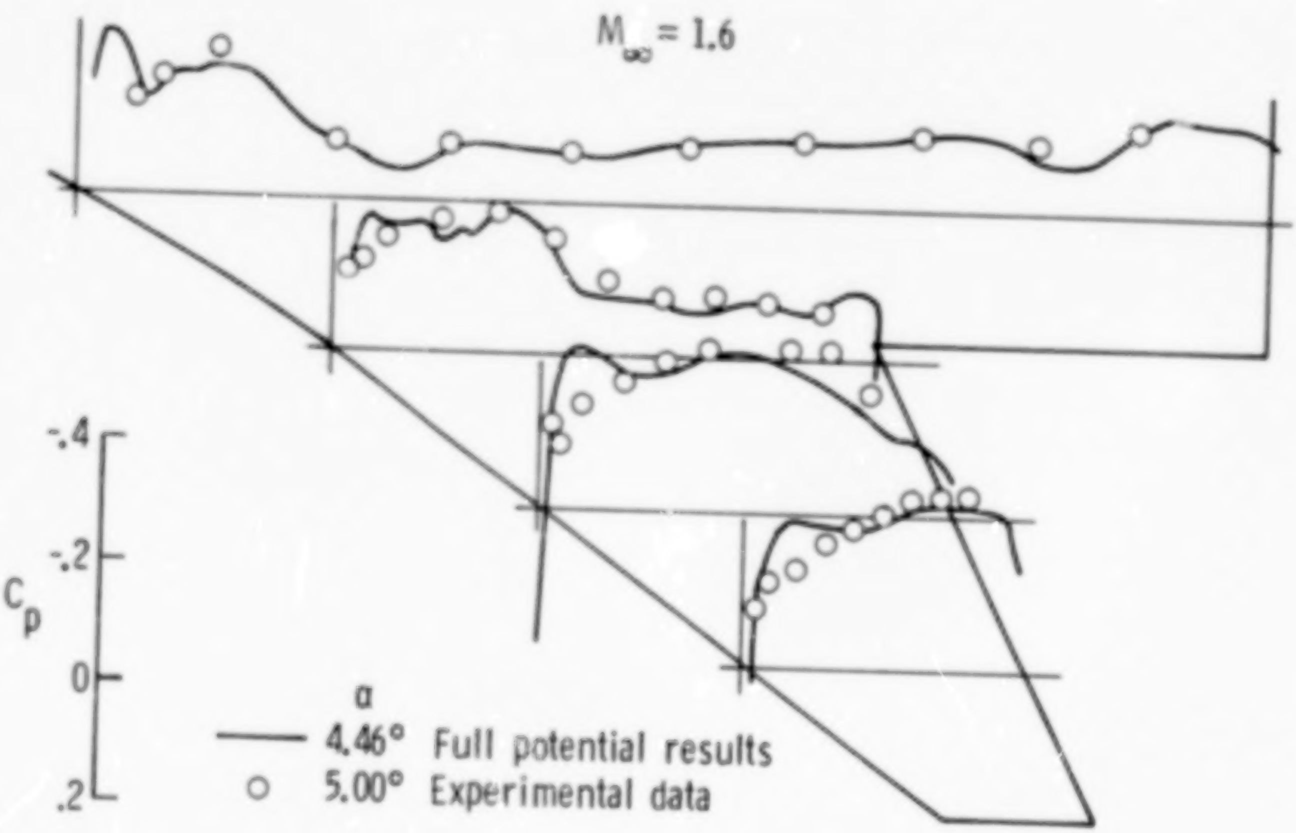

ROCKWELL FIGHTER CONFIGURATION

Lower Surface Pressure Distribution

The lower surface pressure comparisons for the 55° sweep configuration at $M_\infty = 1.6$ are also shown in the comparison between theory and experiment and are very good. Similar good agreement has been observed for the 48° sweep wing tested earlier in the Rockwell Trisonic facility prior to the UPWT test. Research (Kenneth M. Jones and Barrett L. Shrout, NASA Langley) is in preparation which will include the complete force and pressure data for the five wing panel geometries tested. These data should provide a strong data base for advanced supersonic fighter designs.

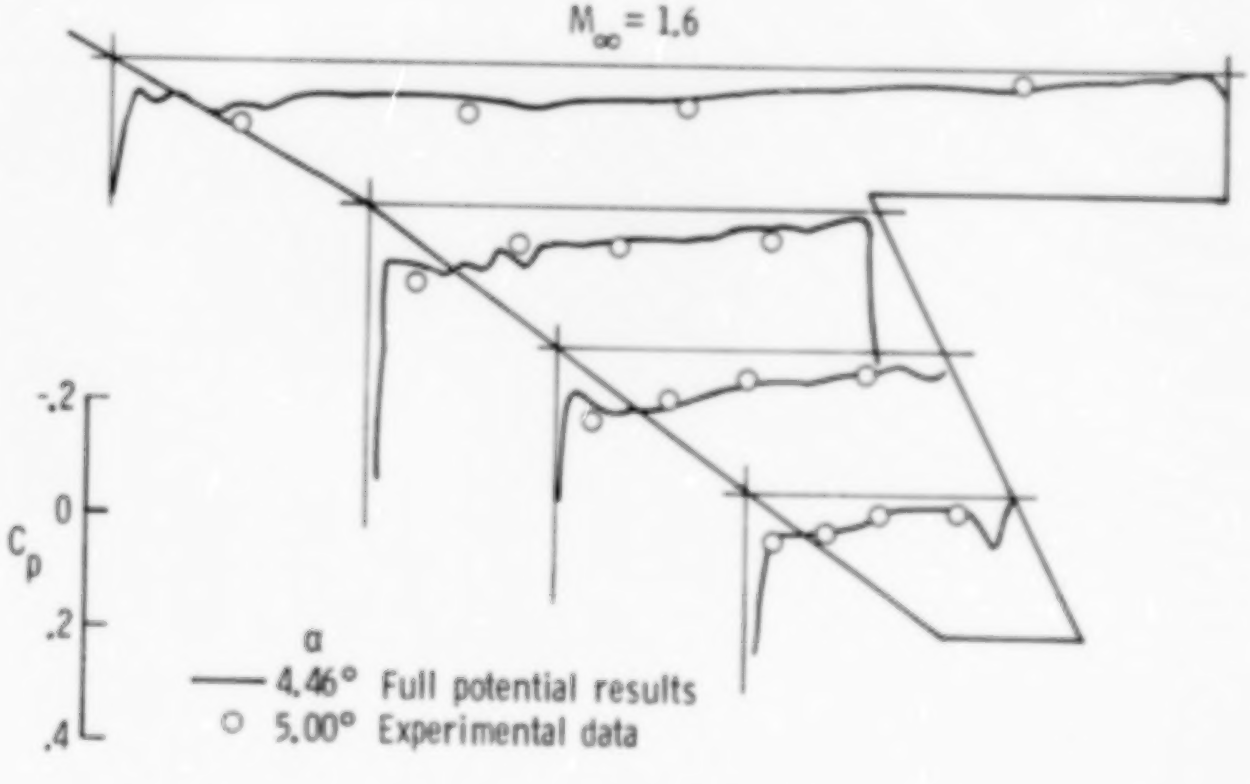

ROCKWELL FIGHTER CONFIGURATION

Force Comparisons

Comparisons of the analysis and the experimental force data for the twisted and cambered 55° sweep wing panel are presented in the figure. The agreement between the potential flow analysis and the UPWT data at the design point ($M = 1.6$, $C_L = 0.32$, $\alpha = 4.46^\circ$) is quite good. To achieve the desired C_L of 0.32 the angle-of-attack must be increased to 5.25° with a corresponding performance penalty (L/D reduction). The 55° twist and camber distribution from the linear design code was not refined via the potential flow code since the flow quality was deemed satisfactory. However, if the performance loss is important, then a refinement of the twist and camber distribution followed by reanalysis with the potential flow code should be investigated to more closely achieve the design goal.

M = 1.6, Nacelle Off

	Linear Analysis	Full Potential Analysis	UPWT Data	UPWT Data
α	4.46	4.46	4.46	5.25
C_L	0.32	0.292	0.283	0.32
C_D	0.0438	0.0402	0.0398	0.045
C_M	-0.061	-0.0565	-0.0530	
L/D	7.31	7.26	7.11	7.0

CONCLUDING REMARKS

A supersonic potential flow solver has been developed to analyze the flow over complex realistic aircraft geometries. Enhancements to the method have been made to accommodate regions of subsonic flow, the effect of trailing wakes on other aircraft components (wing, body, tail, etc), and the modeling/gridding of complete configurations. Validation of the method has been demonstrated by comparisons with experimental aerodynamic force and surface pressure measurements. The predicted results are in very good agreement with the experimental data. The bibliography contains additional information on the use of the potential flow code to predict the aerodynamics of high-speed wing/body configurations, waverider concepts, TAV, and the Space Shuttle orbiter package.

Further work is planned to investigate the quality of the flow field results obtained with the potential code. This capability is important in assessing inlet and control surface placement. Additional analysis of supersonic aircraft concepts is planned to complete the validation of the method and the gridding package. A vectorized version of the code is under development.

Future code development will be in the area of a supersonic Euler solver which is compatible with the geometry and gridding package employed in the present technique. The Euler solver will overcome the isentropic restrictions of the potential method and hopefully retain the ability to treat complex aircraft geometries.

- A Supersonic Full Potential Method Has Been Applied To The Analysis Of Realistic Aircraft Configurations
  - Good Agreement With Experimental Data
    - Surface Pressure Distributions
    - Aerodynamic Force Estimates
- Additional Validation Of Method
  - Investigate Quality Of Results In The Flow Field
  - Analyze Additional Complex Geometry Configurations
  - Vectorize Code
- Future Work
  - Investigate Supersonic Euler Solver

BIBLIOGRAPHY

1. Clever, W. C. and Shankar, V., "Nonlinear Potential Analysis Techniques for Supersonic/Hypersonic Configuration Design," NASA CR-166078, March 1983.

2. Shankar, V. and Clever, W. C., "Nonlinear Potential Analysis Techniques for Supersonic/Hypersonic Aerodynamic Design," NASA CR-172299, March 1984.

3. Shankar, V. and Szema, K. Y., "Nonlinear Potential Analysis Techniques for Supersonic Aerodynamic Design," NASA CR-172507, March 1985.

4. Jones, K. M., "Application of a Full Potential Method for Predicting Supersonic Flow Fields and Aerodynamic Characteristics," AIAA Paper No. 83-1802, July 1983.

5. Jones, K. M., Talcott, N. A., Jr., and Shankar, V., "Application of a Full Potential Method for Computation of Three-Dimensional Supersonic Flows," AIAA Paper No. 84-0139, January 1984.

6. Szema, K. Y. and Shankar, V., "Nonlinear Computation of Wing-Body-Vertical Tail-Wake Flows at Low Supersonic Speed," AIAA Paper No. 84-0427, January 1984.

7. Szema, K. Y., Riba, W. L., Shankar, V., and Gorski, J. J. "Full Potential Treatment of Flows Over 3-D Geometries Including Multibody Configurations," AIAA Paper No. 85-0272, January 1985.

D5

N88-14931

S6--02

117229

19P.

UPWIND RELAXATION ALGORITHMS
FOR EULER/NAVIER-STOKES EQUATIONS

J. L. Thomas
R. W. Walters
D. H. Rudy
R. C. Swanson
NASA Langley Research Center
Hampton, Virginia

PRECEDING PAGE BLANK NOT FILMED

PAGE 88 INTENTIONALLY BLANK

* C-2

[redacted]

Abstract

The present paper will present a description of and results from a new solution algorithm for the compressible Navier-Stokes equations developed by a team of researchers at Langley Research Center. The main features of the algorithm are second- or third-order accurate upwind discretization of the convective and pressure derivatives and a relaxation scheme for the unfactored implicit backward Euler time method, implemented in a finite-volume formulation.

Upwind methods have been successfully used to obtain solutions to the Euler equations for flows with strong shock waves. One reason for this success is that these methods directly simulate the signal propagation features of hyperbolic equations. Furthermore, these methods have the advantage of being naturally dissipative. Upwind differencing has been used for the pressure and convective terms in the present Navier-Stokes algorithm while central differencing has been used for the viscous terms. The particular upwind method being used is based on the flux-vector-splitting technique developed by Van Leer (ref. 1) and both second- and third-order accurate discretizations have been developed.

Currently, the most widely used implicit solution techniques for the Navier-Stokes equations use approximate factorization (AF) methods to treat multi-dimensional problems. Although the implicit AF methods are unconditionally stable in two dimensions, they require an optimal set of iteration parameters, which are difficult to obtain, for rapid convergence. Furthermore, the implicit AF schemes are only conditionally stable for the three-dimensional Navier-Stokes equations. However, the upwind discretization leads to a diagonally dominant matrix structure which allows large time steps to be taken in multi-dimensional problems. The time integration scheme being used in the present algorithm corresponds to a line Gauss-Seidel relaxation method. This method produces good convergence rates for steady-state flows, and most of the algorithm has been vectorized on the NASA Langley VPS 32 computer.

The Navier-Stokes algorithm has been tested for several two-dimensional flow problems such as the laminar boundary layer flow on a flat plate and the flow produced by an oblique shock wave impinging on a laminar boundary layer developing on a flat plate. Solutions for both problems gave excellent results which are presented in this paper. Present effort is directed toward the extension of the scheme to the full three-dimensional Navier-Stokes equations.

Upwind Relaxation Algorithms for the Euler/Navier-Stokes Equations

The purpose of this paper is to present upwind relaxation algorithms for accurate and reliable steady-state solutions to either the compressible Euler (inviscid) or Navier-Stokes (viscous) equations. The main feature of the algorithms is the use of second- or third-order accurate upwind discretizations of the convective and pressure terms, which enables implicit line relaxation strategies to be developed for rapid solutions to the steady-state equations. The basic algorithm for three-dimensional flows is discussed. Both inviscid and viscous (using thin-layer Navier-Stokes approximations) computations are shown for a series of two-dimensional flows.

3-D Relaxation Algorithm

The relaxation algorithm for the time-dependent Euler equations written in conservation form and generalized coordinates is shown. The equation to be solved with relaxation corresponds to the linearized, backward-time approximation in delta form. The inviscid flux is split according to the eigenvalues of the characteristic equation, which recognizes the signal propagation features of the hyperbolic equations and enables relaxation approaches to be exploited for solutions to the steady-state equations. The particular flux splitting technique used corresponds to that developed by Van Leer (ref. 1), although the advantages resulting from upwind differencing would apply equally as well to other splitting techniques. Applying upwind differencing in the streamwise (ξ) direction on the implicit (left-hand) side of the equation in delta form leaves an equation to be solved in the cross flow (η-ζ) plane. The streamwise relaxation is effected by sweeping in the ξ-direction through the mesh, alternating the direction of the sweep every other pass in order to maintain stability for higher order differencing.

Non-linear updating of the residual is indicated, corresponding to upstream cross-flow planes evaluated at time level n+1 when sweeping from upstream to downstream, and vice-versa. The upwind relaxation scheme indicated is unconditionally stable and maximal damping occurs at large time steps. This is in contrast to approximately factored approaches, which require an optimal set of iteration parameters, which are difficult and time consuming to obtain, for rapid convergence. The relaxation scheme also has the advantage that it recovers conventional space marching techniques for supersonic flows in the ξ-direction.

Time-dependent Euler equations in generalized coordinates

$$\frac{\partial \hat{Q}}{\partial \tau} + \frac{\partial \hat{F}}{\partial \xi} + \frac{\partial \hat{G}}{\partial \eta} + \frac{\partial \hat{H}}{\partial \zeta} = 0$$

Linearized implicit time integration

$$\left[\frac{I}{J\Delta\tau} + \delta_\xi \frac{\partial \hat{F}}{\partial Q} + \delta_\eta \frac{\partial \hat{G}}{\partial Q} + \delta_\zeta \frac{\partial \hat{H}}{\partial Q}\right] \Delta Q = -R^n$$

Applying upwind relaxation in the streamwise (ξ) direction leaves an equation to be solved in the cross-flow (η - ζ) plane

$$\left[M + \delta_\eta \frac{\partial \hat{G}}{\partial Q} + \delta_\zeta \frac{\partial \hat{H}}{\partial Q}\right] \Delta Q = -R(Q^n, Q^{n+1})$$

Where

$$M = \frac{I}{J\Delta\tau} + \frac{\partial F^+}{\partial Q} - \frac{\partial F^-}{\partial Q} \qquad \Delta Q = Q^{n+1} - Q^n$$

Solution of Cross-Flow Equations

The upwind differenced equation in the cross-flow plane can be solved using either relaxation or approximate factorization. The upwind relaxation shown corresponds to alternate line Gauss-Seidel sweeping with nonlinear updating of the residual indicated, although in practice the residual is updated linearly using the Jacobian matrices from the implicit side of the equation. With first-order implicit upwind differencing, either approach leads to two sweeps across the plane, solving a system of tridiagonal equations on each line. With relaxation in the cross-flow plane, the scheme is unconditionally stable for the linear wave equation and maximum damping occurs with large time steps. However, because the algorithm is recursive in nature, it cannot be completely vectorized on current pipeline supercomputers such as the CDC CYBER 205. The time step is limited to obtain optimal convergence with the approximate factorization in the cross-flow plane, but the scheme is completely vectorizable. Thus, a tradeoff exists between convergence rate and computational rate in determining the most efficient strategy. Vectorizable relaxation strategies, such as checkerboard algorithms, lead to faster computational rates with slightly lower convergence rates, owing to the underrelaxation required for stability.

$$\left[M + \delta_\eta \frac{\partial \hat{G}}{\partial Q} + \delta_\zeta \frac{\partial \hat{H}}{\partial Q} \right] \Delta Q = -R(Q^n, Q^{n+1})$$

Upwind relaxation (Line Gauss-Seidel — alternate sweeping)

$$\left[M + \frac{\partial \hat{G}}{\partial Q}^{+} - \frac{\partial \hat{G}}{\partial Q}^{-} + \delta_\zeta \frac{\partial \hat{H}}{\partial Q} \right] \Delta Q = -R(Q^n, Q^{n+1}) \quad \zeta\text{ - line implicit}$$

$$\left[M + \frac{\partial \hat{H}}{\partial Q}^{+} - \frac{\partial \hat{H}}{\partial Q}^{-} + \delta_\eta \frac{\partial \hat{G}}{\partial Q} \right] \Delta Q = -R(Q^n, Q^{n+1}) \quad \eta\text{ - line implicit}$$

Approximate factorization

$$\left[M + \delta_\eta \frac{\partial \hat{G}}{\partial Q} \right] \left[M^{-1} \right] \left[M + \delta_\zeta \frac{\partial \hat{H}}{\partial Q} \right] \Delta Q = -R(Q^n, Q^{n+1})$$

Spatial Differencing

The convective and pressure terms are split according to the flux vector splitting technique developed by Van Leer, which is implemented in a control-volume formulation. The flux difference is computed from the difference of split fluxes across all boundaries, where the upwinding is incorporated through an interpolation of conserved variables. A one-parameter family of interpolations is used. This family ranges from fully upwind second-order to upwind-biased third-order approximations. Viscous terms are differenced using second-order central differences, so that the method for viscous flows is limited currently to second order.

Upwind flux splitting for convective and pressure terms

$$\delta_\xi F = \delta_\xi^- F^+ + \delta_\xi^+ F^-$$

Where upwind differences effected through interpolation of conserved variables in terms of 1-parameter family

$$\delta_\xi^- F^+ = F^+ (Q^-)_{i+\frac{1}{2}} - F^+ (Q^-)_{i-\frac{1}{2}}$$

$$Q^-_{i+\frac{1}{2}} = Q_i + \frac{1}{4} \left[(1-K)\nabla + (1+K)\Delta \right] Q_i$$

$$K = \begin{cases} -1 & \text{Second order fully upwind} \\ +1 & \text{Second order central difference} \\ 1/3 & \text{Third order upwind - biased} \end{cases}$$

Viscous terms differenced with second-order central differences

Inviscid Shock Reflection From Flat Plate

Application of the relaxation algorithm to the solution of an inviscid shock reflection from a flat surface is shown. The freestream Mach number is 2.9 and the shock angle is 29°. Fully upwind spatial differencing in the streamwise direction is used along with vertical Gauss-Seidel line relaxation; this leads to the quadratic convergence shown since the flow is fully supersonic. First-order differencing leads to block tridiagonal line inversions; second- or third-order differencing leads to block pentadiagonal line inversions. The residual history shown is for a global line relaxation strategy (sweeping downstream through the mesh). Further improvements in efficiency can be realized by removing linearization errors completely on a line before moving to the next line, and, thus, recovering a space marching method. The space marching strategy has also been extended to efficiently treat supersonic flows with embedded subsonic regions.

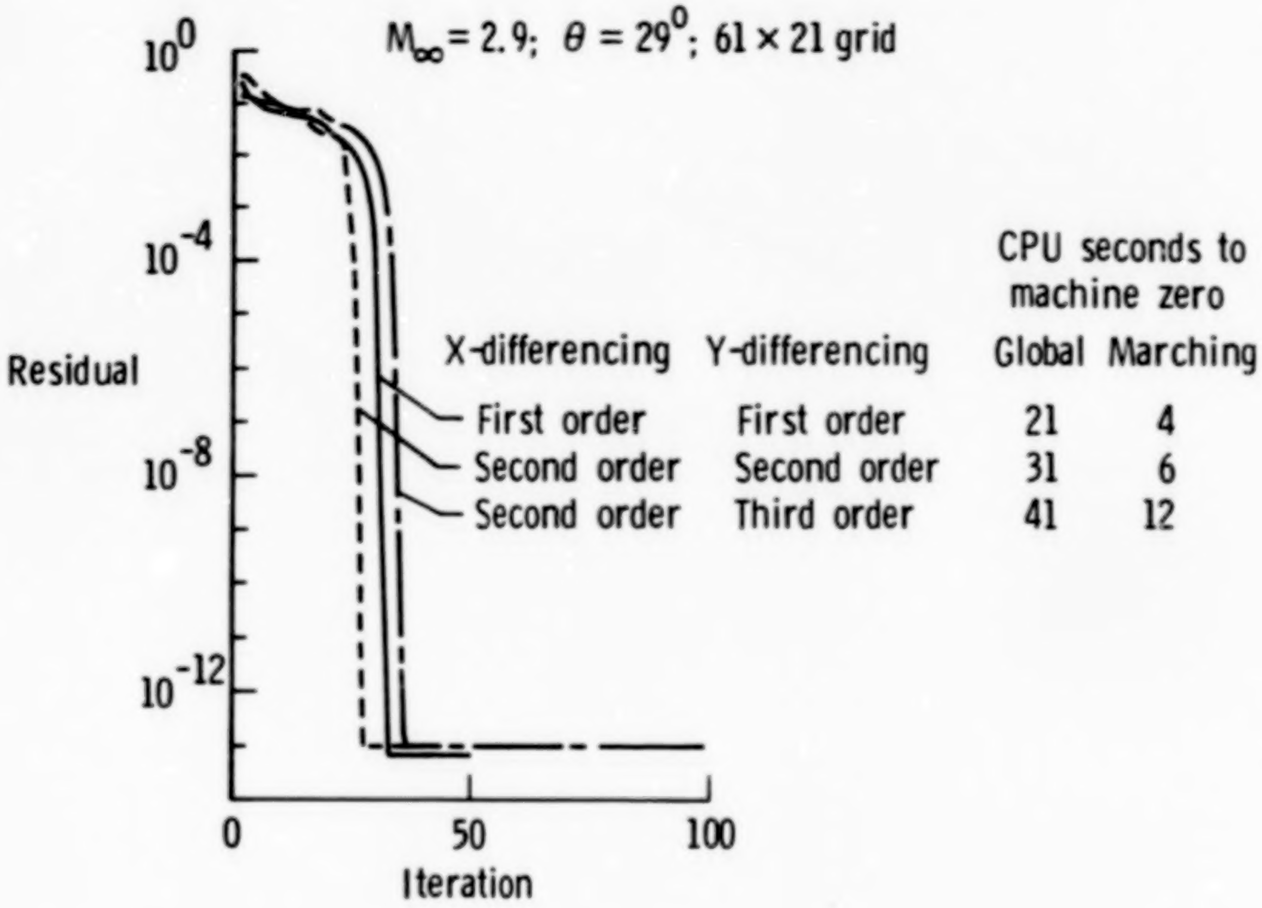

X-differencing	Y-differencing	CPU seconds to machine zero Global	Marching
First order	First order	21	4
Second order	Second order	31	6
Second order	Third order	41	12

Pressure Contours For Inviscid Shock Reflection

Pressure contours for the inviscid shock reflection are shown with various orders of spatial differencing. The grid for each case is uniformly spaced in each of the two directions. The higher order methods are much less dissipative then the first-order scheme and show much higher resolution of the shock wave.

$M_\infty = 2.9$; $\theta = 29°$; 61 × 21 grid

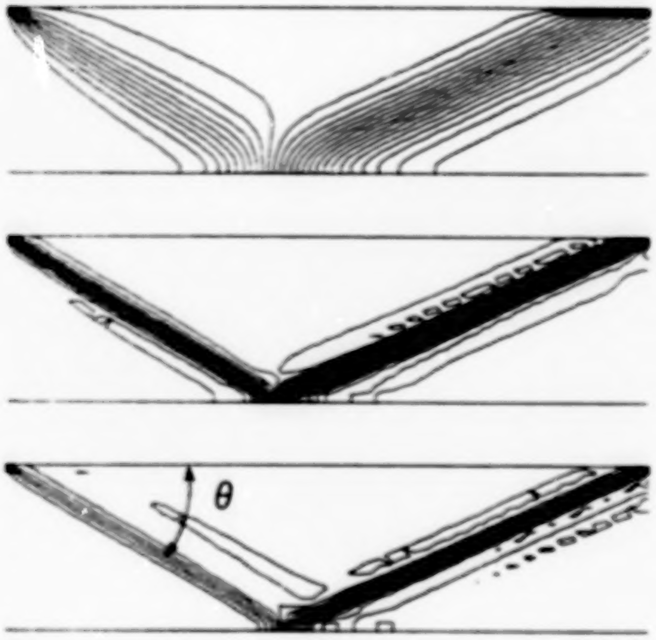

X-differencing	Y-differencing
First order	First order
Second order	Second order
Second order	Third order

Residual Histories for First- and Second-Order Schemes

Residual histories for the transonic flow over a bump in a channel are shown. The incoming Mach number is 0.85, and a significant region of transonic flow exists as shown subsequently. The particular results shown were obtained with approximate factorization (AF) and with vertical line relaxation (LR) methods on a 34 × 18 H-mesh with uniform spacing. The Courant number for the LR scheme is on the order of 200, while that of the AF scheme is limited to 20. One iteration refers to two passes through the mesh using AF and one pass through the mesh using LR. The computational work per iteration on a scalar processor is roughly equal for the two methods and thus the LR scheme is much more efficient. On a vector processor, the computational rate per iteration for the LR scheme is two to three times slower than the AF scheme, even though more than 90 percent of the LR scheme has been vectorized. The only scalar operations in the LR scheme are the recursive forward-backward substitutions on a line; the lower-upper decomposition of the matrix equations is completely vectorizable. Thus, the relative efficiency of the two schemes depends on the type of computer on which the two approaches are implemented.

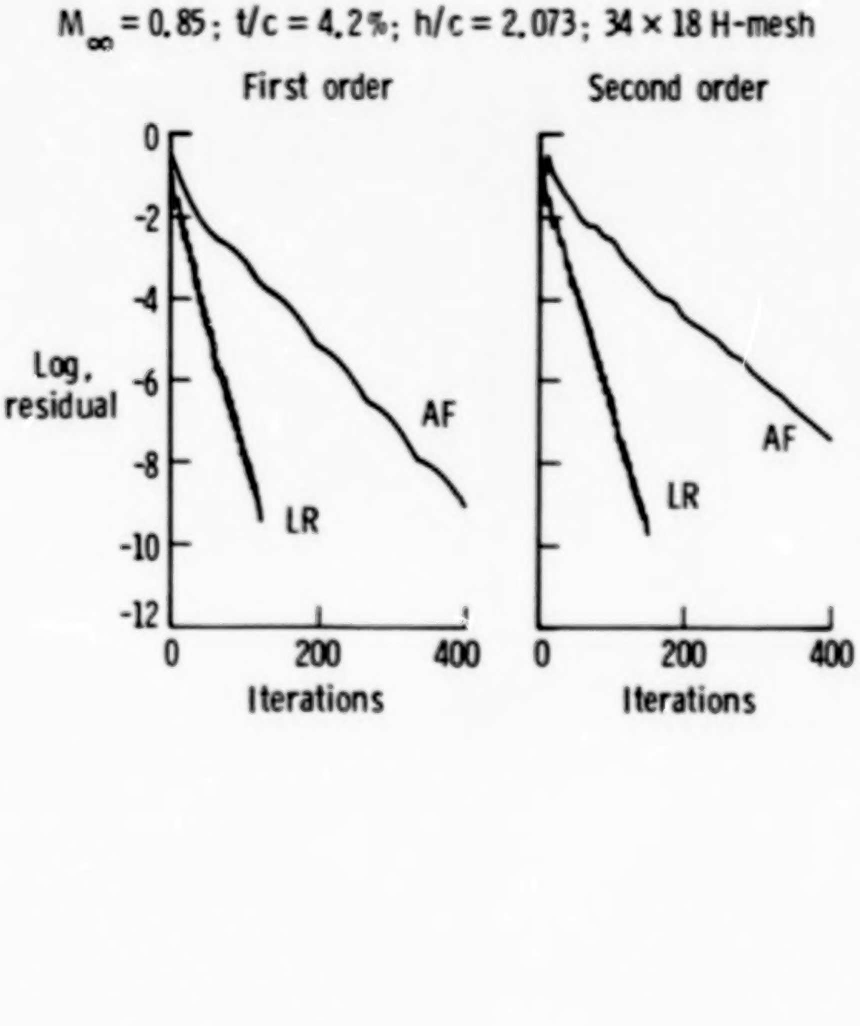

Computational Grid for Bump in Channel

A computational grid for the transonic flow over a bump in a channel is shown. The thickness of the bump is 4.2 percent of the chord, and the channel is approximately two chords in height. The computational grid extends two chords ahead of and behind the bump and is clustered in the region near the bump. The grid is uniform in the vertical direction.

h/c = 2.073; t/c = 4.2 %; 85 × 41 H-mesh

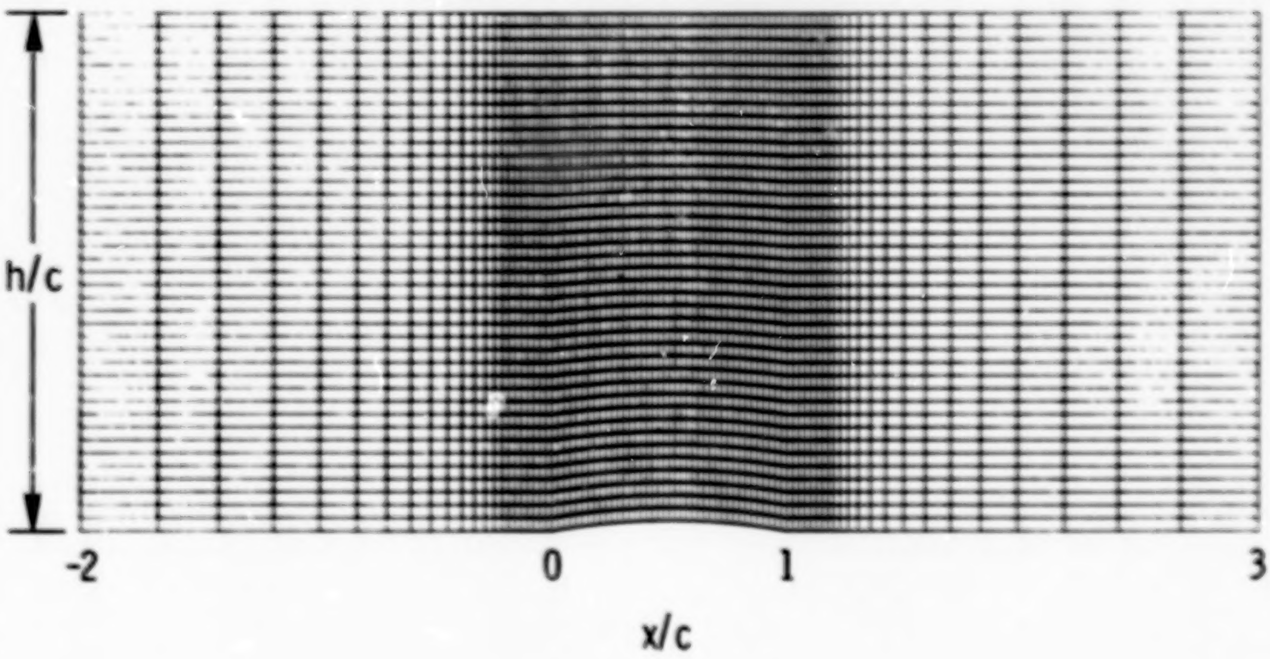

Pressure Contours for Bump in Channel

Pressure contours for the transonic flow over a bump in a channel obtained on the 85 × 41 computational grid are shown. A substantial region of transonic flow exists over the bump, and the shock is captured with two transition zones using the present method. The results shown were obtained with the fully upwind second-order scheme ($\kappa = -1$).

$M_\infty = 0.85$; $t/c = 4.2\%$; $h/c = 2.073$; 85 × 41 H-mesh

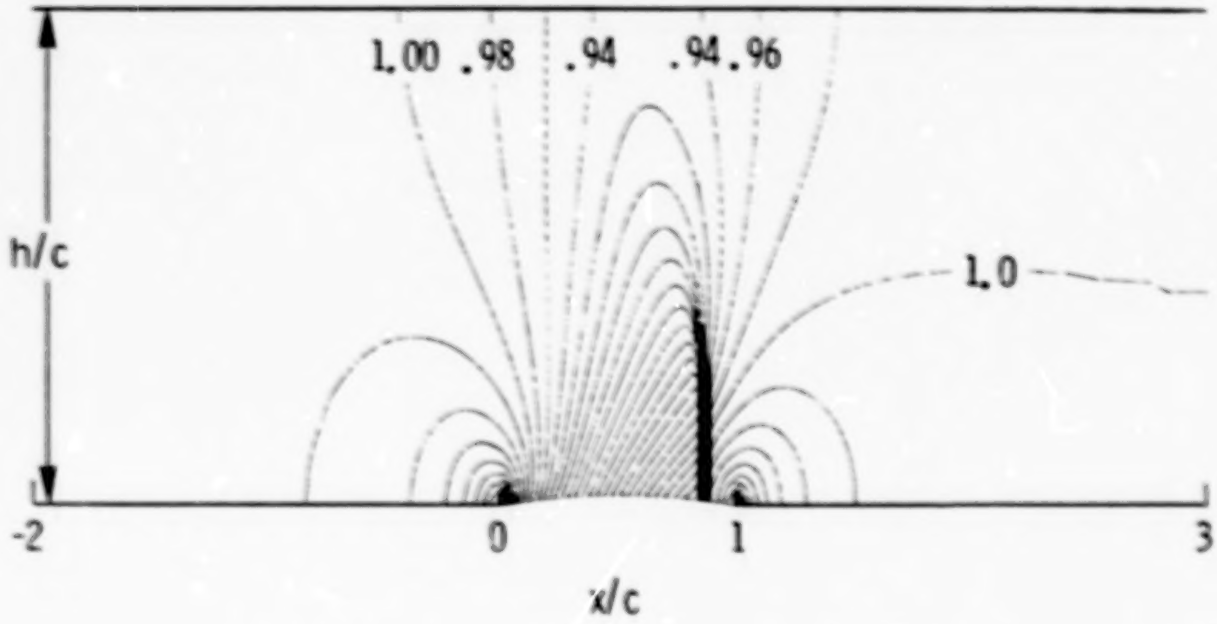

One-Dimensional Couette Flow

Applications of the relaxation algorithm to a series of viscous model problems are shown. The first is one-dimensional Couette flow between a fixed lower plate and a moving upper plate at low Reynolds number and Mach number. Velocity profiles obtained with third-order upwind-biased differencing for the convective and pressure terms and second-order central differencing for the viscous shear terms are shown where the parameter B represents an applied pressure gradient term. No-slip velocity and fixed-wall temperature boundary conditions were used. The relaxation method at large time steps in one-dimension corresponds to Newton's method for finding solutions to nonlinear systems of equations and convergence of the residual to machine zero can be obtained in less than ten iterations. The computed velocity profiles agree very closely with the exact result.

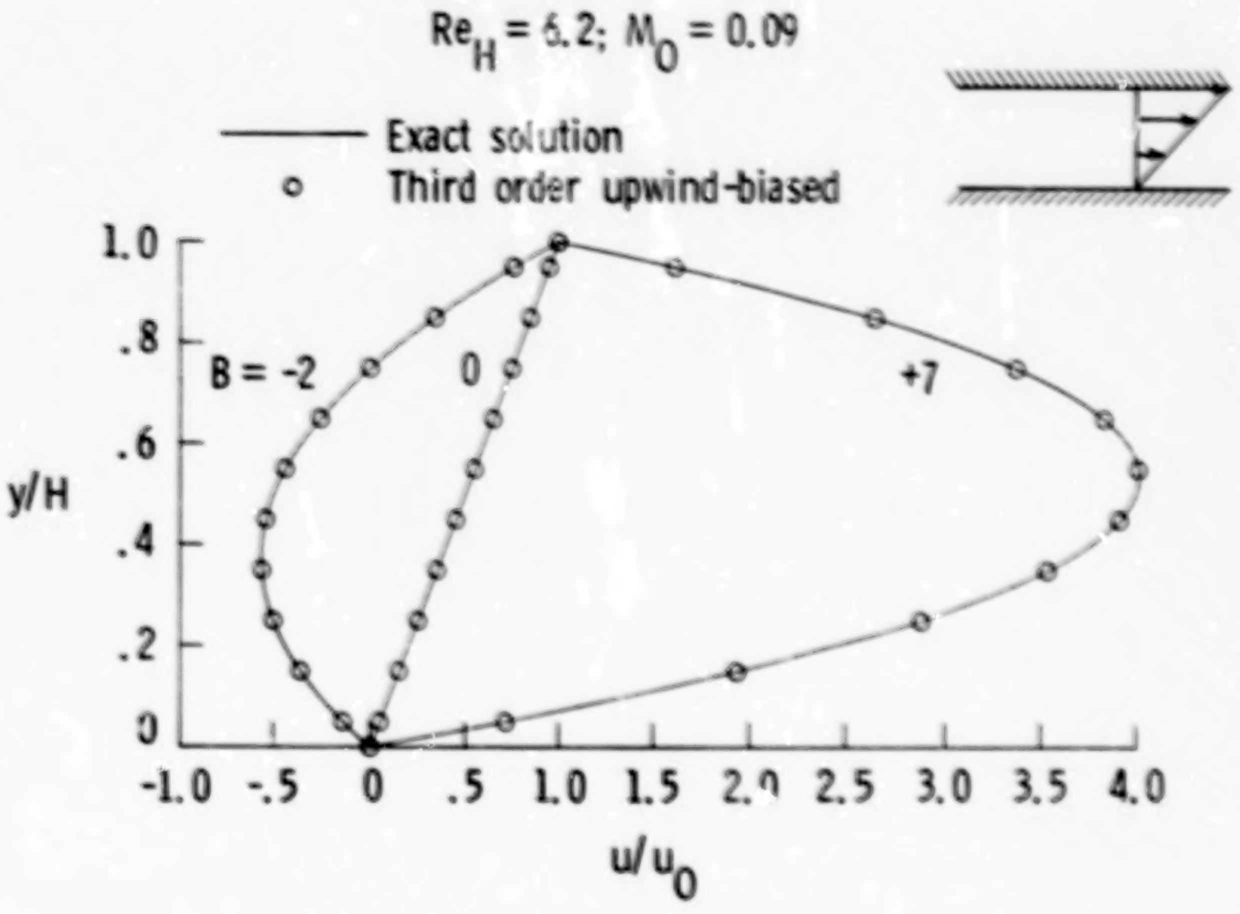

Flat-Plate Boundary Layer: Second-Order Differencing

The accurate computation of viscous effects with an upwind method is an important concern. Results are shown for the laminar flow over a flat plate using second-order ($\kappa = -1$) differencing for the pressure and convective terms. The freestream Mach number is 0.5 and the Reynolds number based on the length of the plate is 10,000. The results were obtained on a 30 × 40 computational grid, which is uniform in the streamwise direction and stretched in the direction normal to the plate. The computational domain is sketched; inflow conditions were applied upstream of the plate and outflow conditions above and downstream of the plate. No-slip, adiabatic wall conditions were specified on the plate. The computations recover the similarity velocity profiles, which develop very quickly downstream of the leading edge. The second-order scheme resolves the boundary layer adequately with approximately twenty points in the layer.

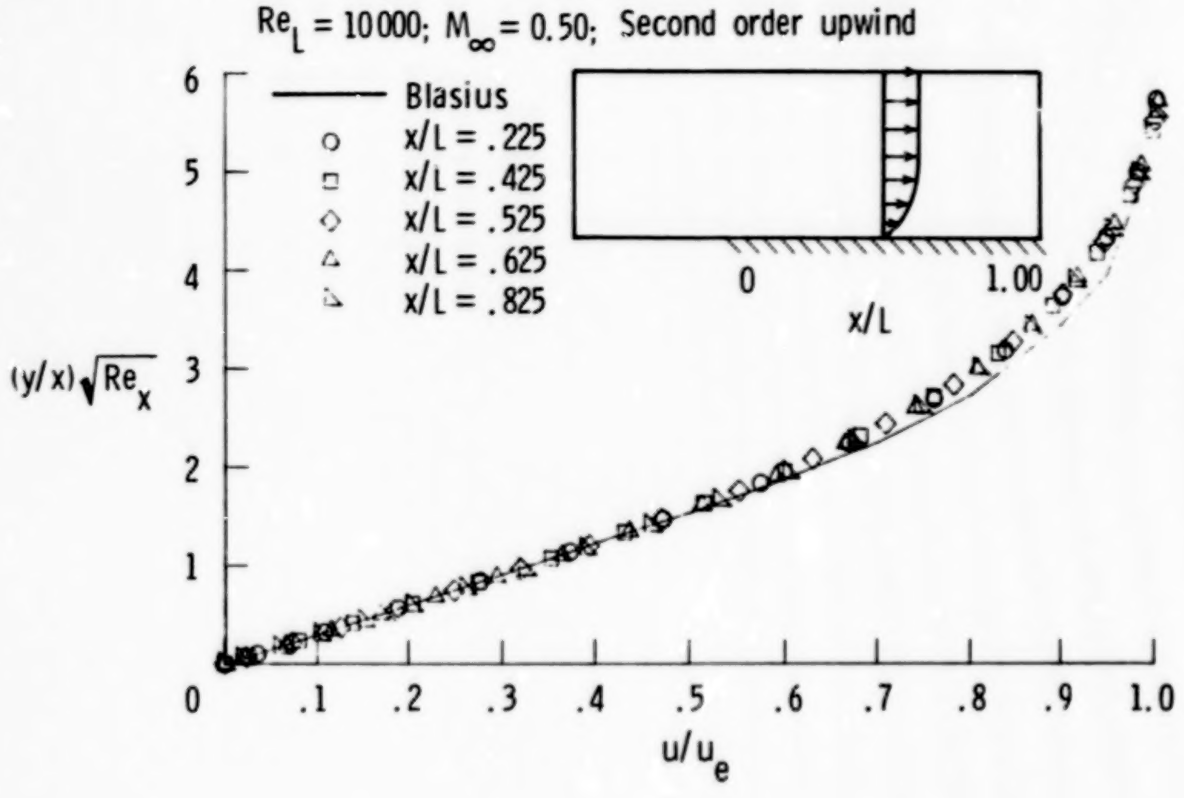

Flat-Plate Boundary Layer: Third-Order Differencing

Results are shown using third-order upwind-biased differencing ($\kappa = 1/3$) for the convective and pressure terms. The accuracy relative to the second-order differencing is evident by comparison with the previous figure. The third-order differencing can be implemented with only a very small additional computational effort relative to the second-order scheme, since the computational molecule for both schemes only involves five points in any one direction. Central difference methods and the present upwind method are formally of the same order (second order) for viscous flows and one should expect roughly the same truncation error level. This has been verified in the present effort both analytically and numerically. In contrast, first-order upwind differencing leads to a boundary layer thickness four to five times that shown.

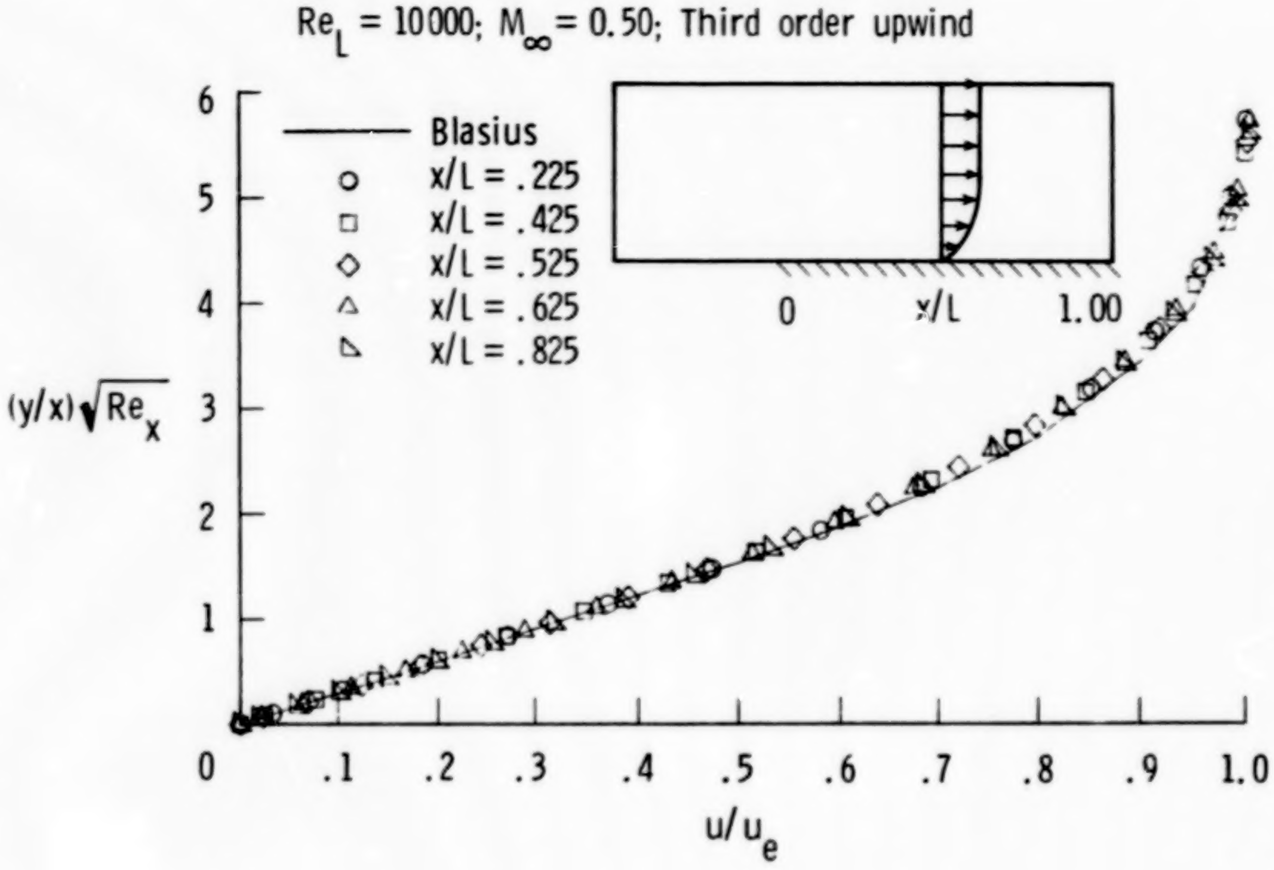

Shock-Boundary Layer Interaction

The final problem is that of an oblique shock wave impinging on a laminar boundary layer developing on a flat plate. The conditions correspond to the experiments of Hakkinen et al. (ref. 2) at a free-stream Mach number of 2.00 and a Reynolds number based on the length from the leading edge to the shock impingement point of 2.96×10^5. The shock is of sufficient strength to cause a separation of the developing laminar boundary layer, as evident in the computational results shown using thin-layer approximations to the Navier-Stokes equations. The pressure contours show the compression and expansion waves downstream of the shock impingement, which are caused by the interaction of the incoming shock wave with the separated boundary layer.

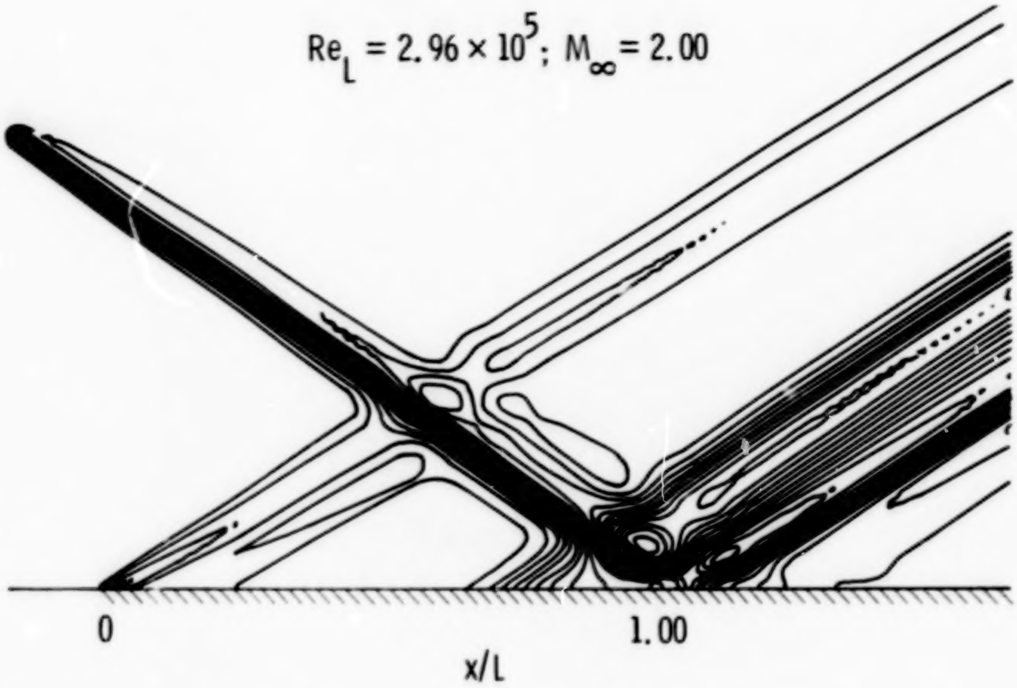

Shock-Boundary Layer Interaction: Grid Convergence

In order to assess the accuracy of the present upwind method, results from a grid convergence study are shown. Mesh densities two and three times the original grid were used. Details of the separated flow region are generally resolved with the second mesh, although a small difference exists between the second and third meshes near reattachment. Outside the separated flow region, very little difference in wall pressure exists in the results shown. The details in the present calculations clearly show the pressure plateau in the separation region.

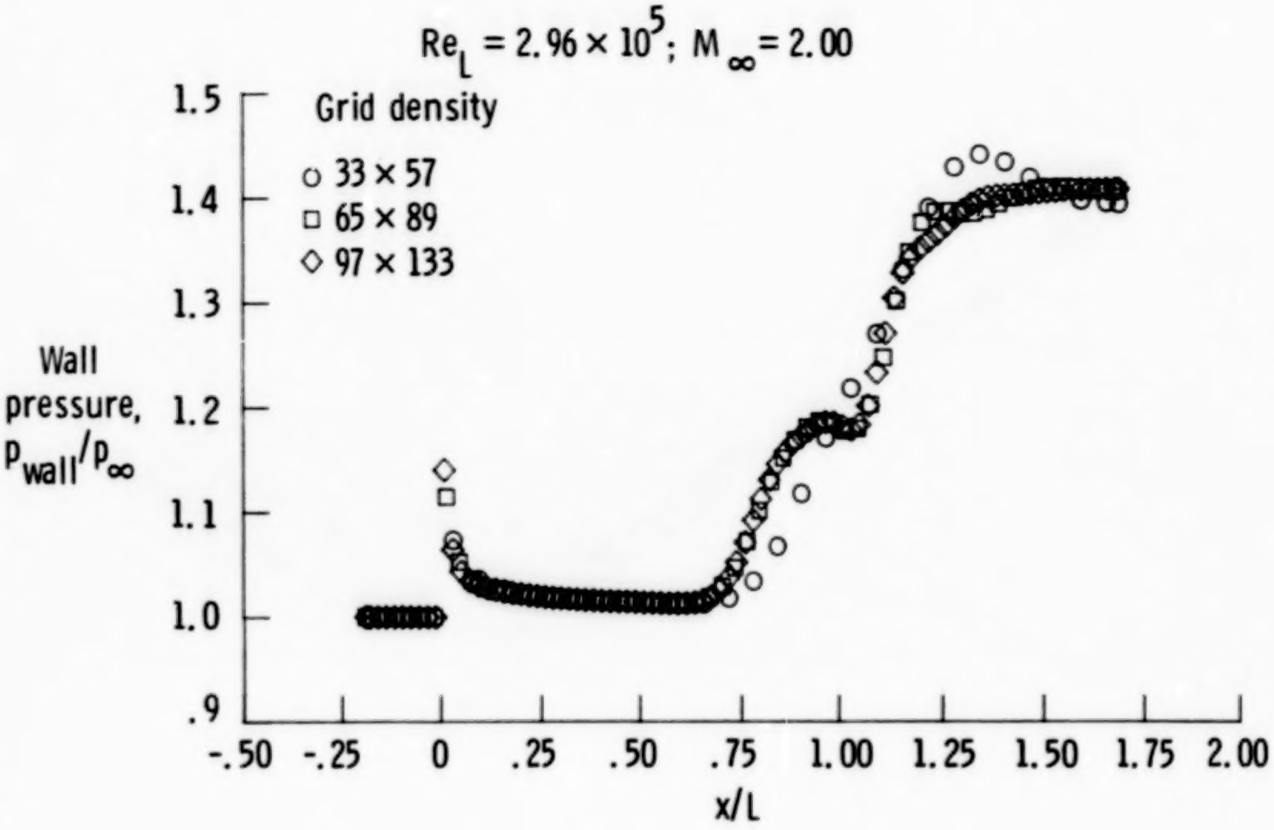

Shock-Boundary Layer Interaction: Skin Friction Coefficient

The skin friction coefficient predicted with the present method for the three meshes is shown. The skin friction exhibits three local extremum, two minimums and one maximum, in the separation zone. The separation extends from approximately 0.75 to 1.20 reference lengths from the leading edge of the plate.

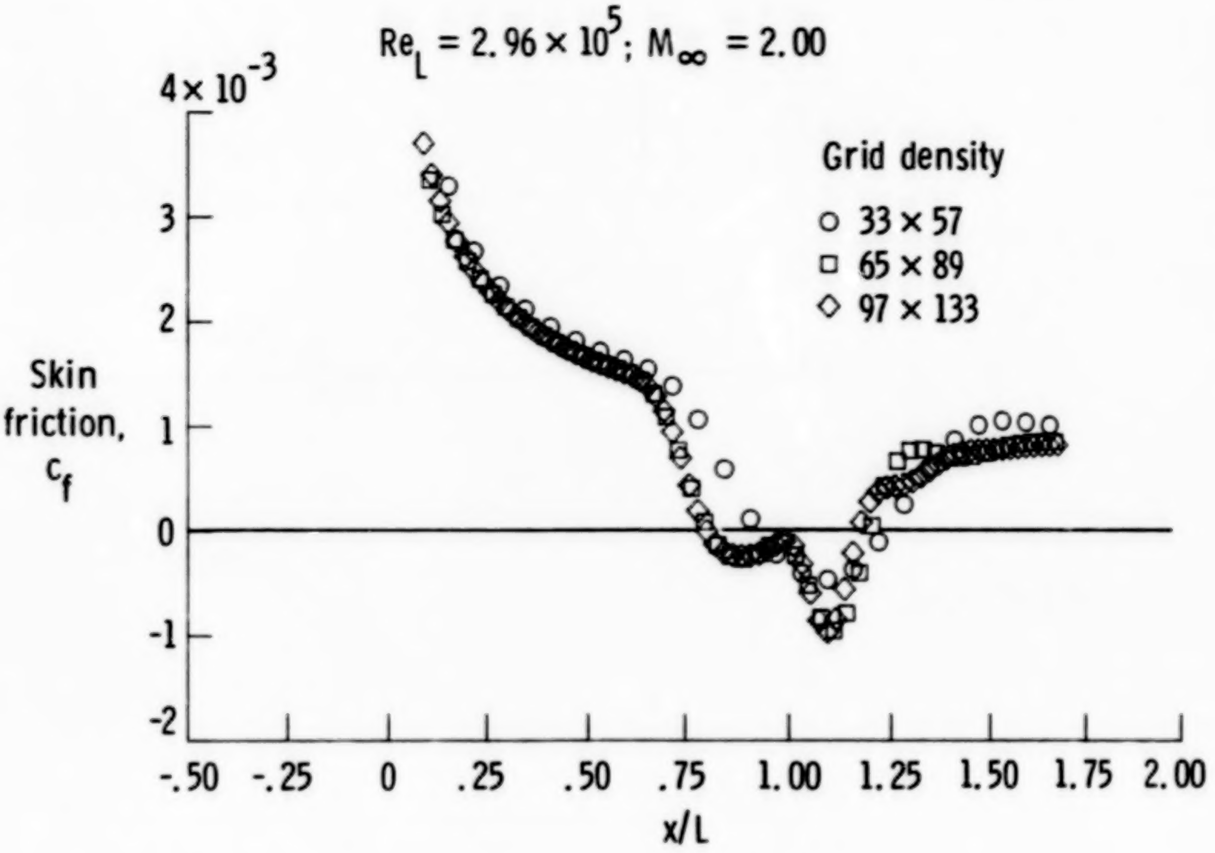

Shock-Boundary Layer Interaction: Wall Pressure and Skin Friction

A comparison of wall pressure and skin friction from the present results with experiment is shown. The pressure plateau and the extent of separation are closely predicted. The arrows in the figure indicate that only the presence of separation was deduced from the experiment; the actual level of skin friction in the separation was not measured.

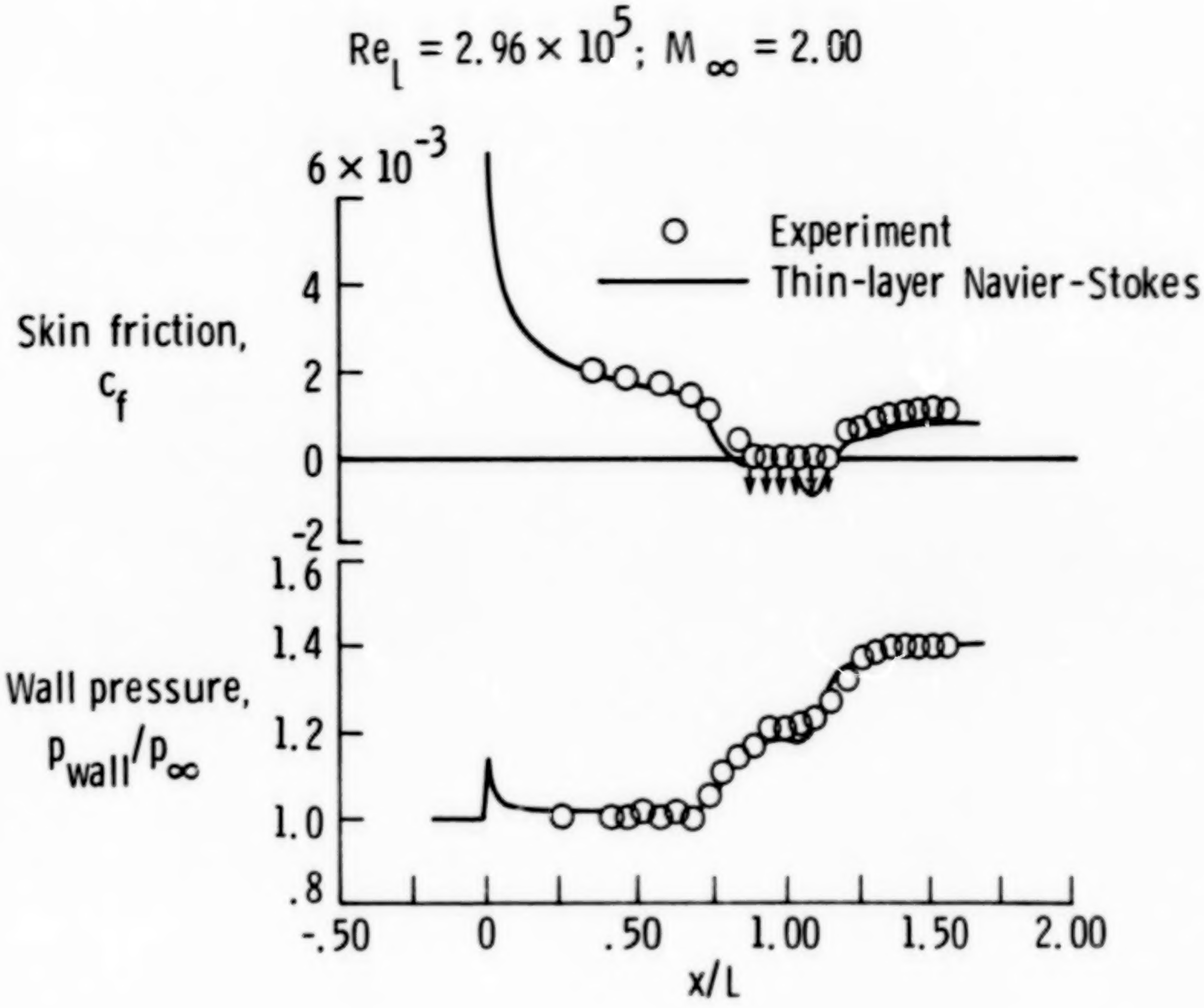

Concluding Remarks

Efficient solutions to steady-state Euler and Navier-Stokes equations are possible through the upwind relaxation algorithms discussed previously. The methods recover conventional space marching methods for fully supersonic flows and can be shown to be unconditionally stable in three dimensions. Accurate solutions to several inviscid and viscous model problems, including flat-plate boundary layer flow and shock/boundary layer interaction with separation, have been demonstrated. The method is currently being implemented in three dimensions.

Efficient solutions to steady-state equations possible through upwind relaxation

- Recovers space marching method for supersonic flows
- Unconditionally stable in three dimensions

Accurate solutions to several viscous flows demonstrated using second/third-order upwind differencing for convective and pressure terms

- Flat plate boundary layer
- Shock/boundary-layer interaction with separation

D6

N88-14932

56-02

117230

27P

A MULTISTAGE TIME-STEPPING SCHEME FOR THE THIN-LAYER NAVIER-STOKES EQUATIONS

R. C. Swanson, Jr.
NASA Langley Research Center
Hampton, Virginia

Eli Turkel
Tel Aviv University
Tel Aviv, Israel

V. N. Vatsa
NASA Langley Research Center
Hampton, Virginia

PRECEDING PAGE BLANK NOT FILMED

PAGE 108 INTENTIONALLY BLANK

[redacted]ITE-VOLUME FORMULATION

The integral form of the conservation laws for mass, momentum, and energy is given in equation (1). The solution vector

$$W = \left[\rho,\ \rho u,\ \rho v,\ \rho E\right]^T,$$

where ρ, (u,v), and E denote the density, Cartesian velocity components, and total internal energy, respectively. The quantities F and G are flux vectors. The variables x and y are Cartesian coordinates, and t represents time. In equation (1), Ω denotes the region of interest and $\partial\Omega$ is the boundary curve. If the computational region is partitioned with quadrilaterals and equation (1) is applied to each one, a system of ordinary differential equations is obtained. One of these equations is given in the figure. The quantity S is the area of the cell being considered. The vector W is evaluated at the cell center, and the indices i and j identify the cell.

$$\frac{\partial}{\partial t}\iint_{\Omega} W dx dy + \int_{\partial\Omega} (F dy - G dx) = 0 \qquad (1)$$

Applying Eq. (1) to the quadrilateral ABCD

$$\frac{d}{dt}\left(S_{ij}W_{ij}\right) + \left(H_{AB} + H_{BC} + H_{CD} + H_{DA}\right) = 0$$

where

$H_{AB}, H_{BC}, H_{CD}, H_{DA}$ -- fluxes through sides of cell

ORIGINAL PAGE IS
OF POOR QUALITY

FINITE-VOLUME MESH

The fluxes H_{AB}, H_{BC}, H_{CD}, H_{DA}, in the case of the momentum equations, account for momentum flow into and out of a cell by convection and by molecular transport. If the thin-layer Navier-Stokes equations are considered, viscous fluxes are included in only H_{BC} and H_{DA}. Consider cell face BC. The viscous stresses at this face are determined by applying Green's theorem to cell A'B'C'D'. In a similar manner, the viscous stresses at cell face DA are obtained.

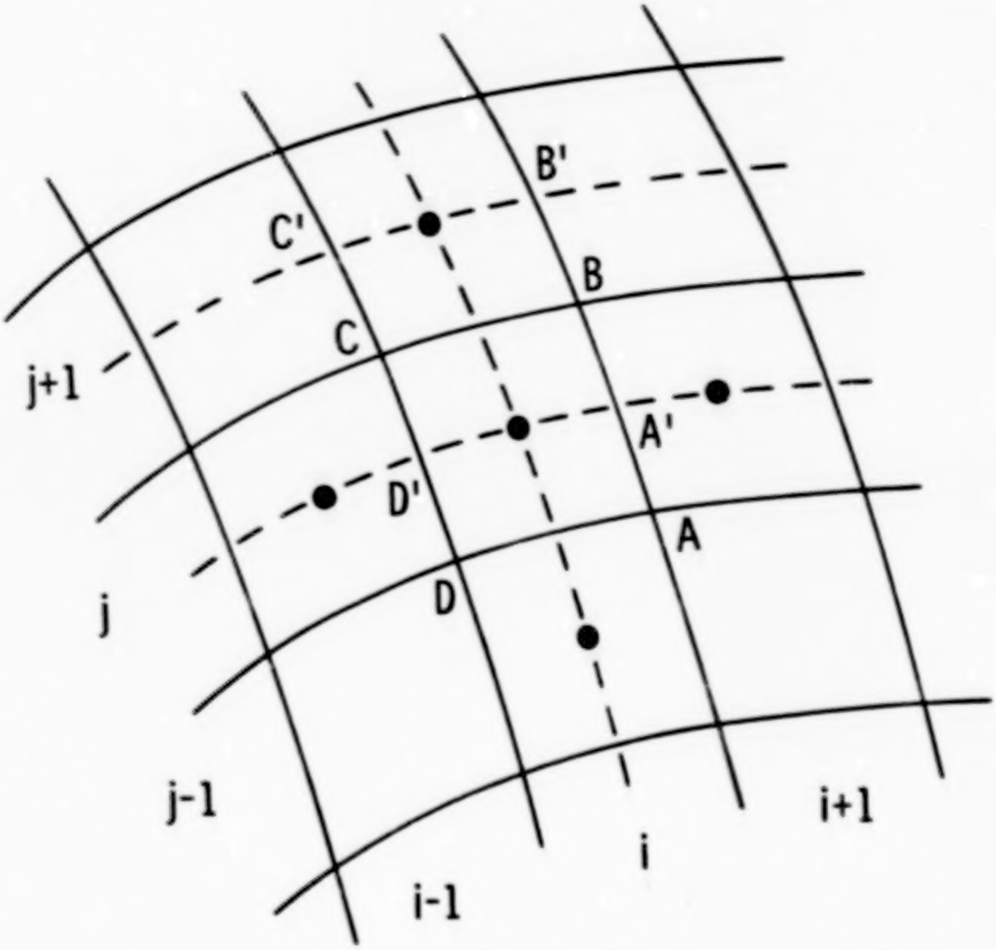

NUMERICAL PROCEDURE

In this figure, the basic elements of the present procedure for the numerical solution of the thin-layer Navier-Stokes equations are given. A modified four-stage Runge-Kutta scheme is used to advance the solution in time. Artificial dissipation terms are added to the difference equations, and they are third order in smooth regions of the flow field. These terms are included for several reasons: (1) to enhance the coupling of the difference equations, (2) to control nonlinear instabilities, and (3) to eliminate oscillations at shock waves. Three techniques are employed to accelerate convergence to steady state. With local time stepping, the solution at any point in the domain is advanced at the maximum time step allowed by stability. This results in faster signal propagation and thus faster convergence. Enthalpy damping involves, in general, adding damping terms to the flow equations that are proportional to the difference between the local total enthalpy and the free-stream value. These terms vanish at steady state. Finally, residual smoothing is an implicit procedure to extend the local stability range.

- Modified four-stage Runge-Kutta scheme

- Artificial dissipation terms added (blending of 2nd and 4th differences)

- Acceleration techniques
  (1) Local time stepping
  (2) Enthalpy damping
  (3) Residual smoothing--extend stability range

NUMERICAL PROCEDURE

The computer code for the scheme is vectorized for efficient processing. The algebraic method of LeBalleur (ref. 1) is used to construct C-type meshes for airfoil calculations. The algebraic eddy viscosity model of Baldwin and Lomax (ref. 1) is employed for turbulence closure.

- Computing efficiency enhancement -- vectorization of scheme
- Algebraic mesh generation -- C-type for airfoils
- Algebraic turbulence model -- Baldwin-Lomax

FOUR-STAGE TIME-STEPPING SCHEME

The four-stage scheme presented in the figure is used to integrate the flow equations in time. The quantities R, L, and D are spatial discretization operators. The operator L is associated with convection, and the operator D is associated with the physical viscous terms and artificial dissipation terms. The terms of D operating on W are evaluated at the first stage and frozen for the remaining stages. For the given values of α_i $(i = 1,2,3)$, this scheme is second-order accurate in time for nonlinear problems. The advantage of the modified scheme over the standard Runge-Kutta scheme is that it requires less array storage in computer processing (an important consideration for three-dimensional problems). Central difference operators are employed for the spatial derivatives in the flow equations. The scheme is second-order accurate in space for sufficiently smooth grids.

$$W^{(1)} = W^n - \alpha_1 \Delta t R W^n$$

$$W^{(2)} = W^n - \alpha_2 \Delta t R W^{(1)}$$

$$W^{(3)} = W^n - \alpha_3 \Delta t R W^{(2)}$$

$$W^{(4)} = W^{n+1} = W^n - \Delta t R W^{(3)}$$

where on the $(q + 1)$ st stage

$$RW^{(q)} = \frac{1}{S}\left(LW^{(q)} - DW^n\right)$$

and

$$\alpha_1 = 1/4,\ \alpha_2 = 1/3,\ \alpha_3 = 1/2$$

ENTHALPY DAMPING

In the present work, a damping term is added to the energy equation only. Note that in the absence of viscous terms, the total enthalpy (H) is constant throughout the flow field if there is a uniform free stream. In the case of viscous flows, constant H can be a solution of the energy equation. Moreover, if the dominant viscous terms (boundary-layer type approximations) are retained in the flow equations, the equation at the bottom of the figure is obtained. Then, if the Prandtl number is unity and the solid boundaries are adiabatic, constant H is a solution of the energy equation. With similar assumptions, the total enthalpy can be shown to be constant for turbulent flows. As indicated previously, enthalpy damping can accelerate convergence. It is especially helpful during the initial time steps of a calculation. At the present time, we are investigating other forms of damping so as to not preclude the capability to solve problems where heat-transfer effects are important.

Consider the energy equation

$$\frac{\partial}{\partial t}(\rho E) + \frac{\partial}{\partial x}(\rho u H) + \frac{\partial}{\partial y}(\rho v H) + \underbrace{\alpha \rho (H - H_{\infty})}_{\text{damping term}} = \text{viscous terms} \qquad (1)$$

Retaining the dominant viscous terms, we obtain for laminar flow

$$\text{LHS (1)} = \frac{\partial}{\partial y}\left\{\frac{\mu}{Pr}\left[\frac{\partial}{\partial y}(H) + (Pr - 1)\frac{\partial}{\partial y}\left(\frac{u^2}{2}\right)\right]\right\}$$

RESIDUAL SMOOTHING

In this figure, some details of implicit residual smoothing are examined. A two-step scheme is considered. The quantity L is the spatial discretization operator. If residual smoothing is applied to the second stage, the factored form given in the figure is used. In this equation, the product symbol is taken over the number of spatial dimensions (ℓ), β is the smoothing parameter, and δ_{XX} is the standard central difference operator. The quantities $\left(u^{n+1} - u^n\right)$ and $\left(u^{(2)} - u^n\right)$ are the updated and explicit residuals, respectively. If β is sufficiently large, the scheme is unconditionally stable. However, as revealed through linear stability analyis, the fastest convergence to steady state is not realized with a very large time step.

Consider the two-step scheme

$$u^{(1)} = u^n - \alpha \Delta t L u^n$$

$$u^{(2)} = u^n - \Delta t L u^{(1)}$$

Residual smoothing for the second stage is given by

$$\prod_{\ell} \left(1 - \frac{\beta_\ell}{4} \delta_{xx}^{(\ell)}\right)\left(u^{n+1} - u^n\right) = u^{(2)} - u^n$$

where δ_{xx} is central difference operator.

COMPUTATIONAL DOMAIN FOR AIRFOIL CALCULATIONS

This figure shows a sketch of the computational domain for airfoil calculations. The outer boundary (ABC) is a C-type curve, and it reflects the type of mesh used.

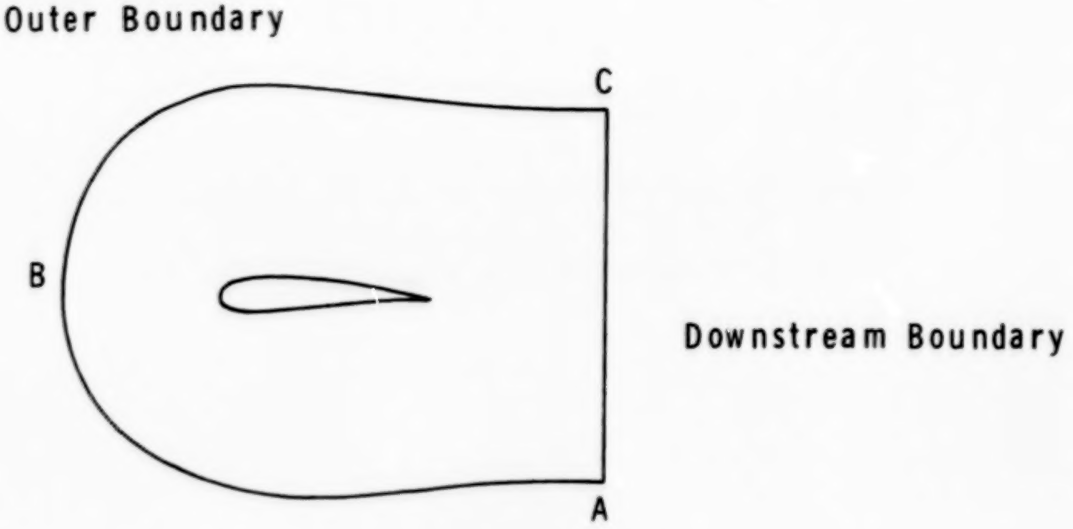
Outer Boundary
C
B
Downstream Boundary
A

BOUNDARY CONDITIONS

During a calculation, a test is performed to determine if there is inflow or outflow at a given location along the outer boundary curve. If there is inflow, the total enthalpy H, entropy S, and tangential velocity component U are specified. If there is outflow, the Riemann invariant is specified. The quantities V, a, and γ are the normal velocity component, speed of sound, and specific heat ratio, respectively.

- SURFACE BOUNDARY
  - (1) No slip
  - (2) Adiabatic condition
- OUTER BOUNDARY
  - (1) Inflow--specify H, S, U
  - (2) Outflow--specify Riemann invariant

$$V - \frac{2a}{\gamma-1}$$

- DOWNSTREAM BOUNDARY--SPECIFY P

TURBULENT FLAT-PLATE FLOW

The Runge-Kutta time-stepping scheme was used to compute turbulent flow ($M_\infty = 0.5$, $Re_\infty = 10^6$) over a semi-infinite flat plate. In the figure on the left, the variation of the skin friction (based on free-stream conditions) with local Reynolds number is presented. The computed result is compared with an incompressible correlation. There is fairly good agreement except in the leading-edge region. Note that since the thin-layer Navier-Stokes equations were solved in the calculation, no attempt was made to resolve the leading-edge region of the plate. In the figure on the right, velocity profiles at X/L = 0.875 are compared. The present result agrees very well with that obtained with the implicit code of Steger (uses Beam and Warming scheme, ref. 1).

($M = 0.5$, $Re = 10^6$)

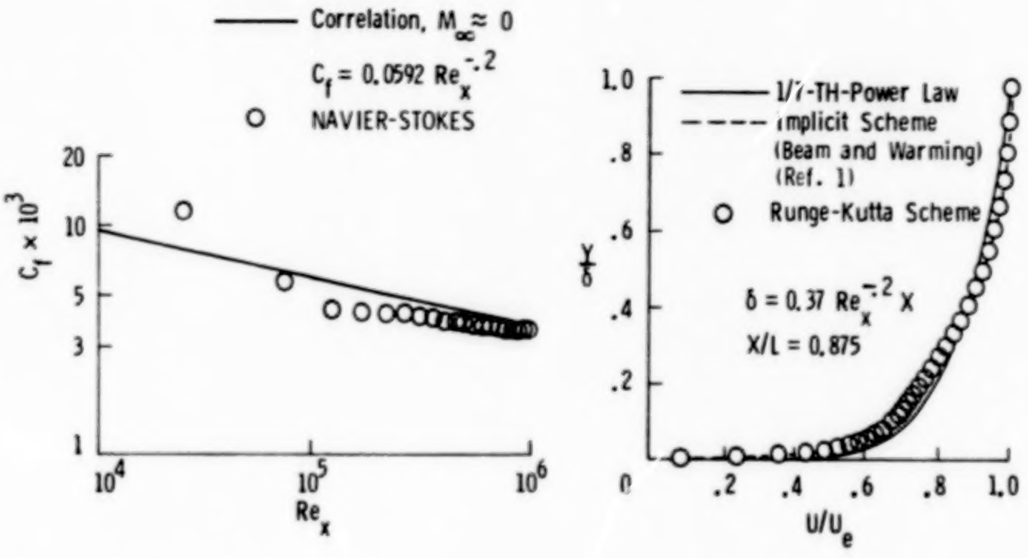

PARTIAL VIEW OF AIRFOIL GRID

This figure shows a partial view of a representative C-type grid used in airfoil calculations. There is grid clustering in the leading- and trailing-edge regions of the airfoil. In addition, there is fine mesh spacing adjacent to the airfoil surface in order to resolve the boundary layer.

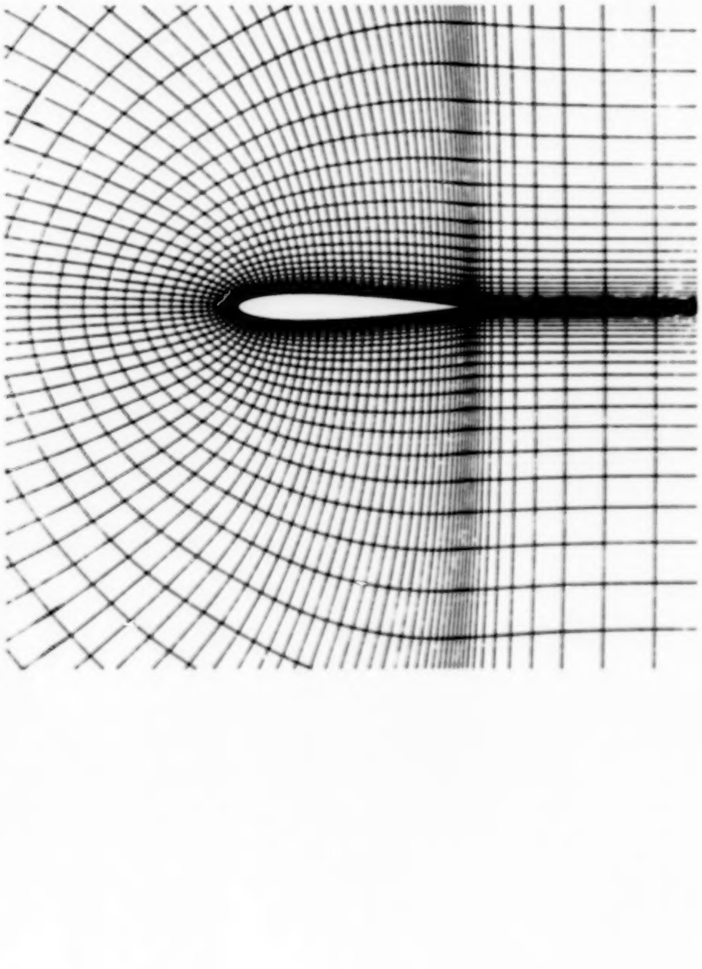

LAMINAR FLOW OVER AN NACA 0012 AIRFOIL

This figure shows results for laminar flow over an NACA 0012 airfoil. The free-stream Mach number and Reynolds number for this case are 0.5 and 5×10^3, respectively. In the figure on the left, the variation of pressure coefficient with nondimensional axial distance (X/C, where C is the airfoil chord) is presented. The viscous solution is compared with the inviscid solution. There are significant viscous effects in the leading- and trailing-edge regions. In the figure on the right, the computed skin-friction distribution is shown. Flow separation is indicated at the 0.82 chord location.

$(M = 0.5, \ Re = 5 \times 10^3, \ \alpha = 0)$

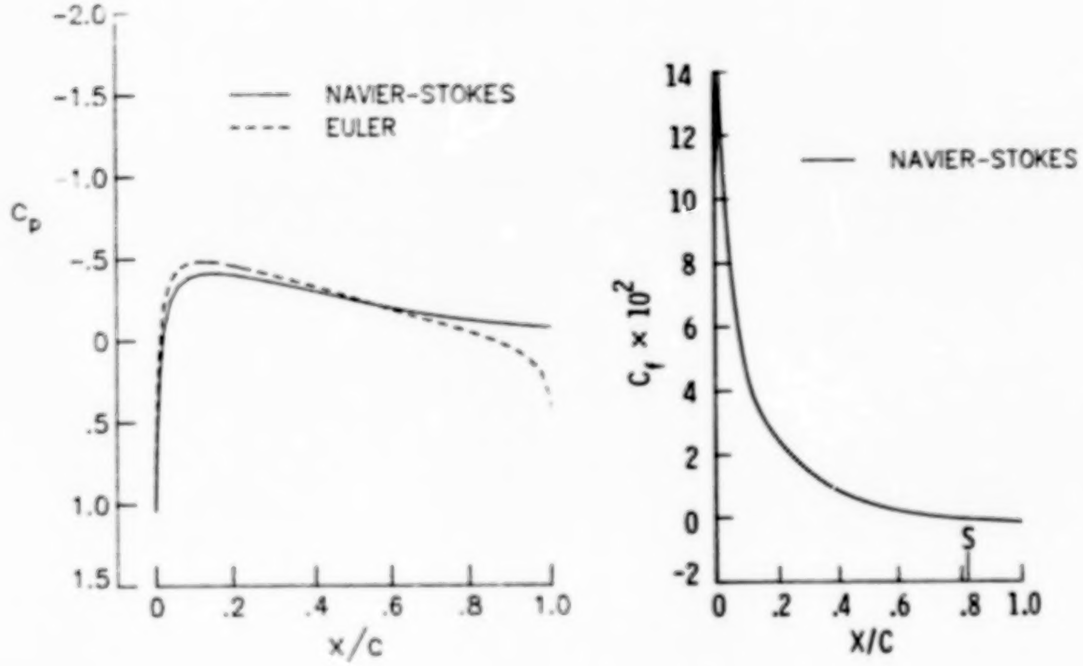

LAMINAR AIRFOIL FLOW---STREAMLINES

This figure shows the streamlines on the upper trailing-edge surface of the airfoil. The indicated separation bubble is thin and elongated. Since the velocities inside the bubble are small, accuracy of the solution is of special concern. Therefore, two calculations were done. In the first case, the grid consisted of 128 cells around the airfoil and 32 cells in the normal-like direction. In the second case, a 128×64 mesh was used. The cell spacing in the normal-like direction was half as large. The solutions were essentially the same except for the reverse flow region. This region was about 7 percent larger in longitudinal extent in the finer grid case.

(M = 0.5, Re = 5×10^3, α = 0)

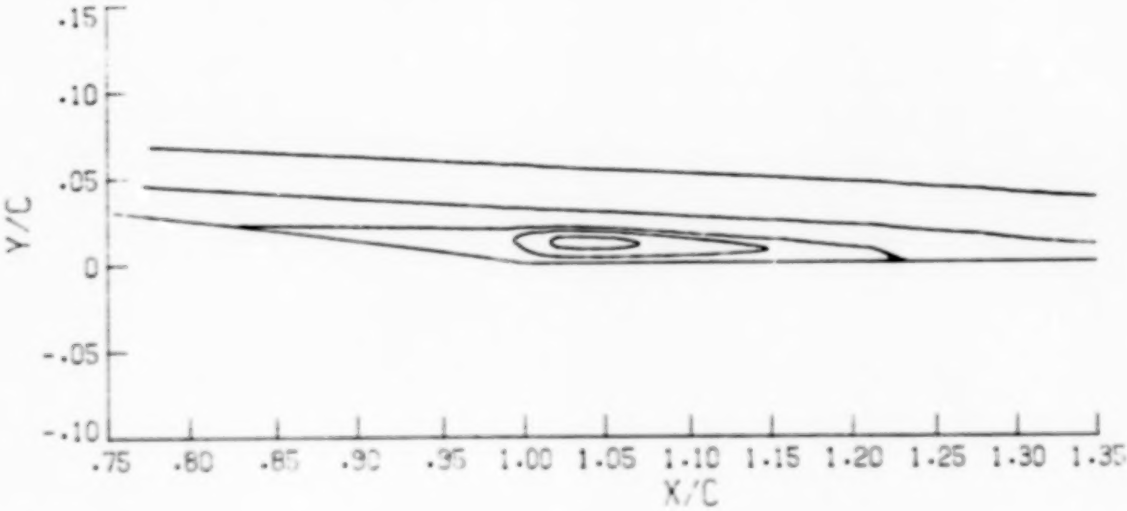

TURBULENT FLOW OVER AN NACA 0012 AIRFOIL

Pressure and skin-friction distributions for turbulent flow over an NACA 0012 airfoil ($M_\infty = 0.5$, $Re_\infty = 2.89\times10^6$) are presented in this figure. There is good agreement between the computed and experimental pressure distributions. In the figure on the right, the skin-friction distribution calculated with the present Navier-Stokes code is compared with that determined with a boundary-layer code. The mesh spacing at the surface in the boundary-layer calculation was more than an order of magnitude smaller than that used in the Navier-Stokes calculation. There is fairly good agreement between these solutions except in the immediate vicinity of the airfoil leading edge. The present solution probably does not have adequate resolution of the very thin turbulent boundary layer at the leading edge.

($M = 0.5$, $Re = 2.89\times10^6$, $\alpha = 0$)

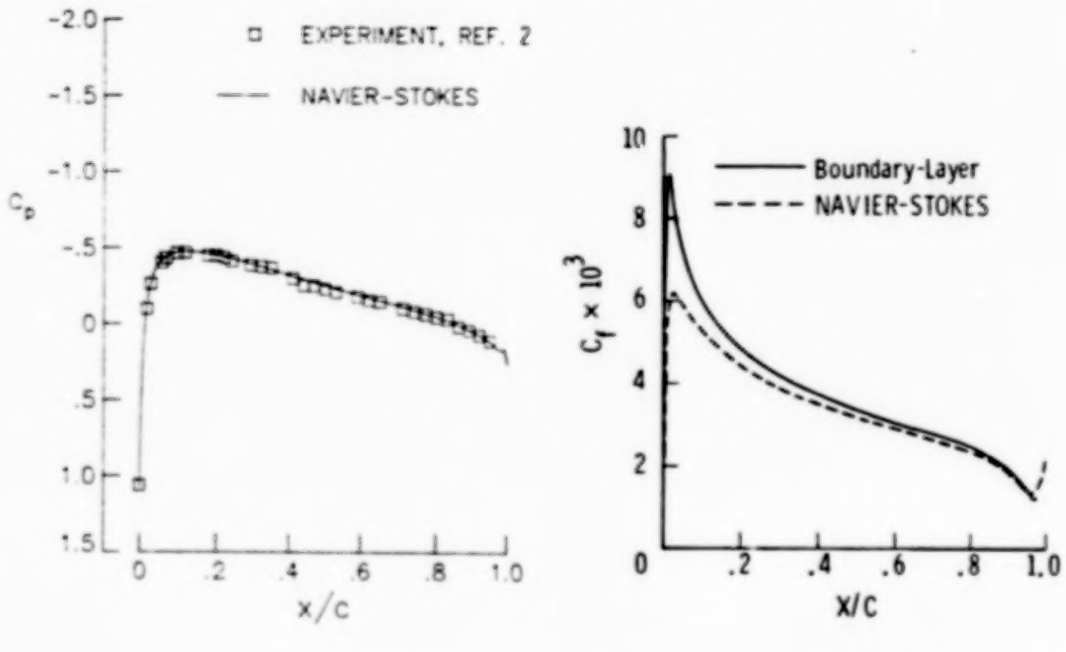

SUBSONIC FLOW OVER AN NACA 0012 AIRFOIL

In this figure, the predicted pressure distribution for subsonic viscous flow ($M_\infty = 0.5$, $Re_\infty = 2.93\times10^6$) over an NACA 0012 airfoil at angle of attack (3.51°) is compared with that for inviscid flow and with experimental data. The angle of attack has been corrected for wind tunnel wall effects. There is good agreement between the present Navier-Stokes results and experiment. The influence of viscosity on this solution, in particular at the suction peak, is evident.

($M = 0.5$, $Re = 2.93\times10^6$, $\alpha = 3.51$)

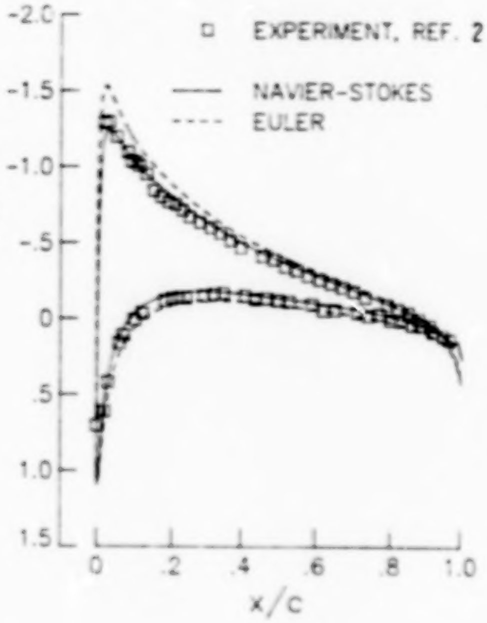

	C_L
EXP.	0.386
VISCOUS	0.388
INVISCID	0.429

TRANSONIC FLOW OVER AN NACA 0012 AIRFOIL

This figure presents pressure distributions for transonic flow (M_∞ = 0.756, Re_∞ = 4.01×10^6) over an NACA 0012 airfoil. The results from the viscous and inviscid calculations show good agreement with the experimental data. The shock in this case is very weak, and this is evident in the Mach number contours in the next figure.

(M = 0.756, Re = 4.01×10^6, α = 0)

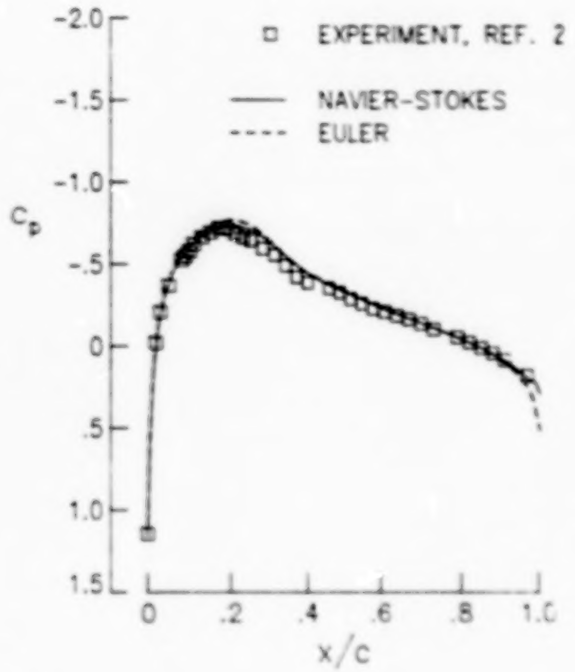

ORIGINAL PAGE IS
OF POOR QUALITY

MACH NUMBER CONTOURS

The supersonic region is indicated in this figure.

$(M = 0.756, \ Re = 4.01 \times 10^6)$

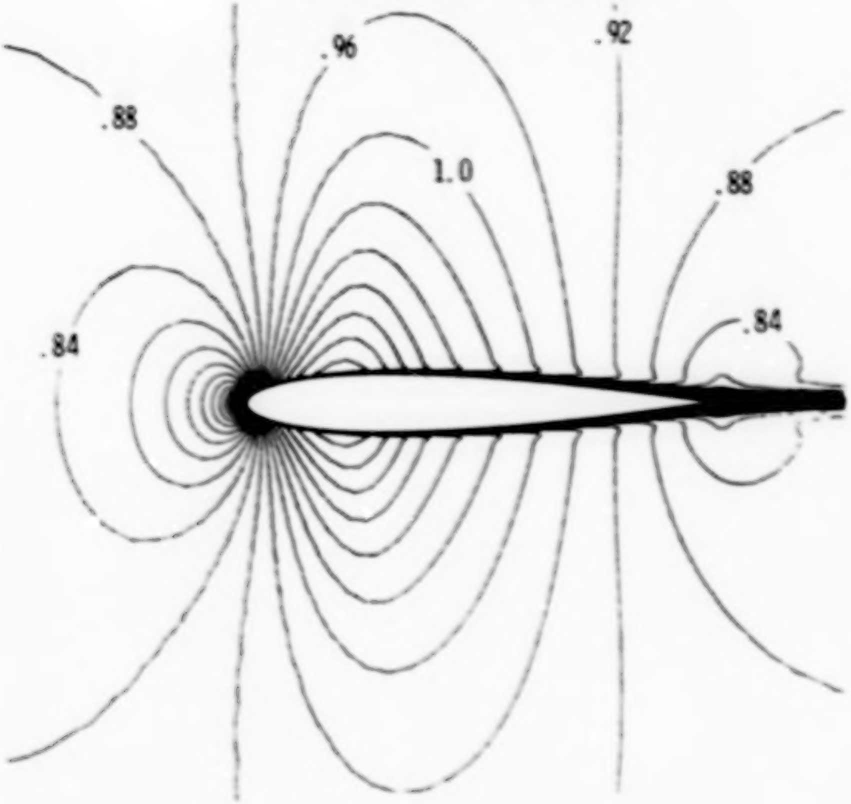

TRANSONIC FLOW OVER AN RAE 2822 AIRFOIL

This figure shows the pressure distribution for supercritical flow over an RAE 2822 airfoil. The free-stream Mach number and Reynolds number are 0.730 and $6.5\text{x}10^6$, respectively. The wind tunnel corrected angle of attack is 2.79°. Transition of the boundary layer was fixed at the experimental value of 3-percent chord. In this calculation, a C-type grid with 260 cells around the airfoil and 96 cells in the normal-like direction was used. There is good agreement between the computed and experimental pressure distributions. The predicted lift and drag coefficients are also compared with those of the experiment.

($M = 0.730$, $Re = 6.5\text{x}10^6$, $\alpha = 2.79$)

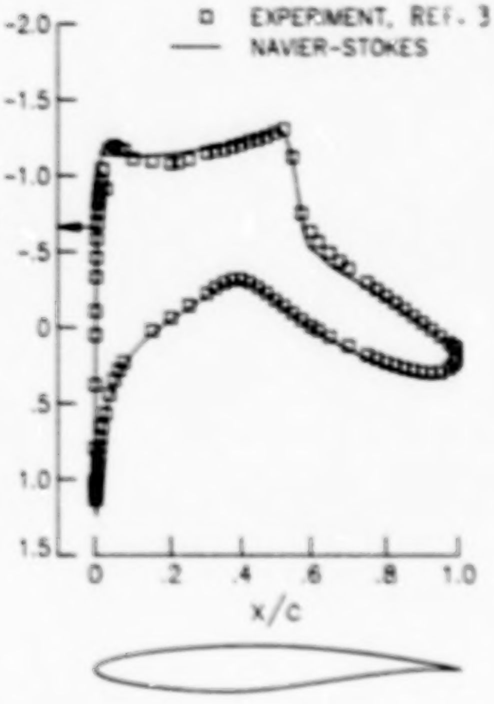

	C_L	C_D
EXP.	0.803	0.0168
VISCOUS CALC.	0.820	0.0193

UPPER SURFACE SKIN FRICTION FOR RAE 2822 AIRFOIL

This figure presents a comparison of the calculated and experimental skin-friction distributions. The skin-friction coefficient is based on boundary-layer edge conditions. In general, there is fairly good agreement with the experimental data. However, the computation shows a small shock-induced separation bubble and incipient trailing-edge separation, which are not indicated by the experimental data. The present computed result is generally consistent with those of other investigators. The predicted rise in skin friction at the airfoil trailing edge is probably due to inadequate representation by the basic Baldwin-Lomax algebraic eddy viscosity model of the transition from the wall boundary layer to the free shear layer.

($M = 0.730$, $Re = 6.5 \times 10^6$, $\alpha = 2.79$)

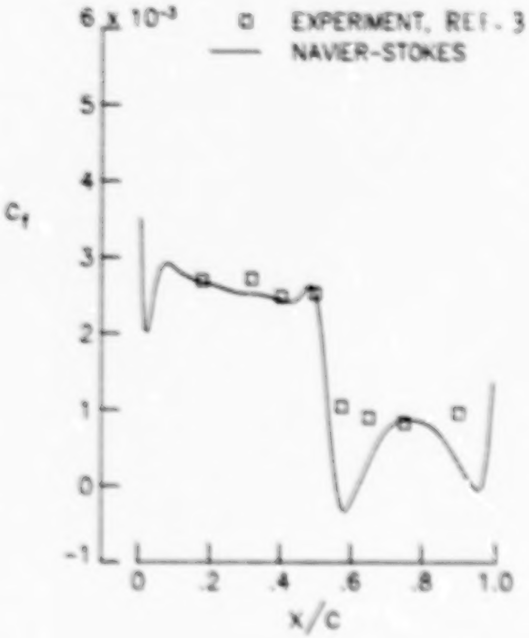

CONVERGENCE HISTORIES FOR LAMINAR AIRFOIL FLOW

This figure displays variations of the common logarithm of the root mean square of the residual of the continity equation with the number of time steps. Curve A shows the residual decay when enthalpy damping is added to the Runge-Kutta time-stepping scheme. Curve B indicates the improvement in the convergence rate with the inclusion of implicit residual smoothing. Satisfactory convergence for engineering applications is achieved in 1,300 time steps, which corresponds to 2.5 minutes on the Vector Processing System (VPS) 32 at Langley Research Center.

(M = 0.5, Re = 5×10^3, α = 0, 128x32 GRID)

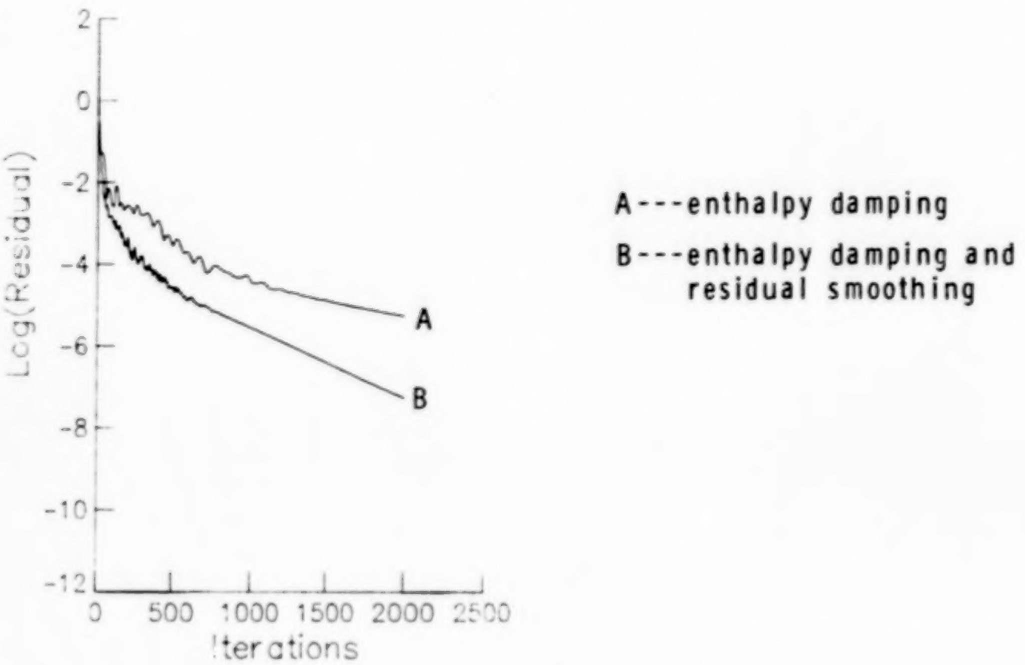

CONVERGENCE HISTORIES FOR TURBULENT AIRFOIL FLOW

The figure on the left shows the convergence history when only local time stepping is employed to accelerate convergence. This convergence history is highly oscillatory. In the figure on the right, the convergence behavior for a computation using enthalpy damping and residual smoothing is much more monotonic. For this case, acceptable convergence is realized in about 1,250 time steps (4 minutes on the VPS-32). Note that the present computer code is not optimized for the VPS-32 system. With optimization the computer processing times can be reduced by a factor of 2 to 3. In conclusion, the final rate of reduction of the residual for the turbulent flow cases can be quite slow. Based on previous work with Euler equations, significant improvement in this rate appears to be possible with a multigrid scheme. At the present time, this is being investigated.

(M = 0.5, Re = 2.89×10^6, α = 0, 120x50 GRID)

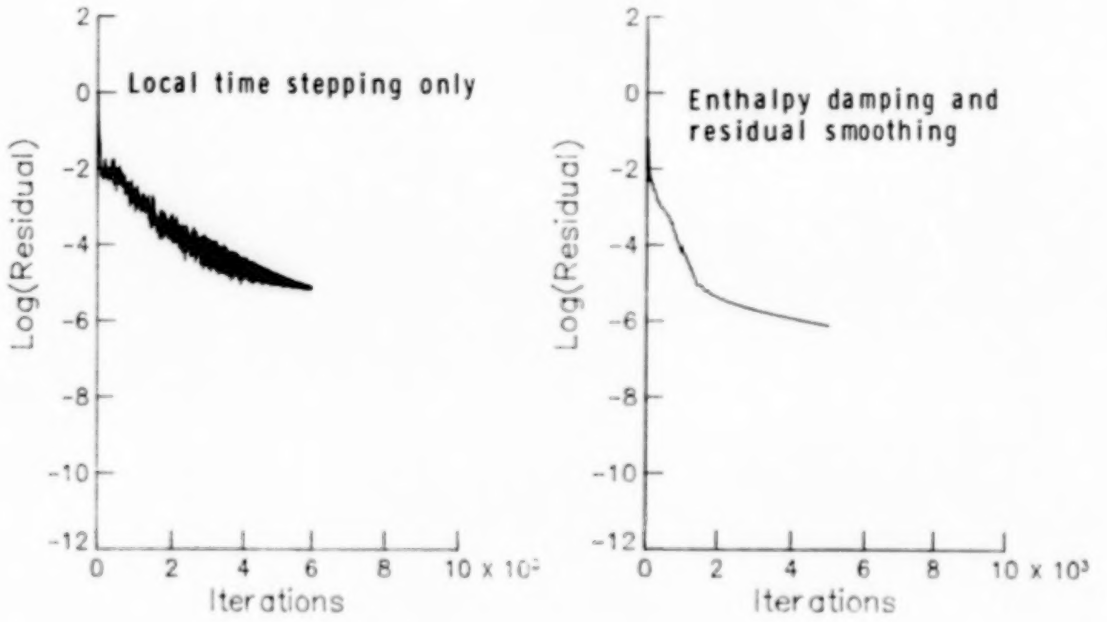

THIN-LAYER NAVIER-STOKES (LAMINAR) SOLUTIONS FOR INFINITE RECTANGULAR WING

In this figure, the velocity profiles computed from two- and three-dimensional thin-layer Navier-Stokes codes are compared at selected axial locations for an infinite, rectangular wing. The wing is constructed with constant chord NACA 0012 airfoil sections. Numerical solutions for this configuration were obtained at $M_\infty = 0.5$ and $Re_c = 5000$. A 96×32 C-grid at each spanwise station was employed, and a total of four spanwise stations were used for the three-dimensional calculations. As expected, the solutions at each spanwise station were identical; and, as indicated by the results shown in this figure, these are in excellent agreement with the solutions obtained from two-dimensional analysis.

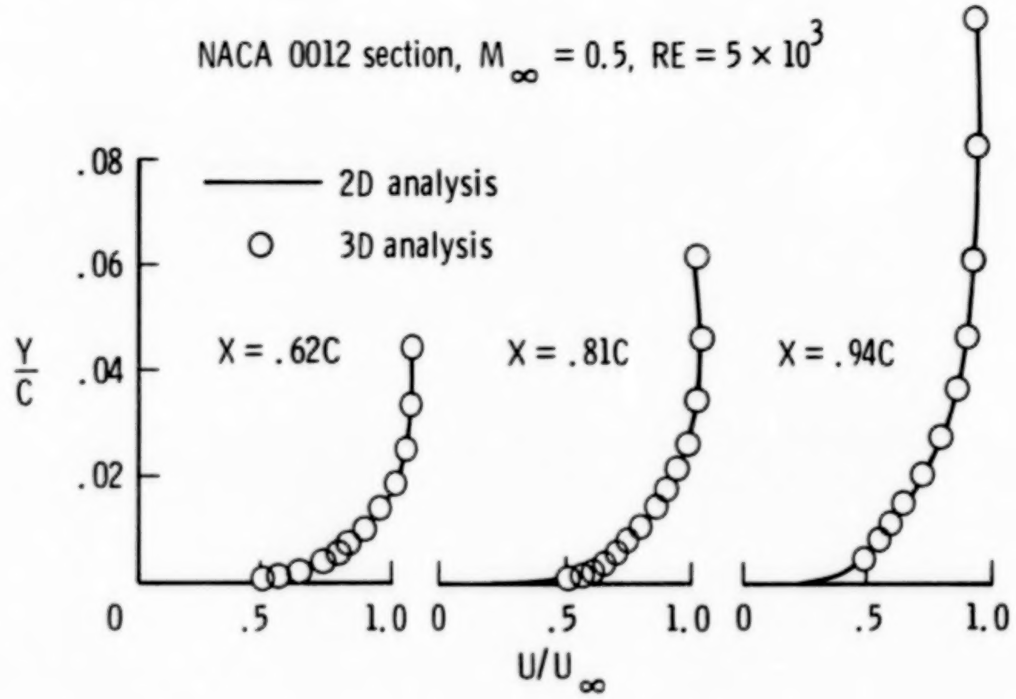

THIN-LAYER NAVIER-STOKES (TURBULENT) SOLUTIONS FOR INFINITE RECTANGULAR WING

The configuration selected for the results shown in this figure is identical to the one shown in the previous figure. However, the flow here is assumed to be fully turbulent and the Reynolds number is taken to be 2.89×10^6. A 120×50 C-grid was employed in each cross section for these calculations. Again, the results from the two- and three-dimensional analyses are found to be in excellent agreement.

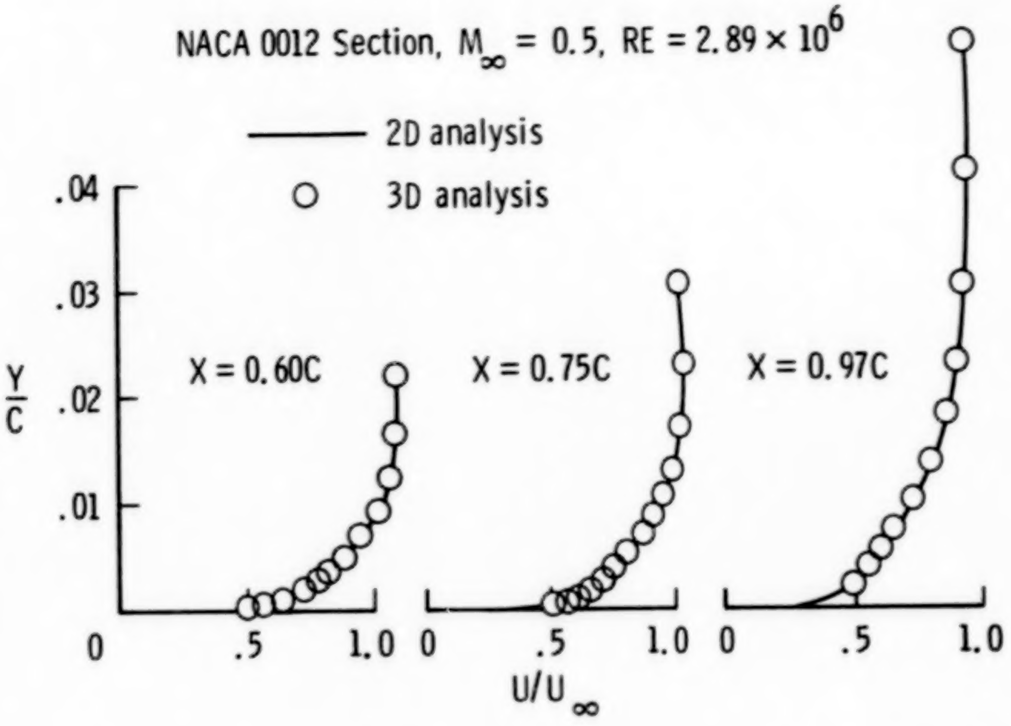

PARTIAL VIEW OF GRID EMPLOYED FOR WING CALCULATIONS

A partial view of a typical grid employed for wing calculations is shown in this figure. A C-H type grid topology is employed here; i.e., sections of C-type grids are stacked at various spanwise stations. Strong grid-clustering is employed near the wing surface to resolve extremely thin turbulent boundary layers that develop at high Reynolds numbers. The grid is also clustered near leading- and trailing-edge regions of the airfoil. A 121×51×17 grid is selected for an initial set of calculations.

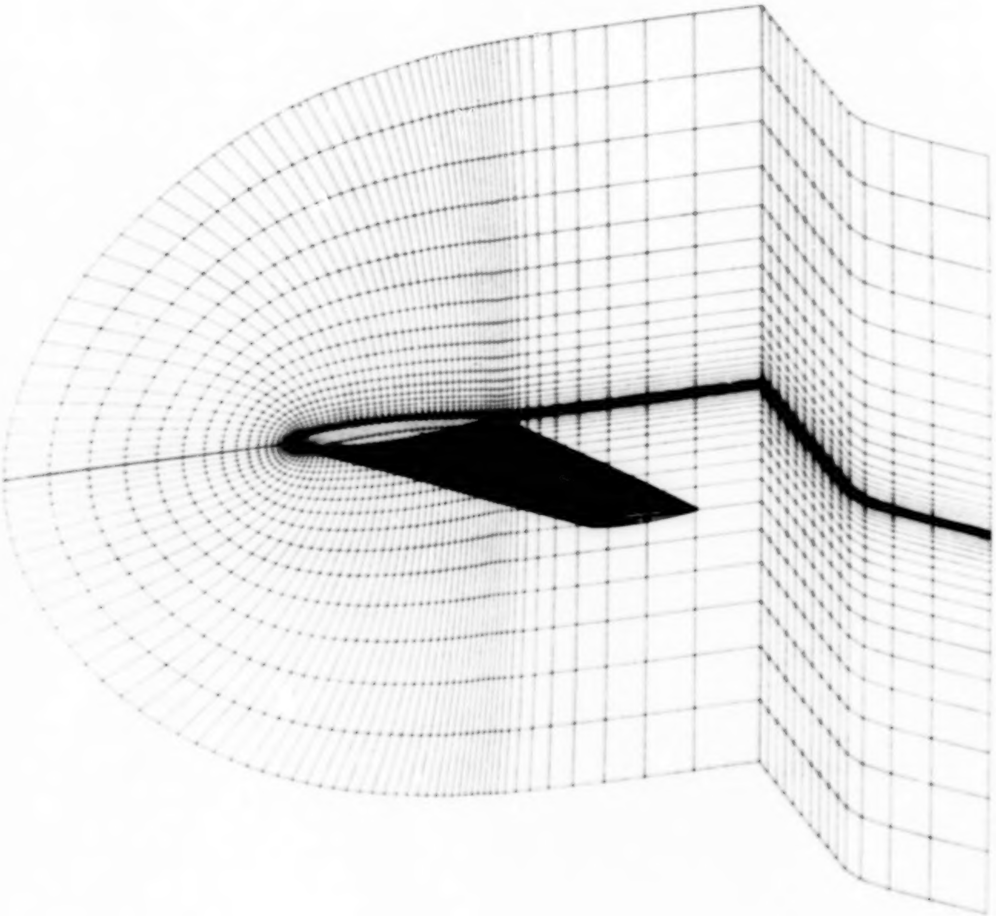

CONCLUDING REMARKS

A finite-volume scheme for numerical integration of the Euler equations has been extended to allow solution of the thin-layer Navier-Stokes equations in two and three dimensions. The extended algorithm, which is based on a class of four-stage Runge-Kutta time-stepping schemes, has been made numerically efficient through the following convergence acceleration techniques: (1) local time stepping, (2) enthalpy damping, and (3) residual smoothing. Also, the high degree of vectorization possible with the algorithm has yielded an efficient program for vector processors. The scheme has been evaluated by solving laminar and turbulent flows. Numerical results have compared well with either theoretical or other numerical solutions and/or experimental data.

- Algorithm for Navier-Stokes equations constructed from a class of explicit multistage time-stepping schemes
- Flexibility in treating arbitrary geometries obtained with a finite-volume formulation
- Numerical efficiency achieved by acceleration techniques
- Computer processing enhanced through vectorization
- Scheme evaluated by solving laminar and turbulent flows

REFERENCES

1. Swanson, R. C.; and Turkel, Eli: A Multistage Time-Stepping Scheme for the Navier-Stokes Equations. NASA CR-172527, Feb. 1985.

2. Thibert, J. J., Granjacques, M., and Ohman, L. H.: NACA 0012 Airfoil. AGARD Advisory Report No. 138, Experimental Data Base for Computer Program Assessment, May 1979.

3. Cook, P. H., McDonald, M. A., and Firmin, M. C. P.: Aerofoil RAE 2822 - Pressure Distributions, and Boundary Layer and Wake Measurements. AGARD Advisory Report No. 138, Experimental Data Base for Computer Program Assessment, May 1979.

D7

N88-14933

57-34

NUMERICAL SIMULATION OF A CONTROLLED BOUNDARY LAYER

117231

16P.

Thomas A. Zang
NASA Langley Research Center
Hampton, Virginia

M. Yousuff Hussaini
ICASE, NASA Langley Research Center
Hampton, Virginia

PRECEDING PAGE BLANK NOT FILMED

PAGE 136 INTENTIONALLY BLANK

[redacted]WING BOUNDARY LAYER

The problem of interest is the boundary layer over a flat plate. The boundary layer grows in space and the transition process is one which occurs in space (in the streamwise direction along the plate). The figure illustrates the growth of the displacement thickness δ^*. The Reynolds number Re depends on x and is based on the free-stream velocity u_∞, the displacement thickness, and the free-stream kinematic viscosity ν_∞. With present computers, 3-D nonlinear simulations of the growing boundary layer can cover only a very small portion of the transition process due to the extreme demands on resolution in the streamwise direction.

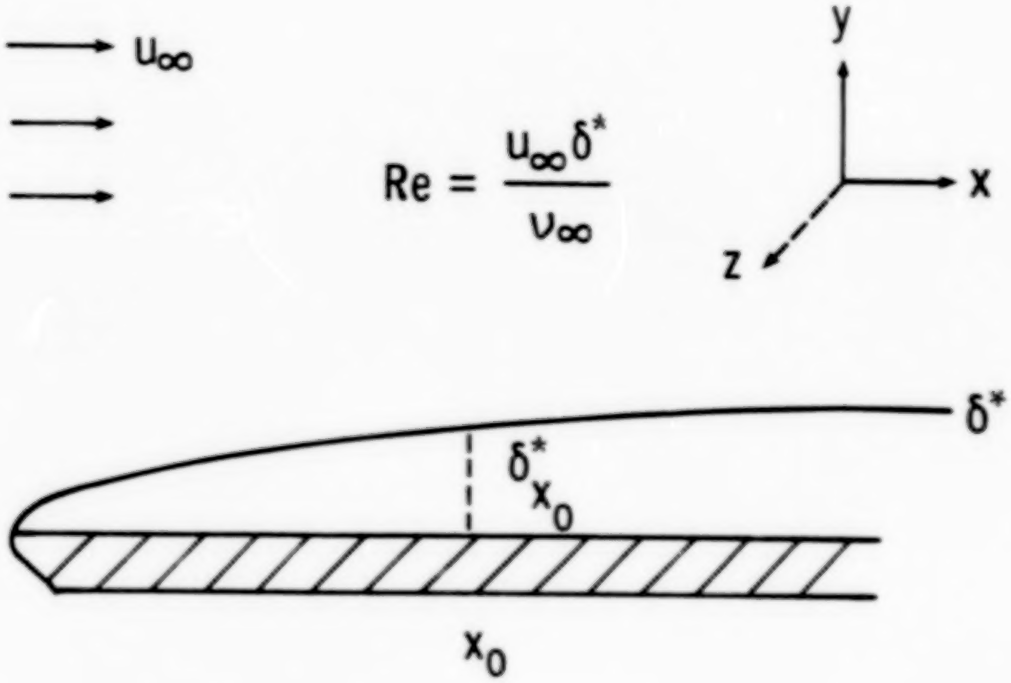

ORIGINAL PAGE IS
OF POOR QUALITY

PARALLEL BOUNDARY LAYER

The parallel flow assumption ignores the growth of the boundary layer in the streamwise direction. It reduces the resolution demands by making feasible the use of periodic boundary conditions in the streamwise direction. Some typical point x_o is chosen as the reference location, and the computational domain extends over 1 or 2 Tollmein-Schlichting (TS) wavelengths λ_{TS}.

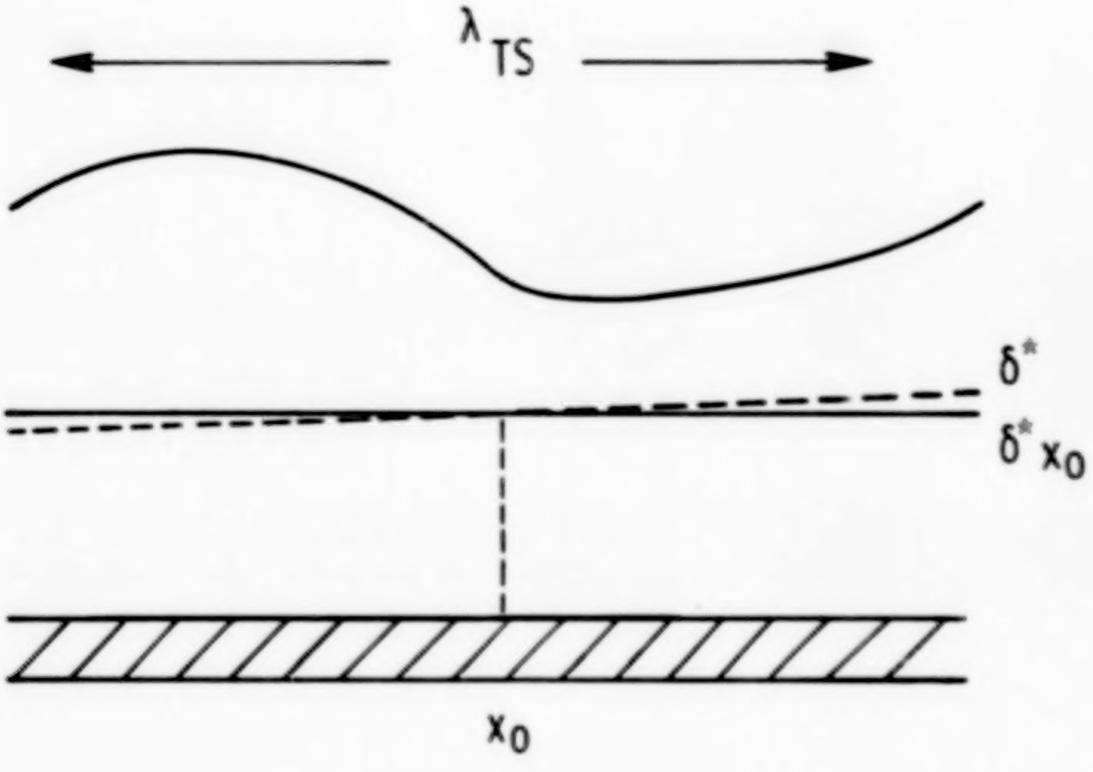

BOUNDARY LAYER CONTROLS

The three standard laminar flow control (LFC) techniques are pressure gradient, suction, and heating. The figure illustrates how each technique affects the mean flow. It also introduces the parameters used to describe the amount of control in the context of the boundary layer equations: β for the pressure gradient, F_w for suction, and τ for heating. The latter influences the flow through the dependence of the viscosity upon temperature.

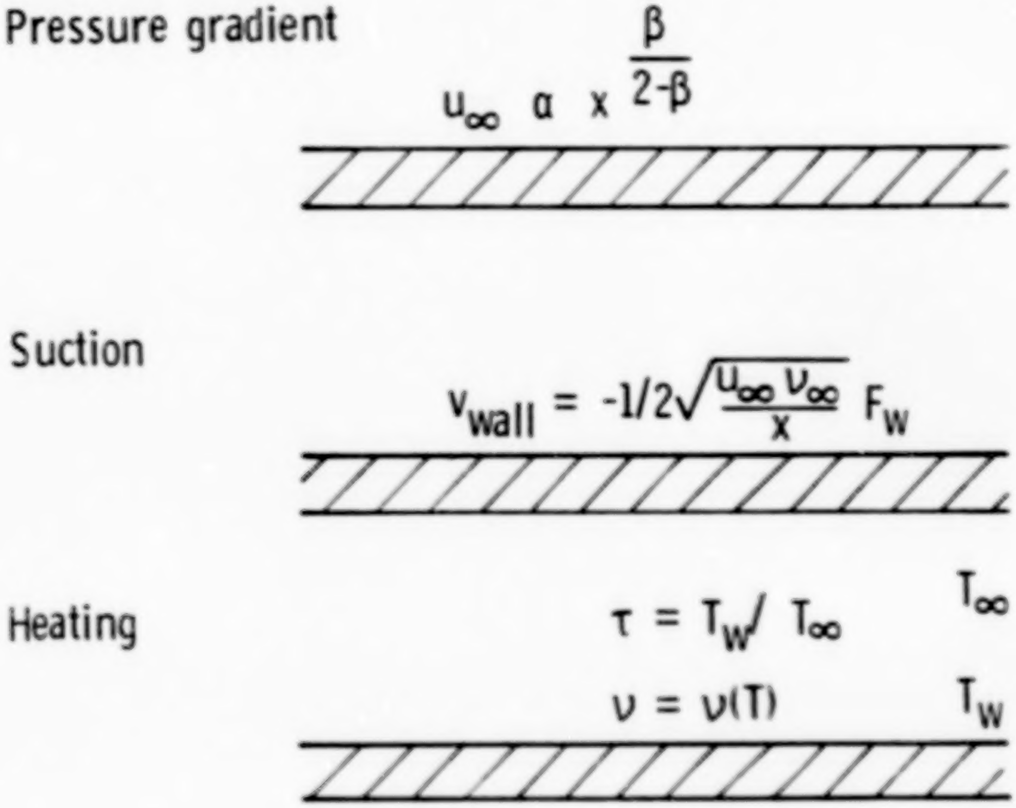
Pressure gradient
$u_\infty \propto x^{\frac{\beta}{2-\beta}}$
Suction
$v_{wall} = -1/2\sqrt{\frac{u_\infty \nu_\infty}{x}}\, F_w$
Heating
$\tau = T_w / T_\infty$
$\nu = \nu(T)$
T_∞
T_w

ORIGINAL PAGE IS
OF POOR QUALITY

CONTROLLED, PARALLEL BOUNDARY LAYER

The parallel flow assumption permits the use of Fourier series in the streamwise (x) and spanwise (z) directions. The wavenumbers α and β are real. The basic equations describing the mean flow are discussed on the figure.

- Parallel flow assumption

$$U(X, Y, Z, T) = \hat{U}(Y)\, e^{i(\alpha X + \beta Z - \omega T)}$$

- Mean flow described by Faulkner-Skan equation with pressure gradient, suction and/or heating controls
- Viscosity and conductivity based on empirical formulas for water
- Reynolds numbers based on displacement thickness and free-stream conditions

NUMERICAL METHODS

Numerical methods are required to find the mean flow, the linear eigenvalues of the Orr-Sommerfeld equation, and the full, nonlinear, 3-D solution of the Navier-Stokes equations. The specific numerical methods used in this work are outlined on the figure.

- Nonlinear mean flow

  4th-order compact finite difference scheme

- Linear modes

  Chebyshev Tau method (ref. 1)

- Navier-Stokes solution

  - Fourier-Chebyshev collocation in space
  - 3rd-order Adams-Bashforth on explicit terms
  - Crank-Nicholson on implicit terms
    (vertical diffusion, pressure and continuity)

NAVIER-STOKES ALGORITHM

The full, nonlinear 3-D, incompressible codes have been implemented on the NASA Langley VPS 32 in both 32-bit and 64-bit arithmetic. The characteristics of the machine and the performance of the code are listed on the chart for 64-bit arithmetic. The storage and speed figures are twice as large for 32-bit arithmetic. Calculations have been performed on 128^3 grids with the Fourier-Chebyshev code in 32-bit arithmetic. They take 25 sec/step and run at a sustained speed of 220 MFLOPS. About 25% of the CPU time is devoted to transposing the data. Hence, the actual computations are being performed at nearly 300 MFLOPS.

- Implemented on VPS 32
  - Cyber 205 architecture (2 pipes)
  - 16 million words (64-bit)
  - 200 Mflops peak speed (64-bit)
  - 80-120 Mflops sustained (64-bit)
- Performance of the Fourier-Chebyshev code
  - 32^3 grid: 2.5 sec/step
  - 64^3 grid: 10 sec/step
- Performance of the Fourier-FD code
  - 32^3 grid: 0.5 sec/step
  - 64^3 grid: 3.0 sec/step

INITIAL CONDITIONS

The initial conditions for the nonlinear simulations consist of the mean flow (U_O) plus a combination of 2-D and 3-D eigenvalues. The eigenfunctions U_{2D} and U_{3D} are normalized so that their maximum value is 1.

$$
\begin{aligned}
U(X,\ Y,\ Z,\ O) = \mathrm{RE} \Big\{ & U_O(Y) \\
& + \varepsilon_{2D}\, U_{2D}(Y)\, e^{i\alpha X} \\
& + \varepsilon_{3D}\, U_{3D}(Y)\, e^{i(\alpha X + \beta Z)} \Big\} \\
& + \varepsilon_{3D}\, U_{3D}(Y)\, e^{i(\alpha X - \beta Z)}
\end{aligned}
$$

$$
\max_{Y} \left| U_{2D}(Y) \right| = \max_{Y} \left| U_{3D}(Y) \right| = 1
$$

FOURIER DECOMPOSITION

The importance of individual components of the flow field can be ascertained by examining the amplitudes of the horizontal Fourier harmonics of the solution. The individual harmonics are labelled by the rational numbers k_x and k_z which measure the horizontal wavenumbers relative to those present in the initial condition.

$$U(X, Y, Z, T) = \sum_{k_x} \sum_{k_z} U_{k_x, k_z}(Y, T) \, e^{i(k_x \alpha X + k_z \beta Z)}$$

$$E_{k_x, k_z}(T) = \int \left| U_{k_x, k_z}(Y, T) \right|^2 DY$$

BOUNDARY LAYER MODES FOR Re = 8950

This table lists the linear TS waves which are used to form the initial conditions for the numerical simulation. The control parameters are $\beta = 0.55$, $F_w = 0.895$, and $\tau = 1.10$. The numerical code does an excellent job of reproducing the linear results.

Control	Mode	α	β	Linear growth rate	Computed growth rate
Pressure	TS 2-D	0.168	0.000	0.000095	0.000096
	TS 3-D	0.168	0.168	-0.001012	-0.001028
Suction	TS 2-D	0.162	0.000	0.000093	0.000093
	TS 3-D	0.162	0.162	-0.000968	-0.000993
Heating	TS 2-D	0.150	0.000	0.000093	0.000097
	TS 3-D	0.150	0.150	-0.000798	-0.000793

SECONDARY INSTABILITY OF HEATED BOUNDARY LAYER

This figure lists the energy in several Fourier harmonics for a simulation of a boundary layer at Re = 8950 with $\tau = 1.10$ and a wall temperature of 293K. The initial conditions were a 2-D and a 3-D TS wave, with $\varepsilon_{2D} = 0.05$ and $\varepsilon_{3D} = 0.0001$. The harmonics are labelled by (k_x, k_z). Both TS waves are linearly stable. Nonlinear effects induce an instability which ultimately leads to turbulence.

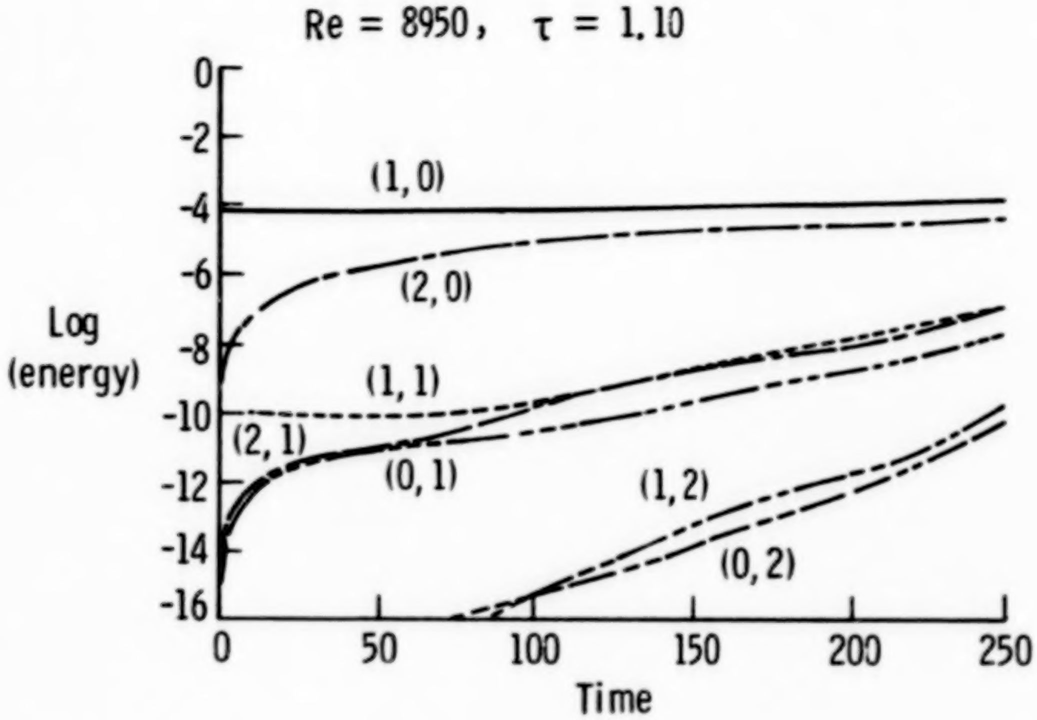

3-D ENERGY VERSUS WALL HEATING

The secondary instability is sensitive to the amount of heating. In these calculations $\epsilon_{2D} = 0.05$ and $\epsilon_{3D} = 0.0001$, and the energy for the 3-D mode is shown. It is the mode labelled (1,1) in the earlier figure. A 1% wall heating has a slight stabilizing effect. If this is combined with a selective control of the (0,1) spanwise mode, then the secondary instability is eliminated entirely.

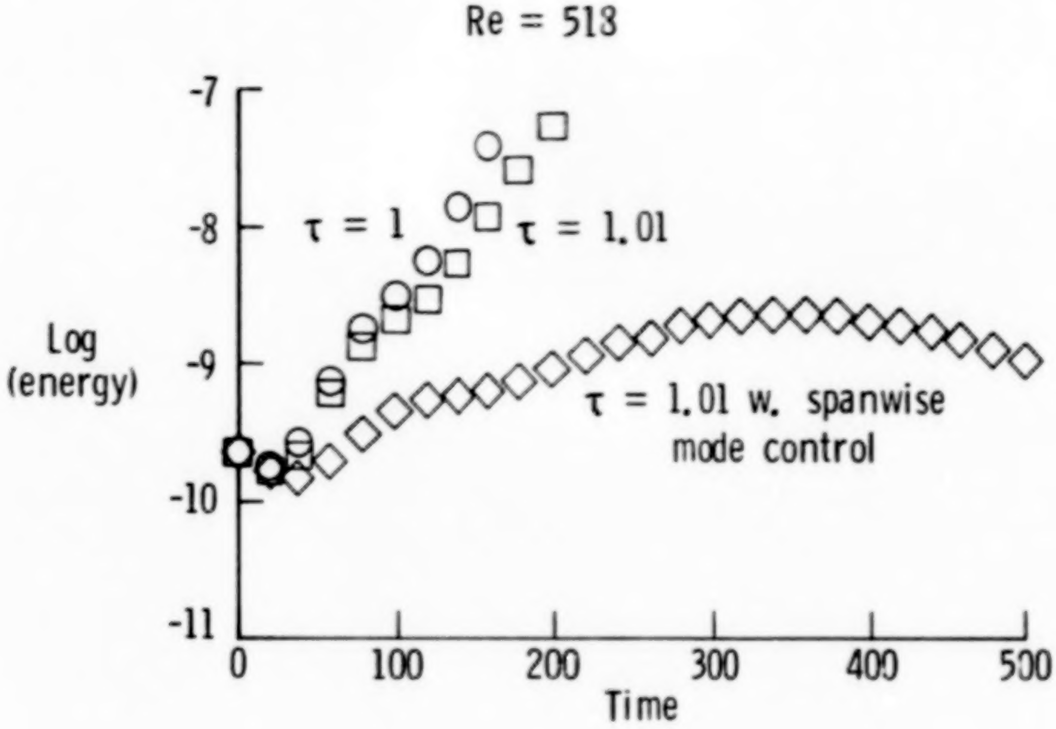

3-D ENERGY VERSUS 2-D AMPLITUDE (UNIFORM HEATING)

Even a 1% 2-D TS wave is sufficient to induce the secondary instability in the boundary layer with wall heating. The instability at this Reynolds number is so severe that selective control of the spanwise mode cannot remove it.

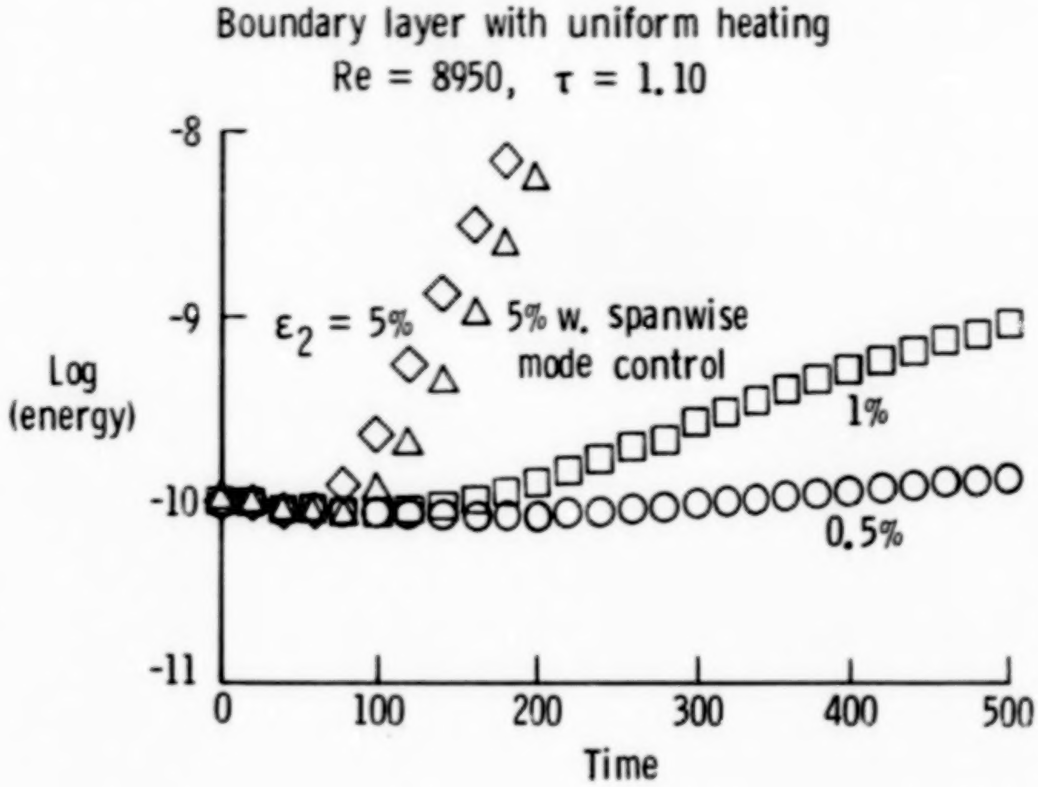

3-D ENERGY VERSUS 2-D AMPLITUDE (UNIFORM PRESSURE GRADIENT)

Even a 1% 2-D TS wave is sufficient to induce the secondary instability in the boundary layer with pressure gradient. The instability at this Reynolds number is so severe that selective control of the spanwise mode cannot remove it.

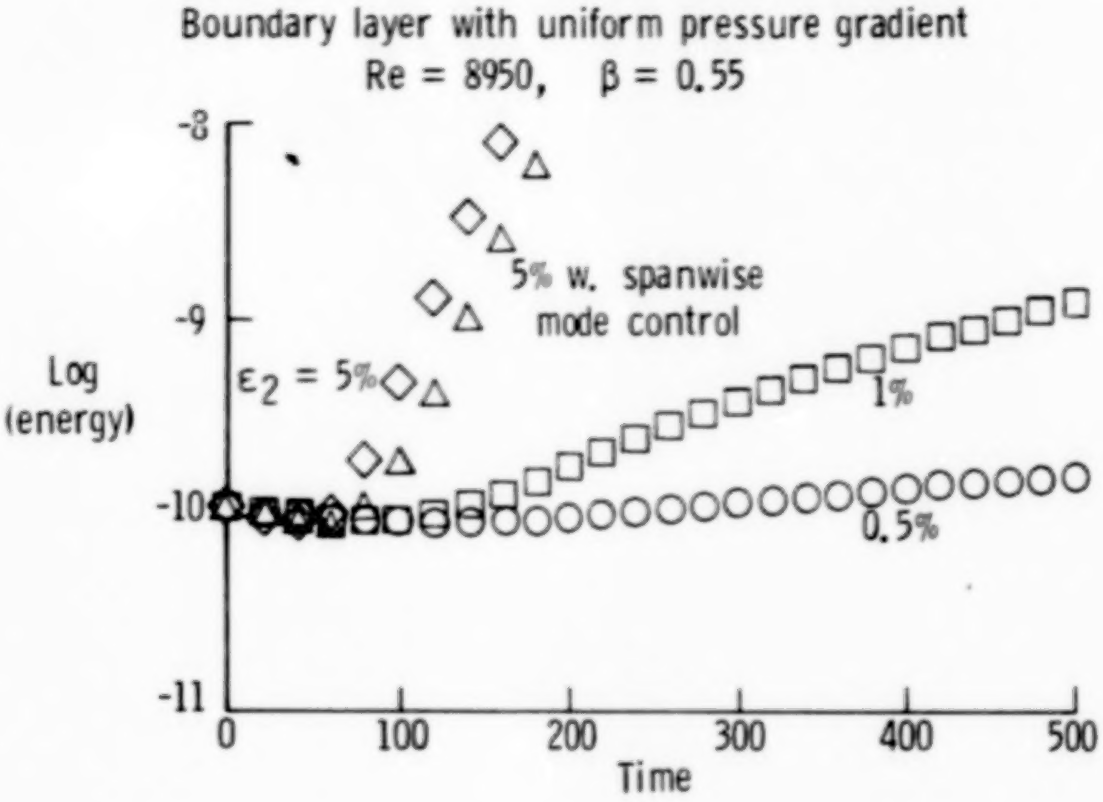

3-D ENERGY VERSUS 2-D AMPLITUDE (UNIFORM SUCTION)

Even a 1% 2-D TS wave is sufficient to induce the secondary instability in the boundary layer with suction. The instability at this Reynolds number is so severe that selective control of the spanwise mode cannot remove it.

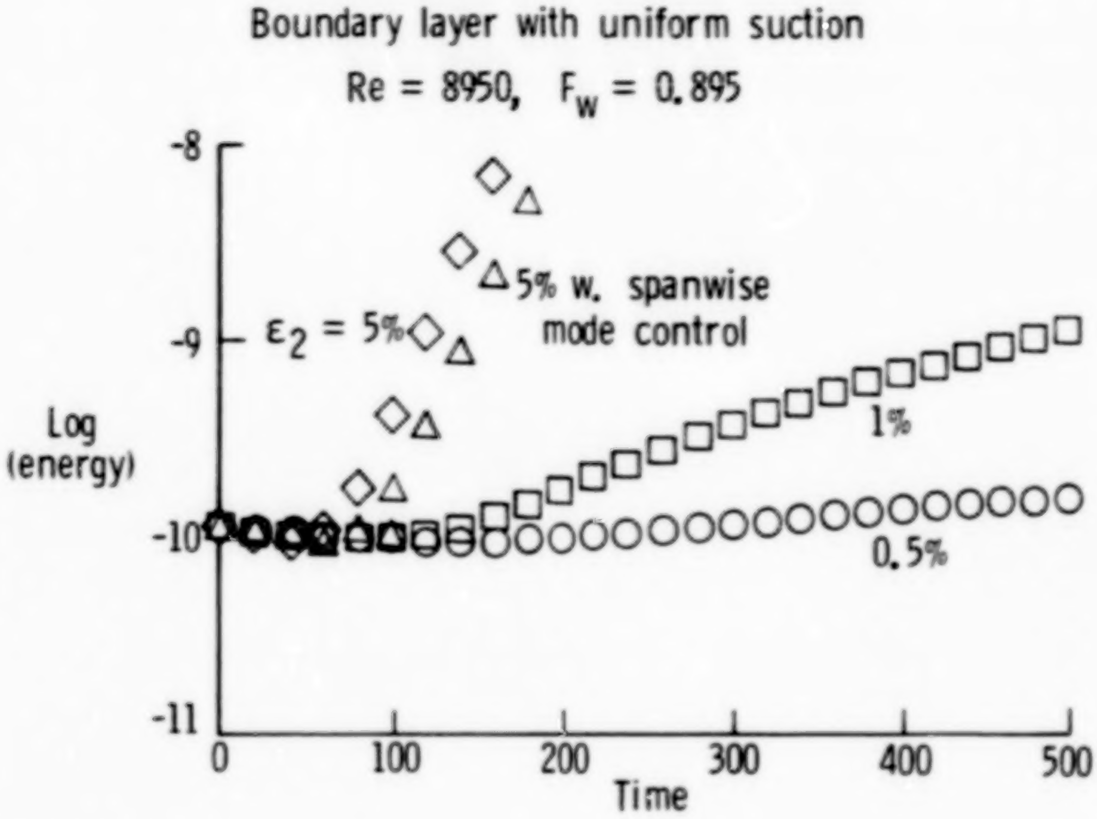

SUMMARY

- A secondary instability exists for the parallel boundary subject to uniform pressure gradient, suction or heating
- Selective control of the spanwise mode reduces the secondary instability in the parallel boundary layer at low Reynolds number

REFERENCE

1. Gottlieb, D. and Orszag, S.: Numerical Analysis of Spectral Methods. SIAM, Philadelphia, PA, 1977.

D8

N88-14934

58-02

117232
16P

VISCOUS VORTEX FLOWS

R. P. Weston, J. P. Chamberlain,
C. H. Liu, and Peter-Michael Hartwich*
NASA Langley Research Center
Hampton, Virginia

---

*NRC - NASA Resident Research Associate

[redacted]

INTRODUCTION

Several computational studies are currently being pursued that focus on various aspects of representing the entire lifetime of the viscous trailing vortex wakes generated by an aircraft. The computational regions are indicated in the figure below, with the vicinity around the vortex-generating aircraft designated as region A. The formation and subsequent near-wing development of the leading-edge vortices formed by a delta wing are being calculated at modest Reynolds numbers using a three-dimensional, time-dependent Navier-Stokes code. The calculations exhibit realistic vortex characteristics including behavior similar to vortex bursting at high angles of attack. Another computer code has been developed to focus on the roll-up, the trajectory, and the mutual interaction of the trailing vortices further downstream from the wing (region B) using a two-dimensional, time-dependent Navier-Stokes algorithm. This code has also been used to study the modification of the vortex behavior due to ground-proximity effects and the enhanced vortex decay induced by atmospheric temperature gradients. To investigate the effect of a cross-wind ground shear flow on the drift and decay of the far-field trailing vortices (region C), yet another code has been developed that employs Euler equations along with matched asymptotic solutions for the decaying vortex filaments. And finally, to simulate the conditions far downstream after the onset of the Crow instability in the vortex wake (region D), a full three-dimensional, time-dependent Navier-Stokes code has been developed to study the behavior of interacting vortex rings.

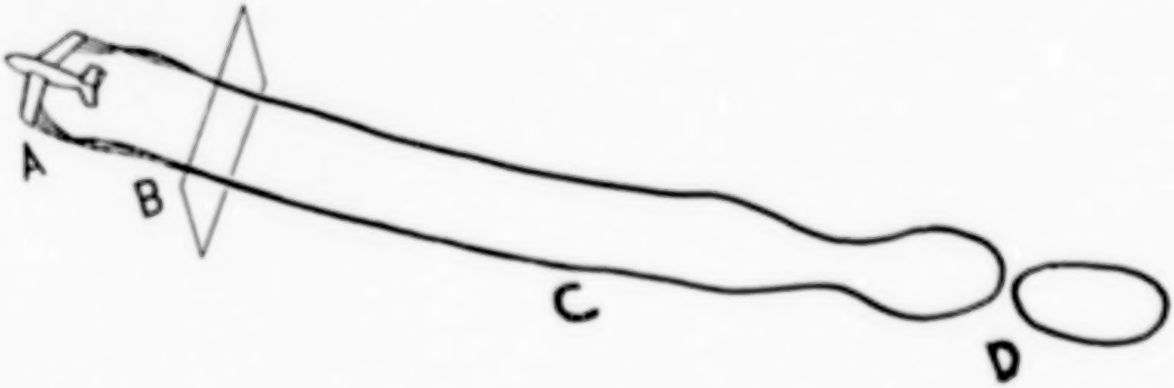

3-D NAVIER-STOKES CALCULATIONS

The formation and the subsequent near-wing development of the leading-edge vortices formed by a delta wing are simulated by time-accurate finite-difference solutions to the Navier-Stokes equations for three-dimensional, incompressible flows with moderate Reynolds numbers. This particular aspect of an extensive numerical study of vortex flow fields generated by aircraft was chosen because a broad experimental data base allows thorough evaluation of the numerical results. The discretized momentum equations are integrated by an Euler-explicit, time-marching procedure that is first and second-order accurate in time and space, respectively. The pressure field is computed simultaneously by a simplified Jacobi method applied to the Poisson equation for the pressure. Truly transient solutions are achieved by repeating the iterative procedure as with time level until the flow is source free.

- Body-fitted coordinates
- Incompressible
- Time-dependent
- Explicit finite-difference

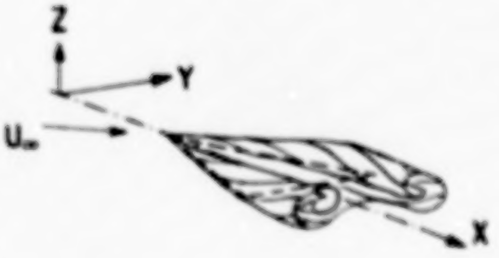

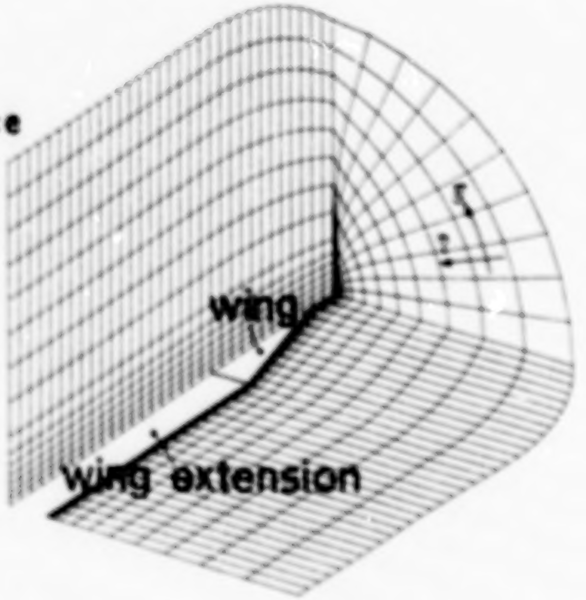

COMPARISON WITH EXPERIMENT AT $\alpha = 20.5^{\circ}$

This figure shows a comparison of streamline patterns that were determined from the velocity fields as steady-state solutions to the Navier-Stokes equations (Re = 250 and Re = 1500) and to the Euler equations ($Re \rightarrow \infty$), and also those that were photographed in a water tunnel (Re = 900). In all four cases the lateral deviations of the vortex streamlines are quite similar. The circumferential velocities of the experimentally observed vortices are judged to be greater than those in the computed flow fields since the number of coils per axial length in the photograph is higher than in the computations. The values for κ give an estimation of the additional numerical viscosity which has to be added to numerically stabilize the finite-difference solutions of the Navier-Stokes equations (Re = 1500) and of the Euler equations ($Re \rightarrow \infty$). The quantity κ can be interpreted as the reciprocal of a Reynolds number, giving the effective Reynolds number during the computations as $(\frac{1}{Re})_{effective} = (\frac{1}{Re})_{nominal} + \kappa$.

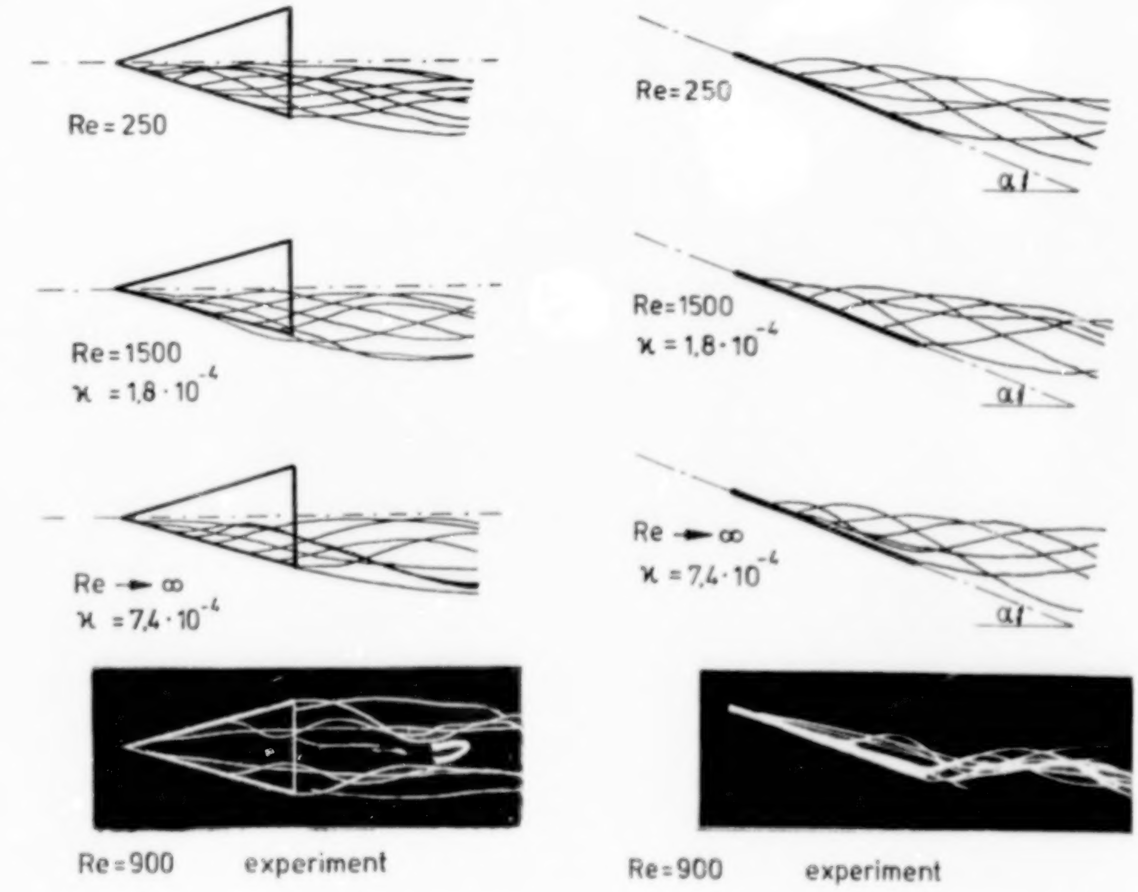
Re = 250
Re = 250
α
Re = 1500
$\kappa = 1{,}8 \cdot 10^{-4}$
Re = 1500
$\kappa = 1{,}8 \cdot 10^{-4}$
α
$Re \rightarrow \infty$
$\kappa = 7{,}4 \cdot 10^{-4}$
$Re \rightarrow \infty$
$\kappa = 7{,}4 \cdot 10^{-4}$
α
Re = 900 experiment
Re = 900 experiment

ORIGINAL PAGE IS
OF POOR QUALITY

VELOCITY FIELD FOR 78.6% CHORD, $\alpha = 20.5^{\circ}$

This figure shows the projections of the velocities in planes which intersect the delta wing perpendicularly at 78.6% of the root chord. The aspect ratio is AR = 1 and the angle of attack is 20.5 degrees. The velocity fields represent steady-state solutions to the Navier-Stokes equations ($Re = 250$ and $Re = 1500$) and to the Euler equations ($Re \to \infty$). For $Re = 250$, no additional numerical damping was necessary, whereas numerically stable solutions for $Re = 1500$ and $Re \to \infty$ were obtained only after additional damping, indicated by κ, has been introduced in the discretized momentum equations. The vortex for $Re = 250$ lies higher and closer to the plane of symmetry than in the other two cases. The velocity distributions for $Re = 1500$ and $Re \to \infty$ look quite similar if a small region in the neighborhood of the wing is neglected where the different boundary conditions for viscous and inviscid flows affect the solution. The small size of this region suggests that for the computation of vortex flows around sharp-edged delta wings with $Re > O(10^3)$ the friction forces may be neglected. To provide further evidence for this conclusion, additional investigations are in progress.

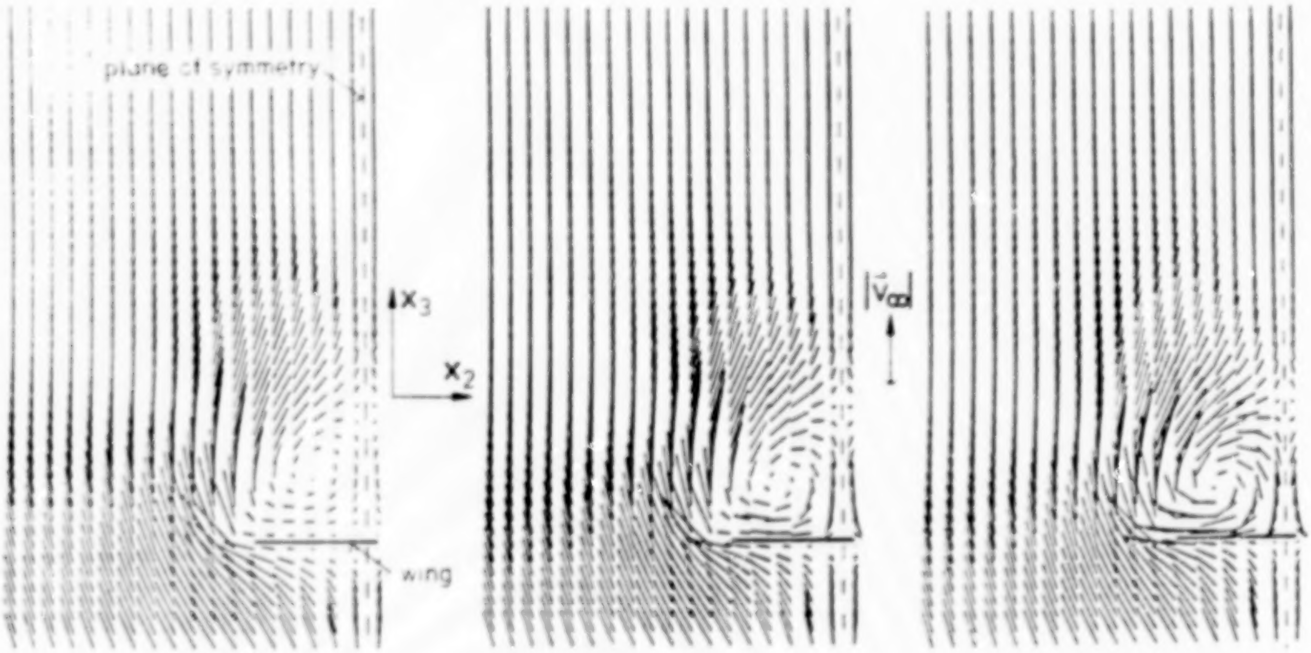

$Re = 250$ $\qquad$ $Re = 1500 \quad \kappa = 1.8 \cdot 10^{-4}$ $\qquad$ $Re \to \infty \quad \kappa = 7.4 \cdot 10^{-4}$

ORIGINAL PAGE IS
OF POOR QUALITY

TWO-DIMENSIONAL INITIAL VALUE PROBLEM

The governing equations are expressed in terms of the variables of stream function (ψ) and vorticity (ω). The equation of continuity can then be cast as a Poisson equation and the curl of the momentum equation becomes the vorticity transport equation, where t is time, ν is the kinematic viscosity, and v and w are the velocity components in the y and z directions, respectively. The subscripts denote partial derivatives. The initial vorticity distribution provides the initial condition and the boundary condition for the unbounded flow is based on the fact that the vorticity distribution is confined to one area and decays exponentially with distance from that area. The exact solution for the Poisson equation is given by the Biot-Savart law. However, the computation of the boundary conditions using this law directly is extremely expensive. A considerable time savings can be achieved by expanding the Biot-Savart integral in a power series in terms of vorticity. The coefficients of the terms in the power series are moments of the vorticity distribution. Previous studies have shown that the first moments and several linear combinations of higher moments are time invariant. These results can be used to determine the boundary condition for the numerical calculations and are also used in checking the accuracy of the numerical solutions as they proceed.

Incompressible, Navier-Stokes Eqns.

Continuity: $\nabla \cdot \vec{V} = 0 \Rightarrow \Delta \psi = -\omega$ (Poisson eqn)

Vorticity
Transport : $\omega_t + v\,\omega_y + w\,\omega_z = \nu\,\Delta\,\omega$

I.C. $\omega(\vec{x},0) = \omega_o(\vec{x})$

B.C. $\omega(x,t) \rightarrow 0$ exponentially as $x \rightarrow \infty$

Boundary values of ψ are evaluated using a moment expansion of the Biot-Savart law

FLOWCHART

The basic algorithm performed by the program is outlined below:

1. The volume integrals are evaluated using Simpson integration over the computational domain. The time varying integrals are evaluated at each time step, while the time-invariant integrals are evaluated initially and then only periodically to monitor the accuracy of the solution.

2. The results from step one are used to obtain the expansion coefficients which are in turn used to determine values of ψ at the boundary.

3. A fast Poisson solver is used to determine the values of ψ in the interior of the computational domain. The solver currently in use is a direct method developed by the National Center for Atmospheric Research (NCAR). The method uses a finite-difference formulation and is second-order accurate in the spatial directions.

4. The velocity field is obtained by using second-order centered differences to obtain the curl of ψ. The velocity values are written over the stream function values to minimize the required computer storage.

5. The vorticity field is advanced in time by using a finite-difference representation of the vorticity transport equation. The program currently uses the Dufort-Frankel method (ref. 1) for solving the vorticity transport equation; this explicit method is accurate to $O[(\Delta t)^2, (\Delta x_i)^2, \nu(\Delta t/\Delta x_i)^2;\ i = 1, 2, 3]$. Explicit methods for solving the vorticity transport equation appear to be more appropriate than implicit methods in this case.

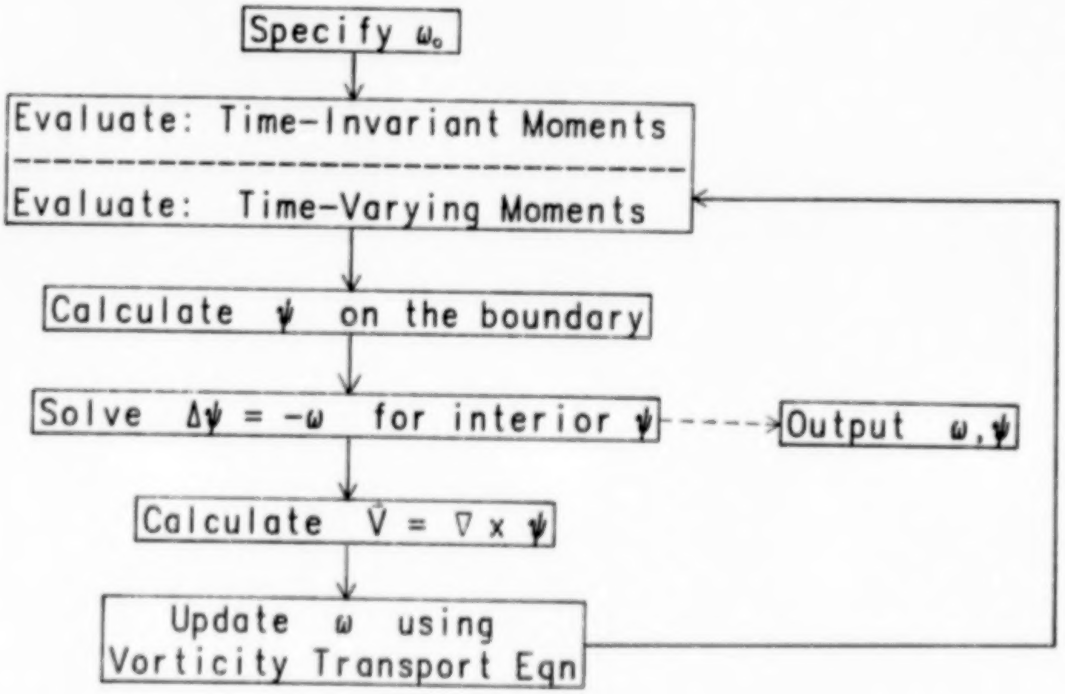
Specify ω_o
Evaluate: Time-Invariant Moments
Evaluate: Time-Varying Moments
Calculate ψ on the boundary
Solve $\Delta\psi = -\omega$ for interior ψ
Output ω, ψ
Calculate $\vec{V} = \nabla \times \psi$
Update ω using Vorticity Transport Eqn

EVOLUTION OF VORTICITY FOR SPANLOAD OF TRANSPORT IN LANDING CONFIGURATION

This figure displays the resultant contours of vorticity for successive planes downstream of the wing. The calculations were performed at a Reynolds number (Γ/ν) of 20,000. The results are shown for only the right half-plane since the flow is assumed to exhibit mirror symmetry about the line $y = 0$. Since the computational grid follows the vortices, the projection of the wing trailing edge appears as the horizontal line that rises in successive planes.

The example is for a spanload distribution like that obtained with a transport aircraft using flaps on landing or takeoff. The resulting initial vorticity distribution has been simplified by distributing the vorticity along a horizontal line, unlike the more complicated positions expected in reality. Note the negative vorticity values associated with the reduction in lift around the fuselage-wing junction.

Successive frames illustrate the evolution of the vortex system in time and demonstrate the ultimate merging of the vortices from the wing tip and flap tip. A movie generated from these calculations has been useful in observing the progress of these vortex interactions.

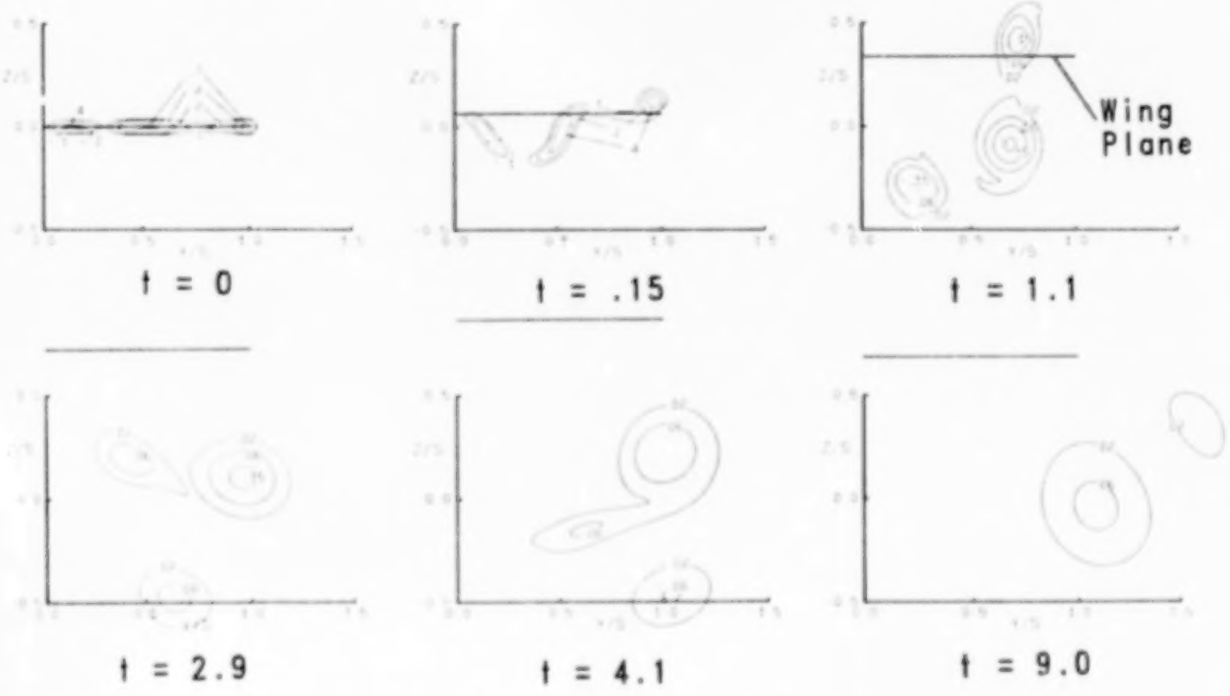

t = 0

t = .15

t = 1.1

t = 2.9

t = 4.1

t = 9.0

ORIGINAL PAGE IS
OF POOR QUALITY

INTERACTION OF DECAYING TRAILING VORTICES IN SPANWISE SHEAR FLOW

The drift of trailing vortices in a crosswind near to the ground is modeled by an unsteady, two-dimensional, rotational flow field with a concentration of large vorticity in spots having a finite but small effective size and finite total strength. The problem is analyzed by a combination of the method of matched asymptotic analyses for the decay of the vortical spots and the Euler solution for the unsteady rotational flow. Using the method of averaging, a numerical scheme is developed in which the grid size and time step depend only on the length and velocity scales of the background flow and are independent of the effective core size of a vortical spot. The core size can be much smaller than the grid size while the peak velocity in the core is inversely proportional to the spot size. Numerical results are presented to demonstrate the strong interaction between the trajectories of the vortical spots and the redistribution of vorticity in the background flow field (ref. 2).

COORDINATE TRANSFORMATION

The problem of a steady far-wake vortex can be simplified by reducing the problem to an equivalent unsteady two-dimensional problem in a plane normal to the flight direction. This simplification is performed by changing the coordinate z to a time variable t using $z=z^*-W_\infty t$, where z is stationary and z^* points in the downstream direction and moves with the airplane at velocity W_∞ (see figure). This assumption ignores the streamwise curvature of the trailing vortex filaments, their initiation at the trailing edge, and the variation of the velocity parallel to the z axis. Mathematically, we assume that $d/dz \ll d/dx$ and d/dy with x,y as the span and vertical direction, respectively. In the x-y plane at a station z, the trailing vortices are represented by "vortex spots" of small effective size inside of which there is a strong vorticity distribution with finite total strength.

This model is employed to study the drift and decay of farfield trailing vortices (vortical spots) in a cross wind (a spanwise shear flow) near the ground.

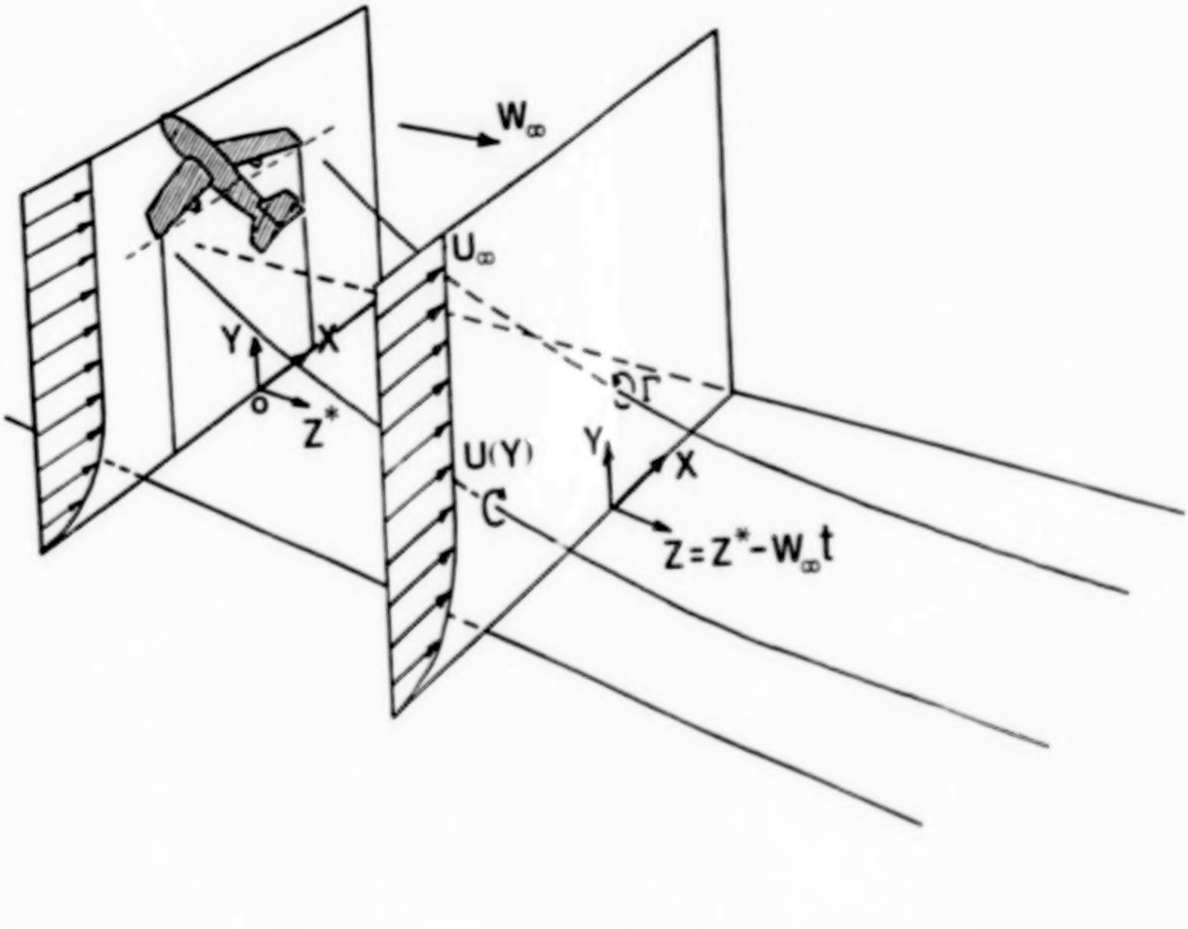

EFFECT OF VORTEX STRENGTH ON TRAJECTORY

To gain a qualitative understanding of the interaction of vortical spots with a background shear flow, we study first the case of a single vortical spot. This figure shows the trajectories of a single concentrated decaying vortical spot of various strengths submerged in a background shear flow. The initial vertical position of the spot is at $y=1$ and the initial background shear flow is chosen as $U_0(y)=1-e^{-y}$. The results show that the vortical spots with positive circulation drift downstream and upward while the vortical spots with negative circulation drift downstream and downward but eventually turn backward ($t>t^*$). This phenomenon is more pronounced as the strength of the vortical spot increases. To explain this phenomenon we consider the case of a single vortical spot with $\Gamma>0$. The disturbed flow moves downward behind the spot, $x<X$, and upward ahead of the spot, $x>X$. For an initial background vorticity ω_0 with $\omega_0'(y)>0$, the disturbed flow increases the vorticity behind the spot and decreases the vorticity ahead of it, i.e., $\tilde{\zeta}>0$ for $x<X$ and $\tilde{\zeta}<0$ for $x>X$. The background vorticity variation $\tilde{\zeta}$ in turn induces an upward motion of the vortical spot for $\Gamma>0$. From similar arguments, we can explain that the background vorticity variation $\tilde{\zeta}$ will induce a downward motion of the vortical spot with $\Gamma<0$. The reason that a vortical spot of negative strength turns around and drifts upstream as it gets closer and closer to the ground can be attributed to the decrease of the contribution of the background shear flow to the forward velocity of the spot and to the increase of the induced velocity by the image of the vortical spot with respect to the ground, $y=0$. It should be pointed out here once more that the vortical spot will drift horizontally when the background shear flow is either a uniform flow ($\omega_0=0$) or a constant shear flow ($\omega_0=$constant) and there will be no change in the background flow, $\tilde{\zeta}\equiv0$.

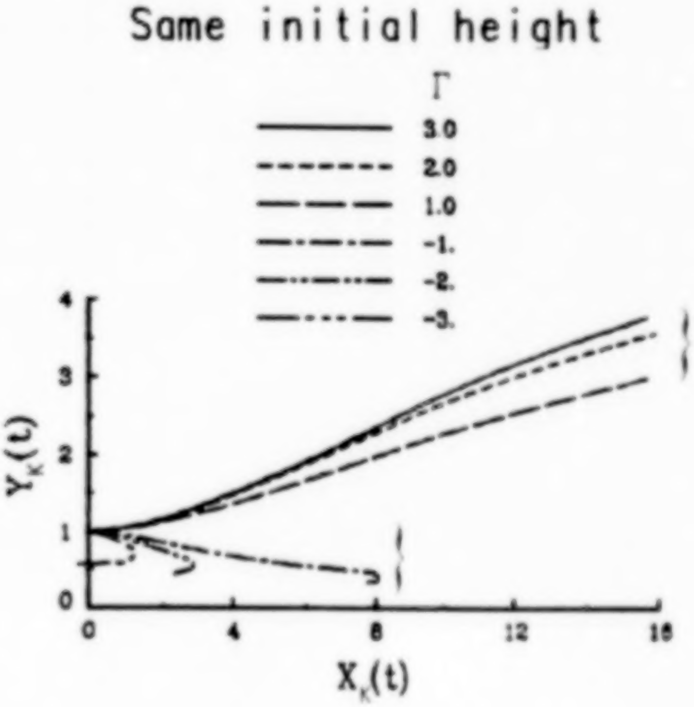

VORTICAL PAIRS SIMULATING TRAILING VORTICES IN A CROSSWIND

The trailing vortex wakes far downstream of an aircraft are modeled by a simple vortex pair whose vorticity distributions are concentrated and are centered at $(\mp X_k(0), Y_k(0))$ with strength $\mp\Gamma$ and effective vortical size $\delta(0)$. The goal of the following numerical examples is to simulate the interaction of the decaying trailing vortical pairs subjected to a cross-flow (spanwise) ground shear. The background shear flow used in the examples is an exponential profile.

In order to find out when we have to use the shear layer solution, we studied the trajectories of a pair of vortices in a shear layer for different initial vortex heights. The $Y_{R,min}$ approaches an asymptotic value of 2.6 when $Y_k(0)$ is greater than 7.0. This means that when the vortex spots are above $y=7$, they are far above the shear layer and the interaction with the shear layer is negligible. The corresponding trajectories (in real spanwise positions) of the vortical pair, starting at different heights $Y_k(0)=1,2,3,4,5$ in the shear layer, are displayed in this figure to show that the trajectories of the vortical spots are sensitive to the starting height, i.e., the altitude of the airplane relative to the thickness of the shear layer.

EFFECT OF DIFFERENT INITIAL POSITIONS

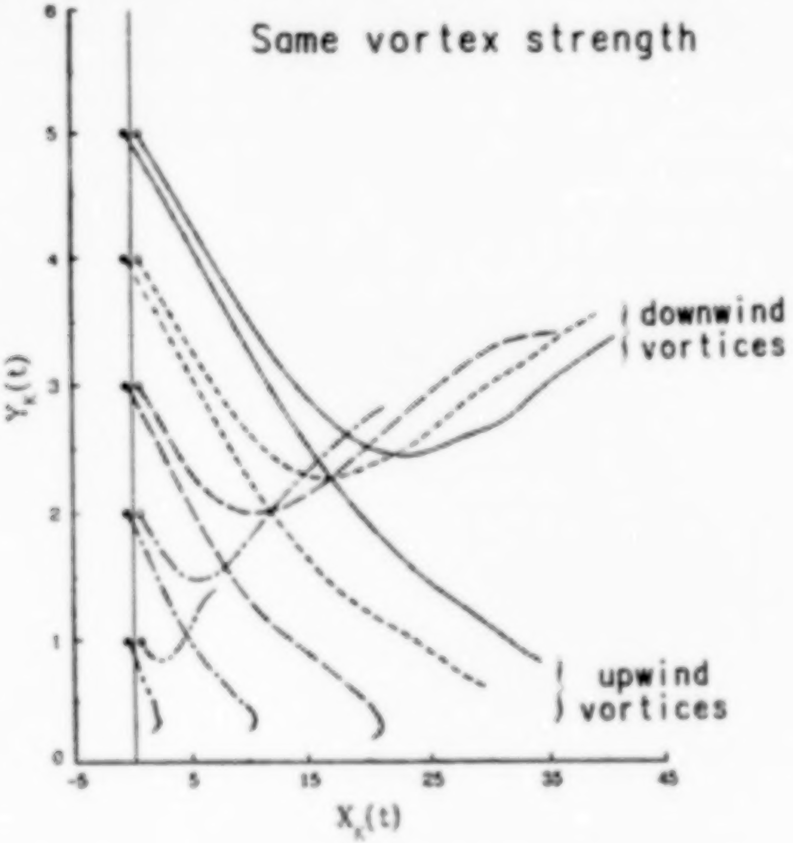

NAVIER-STOKES CALCULATIONS FOR UNSTEADY, THREE-DIMENSIONAL VORTEX-DOMINATED FLOWS

A finite-difference Navier-Stokes code has been developed for calculating unsteady, three-dimensional, vortex-dominated flows in unbounded fluid domains. The algorithm uses an improved boundary condition specification which allows the unbounded nature of the physical problem to be represented on a finite computational domain. This boundary condition specification permits the efficient computation of flows due to closed ring-like vortical tubes or structures. These structures are important elements in fluid flows such as free jets, atmospheric turbulence, and the far-field wakes of aircraft, and studies of their interaction may aid in an understanding of complex vortical fluid flows.

The primary variables used in the computations are the vorticity and the vector velocity potential, which is defined as a divergence-free vector field whose curl yields the velocity. This definition of the vector velocity potential automatically satisfies the incompressible continuity equation, and for unbounded flow relates the vector potential directly to the vorticity through an integral relationship (the vector Poisson integral). In theory, this integral relationship could be used to yield the velocity directly from the vorticity, but the numerical evaluation of the Poisson integral throughout the computational domain is very time consuming. The current algorithm avoids the expense of directly computing the integral by approximating the integral values at the domain boundary with a series representation, and then using these values along with a fast Poisson solver in the domain interior. This technique yields a fast, accurate solution for the velocity field of the unbounded-domain physical problem with a finite computational domain.

Incompressible, Laminar Flow

Continuity: $\nabla \cdot \vec{V} = 0 \Rightarrow \Delta \vec{A} = -\vec{\omega}$ (Poisson eqn)

Vorticity Transport: $\vec{\omega}_t = \nabla \times (\vec{V} \times \vec{\omega}) + \nu \Delta \vec{\omega}$

I.C. $\vec{\omega}(\vec{x},0) = \vec{\omega}_0(\vec{x})$

B.C. $\vec{\omega}(\vec{x},t) \to 0$ exponentially as $x \to \infty$

Boundary values of $\vec{A}$ are evaluated using a moment expansion of the Biot-Savart law

BOUNDARY CONDITION ACCURACY

The accuracy and efficiency of two approximate vector-potential boundary condition methods were evaluated by comparing them with an exact solution that used Poisson integral evaluations to generate the boundary conditions. The two approximate methods were the truncated series method mentioned in the previous figure and a method that enforces zero normal velocity at the boundary by setting $\hat{A}$ to zero at the boundary.

The vorticity distribution chosen for the boundary condition checks is shown in the upper right figure as a vorticity-magnitude isosurface. This distribution represents two Gaussian-core vortex rings with equal strengths, radii, and core diameters whose axes of symmetry lie in the x-y plane and cross the x-axis at an angle of ±22.5°. The centers of the rings lie on the y-axis at ±1.5 units, where a unit of length is the toroidal radius of each ring. The effective core radius (the radius at which the vorticity magnitude has fallen to 1/e of the maximum vorticity magnitude) is 0.5. The computational domain is a cube with edges of length 8 centered about the origin. This domain size is the practical minimum cubical size that will still enclose both vortical rings and thus represents a "worst-case" test condition.

The three boundary condition figures show contour plots of the magnitude of $\hat{A}$ in the x-y plane of the domain for each of the three boundary condition methods. It is evident from the figures that the finite solution domain affects both the series method and zero normal-velocity method solutions, although the series solution is not affected to nearly as great an extent. For slightly larger domains the series method solution closely approximates the Poisson method solution, whereas the global character of the zero normal-velocity solution is altered by the closed boundary.

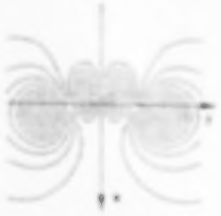

POISSON INTEGRAL B.C.'S

VORTICITY DISTRIBUTION

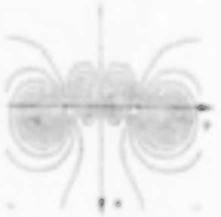

SERIES B.C.'S

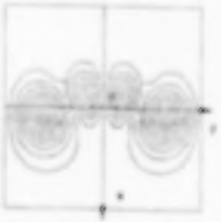

$|\hat{A}| = 0$ B.C.'S

MERGER OF VORTEX RING PAIR

This figure shows the oblique collision, merging, and deformation of two circular, Gaussian-core vortex rings. The first two plots show representative isosurfaces of the initial vorticity and vector velocity potential magnitudes, respectively, and the last four plots show the time development of the vector potential isosurface. The intersections on the surfaces represent grid point locations, and the cube represents the computational domain boundary. The rings collide and merge to form a single distorted oblong ring, which continues to deform until the major and minor axes have switched their orientation. This behavior has been observed experimentally, and work is currently in progress to further correlate the code results with experiment. It is hoped that this algorithm will be useful in understanding and analyzing the physics of vortex-dominated flows.

(VECTOR POTENTIAL STREAM SURFACES)

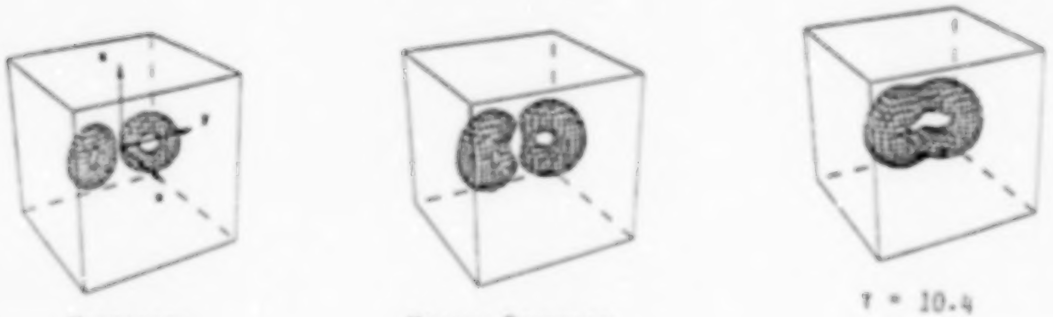

Vorticity $\tau = 0$

Vector Potential $\tau = 0$

$\tau = 10.4$

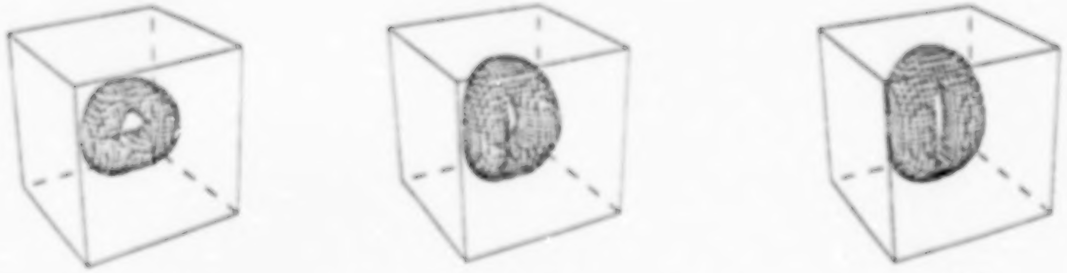

$\tau = 20.2$

$\tau = 40.9$

$\tau = 60.1$

REFERENCES

1. Dufort, E.C., and Frankel, S.P.: "Stability Conditions in the Numerical Treatment of Parabolic Differential Equations," Math. Tables and Other Aids to Computation, Vol. 7, 1953, pp. 135-152.

2. Liu, C. H. and Ting, L.: "Interaction of Decaying Trailing Vortices in Ground Shear," Proceedings of 4th International Conference on Applied Numerical Modeling, Tainan, Taiwan, Dec. 1984, pp. 546-655.

D9

N88-14935

S9-02

A THEORY FOR THE CORE FLOW OF LEADING-EDGE VORTICES

117233

17P.

James M. Luckring
NASA Langley Research Center
Hampton, Virginia

[redacted]

ABSTRACT

Separation-induced leading-edge vortices can dominate the flow about slender wings at moderate to high angles of attack, often with favorable aerodynamic effects. However, at the high angles of attack which are desirable for take-off and landing as well as subsonic-transonic maneuver the vortices can break down or "burst" in the vicinity of the aircraft causing many adverse effects; these include lift loss, pitchup, and buffet. The flow in the core of leading-edge vortices is generally affiliated with the vortex breakdown phenomenon.

A theory is presented for the flow in the core of separation-induced, leading-edge vortices at practical Reynolds numbers. The theory is based on matching inner and outer representaions of the vortex. The inner representation models continuously distributed vorticity and includes an asymptotic viscous subcore. The outer representation models concentrated spiral sheets of vorticity and is fully three dimensional. A parameter is identified which closely tracks the vortex breakdown stability boundary for delta, arrow, and diamond wings.

A THEORY FOR THE CORE FLOW OF LEADING-EDGE VORTICES

Shown in this figure is an outline of the presentation. The chief concepts of the theoretical formulation will first be reviewed, followed by some computed results which highlight the general character of the solutions. An analysis for incipient vortex breakdown is also discussed. Additional details of the theory have recently been given by Luckring (1985).

- Theoretical formulation
    - Inner/outer representation
    - Initial conditions
    - Boundary conditions
- Computed results
    - Experimental correlation
    - Vortex breakdown analysis
- Concluding remarks

THEORETICAL FLOW MODEL

Previous theoretical studies have been focused primarily on either (1) modeling the global vortex flow field with a simplified vortex core representation, or (2) modeling detailed vortex core flow for simplified external conditions. At practical Reynolds numbers, the composite leading-edge vortex flow can be subdivided into overlapping regions which can be modeled with appropriate subclasses of the full governing equations; it is this feature of the flow which is exploited by the present approach. With this approach, considerable advantage can be taken of previous modeling studies of the isolated core and the leading-edge vortex so long as appropriate matching conditions can be established between the two models.

The outer flow is modeled by the free-vortex-sheet theory of Johnson, et al. (1980), a higher-order panel method which solves the Prandtl-Glauert equation including nonlinear boundary conditions pertinent to the concentrated vorticity representation of the leading-edge vortex. This method generally provides good estimates of inviscid wing pressure distributions as well as force/moment properties. The inner flow is modeled by the quasicylindrical Navier-Stokes equations and is initiated with an asymptotic solution valid for conical external conditions. Additional details of the inner flow model as well as matching the inner flow to the outer flow are described subsequently.

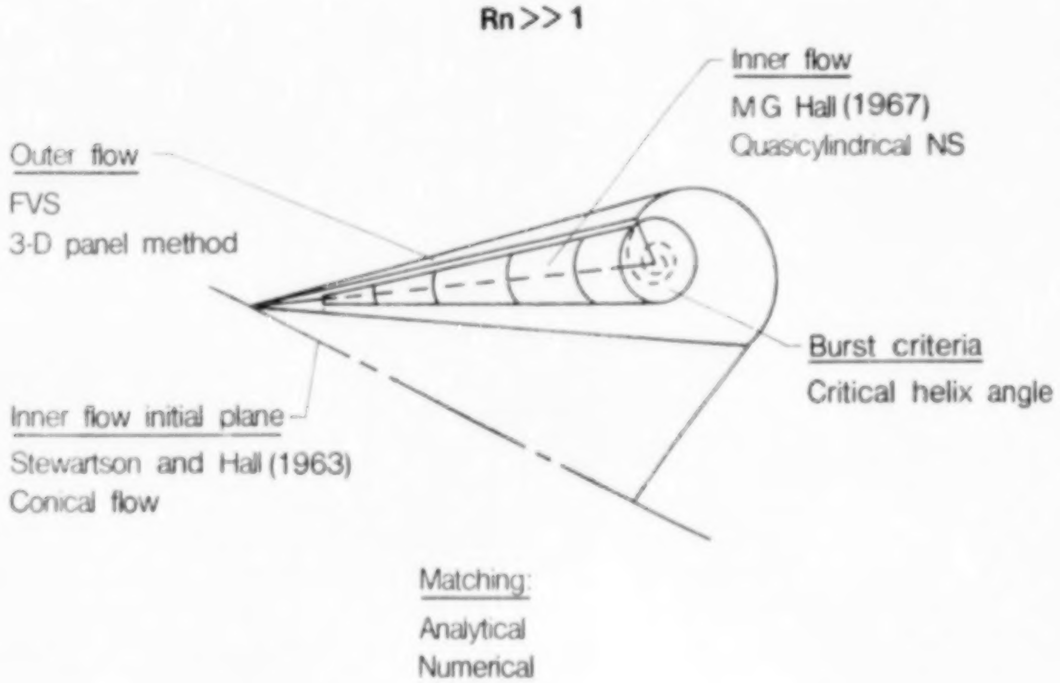
Rn>>1
Inner flow
M G Hall (1967)
Quasicylindrical NS
Outer flow
FVS
3-D panel method
Burst criteria
Critical helix angle
Inner flow initial plane
Stewartson and Hall (1963)
Conical flow
Matching:
Analytical
Numerical

QUASICYLINDRICAL VORTEX CORE

The purpose of the inner flow fomulation is to provide a physically realistic representation of the flow in the core of a three-dimensional, leading-edge vortex, chiefly by accounting for the effects of distributed vorticity as well as viscosity. The unburst cores tend to be slender and, as a consequence, exhibit large gradients in the radial direction as compared to the axial direction. Therefore, the quasicylindrical Navier-Stokes equations of Hall (1966) were chosen as the pilot model of the core flow. The steady flow is assumed to be laminar, incompressible, and axially symmetric; in addition, the slenderness condition renders the equations parabolic in the axial direction. The solution is advanced in space by standard finite difference techniques from the initial plane solution of Stewartson and Hall (1963) with centerline boundary conditions appropriate to the axisymmetric assumption and with edge boundary conditions obtained from the free-vortex-sheet theory.

M.G. Hall (1966)

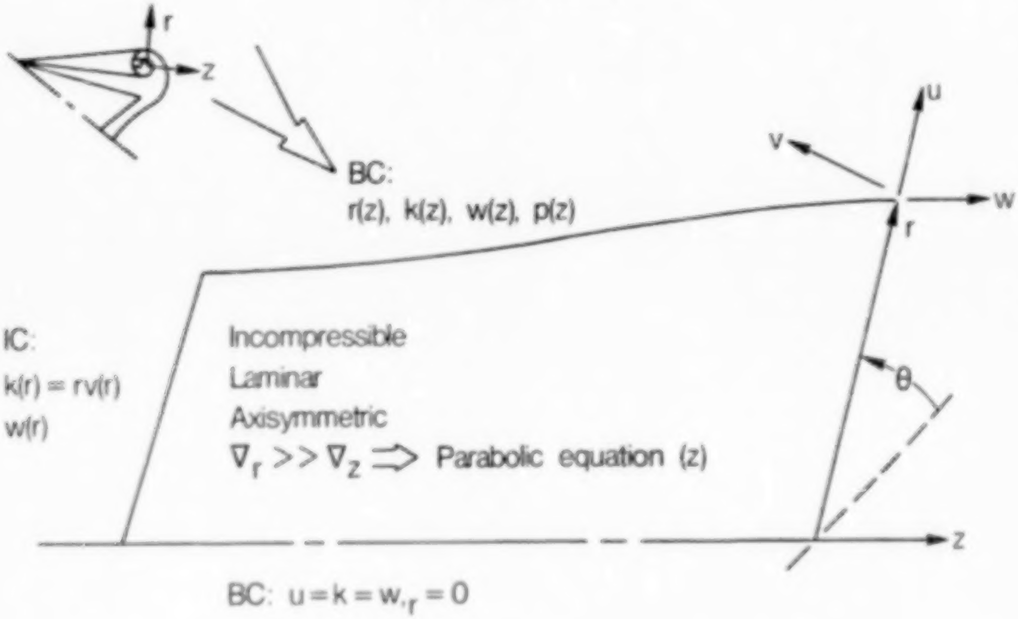
r
z
u
v
w
r
θ
z
BC:
r(z), k(z), w(z), p(z)
IC:
k(r) = rv(r)
w(r)
Incompressible
Laminar
Axisymmetric
$\nabla_r >> \nabla_z \Rightarrow$ Parabolic equation (z)
BC: $u = k = w_{,r} = 0$

INNER/OUTER MATCHING--NONAXISYMMETRIC EFFECTS

The inner-flow representation of the vortex core requires "edge" values of axial flow, circulation, and pressure as well as the region of the edge itself. The matching must be accomplished in the vicinity of the vortex (away from the wing) and must account for the differences between the inner and the outer representations of the vortex.

In the overlap region, both theories model inviscid vortices, the former modeling axisymmetric, continuously distributed vorticity and the latter modeling nonaxisymmetric concentrated vorticity. These differences can be reconciled with the theoretical solution of Mangler and Weber (1966) for a spiral sheet of concentrated vorticity embedded in an otherwise irrotational potential flow. The most noteworthy aspect of their asymptotic solution is that "the leading terms of the velocity components for a potential flow with vorticity concentrated along a sheet are the same as for an axisymmetric flow with continuously distributed vorticity," as given by Hall (1961) and used herein. To lowest order, the (axisymmetric) velocity and vorticity fields are aligned, and the pressure may therefore be derived from a Bernoulli relationship.

The Mangler and Weber (1966) solution provides a guide for the extraction of axisymmetric boundary condition quantities from the nonaxisymmetric outer formulation. Nonconical effects for the flow in the vicinity of the wing apex must also be addressed as discussed by Luckring (1985). Viscous-inviscid interaction effects are not presently accounted for.

- Mangler & Weber (1966)

  Slender core
  Asymptotic
  Incompressible
  Inviscid
  Conical

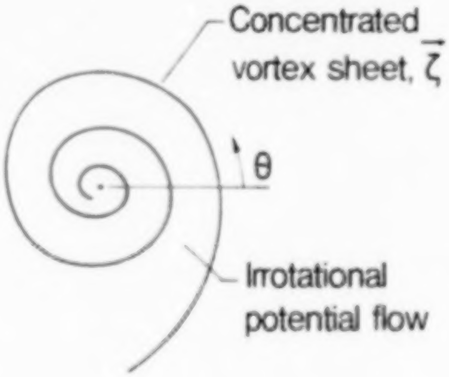
Concentrated vortex sheet, $\vec{\zeta}$
θ
Irrotational potential flow

- Comparison to axisymmetric, distribution ζ sol'n

  $\vec{V}(r/z, \theta; \vec{\zeta}\text{ concentrated}) = \vec{V}(r/z; \vec{\zeta}\text{ distributed}) + \text{HOT}$
  $\vec{\zeta} \times \vec{V} = 0$
  p - Bernoulli Field

COMPARISON OF VORTEX SHEET TRAJECTORIES

One approach to quantifying the matching of the inner and the outer models of the vortex is to compare the vortex sheet trajectories. This correlation stresses all three velocity components, and the outer region of the inner model (vortex core) should agree with the inner region of the outer model (vortex sheet) if the solutions are reasonably matched.

The Mangler and Weber (1966) solution, based on boundary condition data from the datum free-vortex-sheet solution ($\Delta\theta = 0$), shows reasonable correlation with the extended rollup free-vortex-sheet solution ($\Delta\theta = 3\pi$), except in the region given by $\pi < \Delta\theta < 2\pi$. The free-vortex-sheet solution is seen to be somewhat oblate, and nonaxisymmetric effects are, therefore, one cause for differences between the two solutions. Even so, the correlation is encouraging, and improvements based on advanced matching concepts can be expected.

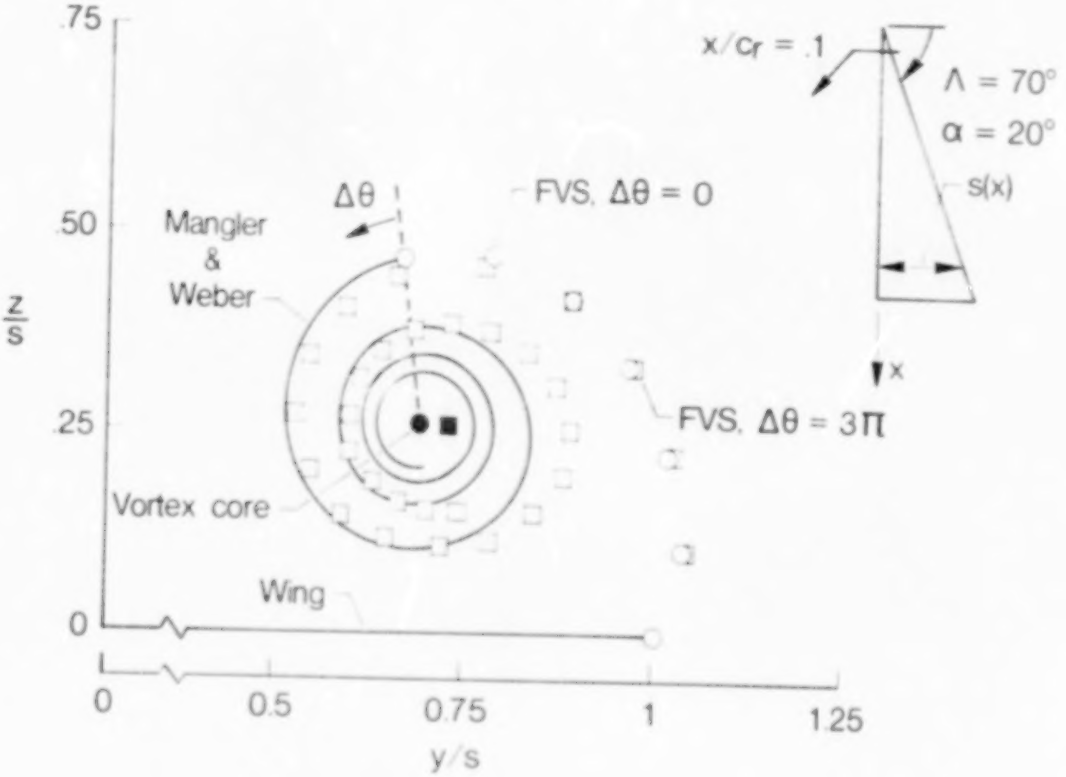

INNER TO OUTER FLOW MATCHING

Another approach to quantifying the matching between the inner and the outer models of the vortex is to directly compare the individual velocity components. The radial distributions of swirl and axial velocity were computed in the datum plane ($\Delta\theta = 0$) and show good correlation between the two representations of the vortex. The correlation for velocities in the plane oriented $\pi/2$ radians from the datum plane was not as good, consistent to the correlation of vortex sheet trajectories shown on the previous figure. Additional studies indicated that the shown correlation was independent of the amount of modeled rollup in the free-vortex-sheet theory.

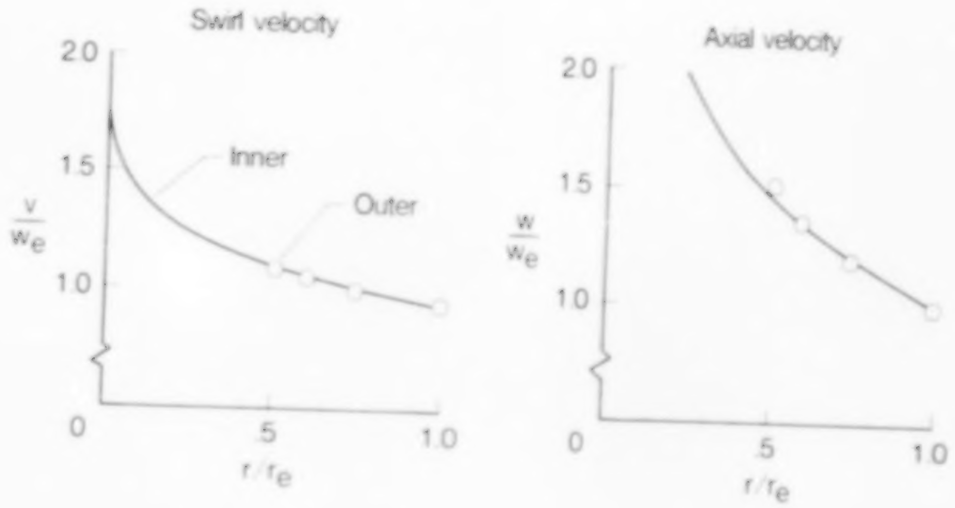

EXPERIMENTAL CORRELATION--VELOCITIES

Calculations have been performed for a wide range of conditions including isolated vortex core flows for generic external conditions as well as composite leading-edge vortex flows for delta, arrow, and diamond wings over a broad range of leading-edge-sweep angles and angles of attack. Typical velocity profiles through the core of the vortex are shown in this figure for a 75-degree delta wing at an angle of attack of 15 degrees. The experimental results of Earnshaw (1962) were obtained for a 76-degree (unit aspect ratio) delta wing at an angle of attack of 14.9 degrees. The freestream reference Mach number was approximately 0.09 and the Reynolds number, based on the wing root chord, was approximately three million.

Comparisons between the theoretical and experimental velocity profiles show reasonable correlations for the outer region of the vortex core and for the radial extent of the viscous subcore. The major discrepancy of this correlation is the centerline axial flow, and both theory and experiment are probable contributors to this discrepancy. Although the five-hole Conrad probe was small as compared to wing dimensions, its diameter is still appreciable as compared to the scale of the viscous subcore. Apart from the probe perturbing the flow itself, gradients across the probe head will also affect the measurements. Theoretically, the major factors affecting the lack of correlation are the incompressible and laminar flow assumptions. Because these flows have a local maximum in velocity at or near the vortex axis, they can be locally compressible at incompressible reference conditions. The inclusion of compressibility effects or turbulence effects would lessen the centerline axial flow.

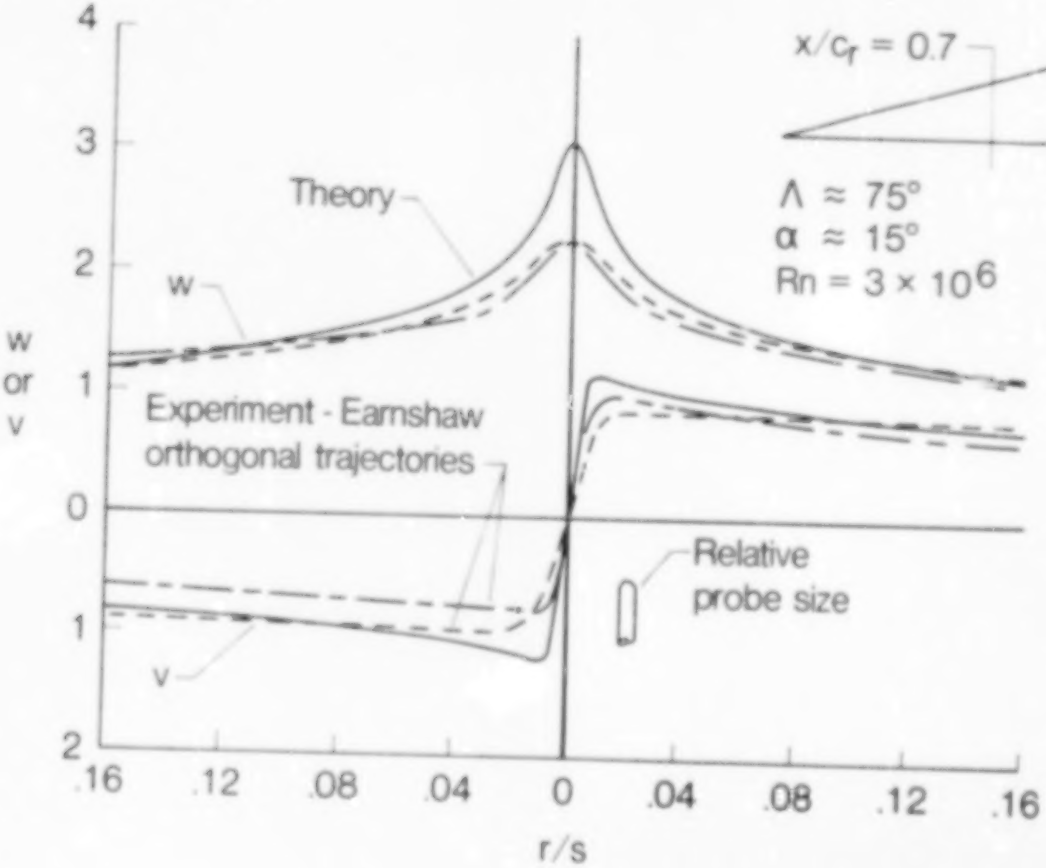

EXPERIMENTAL CORRELATION--PRESSURES

The correlation between theoretical and experimental pressure coefficients is consistent with the velocity correlations. The centerline static pressure coefficient is more negative than the experimental value, chiefly because of the increased centerline axial flow. However, static pressures of this magnitude are not unusual for vortex core flow. At higher angles of attack Earnshaw (1962) recorded C_p values of approximately -24; for a 65-degree swept wing at 15 degrees incidence Lambourne and Bryer (1962) recorded C_p values in the vicinity of -13.

The theoretical total pressure losses are confined to the viscous subcore whereas, experimentally, they are evidenced over the majority of the region shown. However, the theory provides a reasonable estimation of the maximum total losses at the centerline of the vortex.

The computed flow exhibits many of the general features of leading-edge vortex core flow; the flow is weakly singular in the radial direction, has a local maximum axial velocity at the vortex axis several times the freestream value, and has total pressure losses in this same region.

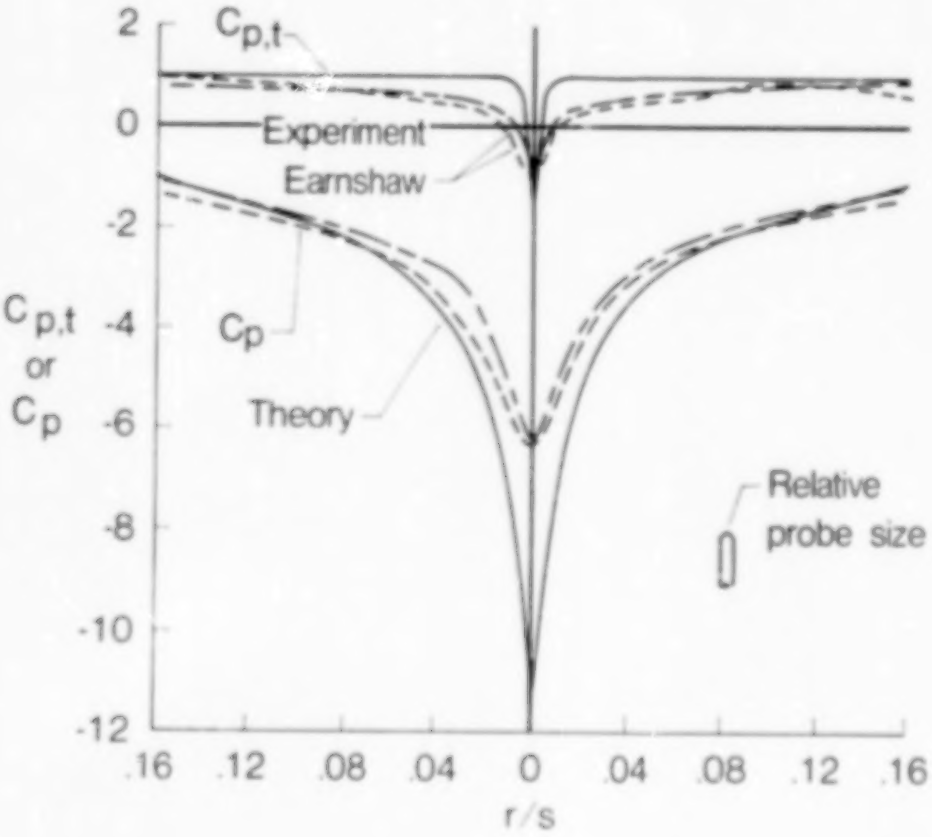

DEFINITION OF HELIX ANGLE

The vortex core flow was analyzed a posteriori by several established criteria for evidence of incipient vortex breakdown. Included in this analysis were the boundary-layer analogy of Hall (1967), the hydrodynamic stability criterion of Ludwieg (1962), and a critical helix angle criterion. Of these criteria, the critical helix angle was found to offer the best correlation with experimental trends.

The tangent of the helix angle is defined as the ratio of the swirl to the axial velocity. It provides a local measure of the flow going through the axisymmetric plane to the flow going down the plane. Previous research has shown that vortex breakdown can occur for values of the helix angle in excess of some critical value, generally in the vicinity of 45 degrees, when accompanied by an adverse longitudinal pressure gradient.

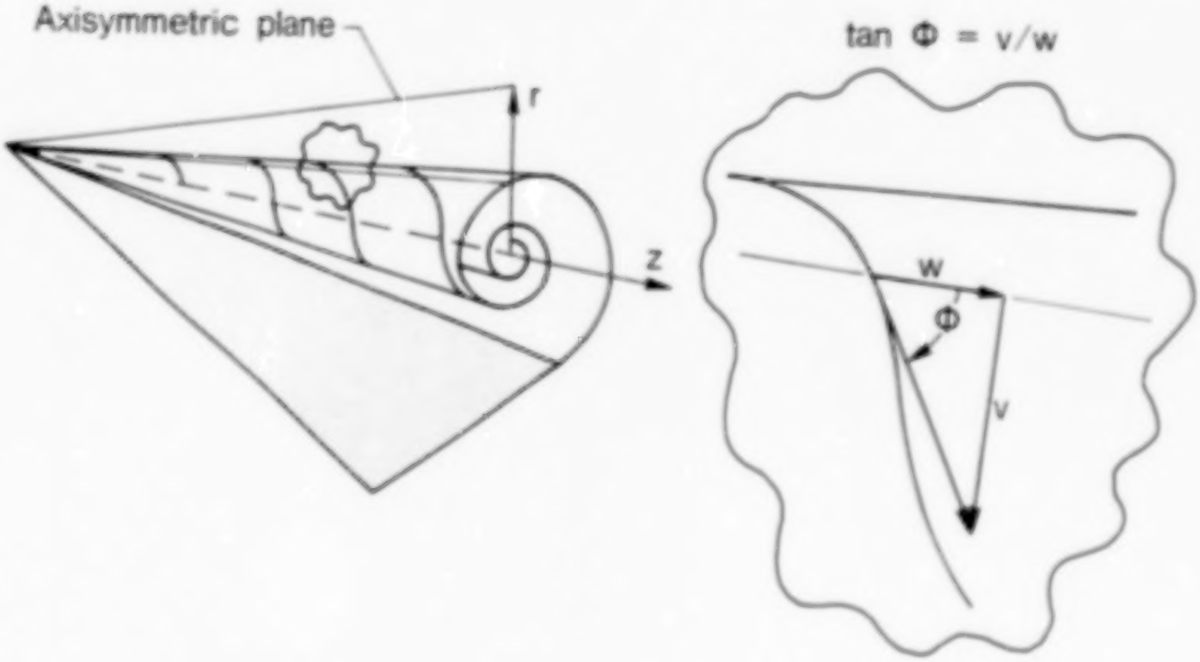

Previous research has shown that tan $\Phi > 1 \Longrightarrow$ breakdown

HELIX ANGLE CONTOURS--ALPHA = 20 DEGREES

Analysis of the vortex core flow for local helix-angle effects is presented in the form of contour distributions. The roughly diagonal edge where the contours terminate corresponds to the edge of the inner computational space as given by the free-vortex-sheet theory. This contour plot is for a 70-degree delta wing at an angle of attack of 20 degrees; the data of Wentz and Kohlman (1968) indicate that breakdown will first occur at the trailing edge of this wing at approximately 29 degrees angle of attack.

Several aspects of the helix angle distribution are noteworthy. There are two regions of maximum helix angle, both of which occur at the edge of the vortex. One is near the apex and the other is in the vicinity of the trailing edge. In addition, the structure of the vortex in terms of this parameter changes from the wing to the wake; over the wing the maximum helix angle occurs radially at the edge of the vortex, whereas in the wake this maximum occurs well within the vortex. Finally, a region of maximum helix angle persists well downstream from the trailing edge.

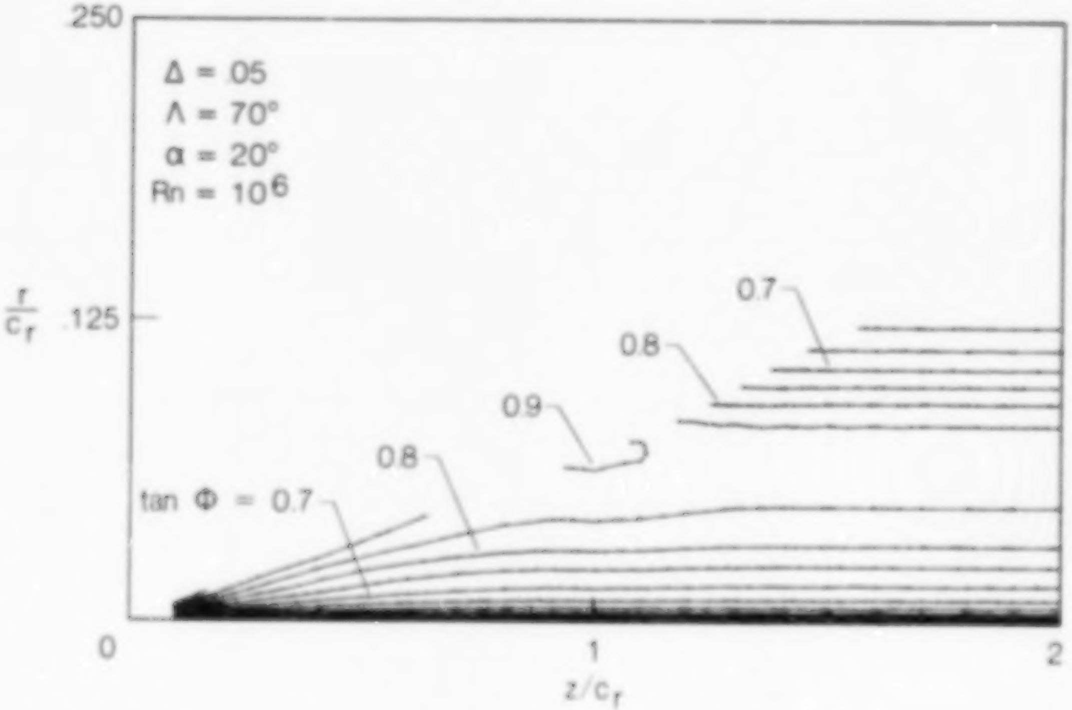

HELIX ANGLE CONTOURS--ALPHA = 30 DEGREES

A similar contour analysis of the flow in the core of the vortex is shown for an angle of attack slightly in excess of the critical value for which breakdown occurs at the trailing edge. The general features of this solution are similar to the 20-degree case of the previous figure. For this case the maximal value of the helix angle tangent exceeds unity.

Additional analysis showed that, in general, near the apex the centerline vortex core flow exhibited a proverse longitudinal static pressure gradient whereas near the trailing edge this gradient was adverse.

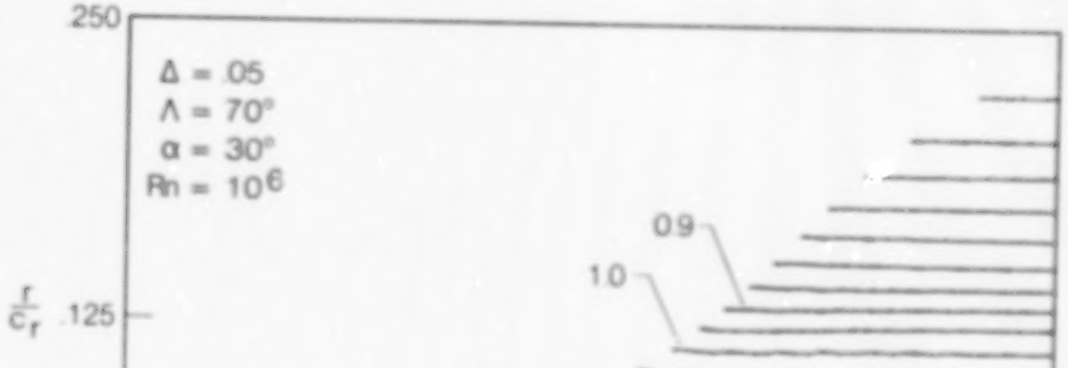

TRAILING-EDGE MAXIMUM HELIX ANGLE

The various solutions were analyzed for the conditions of a maximum helix angle occurring in conjunction with an adverse longitudinal pressure gradient. These conditions occurred in the vortex in the vicinity of the trailing edge. The resultant values are shown for several of the delta wings analyzed along with the experimentally determined values of α_b, the angle of attack for which vortex breakdown first occurs at the trailing edge, from the Wentz and Kohlman (1968) data. The experimental condition of vortex breakdown at the trailing edge of the delta wings correlates roughly with a constant theoretical value of the maximum helix angle at the trailing edge. With the present formulation, this value is slightly greater than one; for reference purposes the conical value of 1.16 is also shown.

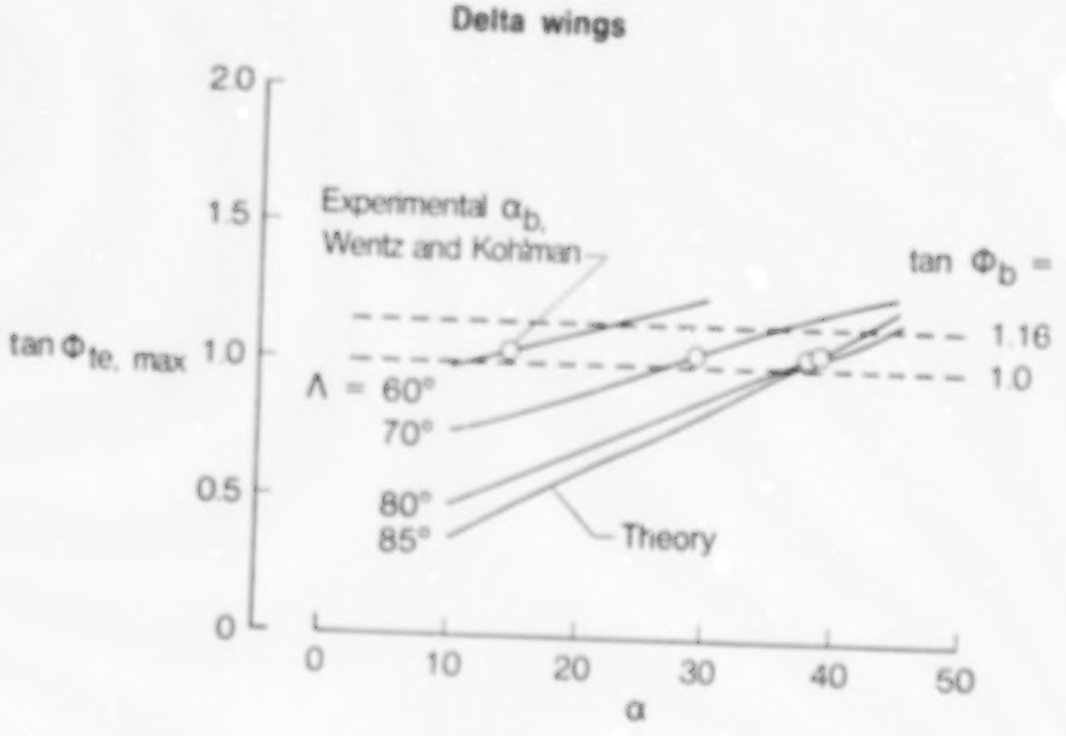

VORTEX BREAKDOWN STABILITY BOUNDARY

This correlation is also shown in a more familiar parameter space; the theoretical results are based on a critical helix angle tangent value of unity. This numerical correlation indicates a good estimation of the strong leading-edge sweep effects on the vortex breakdown stability boundary for delta wings. Additional studies have shown that the same criterion with the same critical value also provided a good estimation of the weak trailing-edge effects on this boundary.

Numerical correlation

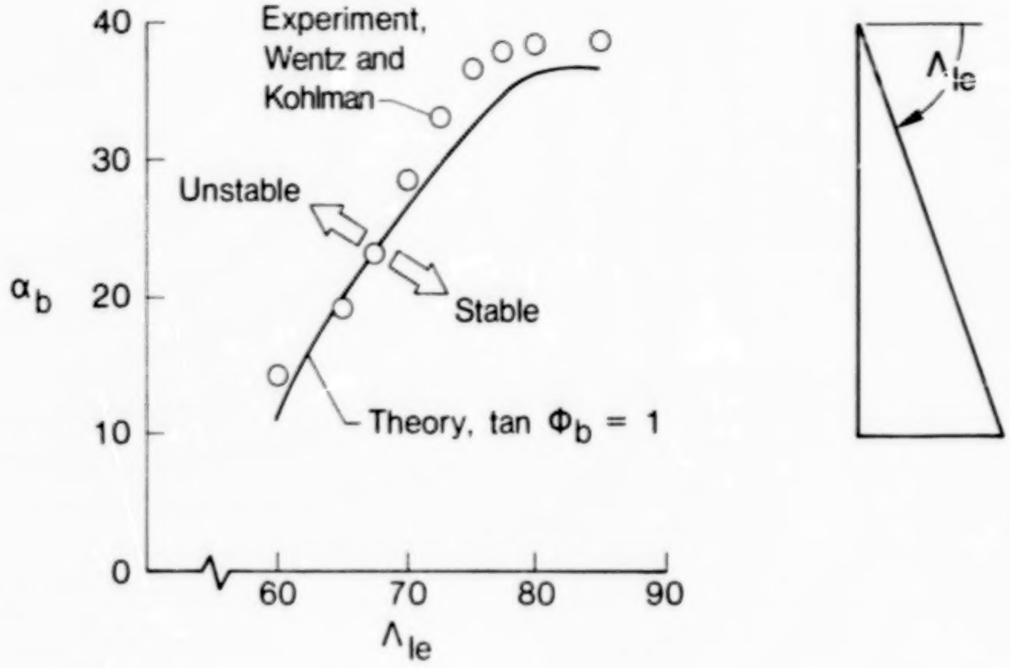

c3

CONCLUDING REMARKS

The flow in the core of a three-dimensional, separation-induced, leading-edge vortex can be calculated by appropriately matching inner and outer representations of the vortex. This approach is not strictly limited to the theories or applications of the present formulation. Other vortical flows (e.g., forebody vortices) could be addressed in a similar fashion with models appropriate to the particular flow.

The computed results of the present formulation exhibit many of the prominent features of the subject flow. These include weak radial singularities in the inviscid, rotational flow, axial velocity excesses at the vortex core axis which are several times the freestream reference value, and total pressure losses in the viscous subcore which arise due to modeled viscous effects. The solutions are, in general, highly three-dimensional, and showed reasonable correlation with experiment.

The experimental condition of incipient vortex breakdown at the trailing edge of delta, arrow, and diamond wings was found to closely correlate with the theoretical condition of a critical helix angle in conjunction with an adverse longitudinal pressure gradient.

The method can readily be extended to account for a number of additional effects. These include compressibility, turbulence, elliptic effects, and viscous/inviscid interaction consequences. Systematic extension of the present formulation should provide additional insights to the vortex breakdown phenomena for three-dimensional flows at practical Reynolds numbers.

- Method demonstrated
    - Matched inner/outer representations
    - Nonconical effects
    - Nonaxisymmetric effects
- Computed results
    - Prominent flow features exhibited
    - Reasonable correlation with experiment
    - Vortex breakdown stability boundary
- Method is readily extendable
    - Compressibility
    - Eddy viscosity
    - Elliptic core
    - Viscous/inviscid interactions

REFERENCES

Earnshaw, P. B. (1962): An Experimental Investigation of the Structure of a Leading-Edge Vortex. Aeronautical Research Council (ARC) R & M No. 3281, England.

Hall, M. G. (1961): A Theory for the Core of a Leading-Edge Vortex. Journal Fluid Mechanics, Vol. 11, p. 209.

Hall, M. G. (1966): The Structure of Concentrated Vortex Cores. Progress in Aeronautical Sciences, Vol. 7, pp. 53-110.

Hall, M. G. (1967): A Numerical Method for Solving the Equations of a Vortex Core. Aeronautical Research Council (ARC) R & M No. 3467, England.

Johnson, F. T.; Lu, P.; Tinoco, E. N.; and Epton, M. A. (1980): An Improved Panel Method for the Solution of Three-Dimensional Leading-Edge Vortex Flows. Volume 1--Theory Document. NASA CR-3278, July.

Lambourne, N. C.; and Bryer, D. W. (1962): The Bursting of Leading-Edge Vortices--Some Observations and Discussion of the Phenomena. Aeronautical Research Council (ARC) R & M No. 3282.

Luckring, J. M. (1985): A Theory for the Core of a Three-Dimensional Leading-Edge Vortex. AIAA Paper No. 85-0108, January.

Ludwieg, H. (1962): Zur Erklärung der Instabilität der über angestellten Deltaflügeln auftretenden freien Wirkbelkerne. ZFW, Vol. 10, No. 6, pp. 242-248, June. See also, An Explanation of the Instability of the Free Vortex Cores Occurring Over Delta Wings with Raised Edges. NASA TM-75861, September 1980. (Technical translation.)

Mangler, K. W.; and Weber, J. (1966): The Flow Field Near the Center of a Rolled-Up Vortex Sheet. Royal Aircraft Establishment (RAE) TR No. 66324, England.

Stewartson, K.; and Hall, M. G. (1963): The Inner Viscous Solution for the Core of a Leading-Edge Vortex. Journal of Fluid Mechanics, Vol. 15, pp. 306-318.

Wentz, W. H., Jr.; and Kohlman, D. L. (1968): Wind-Tunnel Investigation of Vortex Breakdown on Slender Sharp-Edged Wings. NASA CR-98737, November.

D/10

N88-14936

ANALYSIS AND PERFORMANCE PREDICTION OF SCRAMJET INLETS UTILIZING A THREE-DIMENSIONAL NAVIER-STOKES CODE

S10-07

117234

22P

Ajay Kumar and Carl A. Trexler
NASA Langley Research Center
Hampton, Virginia

PRECEDING PAGE BLANK NOT FILMED

PAGE 186 INTENTIONALLY BLANK

[redacted]MJET INLET FLOW FIELD

Scramjet inlets have high geometric complexity as well as a highly complex flow field. The flow is primarily three-dimensional, possibly turbulent. It involves complex shock and expansion wave interactions. It also involves strong shock/boundary-layer interactions resulting in separated regions. Further, due to the aft placement of the cowl, the internal flow ahead of the cowl is exposed to the external flow resulting in interaction between the two.

- **PRIMARILY THREE-DIMENSIONAL, POSSIBLY TURBULENT**
- **INVOLVES COMPLEX SHOCK AND EXPANSION WAVE INTERACTIONS**
- **INVOLVES STRONG SHOCK/BOUNDARY-LAYER INTERACTIONS RESULTING IN SEPARATED REGIONS**
- **INVOLVES INTERACTION BETWEEN INTERNAL AND EXTERNAL FLOW FIELD RESULTING IN FLOW SPILLAGE**

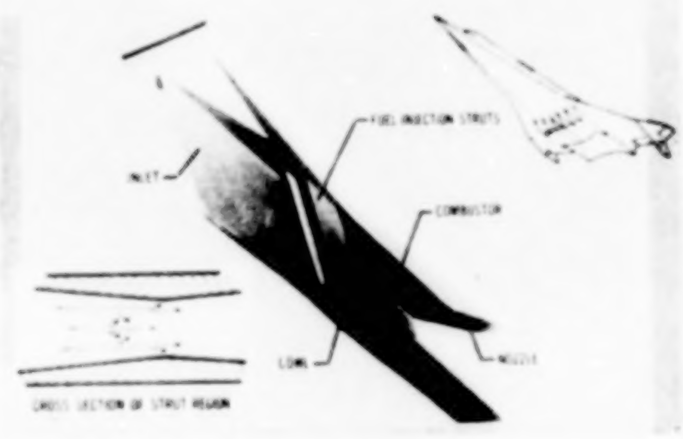

ORIGINAL PAGE IS
OF POOR QUALITY

INLET RESEARCH

Due to the complex nature of the flow, most scramjet inlet research to date has been experimental with little supporting analytical work. However, with the increasing availability of high-speed, large-storage computers and advanced computing techniques, it has become feasible to numerically simulate flow fields associated with high-speed inlets. The goal of the present research is to provide an accurate and efficient inlet analysis tool that allows promising design configurations to be developed with less reliance on extensive wind-tunnel testing.

3-D EULER/NAVIER-STOKES INLET ANALYSIS CODE

The research to provide inlet analysis software started with the development of a two-dimensional Euler and Navier-Stokes code; this was followed by the three-dimensional Euler and Navier-Stokes code. An axisymmetric version of the code is also available. In this presentation, I will discuss only the three-dimensional analysis results. This figure briefly describes the features of the code.

- Governing equations in conservation form
- Boundary-fitted curvilinear coordinates
- Algebraic turbulence model
- MacCormack's explicit or explicit-implicit scheme
- Fully vectorized

CODE ORGANIZATION AND PERFORMANCE

Special attention has been given to organize the code for maximum use of the central core of the computer. The code is fully vectorized and calculations are performed in planes with temporary reusable vectors maintained only in two local planes. Further, to save on storage requirements, the transformation metric data are calculated in each time-step. On the CDC VPS 32 computer, the code can accommodate a maximum of 1.4 x 10^6 grid points without going out of primary memory of the system. It has a compute rate of about .7 x 10^{-5} sec per grid point per time step. For more details, see reference 1.

- The code is written in Star Fortran and uses 32-bit word arithmetic
- Transformation metric data are calculated in each time step
- Calculations are performed in planes with temporary reusable vectors maintained only in two local planes

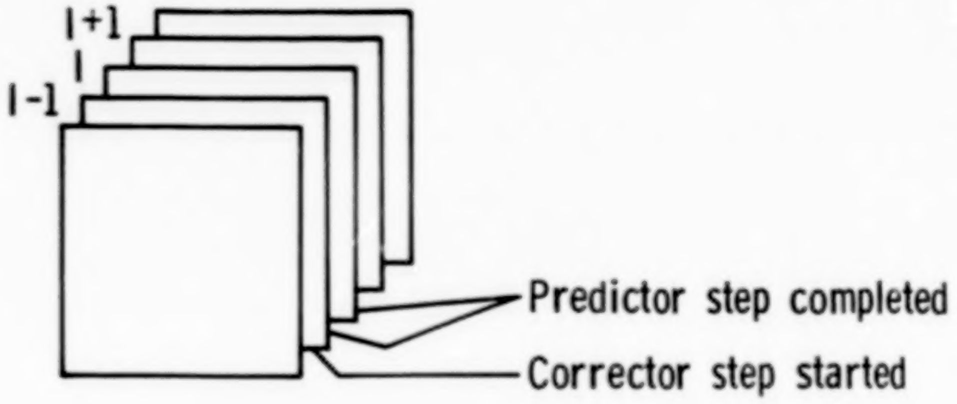

- Maximum grid size that can be used without going out of primary memory is approximately 1.4 million points
- Compute rate is .7 × 10^{-5} sec/grid point for one complete time-step (i.e. both predictor and corrector step)
- Typical solution can be obtained in 20-150 minutes CPU time for up to 100,000 grid points

SYMMETRIC WEDGE CORNER AND SCHEMATIC OF CORNER FLOW

To verify the code, calculations were made for laminar and turbulent flow for a 3-D symmetric wedge corner shown in the figure. The flow in such a corner is representative of the type of flow inside a scramjet inlet. A schematic of the basic characteristics of the corner flow is also presented in the figure. It has very complex structure that includes wall shocks, corner shock, internal shocks, and slip lines.

In the present analysis, a grid of 39 x 61 x 61 points is used with suitable refinement near the corner walls. Calculations are made for the following conditions:

$M_\infty = 3.0$

$N_{R_\infty} = 3.9 \times 10^5$; laminar flow

1.1×10^6; turbulent flow

$T_\infty = 105°K$

$T_w = 294°K$

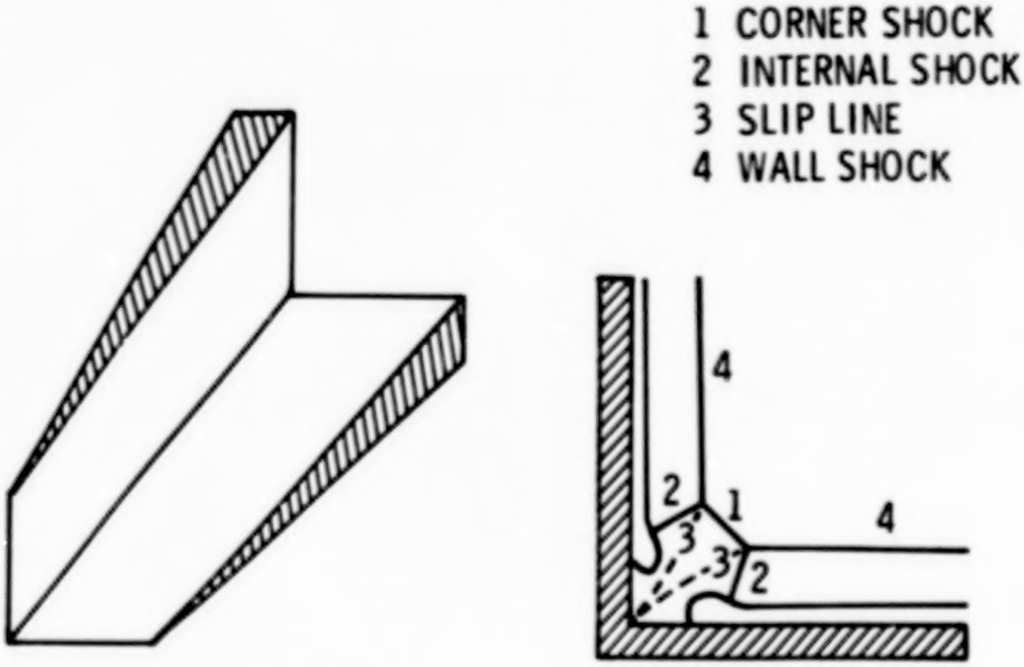

(a)

(b)

DENSITY CONTOURS FOR SYMMETRIC WEDGE CORNER

The figure shows the density contours for the laminar flow as obtained from the present code. Experimentally determined contours are also shown. It is seen that the calculations have predicted the corner flow features very well and are in very good agreement with the experiment.

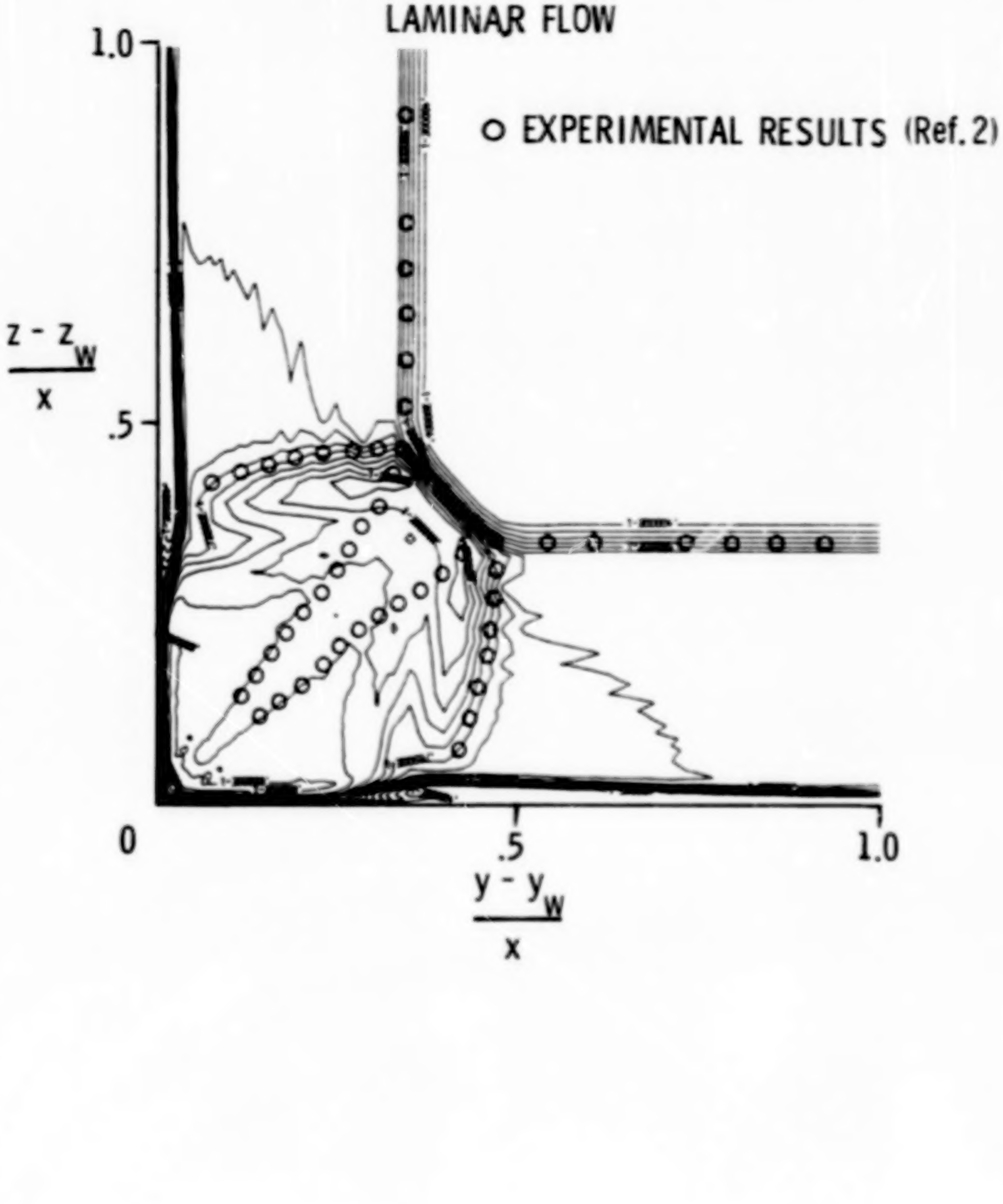

SURFACE PRESSURE DISTRIBUTION FOR SYMMETRIC WEDGE CORNER

This figure presents a comparison of the sidewall pressure distribution with experiment for the laminar and turbulent flow. The predicted results compare well with the experimental results.

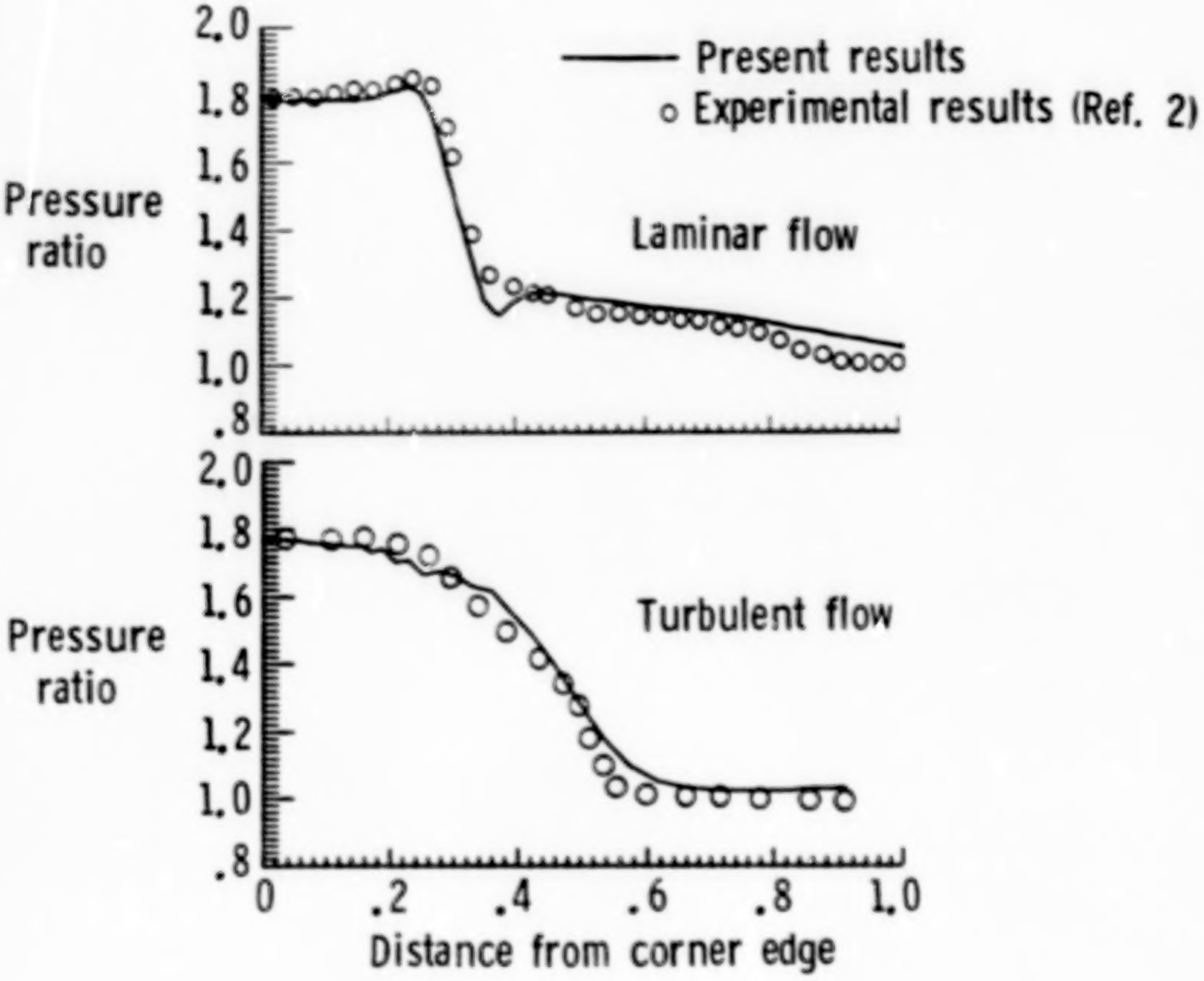

HIGH-SPEED INLET CONFIGURATIONS

The next four figures present a variety of high-speed inlet configurations that have been analyzed with the 3-D Navier-Stokes code. Results on two other configurations will be presented later.

GEOMETRY OF THE PARAMETRIC SCRAMJET ENGINE

$H_1 = 7.2$, $W = 6.4$, $G = 1.6$

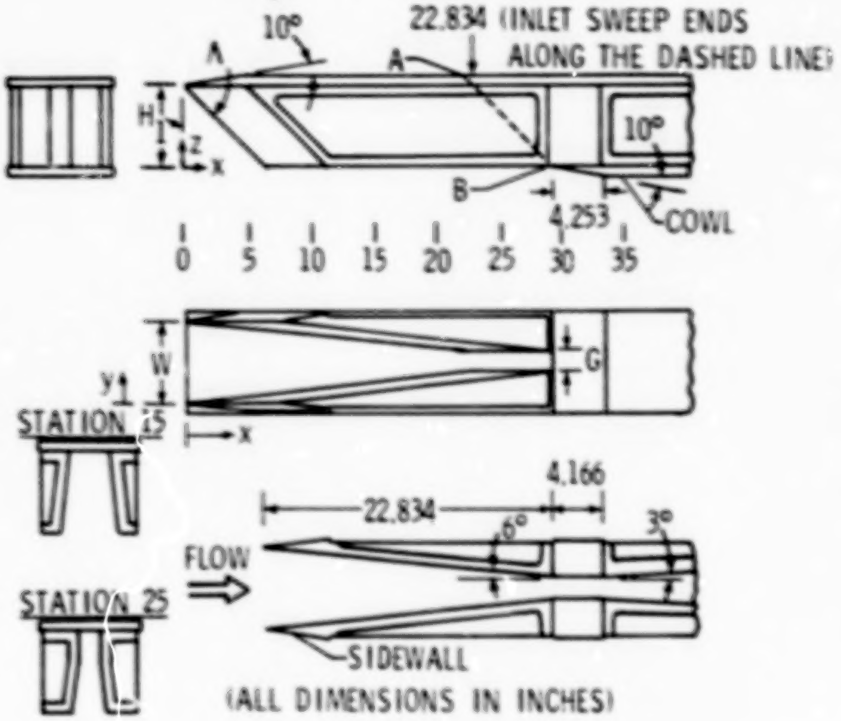
10°
22.834 (INLET SWEEP ENDS ALONG THE DASHED LINE)
A
A
H
z
x
10°
B
4.253
COWL
0
5
10
15
20
25
30
35
W
G
y
x
STATION 15
4.166
22.834
6°
3°
FLOW
STATION 25
SIDEWALL
(ALL DIMENSIONS IN INCHES)

GEOMETRY OF AFT INLET CONFIGURATION

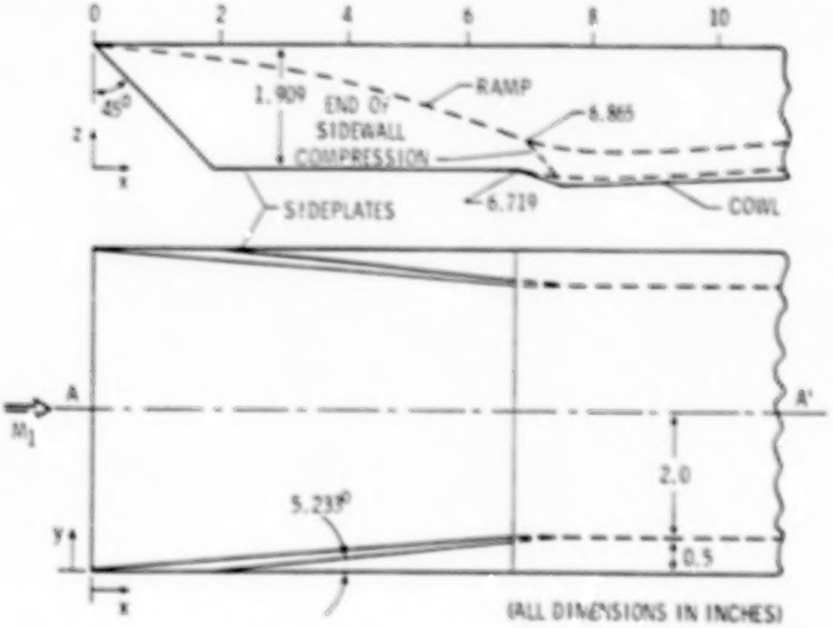
0
2
4
6
8
10
45°
1.909
RAMP
END OF SIDEWALL COMPRESSION
6.865
z
x
6.719
SIDEPLATES
COWL
A
A'
M_1
2.0
5.235°
y
0.5
x
(ALL DIMENSIONS IN INCHES)

TYPICAL MITS INLET CONFIGURATION

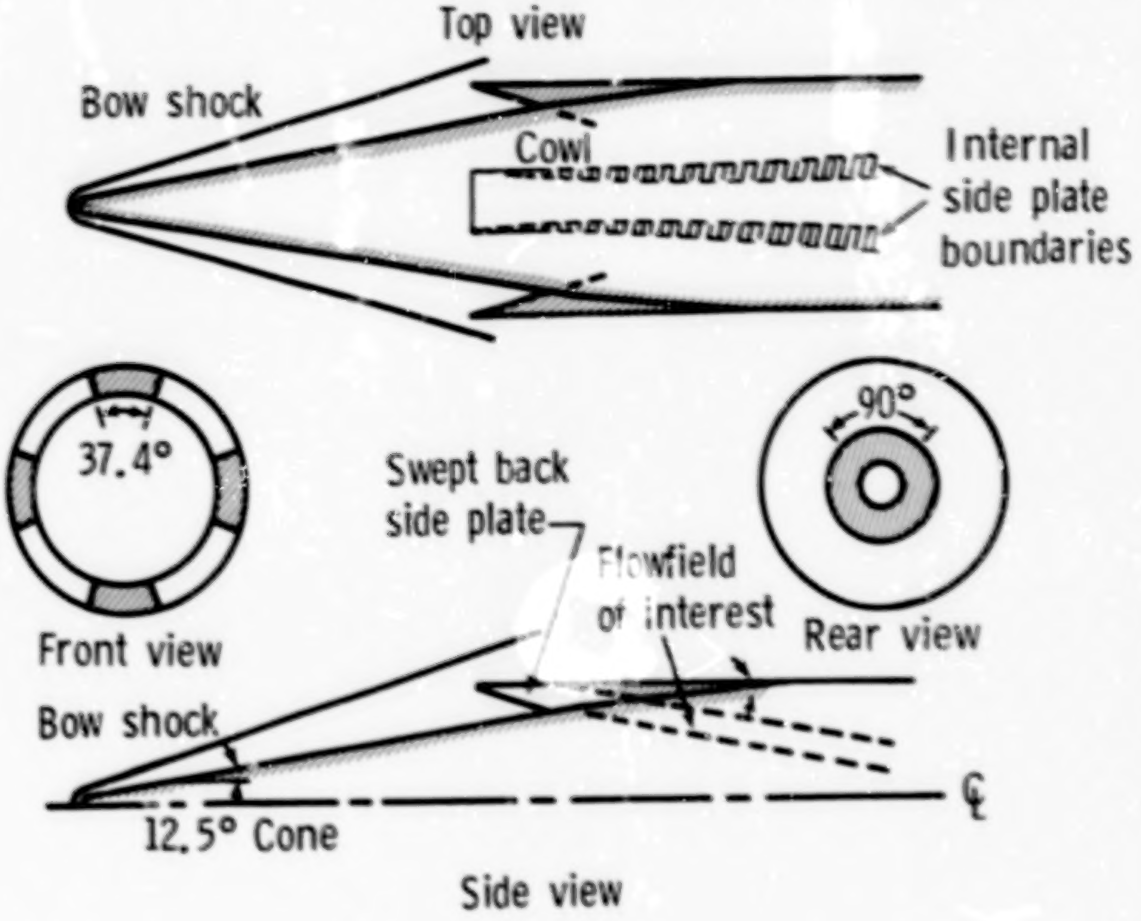
Top view
Bow shock
Cowl
Internal side plate boundaries
37.4°
Front view
Swept back side plate
Flowfield of interest
90°
Rear view
Bow shock
12.5° Cone
℄
Side view

SUPERSONIC INLET DUCT

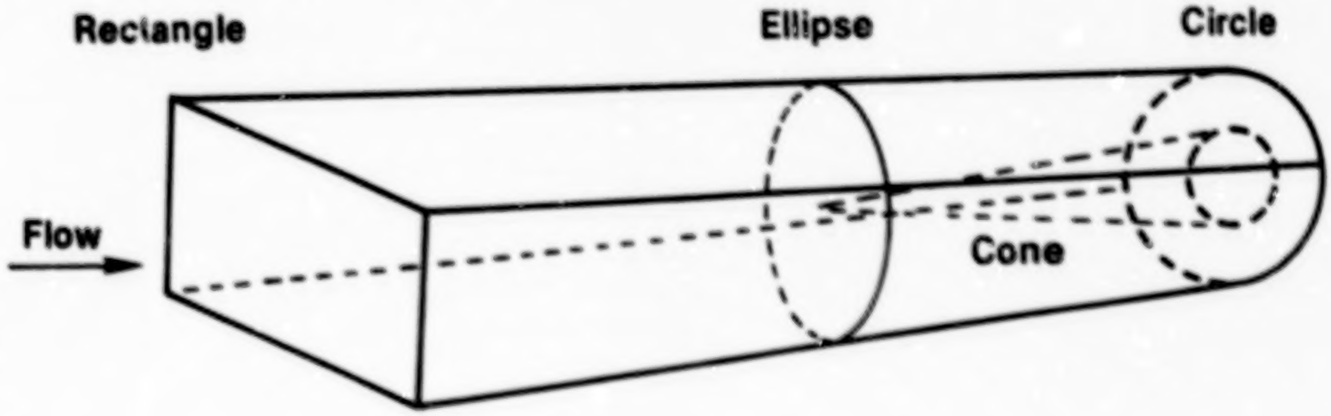
Rectangle
Ellipse
Circle
Flow
Cone

PHYSICAL DOMAIN OF COMPUTATION

Before any results on the inlets are presented, a brief description is given on how the present analysis accounts for the interaction of internal flow with the external flow. As mentioned earlier, this interaction occurs due to the aft placement of the cowl, which exposes the flow inside the inlet to the flow outside the inlet in the region ahead of the cowl. In order to account for this interaction, a portion of the outside flow under the cowl plane must be included in the analysis. Ideally one should go down and around the sidewalls far enough so that the free-stream conditions can be applied on the free boundaries but this would greatly increase the computational requirements. In the present analysis, the region is extended as shown in the figure by the dashed line (only half of the flow is calculated due to symmetry). This limited extension of the computational domain should be sufficient because in the actual engine, several such modules will be placed side by side.

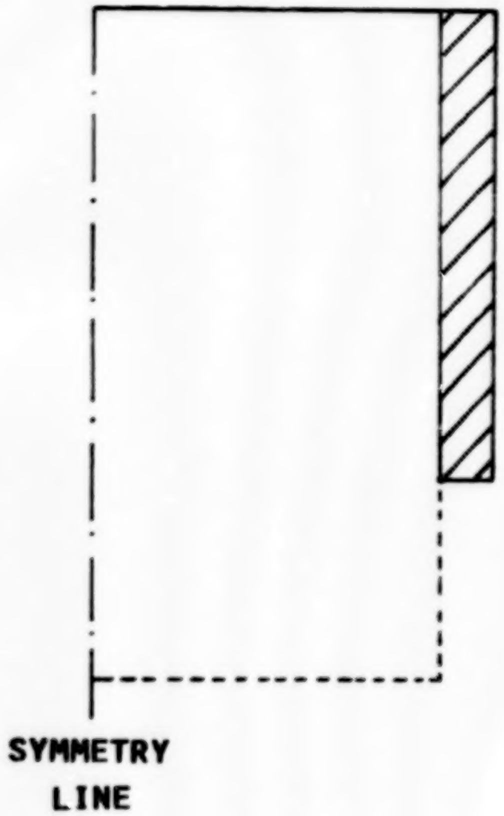

LINE DIAGRAM OF SINGLE-STRUT, REVERSE-SWEEP INLET

The first configuration is a single-strut, reverse-sweep inlet shown here in a line diagram. It has wedge-shaped sidewalls which are swept back at an angle of 30°. A compression strut is located in the center passage of the inlet, which is also swept, but it is swept forward at an angle of 30°. The throat width is held constant at all heights in the inlet, which results in an unswept throat. The cowl closure starts at D. Various other geometrical parameters are shown on the line diagram. Flow is calculated at the following conditions:

$M_1 = 4.03$, $P_1 = 8724\ \mathrm{N/m^2}$, $T_1 = 65°\mathrm{K}$

These correspond to experimental conditions.

$H_1 = 2.75$ in., $W = 1.005$ in., $W/G = 4.16$, $\delta_s = 6°$

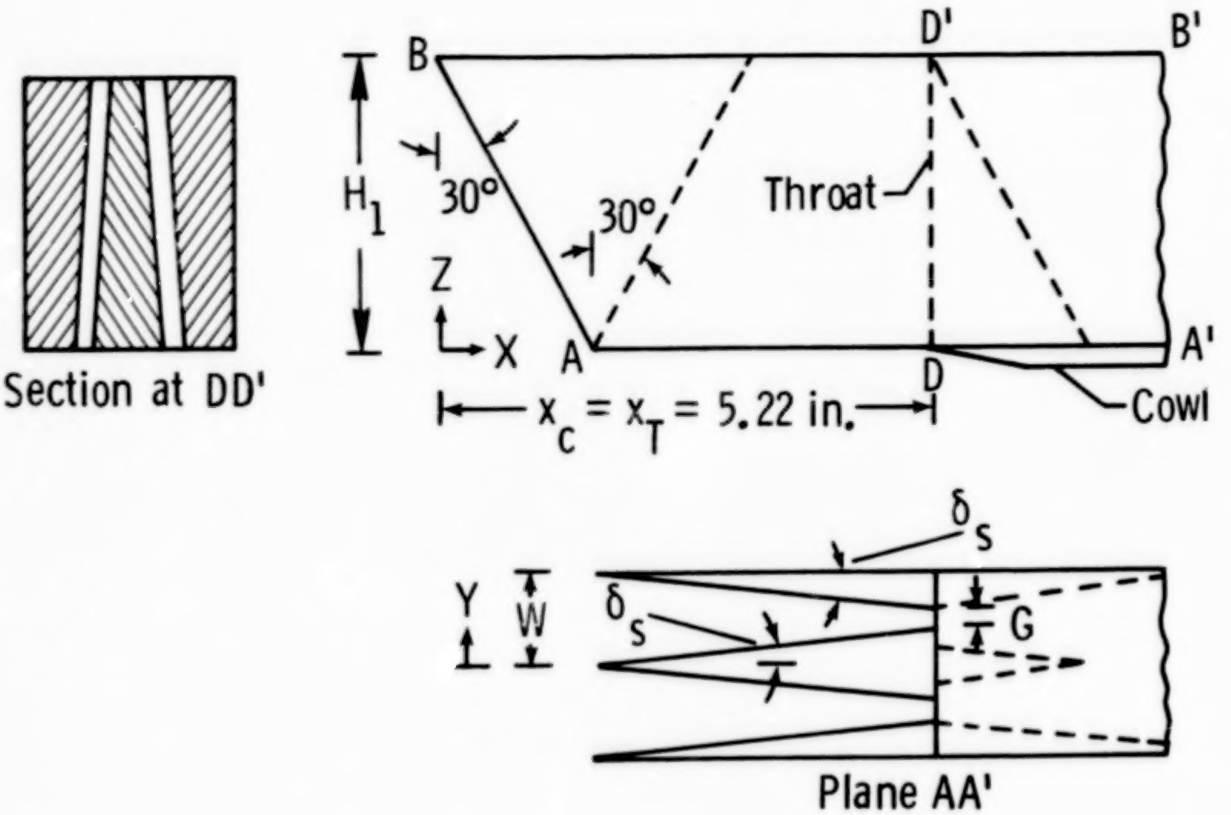

Section at DD'
B
D'
B'
H_1
30°
30°
Throat
Z
X
A
D
A'
Cowl
$x_c = x_T = 5.22$ in.
δ_s
Y
W
δ_s
G
Plane AA'

PRESSURE CONTOURS IN PLANES PARALLEL TO THE COWL PLANE

(M_1 = 4.03)

This figure shows the pressure contours in three planes corresponding to z/H_1 = 0.145, 0.5, and 0.89. One of the problems associated with single-strut inlets with similar sweep on the sidewalls and the strut is that for a given Mach number, the shock waves from the sidewalls and the strut will coalesce into a stronger shock wave which is not desireable for the operation of the inlet over a Mach number range with fixed geometry. In the present configuration, it appears that the shock wave coalescence problem is alleviated. Due to the opposite sweep, shock waves coalesce only in certain planes but not all across the inlet height at a given Mach number. For example, the pressure contours show that for the present conditions, shock waves coalesce in the planes near the top surface but not in the planes near the cowl.

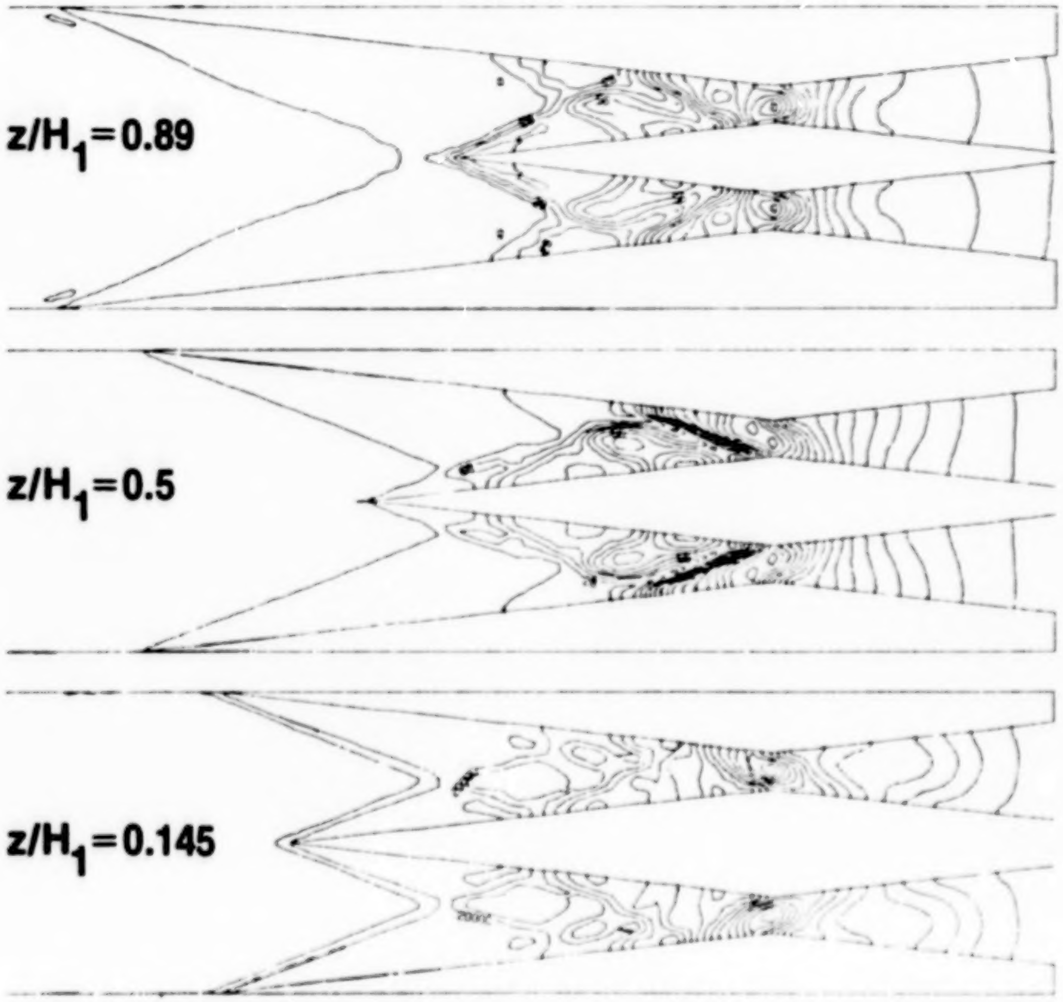

VELOCITY VECTOR FIELD IN PLANES PARALLEL TO THE COWL PLANE

(M_1 = 4.03)

This figure shows the velocity vector field in the same three planes. The separated flow regions on the sidewalls substantiate the observation made from the pressure contours.

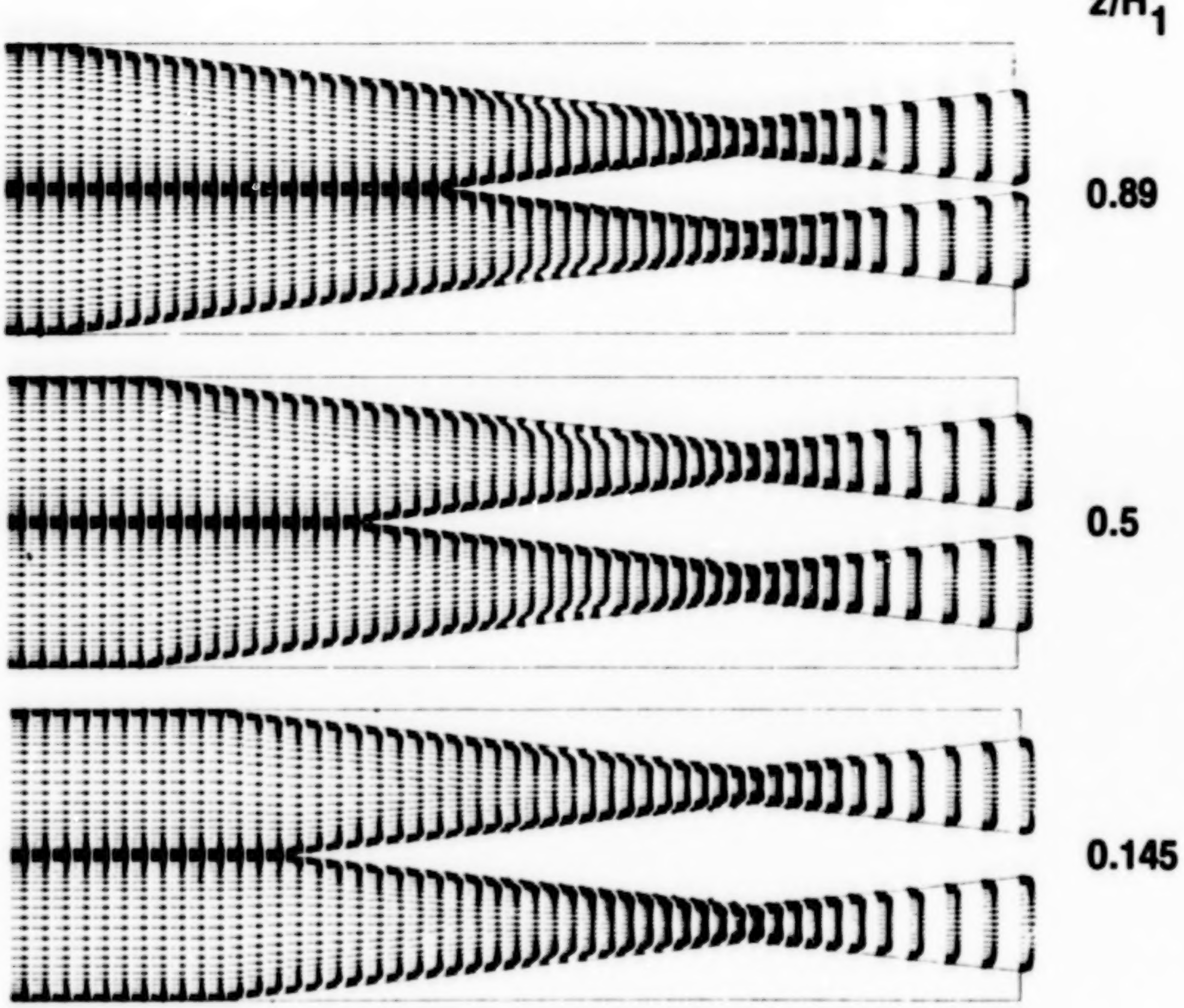

SIDEWALL PRESSURE DISTRIBUTIONS

This figure shows a comparison of the static sidewall pressure distributions with the experiment. It is seen that the predicted pressure levels compare very well with the experimental results up to the inlet throat. Deviations seen downstream of the throat are due to the fact that the experimental model had significantly different geometry than that used in the present calculations.

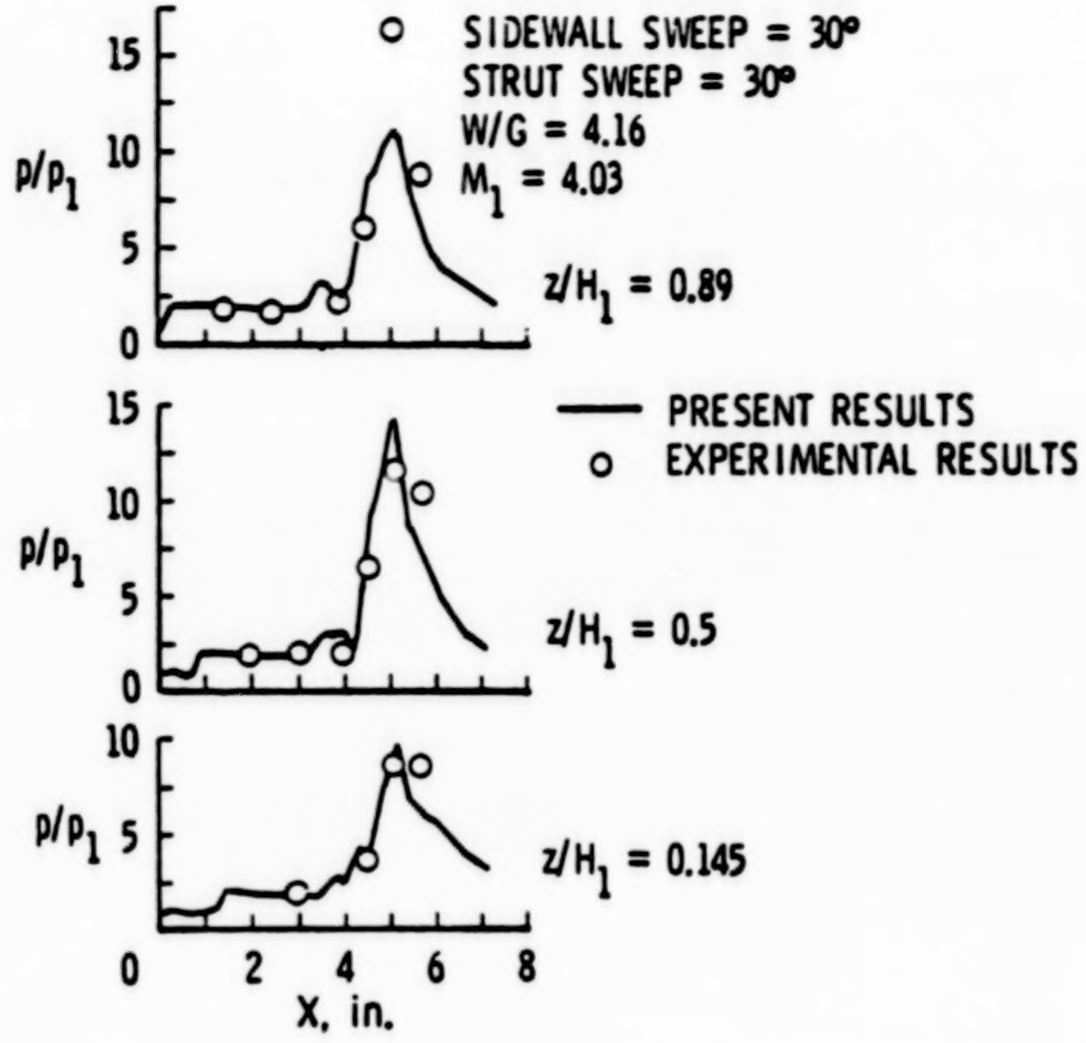

LINE DIAGRAM OF TWO-STRUT INLET

The second configuration for which results are presented here is a two-strut scramjet inlet. A line diagram of the inlet is shown below. This inlet also has wedge-shaped sidewalls which are swept back at an angle of 30°. Two compression struts are located in the center passage of the inlet and are also swept back at an angle of 30°. Sweep of all compression surfaces ends along line EF and the cowl closure starts at F. Various other geometrical parameters are shown on the line diagram. Flow is again calculated at Mach 4.03 in order to be able to compare with the experimental results.

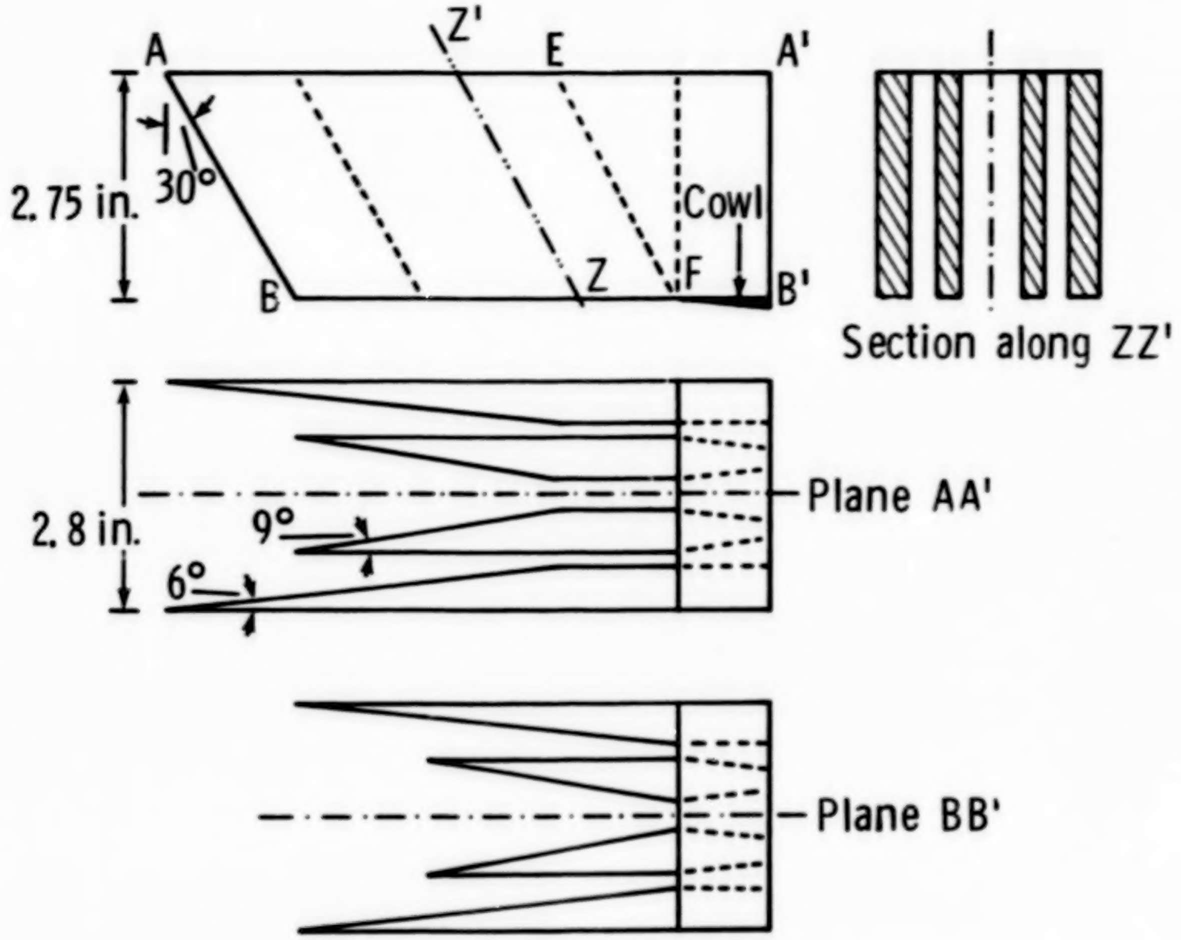

COMPUTATIONAL GRID

This figure shows the computational grid in one of the cross planes and in the symmetry plane. The calculations presented here are made with a grid of 41 x 51 x 37 points in x, y , z-directions, respectively. Out of the 37 planes in the z-direction, 11 planes lie under the cowl plane to account for the interaction between the internal and external flow. Discretization of this inlet is further complicated by the struts embedded in the flow field. In order to accommodate the strut, the present analysis makes the strut surfaces coincident with two grid planes in the y-direction and further allows 10 more grid planes to go through the strut. This results in slight blunting of the strut leading edge, but this blunting is relatively small due to grid concentration in the neighborhood of the strut surfaces. A typical cross-plane grid is shown in the figure. If a particular cross plane lies above the cowl plane, the grid points lying within the strut are disregarded and proper boundary conditions are applied on the strut surfaces, but if the cross plane lies below the cowl plane, all grid points in the plane are used in the calculations.

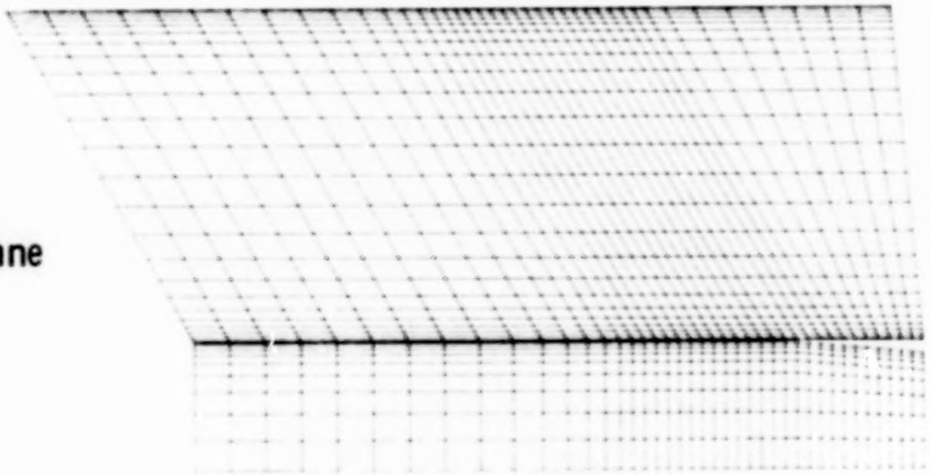

Symmetry plane

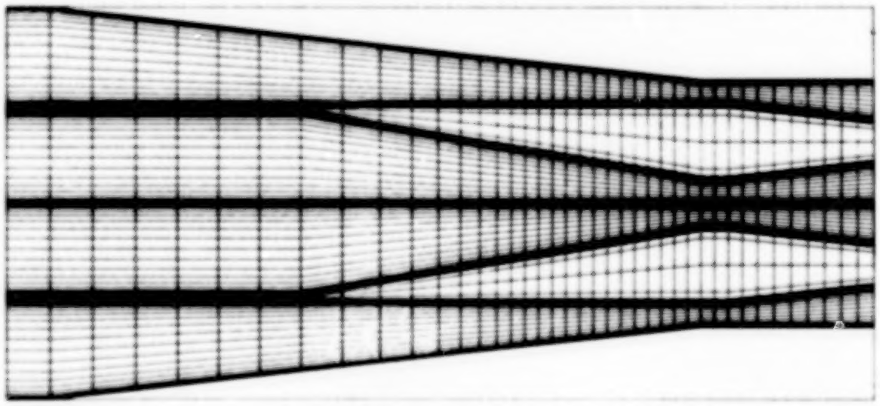

Cross plane

ORIGINAL PAGE IS
OF POOR QUALITY

VELOCITY VECTOR FIELD AND PRESSURE CONTOURS IN PLANE LOCATED AT MID-INLET HEIGHT

This figure shows the velocity vector field and static pressure contours in a plane located at mid-inlet height. Slight blunting of strut leading edges and associated small distortions are obvious from this figure. The velocity vector plot shows several regions of separated flow caused by the shock/boundary-layer interaction and the pressure contour plot shows clearly the shock and expansion waves and their interactions.

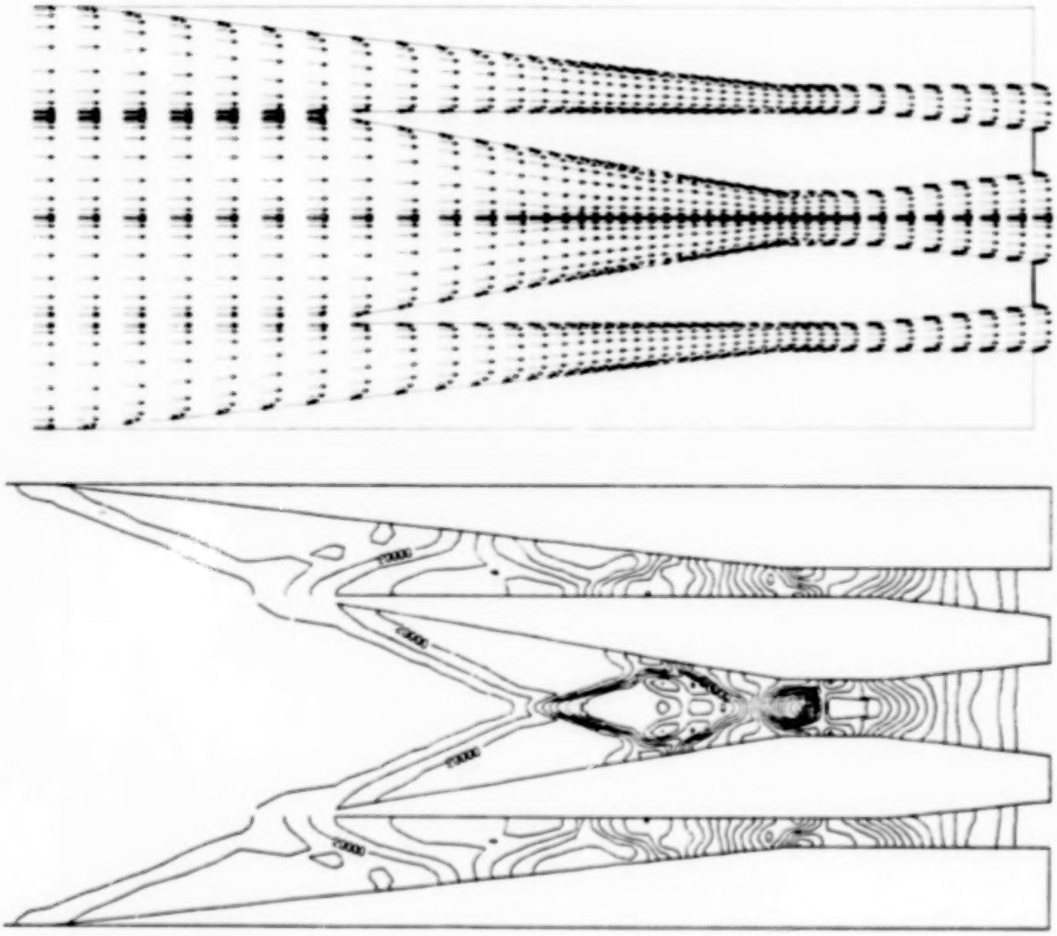

VELOCITY VECTOR FIELD AND PRESSURE CONTOURS

IN THE SYMMETRY PLANE

This figure shows the velocity vector field and static pressure contours in the symmetry plane. The velocity vector field shows a downturn in flow direction ahead of cowl resulting in some flow spillage. The downturn is caused by the sidewall sweep and the interaction between the flow inside and outside of the inlet. Once the inlet flow passes behind the cowl leading edge, it is turned back parallel to the cowl plane, and this turning results in a cowl shock which can be seen in the pressure contour plot on this figure.

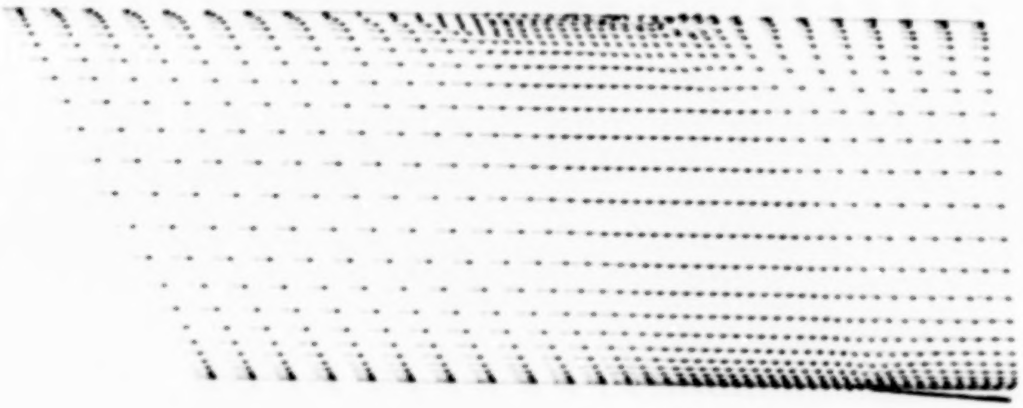

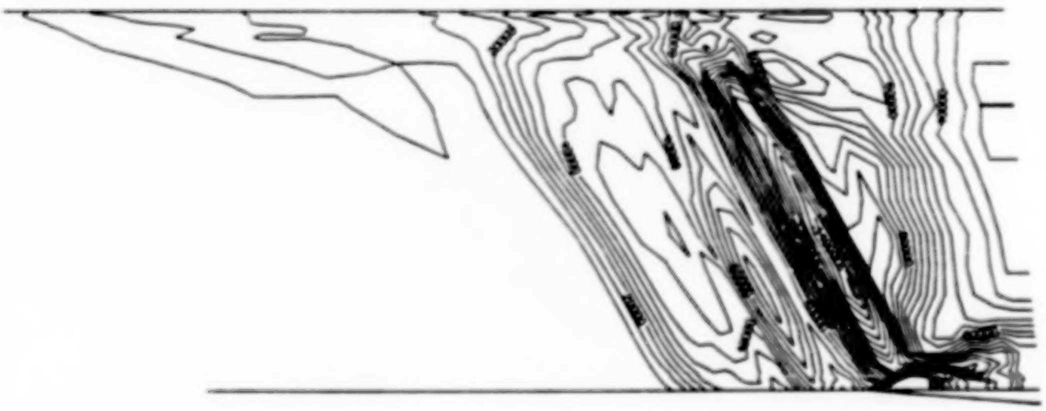

ORIGINAL PAGE IS
OF POOR QUALITY

SURFACE PRESSURE DISTRIBUTIONS IN A TWO-STRUT SCRAMJET INLET

Static pressure distributions on the sidewall at two inlet heights are shown in this figure. As seen from the figure, the predicted pressure distributions compare very well with the experimental data.

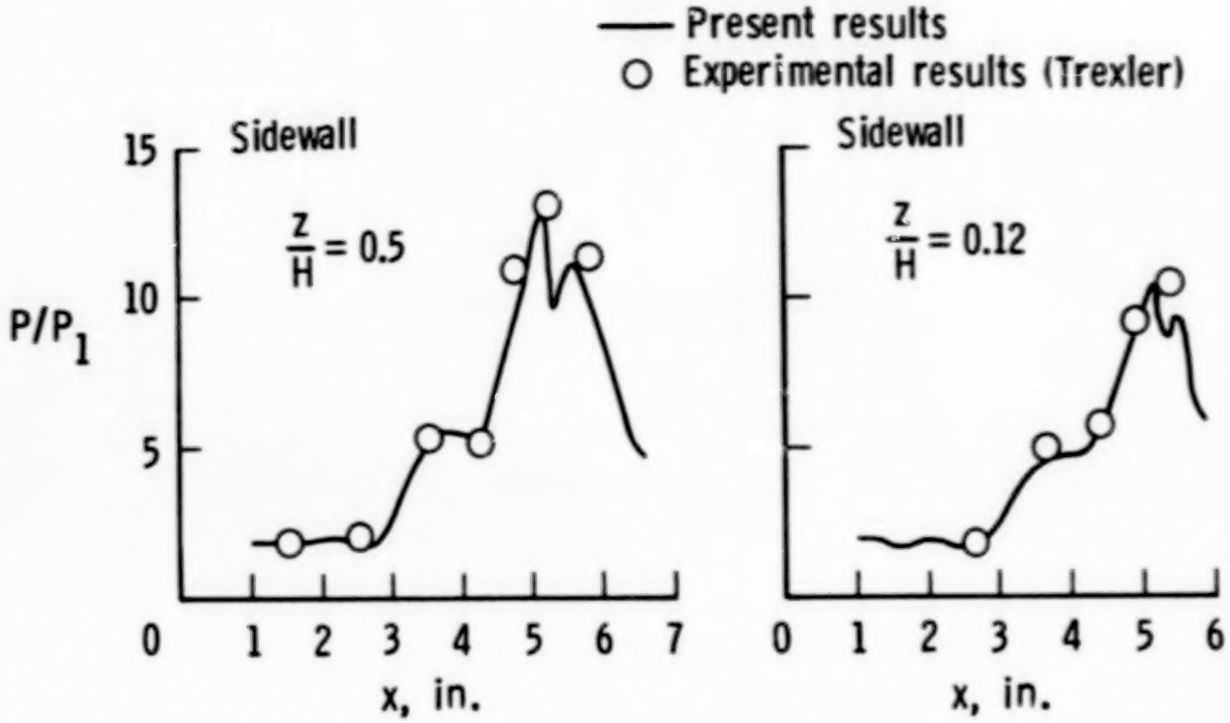

SURFACE PRESSURE DISTRIBUTION IN A TWO-STRUT SCRAMJET INLET

This figure shows a comparison of the predicted static pressure distribution with the experiment on the strut inner surface at mid-inlet height. Here again, the predicted results compare very well with the experiment.

Although not discussed much here, the flow captured by the inlet is an important measure of inlet performance. An accurate prediction of inlet capture also provides support to the procedure used here to account for the interaction between the internal and external flow ahead of the cowl. In the present analysis of the two configurations discussed here, predicted inlet flow capture compared very well with the experimentally predicted value.

Strut (Center Passage)

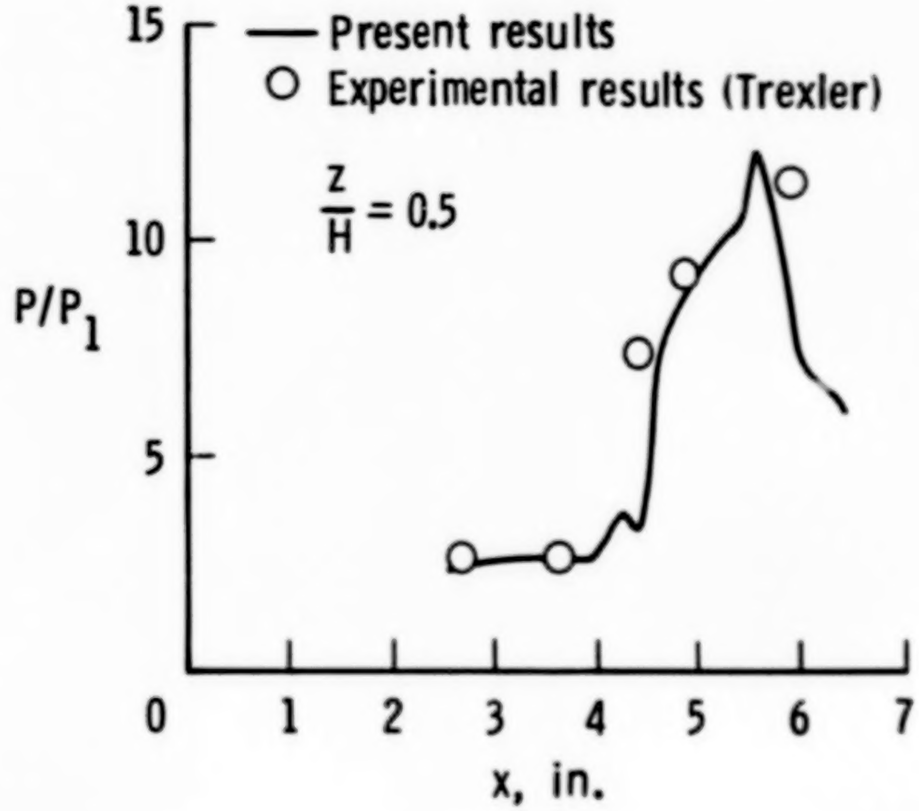

CONCLUDING REMARKS

- A series of inlet analysis codes (2-D, axisymmetric, 3-D) have been developed which can analyze complicated flow through complex inlet geometries in reasonably efficient manner
- The codes have been verified and are being used extensively to analyze practical inlet geometries both at Langley as well as industries
- Newly installed VPS 32 computer will allow more complex configurations to be analyzed
- Scalar Fortran versions available to increase transportability of the codes for use on other Scalar computers and on Cray vector processing computer

REFERENCES

1. Kumar, Ajay: Numerical Analysis of a Scramjet Inlet Flow Field Using the Three-Dimensional Navier-Stokes Equations. CPIA Publication 373, Feb. 1983, pp. 25-39.

2. West, J. E.; and Korkegi, R. H.: Supersonic Interaction in the Corner of Intersecting Wedges at High Reynolds Numbers. AIAA Journal, vol. 10, no. 5, May 1972, pp. 652-656.

N88-14937

LOW-DISTURBANCE WIND TUNNELS

511-09

117235

15P.

I. E. Beckwith, Z. T. Applin,
P. C. Stainback and L. Maestrello
NASA Langley Research Center
Hampton, Virginia

[redacted]

Abstract

During the past several years, there has been an extensive program under way at the Langley Research Center to upgrade the flow quality in several of our large wind tunnels. This effort has resulted in significant improvements in flow quality in these tunnels and has also increased our understanding of how and where changes in existing and new wind tunnels are most likely to yield the desired improvements. As part of this ongoing program, flow disturbance levels and spectra have been measured in several Langley tunnels before and after modifications were made to reduce acoustic and vorticity fluctuations. A brief description of these disturbance control features is given for the Low-Turbulence Pressure Tunnel, the 4- x 7-Meter Tunnel, and the 8-Ft Transonic Pressure Tunnel. These tunnels cover the speed range from low subsonic to transonic. To illustrate typical reductions in disturbance levels obtained in these tunnels, data from hot-wire or acoustic sensors are presented.

A new concept for a subsonic quiet tunnel designed to study boundary-layer stability and transition is also presented. This tunnel avoids some of the disturbance sources in continuous circuit tunnels and also utilizes some special features to reduce fan noise.

Techniques developed at Langley in recent years to eliminate the high intensity and high-frequency acoustic disturbances present in all previous supersonic wind tunnels are described. Freestream measurements of disturbance levels in a Mach 3.5 pilot tunnel which utilizes these techniques are discussed. Data obtained in this tunnel for transition from laminar to turbulent boundary layer on a cone are compared with previous wind tunnel and flight data.

In conclusion, the low-disturbance levels present in atmospheric flight can now be simulated in wind tunnels over the speed range from low subsonic through high supersonic. The special problems that must be solved to reduce flow disturbances in hypersonic wind tunnels will not be considered in this paper.

INTRODUCTION

- DISTURBANCE LEVELS AND SPECTRA MEASURED IN SEVERAL LANGLEY TUNNELS BEFORE AND AFTER MODIFICATIONS/IMPROVEMENTS

- WHAT ARE FEATURES OF THESE TUNNELS REQUIRED TO REDUCE DISTURBANCES OVER SPEED RANGE?

  - LOW-TURBULENCE PRESSURE TUNNEL
  - 4- X 7-METER TUNNEL
  - 8-FT TRANSONIC PRESSURE TUNNEL
  - SUBSONIC QUIET TUNNEL: A CONCEPT
  - MACH 3.5 LOW-DISTURBANCE TUNNEL

Low-Turbulence Pressure Tunnel

The Langley Low-Turbulence Pressure Tunnel was designed especially for research on wing sections. A low-turbulence airstream was required for systematic investigations of large numbers of airfoils at flight Reynolds numbers. The tunnel is of welded steel construction to permit operation at pressures up to 10 atmospheres.

The principal features of this tunnel that account for the low-turbulence levels are, moving upstream from the test section: the relatively large contraction ratio; the nine screens; the heating/cooling coils which function as a honeycomb; the lack of any 90° elbows in the flow circuit along with the splitter vanes and guiding vanes to control separation; and the well-designed drive section and diffuser. This tunnel underwent a major overhaul between December 1979 and March 1982. Two of the major items replaced were the cooler and screens.

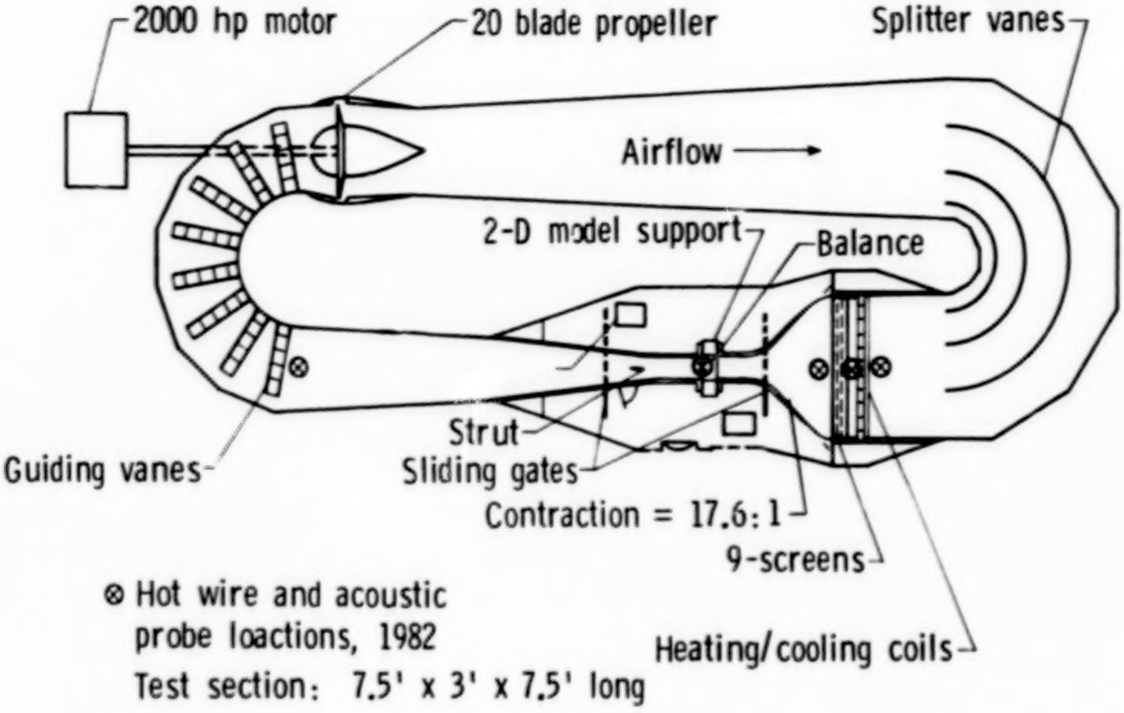
2000 hp motor
20 blade propeller
Splitter vanes
Airflow
2-D model support
Balance
Strut
Guiding vanes
Sliding gates
Contraction = 17.6:1
9-screens
⊗ Hot wire and acoustic probe loactions, 1982
Heating/cooling coils
Test section: 7.5' x 3' x 7.5' long

RMS Velocity Fluctuations in LTPT Test Section

Shown here are the rms velocity fluctuations normalized by the mean velocity (usually referred to as the "turbulence") plotted against the unit Reynolds number. These data were obtained with a hot-wire probe in the center of the test section. The new data obtained in 1982 (ref. 1) are for a range of Mach numbers from 0.05 to 0.3 and indicate the turbulence level generally increases with increasing Mach number. The increasing levels at high unit Reynolds numbers are caused by noise from the fan due to increased power, while the increased levels at the lower unit Reynolds numbers may be due to diffuser separation noise propagating upstream (see ref. 1). The agreement between the new data and the old 1941 data is excellent except for the low point which was for M_∞ = .02. Extrapolation of the new data to this value of M_∞ would give a turbulence level somewhat below the old level.

We conclude that correct design features for low-disturbance wind tunnels in this Mach number range were developed and applied successfully more than 45 years ago. Special acoustic treatment such as used for the Subsonic Quiet Tunnel (considered later in this paper) would probably reduce turbulence levels at the upper and lower ends of the Reynolds number range.

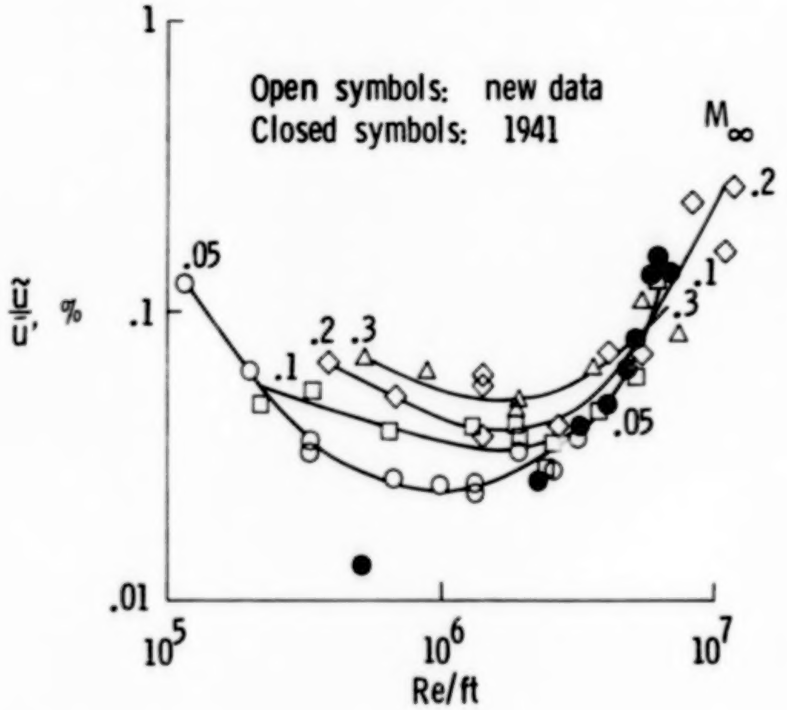

(Ref. 1)

The 4- by 7-Meter Tunnel

The Langley 4- by 7-Meter Tunnel (formerly the V/STOL Tunnel) is used for testing the subsonic aerodynamic characteristics of all types of aircraft, from rotorcraft to the Space Shuttle. Speeds up to 200 knots with unit Reynolds numbers up to 2.1×10^6/ft can be obtained. The tunnel can be operated with closed test section walls (which may be slotted) or with one or more open test section configurations by raising the sidewalls and ceiling. The open test section configuration is particularly useful for flow visualization and acoustic measurements. Earlier investigations (reported in refs. 2 - 4) revealed that the flow quality in the original tunnel suffered from the effects of large-scale unsteadiness and intermittent flow separation in the diffuser downstream of the fan. These disturbances were convected around the circuit with additional input from the fan and flow separations around the third and fourth corners. In addition, for the open test section, the flow quality also suffered due to low-frequency flow pulsations caused by the original flow collector design. The closed test section flow quality has been improved by eliminating the large areas of flow separation by the addition of flow deflectors and replacement of the original debris screen which was too dense. A major facility upgrading is now in progress which includes a perforated grid, honeycomb and screens designed to further improve the test section flow quality. The flow pulsation problem in the open test section has been significantly reduced by triangular vanes and a new flow collector design, tested as a mock-up. A new, permanent flow collector has also been included in the facility upgrade to improve the open test section flow quality.

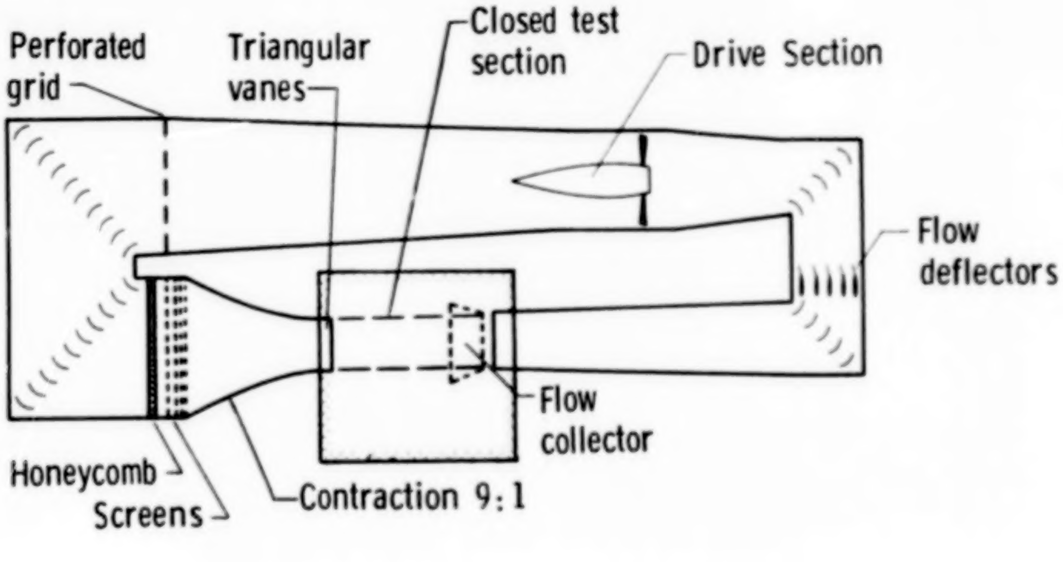

Velocity Fluctuations in the 4- by 7-Meter Tunnel

Shown here are the variations with unit Reynolds number of turbulence levels measured with a hot-wire probe in the center of the test section. Data in the open and closed test sections as obtained in both the original tunnel and with the modifications indicated are given. Nearly an order of magnitude reduction of the low-frequency turbulence levels in the open test section were obtained with the vanes and flow collector. For the closed test section, the original levels were reduced about 50 percent by the flow deflectors (which reduced separation effects) and the new much lower density debris screen. Further reductions are expected with the new perforated plate, honeycomb, and turbulence screens.

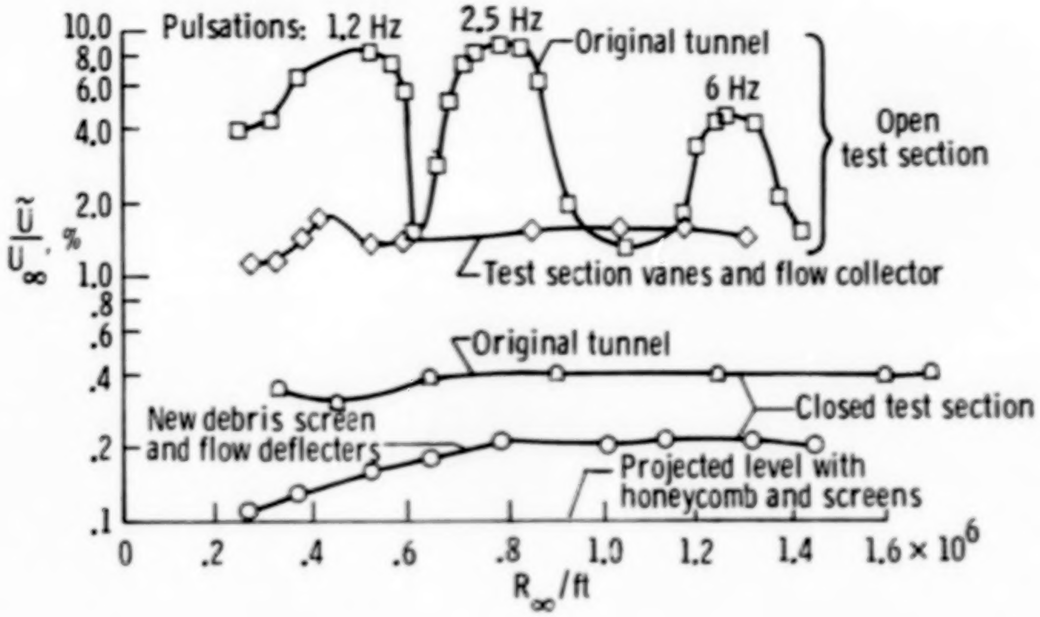

(Ref. 3)

The 8-Ft Transonic Pressure Tunnel

This tunnel has a rectangular cross section with slotted top and bottom walls. The cooler consists of eight staggered rows of finned tubes and it is located just upstream of the 36-Ft diameter settling chamber. Both hot-wire and acoustic probe data have been obtained (refs. 2 and 5) at the indicated locations. These measurements were made in preparation for extensive laminar flow control tests of a large wing (ref. 6). During these latter tests, a honeycomb and five screens were installed upstream of the contraction. However, fluctuation data obtained in the test section with the honeycomb and screens installed are not yet available.

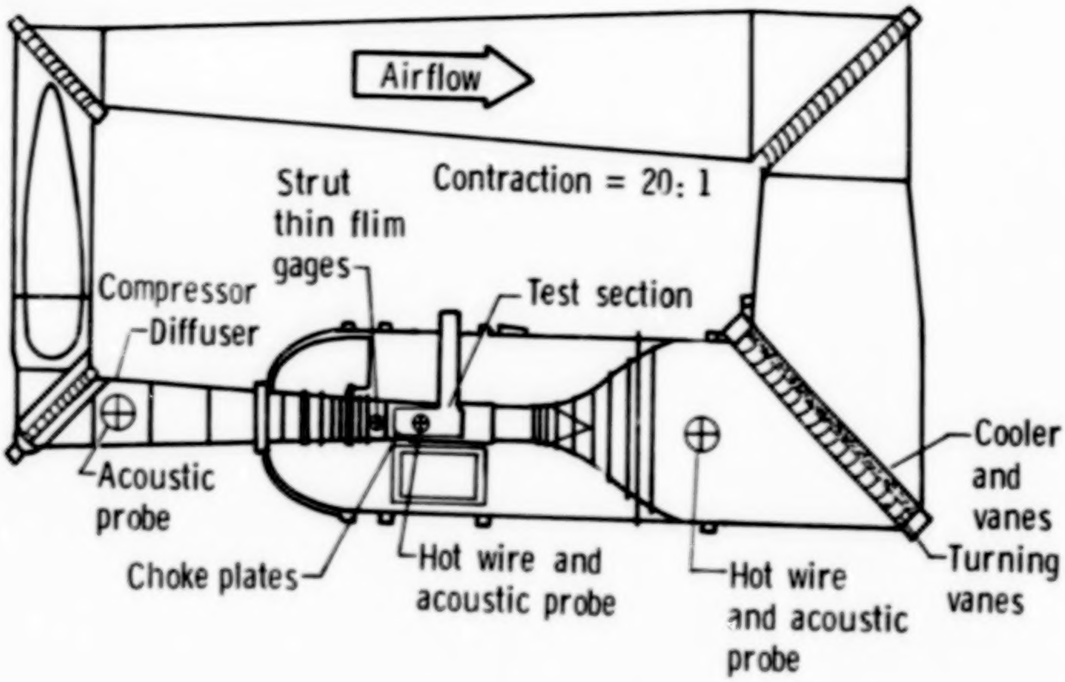
Airflow
Strut
thin flim
gages
Contraction = 20: 1
Compressor
Diffuser
Test section
Cooler
and
vanes
Acoustic
probe
Turning
vanes
Choke plates
Hot wire and
acoustic probe
Hot wire
and acoustic
probe

Pressure Fluctuations in Test Section of 8-Ft TPT

This figure shows the variation with Mach number of the rms static pressure normalized by the mean-static pressure on the centerline of the test section. High-frequency response pressure transducers, cavity mounted within ogive-cylinder probes were used to measure the fluctuating static pressures (ref. 2). For this investigation, the wall slots were covered with 0.25-inch thick metal plates which were beveled and mounted over the slots.

Data are shown for three different choke conditions. With no added chokes, sonic flow was reached near the exit of the test section. The rms pressures then dropped by an order of magnitude since pressure disturbances from the diffuser could not be transmitted upstream through the sonic region. The chokes used for this investigation consisted of streamlined plates that were 3-3/4 feet long by one-inch thick at their location of maximum camber. One side of the plates was flat and this side was attached to the wall with the plate leading edges 5-3/4 feet from the test section entrance. With two of the plates attached to opposite sides of the tunnel, sonic flow occurred at the plate location when the upstream test section Mach number, $M_\infty = .85$. With all four plates attached, the choked condition was reached when $M_\infty = .78$. For all of these choked conditions, the noise level approached the estimated values (ref. 5) caused by the turbulent wall boundary layers. This lower level presumably represents essentially the minimum possible in this type and size of tunnel.

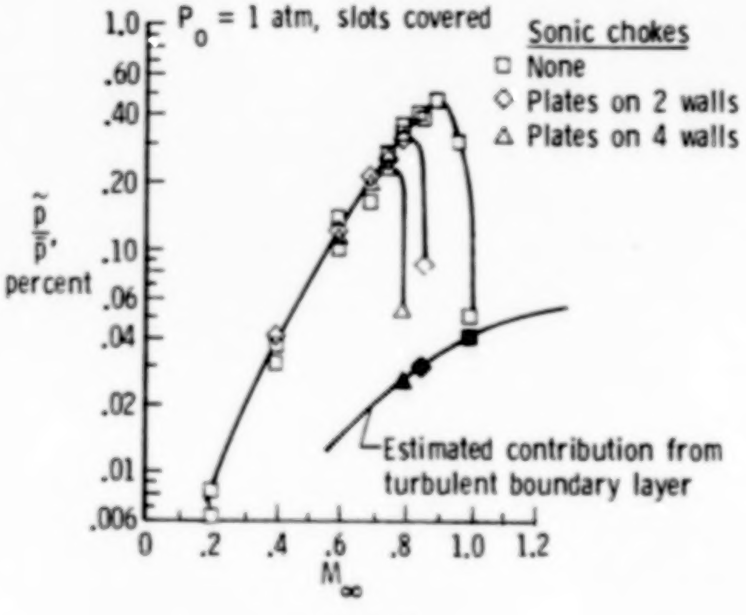

(Ref. 2)

Subsonic Quiet Tunnel

A quiet, high flow quality, transition research apparatus is being designed by L. Maestrello of NASA Langley to study problems of stability, transition, and methods of transition control. The apparatus is open circuit with a 3 x 3-ft test section and a contraction ratio of 20:1. It will operate at speeds up to 240 ft/sec with a corresponding unit Reynolds number of 10^6. Boundary-layer control by suction will be applied on the walls of the contraction and the test section. It is powered by four quiet synchronous fan-motor assemblies with a specially designed variable impedance acoustic muffler placed downstream of the test section. The settling chamber will contain several turbulence screens preceded by a honeycomb-type device consisting of thin-wall tubes aligned with the flow. The facility will be capable of simulating various physical phenomena associated with boundary-layer transition and active control.

The noise from the fan-motor assembly propagating upstream into the test section is attenuated by the specially designed acoustic muffler. The muffler is lined with variable density sound absorbing material of progressively varying depth to provide sound attenuation over a broad range of frequencies. The inside walls of the muffler are slightly diverging to act as a diffuser as well. Estimated noise levels at the highest speed using a 15-Ft long muffler on two or three sides of the diffuser duct are shown. These noise levels are based on experimental data from similar configurations. The noise level obtained with the three-sided muffler is lower than the estimated flow noise in the test section.

Research on Stability, Transition, and Transition Control

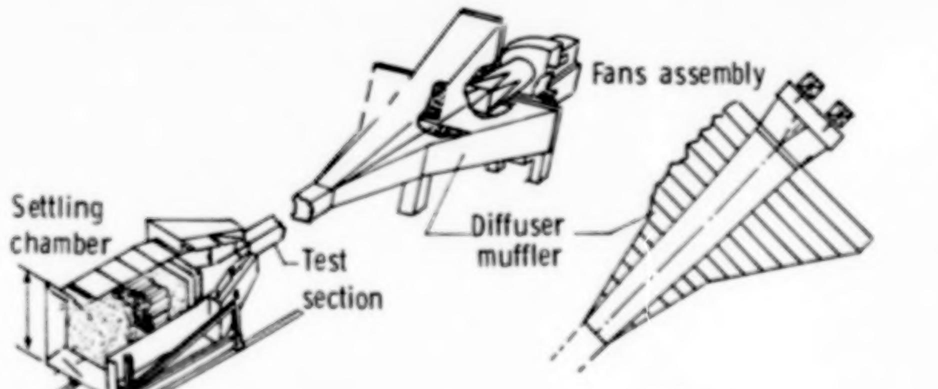

- Test section 3 ft x 3 ft
- Velocity up to 250 ft/sec
- Re/ft up to 10^6
- Contraction = 20:1

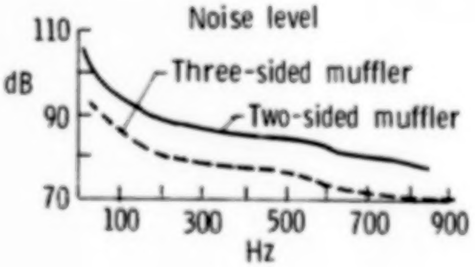

Supersonic Low-Disturbance Tunnel

This figure shows a cross-sectional view of the two-dimensional Mach 3.5 Pilot Nozzle. This small nozzle has exit dimensions of 6 inches high by 10 inches wide and it is installed in a blow-down facility at Langley that has been used over the past several years to develop and test techniques for reducing flow noise at Mach numbers of 3 and 3.5 (refs. 7-9).

The settling chamber is 2 feet in diameter and contains a honeycomb, 7 turbulence screens, and acoustic attenuators consisting of dense porous plates that reduce the high valve and pipe noise to very low levels.

The subsonic approach to the nozzle has a contraction ratio of 49 and has boundary-layer removal slots upstream of the throat as indicated. In this way the new laminar boundary that begins at the slot lip can be maintained laminar to appreciable downstream distances into the supersonic flow. When the nozzle wall boundary layers are laminar, the very high level and high-frequency noise radiated into the test section by the turbulent wall boundary layers in conventional supersonic tunnels is eliminated. The large favorable pressure gradients and highly polished walls help maintain the nozzle wall boundary layers laminar up to unit Reynolds numbers of 6×10^7/m (ref. 8) where the freestream test Reynolds number based on the length of the quiet test region is approximately 7×10^6. Consequently, as illustrated, the upstream most sensitive regions of the laminar boundary layer on a test cone have essentially no incident noise, and transition Reynolds numbers are in the range of flight data.

Mach 3.5 pilot nozzle

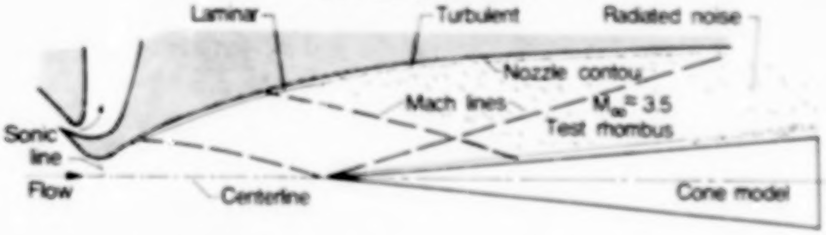

- Blow-down tunnel - high valve and pipe noise

- Settling chamber treatment
- Subsonic boundary-layer removal
- Highly polished walls
- Laminar boundary layer on nozzle walls

- Laminar to turbulent transition on test models same as flight data
- Incident noise can be varied

Effect of Unit Reynolds Number on Noise in Pilot Nozzle

The rms static pressures (normalized by the mean pressures) obtained from hot-wire data on the nozzle centerline are plotted against distance from the nozzle throat. Since acoustic noise is propagated along Mach lines in supersonic flow, the noise levels in the test rhombus are extremely low (within the instrument noise range) when the boundary layer at the upstream acoustic origin regions is laminar. For the lowest unit Reynolds number of $R_\infty = 2.5 \times 10^6$/in, the acoustic origin location at transition on the nozzle wall is indicated and the corresponding locus of the increased noise levels is traced along a Mach line downstream to the centerline. When the probe is traversed through this centerline station, the increased noise is sensed by the hot-wire anemometer. Also, when the test unit Reynolds number is increased, transition on the nozzle wall moves upstream and the length of the quite test core is correspondingly reduced.

Since, at a given Reynolds number the upstream "edge" of the increasing noise region is fixed within the nozzle flow field, the noise levels and onset locations can be varied, as desired, by simply moving the cone downstream within the uniform test flow rhombus. Obviously, the noise onset regions and levels can also be varied by changing the unit Reynolds number. Another technique that has been used extensively to increase the noise levels (ref. 7), is to cut off the subsonic boundary-layer removal flow (see previous figure) with a valve in the exhaust ducts. The result is that the flow spills around the slot lip and the boundary layer on the nozzle walls is then completely turbulent.

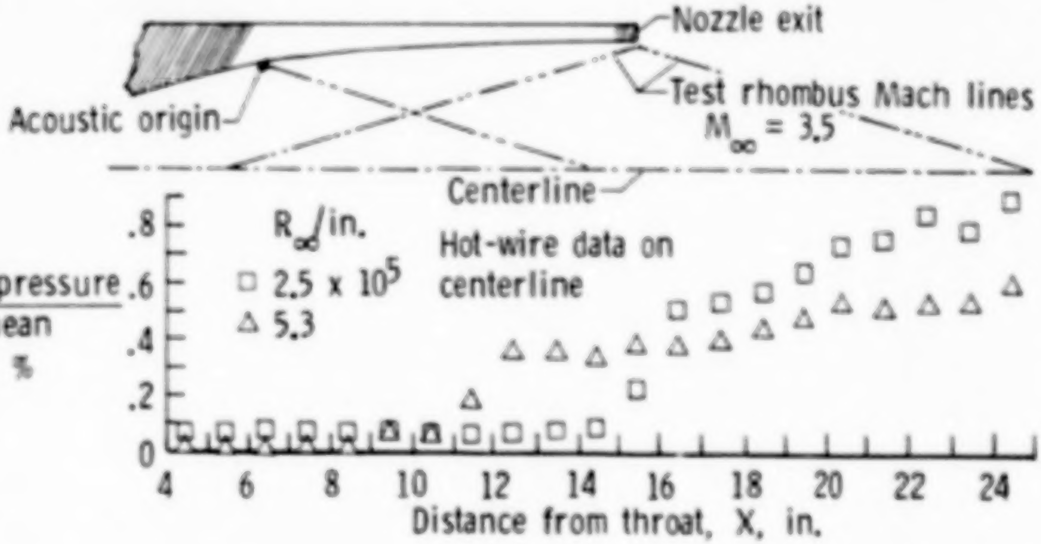

Transition Reynolds Numbers on Sharp Cones

This final figure compares the transition Reynolds numbers, Re_T, (the local length Reynolds numbers at the onset location of transition) on sharp tip cones at zero angle of attack from the present quiet tunnel tests with flight data and conventional wind tunnel data. The data are plotted with the familiar parameters of Re_T against the local unit Reynolds number, Re/in. In the range of 5 to 8 x 10^5/in, the quiet tunnel data are much higher than data from conventional tunnels and are in the lower range of the flight data. As Re/in is increased above 8 x 10^5, the values of Re_T decrease into the range (extrapolated) of the conventional tunnel data. This decrease in Re_T is caused by the corresponding increasing noise levels as illustrated in the previous figure.

It has been discovered that the location of transition on the nozzle wall depends also on the surface finish of the wall. Hence, according to the previous discussion, the location of transition on a test cone would also be affected. This dependence of Re_T on the nozzle surface finish is shown in the figure by data taken before and after extensive polish work on the nozzle surface. The μ-inch finish values given are the highest rms values obtained with a profilometer in the same regions near the nozzle throat. Thus, at Re = 10^6/in, the values of Re_T were increased from 4 x 10^6 up to 8 x 10^6 by the improved nozzle wall finish from 12 rms μ-inch to 3 rms μ-inch.

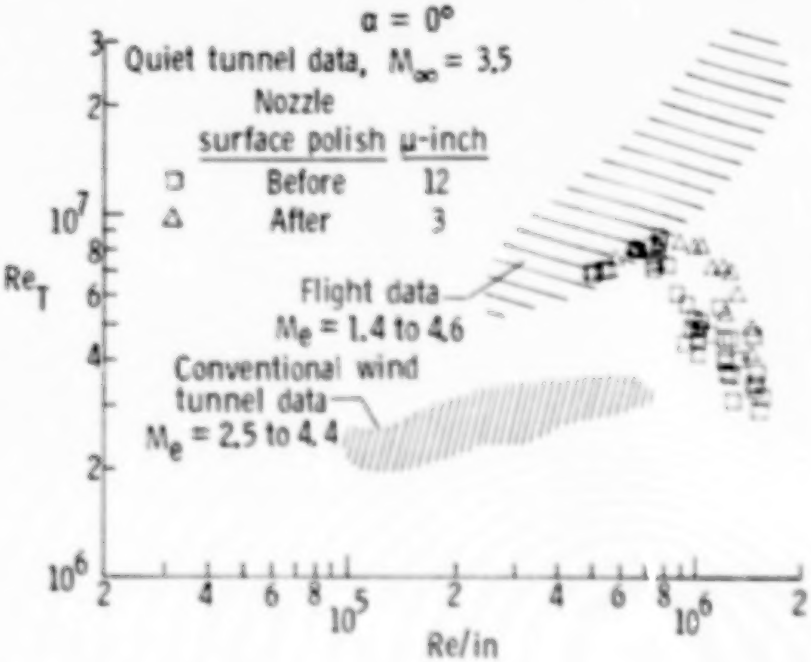

Conclusions

The general requirements for low-disturbance wind tunnels include:

Subsonic and Transonic Tunnels

a. Layout of circuit, turning vanes and diffuser: control separation
b. Acoustic treatment of drive section and diffuser
c. Honeycomb and screens
d. High contraction ratio
e. Sonic chokes
f. Open test section: treatment of entrance and exit

Supersonic Blow-Down Tunnel

a. Settling chamber acoustic components to reduce valve and pipe noise
b. Subsonic boundary layer removal
c. Highly polished walls
d. Laminar boundary layer on nozzle walls

Results

Practical techniques developed at Langley have significantly reduced disturbances in wind tunnels up to Mach number 3.5. The low-disturbance levels of flight can be simulated in wind tunnels over the speed range.

References

1. Stainback, P. Calvin and Owen, F. Kevin: Dynamic Flow Quality Measurements in the Langley Low-Turbulence Pressure Tunnel. AIAA Paper 84-0621, March 1984.

2. Owen, F. K.; Stainback, P. C.; and Harvey, W. D.: An Evaluation of Factors Affecting the Flow Quality in Wind Tunnels. AGARD-CP-348, February 1984.

3. Applin, Zachary T.: Modification to the NASA Langley 4- by 7-Meter Tunnel for Improved Rotorcraft Aerodynamics and Acoustics. Presented at the American Helicopter Society Meeting in Williamsburg, Virginia, Oct. 29-Nov. 1, 1984.

4. Sellers, William L., III; Applin, Zachary T.; Molloy, John K.; and Gentry, Garl L., Jr.: Effect of Jet Exit Vanes on Flow Pulsations in an Open-Jet Wind Tunnel. NASA TM 86299, March 1985.

5. Harvey, William D.; Stainback, P. Calvin; and Owen, F. Kevin: Evaluation of Flow Quality in Two Large NASA Wind Tunnels at Transonic Speeds. NASA Technical Paper 1737, Dec. 1980.

6. Harvey, W. D.; Harris, C. D.; Brooks, C. W.; Clukey, P. G.; and Stack, J. P.: Design and Experimental Evaluation of a Swept Supercritical Laminar Flow Control (LFC) Airfoil. NASA CP-2397, 1986. (Paper 26 in this compilation.)

7. Beckwith, Ivan E.; Creel, Theodore R., Jr.; Chen, Fang-Jenq; and Kendall, James M.: Free-Stream Noise and Transition Measurements on a Cone in a Mach 3.5 Pilot Low-Disturbance Tunnel. NASA Technical Paper 2180, September 1983.

8. Beckwith, I. E.; Malik, M. R.; and Chen, F.-J.: Nozzle Optimization Study for Quiet Supersonic Wind Tunnels. AIAA Paper 84-1628, June 1984.

9. Chen, F.-J.; Malik, M. R.; and Beckwith, I. E.: Instabilities and Transition in the Wall Boundary Layers of Low-Disturbance Supersonic Nozzles. AIAA Paper 85-1573. Presented at the AIAA 18th Fluid Dynamics, Plasma Dynamics, and Lasers Conference, Cincinnati, Ohio, July 16-18, 1985.

D12

N88-14938

52-09
117236
35P.

WIND TUNNEL WALL INTERFERENCE

Perry A. Newman, Raymond E. Mineck, Richard W. Barnwell
NASA Langley Research Center
Hampton, Virginia

William B. Kemp, Jr.
College of William and Mary
Williamsburg, Virginia

PRECEDING PAGE BLANK NOT FILMED

PAGE 224 INTENTIONALLY BLANK

[redacted] TUNNEL WALL INTERFERENCE RESEARCH

About a decade ago, interest in alleviating wind tunnel wall interference was renewed by advances in computational aerodynamics, concepts of adaptive test section walls, and plans for high Reynolds number transonic test facilities. Selection of the NASA Langley cryogenic concept for the National Transonic Facility (NTF) tended to focus our renewed wall interference efforts. A brief overview and current status of some Langley sponsored transonic wind tunnel wall interference research are presented. Included are continuing efforts in basic wall flow studies, wall interference assessment/correction (WIAC) procedures, and adaptive (flexible) wall technology. It should be pointed out that for transonic flow conditions, wind tunnel wall interference is coupled to other tunnel flow phenomena not generally associated with subsonic flow and classical (linear) wall interference theory. Some of these related phenomena, such as flow quality, support interference, flow diagnostics, and transition studies, are discussed in other papers in this compilation. Understanding these phenomena is basic to proper unbounded-flow simulation in wind tunnels; however, it is not appropriate to repeat the material in this brief overview. Furthermore, much of what should be included here cannot be; a list of publications from Langley sponsored research over the past decade or so is included in order to summarize the total effort and to identify some of the individual researchers who have been involved.

NASA Langley focus is transonic

- Basic wall flow studies
- Assessment/correction procedures - WIAC
- Adaptive wall technology - flexible

BASIC WALL FLOW STUDIES

In order to emphasize specific wall interference aspects, the basic wall flow studies summarized here have been grouped as slotted wall test sections, sidewall boundary-layer phenomena, wall interference data bases, and tunnel simulator code development. Activities pertaining to slotted test section walls include parametric studies of wall properties, use of such information in NTF test section design, and subscale design verification tests. These efforts are considered as customary wall interference research. Activities dealing with the response of the (solid) sidewall boundary layer to the model pressure field and its resulting influence on the test conditions are not so customary. It is primarily observed in airfoil testing and should be accounted for or alleviated; its influence is much less in 3-D. NASA Langley work in this area includes theory, experiment, and applications. Wall interference data bases and numerical wind-tunnel flow simulator codes are required for the development and verification of assessment/correction (WIAC) procedures; in addition, these pursuits have their own intrinsic value. Both 2-D and 3-D data bases, including wall pressure signature data, are being generated. Tunnel simulator CFD codes are being continually developed; governing flow equations include linear, transonic potential, and nonpotential approximations. The paper by South et al. in session 1 of this compilation is an example of our work in this area.

- Slotted test section walls
  - 6- by 19-inch TT parametric studies
  - NTF design/subscale NTF tests
- Sidewall boundary layer phenomena
  - Theory and experiment
  - Applications
- Wall interference data bases
  - 2D and 3D
  - Wall pressure data
- Tunnel simulator code development
  - Linear and transonic potential
  - Nonpotential

SLOTTED WALL PARAMETRIC STUDIES

6- by 19-Inch TT

ORIGINAL PAGE IS
OF POOR QUALITY

The experimental phase of Langley's most recent parametric slotted wall flow study was conducted by Joel Everhart throughout 1984 in the 6- by 19-inch Transonic Tunnel (TT). His experimental setup is shown in the photograph; the single-slot test section wall configuration standing at the right has been removed, exposing the airfoil and opposite wall. A flow angularity probe is visible in the slot of the far wall, just ahead of the leading edge of the model. Pressure data were taken on the walls and model; flow angularity data were also taken in the test section. Variation of wall parameters was by means of readily interchangeable test-section "upper and lower" slotted-wall configurations. Wall parameters varied in this study include geometric openness ratio, number of slots at fixed openness, slat thickness, slat lip radius-of-curvature, and sidewall boundary-layer thickness. This was done using a 6-inch-chord NACA 0012 airfoil over a range of angles of attack (-4^{o} to $+4^{o}$) and tunnel Mach numbers (0.1 to 0.95). Data from this study are now being reduced; hopefully these data will aid in understanding the role of such parameters in the slotted-wall boundary condition.

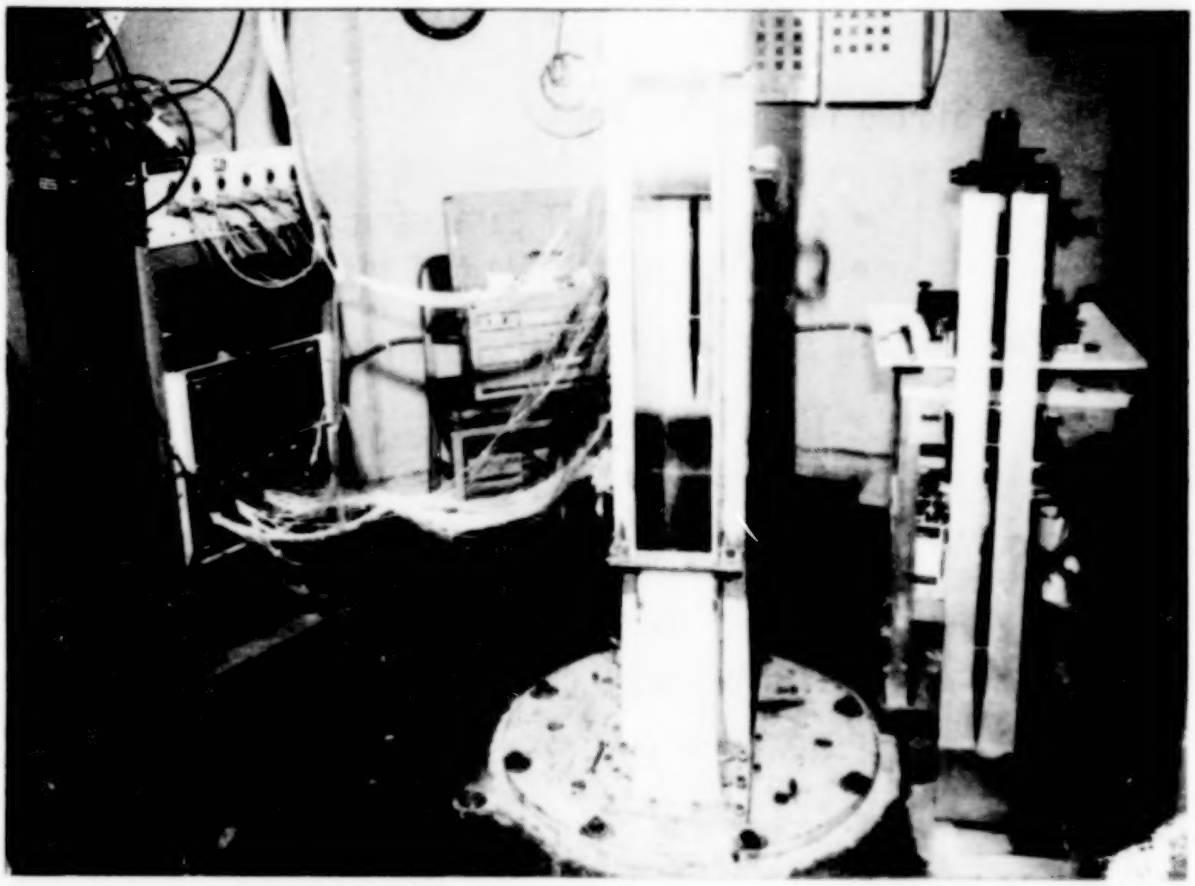

ORIGINAL PAGE IS
OF POOR QUALITY

SIDEWALL BOUNDARY LAYER CONTROL

8- by 24-Inch Airfoil Test Section, 0.3-M TCT

The 0.3-m TCT sidewall boundary layer removal hardware consists of a pair of perforated panels inserted (flush-mounted) in the tunnel sidewalls upstream of the model location. These perforated panels extend from the floor to the ceiling of the test section and are approximately 6 inches wide, as shown in the top view photograph of the test section (top of the plenum chamber and the slotted wall removed). Visible in this photograph are the airfoil model, boundary layer bleed ducting, one of the four boundary layer sidewall rakes, and one of the two perforated panels. The holes in it were drilled using an electron beam technique and the surface was etched; this results in an unusually smooth surface considering the large number of holes in the plate. Two different hole configurations giving different porosities have been tested. The amount of the boundary layer mass flow removed from either of the sidewalls is controlled independently by two digital flow control valves and discharged directly to the atmosphere (passive system). At a Mach number of 0.76, the maximum bleed flow rate is about 2 percent of the test section mass flow rate; this amount of bleed capability is sufficient to significantly reduce the sidewall boundary layer displacement thickness. Recently, a cryogenic reinjection compressor (active system) has been installed and validated; the sidewall boundary layer mass removal capability has been expanded to cover the entire operating envelope of the 0.3-m TCT.

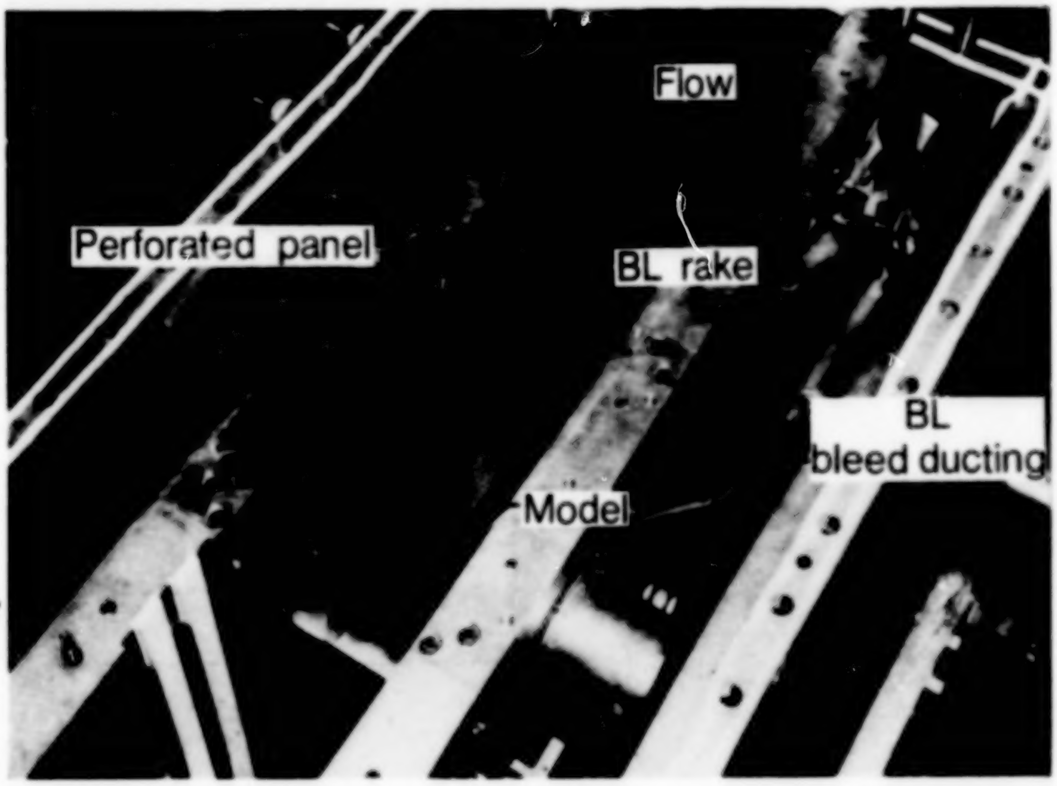

EFFECT OF SIDEWALL BOUNDARY LAYER BLEED

0.3-M TCT

The adverse influence of the sidewall boundary layer/model pressure field interaction on an airfoil test is most pronounced at supercritical flow conditions. Barnwell and Sewall have shown that for attached flow on the sidewall, the Mach number correction is approximately $-2\delta^*/b$, where b is the tunnel span. When the airfoil shock waves intersecting the sidewall separate the sidewall boundary layer, then the resulting flow is very 3-D in nature; one tries to prevent this situation. In the 0.3-m TCT airfoil tests, the effect of upstream sidewall boundary layer bleed is most easily observed at supercritical flow conditions with high lift. Shown in the figure are midspan chordwise and several spanwise presure distributions on an airfoil at the nominal tunnel conditions shown in the subtitle. Results are for tests without (○) and with (□) bleed (passive system); test section Mach numbers (M_t) and their corrected values (M_c), using Barnwell-Sewall approximations, are also given. As can be seen on the left, with bleed applied, there is an improvement of the midspan pressure recovery on the upper surface near the trailing edge of the airfoil; this suggests that with bleed the separation on the upper surface is significantly reduced. The more downstream location of the shock wave and higher normal force coefficient for the lower test section Mach number also indicate less separation. The spanwise distributions are on the right; at $x/c = 0.5$ it is seen that the separation induced by the shock is at the sidewalls. The flow appears to be less 3-D with bleed applied.

0.3 m TCT, $M_{\infty,t} = 0.76$, $R_c = 6 \times 10^6$, $\alpha = 4°$

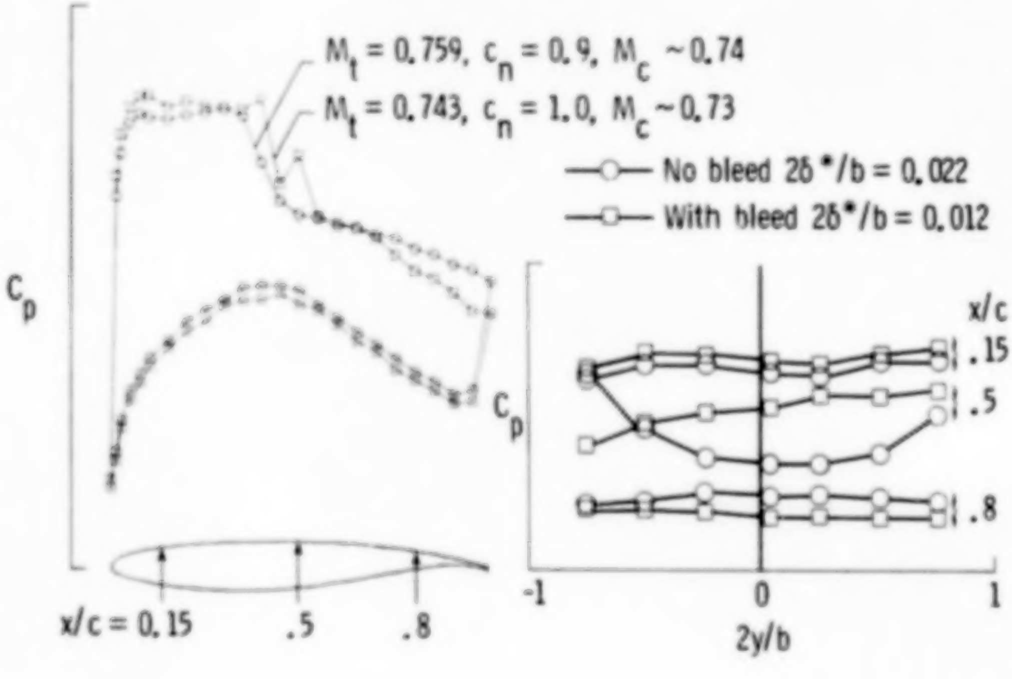

ORIGINAL PAGE IS
OF POOR QUALITY

SIDEWALL BOUNDARY LAYER CONTROL

LFC Experiment, 8-Ft TPT

Suction requirements under the turbulent boundary layer of the contoured test-section liner near the model and on the model surfaces near the liner were determined as part of the liner-design procedure. This was done in the process of determining the effective displacement correction which had to be accounted for in the liner shape. Determination of the suction requirements in these turbulent-flow regions is not to be confused with what is required to determine the laminar-flow-region suction rates over most of the model. Suction is required on the liner "endplates" near the model juncture in order to keep the turbulent boundary layer attached through the adverse pressure-gradient regions which occur in the following regions: on approaching the model leading edge, through the aft-portion pressure-recovery regions, and near the concave corners on the lower surface. The liner blocks in these regions form a collar about the model containing suction panel blocks with slot/plenum/duct construction very similar to that used on the wing. These blocks are metal, but with molded fiberglass outer skin; they move with the model through angle-of-attack adjustments. The figure is a photograph looking downstream through the channel "above" the wing surface, and the suction panel blocks are the dark areas on the top and bottom liner "endplates."

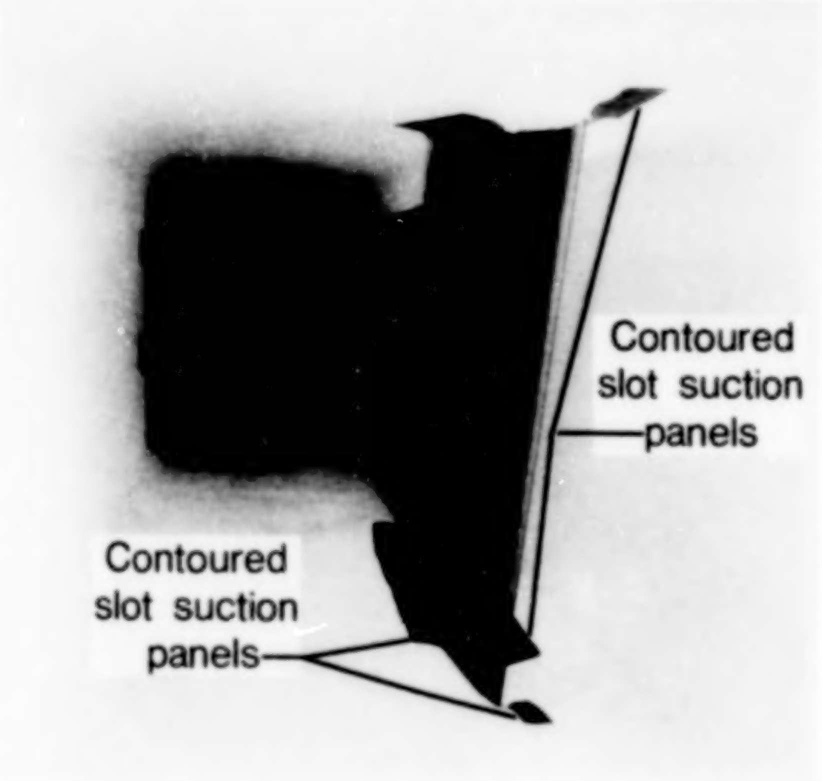

SIDEWALL BOUNDARY LAYER CONTROL

LTPT

In order to reasonably approach two dimensionality in low-speed flows when testing multielement airfoils, some form of tunnel sidewall boundary layer control is needed. The large adverse pressure gradients induced by the high-lift airfoil can cause the tunnel sidewall boundary layer to separate and result in a decrease in airfoil lift. Tangential blowing was selected to provide local sidewall BLC near the airfoil; overall boundary layer thinning upstream of the model is accomplished by single suction slots on each sidewall. Five blowing boxes with tangential slots are available for each side of the tunnel and can be positioned around the airfoil within the confines of the endplates. High-pressure air is supplied to each box through a flexible hose connected to a mobile blowing-box control cart. The tangential wall blowing energizes the sidewall boundary layer, appreciably reducing its displacement thickness. The photograph is a view looking into the trailing edge of a "poor man's" split flap model. Single blowing-box tangential slots are seen on each turntable above the model in the adverse pressure recovery region above the upper airfoil surface. Ahead of the leading edge, the sidewall suction slots are visible. These span each sidewall from top to bottom. In earlier tests on an NACA 4416 airfoil with flap, it was found that tangential blowing through slots located on the model endplates eliminated flow separation at the flap and sidewall juncture. It is required to obtain useful results from two-dimensional tests of high-lift multielement airfoils.

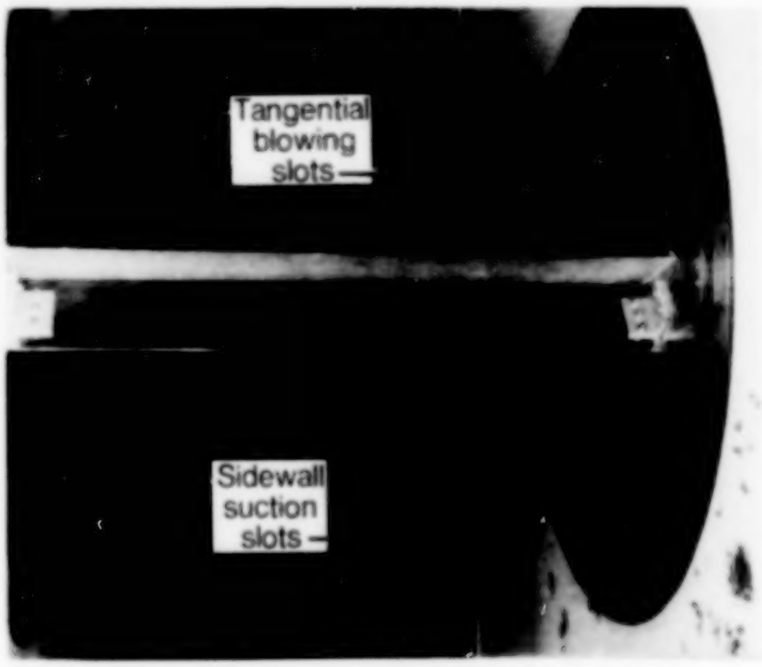

ORIGINAL PAGE IS
OF POOR QUALITY

SIDEWALL BOUNDARY LAYER CONTROL

6- by 28-Inch TT Studies

ORIGINAL PAGE IS
OF POOR QUALITY

Experimental studies on controlling the sidewall boundary layer in airfoil tests at transonic flow conditions via suction through a few discrete orifices have been initiated by Bill Sewall. The photograph shows a 3-inch-chord NACA 0012 model mounted on endplates for the 6- by 28-Inch Transonic Tunnel. Pressure orifices on the model upper surface are visible near midspan. Discrete sidewall orifices are seen on the endplate at the top of the photograph; each of these can be connected to either measure pressure or provide local sidewall boundary layer suction. The tubing stubs for this interchangeable connection are seen on the endplate at the bottom of the photograph; the tubing bundle is from the model upper-surface pressure orifices. The discrete endplate orifices are located along the model-endplate juncture, including one at the leading edge, and in the aft adverse pressure gradient region where shocks would form and tend to separate the sidewall boundary layer. The hardware has not yet been put into the tunnel.

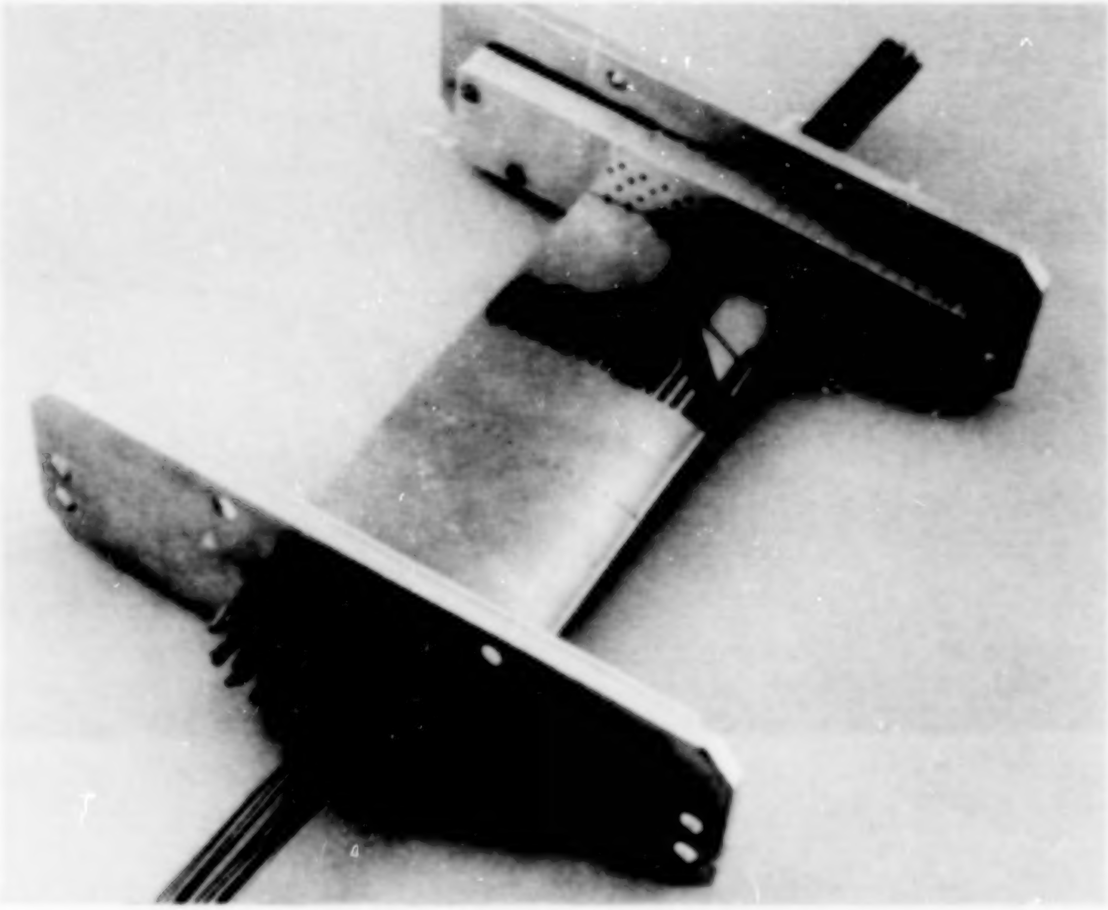

HYPERSONIC MODELS USED IN SUBSCALE NTF INTERFERENCE EXPERIMENT

Three-dimensional transonic data bases suitable for testing and validating WIAC procedures are being taken on this pair of (previously existing) hypersonic models in a subscale NTF facility - the Diffuser Flow Apparatus (DFA). These models are the same shape but differ in size; some wall interference assessment can be made by comparing certain force and moment data between the two models. However, using the measured wall pressures as boundary data in a WIAC code, one would hope to get very similar corrected results independent of the model size. The differences caused by the inability to match the model Reynolds number at the same Mach number have been minimized by the selection of this configuration, which has a highly swept planform and a sharp nosed airfoil.

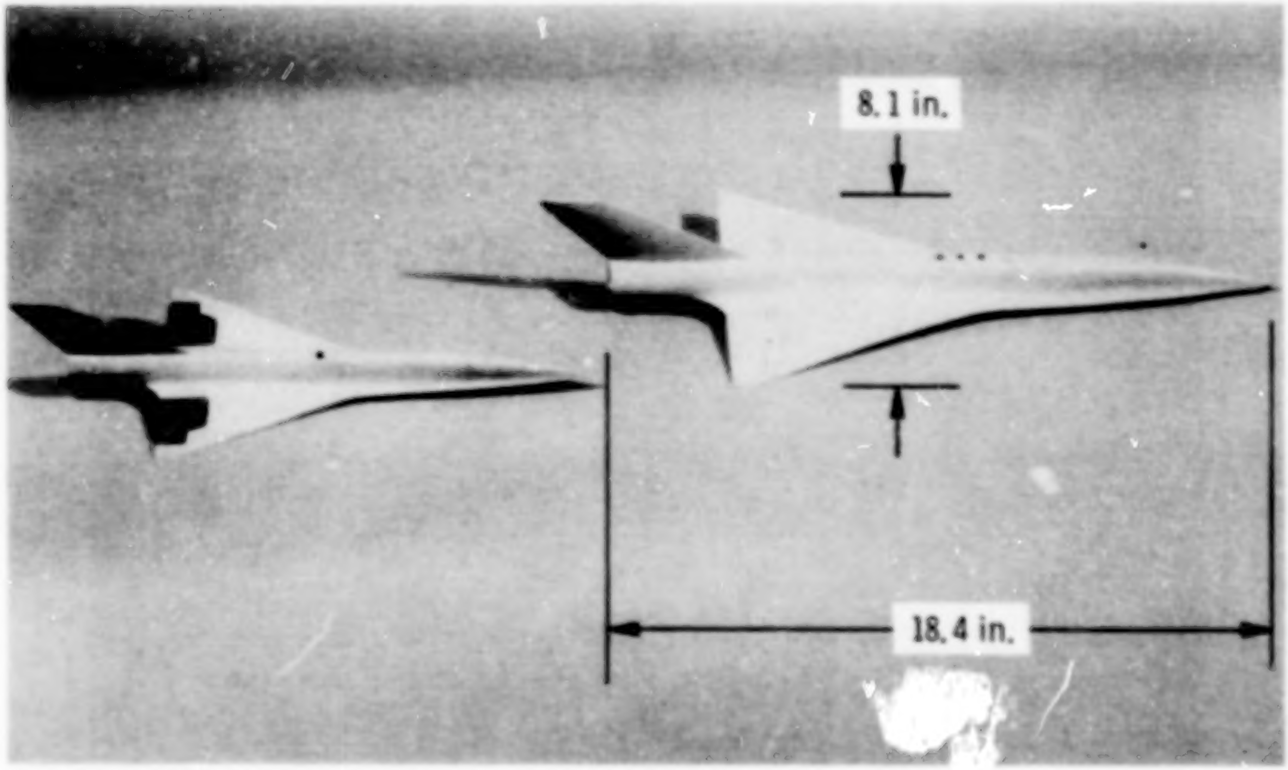

ORIGINAL PAGE IS
OF POOR QUALITY

SUBSCALE NTF WITH LARGE HYPERSONIC MODEL

The wall pressure orifice layout on the DFA floor, ceiling, and sidewall is shown in this schematic. Location of these orifices with respect to the large hypersonic model, its supporting sting, the floor and ceiling wall slots, and reentry flaps can be seen. This particular pattern was determined by NTF slotted wall constraints and a linear theory wall interference code. The suitability of using data obtained with this particular orifice layout in existing 3-D linear and transonic simulation and WIAC codes is being analyzed at present. Another entry and additional testing is to be done in the DFA.

Wall pressure orifice locations

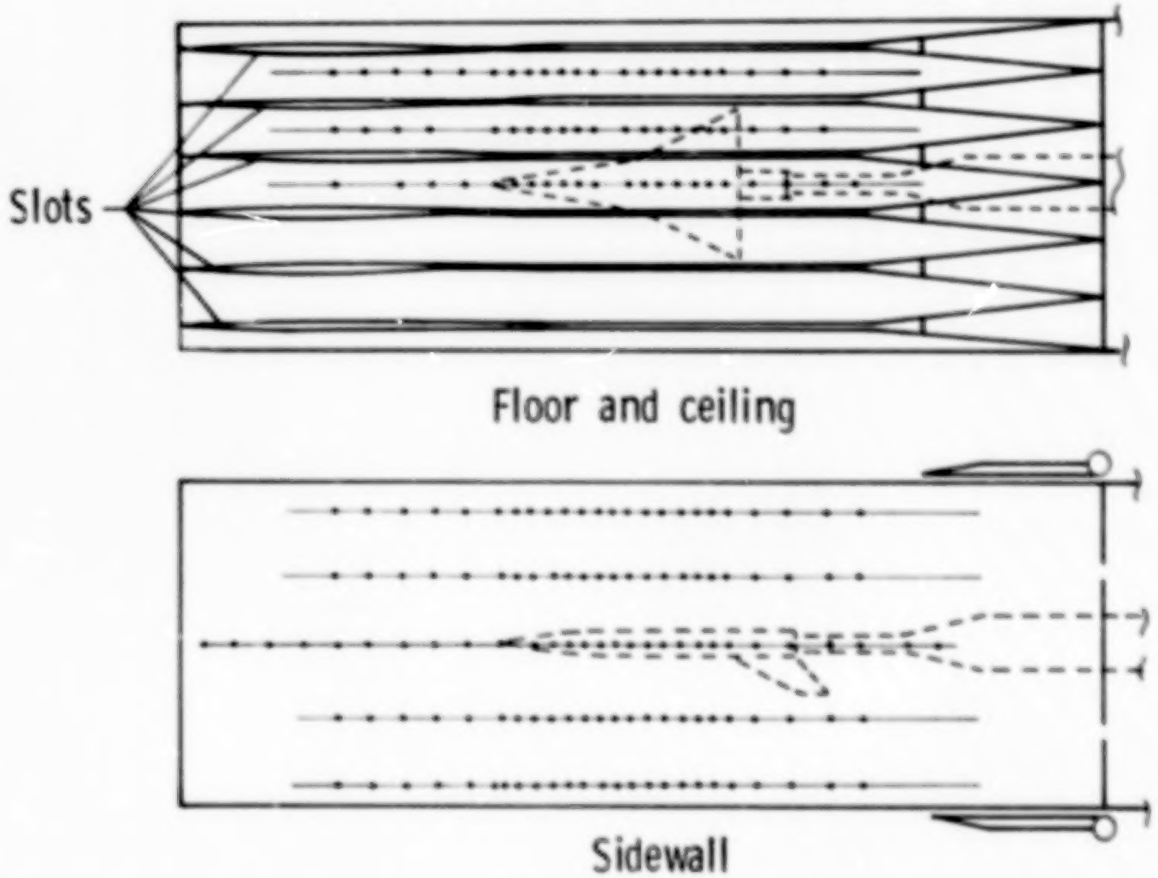

SUBSCALE NTF (DFA) SAMPLE RESULTS

Sample results for Mach number distributions along the centerline of the test section floor are given in the figure. These were for a nominal tunnel Mach number of 0.9 and at very-near-zero lift for both models. The tunnel was initially run empty, without either model or sting support system, to investigate the uniformity of the Mach number distribution in the test section and provide a Mach number calibration for the model tests. Wall Mach number signatures for both models are also shown; the influence of the sting flare can be seen downstream of the model location. This effect must be accounted for either in the WIAC procedure or by taking the sting signature out as a tare-type correction to the wall data. Tests of sting only have also been made.

Mach numbers along ℄ of test-section floor

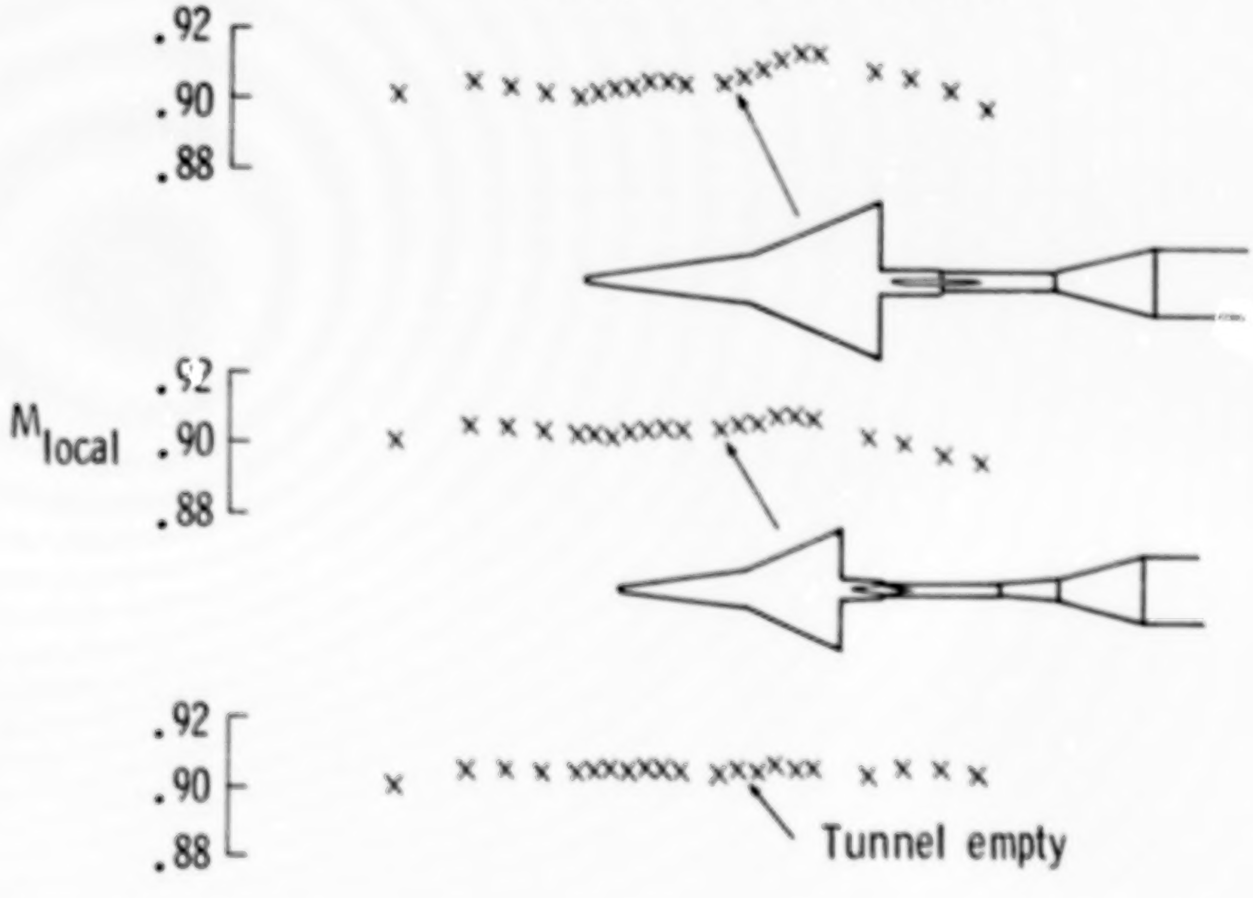

ASSESSMENT/CORRECTION PROCEDURES - WIAC

Wind tunnel wall interference assessment/correction (WIAC) procedures have evolved over the past decade; they are based upon ideas and capabilities from classical wall interference theory, adaptive wall concepts, and computational fluid dynamics. Specific representations have varied from classical-like pretest prediction methods to adaptive-like post-test correction methods; however, it is now generally believed that some flow-field data taken during the test are required in order to make an adequate assessment of or correction for transonic wall interference. The basic idea is to first numerically simulate the tunnel flow field, subject to measured boundary data, and then to search for a corresponding numerical solution in free air. Differences between such solutions are associated with wall interference corrections. When flight Mach and Reynolds numbers are both nearly matched in the tunnel test, then the corrections deduced by this correspondence may be valid well into the transonic flow regime. A nonlinear, transonic small-disturbance equation WIAC procedure has been developed for the airfoil test section of the 0.3-m TCT. It utilizes measured wall pressure data and accounts for interference from all four test section walls. For the NTF, both linear and nonlinear 3-D correction procedures are being developed. Nine longitudinal rows of wall pressure taps are being installed in the test section, and specific wall interference experiments are scheduled. Transonic nonpotential WIAC codes are being developed in order to determine the importance of nonisentropic effects in wall corrections.

- 0.3 m TCT, 8- by 24-inch airfoil TS
    - Wall pressure taps
    - Nonlinear, four-wall correction
    - Advanced technology airfoil test data
- NTF
    - Linear and nonlinear correction codes
    - Subscale NTF (DFA) data
    - Wall pressure taps being installed
    - Planned NTF wall interference tests
- Nonpotential WIAC code development
    - Flow Industries, Inc.
    - NCSU

UNCORRECTED LIFT CURVES, CAST 10-2/DOA 2

A sample of wall interference corrections for airfoil data taken in the 8- by 24-inch test section of the 0.3-m TCT is given in the next two figures. These data were taken in cooperation with the DFVLR as part of NASA's Advanced Technology Airfoil Test program, in which U.S. industry also participated. On the left, uncorrected lift curve data from three tests (identified in the key) are compared with an independent free-air calculation from the GRUMFOIL 2-D transonic (full-potential equation with viscous interaction) airfoil code at the uncorrected tunnel conditions. Test 136 was run about 2 years prior to the other tests, and it was later deemed to have a -0.3° bias in the tunnel angle-of-attack. This bias has been accounted for and is the only difference in the figure on the right. It can be seen that the data are not collapsed in either case; furthermore, none agree with the free-air calculation.

0.3 m TCT data, M ~ 0.73, R ~ 10 million

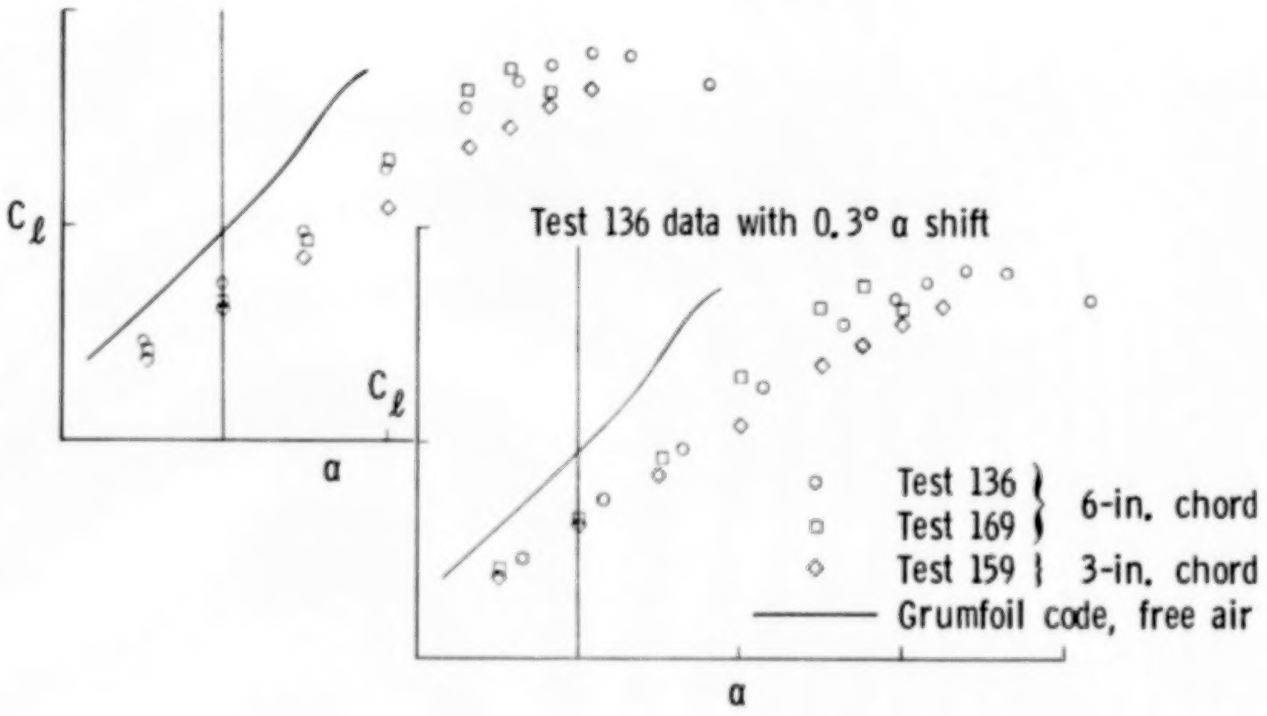

FOUR WALL CORRECTED LIFT CURVES, CAST 10-2/DOA 2

The transonic airfoil WIAC procedure for the 8- by 24-inch test section of the 0.3-m TCT determines corrections for the tunnel Mach number and angle-of-attack. Corrections were obtained for some of the CAST 10-2/DOA 2 airfoil data before we realized that there was an angle-of-attack bias in one of the tests; these results are shown on the left. It can be seen that the corrected data are nearly collapsed and lie very close to the GRUMFOIL free-air results calculated at the corrected conditions. WIAC corrections were then made to the shifted Test 136 data, and these latter results are shown at the right. These results are essentially the same as those on the left, indicating that the WIAC procedure accounted for the bias automatically. In this procedure, the quoted tunnel Mach number and angle-of-attack are more properly only reference values.

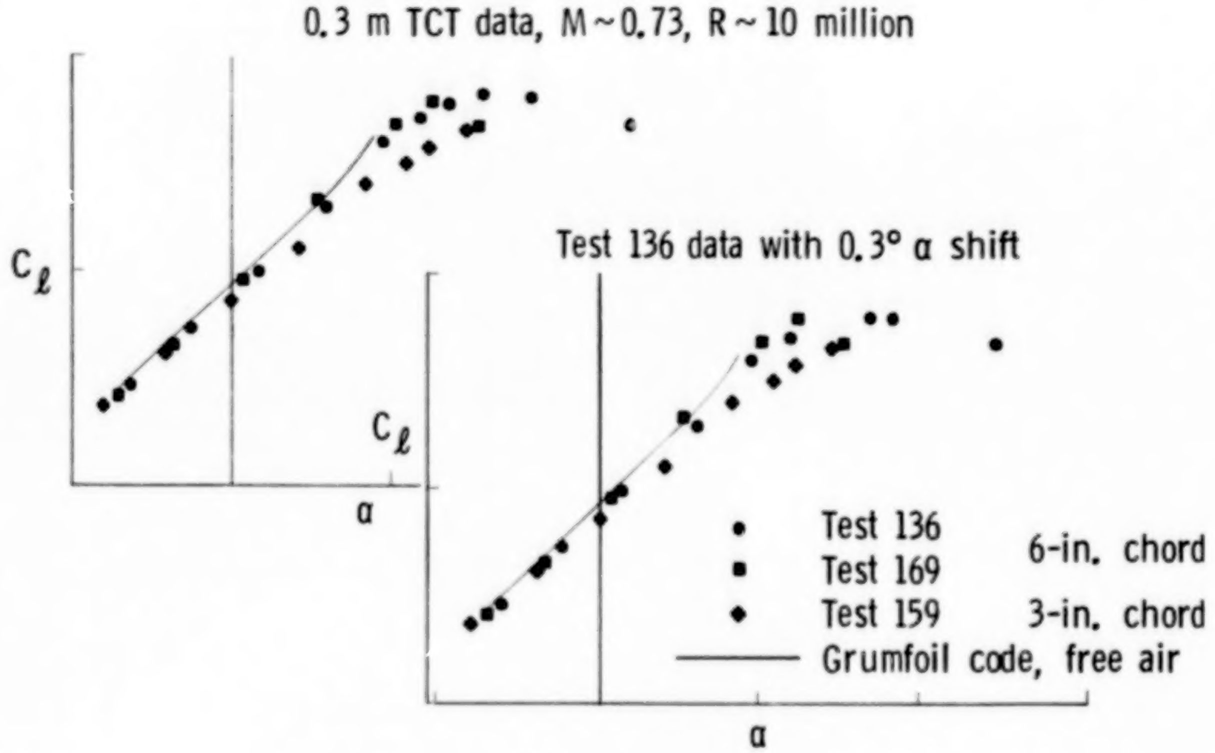

PLANNED NTF WALL INTERFERENCE EXPERIMENTS

NTF experiments specifically designed to study wall interference will be performed using several sizes of geometrically similar simple bodies of revolution and two sizes of Pathfinder I models. Both pointed and blunt bodies of revolution will be tested in order to study Reynolds number effects on blockage corrections and wave drag at Mach numbers near unity. The pointed bodies study will be directed toward very low supersonic flow conditions near maximum drag, whereas the blunt bodies, which are supercritical bodies of revolution, will be studied at very high subsonic flow conditions. Studies on the Pathfinder I model and a 1/2-scale Pathfinder I will evaluate combined blockage and lift interference on this general transport configuration. In all studies, tunnel wall pressures required by the wall interference assessment/correction procedures will be measured.

- Pointed bodies of revolution
- Blunt bodies of revolution
- Pathfinder I models

PATHFINDER I MODELS

ORIGINAL PAGE IS
OF POOR QUALITY

An uninstrumented wing was fabricated to be tested on the Pathfinder I fuselage; this model will be used in conjunction with a 1/2-scale Pathfinder I model to evaluate the wall interference techniques for the NTF. Care was taken to assure that these two models were as geometrically and structurally similar as possible. Both of the wings were fabricated from the same material with the full-sized wing having a fabrication tolerance of ±0.004 inch and the 1/2-scale model having a fabrication tolerance of ±0.002 inch. Six-component strain-gauge balance data obtained from these models will be used in conjunction with static pressures measured on the test section floor, ceiling, and one sidewall to validate wall interference assessment/correction techniques for the NTF. The primary objective of these tests will be to study Reynolds and Mach number effects on combined blockage and lift interference at high subsonic flow conditions appropriate to transport configurations.

PATHFINDER I

ADAPTIVE WALL TECHNOLOGY - FLEXIBLE

The adaptive wall test section concept, using solid flexible walls, attempts to reduce or eliminate wall interference while providing a boundary condition more suitable for mathematical analysis than that of the ventilated wall concepts. Therefore, contouring the solid walls of the test section along free-air streamlines is the basis of the adaptive wall test section concept being pursued at Langley and the University of Southampton under an NASA grant. The concept uses a wind tunnel together with the high-speed digital computer. Both the wind tunnel and the computer are used to provide a part of the total flow field, each working in the region best suited to its unique capability. That is, the tunnel solves the real, viscous, rotational, inner flow field about the model, while the computer solves the imaginary outer flow field extending to infinity. An adaptive wall test section configured for 2-D testing is being installed in the 0.3-m Transonic Cryogenic Tunnel (TCT) circuit. The design of this test section is based upon the work undertaken at Southampton. The self-streamlining wall test section (SSW TS) of the 0.3-m TCT is 13 by 13 inches, whereas that of the transonic self-streamlining wall tunnel (TSSWT) at Southampton is 6 by 6 inches. Initial airfoil tests in the 0.3-m TCT will be for models in two sizes; early attempts at 3-D testing in it will use the AEDC wall interference model. Current research studies at Southampton concern shockwave/adaptive wall interaction control and 3-D model/2-D adaptive wall testing.

- 0.3 m TCT (NASA Langley)
  - 13- by 13-inch SSW TS being installed
  - Airfoil models in two sizes initially
  - AEDC wall interference model for 3D
- TSSWT (Univ. of Southampton)
  - 6- by 6-inch test section
  - Shockwave/wall interaction studies
  - 3D model/2D adaptive testing

ORIGINAL PAGE IS
OF POOR QUALITY

13- by 13-INCH SELF STREAMLINING WALL TEST SECTION, 0.3-M TCT

The 13- by 13-inch self streamlining wall test section is now being installed in the 0.3-m TCT. This new test section, shown in the photograph, is configured for two-dimensional testing. The test section is 56 inches long, and all four walls are solid with the top and bottom walls being flexible. Stepping motors, which drive the wall jacks, can be seen at the top and bottom of the photograph. Models with chords up to 13 inches can be tested over an angle-of-attack range of ±20 degrees. Windows located in the top portion of the turntable allow limited viewing of the region above the model. A traversing mechanism may be installed at several downstream locations. One of the plates for the optional sidewall boundary-layer removal system is barely visible through the test section access port.

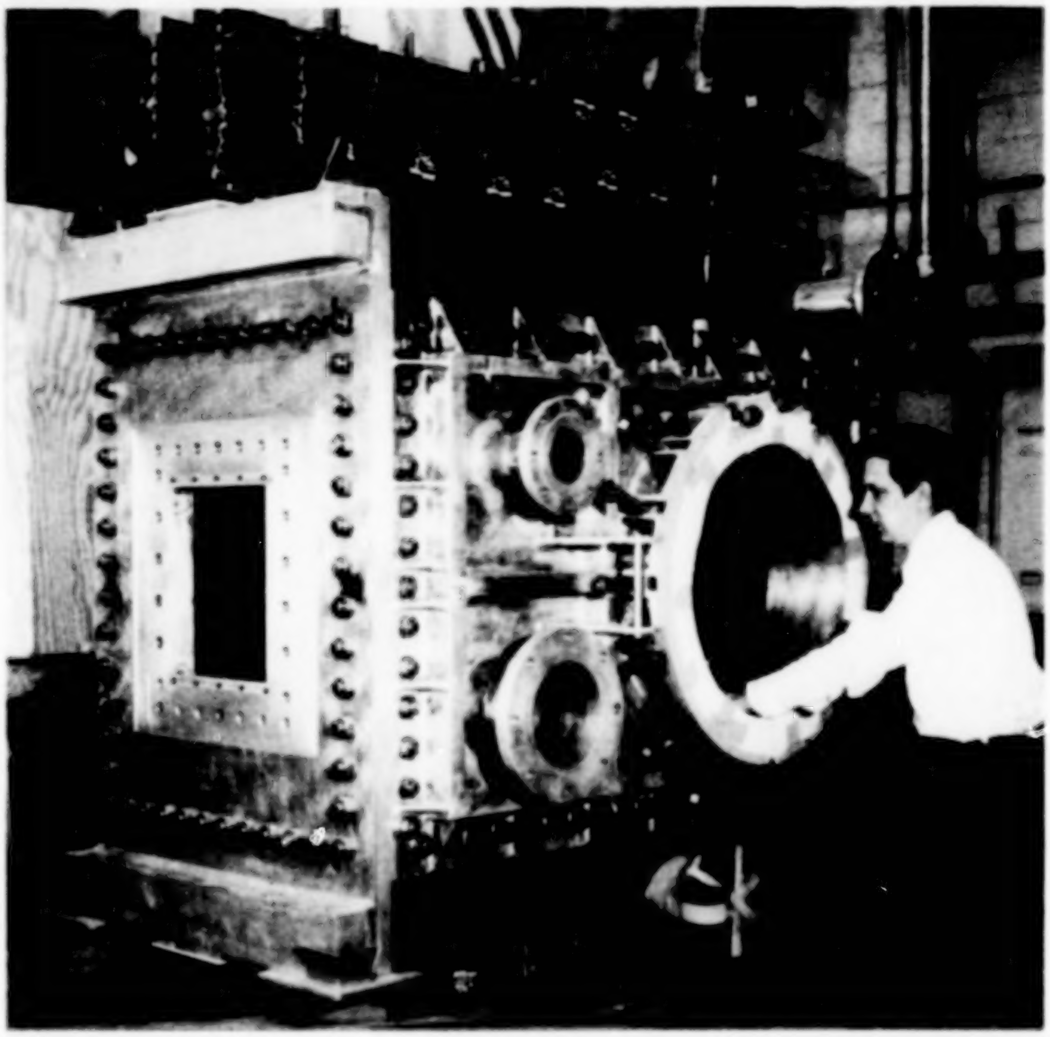

AIRFOIL MODELS IN TWO SIZES

Initial tests in the 13- by 13-inch SSW TS of the 0.3-m TCT will be for tunnel systems checkout, performance, flow quality, and wall adaptation to uniform flow at various conditions. Upon completion of these initial tests, two tests of airfoil pairs are scheduled to determine the operational capabilities of the adaptation software and to investigate 2-D wind tunnel wall interference at high Reynolds numbers. Two NACA 0012 airfoil models, one with a 6.5-inch chord and the other with a 13-inch chord, as shown in the photograph, will be tested to assess the software at values of tunnel height to model chord down to 1.0. The results from these tests can be compared with results from tests of the NACA 0012 in the 0.3-m TCT and other facilities. Two joint cooperative programs, one an NASA/ONERA/DFVLR effort and the other an NASA/NAE effort, have been established to test DOA CAST-10 airfoil models of 7- and 9-inch chords, respectively. These joint data will be used to assess the effects of model manufacturing differences and to compare the results on the same airfoil model in different facilities.

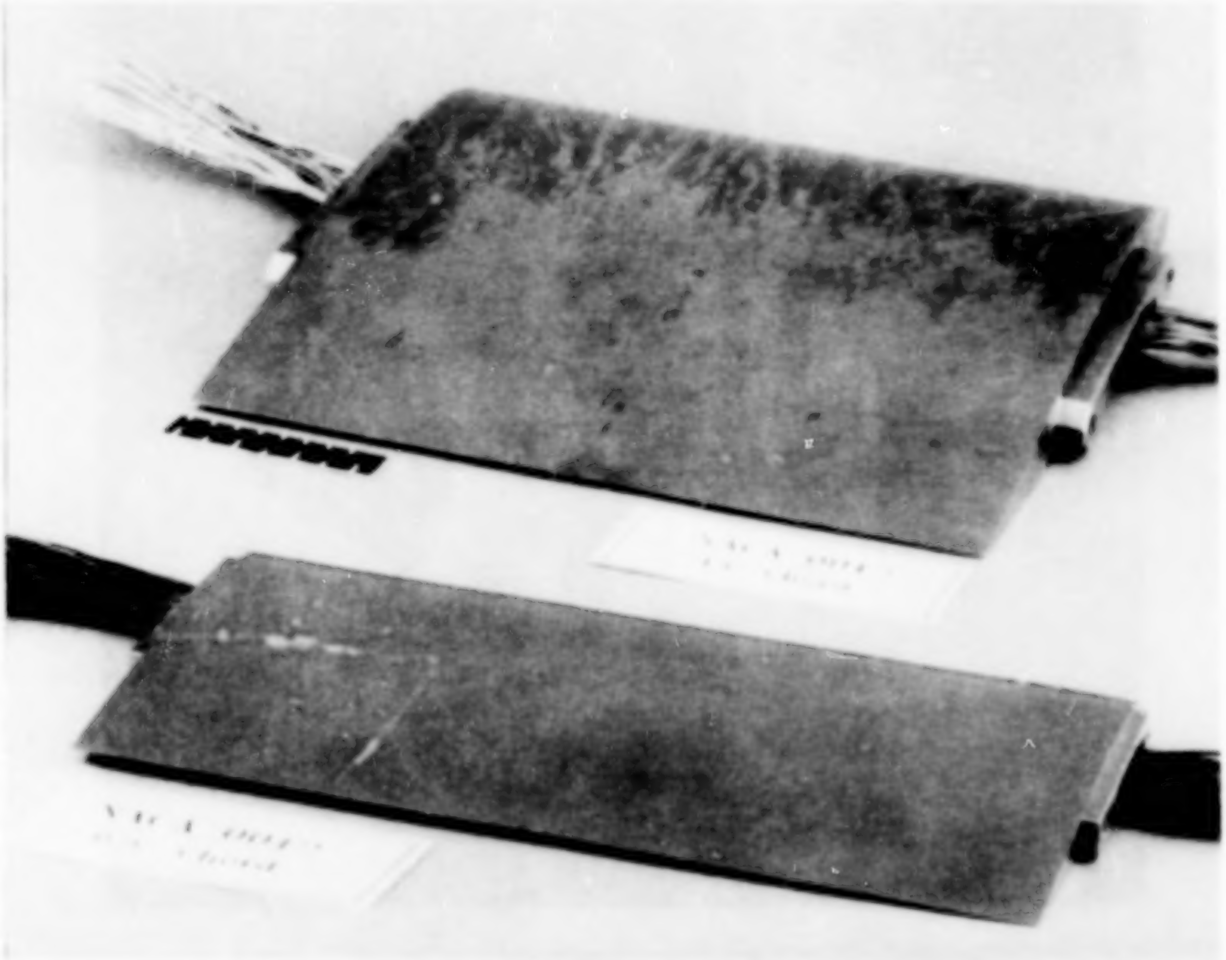

ORIGINAL PAGE IS
OF POOR QUALITY

TRANSONIC SELF STREAMLINING WALL TUNNEL

ORIGINAL PAGE IS
OF POOR QUALITY

University of Southampton

Adaptive wall work at the University of Southampton under NASA Langley sponsorship has been going on for a little more than a decade. Recent accomplishments include successful transonic testing of airfoils down to tunnel height-to-chord ratios of about one and at flow conditions where the supercritical flow region extends to the adapted walls. The facility is automated and has a reasonably rapid response. Good agreement has been seen between results from the TSSWT and several other 2-D adaptive flexible wall tunnels. Current 2-D research is toward use through Mach numbers of unity. Initial research on 3-D model testing within 2-D adaptable walls has also begun. The photograph shows a 3-D model mounted in the University of Southampton TSSWT.

3-D MODEL/2-D WALL ADAPTATION

The 3-D model is viewed here through the access port of the TSSWT as shown on the previous photograph. The edge of the 2-D flexible wall above the model is also seen through the port. Here, the goal of testing free from wall interference cannot be met. The philosophy adopted is to provide the test section with sufficient static pressure taps around and along its length to allow various measures of interference to be quantified. The principal interferences that the model experiences are wall-induced velocities in the streamwise and vertical directions. This induced velocity field can be manipulated by 2-D wall movement, and hence the level of interference can be reduced. Assessment of and correction for residual interference will be made using the wall pressure and location data measured for the final 2-D adapted wall setting in a given test run.

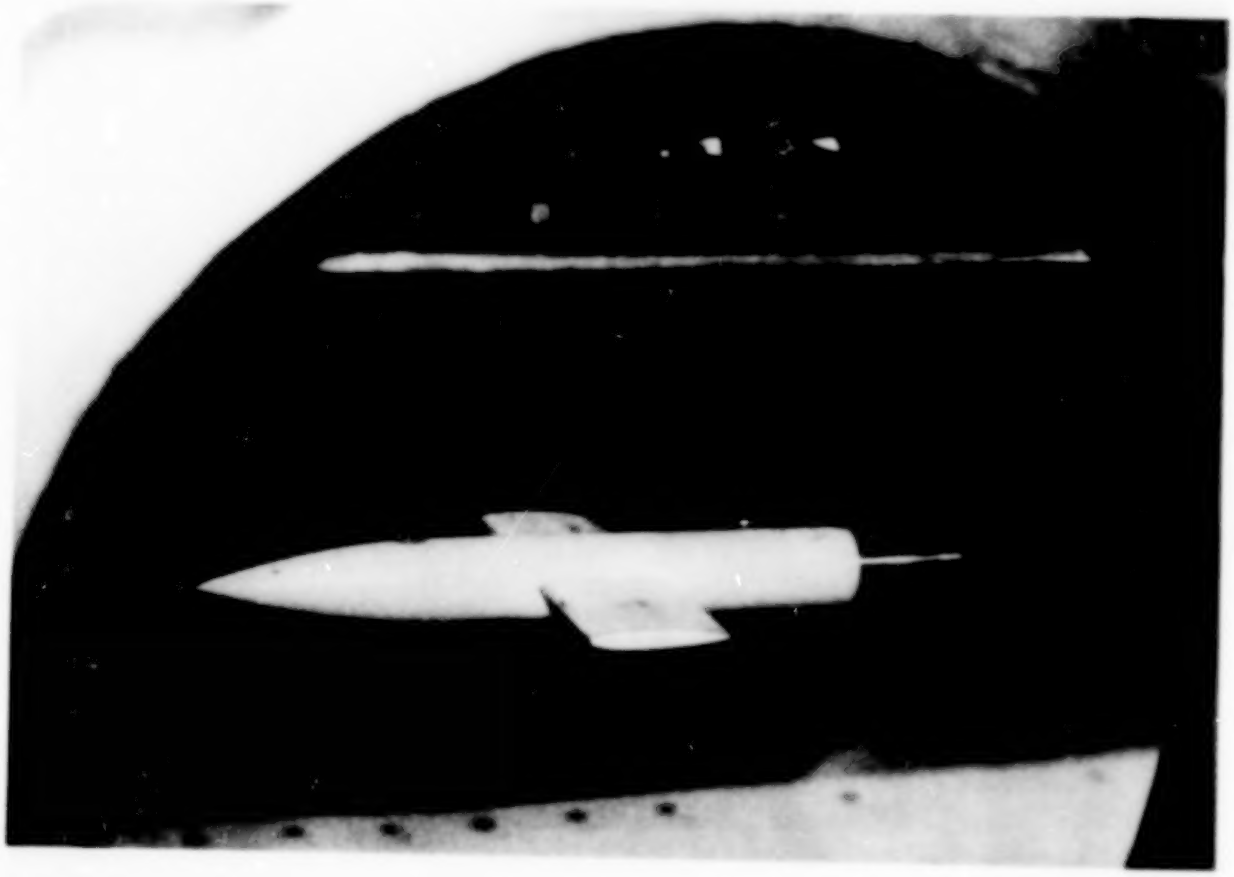

ORIGINAL PAGE IS
OF POOR QUALITY

A DECADE OF RENEWED WIND TUNNEL WALL INTERFERENCE RESEARCH

This last chart characterizes NASA Langley's recently renewed wind tunnel wall interference research. In addition to the points listed, it should be added that most of our wall interference research to date has been directed toward conventional slotted-wall transonic tunnels; solid, flexible, adaptive-wall, transonic tunnels; and assessment/correction methods related to them. The publications list does not include work related to high-lift (V/STOL), supersonic-hypersonic, and unsteady wall interference research, which have also been pursued during this past decade at Langley. Furthermore, one should not assume from the number of researchers listed on the publications that our transonic effort is a large one; few are full-time wall interference players. One tends to become interested in transonic wall interference only when a promising new idea comes along or when all other explanations fail in trying to understand the test results.

- NASA Langley focus is transonic flow
- Both analytical and experimental aspects being pursued
- Applications for prediction, assessment/correction, avoidance, and verification continue
- Work best summarized by publications (list in handout)

A DECADE OF RENEWED NASA LANGLEY SPONSORED TRANSONIC WIND TUNNEL WALL INTERFERENCE RESEARCH

I. GENERAL

A. Wall Interference

1. Kemp, W. B., Jr.: Transonic Wind-Tunnel Wall Interference. NASA CP-2009, 1977, pp. 65-71.
2. Pierpont, P. K. (editor): Advanced Technology Airfoil Research. NASA CP-2045, 1979.
3. Newman, P. A.; and Kemp, W. B., Jr.: Wall-Interference Effects: Status Review and Planned Experiments in NTF. NASA CP-2183, 1981, pp. 123-141.
4. South, J. C., Jr.; and Thames, F. C.: Report of the Panel on Theoretical Aerodynamics. NASA CP-2183, 1981, pp. 277-286.
5. McKinney, L. W.; and Baals, D. D. (editors): Wind-Tunnel/Flight Correlation - 1981. NASA CP-2225, 1982.
6. Tuttle, M. H.; and Plentovich, E. B.: Adaptive Wall Wind Tunnels, A Selected, Annotated Bibliography. NASA TM-84526, 1982.
7. Newman, P. A.; and Barnwell, R. W. (editors): Wind Tunnel Wall Interference Assessment/Correction - 1983. NASA CP-2319, 1984.
8. Bobbitt, P. J.; and Newman, P. A.: Discussion of Wind Tunnel Wall Interference Correction Issues. NASA CP-2319, 1984, pp. 415-423.
9. Gloss, B. B.: Initial Research Program for the National Transonic Facility. AIAA Paper 84-0585, 1984.

B. Langley Facilities

1. Goodyer, M. J.; and Kilgore, R. A.: High Reynolds Number Cryogenic Wind Tunnel. AIAA Paper 72-995, 1972. (AIAA J., vol. 11, no. 5, 1973, pp. 613-619).
2. Kilgore, R. A.; Adcock, J. B.; and Ray, E. J.: Flight Simulation Characteristics of the Langley High Reynolds Number Cryogenic Transonic Tunnel. AIAA Paper 72-80, 1972. (J. Aircraft, vol. 11, no. 10, 1974).
3. Ladson, C. L.: Description and Calibration of the Langley 6- by 9-Inch Transonic Tunnel. NASA TN D-7182, 1973.
4. Kilgore, R. A.; Goodyer, M. J.; Adcock, J. B.; and Davenport, E. E.: The Cryogenic Wind-Tunnel Concept for High Reynolds Number Testing. NASA TN D-7762, 1974.

5. Ray, E. J; Kilgore, R. A.; Adcock, J. B.; and Davenport, E. E.: Test Results From the Langley High Reynolds Number Cryogenic Transonic Tunnel. AIAA Paper 74-631, 1974.

6. Ladson, C. L.: Description and Calibration of the Langley 6- by 28-Inch Transonic Tunnel. NASA TN D-8070, 1975.

7. McKinney, L. W.; and Howell, R. R.: The Characteristics of the Planned National Transonic Facility. Proceedings AIAA Ninth Aerodynamic Testing Conference, 1976, pp. 176-184.

8. Howell, R. R.; and McKinney, L. W.: The U.S. 2.5-Meter Cryogenic High Reynolds Number Tunnel. ICAS Paper 76-04, 1976.

9. Baals, D. D.: Design Considerations of the National Transonic Facility. NASA CP-2001, 1976, pp. 1583-1602.

10. Kilgore, R. A.: Design Features and Operational Characteristics of the Langley 0.3-Meter Transonic Cryogenic Tunnel. NASA TN D-8304, 1976.

11. Baals, D. D. (Editor): High Reynolds Number Research. NASA CP-2009, 1977.

12. Nicks, O. W.; and McKinney, L. W.: Status and Operational Characteristics of the National Transonic Facility. AIAA Paper 78-770, 1978.

13. Kilgore, R. A.; Igoe, W. B.; Adcock, J. B.; Hall, R. M.; and Johnson, C. B.: Full Scale Aircraft Simulation with Cryogenic Tunnels and Status of the National Transonic Facility. NASA TM-80085, 1979.

14. Ray, E. J.; Ladson, C. L.; Adcock, J. B.; Lawing, P. L.; and Hall, R. M.: Review of Design and Operational Characteristics of the 0.3-Meter Transonic Cryogenic Tunnel. NASA TM-80123, 1979.

15. Kilgore, R. A.: Development of the Cryogenic Tunnel Concept and Application to the U.S. National Transonic Facility. AGARD-AG-240, 1979, pp. 2-1 to 2-27.

16. Ray, E. J.: Langley's Two-Dimensional Research Facilities - Capabilities and Plans. NASA CP-2045, 1979, pp. 399-414.

17. Howell, R. R.: The National Transonic Facility: Status and Operational Planning. AIAA Paper 80-0415, 1980.

18. Ladson, C. L.; and Kilgore, R. A.: Instrumentation for Calibration and Control of a Continuous-Flow Cryogenic Tunnel. NASA TM-81825, 1980.

19. Igoe, W. B.: Characteristics and Status of the U.S. National Transonic Facility. AGARD Lecture Series No. 111, 1980.

20. Gloss, B. B.; and Nystrom, D.: Estimation of Fan Pressure Ratio Requirements and Operating Performance for the National Transonic Facility. NASA TM-81802, 1981.

21. Sewall, W. G.: Description of Recent Changes in the Langley 6- by 28-Inch Transonic Tunnel. NASA TM-81947, 1981.

22. McKinney, L. W.; and Baals, D. D. (Editors): High Reynolds Number Research - 1980. NASA CP-2183, 1981.

23. Fuller, D. E.: Guide for Users of the National Transonic Facility. NASA TM-83124, 1981.

24. Polhamus, E. C.: The Large Second Generation of Cryogenic Tunnels. Astronautics and Aeronautics Magazine, Oct. 1981, pp. 38-51.

25. McKinney, L. W.; and Gloss, B. B.: Status of the National Transonic Facility. AIAA Paper 82-0604, 1982.

26. McKinney, L. W.: Operational Experience with the National Transonic Facility. AGARD-CP-348, 1984, pp. 1-1 to 1-8.

27. Bruce, W. E., Jr.; Fuller, D. E.; and Igoe, W. B.: National Transonic Facility Shakedown Test Results and Calibration Plans. AIAA Paper 84-0584, 1984.

28. McGhee, R. J.; Beasley, W. D.; and Foster, J. M: Recent Modifications and Calibration of the Langley Low-Turbulence Pressure Tunnel. NASA TP-2328, 1984.

29. Campbell, J. F.: The National Transonic Facility - A Research Perspective. AIAA Paper 84-2150, 1984.

Unpublished:

30. National Transonic Facility Research Symposium, NASA Langley Research Center, Dec. 5, 1983 (viewgraphs only).

II. BASIC

A. Slotted Walls

1. Mann, M. J.: Low-Speed Upwash Interference on a Transport Model in a Rectangular Slotted-Wall Wind Tunnel. NASA TM X-3218, 1975.

2. Barnwell, R. W.: Improvements in the Slotted-Wall Boundary Condition. Proceedings AIAA Ninth Aerodynamic Testing Conference, 1976, pp. 21-30.

3. Barnwell, R. W.: Design and Performance Evaluation of Slotted Walls for Two-Dimensional Wind Tunnels. NASA TM-78648, 1978.

4. Everhart, J. L.; and Barnwell, R. W.: A Parametric Experimental Study of the Interference Effects and the Boundary-Condition Coefficient of Slotted Wind-Tunnel Walls. AIAA Paper 78-805, 1978.

5. Barnwell, R. W.; Sewall, W. G.; and Everhart, J. L.: Design and Calibration of Slotted Walls for Transonic Airfoil Wind Tunnels. NASA CP-2045, 1979, pp. 433-443.

6. Everhart, J. L.; and Barnwell, R. W.: A Parametric Experimental Study of the Slotted-Wall Boundary Condition. NASA CP-2045, 1979, pp. 459-471.

7. Ramaswamy, M. A.; and Cornette, E. S.: Supersonic Flow Development in Slotted Wall Tunnels. AIAA Paper 80-0443, 1980. (AIAA J., vol. 20, no. 6, 1982, pp. 805-811).

8. Barger, R. L.: A Theory for Predicting Boundary Impedance and Resonant Frequencies of Slotted-Wall Wind Tunnels, Including Plenum Effects. NASA TP-1880, 1981.

9. Everhart, J. L.: Potential Flow Through a Cascade of Alternately Displaced Circular Bodies - The Rod-Wall Wind-Tunnel Boundary Condition. NASA TM-85750, 1984.

B. Sidewall Boundary Layers

1. Barnwell, R. W.: A Similarity Rule for Compressibility and Sidewall Boundary Layer Effects in Two-Dimensional Wind Tunnels. AIAA Paper 79-108, 1979. (AIAA J., vol. 18, no. 9, 1980, pp. 1149-1151).

2. Sewall, W. G.: The Effects of Sidewall Boundary Layers in Two-Dimensional Subsonic and Transonic Wind Tunnels. AIAA Paper 81-1297, 1981. (AIAA J., vol. 20, no. 9, 1982, pp. 1253-1256).

3. Murthy, A. V.; Johnson, C. B.; Ray, E. J.; and Lawing, P. L.: Recent Sidewall Boundary-Layer Investigations with Suction in the Langley 0.3-m Transonic Cryogenic Tunnel. AIAA Paper 82-0234, 1982.

4. Barnwell, R. W.; and Sewall, W. G.: Similarity Rules for Effects of Sidewall Boundary Layer in Two-Dimensional Wind Tunnels. AGARD-CP-335, 1982, pp. 3-1 to 3-10.

5. Sewall, W. G.: Application of a Transonic Similarity Rule to Correct the Effects of Sidewall Boundary Layers in Two-Dimensional Transonic Wind Tunnels. NASA TM-84847, 1982.

6. Adcock, J. B.; and Barnwell, R. W.: Effect of Boundary Layers on Solid Walls in Three-Dimensional Subsonic Wind Tunnels. AIAA Paper 83-0144, 1983. (AIAA J., vol. 22, no. 3, 1984, pp. 365-371).

7. Murthy, A. V.; Johnson, C. B.; Ray, E. J.; Lawing, P. L.; and Thibodeaux, J. J.: Investigation of Upstream Sidewall Boundary Layer Removal Effects on a Supercritical Airfoil. AIAA Paper 83-0386, 1983.

8. Murthy, A. V.; Johnson, C. B.; Ray, E. J.; Lawing, P. L.; and Thibodeaux, J. J.: Studies of Sidewall Boundary Layer in the Langley 0.3-Meter Transonic Cryogenic Tunnel With and Without Suction. NASA TP-2096, 1983.

9. Johnson, C. B.; Murthy, A. V.; Ray, E. J.; Lawing, P. L.; Thibodeaux, J. J.: Effect of Upstream Sidewall Boundary Layer Removal on an Airfoil Test. NASA CP-2319, 1984, pp. 143-163.

10. Adcock, J. B.; and Barnwell, R. W.: Effect of Boundary Layers on Solid Walls in Three-Dimensional Subsonic Wind Tunnels. NASA CP-2319, 1984, pp. 205-218.

11. Jenkins, R. V.: Some Experience With Barnwell-Sewall Type Correction to Two-Dimensional Airfoil Data. NASA CP-2319, 1984, pp. 375-392.

12. Barnwell, R. W.: Effect of Sidewall Suction on Flow in Two-Dimensional Wind Tunnels, AIAA Paper 84-0242, 1984.

13. Murthy, A. V.; Johnson, C. B.; Ray, E. J.; and Stanewsky, E.: Investigation of Sidewall Boundary Layer Removal Effects on Two Different Chord Airfoil Models in the Langley 0.3-Meter Transonic Cryogenic Tunnel. AIAA Paper 84-0598, 1984.

14. Murthy, A. V.: Corrections for the Attached Sidewall Boundary-Layer Effects in Two-Dimensional Airfoil Testing. NASA CR-3873, 1985.

C. Data Bases (With Measured Wall Pressures)

1. Couch, L. M.: Transonic Wall Interference Effects on Bodies of Revolution. AIAA Paper 72-1008, 1972.

2. Couch, L. M.; and Brooks, C. W., Jr.: Effect of Blockage Ratio on Drag and Pressure Distributions for Bodies of Revolution at Transonic Speeds. NASA TN D-7331, 1973.

3. Blackwell, J. A., Jr.; Burdges, K. P.; and Hinson, B.: Effect of Wall Porosity on a NASA 10% Thick Supercritical Airfoil at Transonic Speeds. NASA CR-132712, 1975.

4. Blackwell, J. A., Jr.; and Pounds, G. A.: Wind-Tunnel Wall Interference Effects on a Supercritical Airfoil at Transonic Speeds. J. Aircraft, vol. 14, no. 10, 1977, pp. 929-935. (Also Proceedings AIAA Ninth Aerodynamic Testing Conference, 1976, pp. 1-11.)

5. Baronti, P.; and Roffe, G.: An Experimental Investigation of a Transonic Interference Over a Three-Dimensional Wing. General Applied Science Laboratories, Inc., TR No. 244, 1977.

6. Ladson, C. L.; and Ray, E. J.: Status of Advanced Airfoil Tests in the Langley 0.3-Meter Transonic Cryogenic Tunnel. NASA CP-2208, 1981, pp. 37-53.

7. Wolf, S. W. D.: Model and Boundary Aerodynamic Data From High Blockage Two-Dimensional Airfoil Tests in a Shallow Unstreamlined Transonic Flexible Walled Test Section. NASA CR-165685, 1981.

8. Johnson, W. G., Jr.; Hill, A. S.; Ray, E. J.; Rozendaal, R. A.; and Butler, T. W.: High Reynolds Number Tests of a Boeing BAC I Airfoil in the Langley 0.3-Meter Transonic Cryogenic Tunnel. NASA TM-81922, 1982.

9. Reaser, J. S.: Transonic Testing in a Cryogenic 2-D Wind Tunnel of an Advanced Technology Airfoil. Lockheed-California, Burbank, Report No. LR-30047, 1982.

10. Ray, E. J.: A Review of Reynolds Number Studies Conducted in the Langley 0.3-m Transonic Cryogenic Tunnel. AIAA Paper 82-0941, 1982.

11. Dress, D. A.; Johnson, C. B.; McGuire, P. D.; Stanewsky, E.; and Ray, E. J.: High Reynolds Number Tests of the CAST 10-2/DOA 2 Airfoil in the Langley 0.3-Meter Transonic Cryogenic Tunnel - Phase I. NASA TM-84620, 1983.

12. Reaser, J. S.; Hallissy, J. B.; and Campbell, R. L.: Design and True Reynolds Number 2-D Testing of an Advanced Technology Airfoil. AIAA Paper 83-1792, 1983.

13. Reaser, J. S.: Testing of an Advanced Technology Transonic Airfoil in a 2-D Cryogenic Wind Tunnel. Lockheed-California, Burbank, Report No. LR-30418, 1983.

14. Jenkins, R. V.: Tabulation of Data From Tests of an NPL 9510 Airfoil in the Langley 0.3-Meter Transonic Cryogenic Tunnel. NASA TM-84579, 1983.

15. Jenkins, R. V.: Reynolds Number Tests of an NPL 9510 Airfoil in the Langley 0.3-Meter Transonic Cryogenic Tunnel. NASA TM-85663, 1983.

16. Stanewsky, E.; Demurie, F.; Ray, E. J.: and Johnson, C. B.: High Reynolds Number Tests of the CAST 10-2/DOA 2 Transonic Airfoil at Ambient and Cryogenic Temperature Conditions. AGARD-CP-348, 1984, pp. 10-1 to 10-13.

17. Plentovich, E. B.; Ladson, C. L.; and Hill, A. S.: Tests of a NACA 65_1-213 Airfoil in the NASA Langley 0.3-Meter Transonic Cyrogenic Tunnel. NASA TM-85732, 1984.

18. Sewall, W. G.: Wall Pressure Measurements for Three-Dimensional Transonic Tests. AIAA Paper 84-0599, 1984.

19. Dress, D. A.; Stanewsky, E.; McGuire, P. D.; and Ray, E. J.: High Reynolds Number Tests of the CAST 10-2/DOA 2 Airfoil in the Langley 0.3-Meter Transonic Cryogenic Tunnel - Phase II. NASA TM-86273, 1984.

20. Jenkins, R. V.; Johnson, W. G., Jr.; Hill, A. S.; Mueller, R.; and Redeker, G.: Data From Tests of an R4 Airfoil in the Langley 0.3-Meter Transonic Cryogenic Tunnel. NASA TM-85739, 1984.

21. Ray, E. J.; and Ladson, C. L.: Review of the Advanced Technology Airfoil Test Program in the 0.3-M Transonic Cryogenic Tunnel. NASA CP-2319, 1984, pp. 361-373.

22. Johnson, W. G., Jr.; Hill, A. S.; and Eichmann, O.: Pressure Distributions from High Reynolds Number Tests of a NASA SC(3)-0712(B) Airfoil in the Langley 0.3-Meter Transonic Cryogenic Tunnel. NASA TM-86370, 1985.

23. Johnson, W. G., Jr.; Hill, A. S.; and Eichmann, O.: High Reynolds Number Tests of a NASA SC(3)-0712(B) Airfoil in the Langley 0.3-Meter Transonic Cryogenic Tunnel. NASA TM-86371, 1985.

D. Simulator Codes

1. Barnwell, R. W.: Transonic Flow About Lifting Wing-Body Combinations. AIAA Paper 74-185, 1974.

2. Newman, P. A.; and Klunker, E. B.: Numerical Modeling of Tunnel-Wall and Body-Shape Effects on Transonic Flows Over Finite Lifting Wings. NASA SP-347, 1975, pp. 1189-1212.

3. Barnwell, R. W.: Approximate Method for Calculating Transonic Flow About Lifting Wing Body Combinations. NASA SP-347, 1975, pp. 1281-1303.

4. South, J. C., Jr.; and Keller, J. D.: Axisymmetric Transonic Flow Including Wind Tunnel Wall Effects. NASA SP-347, 1975, pp. 1233-1267.

5. Ruger, C.; and Baronti, P.: A Linear Solution of Lift Interference in Square Tunnels With Slotted Test Sections of Finite Length. NASA CR-144980, 1975.

6. Doria, M. L.; and South, J. C., Jr.: Transonic Potential Flow and Coordinate Generation for Bodies in a Wind Tunnel. AIAA Paper 82-0223, 1982.

7. Wedan, B.; and South, J. C., Jr.: A Method for Solving the Transonic Full-Potential Equation for General Configurations. AIAA 83-1889, 1983.

8. Kemp, W. B., Jr.: An Interference Assessment Approach for a Three-Dimensional Slotted Tunnel With Sparse Wall Pressure Data. NASA CP-2319, 1984, pp. 323-334.

9. Kemp, W. B., Jr.: A Slotted Test Section Numerical Model for Interference Assessment. AIAA Paper 84-0627, 1984. (J. Aircraft, vol. 22, no. 3, 1985, pp. 216-222).

10. South, J. C., Jr.; Doria, M. L.; and Green, L. L.: Finite-Volume Scheme for Transonic Potential Flow About Airfoils and Bodies in an Arbitrarily-Shaped Channel. Third Symposium on Numerical and Physical Aspects of Aerodynamic Flows, 1985.

III. WIAC

1. Kemp, W. B., Jr.: Toward the Correctable-Interference Transonic Wind Tunnel. Proceedings AIAA Ninth Aerodynamic Testing Conference, 1976, pp. 31-38.

2. Kemp, W. B., Jr.: Transonic Assessment of Two-Dimensional Wind Tunnel Wall Interference Using Measured Wall Pressures. NASA CP-2045, 1979, pp. 473-486.

3. Blackwell, J. A.: Wind-Tunnel Blockage Correction for Two-Dimensional Transonic Flow. J. Aircraft, vol. 16, no. 4, 1979, pp. 256-263.

4. Kemp, W. B., Jr.: TWINTAN: A Program for Transonic Wall Interference Assessment in Two-Dimensional Wind Tunnels. NASA TM-81819, 1980.

5. Rizk, M. H.: A New Optimization Technique Applied to Wind Tunnel Angle-of-Attack Corrections. Flow Research Company Note No. 198, 1982.

6. Kemp, W. B., Jr.; and Adcock, J. B.: Combined Four-Wall Interference Assessment in Two-Dimensional Airfoil Tests. AIAA Paper 82-0586, 1982. (AIAA J., vol. 21, no. 10, 1983, pp. 1353-1359).

7. Rizk, M. H.; Hafez, M.; Murman, E. M.; and Lovell, D.: Transonic Wind Tunnel Wall Interference Corrections for Three-Dimensional Models. AIAA Paper 82-0588, 1982.

8. Rizk, M. H.; and Smithmeyer, M. G.: Wind-Tunnel Wall Interference Corrections for Three-Dimensional Flows. J. Aircraft, vol. 19, no. 6, 1982, pp. 465-472.

9. Rizk, M. H.: Higher-Order Flow Angle Corrections for Three-Dimensional Wind Tunnel Wall Interference. J. Aircraft, vol. 19, no. 10, 1982, pp. 893-895.

10. Gopinath, R.: Wall Interference Evaluation from Pressure Measurement on Control Surfaces. J. Aircraft, vol. 19, no. 12, 1982, pp. 1097-1098.

11. Rizk, M. H.: A New Approach to Optimization for Aerodynamic Applications. J. Aircraft, vol. 20, no. 1, 1983, pp. 94-96.

12. Rizk, M. H.: The Single-Cycle Scheme: A New Approach to Numerical Optimization. AIAA J., vol. 21, no. 12, 1983, pp. 1640-1647.

13. Rizk, M. H.; and Murman, E. M.: Wind Tunnel Wall Interference Corrections for Aircraft Models in the Transonic Regime. J. Aircraft, vol. 21, no. 1, 1984, pp. 54-61.

14. Kemp, W. B., Jr.: TWINTN4: A Program for Transonic Four-Wall Interference Assessment in Two-Dimensional Wind Tunnels. NASA CR-3777, 1984.

15. Rizk, M. H.; Smithmeyer, M. G.; and Murman, E. M.: Wind Tunnel Wall Interference Corrections for Aircraft Models. NASA CP-2319, 1984, pp. 301-322.

16. Gumbert, C. R.; Newman, P. A.; Kemp, W. B., Jr.; and Adcock, J. B.: Adaptation of a Four-Wall Interference Assessment/Correction Procedure for Airfoil Tests in the 0.3-m TCT. NASA CP-2319, 1984, pp. 393-411.

17. Rizk, M. H.; Lovell, D.; and Jou, W. H.: Wind Tunnel Wall Interference Corrections Based on the Euler Equations. Flow Industries, Inc., Research and Technology Division Report No. 289, 1984.

18. Gumbert, C. R.; and Newman, P. A.: Validation of a Wall Interference Assessment/Correction Procedure for Airfoil Tests in the Langley 0.3-m Transonic Cryogenic Tunnel. AIAA Paper 84-2151, 1984.

19. Gaffney, R. L., Jr.; Salas, M. D.; and Hassan, H. A.: Assessment of Wind Tunnel Corrections for Multielement Airfoils at Transonic Speeds. Third Symposium on Numerical and Physical Aspects of Aerodynamic Flows, 1985.

Unpublished:

20. Newman, P. A.: Wall Interference Theories. National Transonic Facility Research Symposium, NASA Langley Research Center, Dec. 5, 1983.

21. Adcock, J. B.: Wall Interference Experiments. National Transonic Facility Research Symposium, NASA Langley Research Center, Dec. 5, 1983.

22. Newman, P. A.; Gumbert, C. R.; and Kemp, W. B., Jr.: 0.3-m Transonic Cryogenic Tunnel User Mini-Workshop on Airfoil WIAC Procedure - Presentation Viewgraphs. NASA Langley Research Center, Feb. 6, 1985.

23. Gumbert, C. R.: User Manual for 0.3-m TCT Wall-Interference Assessment/Correction Procedure: 8- by 24-Inch Airfoil Test Section. NASA TM-87582, 1985.

IV. ADAPTED WALLS

A. Active

1. Goodyer, M. J.: The Self Streamlining Wind Tunnel. NASA TM X-72699, 1975.

2. Goodyer, M. J.: A Low Speed Self Streamlining Wind Tunnel. AGARD-CP-174, 1976, pp. 13-1 to 13-8.

3. Judd, M.; Goodyer, M. J.; and Wolf, S. W. D.: Application of the Computer for On-Site Definition and Control of Wind Tunnel Shape for Minimum Interference. AGARD-CP-210, 1976, pp. 6-1 to 6-14.

4. Judd, M.; Wolf, S. W. D.; and Goodyer, M. J.: Analytical Work in Support of the Design and Operation of Two Dimensional Self Streamlining Test Sections. NASA CR-145019, 1976.

5. Wolf, S. W. D.; and Goodyer, M. J.: Self Streamlining Wind Tunnel: Low Speed Testing and Transonic Test Section Design. NASA CR-145257, 1977.

6. Wolf, S. W. D.: Self Streamlining Wind Tunnel: Further Low Speed Testing and Final Design Studies for the Transonic Facility. NASA CR-158900, 1978.

7. Goodyer, M. J.: Developments in Airfoil Testing Techniques at University of Southampton. NASA CP-2045, 1979, pp. 415-423.

8. Ladson, C. L.: A New Airfoil Research Capability. NASA CP-2045, 1979, pp. 425-432.

9. Wolf, S. W. D.; and Goodyer, M. J.: Studies of Self Streamlining Wind Tunnel Real and Imaginary Flows. NASA CR-158831, 1979.

10. Goodyer, M. J.; and Wolf, S. W. D.: The Development of a Self-Streamlining Flexible Walled Transonic Test Section. AIAA Paper 80-0440, 1980. (AIAA J., vol. 20, no. 2, 1982, pp. 227-234).

11. Wolf, S. W. D.: Selected Data From a Transonic Flexible Walled Test Section. NASA CR-159360, 1980.

12. Wolf, S. W. D.; Goodyer, M. J.; and Cook, I. D.: Streamlining the Walls of an Empty Two-Dimensional Flexible-Walled Test Section. NASA CR-165936, 1982.

13. Wolf, S. W. D.; Cook, I. D.; and Goodyer, M. J.: The Status of Two- and Three-Dimensional Testing in the University of Southampton Transonic Self-Streamlining Wind Tunnel. AGARD-CP-335, 1982, pp. 15-1 to 15-14.

14. Wolf, S. W. D.: Control Software for Two Dimensional Airfoil Tests Using a Self-Streamlining Flexible Walled Transonic Test Section. NASA CR-165941, 1982.

15. Goodyer, M. J.: Extraction of Model Performance from Wall Data in a Two-Dimensional Transonic Flexible Walled Test Section. NASA CR-165994, 1982.

16. Wolf, S. W. D.: Aerodynamic Data From a Two-Dimensional Cambered Airfoil Section in a Shallow Transonic Flexible Walled Test Section. NASA CR-166005, 1982.

17. Wolf, S. W. D.: A Wake Traverse Technique for Use in a Two Dimensional Transonic Flexible Walled Test Section. NASA CR-165995, 1982.

18. Everhart, J. L.: A Method for Modifying Two-Dimensional Adaptive Wind-Tunnel Walls Including Analytical and Experimental Verification. NASA TP-2081, 1983.

19. Everhart, J. L.: FLEXWAL: A Computer Program for Predicting the Wall Modification for Two-Dimensional, Solid Adaptive-Wall Wind Tunnels. NASA TM-84648, 1983.

20. Webb, J.: Adaptation of Two-Dimensional Transonic Analysis Code, TSFOIL, for Use in Modeling Adaptive Wall Test Sections. NASA CR-173300, 1984, Appendix B.

21. Goodyer, M. J.: Tests on a CAST 7 Two-Dimensional Airfoil in a Self-Streamlining Test Section. NASA CR-172291, 1984.

22. Lewis, M. C.: The Status of Analytical Preparation for Two-Dimensional Testing at High Transonic Speeds in the University of Southampton Self-Streamlining Wind Tunnel. NASA CR-3785, 1984.

23. Wolf, S. W. D.: The Design and Operational Development of Self-Streamlining Two-Dimensional Flexible Walled Test Sections. NASA CR-172328, 1984.

24. Goodyer, M. J.: Computation of Imaginary-Side Pressure Distributions Over the Flexible Walls of the Test Section Insert for the 0.3-m Transonic Cryogenic Tunnel. NASA CR-172363, 1984.

25. Goodyer, M. J.; and Cook, I. D.: Two- and Three-Dimensional Model and Wall Data From a Flexible-Walled Transonic Test Section. NASA CP-2319, 1984, pp. 79-88.

Unpublished:

26. Wolf, S. W. D.: Turbine Blade Cascade Testing in a Flexible Walled Wind Tunnel. B.Sc. Honours Project, University of Southampton, April 1975.

27. Wolf, S. W. D.: Application of Data Acquisition Systems for On-Line Definition and Control of Wind Tunnel Shape. Von Karman Inst. for Fluid Dynamics, 1979.

28. Mason, B. I. F.: Development of a Program for the Flexible Wall Tunnel at Transonic Speeds. B.Sc. Honours Project, Univ. of Southampton, May 1980.

29. Rahman, A.: Comparison of Theoretical and Experimental Data of a CAST 7 Aerofoil Section. M.Sc. Thesis, Univ. of Southampton, 1983.

30. Mineck, R. E.: Status of the Adaptive Wall Test Section for the NASA Langley 0.3-m Transonic Cryogenic Tunnel. Euromech Colloquium 187, Oct. 1984.

B. Passive

1. Ferri, A.; and Roffe, G.: Experimental Investigation of Wall Shock Cancellation and Reduction of Wall Interference in Transonic Testing. NASA CR-144979, 1975.

2. Newman, P. A.; and Anderson, E. C.: Numerical Design of Streamlined Tunnels Walls for a Two-Dimensional Transonic Test. NASA TM-78641, 1978.

3. Newman, P. A.; and Anderson, E. C.: Analytical Design of a Contoured Wind-Tunnel Liner for Supercritical Testing. NASA CP-2045, 1979, pp. 499-509.

4. Anderson, E. C.: User Guide for STRMLN: A Boundary-Layer Program for Contoured Wind-Tunnel Liner Design. NASA CR-159058, 1979.

5. Campbell, R. L.: Computer Analysis of Flow Perturbations Generated by Placement of Choke Bumps in a Wind Tunnel. NASA TP-1892, 1981.

6. Newman, P. A.; Anderson, E. C.; and Peterson, J. B., Jr.: Numerical Design of the Contoured Wind-Tunnel Liner for the NASA Swept-Wing LFC Test. AIAA Paper 82-0568, 1982.

7. Newman, P. A.; Anderson, E. C.; and Peterson, J. B., Jr.: Aerodynamic Design of the Contoured Wind-Tunnel Liner for the NASA Supercritical, Laminar-Flow-Control, Swept-Wing Experiment. NASA TP-2335, 1984.

DB

N88-14939

513-09
117237
17P

STATUS OF MAGNETIC SUSPENSION TECHNOLOGY

Richmond P. Boyden and Ping Tcheng
NASA Langley Research Center
Hampton, Virginia

PRECEDING PAGE BLANK NOT FILMED

PAGE 260 INTENTIONALLY BLANK

[redacted]

ABSTRACT

This paper highlights the reasons for the continuing interest in Magnetic Suspension and Balance Systems (MSBS). Typical problems that can arise because of model-support interference in a transonic wind tunnel are shown to illustrate the need for MSBS. The two magnetic suspension systems in operation at Langley are the only ones active in the U.S. One of these systems is the 13-inch MSBS which was borrowed from the Air Force Arnold Engineering Development Center. The other system is the 6-inch MSBS which was developed by the MIT Aerophysics Laboratory with NASA and DOD funding. Each of these systems is combined with a subsonic wind tunnel. Ongoing research in both of these systems is covered. Last year, Madison Magnetics, Inc., completed a contractual design and cost study utilizing some advanced concepts for a large MSBS which would be compatible with an 8-foot transonic wind tunnel and the highlights of the study are presented. Sverdrup Technology, Inc., recently performed a study under contract for Langley on the potential usefulness to the aerospace industry of a proposed large MSBS combined with a suitable transonic wind tunnel. The results of that study are discussed. Langley has partially funded the MSBS work at the University of Southampton for about 6 years under a grant arrangement and the major results are summarized.

NASA MAGNETIC SUSPENSION AND BALANCE SYSTEM

This is the official NASA logo used to identify the work in Magnetic Suspension and Balance Systems. It consists of a head-on view of a fighter-type aircraft model suspended in an octagonal test section of a wind tunnel without any mechanical model support. The model is surrounded by an artist's conception of magnetic field lines. A symbolic representation of a wind tunnel fan is shown outside of the test section.

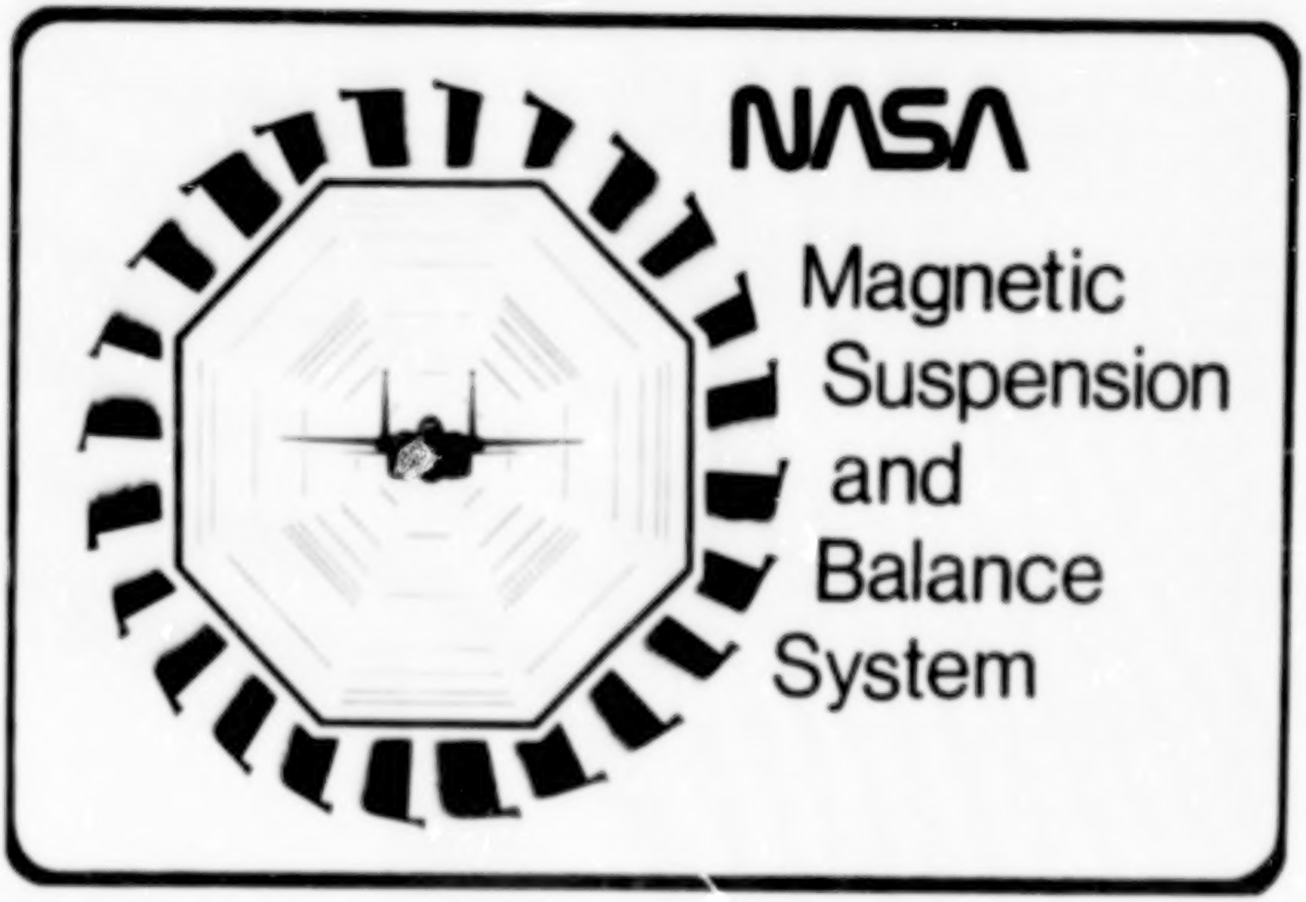

OUTLINE

An outline of the presentation is shown in this figure. We will begin with some background by reviewing the reasons for the basic interest in the magnetic suspension of models in wind tunnels. The effects that can arise from mechanical model supports are well known to those with experience in performing aerodynamic tests in wind tunnels or in analyzing the resultant aerodynamic data. Some examples of model support problems that have been encountered in tests here at Langley will be presented. Model support interference is difficult to predict, especially at transonic speeds. It is very dependent on the particular subtleties of geometry of each different model configuration.

Magnetic suspension of the model in the wind tunnel test section is seen to be the only feasible solution for completely eliminating model support interference for three-dimensional models. Fourteen Magnetic Suspension and Balance Systems (MSBS) are known to have been constructed in this country and abroad since 1957. These MSBS have been used for wind tunnel tests in various facilities at speeds ranging from subsonic to hypersonic. However, the largest of these MSBS can only accommodate a test section that is 13 inches in diameter. Our aim of eliminating support interference for three-dimensional models in transonic wind tunnels requires us, therefore, to develop and to demonstrate the technology required for larger MSBS.

The NASA Langley effort in magnetic suspension involves three aspects. The first is the in-house work which is focused on the two magnetic suspension systems which are operational here at Langley. The second is the work that is accomplished through study contracts and the third is the research grant with the University of Southampton in England.

- Effects of mechanical model supports
- Examples of model support problems
- Solution - Magnetic Suspension and Balance System (MSBS)
- Goal - Develop technology required for larger MSBS
    - In-house work
    - Study contracts
    - Research grant
- Videotape

EFFECTS OF MECHANICAL MODEL SUPPORTS

The primary problem with mechanical model supports in wind tunnels arises from classical support interference. One source of the interference comes from alterations which have to be made to the model geometry to accommodate the model support or sting. In many cases, the aft fuselage must be enlarged or otherwise distorted for rear sting entry. The second source of support interference is the distorted flow pattern resulting from the physical presence of the model support or sting. Support interference increases with increasing tunnel pressure as the size of the model support structure must be made larger to accommodate the higher loads. In addition, as aircraft configurations become more sophisticated with higher and higher fineness ratios, the problems of support interference become more difficult. (For a bibliography on this subject, see ref. 1.)

The constraints imposed by mechanical model support systems make up the other class of problem areas. The first constraint which is listed is the limited movement normally available with a mechanical system both in translation and in rotation. The other constraints listed are related to dynamic testing. These include limits on the amount of dynamic motion and the difficulty in obtaining combined dynamic motions such as pitching and plunging. Also, it is often difficult to provide a dynamic motion about the correct center of gravity location for some vehicle configurations.

- Classical support interference (Bibliography-TM 81909)
    - Altered model geometry
    - Distorted flow
    - Increases with tunnel pressure
    - Increases with aircraft sophistication
- Support related restraints
    - Limited static motion (x, y, z, α, β, Φ)
    - Limited dynamic motion (u, v, w, p, q, r; amplitudes)
    - Difficult to obtain combined motions
    - Difficult to obtain desired c. g. locations

EXAMPLES OF SOME MODEL SUPPORT PROBLEMS

This figure contains three typical examples of problems resulting from model support interference which have been encountered in tests in Langley wind tunnels. In the upper left of this figure, the sketch shows the true lines of the fighter-type aircraft with solid lines. The sting and the enlarged afterbody of the model required for the sting are shown as dashed lines. As indicated by the plot, the afterbody drag at transonic speeds, which accounts for a high percentage of the total drag, was found to be in error by about eighteen percent.

The sketch in the upper right portion of the figure illustrates a transport model mounted on a centerline sting. The proximity of the sting to the horizontal tail surfaces changed the flow pattern enough to give incorrect values of pitching moment versus tail incidence angle as shown for a constant angle of attack.

The two sketches at the bottom of the figure show how the boattailed rear fuselage of a model was enlarged to accommodate a sting for forced-oscillation dynamic stability tests. The measured damping in yaw at transonic speeds was found to be incorrect and even to have the wrong sign over part of the angle-of-attack range. This was caused by the proximity of the enlarged rear fuselage to the horizontal tail surfaces. Modifications had to be made to the model and the test program had to be repeated in a different facility with a smaller sting.

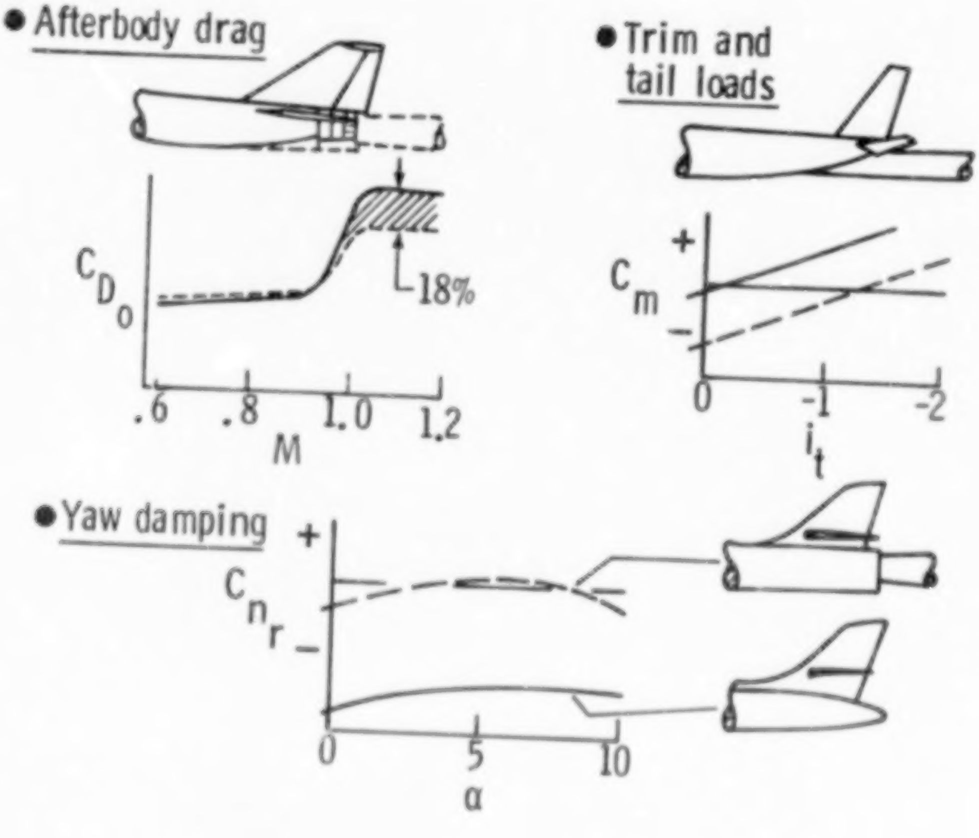

SOLUTION FOR SUPPORT INTERFERENCE

Magnetic suspension of the model is seen to be the only viable solution for three-dimensional testing of aircraft models in order to eliminate completely problems with model support interference. The concept was first demonstrated with a working system by the French in 1957. NASA Langley has been actively studying and sponsoring research on magnetic suspension ever since the publication of the original French technical paper. Abstracts of the known work published relative to Magnetic Suspension and Balance Systems (MSBS) for use in wind tunnels are contained in a 1983 bibliography (ref. 2). The report contains over 200 abstracts and is cross-indexed by subject, author, and corporate source. Reference 3 is an excellent summary of more recent developments.

Four MSBSs are known to be currently active and two out of the four are located here at this Center. One is the 13-inch system which has been on loan to NASA since 1979 from the U.S.A.F. Arnold Engineering Development Center (AEDC). It is the largest MSBS constructed to date, although the French have a system that is only slightly smaller, but not currently active. The 13-inch system was first operated in about 1965 and was later used with a hypersonic wind tunnel at AEDC. This system has been updated recently with a digital controller and an electro-optical position sensor system. The other MSBS, which is now operational at Langley, is the 6-inch system which was constructed by personnel of the MIT Aerophysics Laboratory under sponsorship of NASA and DOD. This system was first operated in 1969. Two unique features of this system are the sophisticated arrangement of the electromagnets and the Electromagnetic Position Sensor which operates as a differential transformer to sense model position. This system was acquired from MIT in 1982 when the Aerophysics Laboratory was closed and the system was just put back into operation here at Langley last year.

The other two MSBSs known to be active are located in England. The 7-inch system at the University of Southampton has been operational in various forms since 1964. Langley has partially supported the magnetic suspension work at Southampton since 1979 by means of a research grant. At the present time, this system is the most technically advanced in terms of capabilities such as an available angle-of-attack range of about sixty degrees. The 3-inch MSBS at Oxford University was recently being utilized to measure non-adiabatic wall effects on the drag of slender cone configurations at hypersonic speeds.

Since all of these MSBSs are relatively small, our research is directed towards the development and demonstration of the technology required for larger MSBS of a practical size for aerodynamic testing.

- Magnetic Suspension of the model is the only solution for 3-D testing
- Several small tunnels have operational MSBS
  - MSBS bibliography (TM 84661 - July 1983)
  - Four are active
    - 13 inch NASA/AEDC
    - 6 inch NASA/MIT
    - 7 inch University of Southampton
    - 3 inch Oxford University

AREAS OF ACTIVE RESEARCH

The areas of research currently being investigated in order to extend the usefulness of Magnetic Suspension and Balance Systems (MSBS) to larger sizes for wind tunnel applications are listed in the accompanying figure. A digital controller has been in operation with the Southampton 7-inch MSBS for several years and one was more recently put into operation with the 13-inch system here at Langley. However, the full potential of a digital controller must be further developed by optimizing the control algorithms. An ideal controller would be self-adaptive and, for example, would independently vary the loop gains with changes in model angle of attack and changes in test conditions.

Although many types of model position sensors have been developed, the "perfect" position sensor has not yet been devised. Also, it appears that for a fail-safe suspension system, redundant position sensing systems will be a necessity.

The areas of MSBS coil configuration design and the application of superconducting technology go hand-in-hand as any system for a test section larger than about two feet in diameter will of necessity have to use superconducting electromagnets. A 6-inch MSBS that used superconducting magnets was built and first operated in 1972 at the University of Virginia with Langley sponsorship. Superconducting electromagnets do have to be immersed in containers of liquid helium and kept at extremely low temperatures to maintain the operating state of essentially zero electrical resistance. In recent years, the use of superconducting electromagnets in such fields as high-energy physics research and in fusion research has matured this technology to the point where superconducting cable can be purchased "off-the-shelf."

The other areas listed on the figure as calibration, internal strain-gage balance, data accuracy, and data telemetry all fall into the very important category of items that must be well understood in order extract useful aerodynamic information from a magnetically suspended model. The concept of using a strain-gage balance inside the model both for load calibration and for the measurement of aerodynamic forces and moments was originated by Langley personnel. Frequency modulation telemetry has been used in the past, primarily by the French, but a new multichannel telemetry system being developed in-house will use an infrared light beam for data transmission.

- Digital controller
- Position sensing
- Coil configurations
- Application of superconducting technology
- Calibration
- Internal strain-gage balance
- Data accuracy
- Data telemetry

IN-HOUSE MSBS STATUS - APRIL 1985

The 13-inch NASA/AEDC system is currently being operated with a subsonic wind tunnel capable of about 0.5 Mach number. The system now has a digital controller in place of the original analog control system. Feedback control of the power amplifiers supplying the electromagnets must be used in all magnetic suspension systems in order to stabilize the model position. The X-ray position sensor originally developed by AEDC for the 13-inch system to fill a specific need has been replaced by an electro-optical system developed by the Langley Instrument Research Division that uses a small laser as the light source and self-scanning photodiode arrays as the sensing element. At the present time, the 13-inch system is being readied for load calibration. One method of doing this will be discussed in more detail later in the paper. As previously mentioned, there is also work in progress on the development of a telemetry system that will be used to transmit pressure and other data from a magnetically suspended model. Later this year, aerodynamic measurements will be made on the models listed in the figure. These tests will enable us to gain some practical testing experience with the system.

The 6-inch NASA/MIT system has been put back into operation complete with the subsonic tunnel that was built for the system at MIT. The Electromagnetic Position Sensor (EPS) which MIT originally developed for use with this system is a unique device. It operates as a differential transformer and is used to sense model position and attitude within the test section volume. The position and attitude information is required by the feedback control system and, of course, is also used for data reduction of the measured forces and moments. The Instrument Research Division is currently doing a complete calibration of the EPS to determine system accuracy, sensitivity, and repeatability. The EPS is a possible candidate for use in larger size suspension systems and an analysis is being made to determine if there are any inherent problems in scaling-up the EPS concept.

Model forces and moments in a MSBS are normally determined after suitable calibration from measurements of the current in each of the suspension electromagnets. An evaluation will be made of the practical data accuracy of both the 13-inch and the 6-inch systems. As previously mentioned, work is underway in developing alternate techniques of measuring model position and model loads.

13-inch NASA/AEDC MSBS and subsonic wind tunnel

- System operational with digital controller
- Work in progress
  - System calibration
  - Telemetry development
- Aerodynamic measurements planned
  - Ogive-nose cylinder
  - Delta-wing model
  - Space shuttle orbiter

6-inch NASA/MIT MSBS and subsonic wind tunnel

- Operational with Electromagnetic Position Sensor
- Evaluate practical MSBS data accuracy
- Develop alternate position and force measuring techniques

13-INCH NASA/AEDC MSBS

A sketch of the 13-inch system is shown in this figure. This system has the four lift electromagnets arranged in a "V" configuration. These four magnets provide the lift force, pitching moment, side force, and yawing moments. The drag solenoid provides the drag force. The test section for the subsonic wind tunnel is not shown in this sketch, but it passes through the drag solenoid. The model contains an iron core which, for a typical model, is normally about one inch in diameter and 6 inches long. The iron core is magnetized by the applied magnetic fields. The 13-inch MSBS has a lift force capability of a few pounds depending on the size of the iron core in the model.

The test section walls are made of clear plastic and the cross-section is a modified octagon that measures about 10.5 inches by 12.5 inches. The model position sensing system is made up of beams of light from three small lasers which, with the aid of suitable lenses and mirrors, are projected across the test section onto self-scanning photodiode arrays as illustrated in the sketch. The size of the light sheet incident on the photodiode arrays is dependent on the model position within the light sheet and the size of the shadow cast by the model.

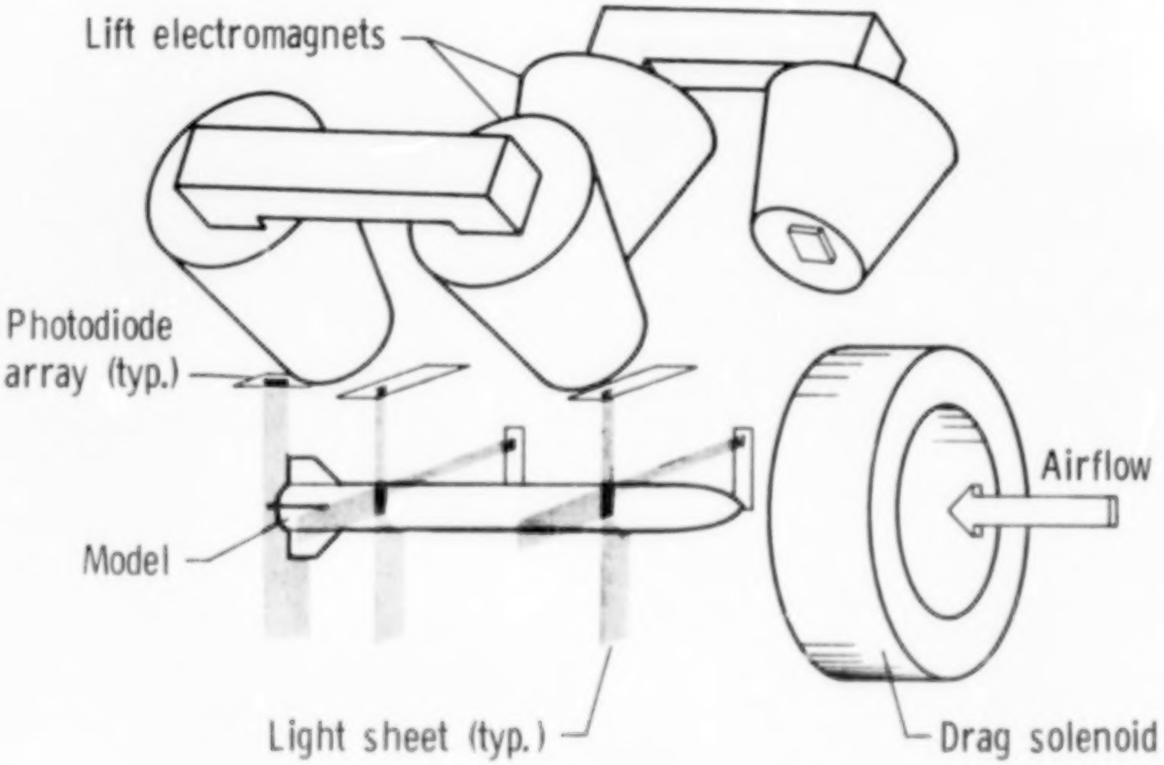

6-INCH NASA/MIT MSBS

This figure is a line drawing of the 6-inch MSBS which was acquired from MIT when the Aerophysics Laboratory was closed. The magnetic coils are contained within the cube-shaped housing which, for purposes of putting scale to the drawing, has a height of about 6 feet. The complete assembly including the subsonic tunnel is about thirty-five feet in length. Air is drawn into the tunnel bell-mouth through the test section and exhausts around the base of the blower back into the room. The associated power supplies and instrumentation racks are not shown in the drawing.

The electromagnets, which are water-cooled, are positioned around the outside of the volume containing the test section and the Electromagnetic Position Sensor (EPS) coils. Model viewing access is available through the sides of the coil housing. The EPS consists of an assembly of coils of fine wire, located immediately outside the walls of the clear plastic test section, and associated electronics. Magnetically soft iron is used for the model core and a pair of coils are dedicated to magnetizing the core.

One of the last series of aerodynamic tests at MIT involved combined spinning and coning motions of some projectile shapes.

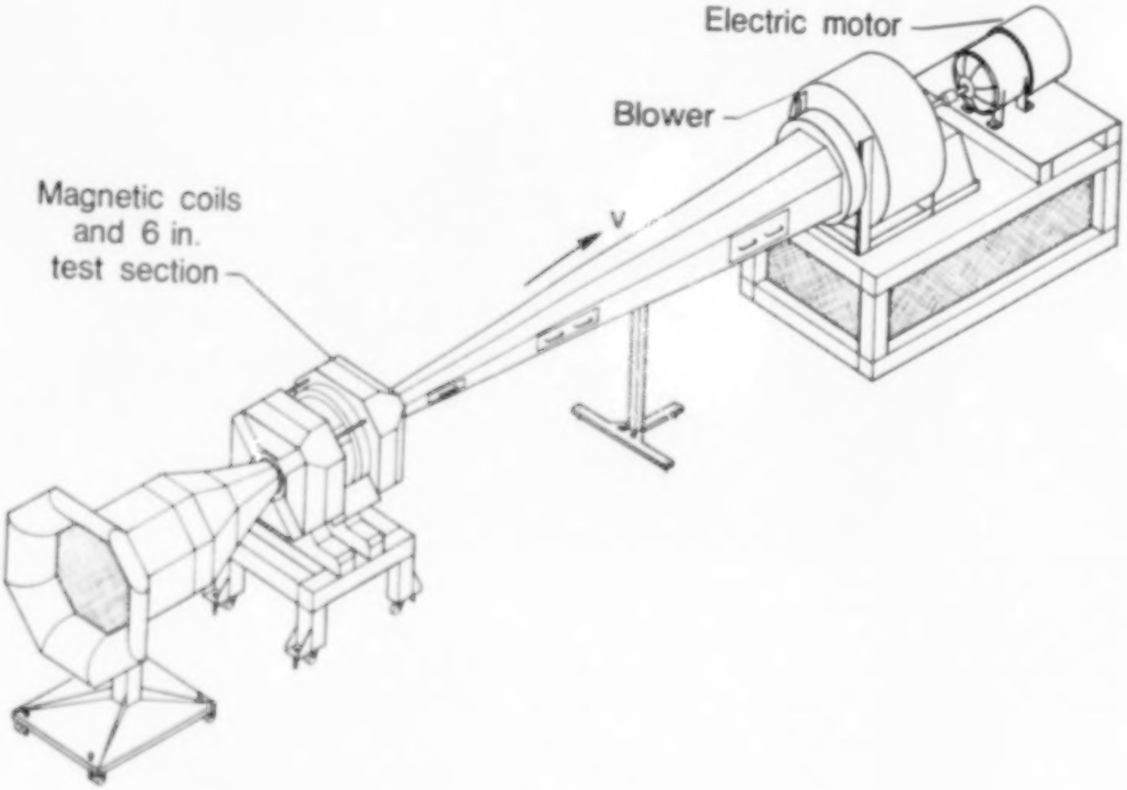

MSBS CALIBRATION MODEL

Force and moment data from a magnetic suspension and balance system have always been obtained in the past from measurements of the currents in the electromagnets. Accurate data can be obtained in this way, but it involves a tedious calibration process with each model core. Absolute model position must be maintained and model rotation in the pitch or yaw plane complicates the calibration process. To overcome some of these problems, personnel in the Langley Instrument Research Division have originated a concept of using an electrical resistance strain-gage balance to calibrate a magnetic suspension system. As illustrated in the sketch, the concept uses a strain-gage balance located between the iron core, which supports the assembly by the action of the magnetic fields, and the calibration fixture. Any load applied to the fixture is sensed by the strain-gage balance which has been calibrated previously using standard procedures for such balances. Initial tests in the 13-inch MSBS using hardware similar to that shown in the sketch were promising. Additional tests with strain-gage balances especially constructed with the correct size and load range are planned for both the 6-inch and the 13-inch MSBS.

Although this concept was originally devised just for wind-off calibration, it was later realized that the same concept can be used for aerodynamic data measurement if the calibration fixture in the sketch is replaced by an aerodynamic model. The internal strain-gage balance then can measure the resultant aerodynamic loads after the tare or weight loads are subtracted from the total loads. A telemetry system for transmitting the strain-gage balance data from the suspended model is being developed in order to demonstrate this capability. A similar strain-gage technique could also be used to measure loads on individual components such as on a wing or a canard.

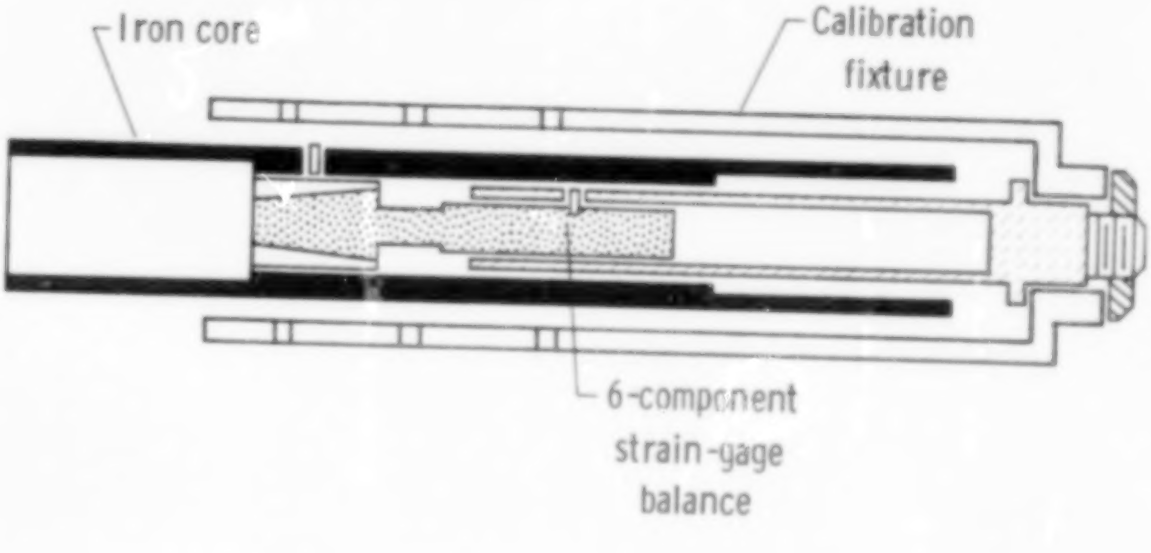

FEASIBILITY STUDY

A study has been made by Madison Magnetics, Inc., under a contract from Langley to investigate the application of advanced concepts in superconducting technology to the design of a MSBS that would be compatible with a large transonic wind tunnel. For the purposes of the study, the specifications for the tunnel were arbitrarily set at an 8-foot by 8-foot test section operating at a Mach number of 0.9 and a stagnation pressure of one atmosphere. The model size and model loads were based on a highly maneuverable fighter design as this class of aircraft had been found to be a more difficult design problem when compared to other types of aircraft because of internal volume and load considerations. The required model angular displacement was ±30 degrees in pitch, ±10 degrees in yaw, and ±20 degrees in roll. Similar specifications were used in an earlier feasibility study in reference 4 by the General Electric Company, but that study was restricted to off-the-shelf equipment and technology.

The concept that had the most impact on the results of the Madison Magnetics study was the replacement of the usual iron core in the model with an isolated persistent superconducting solenoid. This concept was demonstrated at a small scale by researchers at the University of Southampton. The use of a superconducting core rather than an iron or permanent magnet core results in a larger magnetic moment in the model for an 8-foot size facility so that for the same loads the exterior electromagnets can be made smaller.

The most important conclusions from this study were that the combination of a compact model core superconducting solenoid and a unique coil arrangement was feasible and did meet the design requirements. The cost estimate for the construction of this system, not including the wind tunnel, was about $30 million.

This study has been published as reference 5. Further work by Madison Magnetics in refining and optimizing the design is underway.

- Application of advanced concepts
- Design and cost study
    - 8 ft × 8 ft test section
    - Mach = 0.9
    - Fighter-type model
- Conclusions
    - Design is feasible
    - Cost estimate about $ 30 million
- Further study under way

USEFULNESS STUDY

Sverdrup Technology, Inc., has made a study (ref. 6) for Langley which involved surveying the U.S. aerospace industry to determine if, in their opinion, current and future aerodynamic test requirements are sufficient to justify continued work by NASA on magnetic suspension systems for wind tunnels. In essence, the basic question revolved around the potential usefulness to the aerospace industry of a large tunnel fitted with a MSBS.

The approach taken was for the contractor to prepare a written description of the background and the capabilities of MSBS along with an appropriate questionnaire. This material was distributed to individuals in the industry. After the questionnaires were returned, follow-up visits were made for further discussion of all the material. A draft of the final report was prepared following evaluation and analysis of the results.

In summary, there was universal endorsement by the respondents for NASA to continue with its MSBS development program. The aircraft manufacturers, in general, were more enthusiastic than were the missile manufacturers. There was some concern expressed about facility cost and facility availability if only a single facility were to be constructed. A preference was noted for a large transonic MSBS facility as opposed to a midsized transonic, a midsized supersonic, or a large low-speed facility.

- Objective-survey U. S. aerospace industry
- Approach
  - Prepare description and capabilities
  - Distribute questionnaire
  - Follow-up visit and interview
  - Evaluate results
- Conclusions
  - Positive response for continued MSBS research
  - Some concern about facility cost and availability
  - Preference for large transonic MSBS facility
- Status
  - Draft of final report submitted

RESEARCH GRANT

The University of Southampton in England has been very active and productive in magnetic suspension research for many years. The work has been partially supported since 1979 by a NASA research grant to investigate the technology required for large systems. The 7-inch MSBS at Southampton has been operational in several configurations since 1964. The latest configuration has full digital control of the model through a minicomputer in all six degrees of freedom. The bipolar power supplies used with the electromagnets in the 7-inch system are the type that were developed for commercial use with numerically controlled machinery. The symmetrical coil configuration, along with the digital controller and the bipolar power supplies, has allowed the researchers at Southampton to demonstrate a model pitch angle of 60 degrees. This extreme angle of attack capability was shown in a videotape at the conclusion of the presentation. Theoretical computations have not shown any restrictions on an unlimited attitude capability.

As mentioned previously, the concept of the superconducting model core has been demonstrated at Southampton with a working version that met the design requirement of a 30 minute "flying" time. The superconducting model core shows great promise of lowering the cost of large systems by providing a larger magnetic moment in the model than would be possible with a conventional iron core.

- 7-inch MSBS
- Concepts studied and demonstrated
    - Digital controls
    - Bi-polar power supplies
    - Symmetrical coil configuration
    - High angle of attack capability
    - Superconducting model core

CONCLUSIONS

Support interference is the basic problem that arises from the use of mechanical model supports in wind tunnels. Magnetic suspension of the model is the only viable solution for three-dimensional testing of aircraft models in order to eliminate completely model support interference. All of the basic technology for a large Magnetic Suspension and Balance System (MSBS) has been demonstrated at small scale and design studies have shown that a large MSBS is feasible. A survey of the U.S. aerospace industry has shown a positive response for NASA to continue with its MSBS development program. Work is progressing on preliminary engineering designs for a large MSBS and the cost estimates for a large MSBS appear to be reasonable.

- Support interference is a problem
- Magnetic suspension only solution for 3-D testing
- Basic technology has been demonstrated at small scale
- Large MSBS feasible
- Positive industry response for continued MSBS development
- Work progressing on engineering design for large MSBS
- Cost estimates for large MSBS appear reasonable

REFERENCES

1. Tuttle, Marie H.; and Gloss, Blair B.: Support Interference Wind Tunnel Models - A Selective Annotated Bibliography. NASA TM-81909, 1981.

2. Tuttle, Marie H.; Kilgore, Robert A., and Boyden, Richmond P.: Magnetic Suspension and Balance Systems - A Selected, Annotated Bibliography. NASA TM-84661, 1983.

3. Britcher, C. P.: Progress Towards Magnetic Suspension and Balance Systems for Large Wind Tunnels. Journal of Aircraft, vol. 22, no. 4, April 1985, pp. 264-269.

4. Bloom, H. L.; et al: Design Concepts and Cost Studies for Magnetic Suspension and Balance Systems. NASA CR-165917, 1982.

5. Boom, R. W.; Eyssa, Y. M.; McIntosh, G. E.; and Abdelsalam, M. K.: Magnetic Suspension and Balance System Study. NASA CR-3802, 1984.

6. Martindale, W. R.; Butler, R. W.; and Starr, R. F.: Study on Needs for a Magnetic Suspension System Operating with a Transonic Wind Tunnel. NASA CR-3900, 1985.

D14

N88-14940

S14-02

117238

32P.

FLOW DIAGNOSTICS AND VISUALIZATION IN WIND TUNNELS AND FLIGHT

P. C. Stainback, C. B. Johnson, B. J. Holmes, C. J. Obara,* D. Carraway, **
J. F. Meyers, S. P. Wilkinson, W. C. Honaker, P. L. Lawing, R. R. Antcliff,***
O. Jarrett, Jr., R. C. Rogers, and J. P. Stack
NASA Langley Research Center
Hampton, Virginia

*Kentron International, Inc.
Hampton, Virginia

**Old Dominion University
Norfolk, Virginia

***SRI
Hampton, Virginia

PRECEDING PAGE BLANK NOT FILMED

C-4

PAGE 278 INTENTIONALLY BLANK

[redacted]

FLOW DIAGNOSTIC AND VISUALIZATION IN WIND TUNNELS AND FLIGHT

Personnel at the Langley Research Center are conducting research on a variety of flow diagnostic instruments and flow visualization techniques. The figure indicates some of the instruments and techniques being developed and the researchers involved. If additional information is desired on a given subject, the personnel noted should be contacted.

- Conventional testing techniques

Hot wire anemometry

P.C. Stainback
C.B. Johnson

Hot film anemometry

B.J. Holmes
C.J. Obara
D.L. Carraway
J.P. Stack

- Non-intrusive testing techniques

Laser velocimeter (LV)

J.F. Meyers
S.P. Wilkinson

Laser transit anemometer (LTA)

W.C. Honaker
P.L. Lawing

Coherent anti-stokes Raman scattering (CARS)

R.R. Antcliff
O. Jarrett, Jr.
R.C. Rogers

- Flow visualization

Sublimating chemicals

B.J. Holmes
C.J. Obara

FLOW REGIMES FOR HOT-WIRE ANEMOMETRY

At the present time, flow diagnostic work in hot-wire anemometry is being conducted in three flow regimes, namely, incompressible subsonic; compressible subsonic, transonic, and low supersonic (noted hereafter as transonic); and high supersonic and hypersonic (noted hereafter as supersonic) flow regimes. In the incompressible subsonic flow regime, multi-wire probes are used to measure the three components of the fluctuating velocity and total temperature fluctuations. In the transonic flow regime, the longitudinal velocity, density, and total temperature fluctuations are being measured. In the supersonic flow regime, the mass flow and total temperature fluctuations are measured, and for wind tunnel test section disturbances, pressure fluctuations can be computed from these results.

- Subsonic flows - $\tilde{u}$, $\tilde{v}$, $\tilde{w}$, $\tilde{T}_0$
- Transonic flows - $\tilde{u}$, $\tilde{\rho}$, $\tilde{T}_0$
- Supersonic flows - $\tilde{m}$, $\tilde{T}_0$

DATA ANALYSIS TECHNIQUES FOR HOT-WIRE ANEMOMETRY

Much of the hot wire data obtained at Langley is obtained using digital signal analysis techniques since these techniques are much more powerful than analog ones. For example, quantities can be obtained using digital techniques that would be impossible or impractical to obtain using analog methods.

Conditional sampling techniques are used when data are to be taken only when some predetermined condition is satisfied. Using this technique, detail fluctuating quantities can be measured which would otherwise be obscured by other fluctuations in the flow.

There are cases where assumptions have been made for hot-wire anemometry in order to make measurements in the transonic flow regime. Efforts are under way to determine possible errors introduced into the results using these assumptions.

When the signal-to-noise ratios are low, particularly in low disturbance facilities, methods have been devised in an attempt to separate the signal of interest from the noise.

- Digital signal analysis
- Conditional sampling
- Error analysis
- Correction procedures for electronic noise

SCHEMATIC OF 0.3-METER TRANSONIC CRYOGENIC TUNNEL

Hot-wire measurements were made in the 0.3-Meter Transonic Cryogenic Tunnel. This facility is a closed-circuit wind tunnel driven by an axial flow fan. Cryogenic conditions are obtained by injecting liquid nitrogen into the circuit just downstream of the test section. The excess mass is removed from the circuit through an exhaust system located just upstream from the settling chamber. The tunnel operates over a Mach number range from about 0.1 to 0.9, a total pressure range from about 20 to 90 psi and a total temperature range from about 100 to 320 K.

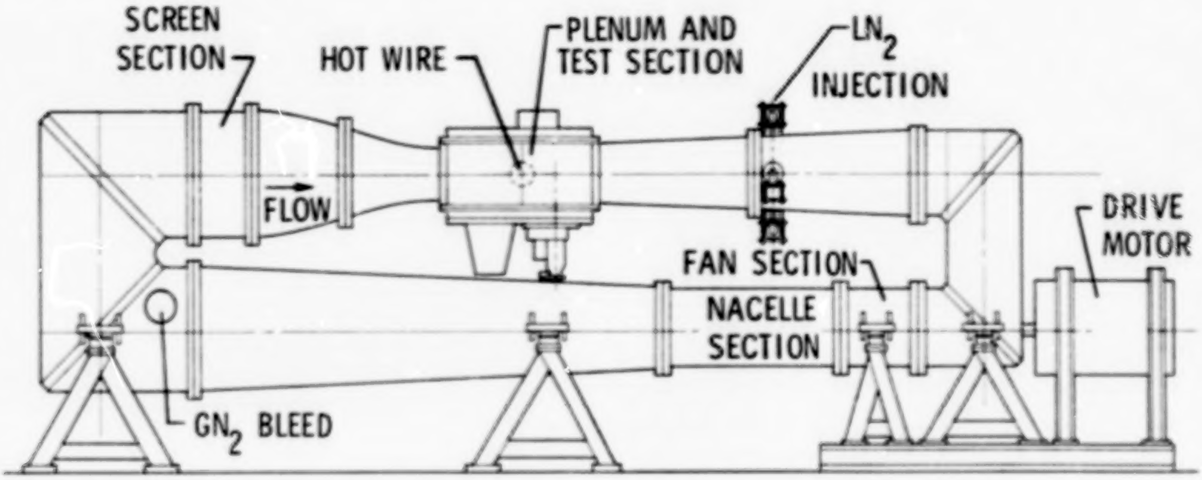
SCREEN SECTION
HOT WIRE
PLENUM AND TEST SECTION
LN_2 INJECTION
FLOW
DRIVE MOTOR
FAN SECTION
NACELLE SECTION
GN_2 BLEED

VELOCITY FLUCTUATIONS MEASURED IN THE TEST SECTION OF THE 0.3-METER TRANSONIC CRYOGENIC TUNNEL

Hot-wire measurements were made in the 0.3-Meter Transonic Cryogenic Tunnel using a three wire hot wire probe and using digital analysis techniques to reduce the data. This technique has made it possible to separate the three coexisting fluctuations of velocity, density, and total temperature. The velocity fluctuations increased with both increased velocity and density and the levels were high at the higher velocities and densities - ranging up to four percent.

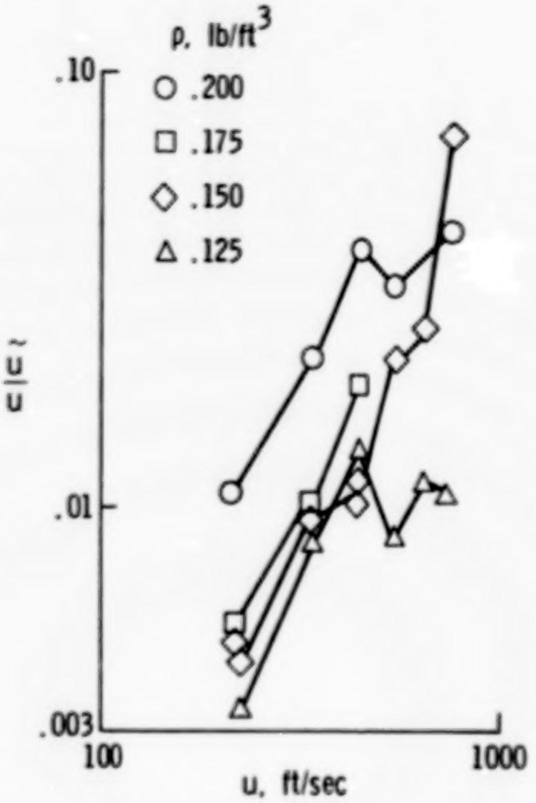

DENSITY FLUCTUATIONS MEASURED IN THE TEST SECTION OF THE 0.3-M TRANSONIC CRYOGENIC TUNNEL

The density fluctuations also increased with increasing velocity and density and had a variation and level very similar to those measured for the velocity fluctuations.

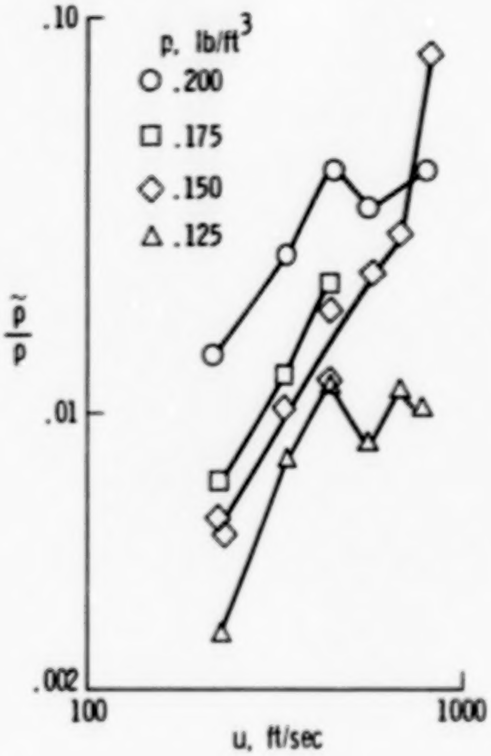

TOTAL TEMPERATURE FLUCTUATIONS MEASURED IN THE TEST SECTION OF THE 0.3-METER TRANSONIC CRYOGENIC TUNNEL

In general, the total temperature fluctuations also increased with increasing velocity and density; however, the levels of the total temperature fluctuations were about an order of magnitude lower than the velocity and density fluctuations. The total temperature fluctuations ranged from about .05 to 0.3 percent.

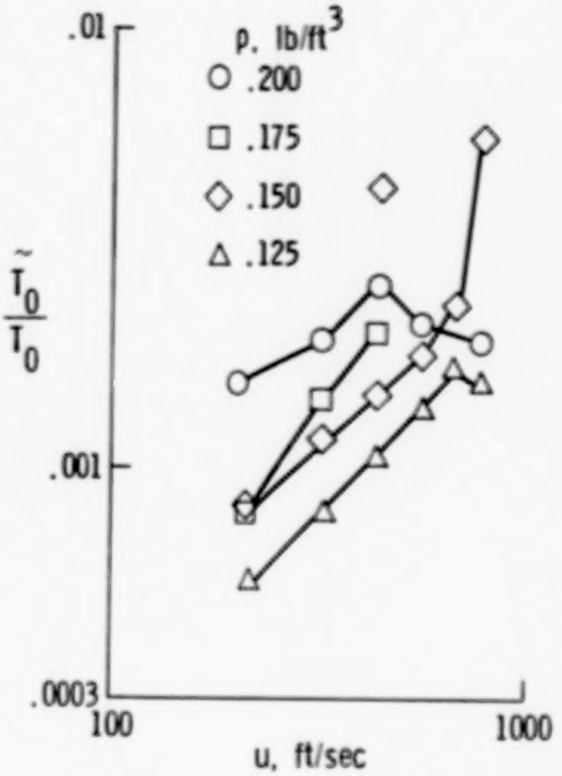

TESTING TECHNIQUES FOR HOT FILM ANEMOMETRY

Hot film anemometry is a very versatile technique and hot film anemometry has been applied to several fluid dynamic problems. Special probes have been procured to apply the three wire hot-wire technique to hot film anemometry. The probes have not been tested to date.

The hot film technique has been used extensively to detect boundary layer transition and the degree of intermittency in the transition region.

Hot films have been developed into a flow reversal measuring device to obtain data on the location of boundary separation and re-attachment.

If a hot film is properly sized and calibrated, shear stresses can be measured over the flow conditions for which the film is calibrated.

Finally, the hot film technique has also been developed into a cross flow vorticity measuring device. This device will measure the spacing of crossflow vortices, give some indication of the local velocity, and indicate when the vortices cause the laminar boundary to break down into a turbulent one.

- Fluctuating fluid quantities
- Transition detection
- Flow reversal
- Shear stress measurements
- Cross flow vorticity

MULTI-ELEMENT HOT-FILM TRANSITION SENSOR

The accurate measurement of the location where a laminar boundary layer breaks down to a turbulent one serves many purposes. In basic research and in developmental testing, this information is needed for validation of theory and design. For example, a complete understanding of performance and stability and control of a laminar flow airplane requires knowledge of transition locations on wing surfaces, empennage surfaces, fuselage, and nacelles.

One very useful device for large-scale wind tunnel and flight applications is the thin, surface-mounted hot-film gage. Hot films indicate transition responding to the different heat transfers in laminar versus turbulent flow. The advantages of these gages relate to installation flexibility and durability. Since the gages and associated wiring are entirely surface mounted, they may be used on test surfaces which do not permit through-the-surface types of instrumentation. Installed gage thicknesses will not be large enough to cause transition for testing at sufficiently large model scales.

The continuous multi-element hot-film transition gage has been developed by integrating the required number and distribution of hot-film sensing elements into a long, continuous thin sheet. Transition data acquisitions are accomplished using an electronic switching system which allows rapid switching of all sensing elements into the data recording system.

The continuous thin sheet of a particular length covers the area of interest for transition measurements beginning at the leading edge and continuing to downstream of the transition region. For example, on an airplane wing of 10-foot chord length, the gage may be as much as seven to eight feet in length. The leading edge of a gage mounted on the upper surface of a wing would wrap around, beneath, and downstream of the wing leading edge. In this fashion, no disturbance from the film leading edge will cause turbulent wedges to disturb the hot-film sensors in the transition region. For situations where the lateral edges could cause transition, the edges may be filled and faired to correct this difficulty.

The multi-element gages are planned for use on both the NASA Lear 28/29 viscous drag reduction flight experiments and the NASA OV-1 natural-laminar-flow engine nacelle flight experiments.

ORIGINAL PAGE IS
OF POOR QUALITY

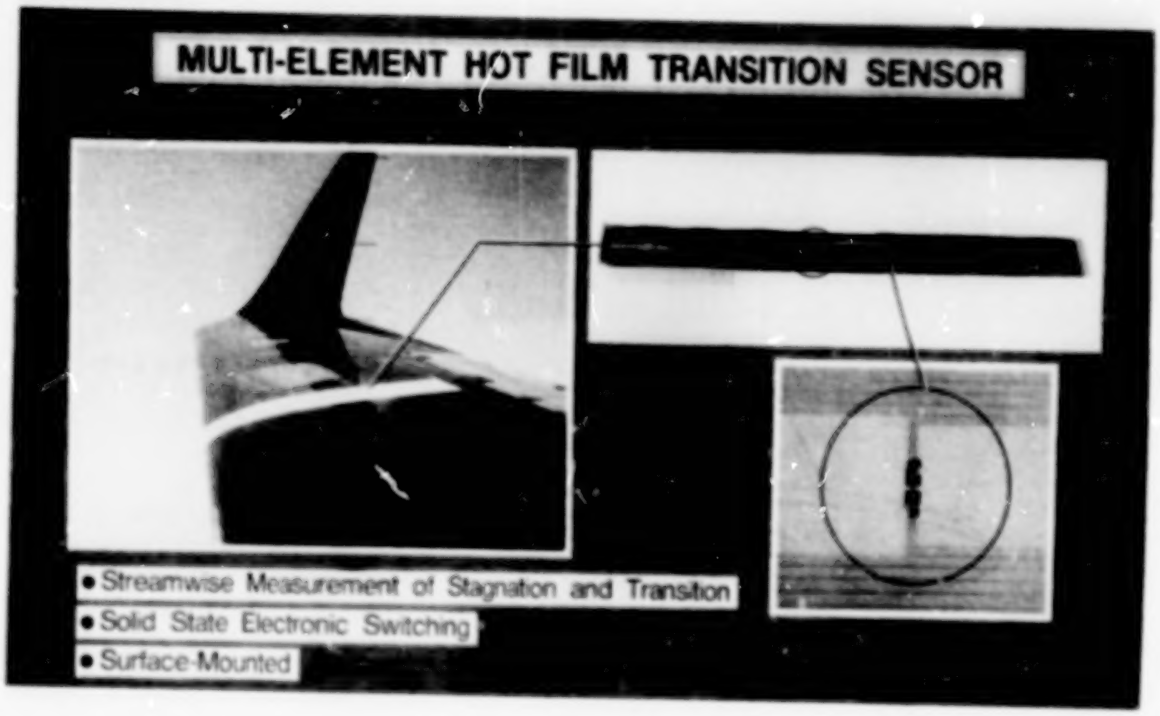

MULTI-ELEMENT HOT FILM TRANSITION SENSOR

- Streamwise Measurement of Stagnation and Transition
- Solid State Electronic Switching
- Surface-Mounted

LAMINAR AND TURBULENT FLOW INDICATED BY HOT FILMS

Near the leading edge of an airfoil where the boundary layer is laminar, the output from the hot film is very low. As the flow progresses along the wing, the Tollmien-Schlichting waves break down into localized turbulent bursts. These bursts produce a positive voltage spike in the output from the anemometer. Farther down the airfoil, the rate of turbulent bursts increases until the flow is approximately fifty percent laminar and fifty percent turbulent. After this, the flow becomes almost completely turbulent with an occasional laminar burst. Finally, the boundary layer becomes completely turbulent.

The "beginning" and "end" of boundary layer transition can be determined from RMS values of the output signal from the anemometer where the minimum RMS value represents the beginning of transitions and the maximum value represents the end of the transition process.

The degree of turbulent intermittency can be obtained through the transition process by measuring the rate of occurrence of turbulent bursts.

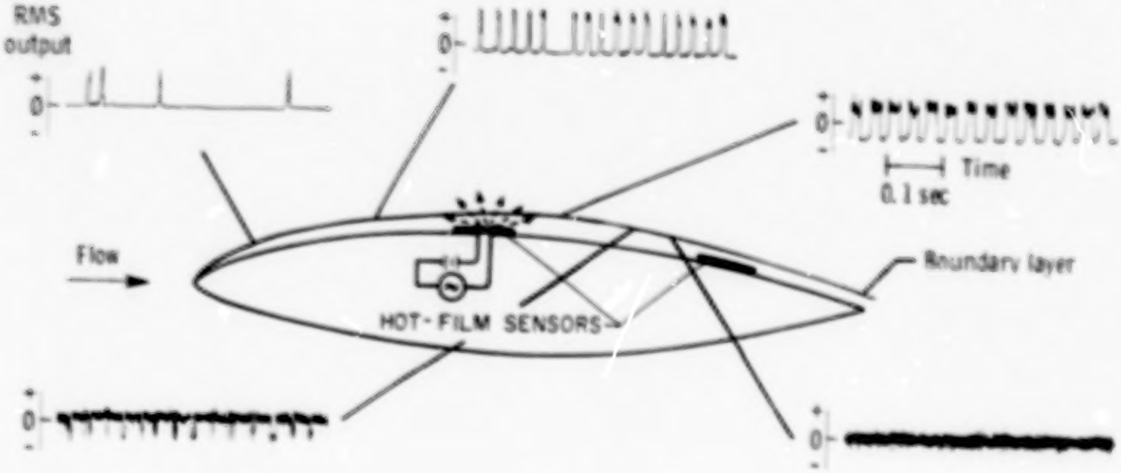

LAMINAR BOUNDARY LAYER SEPARATION SENSOR

The laminar boundary layer separation sensor (BLS sensor), used to detect flow separation and flow reversal, consists of a flush array of three parallel thin films. The center film is electronically heated by a constant temperature anemometer (CTA). The outer films are incorporated into two legs of a bridge for use as resistance thermometers. When the sensor is exposed to airflow, heat is transferred from the center film to either the upstream or downstream film, depending on the direction of the flow. The change in temperature (according to the change in resistance) of the upstream or downstream films is measured by the bridge and differenced by a differential amplifier to determine the direction of the flow, and hence, separation.

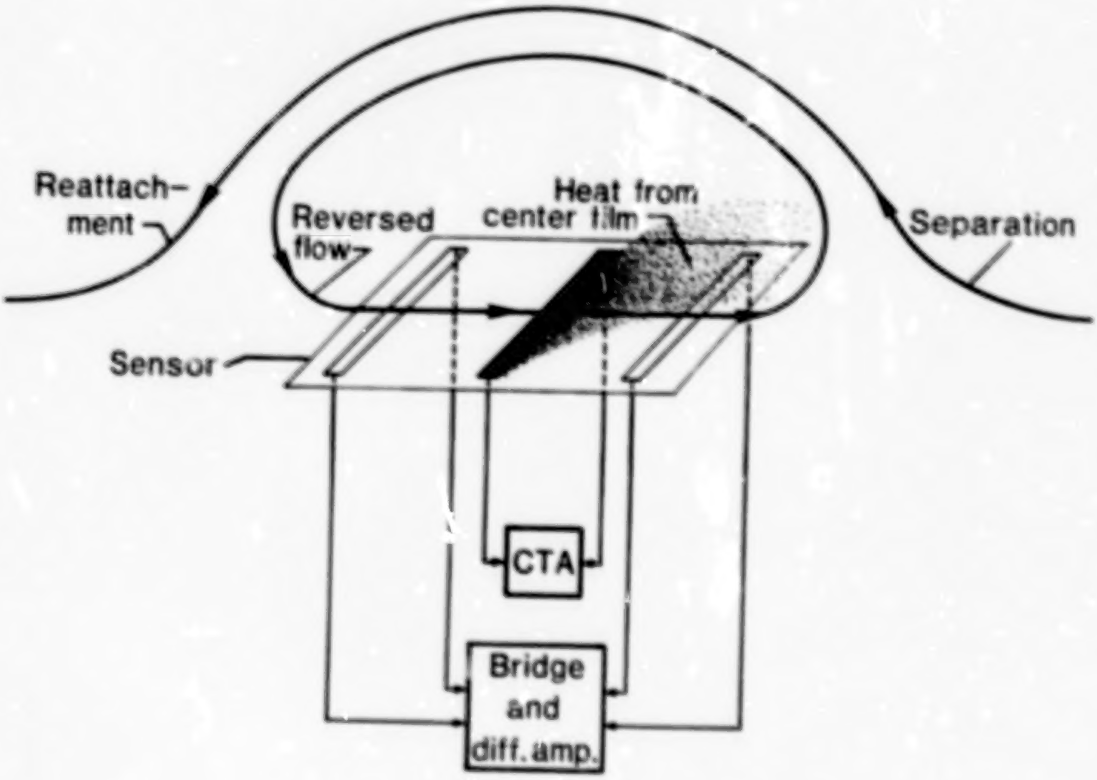
Reattach-
ment
Reversed
flow
Heat from
center film
Separation
Sensor
CTA
Bridge
and
diff. amp.

ORIGINAL PAGE IS
OF POOR QUALITY

BOUNDARY LAYER MEASUREMENTS OBTAINED WITH A BOUNDARY LAYER SEPARATION SENSOR

A preliminary test of the sensor was conducted in the Instrument Research Division's (IRD) small calibration tunnel on a laminar-flow airfoil model. A flow visualization made at 100 m.p.h. indicated the existence and location of a laminar separation bubble, characterized by flow separation, reversal, and reattachment. Subsequent tests were run over a range of tunnel speeds from 45 m.p.h. to 185 m.p.h. with a BLS sensor in the area of the bubble and with other hot-film sensors mounted in various other locations on the model. The results of the tests were favorable. At 45 m.p.h., the polarity of the BLS sensor is positive, indicating reversed flow across the sensor (the presence of a bubble). As the velocity of the tunnel was increased to 185 m.p.h., the polarity of the output changed, indicating the bubble had moved slightly aft of the sensor.

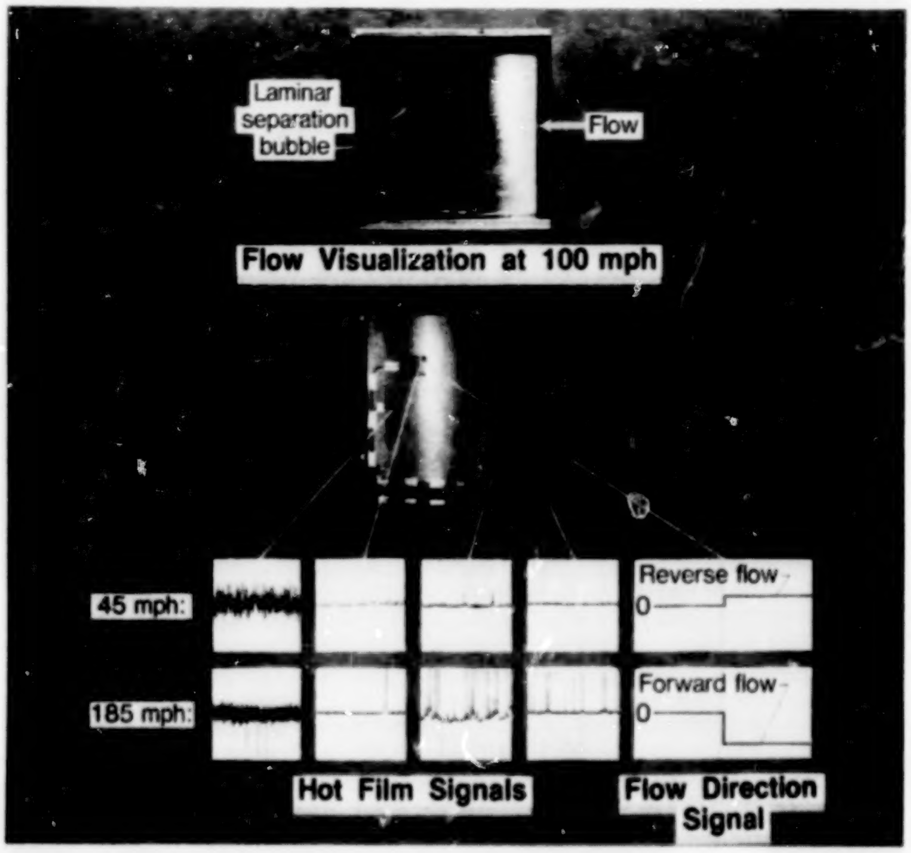

Flow Visualization at 100 mph

Hot Film Signals

Flow Direction Signal

SKIN FRICTION GAGE

A thin film sensor has been calibrated in the Unitary Plan Wind Tunnel at Langley for use in shear stress measurements. A .000127-inch wide by .040-inch long thin film sensor was mounted flush with the tunnel wall in close proximity to a static force-type balance. The heat transfer of the film was measured and compared to shear force data taken simultaneously with the force-type balance.

UPWT Test Setup

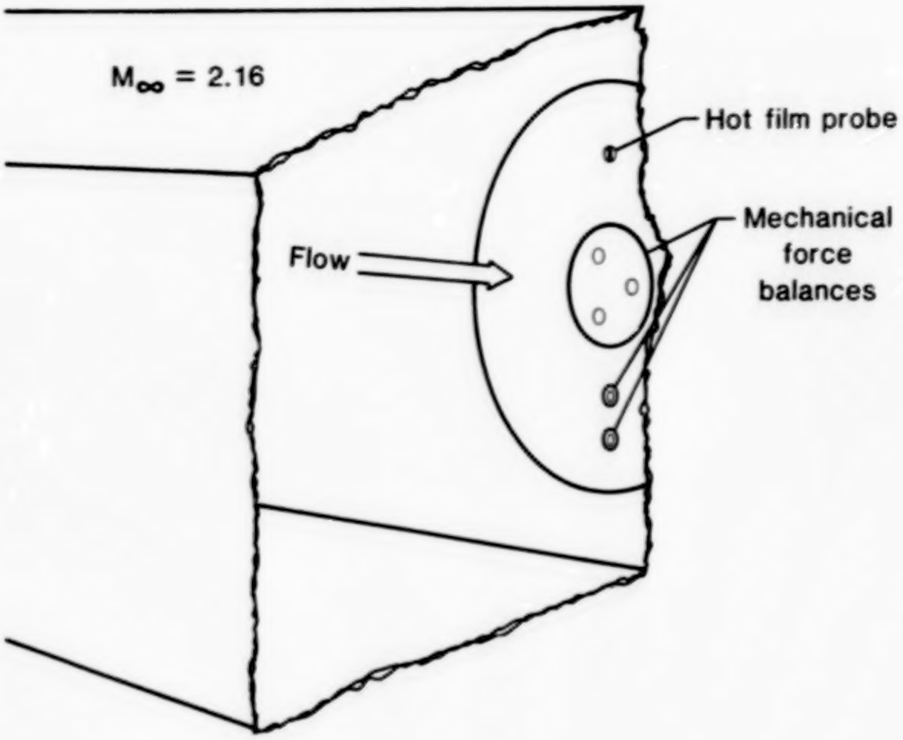
$M_\infty = 2.16$
Hot film probe
Mechanical force balances
Flow

THIN FILM SKIN FRICTION GAGE CALIBRATION

Data were taken at Mach 2.16 over a range of Reynolds numbers from 1 X 10^6 per foot for four different film overheat ratios (film temperatures) from 1.08 to 1.49 (50°C to 180°C).

The results were in good agreement with theoretical analysis for this case which states that the heat transfer of the film is linearly proportional to the cube root of the product of density and shear stress $(\rho\tau)^{1/3}$. The calibration was subsequently repeated, and the worst error in heat transfer for a given shear stress was 0.7 percent.

Some of the current research objectives in this area are:

1. Uniformity between sensors to lessen the amount of calibrations and instrumentation
2. Sensors which can fit various surface contours
3. Sensors for high Reynolds number flow
4. Rugged and reliable sensors for flight and cryogenic applications

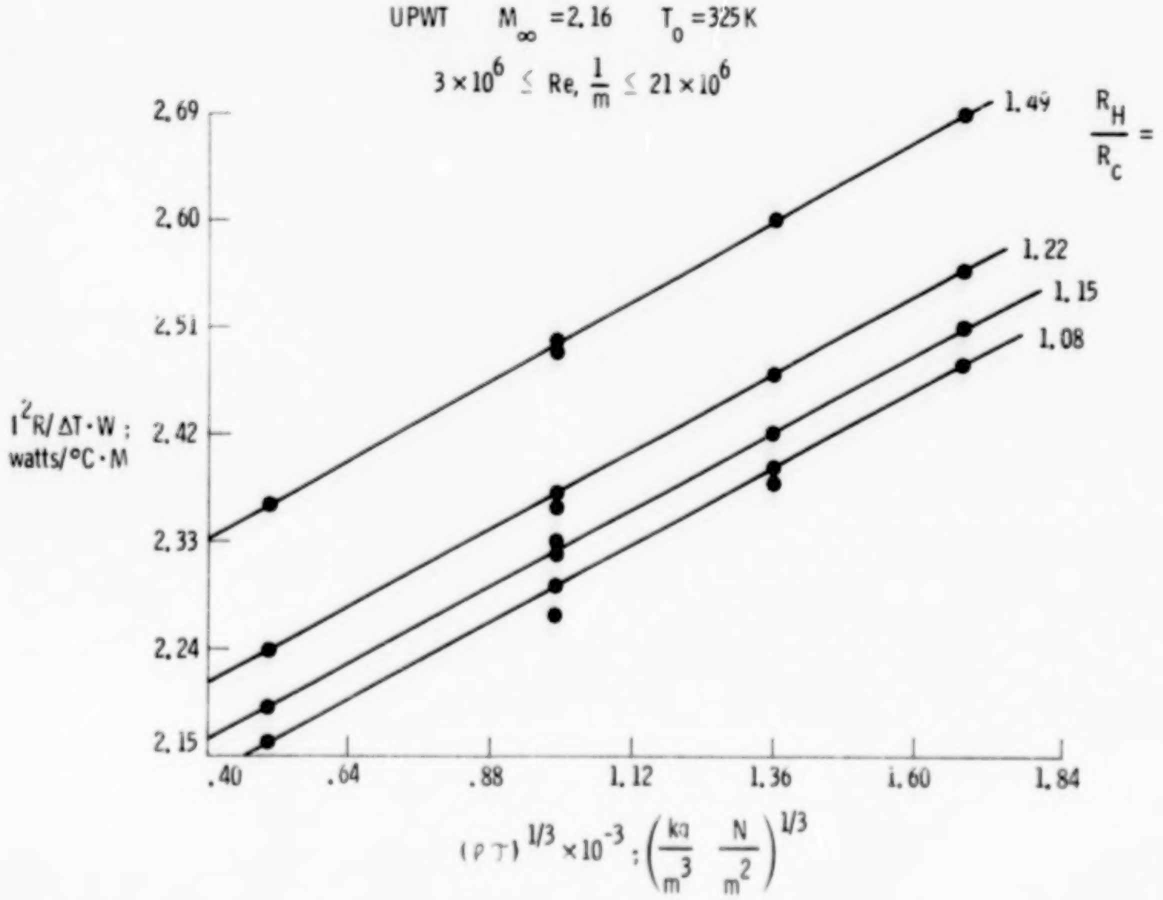

CROSSFLOW VORTICES

When a wing is swept with respect to the incoming velocity vector, a crossflow component of velocity is formed in the boundary layer. In a laminar boundary layer, this crossflow generates vortices in the boundary layer, and the vortices can cause premature transition from laminar to turbulent flow conditions. A schematic of these vortices is shown in the figure. The vortices are narrow and closely spaced, and in general, are aligned in the direction of the freestream velocity vector. The vortices produce high and low shearing stresses and high and low heat transfer rates which can be detected with a heated thin film. Since the vortices can cause transition, it is important that information be obtained on their nature if extensive amounts of laminar flow are expected on swept wings.

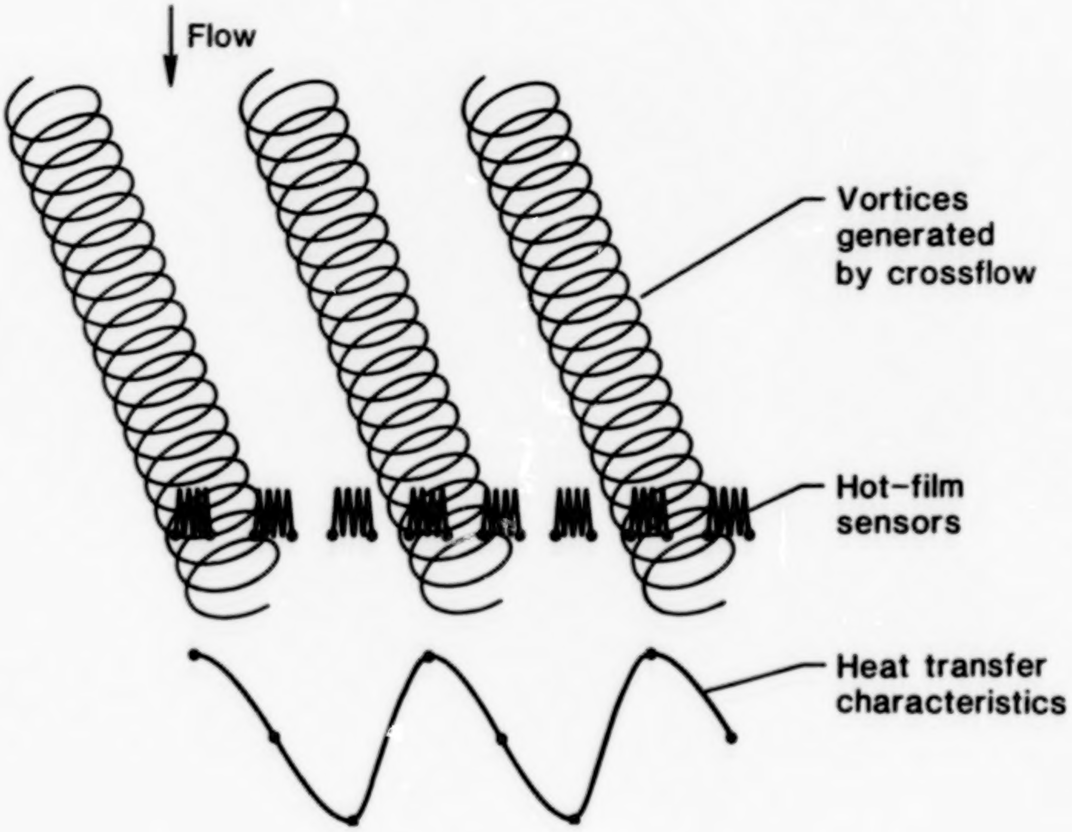
Flow
Vortices generated by crossflow
Hot-film sensors
Heat transfer characteristics

ORIGINAL PAGE IS
OF POOR QUALITY

CROSSFLOW VORTEX SENSOR

The thin film crossflow vortex sensor detects the large variations in local heat transfer and skin friction caused by crossflow vortices. An array of several hot-film elements is electronically heated by a constant temperature anemometer. When exposed to the airflow, the elements respond to the local heat transfer in the boundary layer. Depending on the size and spacing of the elements, the sensor will detect not only the existence of crossflow vortices but will also obtain good resolution of the wavelengths of the vortices.

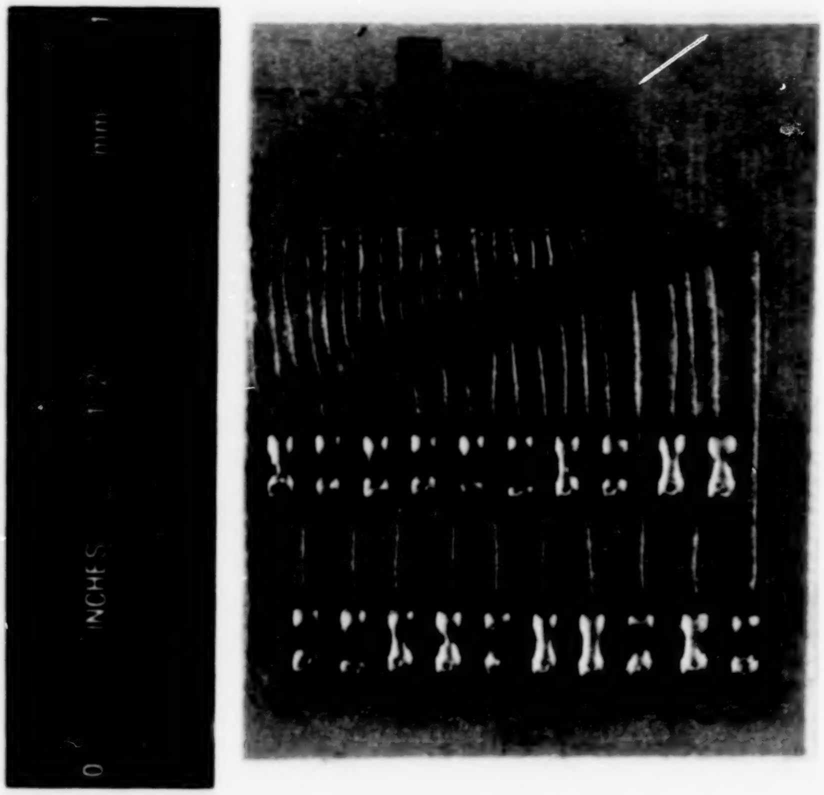

LASER VELOCIMETER SYSTEMS AND FACILITIES

In recent years, the Laser Velocimeter (LV) has been developed into a valuable flow diagnostic tool. At the present time, the Langley Research Center has two- and three-component systems in operation. These systems have been used to make mean and fluctuating velocity measurements in flows which range from low-speed pipe flows to transonic flow speeds. There are dedicated LV systems located in three facilities: the 4- by 7-Meter Tunnel, the 16-Foot Transonic Tunnel, and the Vortex Facility. A portable system is available for exploratory measurements in other facilities.

- Two and three component systems
- Test facilities
    - Pipe flow
    - Vortex facility
    - 4 × 7 - m tunnel
    - LTPT
    - 16 - ft transonic tunnel

PHOTOGRAPH OF A THREE-COMPONENT LASER VELOCIMETER SYSTEM

The laser velocimeter (LV) was an orthogonal three-component fringe-type system used in an off-axis, forward-scatter mode. For the purposes of the present study, only one component was used to compare with the results from the hot wire. A Bragg cell was not used in the LV in order to maintain compatibility with the hot wire, since the hot wire is not sensitive to flow reversal. A 5.0 W Argon ion laser was used as the light source with the 496.5 nm output line being selected. The output power at 496.5 nm was set to 0.2 W. The focal length was 0.38 m and the cross beam angle was 7.52 degrees which yielded a fringe spacing of 3.78 micrometers with a sample volume diameter of 160 micrometers. The collecting optics were rotated 37 degrees off of the optical centerline in the plane of the laser beams, which reduced the sample volume length, (measured to the points where the collected scattered light intensity value was $1/e^2$ of the peak), to 0.62 mm. The receiving optical system had a focal length of 0.38 m with a 7.5 cm clear aperture. The collected light was converted to electrical energy using a photomultiplier with a quantum efficiency of 0.21. This configuration yielded signal levels of approximately 0.2 V, peak-to-peak, from 0.35 - 0.55 micrometer polystyrene particles.

The output signals from the photomultiplier were processed by a high-speed burst counter which contained a double threshold triggering circuit and a 5:8 count comparison error detection circuit set to two percent. The digital output from the counter was input to a high-speed buffer memory which will accept up to 4096 velocity measurements, and the associated measured interarrival times. The data contained within this buffer system were then transferred to a 16-bit minicomputer for data processing and analysis.

ORIGINAL PAGE IS
OF POOR QUALITY

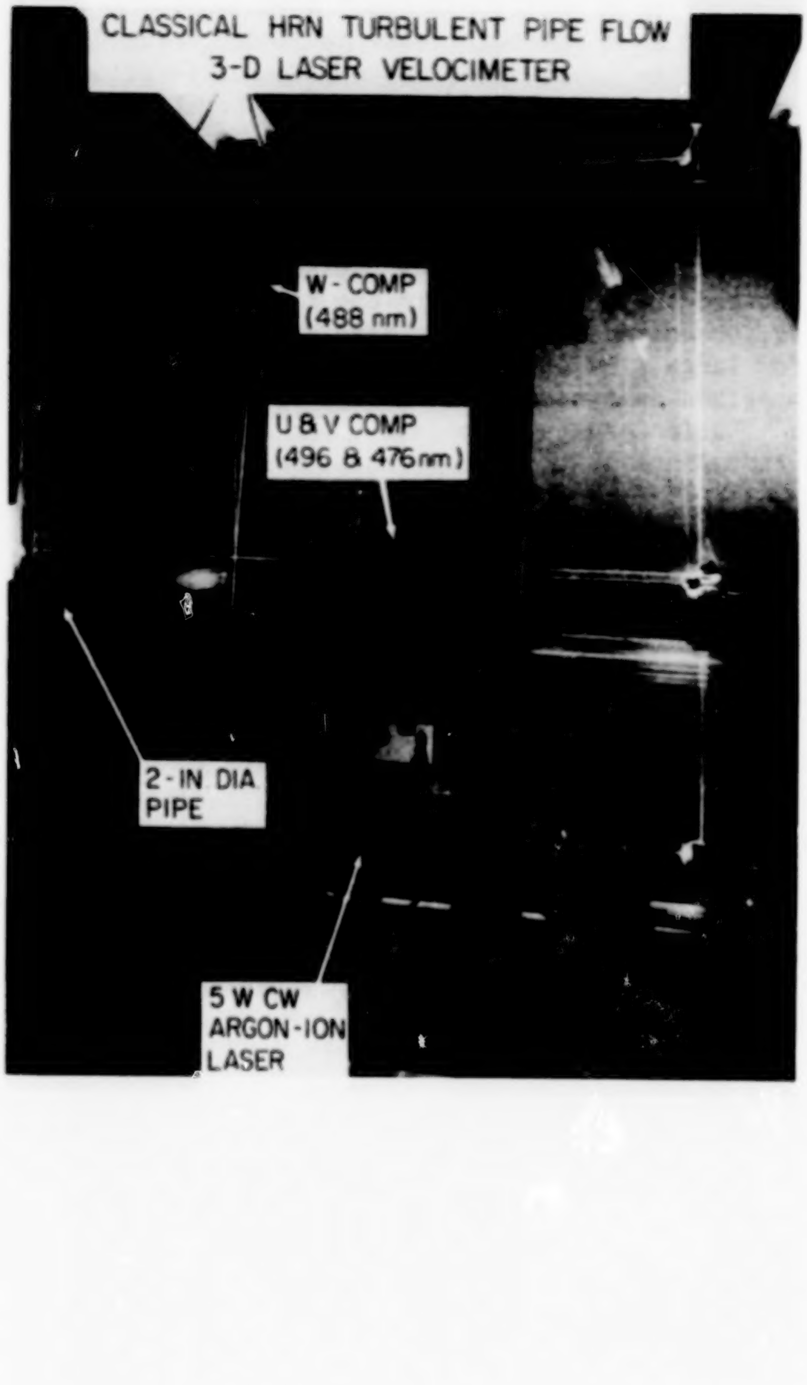
CLASSICAL HRN TURBULENT PIPE FLOW
3-D LASER VELOCIMETER
W - COMP
(488 nm)
U & V COMP
(496 & 476nm)
2 - IN DIA
PIPE
5 W CW
ARGON - ION
LASER

COMPARISON OF HOT-WIRE AND LV MEASUREMENTS

The investigations conducted in the turbulent jet flow from a two-inch pipe were to determine the characteristics of the laser velocimeter when used to measure turbulence quantities. The investigations consisted of comparisons of simultaneous measurements of turbulence with a single-component hot wire and a three-component laser velocimeter. The hot wire was approximately the same size as the laser velocimeter sample volume and located two millimeters downstream of the sample volume. The data from the hot wire were collected by a digital oscilloscope at a sample rate of 1000 data points per second and converted point-by-point via a spline fit calibration curve to velocity. The calibration was performed in a low-turbulence jet (one percent) with the mean velocities determined by the laser velocimeter. The calibration jet was seeded with the same 0.5 micron diameter polystyrene particles as the two-inch pipe to account for the effects of the seed material on the hot-wire heat transfer.

The flow from the two-inch pipe was adjusted to a Reynolds number of 50,000 to match the test conditions used by Laufer (ref. 1). Although the primary comparisons were between the U-component in the laser velocimeter and the hot wire, the remaining two components in the laser velocimeter were used to monitor the flow for large flow angles, which would invalidate the hot-wire measurements. Comparison measurements were made of mean velocity, turbulence intensity (circles - Laufer's data, diamonds - hot wire, and squares - laser velocimeter), and turbulence power spectra at several downstream locations.

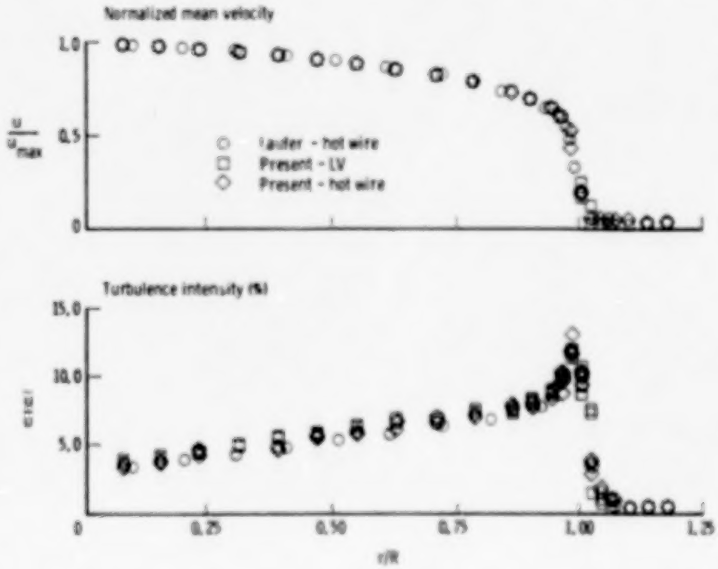

LASER TRANSIT ANEMOMETER SYSTEMS AND FLOW REGIMES

In addition to LV systems, Laser Transit Anemometer (LTA) systems are also under development. At the present time only two component systems are in operation and they have been used in flow regimes which range from subsonic to supersonic speeds. The LTA systems are used to measure mean flow velocities under conditions where it would be difficult or impossible to make these measurements using conventional methods.

- Two component systems
- Test facility flow regimes
  - Subsonic
  - Transonic
  - Supersonic

LASER TRANSIT ANEMOMETER

The LTA was developed to handle applications where conventional Laser Doppler Velocimetry (LDV) was difficult to apply. The LTA measures the transit time of particles that crosses two focused laser beams. The optical package shown here forms "two spots" in space and detects light scattered from particles passing through them. The detected signals are correlated in time and this auto correlation allows an estimate of the average transit time, t. This average transit time in conjunction with the known spot separation, d, provides a measurement of the velocity, V, of the particles by

$$V = d/t$$

LTA system control, data acquisition and data processing are performed by microprocessor-based computer system.

The optics package is designed so that the plane formed by the optical axis of the two beams may be rotated about an axis that is equal distance from and parallel to the two beams. This capability permits the determination of the flow angularity using a "best angle" search. The procedure is to make a velocity magnitude measurement at several spot rotation angles at fixed preselected incremental steps. A plot is then made of "two spot" angular position against contrast, where contrast is defined as

$$(h - b)/\mathrm{sqrt}\ b$$

where h is the value in the peak store and b is the background level. A least-squares fit of a parabolic equation through the maximum three adjacent points is performed and the abscissa of the parabolic vertex is taken to be the mean flow angle or best angle. Finally, the system is positioned at this angle and a velocity magnitude measurement is performed. This calculation assumes a constant particulate concentration.

The Spectron Development Laboratory (SDL) model 104 LTA system has a specified accuracy of 0.1 degrees for flow angle and 0.1 m/s in velocity. Both measurements are affected by diameter to separation distance ratio as well as local turbulence intensity levels.

LASER TRANSIT ANEMOMETER

Electro-optics Head

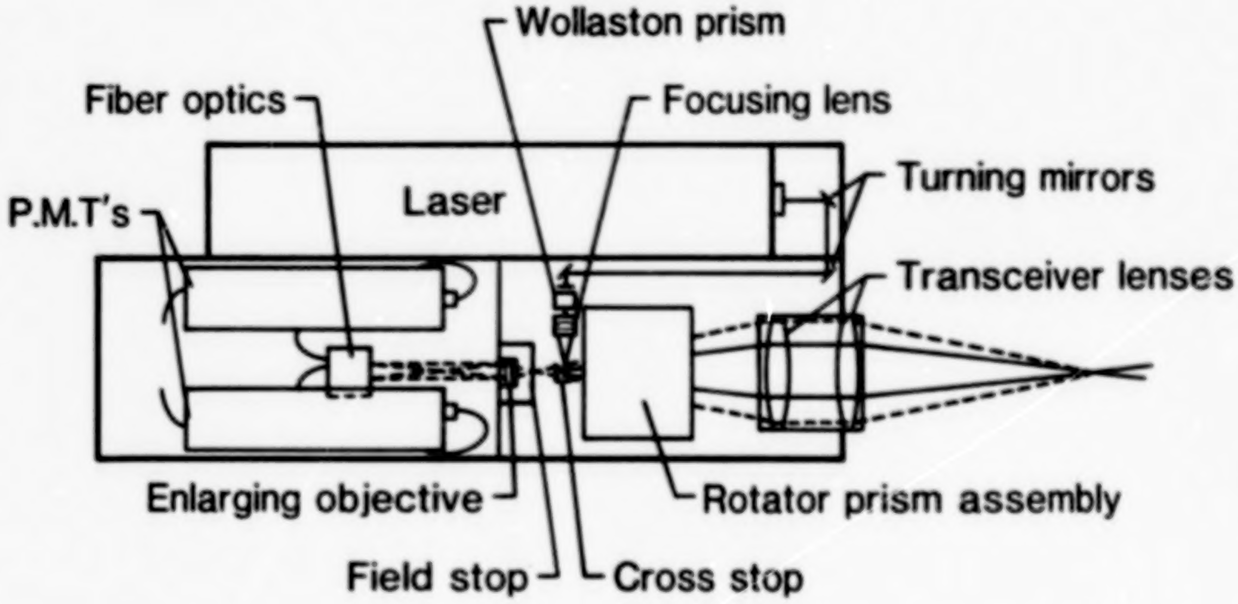
Wollaston prism
Fiber optics
Focusing lens
Laser
Turning mirrors
P.M.T's
Transceiver lenses
Enlarging objective
Rotator prism assembly
Field stop
Cross stop

STAGNATION LINE SURVEY

One of the major objectives of a recent 0.3-m Transonic Cryogenic Tunnel entry was to make measurements in the flow field of a cylinder. The size of tunnel windows did not permit a complete scan into the free stream, but with the "D" window rotated 90 degrees from the normal position a vertical scan was made to locate the stagnation line. This could be accomplished by searching for the location with zero degree flow angle, which occurs on the stagnation line of this model.

The plot shows the ratio of the velocity at each data point position to free-stream velocity as a function of x/D where x is the distance from the model surface and D is the model diameter. For this scan the 0.3-m Transonic Cryogenic Tunnel was operated at a temperature of 225K and a Mach number of 0.3: U was 91 meters/sec and the Reynolds number was 1.87 x 10^6. The solid line is calculated using potential flow theory and the symbols are measurements taken with the LTA system. All errors associated with the measurements are encompassed by the size of the symbols. From a position 3.56 cm (1.4 inches) in front of the model a horizontal scan was made along the flow direction to a point 0.32 cm (0.125 inches) from the model surface. The velocity varied from 86.6 m/sec to 34 m/sec along this streamline and these velocities agreed very well with theory.

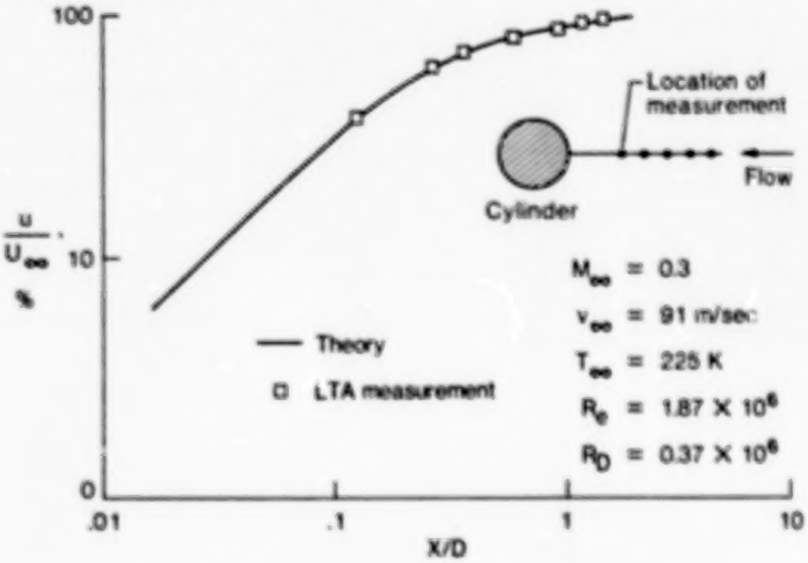

CARS SYSTEM FOR TURBULENT FLAME MEASUREMENTS

Coherent Anti-Stokes Raman Spectroscopy (CARS) is a non-intrusive diagnostic technique which can measure the temperature and density of a gas in a flame. In the configuration shown here, called BOXCARS, high spatial (a few microns diameter by a millimeter length) and temporal (a complete data event in 10 nanoseconds) resolutions are achieved. In addition, CARS has high conversion efficiency and a laser-like signal; thus simple optics may be used to collect the strong signal. The process is Anti-Stokes in character, thus avoiding interference from the laser beams used to create the signal and any naturally occurring fluorescence.

The spectral shape of the CARS signal is temperature dependent; temperature is determined by fitting the CARS signal to a library of previously calculated spectra (typically nitrogen). The intensity of the CARS signal is density dependent; a partial reflector is used to create a second CARS signal in room air. The ratio of the two signals is used to calculate density.

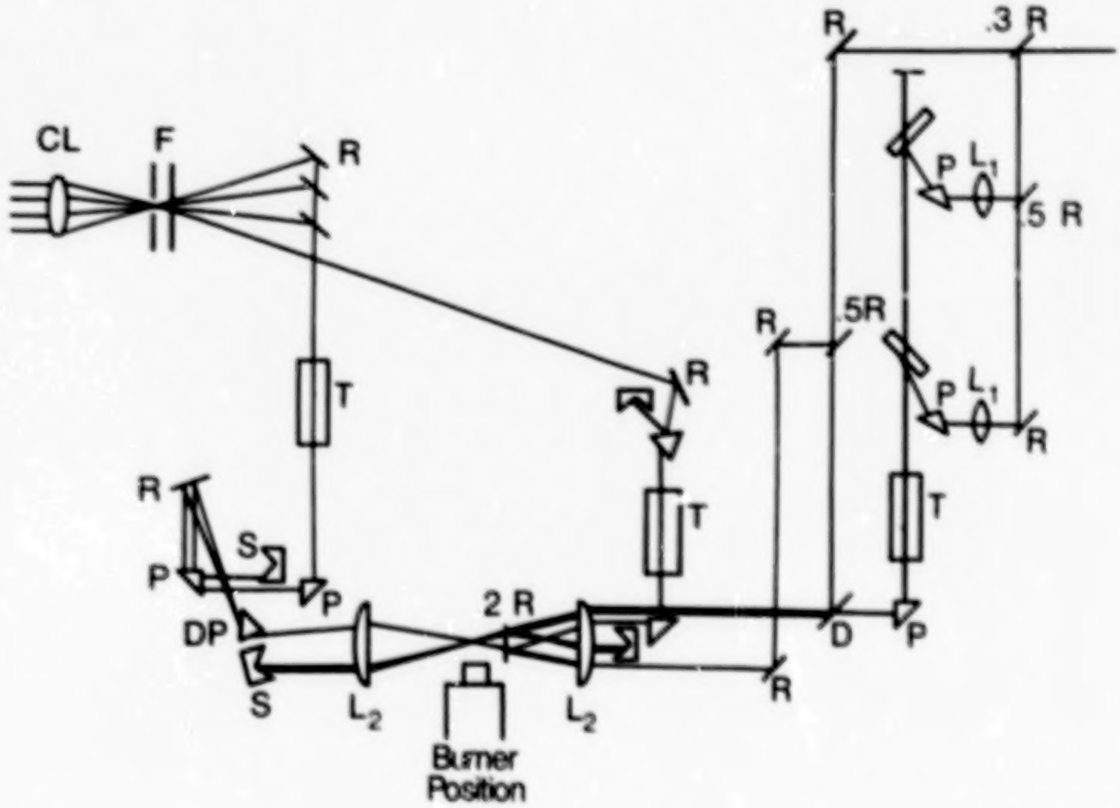

CARS optical schematic including arrangements for referencing and dynamic range enhancement.
Symbols: R= total reflector, L= lens, p= 90 deg. prism, T= telescope, D= dichroic mirror, S= beam sink, DP= dispersion prism, F= filter, CL= cylinderical lens.

ORIGINAL PAGE IS
OF POOR QUALITY

SHADOWGRAPH OF COAXIAL DIFFUSION FLAME

A subsonic coaxial diffusion flame was investigated with the CARS system. A comparison of the distribution of temperature and nitrogen density measured with the CARS system was made with modeled results. The combustion was modeled using: parabolized Navier-Stokes equations, a marching finite difference algorithm, a two equation (κ-ε) turbulence model, hydrogen oxygen equilibrium chemistry, and initial velocity profiles from hot-wire measurements in air.

The spark shadowgraph of the flame also shows the tubes which provided the flow. Hydrogen seeded with 20% nitrogen flowed through the central 1/4-inch diameter tube at an average velocity of 100 m/s. Air flowed through the annulus between the 1/4 inch and the 1-inch tube at an average velocity of 15 m/s. Surveys were taken along the centerline and radially at 1 inch and 4 inches from the exit.

AXIAL VARIATION OF TEMPERATURE AND N_2 NUMBER DENSITY

Good agreement was demonstrated between CARS temperature and density measurements and the modeling results. The inherent standard deviations in the CARS temperature measurements are less than 100 degrees, thus, the larger values shown here are an indication of the variation of temperature due to turbulent mixing of hot and cold gases.

Measurements such as those shown here can be used to validate the results of modeling of computational fluid dynamics, as demonstrated here (see bibliography).

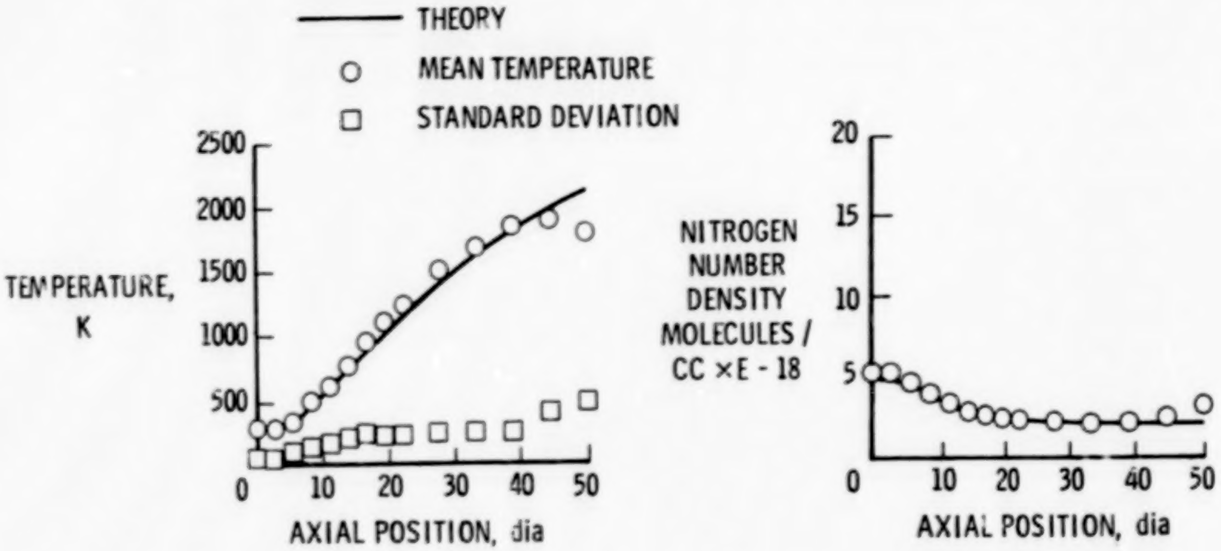

ORIGINAL PAGE IS
OF POOR QUALITY

SUBLIMATING CHEMICALS FOR BOUNDARY LAYER TRANSITION VISUALIZATION

Recent developments which have lead to the practical application of natural laminar flow (NLF) for high performance airplanes require special test techniques for the aerodynamicist. The sublimating chemical method offers an accurate, reliable, low-cost technique for indicating transition from laminar to turbulent flow.

References 2, 3, and 4 discuss the original development of the sublimating chemical technique at the Royal Aircraft Establishment. Refinements by NASA Langley personnel (ref. 5) produced improvements in the simplicity and operational flexibility of the technique which involves coating the surface (using standard paint spraying equipment) with a thin film of volatile solid chemical. When exposed to the airstream, the chemical sublimates more rapidly in the turbulent boundary layer due to higher shear stresses. The chemical coating remains relatively unaffected in the laminar region because of lower shear stresses thus indicating the end of transition at the downstream edge of the remaining chemical coating. Typical sublimation times range from a few minutes to an hour, depending on the chemical selected, ambient temperature, and air speed. For flight testing, use of a slower sublimating chemical at ambient temperatures between 30^{o}F and 90^{o}F (at test altitude) offers the capability of flying to low test altitudes (<20,000 ft), stabilizing the sublimating chemical pattern at the test conditions, and returning to the ground with the chemical pattern unaffected by the off condition portions of the flight required for climb to and descent from the test altitudes. Sublimating chemicals are equally valuable when used for wind tunnel research.

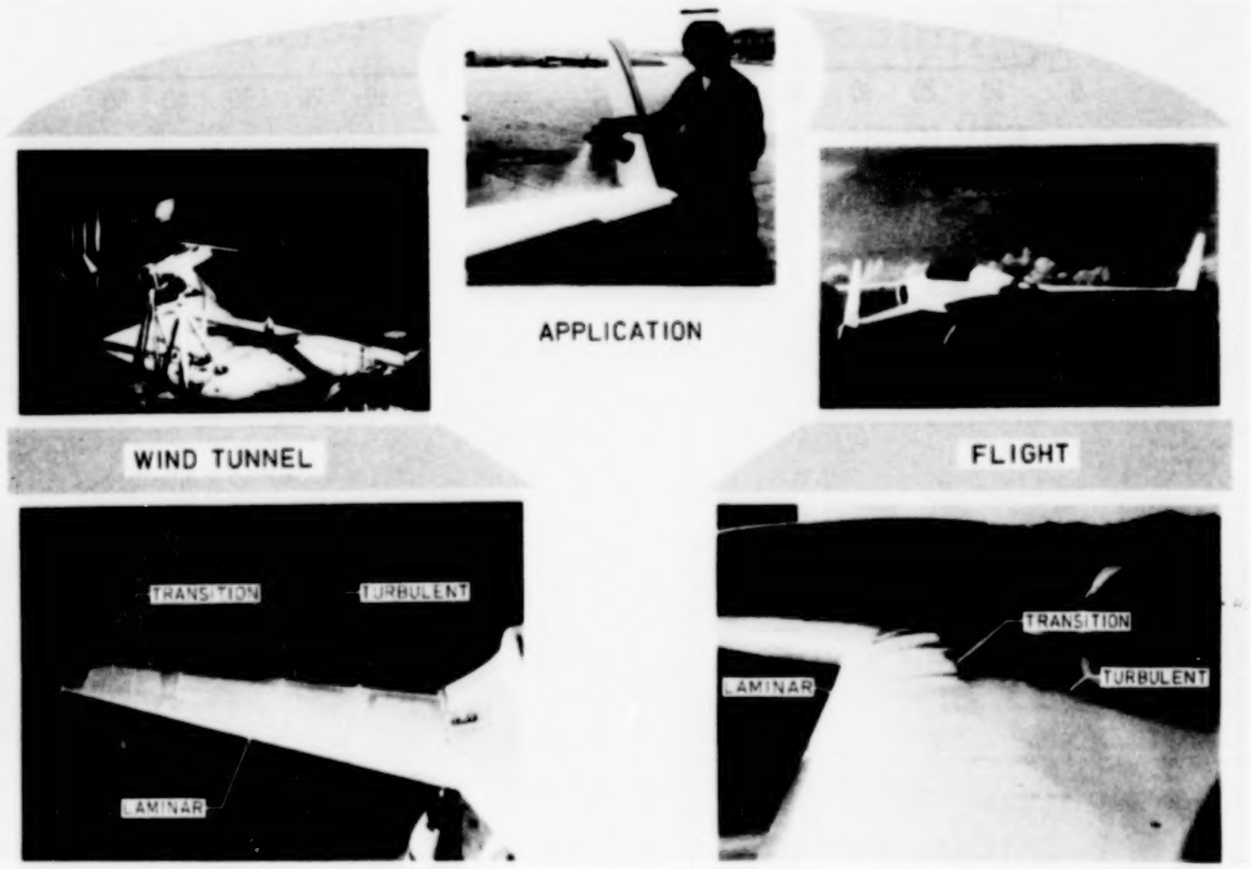

CONCLUSIONS

The Langley Research Center has a concentrated and directed effort under way to develop both conventional and non-intrusive diagnostic instrumentation. These instruments are being developed to operate over large Mach number, total temperature, and total pressure ranges. Efforts are being made to evaluate the measurements made by the various instruments to determine the most accurate and reliable instrument to be used under a given flow environment. Although only one flow visualization technique was described, there are many different types presently being used at the Langley Research Center.

- Developing conventional and non-intrusive diagnostic instrumentation
- Suitable for all Mach number, total temperature and total pressure ranges
- Compare results from different techniques
- Multi-flow visualization techniques

REFERENCES

1. Laufer, J.: Structure of Turbulence in Fully Developed Pipe Flow. NACA Report 1174, 1954.

2. Pringle, G. E. and Main-Smith, J. D.: Boundary Layer Transition Indicated by Sublimation. British RAE Tech. Note AERO No. 1652 (ARC 8892), 1945.

3. Main-Smith, J. D.: Chemical Solids as Diffusible Coating Films for Visual Indication of Boundary Layer Transition in Air and Water. R&M No. 2755, British ARC, 1950.

4. Owen, P. R. and Ormerod, A. O.: Evaporation From the Surface of a Body in an Airstream. R&M No. 2875, British ARC, 1951.

5. Holmes, B. J.; Obara, C. J.; Kelliher, W. C.; and Croom, C. C.: Sublimating Chemical Method for Detecting Laminar Boundary-Layer Transition. NASA Tech Brief LAR 13089, 1983.

BIBLIOGRAPHY

1. Antcliff, R. R.; Jarrett, O., Jr.; and Rogers, R. C.: CARS System for Turbulent Flame Measurements. AIAA Paper 84-1537, 1984.

2. Antcliff, R. R. and Jarrett, O., Jr.: Comparison of CARS Combustion Temperatures with Standard Techniques. AIAA Paper 83-1482, 1983.

3. Antcliff, R. R.; Hillard, M. E.; and Jarrett, O., Jr.: Intensified Silicon Photodiode Array Linearity: Application to Coherent Anti-Stokes Raman Spectroscopy. Applied Optics, Vol. 23, July 15, 1984, pp. 2369-2375.

D15

N88-14941

S15-09

117239

21P.

PRELIMINARY CALIBRATION AND TEST RESULTS FROM THE NATIONAL TRANSONIC FACILITY

Linwood W. McKinney and Dennis E. Fuller
NASA Langley Research Center
Hampton, Virginia

[redacted]IGHTS OF NTF OPERATING EXPERIENCE

The highlights of the National Transonic Facility (NTF) operating experience are shown in the figure below.

- CHECKOUT OF MAJOR SYSTEMS
  - OPERATING ENVELOPE COVERED
  - MODIFICATION TO HEATERS ON MODEL ACCESS SYSTEM
- INITIAL CALIBRATION
  - MACH NUMBER UNIFORMITY
  - TOTAL TEMPERATURE DISTRIBUTION
  - TOTAL PRESSURE DISTRIBUTION
- INITIAL MODEL TESTS
  - PATHFINDER I
  - SPACE SHUTTLE

NATIONAL TRANSONIC FACILITY

ORIGINAL PAGE IS
OF POOR QUALITY

An aerial view of the National Transonic Facility (NTF) site, viewed from the back side, is presented. The large bulk storage nitrogen tank on the left and the vent stack at the right of the tunnel are used to support the cryogenic mode of operation. The cooling tower in the foreground is used with a water-cooled heat exchanger inside the tunnel to support the air mode of operation. The high bay building in the background houses model preparation bays and shop area on the first floor and the control room and tunnel test section entrance on the second floor. The design performance capability is a Mach number range of 0.2 to 1.2, pressure range of 1 to 8.8 atm, and temperature range of 77 to 339K. This will produce a maximum Reynolds number of 120 million at a Mach number of 1.0 based on a chord length of 0.249 meters.

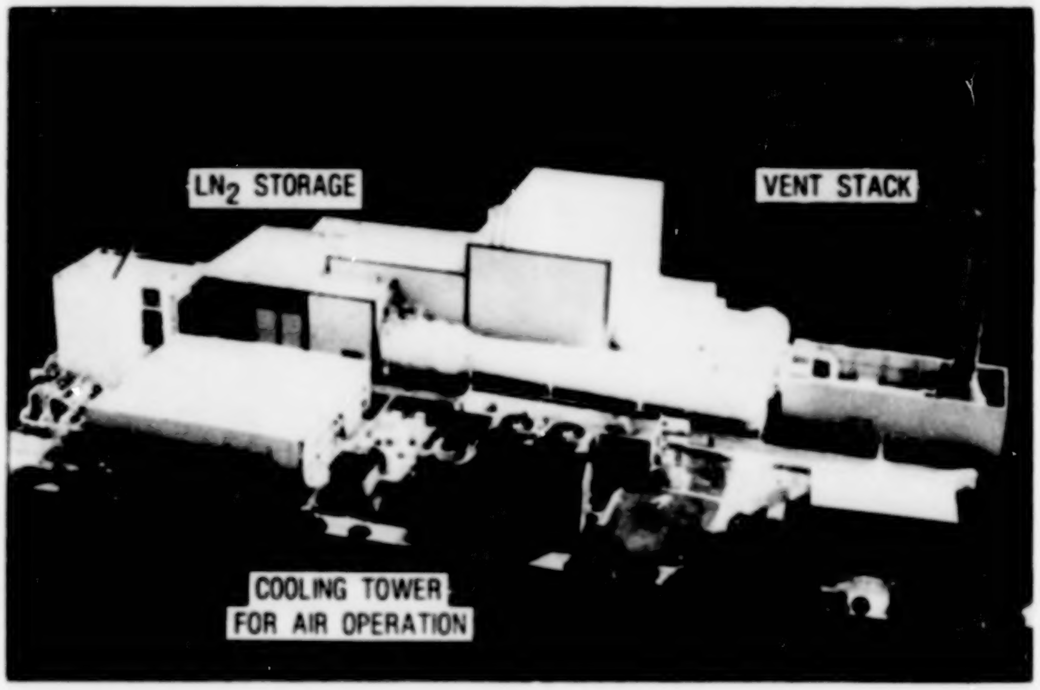

LN_2 PLANT

The majority of the nitrogen is supplied to the onsite 946 cubic meter storage tank by pipeline from a commercial air separation plant. This system has been operational since January 1983 and supplied most of the liquid nitrogen for the NTF during checkout. The onsite storage tank can also be filled from mobile truck units.

NTF
PIPELINE
LN2 PLANT

ORIGINAL PAGE IS
OF POOR QUALITY

NTF PLUME

ORIGINAL PAGE IS
OF POOR QUALITY

The safe venting of the gaseous nitrogen to the atmosphere is closely monitored during all cryogenic test runs. A fan/ejector system mixes ambient air with the gaseous nitrogen expelled from the tunnel in a vent stack 37 meters high. The mixing ratio in the stack is at least one to one under all conditions so that the oxygen content at the stack exit is at least ten percent by volume. The temperature is still low at the exit so that the size of the visible plume emitted is dependent on the atmospheric humidity and wind conditions.

$M=1.0$, $P_T=8.5$ atm, $T_T=119$ K
RELATIVE HUMIDITY=40 percent

REYNOLDS NUMBER ENVELOPE

The maximum operating envelope showing Reynolds number as a function of Mach number is presented and gives a fairly complete picture of the range over which the NTF has been operated. The boundary lines and the lines of constant total and dynamic pressure correspond to operation at minimum cryogenic temperature. The maximum Mach number achieved thus far in the checkout and calibration phase was 1.22. This Mach number was obtained in nitrogen at a pressure of 1.2 atm and at a temperature of 180K. In air, the maximum Mach number was 1.12 at a pressure of 1.4 and at a temperature of 320K.

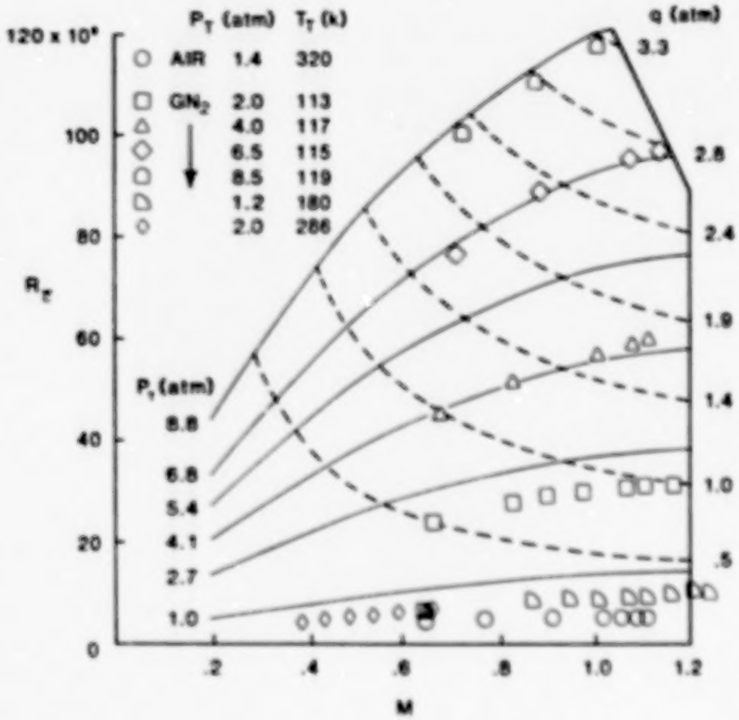

SURVEY RAKE

The survey rake was utilized to determine total pressure and temperature uniformity in the test section. The rake had an array of twenty total pressures and ten total temperatures and was mounted in the NTF roll coupling (internal to the model support arc sector) to provide roll capability of ± 180°. The front of the rake was located at the arc sector center of rotation (station 13). The pressures were measured with the ESP system, and the thermocouples utilized an onboard reference junction to enhance measurement accuracy. The absolute level of the thermocouple measurements was anchored by a platinum resistance thermometer mounted in the settling chamber of the tunnel.

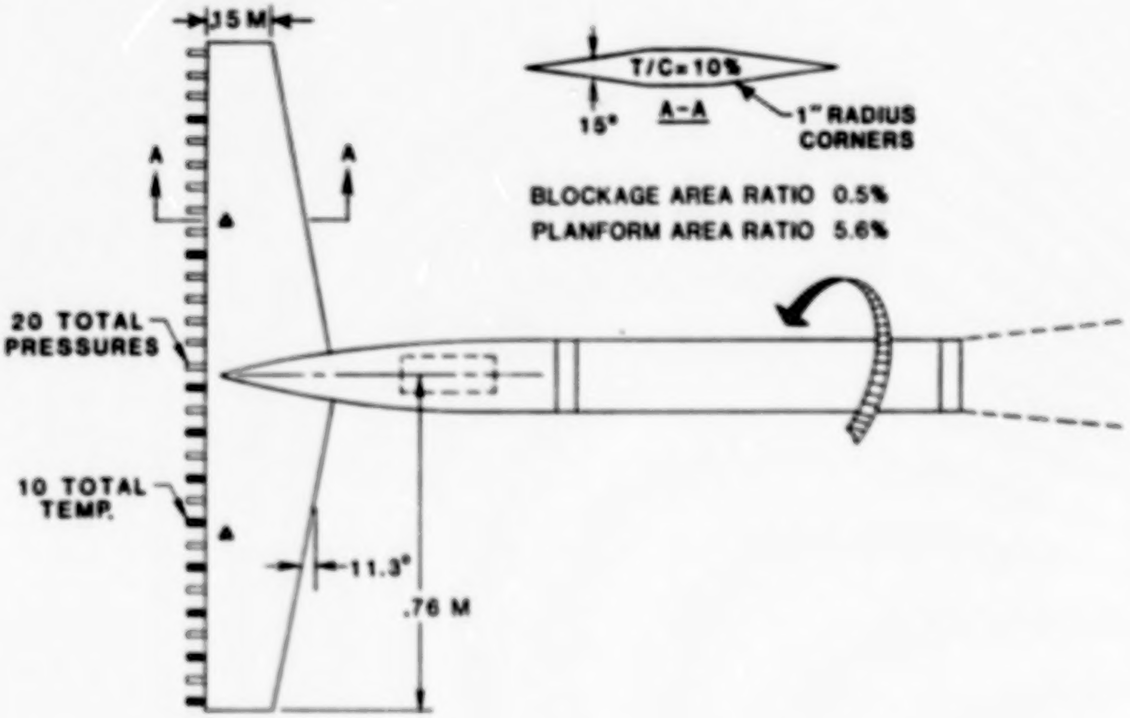
.15 M
A
A
T/C = 10%
15°
A-A
1" RADIUS CORNERS
BLOCKAGE AREA RATIO 0.5%
PLANFORM AREA RATIO 5.6%
20 TOTAL PRESSURES
10 TOTAL TEMP.
11.3°
.76 M

TOTAL PRESSURE DISTRIBUTION - 324K

Typical variations of total pressure across the test section normalized by the reference total pressure for air at 324K are presented. The reference line faired through the data is for a condition of zero gradient. It will be noted from an inspection of the data that a pressure gradient is not detectable in either the horizontal or vertical direction. Data taken at other radial cuts across the test section indicate the same result.

ROTARY RAKE PRESSURES

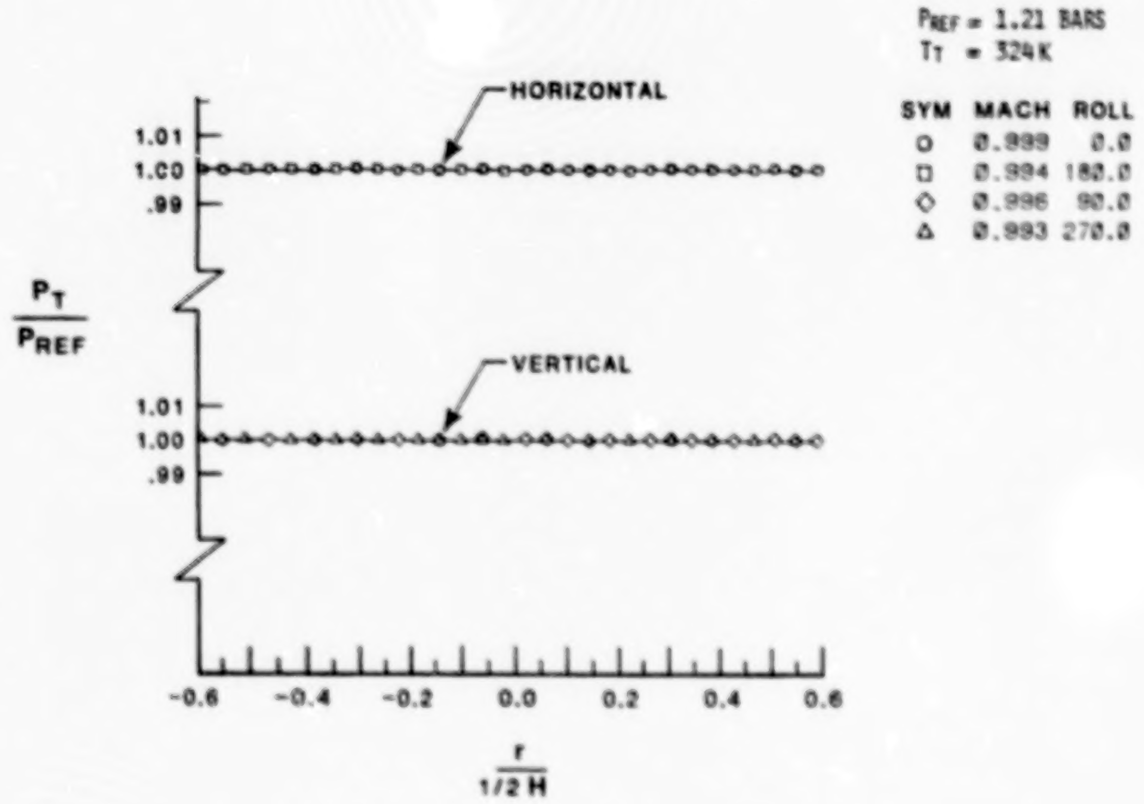

TOTAL PRESSURE DISTRIBUTION - 122K

Typical variations of total pressure across the test section normalized by the reference total pressure for cryogenic operation at 122K are presented. The reference line faired through the data is for a condition of zero gradient. It will be noted from an inspection of the data that a pressure gradient is not detectable in either the horizontal or vertical direction. Data taken at other radial cuts across the test section indicate the same result.

ROTARY RAKE PRESSURES

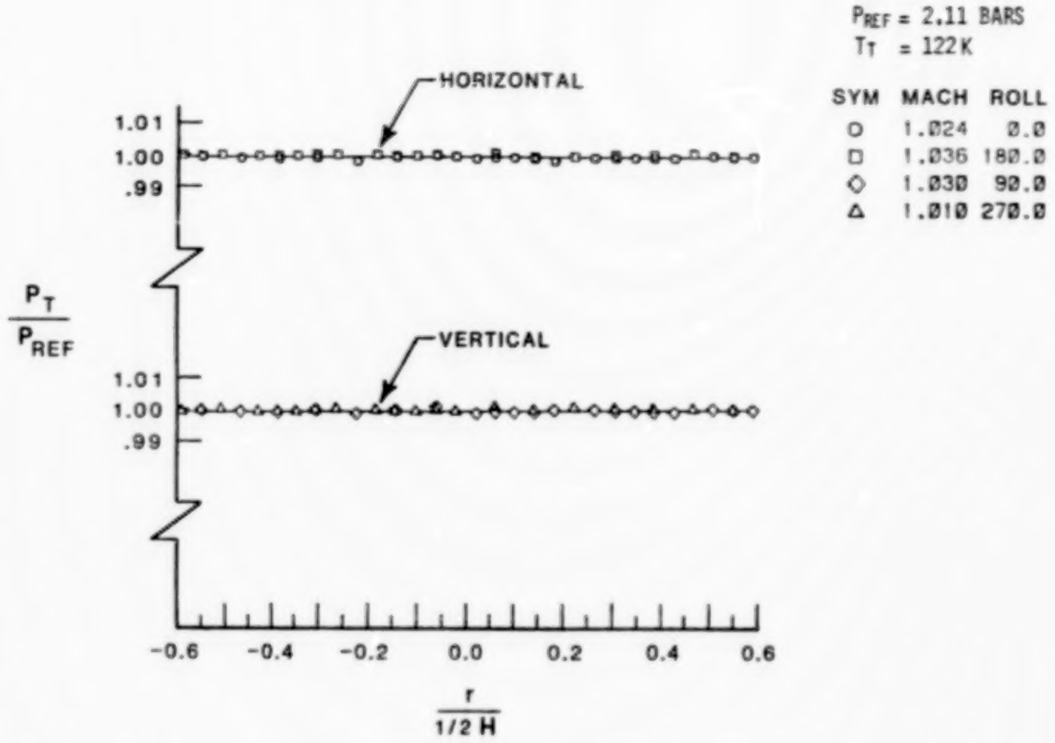

TOTAL TEMPERATURE DISTRIBUTION - 324K

Typical variations in total temperature across the test section normalized by the reference total temperature are presented. The data were taken in air at 324 Kelvin using the cooling coil. The reference lines represent zero gradient. The distribution of data about this line is within plus or minus 1 Kelvin.

ROTARY RAKE TEMPERATURES

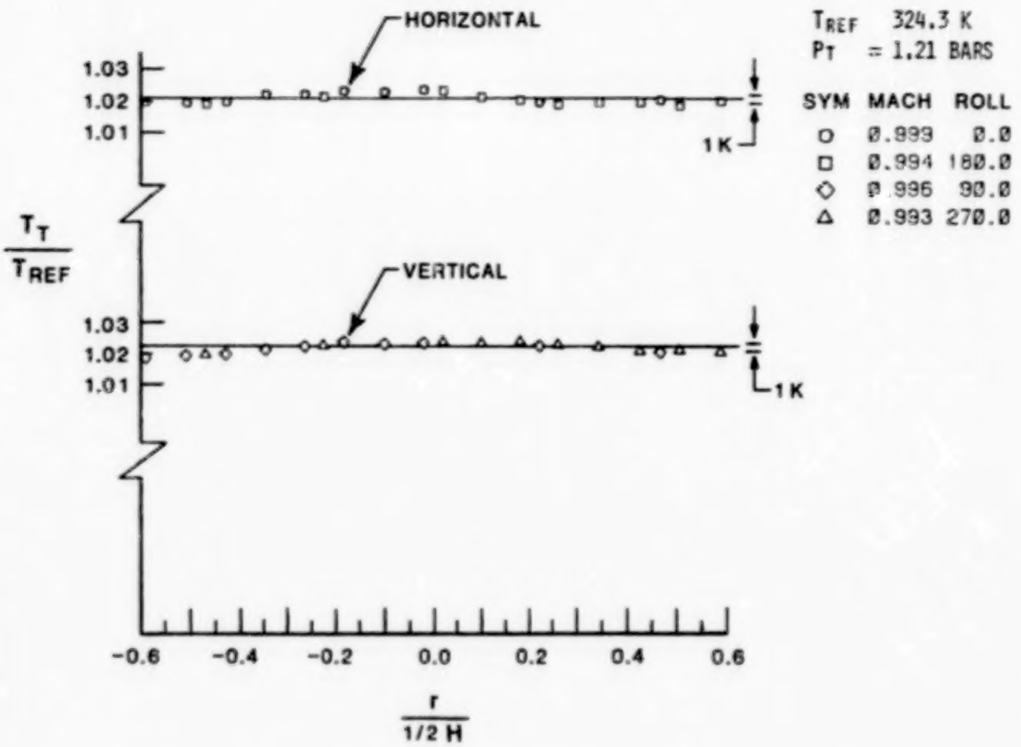

TOTAL TEMPERATURE DISTRIBUTION - 122K

Typical variations in total temperature across the test section normalized by the reference total temperature are presented. The data were taken in the cryogenic mode using the liquid nitrogen injectors for cooling. These data generally fall within a band of plus or minus 0.5 Kelvin. It should be noted that the total temperature ratio is slightly higher than unity. This is due to an offset in the reference temperature junction which was not corrected during the test. This is not important for this discussion since the temperature uniformity across the test section was the primary item of interest and is not affected.

ROTARY RAKE TEMPERATURES

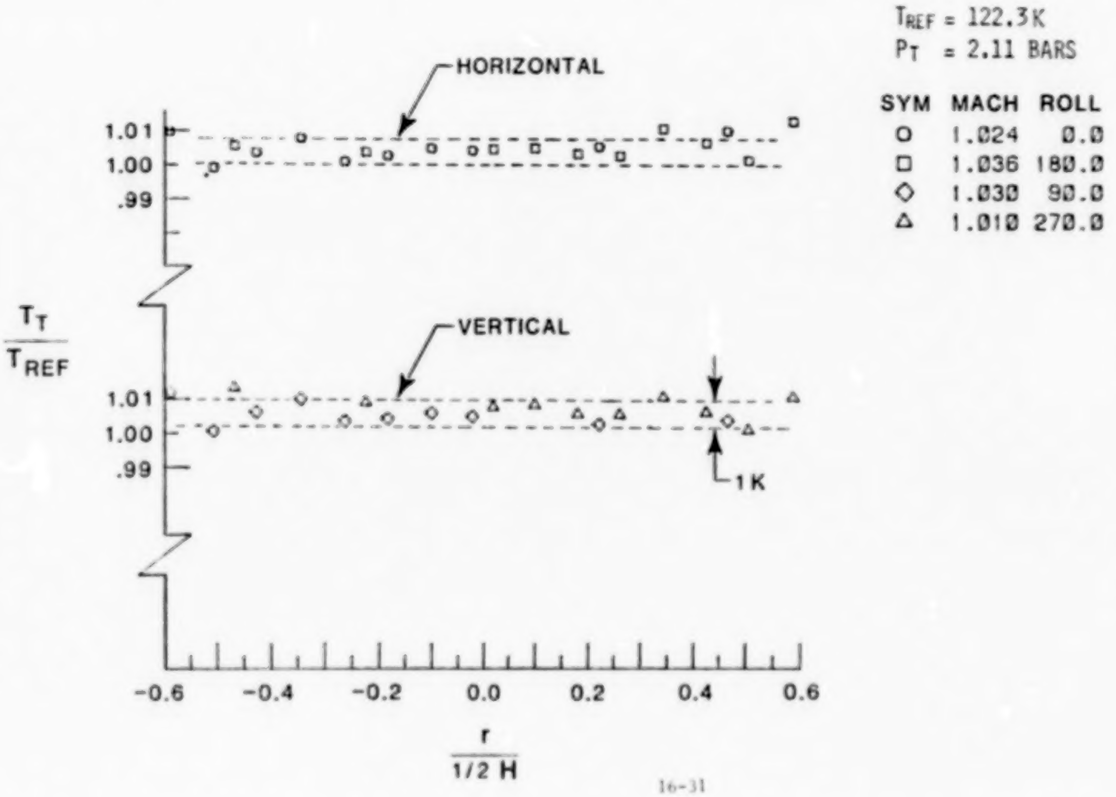

16-31

ORIGINAL PAGE IS
OF POOR QUALITY

The model represents a generic transport with supercritical airfoil and aspect ratio of 9.8. Spots on the left wing are targets used in the checkout of the model deformation system.

TUNNEL FLOW ANGLE

The tunnel flow angularity was investigated using the Pathfinder I model to obtain an integrated value of the flow angle by testing the model upright and inverted. The variation of normal force coefficient with model angle of attack for the model upright and inverted is shown for Mach numbers of 0.60 to 0.82. The near perfect agreement between the upright and inverted runs at both Mach numbers indicates that a correction for flow angle in the NTF at these test conditions will not be required.

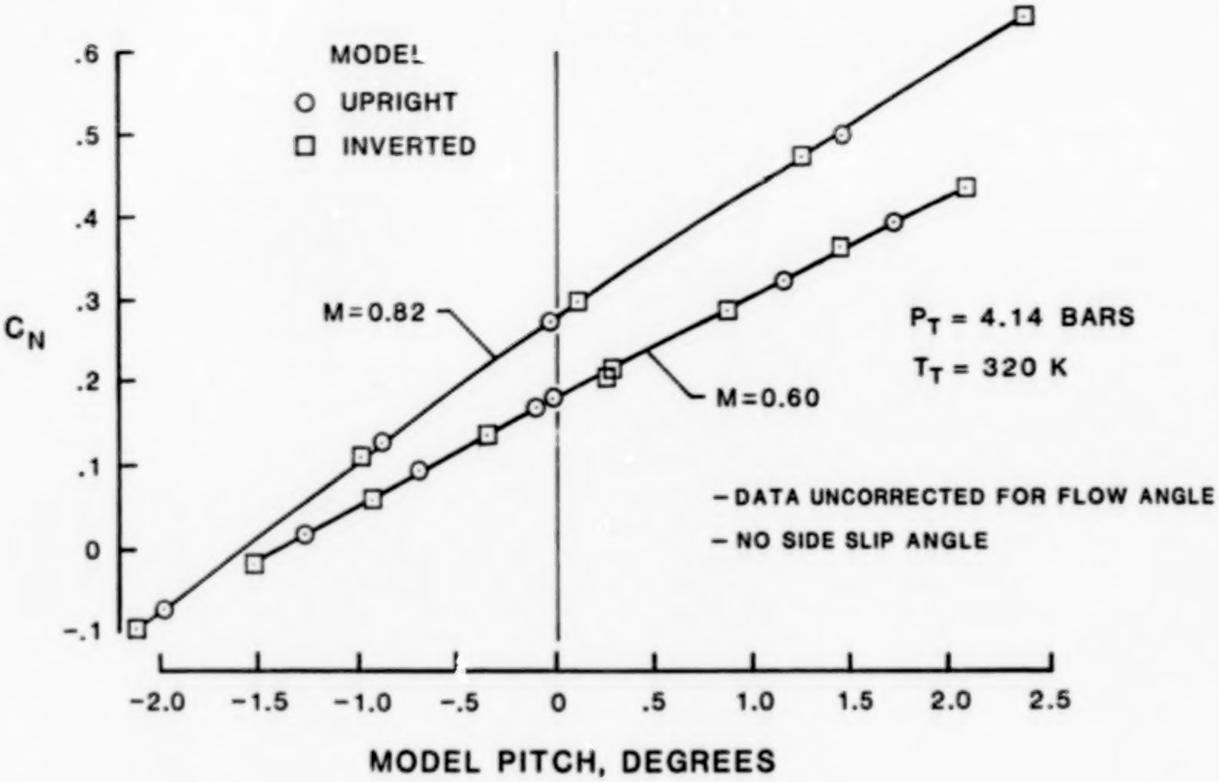

TEST ENVELOPE FOR MODEL INSTRUMENTATION CHECKOUT

For purposes of checking the effects of temperature on model instrumentation performance, it was desirable to have a condition where the flow would be sensitive to Reynolds number and the same test Reynolds number could be obtained at ambient and cryogenic conditions. The Pathfinder I model was used and tested over a Mach number range from 0.40 to 0.82. The test condition of temperature and pressure is shown in the accompanying figure for a Mach number of 0.70. A maximum chord Reynolds number of approximately 5 million was obtained in air at a temperature of 320K at 3 atm stagnation pressure and the same Reynolds number was obtained at 177K and 1.33 atm stagnation pressure. These results will be compared in subsequent figures. Additionally, data will be presented to show the effects of Reynolds number between 2.5 and 29.4 million by varying temperature from 320K to 117K at 1.33 atm stagnation pressure and then increasing pressure to 4 atm.

A Mach number of 0.70 was selected for analysis since any Reynolds number sensitive separation present on the airfoil would not be dominated by shock effects, and thus, would be less sensitive to any changes in model surface conditions that might occur during the test due to particles in the stream.

The internal strain gage balance used to measure model forces and moments was unheated. Temperature measurements were made at the bridges, and corrections to zeroes and sensitivities were applied. For this balance, zero shifts in axial force occurred during the test that were not experienced either during calibration or cryogenic checkout prior to the test. Therefore, drag data were not obtained. The zero shifts were repeatable in post test checks and further evaluation is continuing. Angle of attack and pressure instrumentation was maintained in a heated environment at all times.

M = 0.70

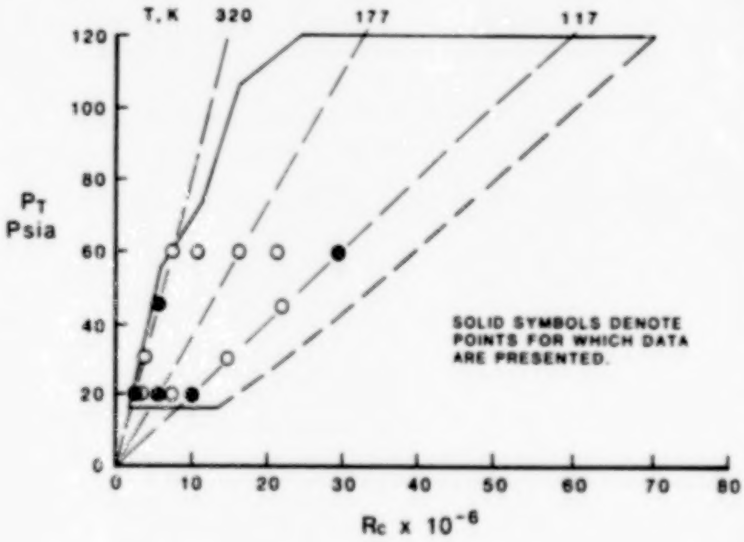

SOLID SYMBOLS DENOTE POINTS FOR WHICH DATA ARE PRESENTED.

EFFECT OF TEMPERATURE ON C_N VERSUS α MEASUREMENT

The accompanying figure shows the variation of normal force with angle of attack and indicates the same result is obtained at a constant Reynolds number for a temperature of both 320K and 177K. The data for a Reynolds number of 2.5 million based on model chord show the familiar characteristics of the supercritical wing tested at low Reynolds number. The nonlinearity of low angles of attack has generally been attributed to flow separation on the lower surface in the cusp region and, of course, trailing-edge separation is apparent at the highest angles of attack.

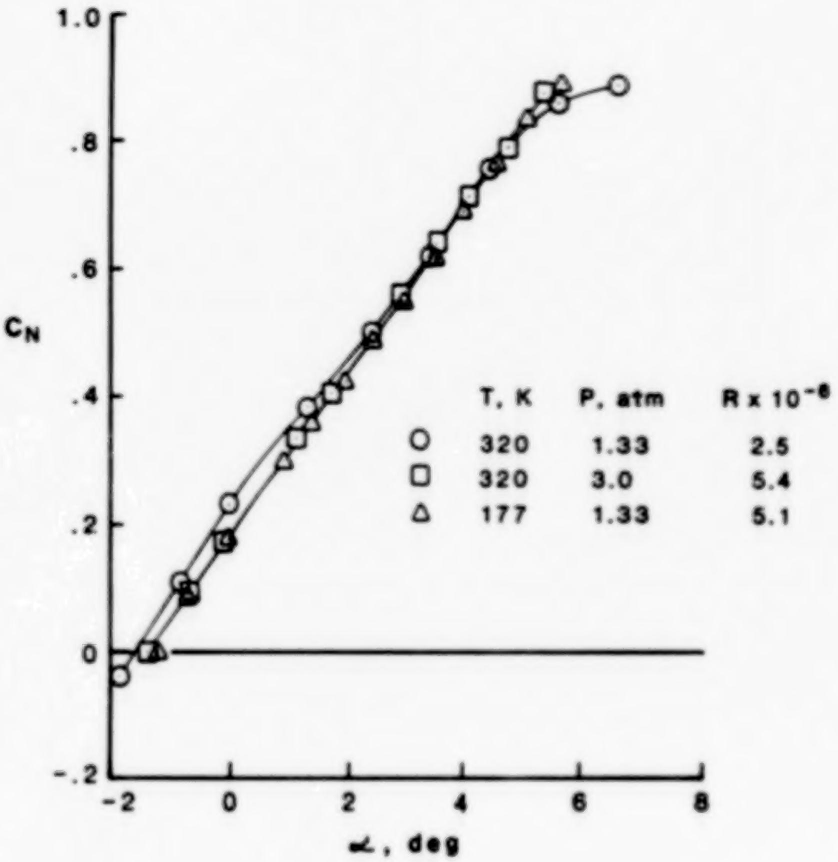
PATHFINDER I ; M = 0.70

EFFECT OF TEMPERATURE ON C_M VERSUS α MEASUREMENT

The accompanying figure illustrates the variation of pitching moment coefficient with angle of attack for essentially the same Reynolds number obtained at temperatures of 320K and 177K. The agreement is very good.

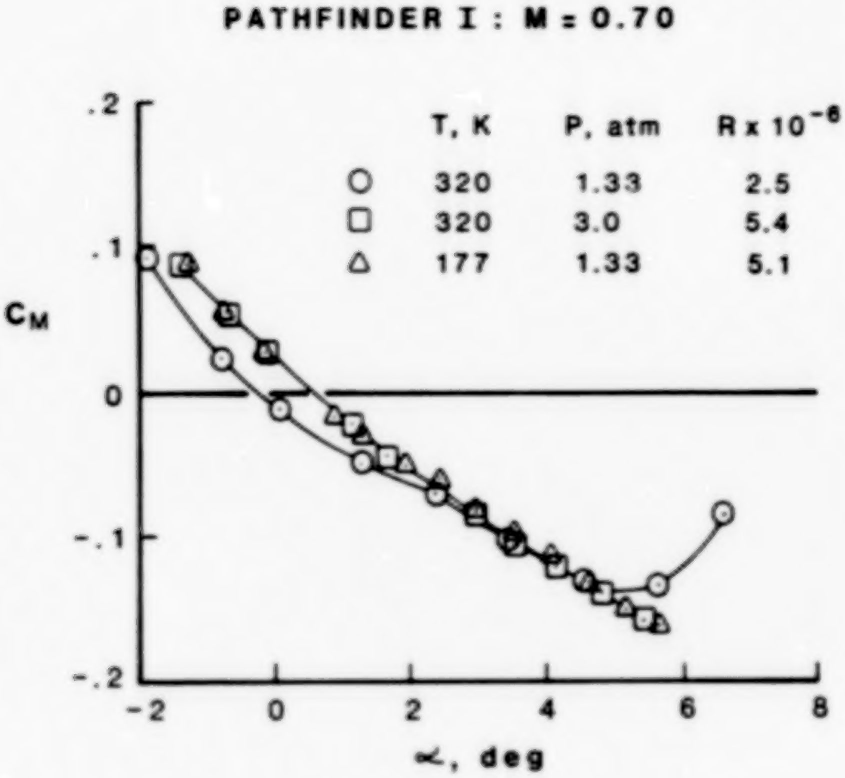

EFFECT OF TEMPERATURE ON C_M VERSUS C_N MEASUREMENT

The accompanying figure illustrates the variation of pitching moment coefficient with normal force coefficient for essentially the same Reynolds number obtained at temperatures of 320K and 177K. The agreement between the two conditions is very good.

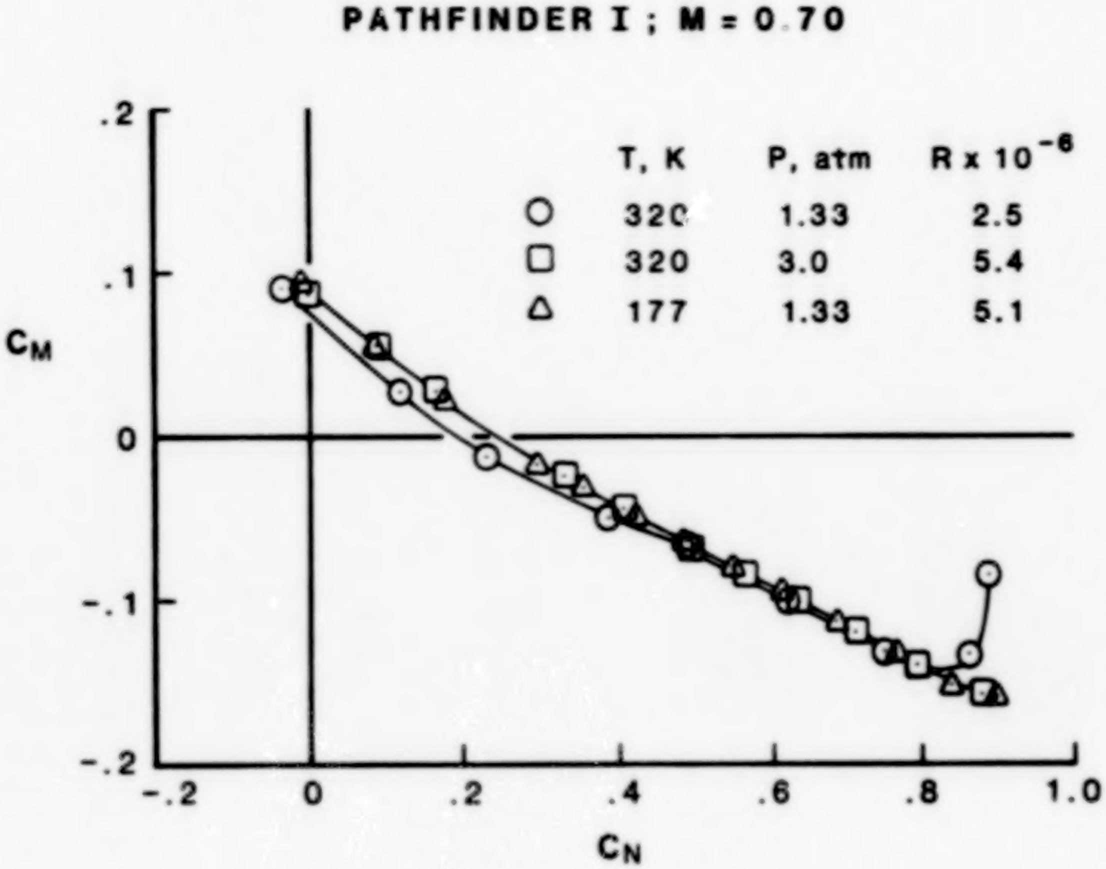

EFFECT OF REYNOLDS NUMBER ON C_N VERSUS α

The accompanying figure illustrates the effect of Reynolds number on the variation of normal force coefficient with angle of attack for the Pathfinder I model. For this case, all of the effect of Reynolds number is obtained by 9 million. The small difference in angle of attack for a constant lift (approximately 0.1 degrees) between 9.1 and 29.4 million appears to be the result of a small shift in angle of attack zero. This is being evaluated.

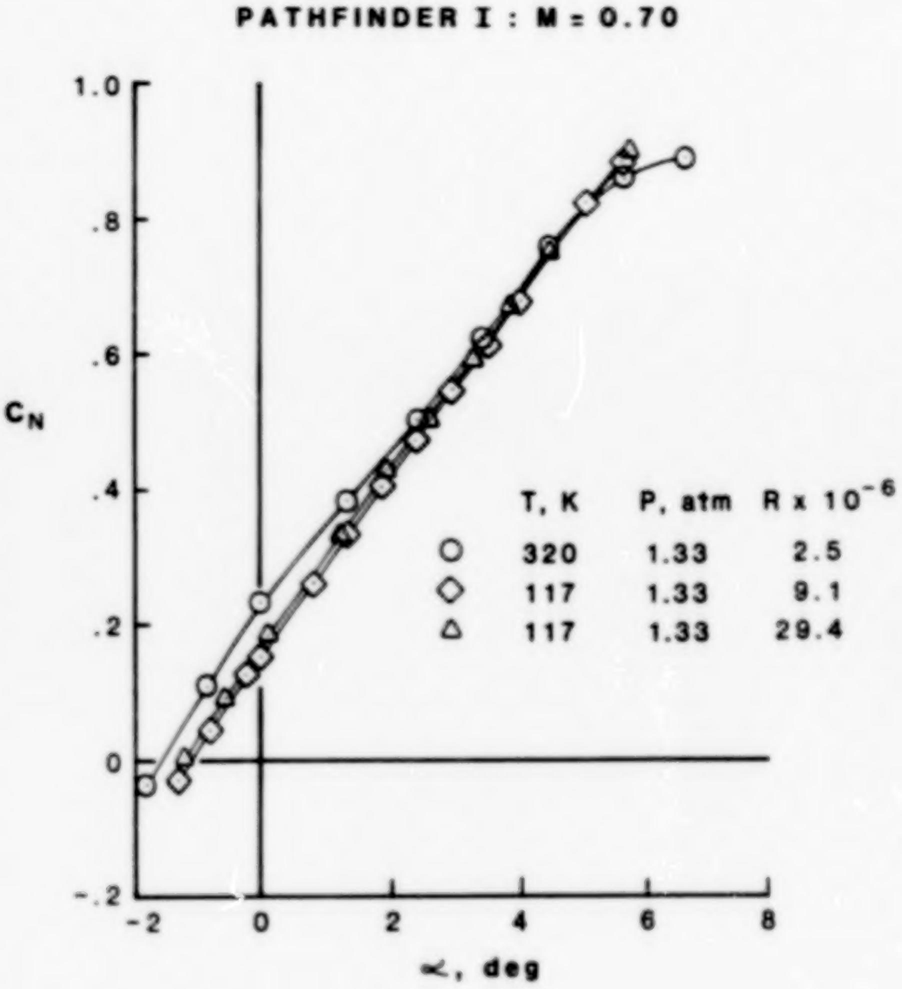

EFFECT OF REYNOLDS NUMBER ON C_M VERSUS α

The accompanying figure illustrates the effect of Reynolds number on the variation of pitching moment coefficient with angle of attack for the Pathfinder I model. As in the case of normal force, essentially all of the effect of Reynolds number is obtained by 9 million. These data also indicate a probable shift in angle of attack between the 9.1 and 29.4 million Reynolds number runs. At the highest angles of attack, a reduction in stability is indicated for the 29.4 million Reynolds number due to aeroelastic effects on the swept wing at 4 atm stagnation pressure.

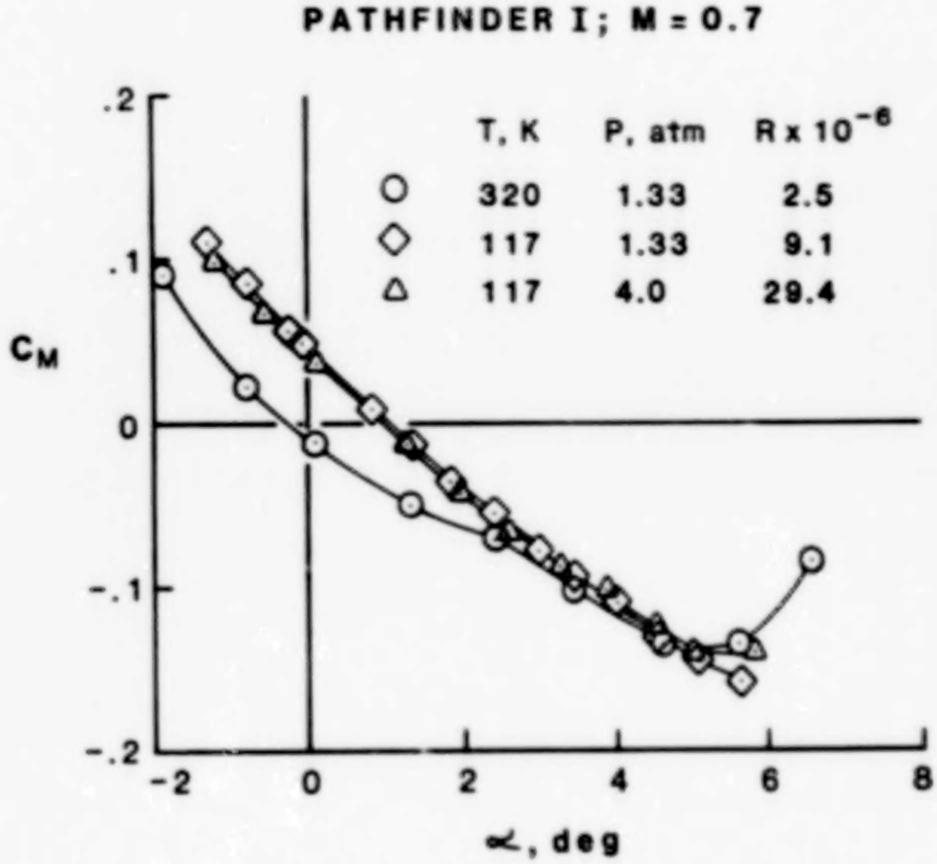
PATHFINDER I; M = 0.7

EFFECT OF REYNOLDS NUMBER ON C_M VERSUS C_N

The accompanying figure illustrates the effect of Reynolds number on the variation of pitching moment coefficient with normal force coefficient for the Pathfinder I model. The near perfect agreement between the data at 9.1 and 29.4 million Reynolds number indicates no change in load distribution between the two cases. This supports the earlier statements that the differences in normal force and moment with angle of attack are most likely due to a small shifts in angle of attack zero between the two runs. The reduction in stability due to aeroelastic effects is readily apparent for the case at 4 atm stagnation pressure.

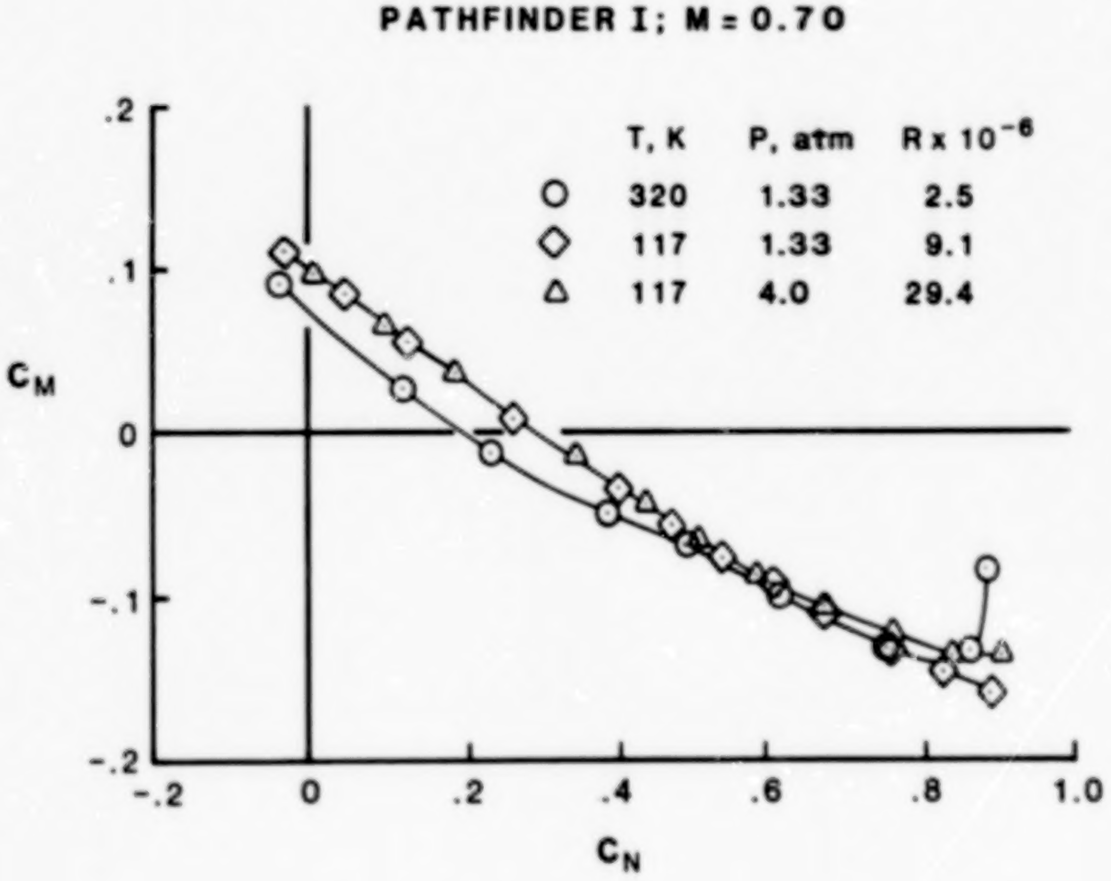

SUMMARY

- The NTF has been operated to design condition of 120 million Reynolds number at a Mach number of 1.0.
- All systems have been checked out except plenum isolation valves; modifications are being made to heaters on the actuators.
- Initial steady-state calibration indicates excellent steady flow characteristics.
- The first test of the Pathfinder I model indicated significant Reynolds number effects.
- Some effects of temperature on instrumentation were obtained. The cause of these effects is being evaluated.

D16

N88-14942

BOUNDARY LAYER TRANSITION

516-34

117240

13P.

L. Maestrello
NASA Langley Research Center
Hampton, Va

A. Bayliss
EXXON Corporate Research Science Laboratories
Annandale, NJ

S. M. Mangalam
Analytical Services & Materials, Incorporated
Hampton, Va

M. R. Malik
High Technology Corporation
Hampton, Va

PRECEDING PAGE BLANK NOT FILMED

PAGE 332 INTENTIONALLY BLANK

[redacted]

ABSTRACT

The boundary layer stability, its active control by sound and surface heating and the effect of curvature are studied numerically and experimentally for subsonic flow. In addition, the experimental and flight test data are correlated using the stability theory for supersonic Mach numbers.

Active transition fixing and feedback control of boundary layer by sound interactions are experimentally investigated at low speed over an airfoil. It is shown that a nonintrusive narrow heating strip causes abrupt changes in velocity profile and triggers instant transition at favorable pressure gradients. Sound interaction at normal incident angles produces significant reduction in velocity perturbations in the region of transition.

Numerical simulation of active control by surface heating and cooling in air shows that by appropriate phase adjustment a reduction in the level of perturbation can be obtained. This simulation is based on the solution of two-dimensional compressible Navier-Stokes equations for a flat plate.

Görtler vortices are studied experimentally on an airfoil in the Low Turbulence Pressure Tunnel (LTPT). The flow pattern is visualized using the sublimating chemical technique and data are obtained using a three component laser velocimeter. It is observed that the vortex wavelength is preserved in the streamwise direction but varies with the Görtler number as predicted by linear stability theory.

The effect of curvature on swept leading-edge stability on a cylinder is numerically studied. The results suggest that transition is dominated by traveling disturbance waves and that the wave with the greatest total amplification has an amplitude ratio of e^{11}. Without the curvature this ratio is increased to e^{17}.

Experimental data from the "quiet" supersonic tunnel and flight tests are analyzed using linear compressible stability theory. The data are obtained on a 5-degree half angle cone with unit Reynolds numbers between 9 to 27 million. The analysis shows that transition could be correlated by the e^N method with N in the range of 9 to 11.

ACTIVE CONTROL OVER AN AIRFOIL

This presentation describes an experiment on active control over an airfoil surface in air. This experiment was conducted at CALTECH where Liepmann et al. (ref. 1) in an earlier experiment demonstrated flow control by active surface heating in water.

Two concepts of control were investigated. The first was active transition fixing by surface heating in the region of favorable pressure gradient to prevent laminar separation at high angles of attack. In this region the flow is highly receptive to surface heating and one can trigger small or large amplitude disturbances as well as trigger instant transition with a single control element shown schematically in the upper part of the figure.

The second control concept investigated was the interaction of sound at near normal incidence with transitional flow over the airfoil to reduce amplitude of the fluctuations.

METHODS OF CONTROL

Control by active surface heating - to prevent separation at high angle of attack

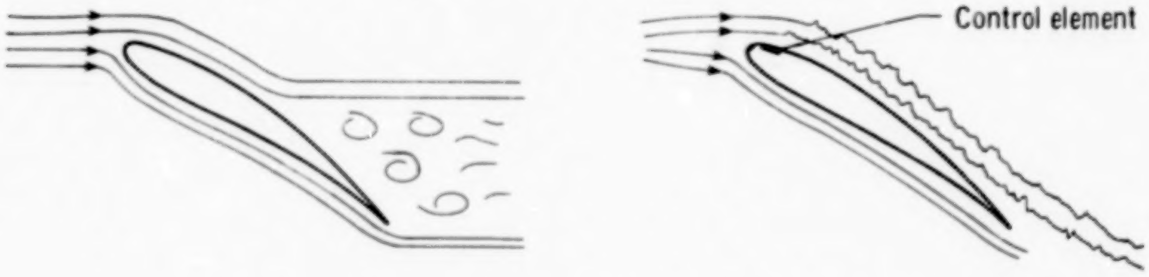

Control by sound - to reduce amplitude perturbation at transition

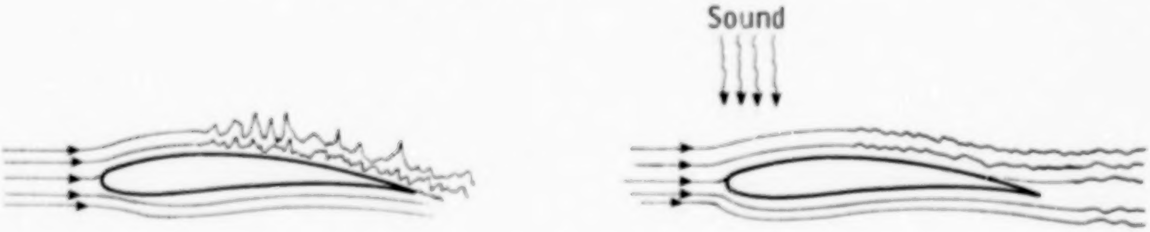

RESULTS

The photograph (next page) on the top left shows a view of the airfoil with two sets of surface heaters mounted flush with the surface - one each in the favorable (near leading edge) and unfavorable pressure gradient (downstream) regions. The experiment was conducted at freestream velocities up to 12 m/s with corresponding Reynolds number of 3.6×10^6 per meter.

Active transition fixing was accomplished by exciting the flow with a wave packet input to the heaters (HO) located near the leading edge. The output response was recorded by a hot-wire (HW) located downstream. The velocity perturbation as a function of time is shown in the bottom left picture where abrupt changes indicate instant transition. Similar input to the heaters located in the unfavorable pressure gradient region showed only marginal effects. This shows that the flow is receptive to outside disturbances only in the region of favorable pressure gradient.

The figures on the right show the effectiveness of boundary layer control by sound interactions in the region of transition. The sound was produced by a speaker mounted in the wall of the tunnel above the airfoil. The speaker was driven by a feedback loop between the heater input and hot-wire output. The top picture shows the uncontrolled response, while the bottom one shows the feedback controlled response. It is evident that dramatic amplitude reduction is achieved. Similar reduction was noticed with pure tone and random signal. It is observed that at the control output the amplitude of the lower frequencies is reduced drastically at the expense of an increase in the background disturbance which is dominated by higher frequencies. Thus, it is clear that the flow will not return to its uncontrolled state.

In conclusion, these methods are powerful and practical techniques of flow control. Nonintrusive transition fixing could be utilized to prevent separation in ducts as well as augment maximum lift on airfoils. Interaction of sound with the flow is an effective way to control amplitude growth even for transitional flow.

ORIGINAL PAGE IS
OF POOR QUALITY

RESULTS

VIEW OF THE AIRFOIL

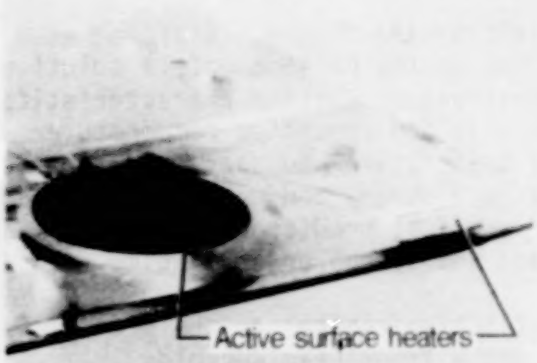
Active surface heaters

PERTURBATION AT TRANSITION

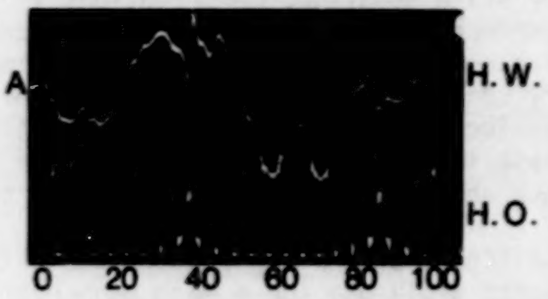

ACTIVE TRANSITION FIXING

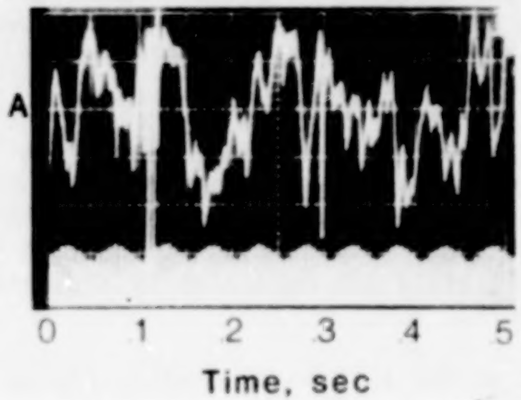

PERTURBATION CONTROLLED BY SOUND

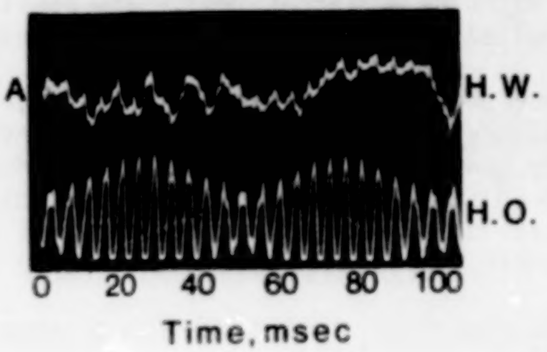

AMPLITUDE CONTROL BY HEATING AND COOLING

This figure concerns a numerical study of the concept of active control by growing disturbances in an unstable, compressible boundary layer by using time periodic, localized surface heating and cooling. The study is based on solving 2-D, compressible, time dependent Navier-Stokes equations on a flat plate.

The computational domain is shown on the left of the figure. Starting with a steady state solution, perturbations in the form of the Orr-Sommerfeld solution are superimposed at inflow. At the top and downstream boundaries characteristics radiation conditions are used. At the plate no slip and specified temperature boundary conditions are used. For control, the temperature boundary condition is modified locally over the width of the strip using a steady and unsteady component with phase input. The method of solution is an explicit predictor-corrector technique which is fourth order accurate in space and second order in time.

The figure on the right shows the effect of active control on the growth of disturbance amplitude for a Mach number of 0.4 and a freestream Reynolds number/foot of $3x10^5$. The disturbance growth is plotted in terms of the RMS of mass flux versus Reynolds number based on the local displacement thickness. The control strip of width equal to three times the displacement thickness is located at the Reynolds number of 1263. The amplitude growths are compared between the uncontrolled and controlled cases with heating and cooling.

Since steady state heating is destabilizing in air while cooling stabilizes, it is necessary to use a 180° phase difference between heating and cooling for unsteady control. The figure shows a reduction in the amplitude growth for both heating and cooling compared to the uncontrolled case. A reduction of about 6% is indicated for heating with an overheat of 1000°F, and a 12% reduction is indicated with cooling for a temperature difference of 300°F.

The numerical simulation demonstrates that either heating or cooling can be used effectively to reduce the level of growing disturbances in a boundary layer. A larger reduction can be obtained by use of multiple control strips placed successively downstream with appropriate phase adjustment.

AMPLITUDE CONTROL BY HEATING AND COOLING

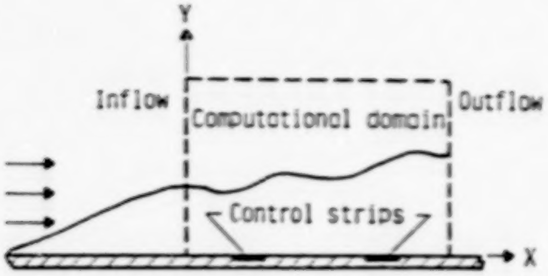
Y
Inflow
Computational domain
Outflow
Control strips
X

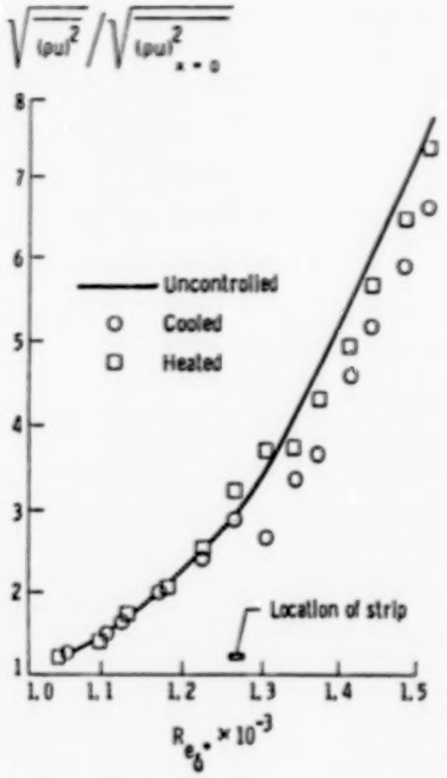

- Solve 2-D unsteady, compressible Navier - Stokes equations
- Control by localized, periodic surface heating and cooling
- $M_\infty = 0.4$, $Re/ft = 3 \times 10^5$

GÖRTLER VORTEX EXPERIMENT

Görtler vortices arise in boundary layers along concave surfaces due to centrifugal effects and are one of three known types of flow instabilities that lead to boundary layer transition. Advanced laminar-flow control (LFC) supercritical airfoils have concave curvature near the leading edge of the lower surface, as shown in the schematic diagram for the airfoil model. Pairs of counter-rotating, streamwise vortices, well known as Görtler vortices, develop in the concave region as shown in the accompanying sketch for the vortex flow pattern. Here, U_∞ is the external flow velocity, δ is the boundary layer thickness parameter, r is the radius of curvature, and λ is the Görtler-vortex wavelength.

The 1.83-meter chord airfoil model shown in the schematic diagram was tested in the NASA Langley Low Turbulence Pressure Tunnel (LTPT). Görtler vortices were observed using a sublimation technique and velocity measurements were made with Laser Velocimetry. The airfoil model has a concave test region extending from 17.5% chord to 27.5% chord. The attached laminar boundary layer was insured by means of suction through a 0.11 × 0.76-meter perforated titanium panel located in the compression part of the concave region. The 10% chord flap at the trailing edge was used to adjust the leading-edge stagnation point. The chord Reynolds number was varied from 1.0 million to 5.9 million, yielding a Görtler number range of 29 to 46.

MODEL SCHEMATIC DIAGRAM

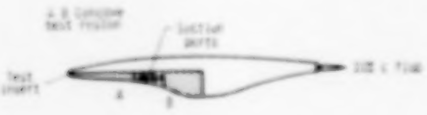

GÖRTLER VORTEX FLOW PATTERN

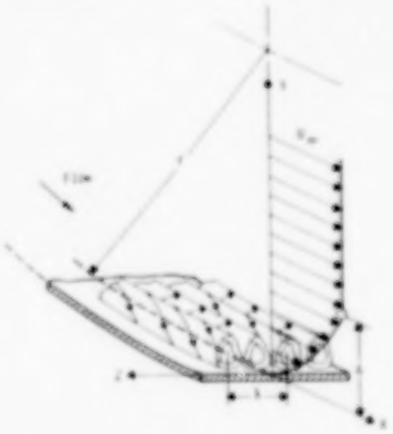

ORIGINAL PAGE IS
OF POOR QUALITY

RESULTS

A thin layer of solid white bephenyl material was sprayed on the black model surface to visualize the flow pattern developed due to the presence of Görtler vortices in the boundary layer along the concave test region. The flow pattern is made visible due to the differential surface shear stress distribution under the layer of counter-rotating pairs of streamwise vortices. A set of black and white bands constitutes a pair of vortices and represents the wavelength of these vortices. A representative flow pattern corresponding to a Görtler number of 36 is shown in the accompanying photograph (flow is from bottom to top in the photograph).

Laser velocimeter measurements of streamwise velocities at different chord locations as well as at various heights above the surface were used to determine the vortex wavelength. A fixed, essentially uniform, vortex spacing was observed in the concave zone by both flow visualization and laser velocity measurements at each external flow condition. As in all previous experiments, the dimensional wavelength was preserved in the flow direction, but unlike the earlier experiments, the wavelength was observed to vary appreciably with Görtler number. The variation in the wavelength with Görtler number is shown in the lower figure where it is compared with results based on linear theory obtained by computing wavelength corresponding to maximum amplification conditions.

FLOW VISUALIZATION

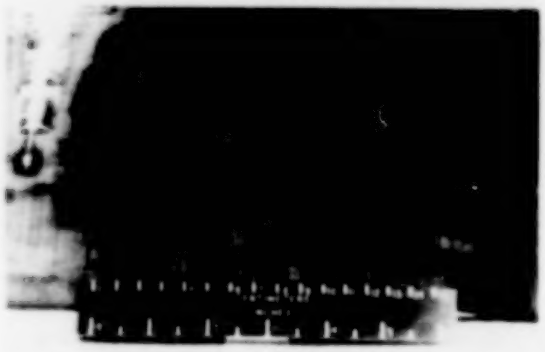

VARIATION OF DIMENSIONAL WAVELENGTH
WITH GORTLER NUMBER, COMPARISON WITH THEORY

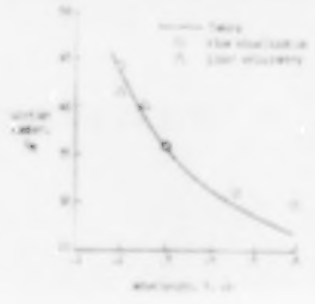

CALIBRATION OF STABILITY THEORY FOR TRANSITION PREDICTION

Linear compressible stability theory was used to analyze supersonic transition data for 10° sharp tip cones at zero angle of attack. Recent flight data at $M = 1.2$ to 1.9 for a cone mounted on the nose of an F-15 aircraft were used. Data obtained in the Langley Mach 3.5 Pilot Low-Disturbance Tunnel were also used. Integration of theoretical disturbance amplification rates for Tollmien-Schlichting (T-S) waves along the cone from the neutral stability point to the measured location of transition onset yields the amplification N factor.

The Görtler instability is usually dominant on concave walls and is observed as small counter-rotating vortices aligned with the flow. Transition was measured for laminar boundary layer flow on the concave walls of quiet wind tunnel nozzles where the local Mach numbers varied from 1.6 to 4.9. The N factors for both types of instabilities varied from about 9 to 11 as illustrated in the next figure.

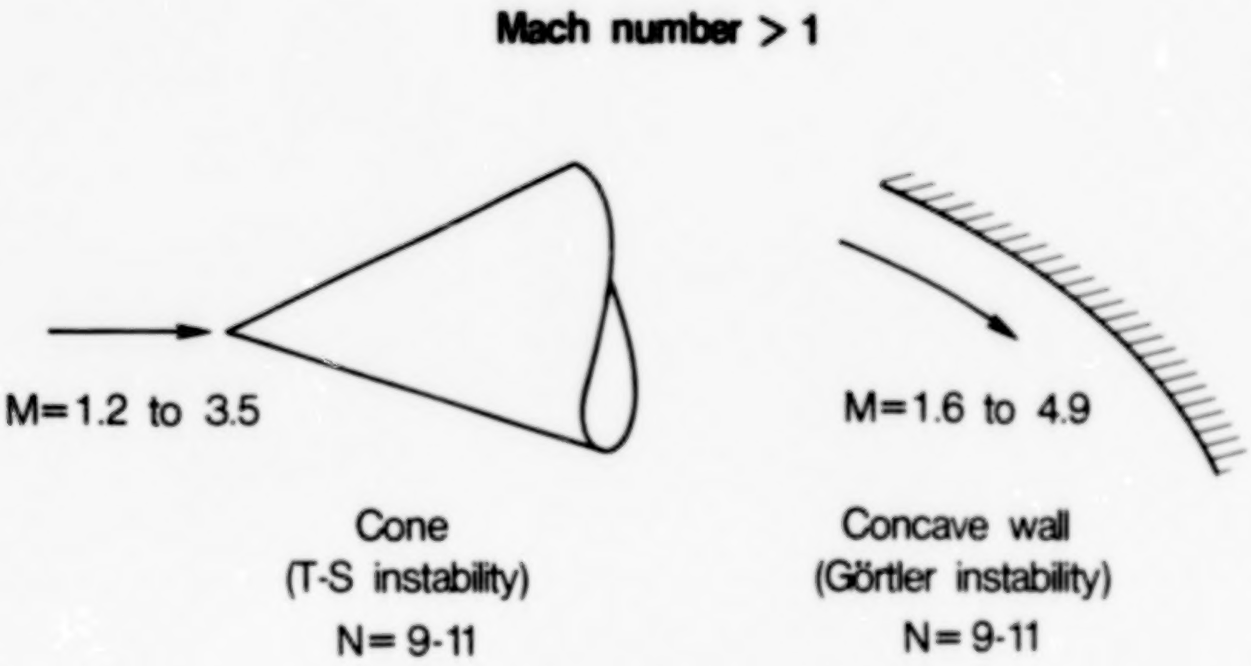

$$N = \ln A/A_o = \int \text{amplification rate}$$

(REF. 2)

The plot on the left shows the envelope curves N as a function of the dimensionless frequency parameter ($F = 2\pi f\ \nu_e/U_e^2 \times 10^5$) for T-S waves on cones. The maximun amplification occurs at the peak of the curves where N varies from about 9 to 11 at the measured location of transition for both the flight data and the quiet wind tunnel data. This agreement indicates that the low-disturbance environment of flight is correctly simulated in this tunnel.

The plot on the right shows the variation of N with the ratio of vortex wavelength (or vortex width) to boundary layer thickness for the Görtler instability on the concave wall of the Mach 3.5 Pilot Low-Disturbance Wind Tunnel over a range of unit Reynolds numbers. Again, the peak values of N vary from about 9 to 11 at the measured locations of transition. Note that transition always occurred when the vortex wavelength was about the same as the local boundary layer thickness.

$N = \ln A/A_0$

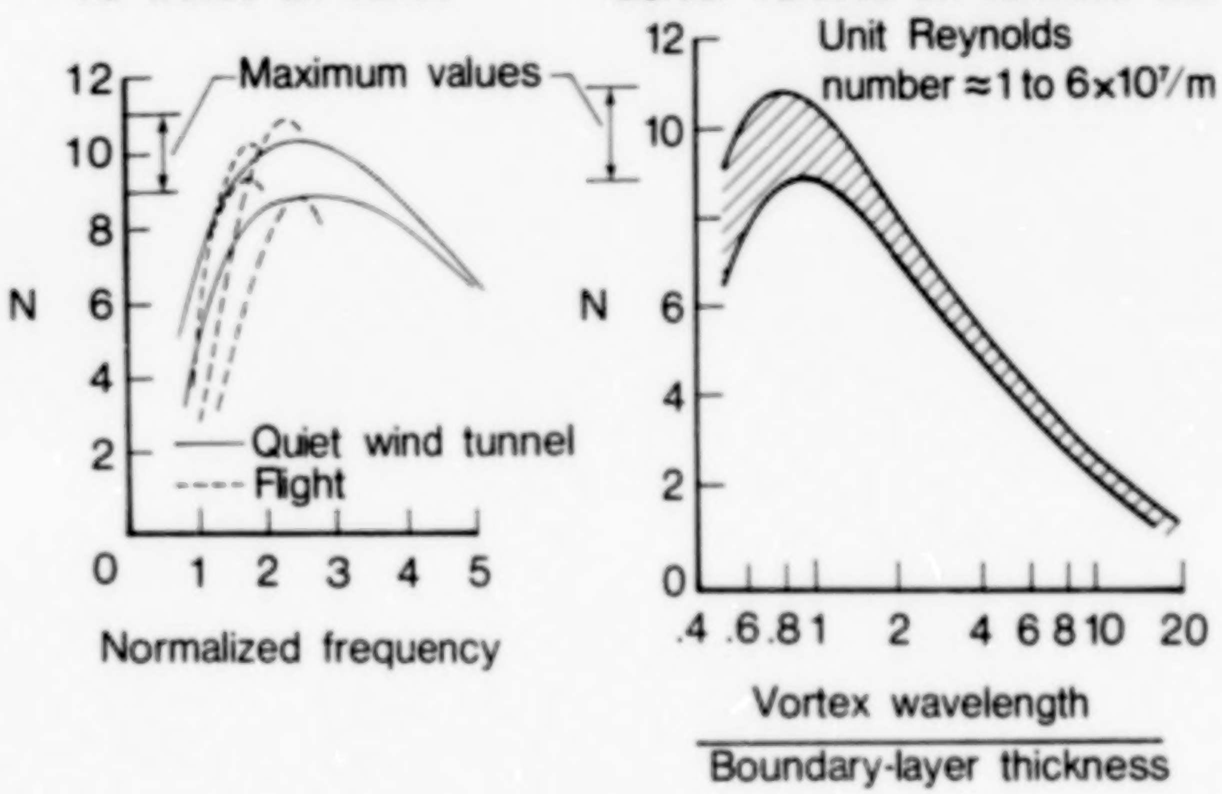

CURVATURE EFFECTS ON SWEPT LEADING-EDGE FLOW STABILITY

The stability of the three-dimensional laminar boundary layer on the windward face of a long cylinder was solved by a computational scheme that includes the body curvature R_1 and the streamline curvature R_2. The maximun growth rates are integrated to the measured locations of transition on a cylinder in a low-speed wind tunnel at velocities from 25 to 180 ft/sec. When the curvature terms are omitted, as in previous investigations, the amplitude ratio was approximately e^{17}. When all curvature terms are properly accounted for, the amplitude ratio is about e^{11} in good agreement with the supersonic results of the two preceding figures as well as with various other types of subsonic flows.

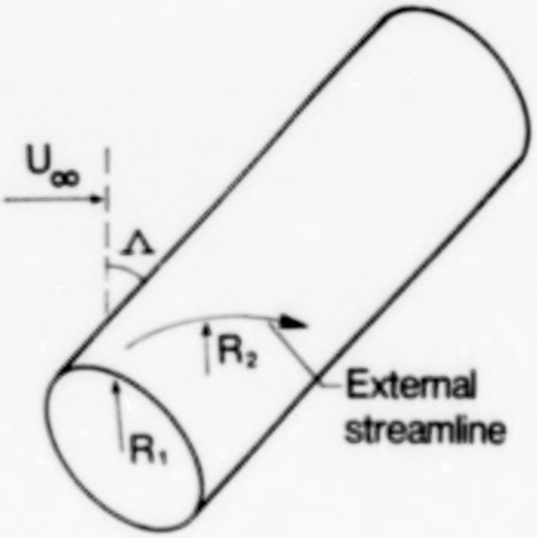

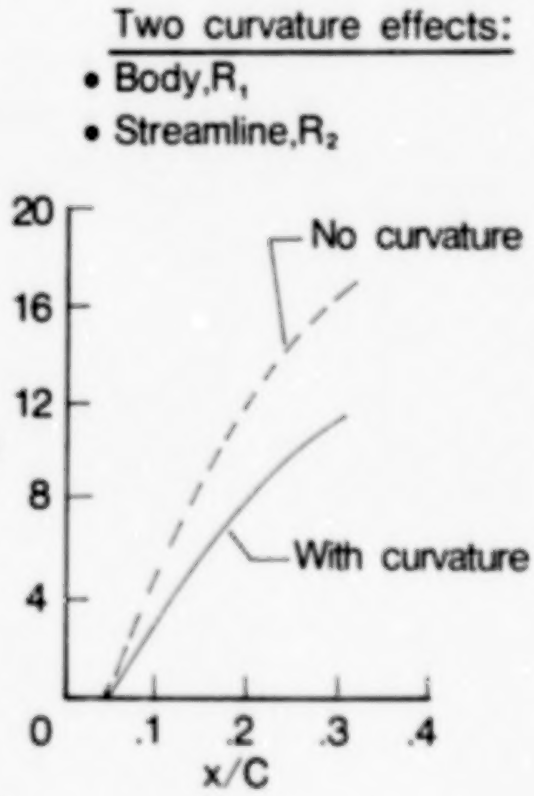

(REF. 3)

REFERENCES

1. Liepmann, H. W. and Nosenchuck, D. M.: Active Control of Laminar Turbulent Transition. J. of Fluid Mechanics, vol. 118, 1982, pp. 201-204.

2. Beckwith, I. E.; Malik, M. R.; and Chen, F. J.: Nozzle Optimization Study for Quiet Supersonic Wind Tunnels. AIAA Paper No. 84-1628, June 1984.

3. Malik, M. R.: Instability and Transition in Supersonic Boundary Layers. ASME Symposium on Turbulent and Laminar Boundary Layers--Their Control and Flow Over Compliant and Other Surfaces, New Orleans, LA, February 12-16, 1984.

BIBLIOGRAPHY

1. Maestrello, L.: Active Transition Fixing and Control of the Boundary Layer in Air. AIAA Paper 85-0564, March 1985.

2. Bayliss, A.; Maestrello, L.; Parikh, P.; and Turkel, E.: Numerical Simulation of Boundary Layer Excitation by Surface Heating/Cooling. AIAA Paper 85-0565, March 1985.

3. Mangalam, S. M.; Dagenhart, J. R.; Hepner, T. E.; and Meyers, J. F.: The Görtler Instability on an Airfoil. AIAA Paper 85-0491, January 1985.

4. Malik, M. R. and Poll, D. I. A.: Effect of Curvature on Cross-Flow Instability. Second IUTAM Symposium on Laminar-Turbulent Transition, Novosibirsk, USSR, July 9-13, 1984.

D17

N88-14943

WALL TURBULENCE CONTROL

517-09

117241

14P.

Stephen P. Wilkinson, A. Margrethe Lindemann, George B. Beeler,
Catherine B. McGinley, Wesley L. Goodman, and R. Balasubramanian
NASA Langley Research Center
Hampton, Virginia

PRECEDING PAGE BLANK NOT FILMED

PAGE 346 INTENTIONALLY BLANK

Abstract

[redacted]

A variety of wall turbulence control devices which have been experimentally investigated are discussed; these include devices for burst control, alteration of outer flow structures, large eddy substitution, increased heat transfer efficiency and reduction of wall pressure fluctuation intensity.

Control of pre-burst flow has been demonstrated with a single, traveling surface depression which is phase-locked to elements of the burst production process. It was shown that the near-wall streamwise flow could be accelerated and thereby reduce the tendency of a retarded streamwise velocity profile to inflectionally break down (burst).

Another approach to wall turbulence control is to interfere with outer layer "coherent structures." Studies have shown that a cylinder adjacent to a flat plate produces a modified Karman vortex street. If the cylinder is sufficiently close to the plate, one component of shed vorticity will be suppressed altogether. Such a device in the outer part of a boundary layer was shown to suppress turbulence and reduce drag by opposing both the mean and unsteady vorticity in the boundary layer.

Large eddy substitution is a method in which streamline curvature (known to suppress turbulence) is introduced into the boundary layer in the form of streamwise vortices. Several systems of streamwise vortices were generated in a turbulent boundary layer. It was shown that boundary layer entrainment rates were reduced below normal flat plate values and indicated the successful suppression of turbulence.

Riblets, which have already been shown to reduce turbulent drag, have also been shown to exhibit superior heat transfer characteristics. Heat transfer efficiency as measured by the Reynolds Analogy Factor was shown to be as much as 36 percent greater than a smooth flat plate in a turbulent boundary layer.

Large Eddy Break-Up devices (LEBU) which are also known to reduce turbulent drag have been shown to reduce turbulent wall pressure fluctuation.

Wall Turbulence Control

Research conducted by the Viscous Flow Branch/High-Speed Aerodynamics Division has shown that it is now possible to reduce or enhance a number of turbulent boundary layer flow properties. This presentation will review our progress in the wall turbulence control area starting with new uses for existing turbulence control devices and following with a variety of new concepts aimed primarily at turbulent, viscous drag reduction. New uses for existing devices include riblets used as high-efficiency heat transfer surfaces and LEBU's (large eddy break-up device) used to control wall pressure fluctuations. New concepts for drag reduction include Large Eddy Substitution which shows that the favorable influence of wall curvature on turbulence may also be obtained with streamline curvature on a flat plate; Opposing Unsteady Vorticity which shows the feasibility of altering large-scale structures in the boundary layer by introducing opposite sense vortices; and Active Phase-Locked Wall Deformation which shows the possibility of controlling turbulent wall bursting through flow-triggered, electromagnetically actuated wall motion.

- Reduce or enhance properties of turbulent wall boundary layers (drag, heat transfer, noise, etc.)
- New uses of existing devices
    - Riblet: efficient heat transfer surface
    - LEBU: reduces wall pressure (density) fluctuations
- New concepts for drag reduction
    - Large eddy substitution
    - Opposing unsteady vorticity
    - Active phase-locked wall deformation

Heat Transfer Efficiency of Riblet Drag Reducing Surfaces

In addition to the drag reducing property of a riblet surface, it also allows for greater heat transfer efficiency than a smooth or rough surface. This finding is based on low-speed heat transfer and drag measurements on a flat, heated riblet model. Heat transfer efficiency is defined by the Reynolds analogy factor. Potential application for this finding is in the field heat exchanger design where an increase in the Reynolds analogy factor allows for multiparameter optimization studies (heat transfer, pumping power, size, weight, etc.).

- Riblets show higher heat transfer efficiency than smooth or rough surfaces
- Efficiency determined by experimentally measuring Reynolds Analogy factor

  ($2\ St/C_f$ St = Stanton #, C_f = skin friction coefficient)
- Application to heat exchanger optimization/efficiency

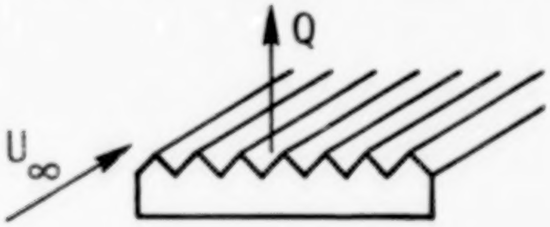

Reynolds Analogy Factor for Riblets

This plot shows the results of measurement of the Reynolds analogy factor for the riblet heat transfer model as well as a reference smooth flat plate. The ordinate is the Reynolds analogy factor (the ratio of two times the Stanton number to the skin friction coefficient). The abscissa is the Reynolds number based on the stream velocity and momentum thickness. As can be seen, the flat plate data remain roughly constant at approximately 1.2 which is the usually quoted value for a flat plate in air. Two types of riblet surfaces, both exhibiting drag reduction, were tested and have Reynolds analogy factors 30 percent higher than the smooth flat plate.

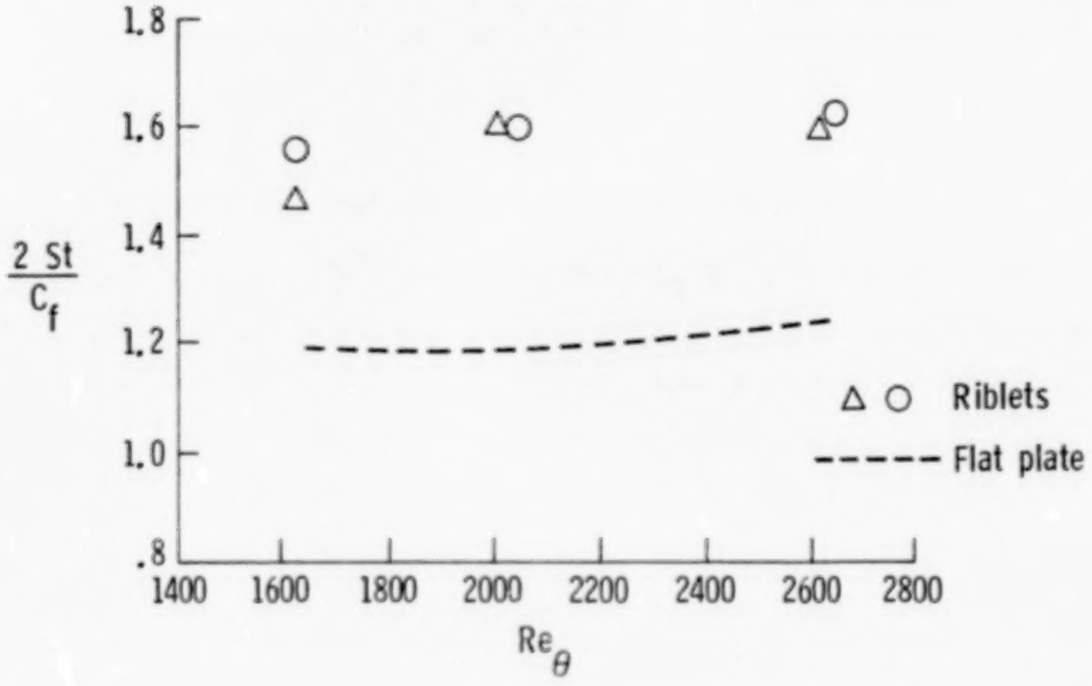

Effect of LEBU on Wall Pressure Spectra

LEBU's affect turbulent, viscous drag apparently by their effect on the large-scale structures in the outer part of the boundary layer. Since these same large-scale structures are responsible for a significant portion of indicated wall pressure fluctuation intensity, reduction in the large scales should cause a similar reduction in wall pressure intensity. To test this hypothesis, a pinhole microphone was used to measure wall pressure spectra downstream of a tandem LEBU at the streamwise location of maximum skin friction reduction. It was found that in the frequency range of the large eddies, the fluctuation intensity was reduced by 25 percent below the reference smooth flat plate level. This finding has potential application to boundary layer noise reduction on aircraft allowing for reduced weight of sound insulation. Density fluctuation intensity should also be reduced to allow for improved performance of aircraft radar domes and laser or IR windows.

- Expect change in wall pressure due to breakup of large scale structures
- Measured wall pressure (P'_W) spectra downstream of LEBU
- P'_W reduced 0(25%)
- Applications: Reduced self noise on sonar domes
  Improved laser and IR window performance
  Reduced weight of sound insulation on aircraft

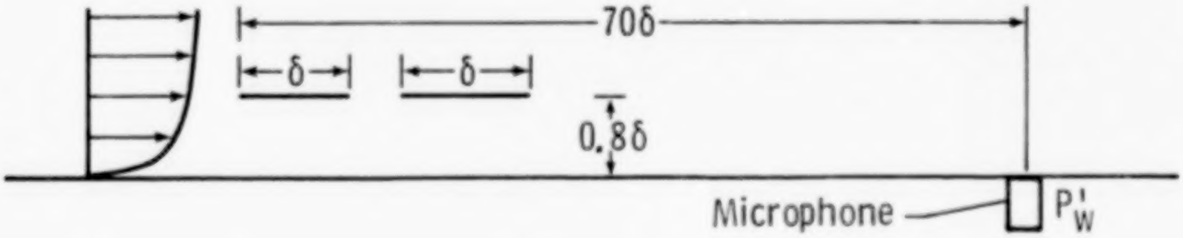

Wall Pressure Spectra Downstream from LEBU

This plot shows the results of the LEBU wall pressure spectral measurements. The ordinate is the mean-square spectral intensity; the abscissa is frequency. For data above 2000 Hz and less than 15000 Hz, there is a clear drop in mean-square spectral intensity. Above 15000 Hz, the LEBU data rejoin the reference flat plate data indicating that the LEBU is affecting the large-scale structures. Since the diaphragm-type microphone beneath the pinhole was sensitive to structural vibrations, the indicated pressure spectra (actually due to vibration) were determined by covering the pinhole during a run. Results shown in the figure indicate that the data below 2000 Hz are excessively distorted by structural vibration and are not correct.

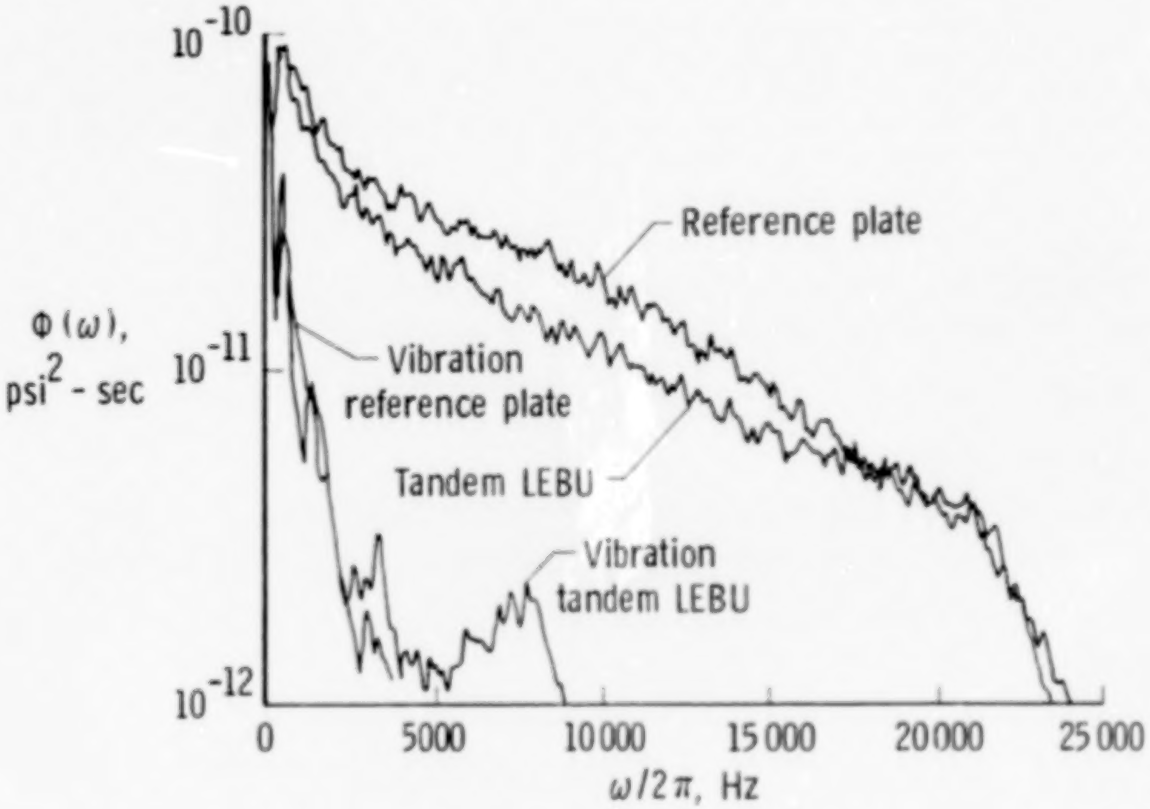

Large-Eddy Substitution via Vortex Cancellation

The large-eddy substitution concept is an extension of turbulence suppression by convex wall curvature. By introducing streamline curvature (as opposed to wall curvature) into turbulent wall flows via co-rotating streamwise vortices, similar turbulence suppression may be possible. The idea is to "wrap-up" and suppress the turbulence in vortex-induced curvature over a streamwise processing region and then remove the vortices. Two techniques were studied: vortex cancellation and vortex self-annihilation. Vortex cancellation employs widely spaced rectangular strakes to generate a spanwise array of co-rotating wall vortices. Opposite sign generators (i.e., unwinders) are placed 20 boundary layer thicknesses downstream to remove the vortices. Vortex self-annihilation employs closely spaced generators which produce vortices which self-destruct downstream of the generators. To determine the effectiveness of the devices, boundary layer growth was measured to estimate the rate at which free-stream air was entrained by the turbulence into the boundary layer. Lower entrainment rates indicate suppression of turbulence. In each case, the entrainment rate was reduced below flat-plate reference levels. Details of this work are presented in Reference 1.

- Co-rotating, longitudinal vortices used to study effect of streamline curvature (induced by vortex) on turbulent wall flow
- "Wrap-up" turbulence in curvature substituting vortex for turbulence
- Two methods employed:
    - Widely spaced generators with unwinders (cancellation)
    - Closely spaced generators without unwinders (self-annihilation)
- Boundary layer entrainment decreased in both cases

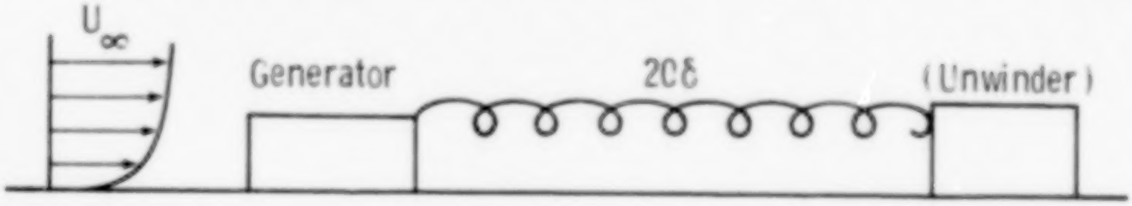

Large-Eddy Substitution

This figure shows the effect of the two techniques of creating and eliminating wall vortices. The left-hand figures demonstrate vortex cancellation. The top figure shows spanwise contours of constant velocity 149 boundary layer thicknesses downstream of the vortex generators without vortex unwinders. The bottom figure shows the same streamwise location with vortex unwinders located 20 boundary layer thicknesses downstream of the generators. As can be seen, the unwinders are very effective in removing the vortices.

The right-hand figures demonstrate the vortex self-annihilation concept. The top figure shows the generated vortices 20 boundary layer thicknesses downstream of the generators. The bottom figure shows the absence of vortices 149 boundary layer thicknesses downstream of the generators due to the self-annihilation process.

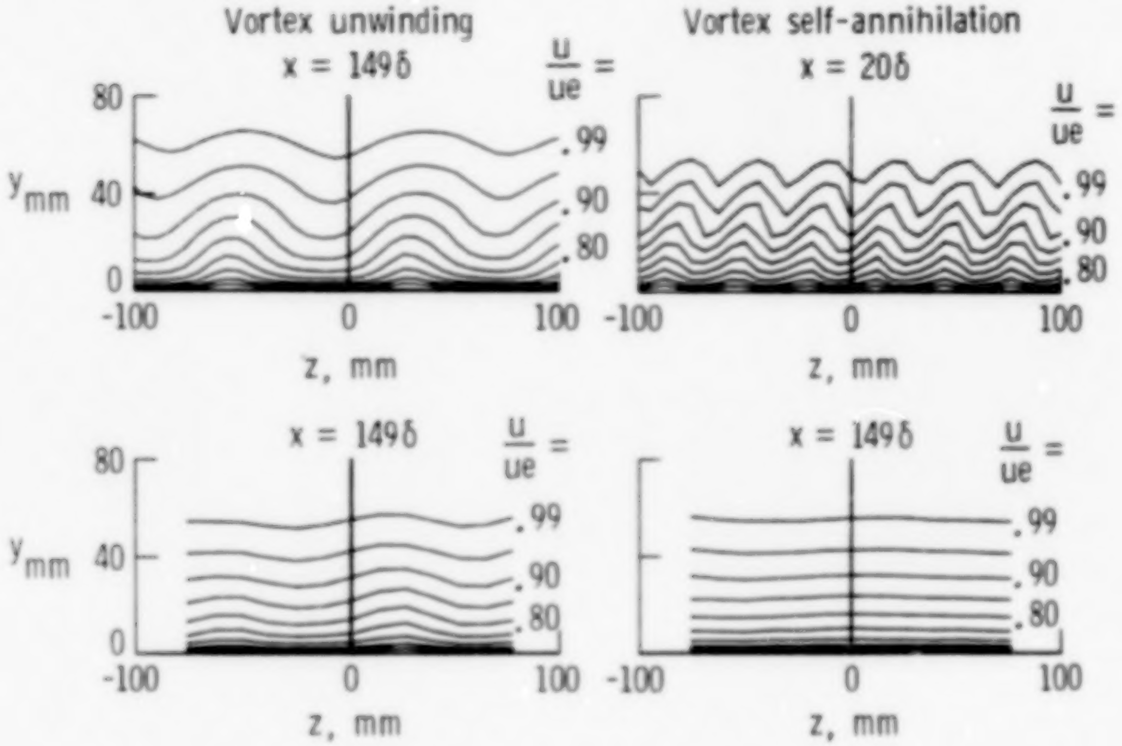
Vortex unwinding

Vortex self-annihilation

Effect of Opposing Unsteady Vorticity on Turbulent Structures in Wall Flows

Coherent structures in the outer part of a wall boundary layer have fluctuating vorticity of the same sign as that of the mean boundary layer. A possible technique for controlling these structures is to introduce vorticity of the opposite sign to counteract the existing coherent structures. A two-dimensional rod in a flow normally produces an alternating vortex pattern downstream of the rod (Karman vortex street). By placing a thin control plate at a proper distance from the rod, one side of the vortex street will be reduced. This method may be used to introduce the vortices required to counteract the coherent structures in the outer part of the boundary layer. Total drag reduction on the order of 25 percent was measured with this technique of which 20 percent was due to the momentum deficit introduced by the device and an additional 5 percent presumably due to turbulence modification by the device. Details of this work are presented in Reference 2.

- Counteract outer layer "coherent structures" by introducing vorticity of opposite sign
- Use Karman vortex street from 2-D rod with one side of street suppressed by control plate
- Viscous drag reduced 0(25%): 20% momentum deficit
  5% turbulence modification

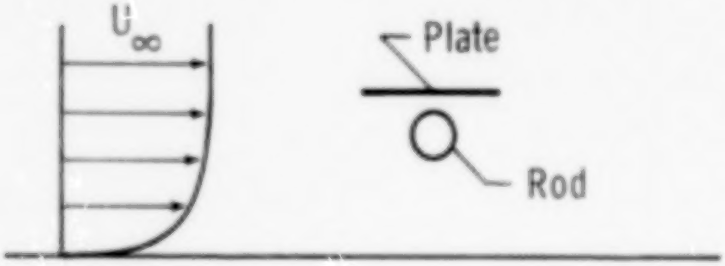

ORIGINAL PAGE IS
OF POOR QUALITY

Production of Control Vortices for Turbulence Modification

This figure shows the effect of the vortex street control plate for a rod in a uniform flow. The arrangement of the device is shown schematically on the left with smoke-wire flow visualization of the downstream vortices on the right. Part A shows the unaltered Karman vortex street. Part B shows the effect of optimum placement of the control plate. Note the reduction in strength of the upper part of the vortex street. Part C shows the effect of placing the control plate too close to the rod. In this case, the rod and control plate act as a single obstacle to the flow.

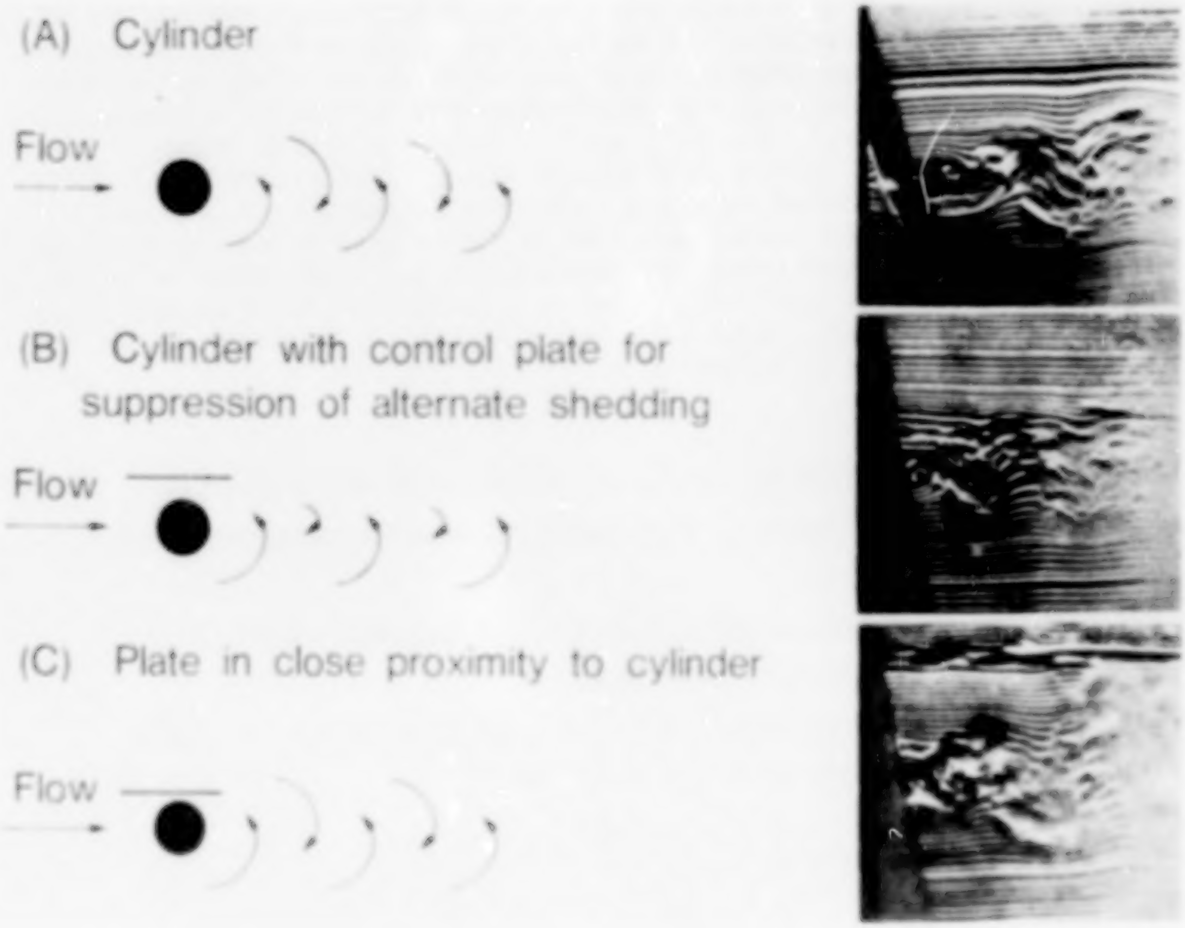
(A) Cylinder
Flow
(B) Cylinder with control plate for suppression of alternate shedding
Flow
(C) Plate in close proximity to cylinder
Flow

Turbulent Burst Control Through Phase-Locked Wall Deformation

Data on coherent structures close to the wall suggest the possibility of controlled wall motion as a means of altering the bursting process. An inflectional instability model of the bursting process was used as a basis for design of the control mechanism. Briefly, the flow model states that low-speed wall streaks and "typical" eddies play a synergistic role in burst production. Wall streaks start the inflection of an initially quiescent, preburst streamwise velocity profile near the wall and the moving, adverse pressure gradient associated with the "typical" eddy adds to the inflection causing turbulent breakdown (bursting). Calculations have shown that a traveling wall depression phase-locked on the low-pressure region beneath a convecting "typical" eddy will raise the local pressure (i.e., decreasing the moving adverse pressure gradient) and decrease the slope of the instantaneous velocity profile. An experimental model was constructed using a flexible, ferromagnetic membrane with discrete, electromagnetic actuators to create the traveling wall depression. Ideally, wall triggering should occur at the simultaneous detection of both a wall streak and a "typical" eddy. A noisy tunnel environment prohibited detection pressure signature of a "typical" eddy. Therefore, wall shear stress was used as the trigger signal to evaluate the effectiveness in stabilizing the preburst flow. No data on actual bursting was taken. (This approach is currently restricted to low-speed flows due to the limited frequency response of most wall motion actuators.) Details of this work are presented in Reference 3.

- Stop turbulent bursting by stabilizing inflectional pre-burst flow
- Based on cancelling moving, instantaneous adverse pressure gradient due to typical eddy
- Calculations of vortex convecting in laminar boundary layer show favorable effect of phased-locked wall motion
- Experiment with electromagnetically actuated wall membrane shows stabilizing effect of phase-locked wall motion

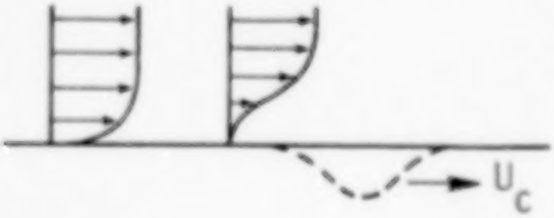

Streamwise Velocity Fluctuation Component for Phase-Locked Wall

In order to determine whether the traveling wall depression model could stabilize preburst flow, wall motion was triggered on various levels of wall shear-stress measured at a point just upstream of the wall device. A depression convection speed of 0.75U was used. Hot-wire anemometry was used to measure turbulent velocity fluctuations above the first actuator in the wall device. These data were then ensemble averaged over three short time intervals for 250 cycles of wall motion. The time intervals or windows were chosen to bracket the time during which the wall was depressed immediately beneath the hot-wire probe. The figure shows the normalized, ensemble-averaged, streamwise velocity fluctuation component for the three time windows both with and without wall motion. It is evident in window 2 that the effect of the wall motion is to accelerate the streamwise flow near the wall. The first window shows no significant effect of secondary, propagating wall waves (caused by the impulsively started wall motion) which travel faster than the wall depression. The third window shows that wall continued to oscillate after the wall depression passed. The primary finding, however, is that the traveling wall depression can stabilize preburst flow.

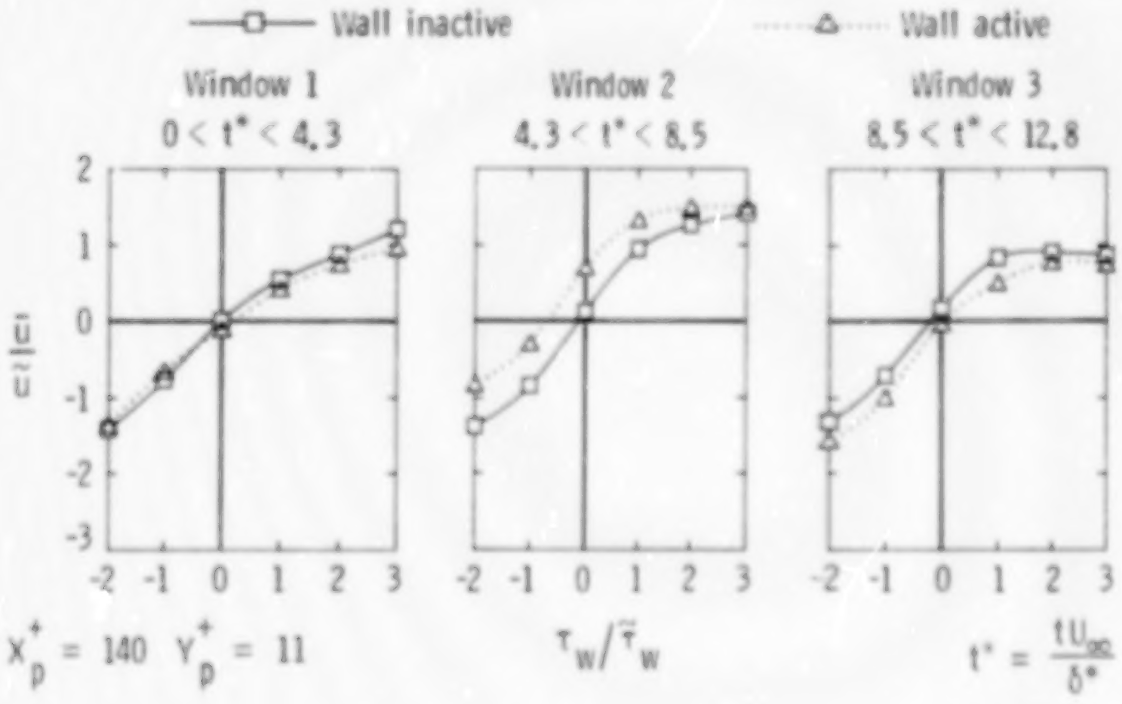

CONCLUSION

We have shown in these initial experiments that wall turbulence can be reduced or amplified by a variety of techniques including embedded bodies, non-planar wall geometries and phase-locked control. The payoff of such control includes drag reduction, reduced sound insulation, increased heat exchanger efficiency, improved performances of laser and IR windows and reduced self noise on sonar domes.

References

1. McGinley, C. B.; and Beeler, G. B.: Large-Eddy Substitution via Vortex Cancellation for Wall Turbulence Control. AIAA Paper 85-0549, March 12-14, 1985.

2. Goodman, W. L.: The Effect of Opposing-Unsteady Vorticity on the Turbulent Structures in Wall Flows. AIAA Paper 85-0550, March 12-14, 1985.

3. Wilkinson, S. P.; and Balasubramanian, R.: Turbulent Burst Control Through Phase-Locked Traveling Surface Depressions. AIAA Paper 85-0536, March 12-14, 1985.

D18

N88-14944

S18-34

117242

14P.

SEPARATED FLOW

W. L. Sellers, III,
R. E. Dunham, Jr.,
W. L. Goodman,
F. G. Howard,
R. J. Margason,
D. H. Rudy,
C. L. Rumsey,
H. P. Stough, III, and
J. L. Thomas
NASA Langley Research Center
Hampton, Virginia

[redacted]

Abstract

This paper provides a brief overview of flow separation phenomena. Langley has many active research programs in flow separation related areas. Most of these programs were reviewed for inclusion in this paper. Three cases were selected which describe specific examples of flow separation research. In each example, a description of the fundamental fluid physics and the complexity of the flow field is presented along with a method of either reducing or controlling the extent of separation. The following examples are discussed in the present paper: (1) flow over a smooth surface with an adverse pressure gradient; (2) flow over a surface with a geometric discontinuity; and (3) flow with shock-boundary layer interactions. These results will show that improvements are being made in our understanding of flow separation and its control.

Flow Separation

Flow separation is an important fluid dynamic problem which can cause a drastic reduction in the performance of aircraft, diffusers, pumps and compressors. The resulting flow fields are also some of the most complex to measure since they typically include regions with steep velocity gradients and unsteadiness as well as bidirectional or reverse flow.

This paper provides a brief overview of flow separation phenomena. Langley has many active research programs in flow separation related areas. Most of these programs were reviewed for inclusion in this paper. Three cases were selected which describe specific examples of flow separation research. In each example, a brief description of the fundamental fluid physics and the complexity of the flow field is presented along with a method for either reducing or controlling the extent of separation. The following examples are discussed in the present paper: (1) flow over a smooth surface with an adverse pressure gradient; (2) flow over a surface with a geometric discontinuity; and (3) flow with shock-boundary layer interactions.

The classical description of flow separation usually states that, in general, for separation to occur the fluid must be subjected to an adverse pressure gradient (increasing pressure) with laminar or turbulent viscosity effects. The energy in the low momentum fluid in the boundary layer is expended in overcoming the rise in pressure. Eventually the surface streamline reaches a point where the shear stress at the wall reaches zero ($\frac{\partial u}{\partial y} = 0$) and the streamline breaks away from the surface. This description represents a considerable over-simplification of the process and may only be applicable to perhaps the simplest of two-dimensional steady separation cases. The modern concept of separation describes the process as beginning intermittently at a given location with the actual streamline detachment point occurring over a zone.

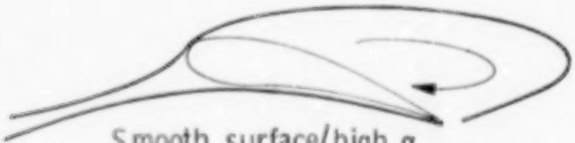

Smooth surface/high α

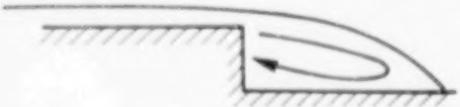

Discontinuous surface

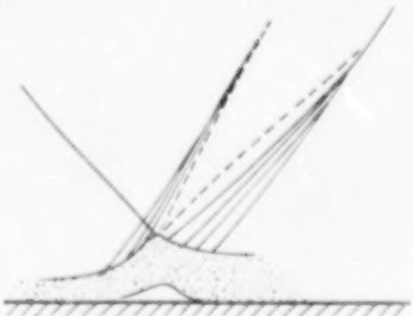

Shock - B.L. interaction

2D Airfoil Separation Analysis

An airfoil at a high angle of attack provides an example of separation from a smooth surface with an adverse pressure gradient. In this case, separation is usually a gradual process with the stall region increasing up to the point of C_{Lmax}. Separation is further complicated by the formation of laminar leading-edge bubbles which may be of either the short or long bubble type. The long bubble may trigger the transition of the boundary layer to a turbulent layer near the reattachment point, whereas the short bubble separation may contract and burst leading to massive upper surface separation.

Additional complications may occur at angles of attack beyond that required to obtain C_{Lmax}. The figure shows the separation characteristics of an NACA 0012 airfoil at 18 degrees angle of attack and a chord Reynolds number of 1 million. The experimental data are compared with solutions of the thin-layer Navier-Stokes equations which were obtained by Chris Rumsey.[1] The calculations show very good agreement with experimental data and also illustrate another phenomenon which is not well defined by experiment. The experimental data show a gradual increase in lift up to a maximum C_L of 1.53 at an angle of attack of 16.9 degrees; then a drastic loss of lift as angle of attack is increased further. At angles of attack greater than that required to achieve C_{Lmax}, the calculations predict an unsteady solution. The separation bubble located above the airfoil leading edge alternately grows and shrinks with respect to time as illustrated in the figure. The vector plots correspond to the minimum and maximum lift coefficient values in the shedding cycle. When the calculations are time averaged, they show very good agreement with the mean values of the experimental data. Experiments designed to measure separated flows must strive to measure the unsteady features as well as the mean or time-averaged quantities.

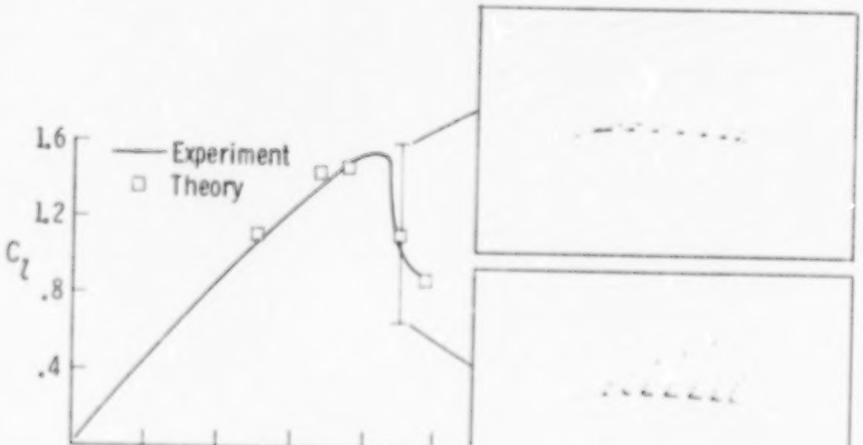

3D Wing Separation

The complexity of the flow field increases as three-dimensional effects are included. Recent experimental investigations have provided new insight into the complex nature of flow separation on wings and wing bodies.[2] The left half of the figure shows results obtained by Winkelmann[3] in which he photographed fluorescent oil flow on a series of simple, unswept, rectangular planform wings of whose aspect ratios ranged from 3 to 12. All of the wings had a 3.5 in chord and a 14 percent thick Clark-Y airfoil section. Test conditions correspond to a chord Reynolds number of 385,000 and an angle of attack of 18.4 degrees. The oil flow patterns on all three wings show a "bead-like" pattern near the wing leading edge which indicates the presence of a laminar leading-edge separation bubble. The aspect ratio 3 wing illustrates the presence of one large "mushroom" stall cell on the upper surface of the wing. A close examination of the oil pattern indicates that only at the centerline of the wing could the flow pattern even remotely be called two-dimensional. There are indications of strong spanwise flow everywhere else on the wing along with vortical flow nodes near both mid semispan positions. An increasing number of "mushroom" cells are observed as the wing aspect ratio is increased; in addition it is not apparent that the flow tends toward two-dimensional characteristics with increased aspect ratio. In this investigation relatively symmetrical patterns are observed on the wings.

The addition of a body to a configuration results in a more complicated flow field. In a recent investigation by Sellers and Kjelgaard, (NASA Langley Research Center, unpublished data) oil flow patterns were observed on an aspect ratio 7 wing with a 14 in chord NACA 0012 airfoil section. The wing was mounted in a high-wing position on a small cylindrical body as shown in the upper right portion of the figure on the next page. Test conditions corresponded to a chord Reynolds number of 1 million with angle of attack ranging from 6 to 22 degrees. The oil flow pattern on the upper surface of the wing at an angle of attack of 20 degrees is shown in the lower right of the figure. A complex and asymmetrical pattern develops with large regions of reverse flow on each wing and spiral nodes forming from the flow at the wing-body juncture. The oil flow patterns change dramatically as the angle of attack is increased above $C_{L\max}$. At 16 degrees angle of attack the flow pattern is steady and asymmetric with only the left wing separated. At 17 degrees angle of attack, an unsteady separation occurs where the left wing remains separated and the right wing alternates between attached and separated flow. Between 18 and 20 degrees the pattern remains steady and asymmetric as shown in the lower right of the figure. Two features from these photographs are noteworthy: (1) the flow separation patterns are very complex and three-dimensional; and (2) the small fuselage appears to cause large flow asymmetries which were not apparent in Winkelmann's observations on wings without bodies. These asymmetries are expected to be more significant with larger bodies and with more complex configurations.

3D Wing Separation

ORIGINAL PAGE IS
OF POOR QUALITY

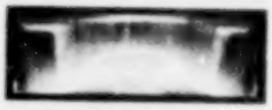

AR = 3

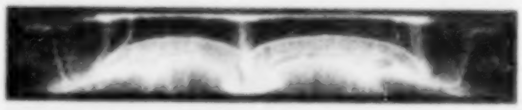

AR = 6

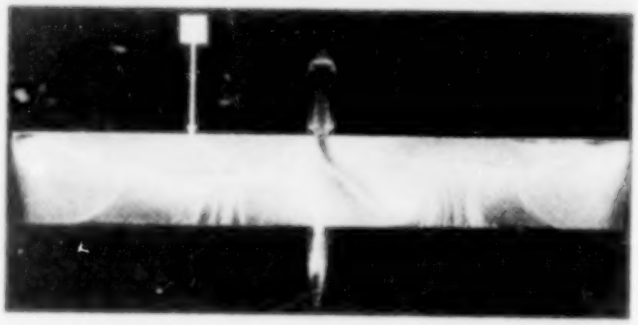

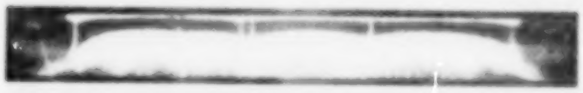

AR = 9

Two-Phase Flow Induced Separation

NASA is conducting research to find if heavy rain concentration is a factor in airfoil flow separation.[4] Analysis has shown that significant increases in drag can occur when an aircraft encounters rain with liquid water content from 15 to 60 g/m^3, which corresponds to between 19 and to 70 in of rain per hour. Flight measurements have demonstrated that these levels can be encountered during thunderstorms.

A preliminary experiment was conducted in the Langley 4- by- 7 meter tunnel to investigate the sensitivity of airfoil performance to heavy rain encounters. The sketch on the left side of the of the figure illustrates the experimental setup. For this test, a 2.5 ft chord NACA 64-210 airfoil was installed in the aft portion of the test section and a water spray manifold system was located in the forward part of the test section. The spray system was capable of generating a two-phase flow of 4.5 percent water by weight, which is equivalent to 57 in of rain per hour.

The right side of the figure shows the section lift coefficient data obtained at a Reynolds number of 2.6 million. The baseline data (water spray off) indicated that stall was beginning to occur at an angle of attack of about 18 to 20 degrees. For the highest spray rate (4.5 percent water by weight or 57 in/hr) the data indicate that separation begins at a lower angle of attack and that stall occurs at an angle of attack of 12 degrees. The maximum lift coefficient is reduced by 25 percent.

Continuing tests will attempt to identify the mechanisms which cause premature separation in two-phase flow and to determine the sensitivity of full scale wings to these phenomena.

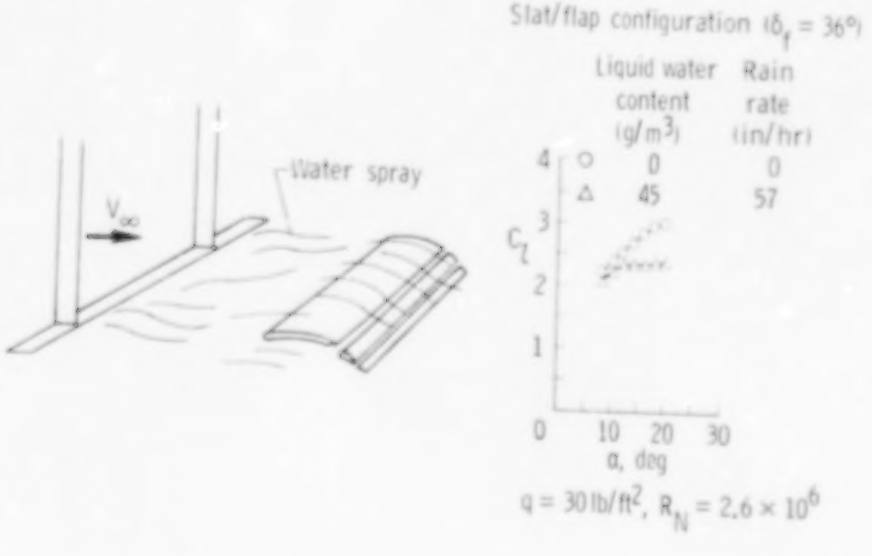

Leading-Edge Droop Separation Control

NASA Langley is conducting research oriented toward improving the spin resistance of light airplanes.[5] The research has shown that the addition of a discontinuous, outboard wing leading-edge droop can provide significant improvements in aircraft stall characteristics and spin resistance. Wind tunnel tests at NASA Langley and the University of Maryland explored the effect of these wing leading-edge modifications and flight tests have verified the results.

The graph on the left side of the figure shows the variation of the total resultant force coefficient for the outer wing panel $C_{r_{o.w.}} = (C_L^2 + C_D^2)^{1/2}$ versus angle of attack from a 1/6 scale wind tunnel model at a Reynolds number of 320,000. Resultant force is more relevant to autorotative characteristics than lift, at high angles of attack. A negative resultant force curve slope is indicative of unstable roll damping and a tendency to spin. The addition of the leading-edge droop has a negligible effect on the resultant force coefficient at low angles of attack. Beyond the stall angle of the basic wing, however, the lift of the modified wing continues to increase and produces a stabilizing force slope up to 30-35 degrees angle of attack. The fluorescent oil flow visualization photographs on the right side of the figure show the effect of the leading-edge droop on the flow patterns on the wing. A close examination of the photographs shows a vortex-type flow emanating from the leading-edge discontinuity which prevents the outward progression of the separated flow.

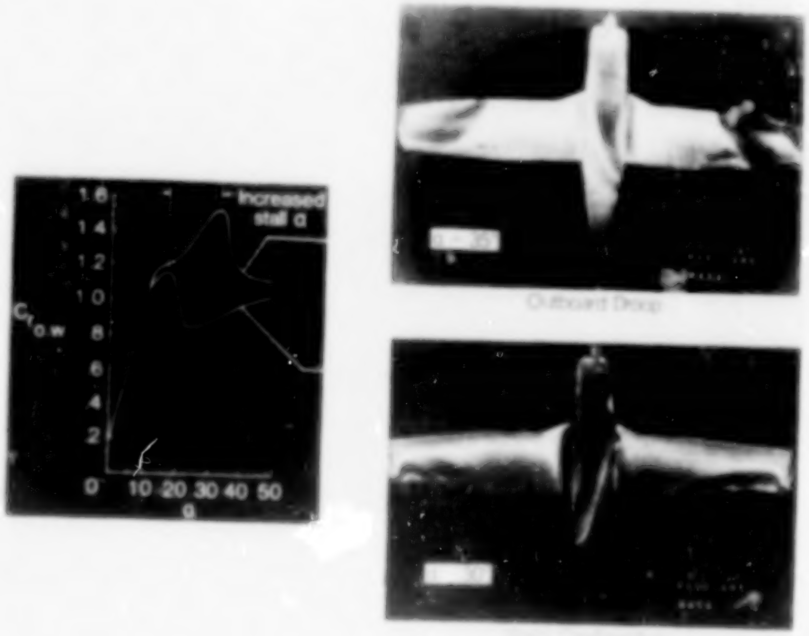

Outboard Droop

ORIGINAL PAGE IS
OF POOR QUALITY

ORIGINAL PAGE IS
OF POOR QUALITY

Blunt Body Separation Analysis

The separated flow in the base region of a blunt body produces a drag force which can contribute significantly to the total drag of the body. In general, the nature of the near-wake flow is strongly dependent upon the geometry of the body and the Mach number regime and Reynolds number of the external flow. For example, a two dimensional bluff body in a subsonic stream generates a wake dominated by alternately shed vortices over a wide range of Reynolds numbers. Since the base drag in this case is associated with the vortex shedding, methods for reducing the base drag must be directed toward eliminating or weakening the vortex shedding or delaying the formation of the vortices. Two of the methods that have been found to reduce base drag in wind tunnel experiments are being studied numerically using solutions of the time-dependent Navier-Stokes equations. These two methods include the use of either a base cavity or the injection of mass through the base into the wake. The finite-difference scheme used in the present study is the unsplit MacCormack (ref. 6) explicit predictor-corrector technique which can be vectorized efficiently for calculations which use the CDC VPS-32 computer at Langley.

Shown in the figure are calculations of subsonic flow for a slender body with and without a rectangular base cavity.[7] Velocity vectors are shown in the near-wake region, for Mach 0.6 flow with a Reynolds number based on chord length of 9.62×10^3, at a point in time after periodic flow has been established. The presence of the cavity allows the vortex formation region to extend into the cavity. As a result, the pressure along the rear wall of the cavity is now higher than that along the base of the unmodified configuration which reduces the base drag.

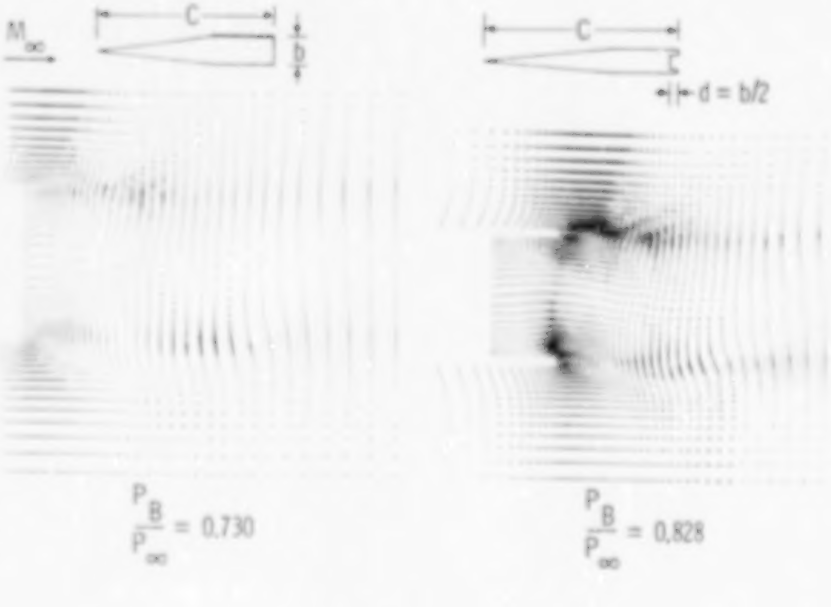

Bluff Body Separation Control

The drag of afterbodies in fluid flow can be kept low if the closure angle is low enough that attached flow is maintained over the afterbody (streamline body).[8] However, in many situations this approach is not practical because the length required becomes excessive. Therefore, in these situations (such as ground transportation) the afterbodies are typically truncated rather sharply. The parameter which causes separation is the magnitude of the adverse pressure gradient which occurs in the region where the flow is being expanded. Non-attached (or separated) flow on an axisymmetric bluff afterbody is shown in the photo on the upper right (flow from left to right). It can be seen that separation occurs just downstream of the shoulder of the body boattail. This separated flow results in high drag as shown by the drag measurements for the non-grooved bluff afterbody. Previous investigations have indicated that transverse grooves can be effective in delaying separation for two-dimensional diffusers (internal flow). The photo on the lower right illustrates how the flow remains attached over a much greater region of the bluff afterbody when transverse grooves are employed in the shoulder region. Measurements show that the better flow attachment reduces drag coefficient measurements at intermediate Reynolds numbers (approximately 0.3 to 1.3 × 105) for the grooved afterbody. The mechanism of the transverse grooves appears to be one of substituting several small regions of separation (which provide a wall slip boundary condition) for a larger separated flow region. It appears that the grooves should be located in the region of high longitudinal pressure gradient. The grooves may need to be tailored to provide a reduced drag coefficient at a particular Reynolds number.

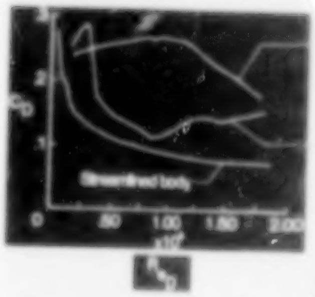

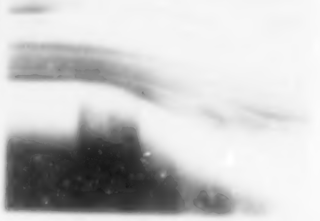

ORIGINAL PAGE IS
OF POOR QUALITY

ORIGINAL PAGE IS
OF POOR QUALITY

Shock-Boundary Layer Interaction

As the velocity increases over a body, shock waves form and interact with the boundary layers developing near the surface. If the shock wave is weak, the flow remains attached and the effect of the thickening boundary layer is to convert the sharp pressure rise into a more gradual one. If the shock wave is of sufficient strength, the boundary layer will separate due to the strong adverse pressure gradient through the shock. The interaction region, in the case of laminar boundary layer separation, is larger than that for a turbulent boundary layer separation.[9]

The separation of a boundary layer due to an impinging shock wave is a classical example of the process and can commonly occur in supersonic inlets. The analysis of Thomas and Wallace[10] corresponds to the experiments of Hakkinen et al.[11] at a free-stream Mach number of 2.00 and a Reynolds number based on the length from the leading edge to the shock impingement point of 2.96 × 105. The pressure contours are presented on the left of the figure and show several distinct features of this flow. The oblique shock formed at the leading edge of the plate is shown at x/L = 0. The impinging shock intersects the plate at x/L = 1.0 and is of sufficient strength to cause separation of the laminar boundary layer. The interaction region is large compared to the boundary layer thickness and encompasses the region from x/L = 0.77 to 1.15. In the separated zone, the plateau region of nearly constant static pressure is evident. The streamlines and velocity vectors in the vicinity of the interaction region are shown on the right of the figure. A separation bubble with reversed flow is shown in the interaction region.

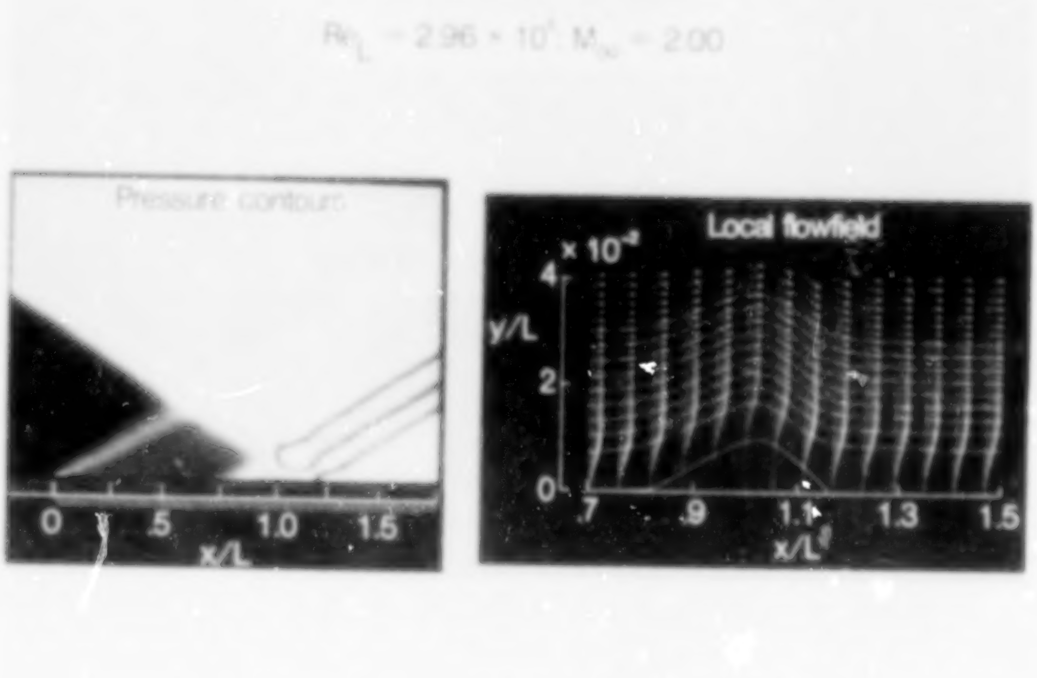

ORIGINAL PAGE IS
OF POOR QUALITY

ORIGINAL PAGE IS
OF POOR QUALITY

Control Plate for Shock-Boundary Layer Interaction

Numerical and experimental studies have been done on a new, passive approach for separation control in shock-boundary layer interaction.[12] The device consists essentially of a horizontal plate suspended in the outer part of the boundary layer. This plate is positioned such that the incident shock reflects from this plate rather than the wall, thus effectively shielding the low momentum flow near the wall from the tremendous adverse pressure gradient engendered by shock impingement.

The figure shows a plot of the normalized wall static pressure versus the distance downstream on the experimental test plate along with the corresponding Schlieren photograph of the flow field with the control plate in place. The square symbols correspond to the reference case without the control plate and the diamond symbols correspond to the case with the control plate. From this plot it can be seen that with the addition of the control plate the interaction region has been shortened. Further investigations will be conducted to identify the total drag reduction.

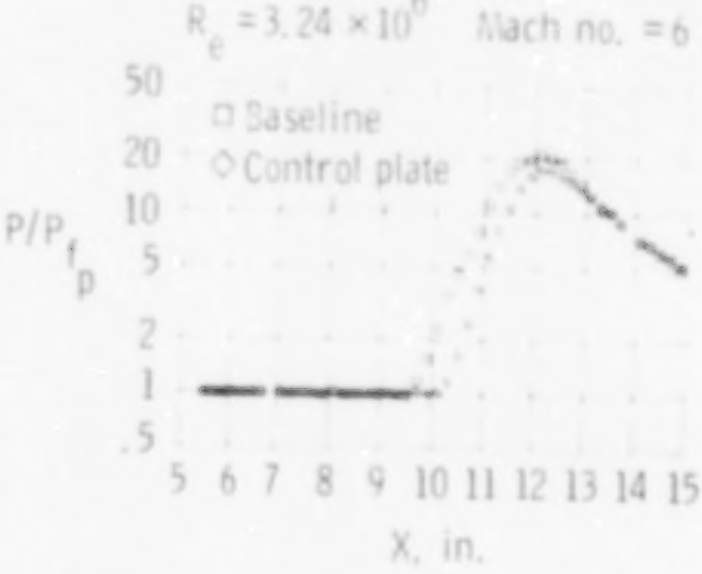

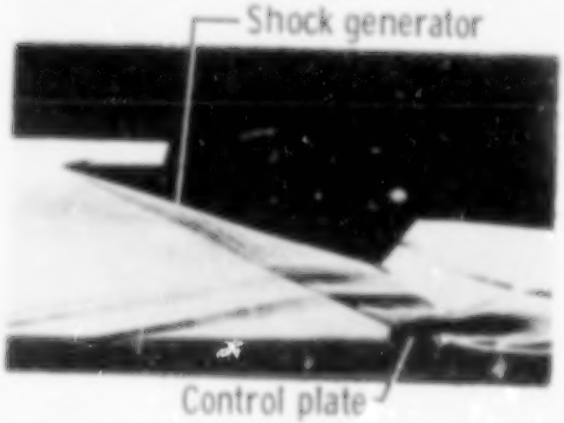

C-5

Summary

Flow separation generated by an airfoil or an aircraft at high angles of attack is an extremely complicated process. The basic physics are becoming better understood, but additional research is required. NASA Langley has recently started an experimental and analytical effort directed toward understanding the complexities of flow separation. Related research is also providing information on how to control separation with simple yet effective modifications to wing leading edges and on the effect of very heavy rain on flow separation.

Flow separation from blunt bases or bluff bodies represents a significant portion of body drag. For the case of the blunt base, vortex shedding is the dominant feature which produces higher base pressures and thereby larger drag. Recessing the base to form a cavity has been shown both experimentally and numerically to reduce the base drag. Spanwise grooves have been shown to reduce flow separation on bluff bodies.

Shock-boundary layer interactions commonly occur at high speed and can seriously degrade the performance of engine inlets and diffusers. A small control plate to shield the boundary layer from the impinging shock has been effective in modifying the interaction region.

OVERALL OBJECTIVES - BETTER UNDERSTAND THE FUNDAMENTAL PHYSICS AND TO IDENTIFY EFFECTIVE SEPARATION CONTROLS

- HIGH-α
  - HEAVY RAIN AGGRAVATES FLOW SEPARATION
  - LEADING EDGE DROOP REDUCES SEPARATION IN OUTBOARD REGIONS

- BLUNT/BLUFF BODY SEPARATION
  - BASE CAVITY REDUCES BASE DRAG
  - SPANWISE GROOVES REDUCE SEPARATION ON BLUFF BODIES

- SHOCK-BOUNDARY LAYER INTERACTION
  - CONTROL PLATE CAN DELAY SEPARATION

References

1. Christopher L. Rumsey: Time-Dependent Navier-Stokes Computations of Separated Flows Over Airfoils. AIAA Paper No. 85-1684, July 1985.

2. Richard J. Margason: Computational Methods for Subsonic Aerodynamic Flow Separation. 4th International Conference on Applied Numerical Modeling, Tainan, Taiwan, December 1984.

3. A. E. Winkelmann: On the Occurrence of Mushroom Shaped Stall Cells in Separated Flow. AIAA Paper No. 83-1734, July 1983.

4. R. Earl Dunham, Jr., Gaudy M. Bezos, Garl L. Gentry, Jr., and Edward Melson, Jr.: Two-Dimensional Wind Tunnel Tests of a Transport-Type Airfoil in a Water Spray. AIAA Paper No. 85-0258, January 1985.

5. H. Paul Stough, III, Daniel J. DiCarlo, Kenneth E. Glover, and Eric C. Stewart: Wing Design for Spin Resistance. AIAA Paper No. 84-2223, July 1984.

6. MacCormack, R. W.: The Effect of Viscosity in Hypervelocity Impact Cratering. AIAA Paper 69-354, April 1969.

7. David H. Rudy: Navier-Stokes Solutions for Two-Dimensional Subsonic Base Flow. Southeastern Conference on Theoretical and Applied Mechanics, Pine Mountain, Ga., May 1984.

8. F. G. Howard, W. L. Goodman, and M. J. Walsh: Axisymmetric Bluff-Body Drag Reduction Using Circumferential Grooves. AIAA Paper No. 83-1788, July 1983

9. P. K. Chang: Control of Flow Separation: Energy Conservation, Operational Efficiency, and Safety. McGraw-Hill Book Co., Washington, D.C., 1976.

10. James L. Thomas and Robert W. Walters: Upwind Relaxation Algorithms for the Navier-Stokes Equations. AIAA Paper No. 85-1501, July 1985.

11. R. J. Hakkinen, I. Greber, L. Trilling, and S. S. Abarbanel: The Interaction of an Oblique Shock Wave with a Laminar Boundary Layer. NASA Memo-2-18-59W, March 1959.

12. W. L. Goodman, E. L. Morrisette, M. Y. Hussaini and D. M. Bushnell: Control Plate for Shock-Boundary Layer Interactions. AIAA Paper No. 850523, March 1985.

C-5

D19

N88-14945

5,9-02

117243

18P.

VORTEX DYNAMICS

George C. Greene, John E. Lamar, and C. H. Liu
NASA Langley Research Center
Hampton, Virginia

L. R. Kubendran
National Research Council
Washington, DC

[redacted]

VORTEX DYNAMICS

Vortex flows of interest to aerodynamicists cover a wide range of scales from a fraction of an inch in boundary layer flows to many feet in wake flows. In many applications these flows are poorly understood and, due to their complexity, present a challenge both analytically and experimentally. This paper describes four topics representing the spectrum of experimental and analytical vortex research.

- Long research history
- Many scales and applications
- Challenging research area

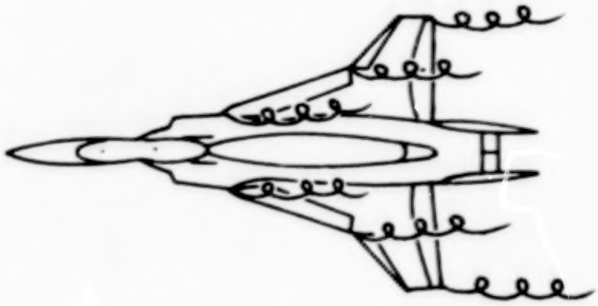

JUNCTURE VORTEX CONTROL

Juncture vortex control is important not only because of its direct contribution to drag but also because of its potentially unfavorable interaction with the wing boundary layer or other vortices.

- Drag reduction
- Boundary layer control
- Vortex interactions

JUNCTURE FLOWFIELD SCHEMATIC

This figure shows a schematic of a juncture flowfield. A wing at zero incidence is mounted perpendicular to a flat surface. The x cordinate is aligned with the freestream velocity vector, y is perpendicular to the surface, and z is the lateral coordinate as shown. The flow direction angle, θ, is in the lateral or x-z plane. As the boundary layer encounters the adverse pressure gradient near the wing leading edge, it can separate with the separated region forming the core of the juncture vortex.

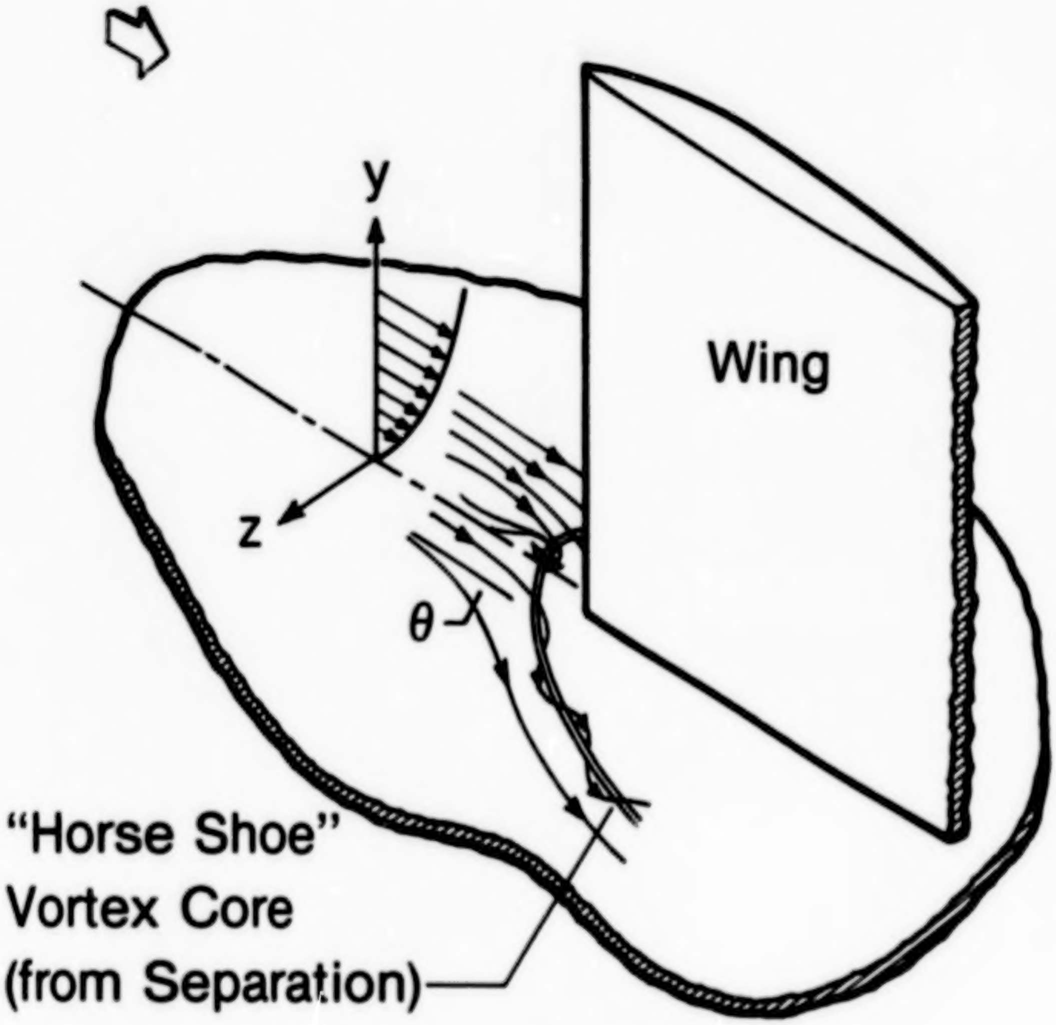

FLOW ANGLE MEASUREMENTS

This figure illustrates one type of measurement used to understand the juncture flow. The lateral flow direction angle, θ, is shown as a function of the lateral coordinate, z, for a streamwise location just ahead of the wing. The symbols represent different heights above the surface. Near the surface there is a flow reversal ($\theta = 180^{\circ}$) near the wing centerline (near $z = 0$). Above the separated region, the flow angle behaves as expected allowing smooth flow around the wing. Although the measurements shown were made with a hot wire anemometer, a variety of techniques, including pressure probes and a laser velocimeter, are being used to study juncture flow control by fillets or other geometry modifications. Additional details of this research are described in reference 1.

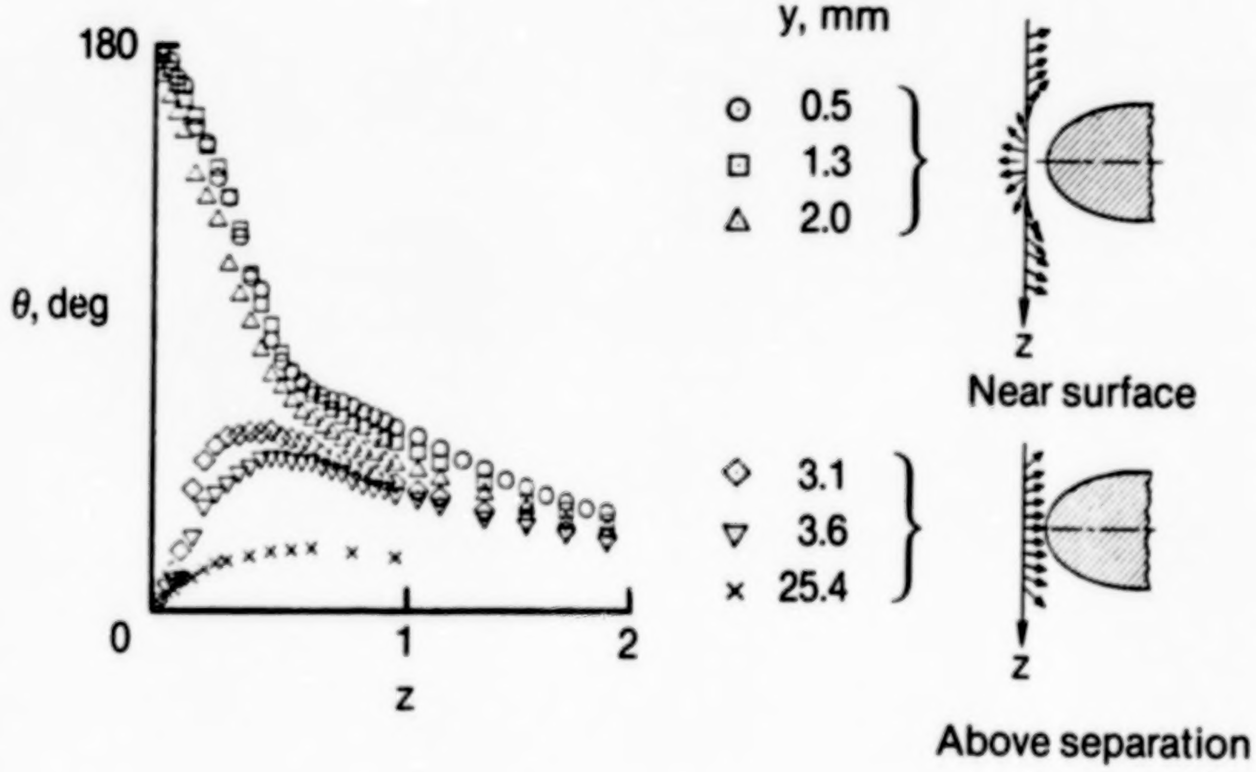

IN-FLIGHT FLOW VISUALIZATION

The purpose of this resarch is to develop vapor-screen technology for in-flight visualization of the leading edge vortex over the wing of an F-106B aircraft and to understand the effects of Mach and Reynolds numbers on the overall flowfield.

- Develop vapor screen technology for in-flight flow visualization
- Observe leading edge vortex system
- Understand Mach and Reynolds numbers effects

F-106B AIRCRAFT

ORIGINAL PAGE IS
OF POOR QUALITY

This photograph of the F-106B aircraft shows the location of the vapor screen light source on the side of the fuselage just forward of the vertical tail, the camera system on top of the fuselage just aft of the canopy, and the seeding probe just underneath the wing leading edge near the apex.

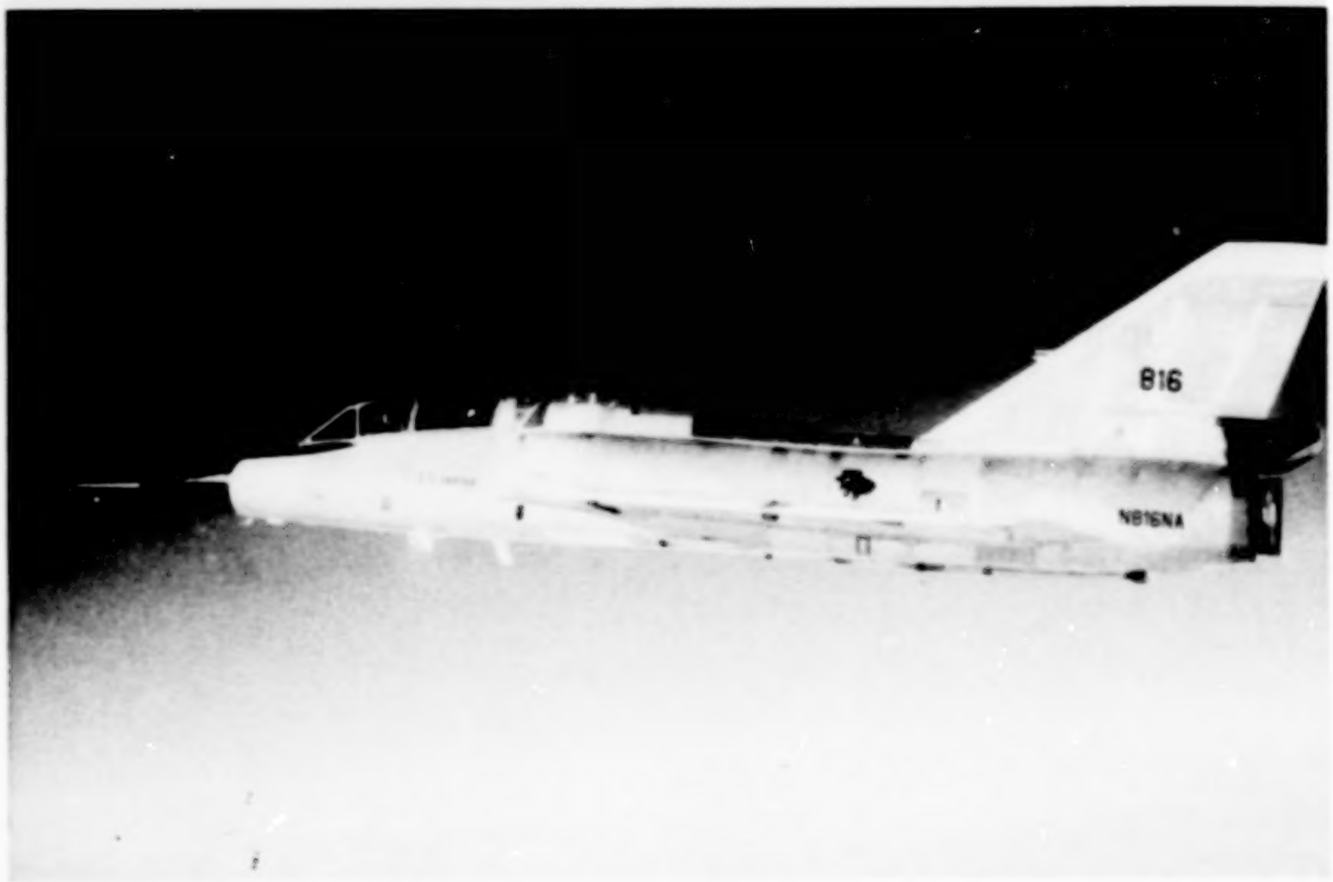

VISUALIZATION SCHEMATIC

This figure shows the relative locations of the seeding probe, vapor screen light sheet, and camera field of view on the F-106B aircraft. The field of view on the TV monitor screen illustrates the relative positons of the light sheet, fuselage, and wing leading and trailing edges.

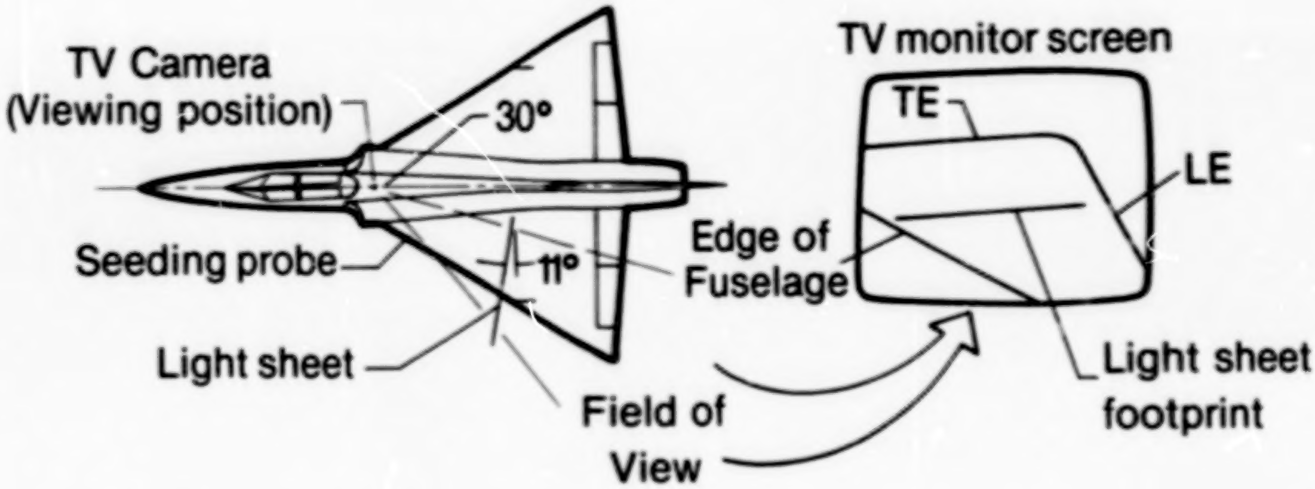
TV Camera
(Viewing position)
30°
Seeding probe
11°
Light sheet
Field of View
Edge of Fuselage
TV monitor screen
TE
LE
Light sheet footprint

VORTEX VISUALIZATION

ORIGINAL PAGE IS
OF POOR QUALITY

The photographs of the TV monitor screen shown in this figure illustrate the observed variation of the leading-edge vortex system on the F-106B aircraft under two different flight conditions at an angle of attack of 18°. The photograph on the left was taken during a constant altitude deceleration maneuver in which the angle of attack was slowly increased to maintain constant lift (1g flight). The photograph on the right was taken during a spiral descent (5g) maneuver during which the Mach number was held constant. Although the Mach and Reynolds numbers are different for these cases, they are representative of the wide variety of conditions which are routinely encountered in cruise and maneuver flight.

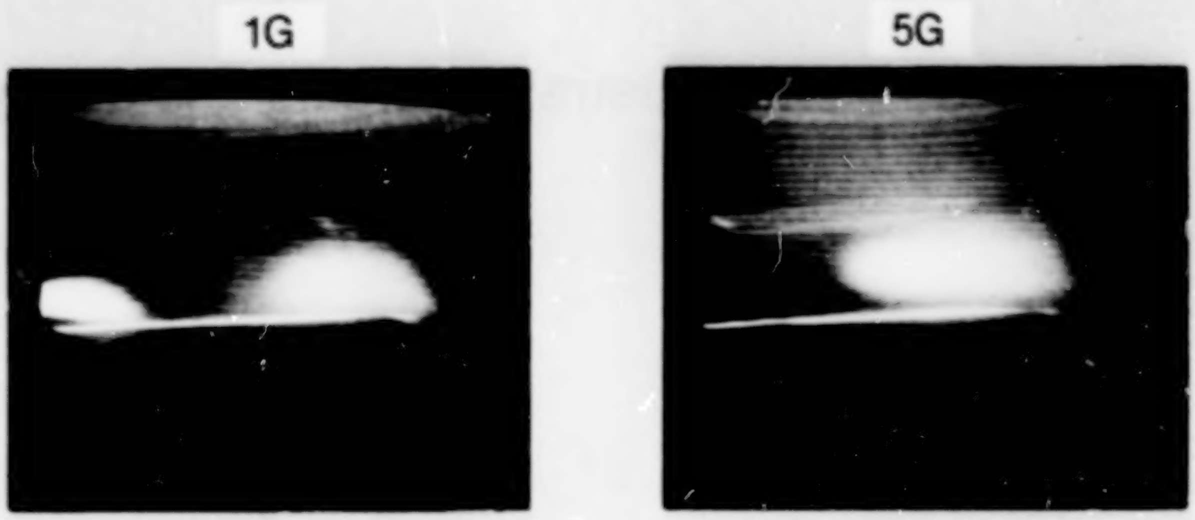

1G

Constant altitude - deceleration

5G

Left spiral descent

$\alpha = 18°$

NUMERICAL STUDIES OF VORTEX FLOWS

Complex vortex flows occur frequently in many areas of fluid mechanics and are often poorly understood. Numerical techniques have been developed and applied to study three-dimensional flows. An example problem is the merging and decay of a pair of vortex rings.

- Physical intuition is lacking
- Example problem is interacting vortex rings
- Numerical results illustrate merging and decay

INITIAL GEOMETRY

This figure shows the initial geometry for the vortex ring calculations. Both rings have the same strength (Γ), radius (R_o), and core size (δ_o) and are separated by a distance D_o.

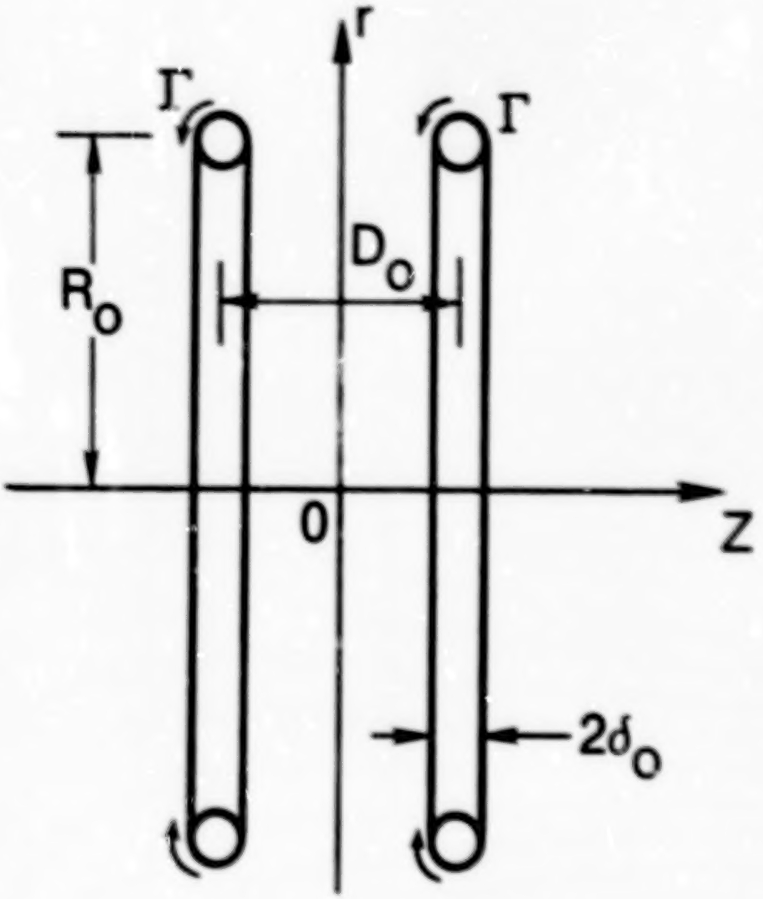

VORTICITY CONTOURS

ORIGINAL PAGE IS
OF POOR QUALITY

This figure illustrates a typical evolution of the vorticity for two right-moving interacting vortex rings with Reynolds number = 754 and $D_0/\delta_0 = 6$. Note that the displayed vorticity contours represent the vorticity distribution on a meridian plane cutting through the torus with only the contours centered at R_0 being shown. The center of the torus is far below the contours and is not shown. The first ring, moving ahead initially, is stretching its radius and slowing down. In contrast, the second ring, moving behind initially, is contracting its radius and speeding up. The plane of the second ring passes over that of the first ring at $t = 1.83$. At this instant, the two rings switch the roles of leading and lagging. It is observed that the two points of local maximum vorticity cross over each other two more times at $t = 3.11$ and 3.81. Finally, the two points of local maximum vorticity merge into a single point for $t = 3.81$. A more detailed description of these calculations is presented in reference 2.

Two Vortex Rings, $R_0 = 15$, $D_0 = 6$, Re = 754

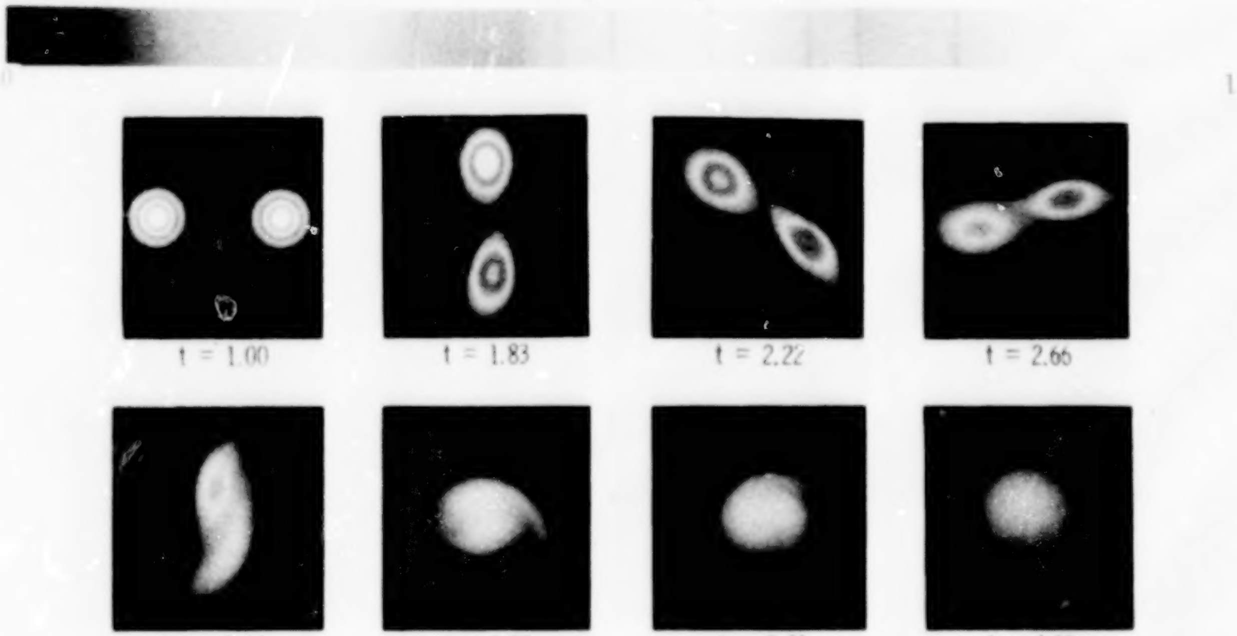

t = 3.11 t = 3.57 t = 3.81 t = 4.89

VORTEX DECAY IN THE ATMOSPHERE

Measurements of wake decay in ground facilities and in the atmosphere have shown considerable variation. Analytical predictions of atmospheric effects also vary greatly. An approximate analytical model has been developed to predict the effects of stratification, turbulence, and Reynolds number on wake lifetime.

- Understand effects of stratification, turbulence, and Reynolds number on wake persistence
- Historically difficult problem
- Approximate analytical model developed

FLOWFIELD SCHEMATIC

This figure shows a schematic of the flowfield in the wake of a lifting wing, viewed in a coordinate system moving downward with the wake. As the roughly oval region of fluid descends, it is subject to several types of interaction with the surrounding atmosphere which promote decay. One interaction is proportional to the square of the wake descent velocity and is roughly analogous to the viscous forces which a solid body would experience. Wake decay is also enhanced by atmospheric turbulence which, in the absence of large scale instabilities, has an effect proportional to the vortex strength and turbulence level. In addition, if the atmosphere is stably stratified, the wake experiences a buoyancy force proportional to the density difference between the wake and surrounding atmosphere. These effects have been simulated in an approximate analysis to predict the motion and decay characteristics of wakes in the atmosphere.

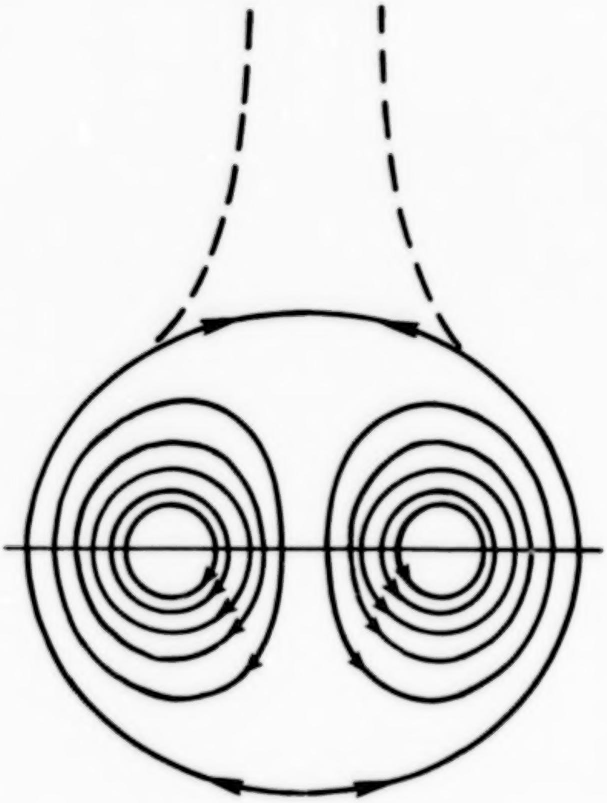

This figure shows a comparison of predicted wake trajectories and ground facility data from reference 3 for the range of density stratification commonly encountered in the atmosphere. The term "neutral" refers to an adiabatic decrease in density with altitude while the term "inversion" refers to a more rapid decrease which occurs when the temperature is increasing with altitude (ground colder than the atmosphere). As shown in the figure, this can have a large effect on wake lifetime.

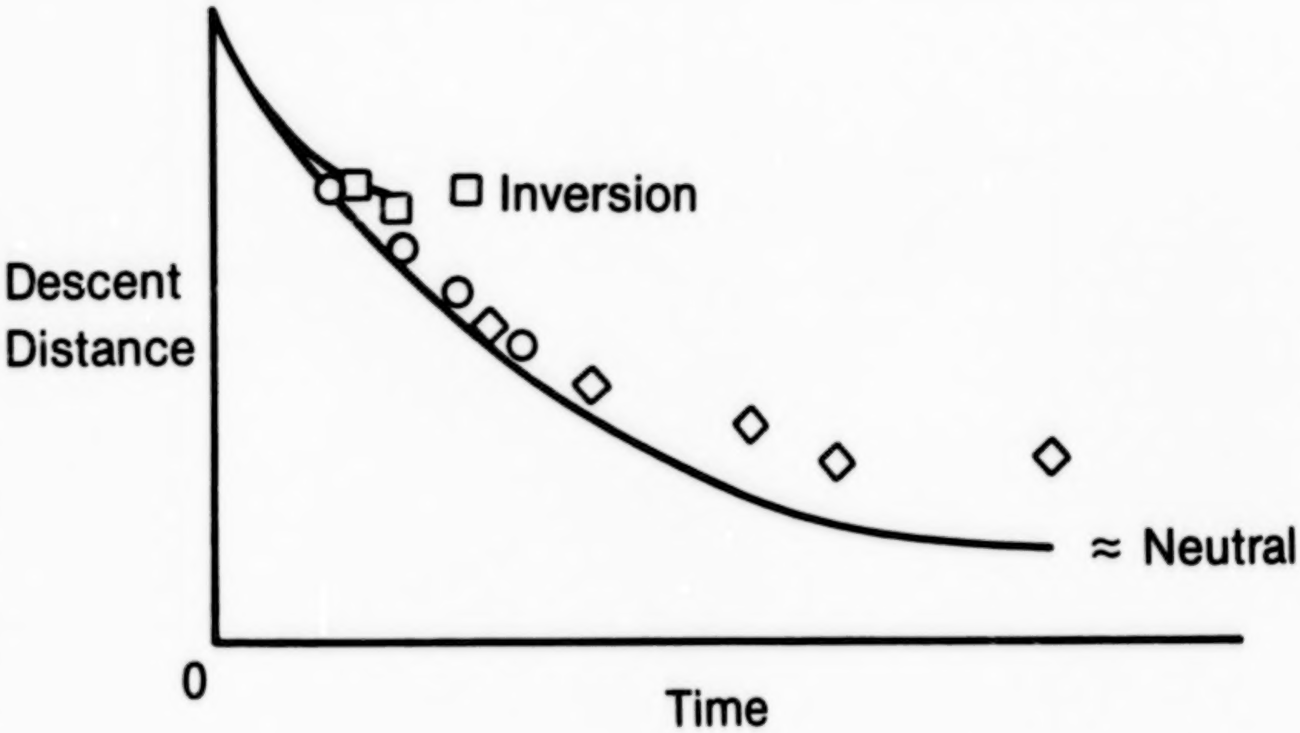

PREDICTED WAKE DECAY

This figure shows predicted effects of stratification and turbulence on the decay of vortex strength. The curves labeled "neutral" and "inversion" correspond to the range of density stratification commonly encountered in the atmosphere with no turbulence effects included. The broken lines correspond to the "neutral" case with turbulence effects included and, for a large transport aircraft, represent approximate boundaries between negligible, light, and light-to-moderate turbulence. Typical aircraft separations in the terminal area correspond to normalized time values between about 4 and 8. Atmospheric conditions are therefore predicted to play a dominant role in determining wake lifetimes. Conditions of low turbulence and near neutral atmospheric stability are predicted to be especially conducive to long wake lifetimes.

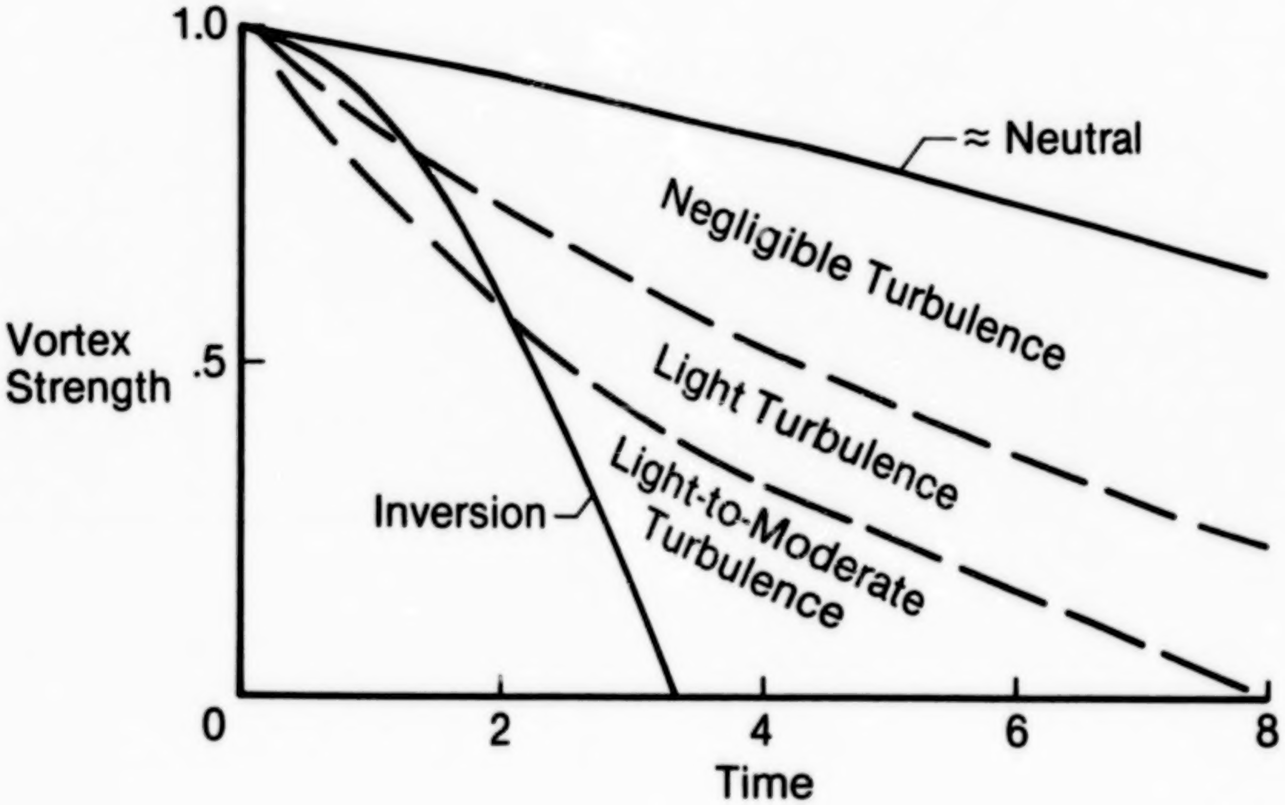

SUMMARY

Due to the many applications in aerodynamics there is a broad spectrum of vortex-flow research. The level of physical understanding varies considerably; therefore the research technique is often tailored to the application.

- Experimental research underway to understand a wide variety of complex vortex flows
- Analytical techniques being applied to numerically simulate basic vortex physics and predict decay trends in the atmosphere

REFERENCES

1. Kubendran, L. R.; McMahon, H.; and Hubbart, J.: Turbulent Flows Around a Wing-Fuselage Type Juncture. AIAA Paper 85-0040, January 1985.

2. Liu, Grace C.; and Hsu, Chung-Hao: Numerical Studies of Interacting Vortices. NASA TM 86325, 1985.

3. Satran, Dale R.; Neuhart, Dan; Holbrook, G. Thomas; and Greene, George C.: Vortex Research Facility Improvements and Preliminary Density Stratification Effects on Vortex Wakes. AIAA Paper 85-0050, 1985.

D20

N88-14946

520-02
117244
7P.

OVERVIEW OF THE LANGLEY VISCOUS DRAG REDUCTION PROGRAM

Jerry N. Hefner
NASA Langley Research Center
Hampton, Virginia

[redacted]

VISCOUS DRAG REDUCTION

As a result of reductions in form drag and roughness drag, skin friction drag or viscous drag now represents a major contributor to the cruise drag of subsonic business and transport aircraft, and hence, is considered a barrier problem to further significant improvements in the aerodynamic efficiency of these aircraft. In fact, viscous drag accounts for as much as 50 percent of the total cruise drag for subsonic transports and as much as 35-40 percent of the cruise drag for supersonic aircraft. To meet the challenge of reduced viscous drag and improved aerodynamic efficiency, research in the areas of laminar-flow control and turbulence control/drag reduction was initiated at the NASA Langley Research Center in the mid-1970's under the Aircraft Energy Efficiency Program and the Aeronautics Research and Technology Base. The significance of this research is that even small reductions in viscous drag should provide important design tradeoffs including: significant resizing options for new aircraft designs, increased range capability without increased take-off gross weight, increased speed and productivity, and reduced fuel volume and cost. Only a 10-percent reduction in viscous drag could provide an annual fuel savings of the order of $200-300 million assuming an annual civil aviation fuel bill in the United States of $10 billion.

- Viscous (skin friction) drag is barrier problem
- Accounts for approximately
  - 50 percent of cruise drag for subsonic transports
  - 35-40 percent for supersonic aircraft
- Reductions in viscous drag provide
  - Significant re-sizing options for new aircraft designs
  - Increased range capability
  - Increased speed and productivity
  - Reduced fuel volume/cost

MAINTENANCE OF LAMINAR FLOW FOR VISCOUS DRAG REDUCTION

The research being conducted under the Viscous Drag Reduction Program focuses on two approaches to reduce the skin friction drag. Where the chord or length Reynolds numbers (R_c) are of the order of 60×10^6 or less (i.e., wings, nacelles, empennage), the maintenance of laminar flow appears most promising and provides the largest net benefits. For Reynolds numbers much larger than this (i.e., 100×10^6 or greater), it is unclear whether laminar flow can be maintained over relatively large surface areas of the aircraft; hence, turbulence control/drag reduction is being investigated for these surfaces (i.e., fuselage).

Three concepts are being investigated to delay the boundary layer transition process and maintain laminar flow beyond the usual transition Reynolds numbers of 4×10^6 or less. These include: (1) the use of favorable pressure gradient or surface shaping (natural laminar flow); (2) suction through slotted or perforated surfaces (laminar flow control); and, (3) combinations of suction and favorable pressure gradient (hybrid laminar flow control). The advantage of natural laminar flow is that it is a passive approach to the maintenance of laminar flow but it may be limited to wing sweep angles of approximately 20 or less and chord Reynolds numbers of 20×10^6 or less. Laminar-flow control, using full-chord suction, will probably be required for applications where extensive laminar flow is necessary for chord Reynolds numbers approaching $50\text{–}60 \times 10^6$ and sweep angles of 30 or greater. Hybrid laminar-flow control minimizes suction requirements and provides increased operational flexibility and improved off-design performance compared to natural laminar flow.

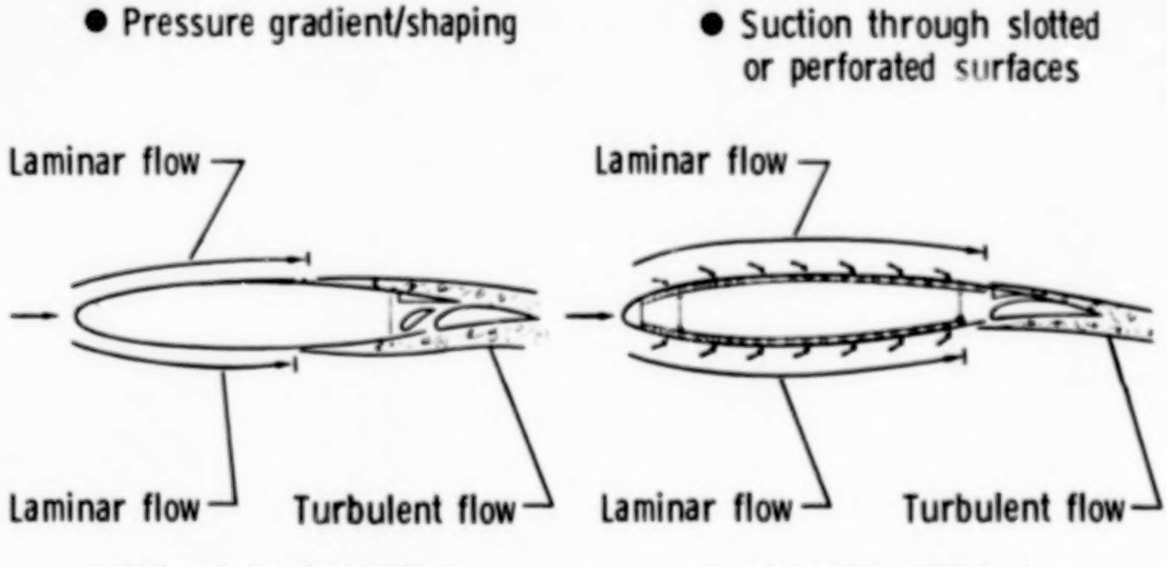
- Pressure gradient/shaping
- Suction through slotted or perforated surfaces

Natural Laminar Flow

Laminar Flow Control

TURBULENCE CONTROL FOR VISCOUS DRAG REDUCTION

Turbulence control/drag reduction research attempts to identify and develop highly innovative concepts employing surface micro-geometry modifications to alter and control the turbulence production process and to reduce turbulent surface shear. Although the payoff from this approach to viscous drag reduction is generally much less than that for the maintenance of laminar flow, it does provide an alternative that is applicable to high length Reynolds numbers, may be retrofittable to existing aircraft, and has less operational sensitivities.

Twelve turbulence control concepts are currently being explored at Langley with two of these concepts (i.e., riblets and large-eddy breakup devices) producing net viscous drag reductions of the order of 10 percent. Riblets are very small, flow-aligned, triangular grooves cut into the surface. If the height and spacing of these grooves are scaled properly, based on particular fluid physics properties, then net skin-friction drag reductions can be obtained; for practical flight applications riblets would typically have a height and spacing of between 0.0015-0.003 inch. Large-eddy breakup devices are thin flat plates or small airfoils immersed within the turbulent boundary layer to alter the large-scale turbulent structures within the boundary layer. The unique feature of both concepts is that the skin-friction reductions produced by their interaction with the turbulent boundary layer are sufficiently large, such that they more than compensate for the drag penalties associated with the particular concept (i.e., increased wetted area for riblets and device drag for large-eddy breakup devices).

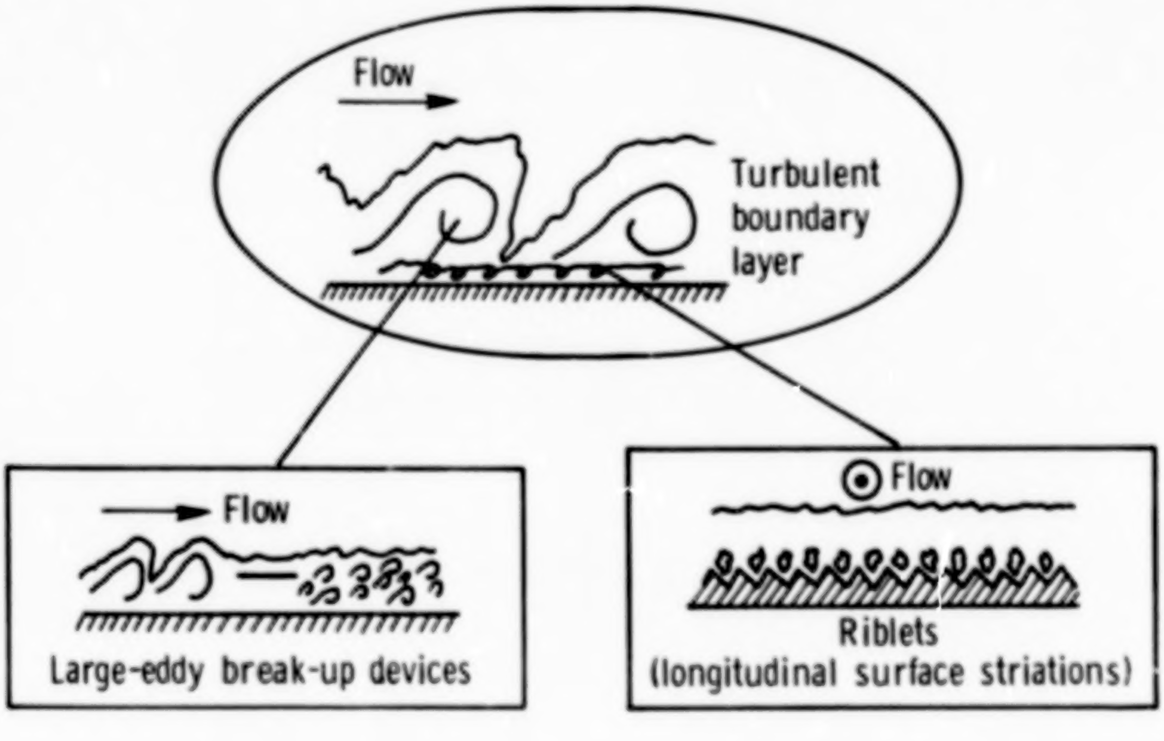
Flow
Turbulent boundary layer
Flow
Large-eddy break-up devices
Flow
Riblets
(longitudinal surface striations)

VISCOUS DRAG REDUCTION RESEARCH

Wind tunnel, flight, computational, and systems research programs are aimed at providing the data base and design methodology necessary to ensure the technology readiness of viscous drag reduction for the 1990's and to reduce the risks associated with both the near-term and far-term application to business, commuter, and transport aircraft. Other important objectives include: determining the limits of applicability of natural laminar flow with regard to wing sweep, pressure gradient, Reynolds number, and disturbance environment; providing the experience and data base to ensure that laminar flow can be maintained economically and reliably in practical airline environments; and demonstrating that turbulent drag reduction is more than a laboratory curiosity and can provide significant benefits in practical flight applications.

Objectives

- Data base and design methodology necessary to accelerate technology readiness and reduce risks for application to business, commuter, and transport aircraft
- Limits of applicability of natural laminar flow
- Economic maintenance and reliability of laminar-flow control concepts
- Flight application of turbulent drag reduction concepts

CURRENT VISCOUS DRAG REDUCTION RESEARCH

Key elements of the Viscous Drag Reduction Program are highlighted on this figure. Laminar flow research focuses on the following: developing advanced airfoils for all classes of aircraft, providing guidelines for fuselage and nacelle laminarization, determining allowable manufacturing tolerances, determining the acoustic environment on transport aircraft at cruise conditions including critical noise sources and their influence on the maintenance of laminar flow, understanding the fluid physics and providing a boundary layer transition criterion for the interaction of crossflow (CF) and Tollmien-Schlichting (TS) instabilities, establishing design criteria for perforated and slotted suction surfaces with improved tolerances to spanwise and chordwise pressure gradients, developing control concepts for separation on laminar-flow airfoils, and conducting systems research to explore the near-term application of hybrid laminar-flow control to transport aircraft. Turbulent drag reduction research focuses on concept invention and development, and the optimization and flight evaluation of riblets and large-eddy breakup devices.

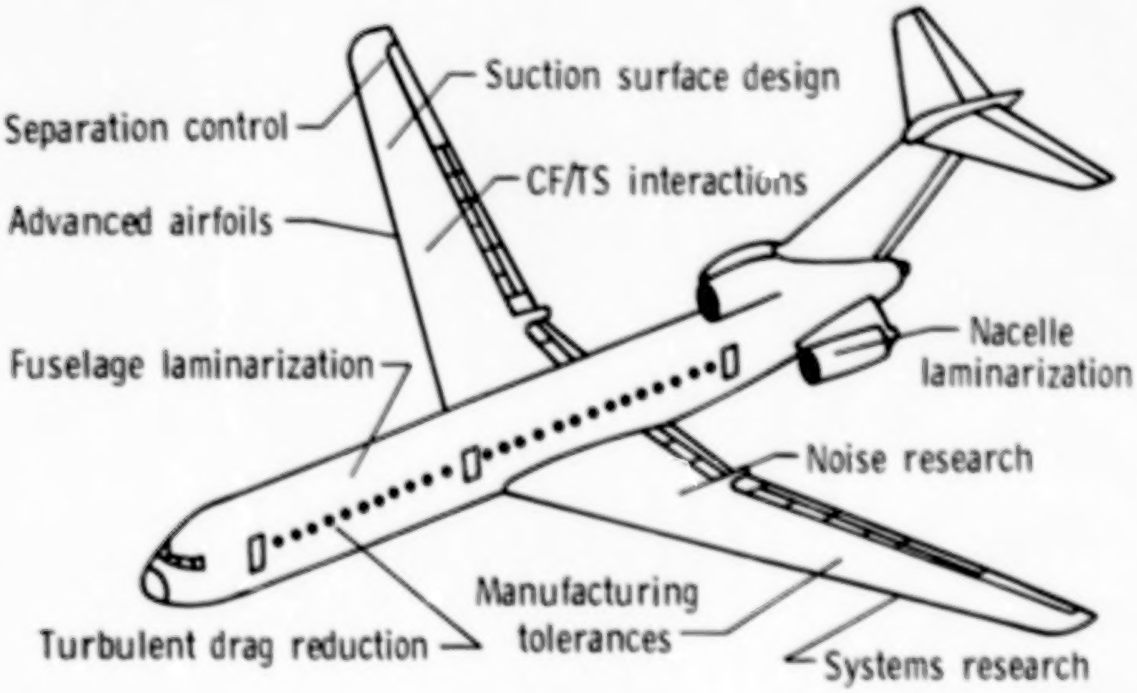
Suction surface design
Separation control
CF/TS interactions
Advanced airfoils
Fuselage laminarization
Nacelle laminarization
Noise research
Manufacturing tolerances
Turbulent drag reduction
Systems research

POTENTIAL PAYOFFS FOR VISCOUS DRAG REDUCTION APPROACHES

Significant progress has been made in the areas of natural laminar flow, laminar-flow control, and turbulent drag reduction over the past seven to ten years and viscous drag reduction is now recognized as one of the two technologies having the greatest potential for improving the performance of future aircraft (propulsion and the advanced turboprop constitute the other technology). Potential payoffs could include 15 percent reductions in cruise drag for natural laminar flow applied to only wing surfaces, 20 percent reductions for laminar-flow control wings, and 5-10 percent reductions for riblets and/or large-eddy breakup devices applied to transport fuselages. These payoffs would reduce fuel volume and cost, increase the sales of business and transport aircraft employing viscous drag reduction, and provide the technology for global military transports and for missiles and supercruisers with increased range.

- Natural laminar flow
    - Order of 15 percent reductions in aircraft drag
    - Greatly increased export sales; reduce fuel costs
- Laminar flow control (suction)
    - Order of 20 percent reductions in aircraft drag
    - $2 billion/year in fuel savings
    - Global military transports
- Turbulent drag reduction
    - Order of 5-10 percent reductions in aircraft drag
    - $700 million/year in fuel savings
    - Increased missile/supercruiser range

D21

N88-14947

1N-02

117245
14P.

ADVANCED NATURAL LAMINAR FLOW AIRFOIL WITH HIGH LIFT TO DRAG RATIO

Jeffrey K. Viken and Werner Pfenninger
ESCON
Grafton, Virginia

Robert J. McGhee
NASA Langley Research Center
Hampton, Virginia

PRECEDING PAGE BLANK NOT FILMED

PAGE 400 INTENTIONALLY BLANK

[redacted]

ABSTRACT

An experimental verification of a high performance natural laminar flow (NLF) airfoil for low speed and high Reynolds number applications has been completed in the Langley Low Turbulence Pressure Tunnel (LTPT). The airfoil was designed for a $c_\ell = 0.4\text{-}0.45$ at a Reynolds number of 10 million and $M_\infty < 0.4$ with a thickness of 0.14 chord. Theoretical development allowed for the achievement of 0.70 chord laminar flow on both surfaces by the use of accelerated flow as long as tunnel turbulence did not cause upstream movement of transition with increasing chord Reynolds number. With such a rearward pressure recovery, a concave type deceleration was implemented. This type of recovery efficiently recovers pressure by decelerating most when the boundary layer has the most energy, then continuously decreasing the gradient toward the trailing edge. The airfoil's leading edge is moderately sharp representing a compromise between a sharp nose needed for a wide low drag c_ℓ range and a blunt nose for better $c_{\ell max}$ performance. A 0.125 chord simple flap is incorporated to substantially increase the low drag c_ℓ range by keeping the stagnation point at the leading edge at different c_ℓ's.

Two-dimensional theoretical analysis indicated that a minimum profile drag coefficient (c_{d_∞}) of 0.0026 was possible with the desired laminar flow at the design condition. With the three-foot chord two-dimensional model constructed for the LTPT experiment, a minimum profile drag coefficient of 0.0027 was measured at a $c_\ell = 0.41$ and $Re_c = 10 \times 10^6$. The low drag bucket was shifted over a considerably large c_ℓ range by the use of the 12.5% chrod trailing edge flap. At a Reynolds number of 10 million and $\delta_f = -10°$, the lower end was shifted to $c_\ell \approx 0$. With a positive flap deflection of 12.5°, the upper end was shifted to $c_\ell = 0.81$. This yielded a two-dimensional lift to drag ratio (L/D) of 245.

Suprisingly high $c_{\ell max}$ values were obtained for an airfoil of this type. A $c_{\ell max}$ of 1.83 was obtained for $\delta_f = 0°$ at $Re_c = 10 \times 10^6$ and $M_\infty = 0.12$. The $c_{\ell max}$ decreases slowly with decreasing Reynolds number. A 0.20 chord split flap with 60° deflection was also implemented to verify the airfoil's high lift capabilities. A maximum lift coefficient of 2.70 was attained at Reynolds numbers of 3 and 6 million.

NLF(1)-0414F DESIGN OBJECTIVES

The first and primary objective of the design was to design a natural laminar flow (NLF) airfoil, for low speed applications, that achieved significantly lower profile drag coefficients at cruise than existing NLF airfoils but was still practical to use. This resulted in an exercise to design an airfoil with as extensive favorable gradients ($dp/dx < 0$) as seemed practical without making the far aft pressure recoveries too severe. The airfoil was also designed for reasonably high chord Reynolds numbers, approximately 10 million (fig. 1).

To help lessen the severity of the far aft pressure recoveries with respect to separation, concave type pressure recoveries were utilized. A concave pressure recovery decelerates the flow when the boundary layer has the most energy, tapering the gradient of the deceleration downstream on the airfoil as the boundary layer loses energy. For off-design conditions, the possibility of utilizing boundary layer re-energizers or momentum redistributors was also examined as a means of alleviating the problem of turbulent separation in the pressure recovery.

To improve $c_{\ell max}$ performance, a thicker leading edge was utilized than is normally considered for airfoils with such extensive laminar flow, operating at such high chord Reynolds numbers. It was known that this thick leading edge would limit the low drag c_ℓ range on the bare airfoil with premature negative pressure peaks, however, the chance of a leading edge type stall would be reduced. Also, Pfenninger's earlier work (ref.1) showed that the use of a small chord simple trailing edge flap could be used to regain a respectable low drag c_ℓ range. Deflection of this small chord flap, both positively and negatively, allows the conversion of lift due to angel of attack into lift due to flap deflection. By changing the lift at the design angle of attack, favorable gradients can be maintained on both surfaces simultaneously for a relatively wide range of lift coefficients.

With the steep pressure recoveries that result on an airfoil of this kind, it was known that there would be problems with laminar separation at lower chord Reynolds numbers. In the far aft pressure rises this results in profile drag penalties due to the formation of separation bubbles. In the leading-edge region this could result in poor high lift performance. The use of boundary layer trips was explored as a means of causing transition before the laminar separation point was reached, thereby eliminating the problem.

Finally, when designing configurations for maximum cruise performance, one is inevitably led to flying as close to $(L/D)_{max}$ as possible. This means increasing the wing loading, and results in the need for greater maximum lift coefficients. NLF(1)-0414F was designed with the intent of integrating it with a slotted Fowler flap arrangement and possibly even a Kruger flap to achieve high maximum lift coefficients.

NLF(1)-0414F DESIGN OBJECTIVES

- 70% CHORD NATURAL LAMINAR FLOW (NLF) ON BOTH SURFACES AT R_{E_C} = 10 MILLION
- COMPROMISE SOME LOW DRAG C_l RANGE (AT $\delta_F = 0°$) TO IMPROVE $C_{l_{MAX}}$ PERFORMANCE BY THICKENING THE LEADING EDGE
- INCREASE LOW DRAG C_l RANGE WITH A SMALL CHORD TRAILING-EDGE FLAP
- IMPLEMENT CONCAVE PRESSURE RECOVERY TO REDUCE THE TURBULENT SEPARATION PROBLEM WHEN TRANSITION OCCURS FAR FORWARD ON THE AIRFOIL. ALSO, POSSIBLY USE SOME FORM OF BOUNDARY LAYER RE-ENERGIZATION OR MOMENTUM REDISTRIBUTION
- USE OF BOUNDARY LAYER TRIPS (TAPE, GRIT, BLEED AIR, ETC.) TO ELIMINATE LAMINAR SEPARATION AT LOWER REYNOLDS NUMBERS, BOTH IN THE REAR PRESSURE RECOVERY AND AT THE LEADING EDGE AT HIGH ANGLES OF ATTACK
- IMPLEMENTATION OF AN EFFICIENT HIGH LIFT SYSTEM: SLOTTED FOWLER FLAPS AND POSSIBLY A KRUGER FLAP

Figure 1

NLF(1)-0414F PROFILE WITH FLAP DEFLECTION

Shown in figure 2 is the profile of NLF(1)-0414F. It is characterized by a moderately sharp leading edge. This leading edge is thicker than a normal high Reynolds number NLF airfoil but sharper than a conventional turbulent flow airfoil. Maximum thickness is 14.3% of the chord, being relatively far aft on the airfoil at the 45% chord location. The trailing-edge region is sharp for low pressure drag penalties. The 12.5% chord trailing-edge flap is illustrated at two deflection angles: -10° and 12.5°.

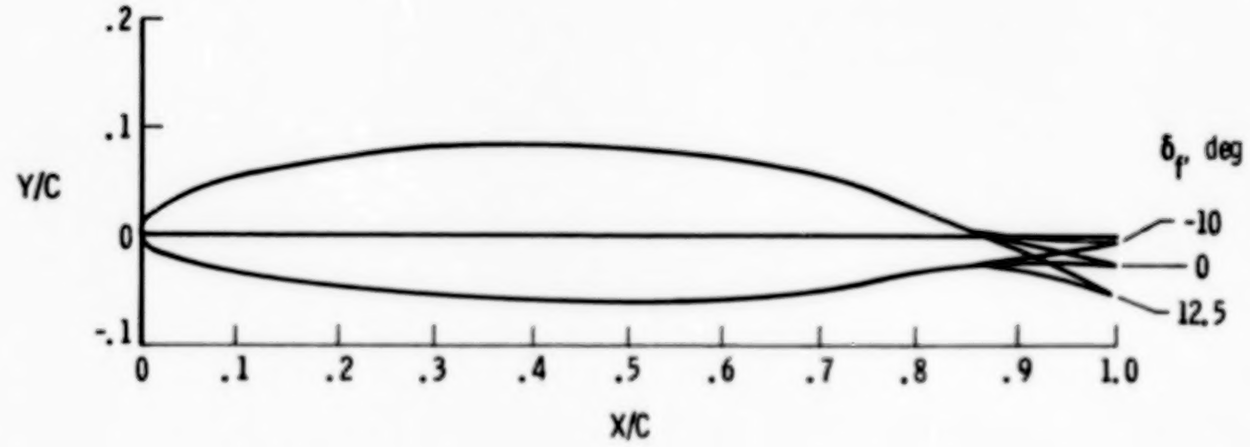

Figure 2

EXPERIMENTAL/THEORETICAL PRESSURE DATA AT DESIGN CONDITIONS

A comparison of the experimental pressure distribution of NLF(1)-0414F at $M_\infty = 0.40$, $Re_c = 10 \times 10^6$, and $\alpha = -1°$ is compared with theoretical pressure distribution calculated by the Korn-Garabedian (ref. 2) potential flow analysis (fig. 3). There are favorable gradients on both surfaces up to the 70% chord location. The steep concave pressure recoveries of NLF(1)-0414F are also illustrated. There is a flat spot in the upper surface pressure distribution at $x/c = 0.15$. This resulted from the addition of thickness in the leading-edge region to improve $c_{\ell max}$ performance. Results form the Tollmien-Schlichting boundary layer stability analysis showed that this flat spot in the pressure distribution yielded a smaller disturbance growth than with a continuous acceleration in this region.

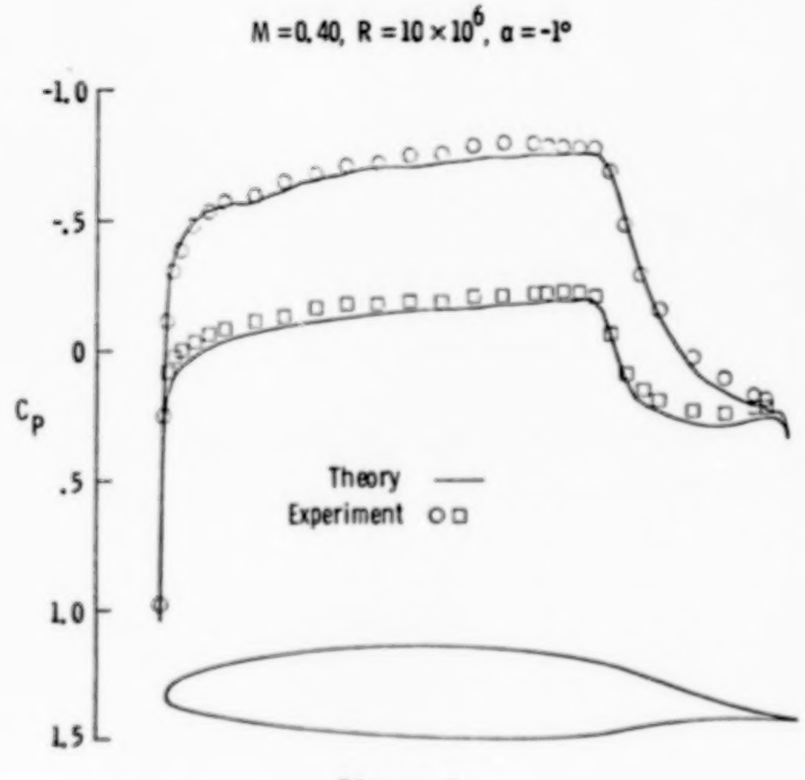

Figure 3

STALL CHARACTERISTICS AND REYNOLDS NUMBER EFFECTS

The section characteristics of NLF(1)-0414F are shown in figures 4 and 5 at chord Reynolds numbers ranging from 2 to 10 million with no flap deflection. For a chord Reynold number of 10 million (the design case) the minimum profile drag coefficient, at $\alpha = -1°$, is 0.0027 with 70% chord laminar flow on both surfaces. This represents a profile drag coefficient that is only 38% that of an unseparated fully furbulent airfoil. The low drag bucket is very narrow at this high Reynolds number in the wind tunnel experiment. The pitching moment coefficient about the quarter chord point is -.079, at $\alpha = -1°$. At the design chord Reynolds number of 10 million $c_{\ell max}$ was 1.83, at $a = 18.0°$, with a gentle stall behavior. If the chord Reynolds number is reduced to 6 million, the $c_{\ell max}$ is still 1.82. However, below $Re_c = 6 \times 10^6$, the $c_{\ell max}$ decreased. This is because of the increased energy losses in the boundary layer due to the increase effects of viscosity. Note that even $Re_c = 2 \times 10^6$, where $c_{\ell max} = 1.45$, the stall is still very gently and there is no indication of a leading edge type stall. As Reynolds number is decreased, the minimum profile drag coefficient increases in a manner greater than unseparated airfoils. Significant laminar separation bubbles start to occur at the beginning of the pressure rise on each surface, resulting in profile drag penalties. Note the character of the low drag bucket at chord Reynolds numbers of 2 and 3 million. at both ends, when the leading edge negative pressure peak eliminates the laminar separation bubble on one surface or the other, the profile drag coefficient is lower than in the middle of the low drag bucket. In the middle of the low drag bucket, there are laminar separation bubbles on both surfaces.

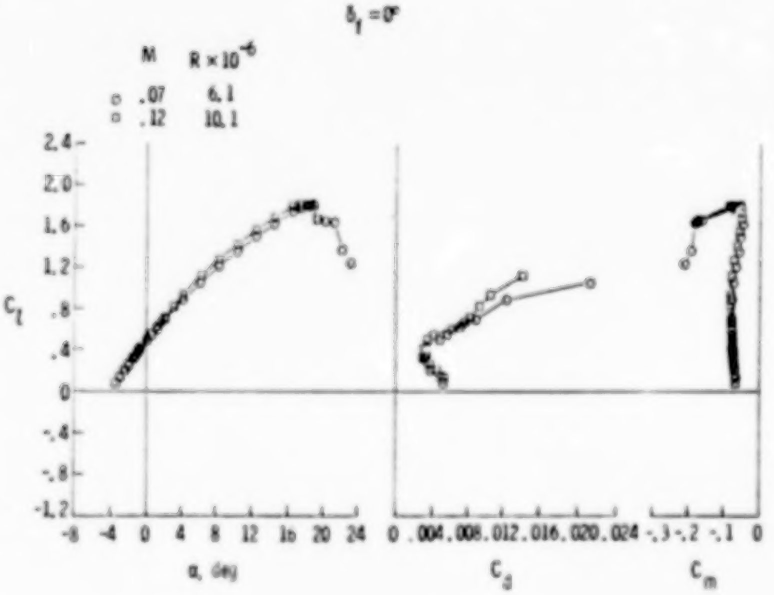

Figure 4

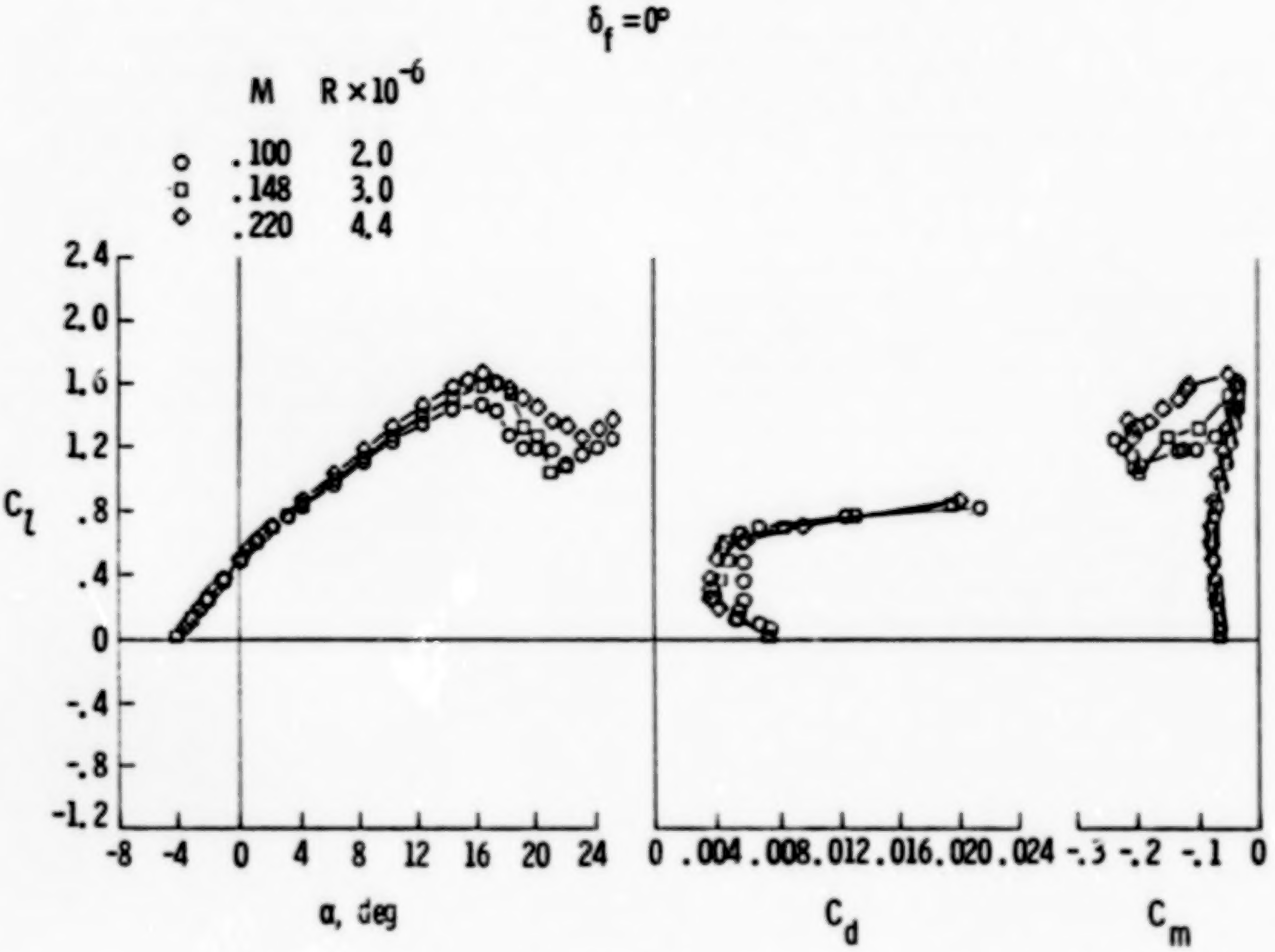
$\delta_f = 0°$
M
$R \times 10^{-6}$
○ .100 2.0
□ .148 3.0
◇ .220 4.4
C_l
2.4
2.0
1.6
1.2
.8
.4
0
-.4
-.8
-1.2
-8
-4
0
4
8
12
16
20
24
α, deg
0
.004
.008
.012
.016
.020
.024
C_d
-.3
-.2
-.1
0
C_m

Figure 5

FLAP DEFLECTION EFFECTS

The drag polar at $Re_c = 6.1 \times 10^6$ for various flap deflections ranging from -10° to 20° is shown in figure 6. Deflecton of this 12.5% chord simple trailing-edge flap gave a c_ℓ rang with a low drag from $c_\ell = -.007$ to nearly $c_\ell = 1.06$. The minimum profile drag coefficient with 0° flap deflection at $Re_c = 6 \times 10^6$ is 0.0032 for a c_ℓ range from 0.273 to 0.417. At the lower end of the drag bucket, with a flap deflection of -10°, the minimum profile drag coeffficient is 0.0036 at $c_\ell = .-007$. At the upper end of the low drag c_ℓ range, with a flap deflection of 20°, the minimum profile drag coefficient is 0.0043 at $c_\ell = 1.06$. This yields a L/D of 247; however, this is only at one c_ℓ and it would be hard to fly at one design point. Examining the 17.5° flap deflection, this same minimum profile drag coefficient, 0.0043, is realized at a section lift coefficient as high as 0.905, yielding a L/D of 210. For this flap deflection, there is a reasonable c_ℓ range to fly in. At the design chord Reynolds number of 10 million, at the upper end of the low drag range (12.5° flap deflection), there was minimum profile drag coefficient of only 0.0033 with $c_\ell = 0.81$. This gives a L/D of 245.

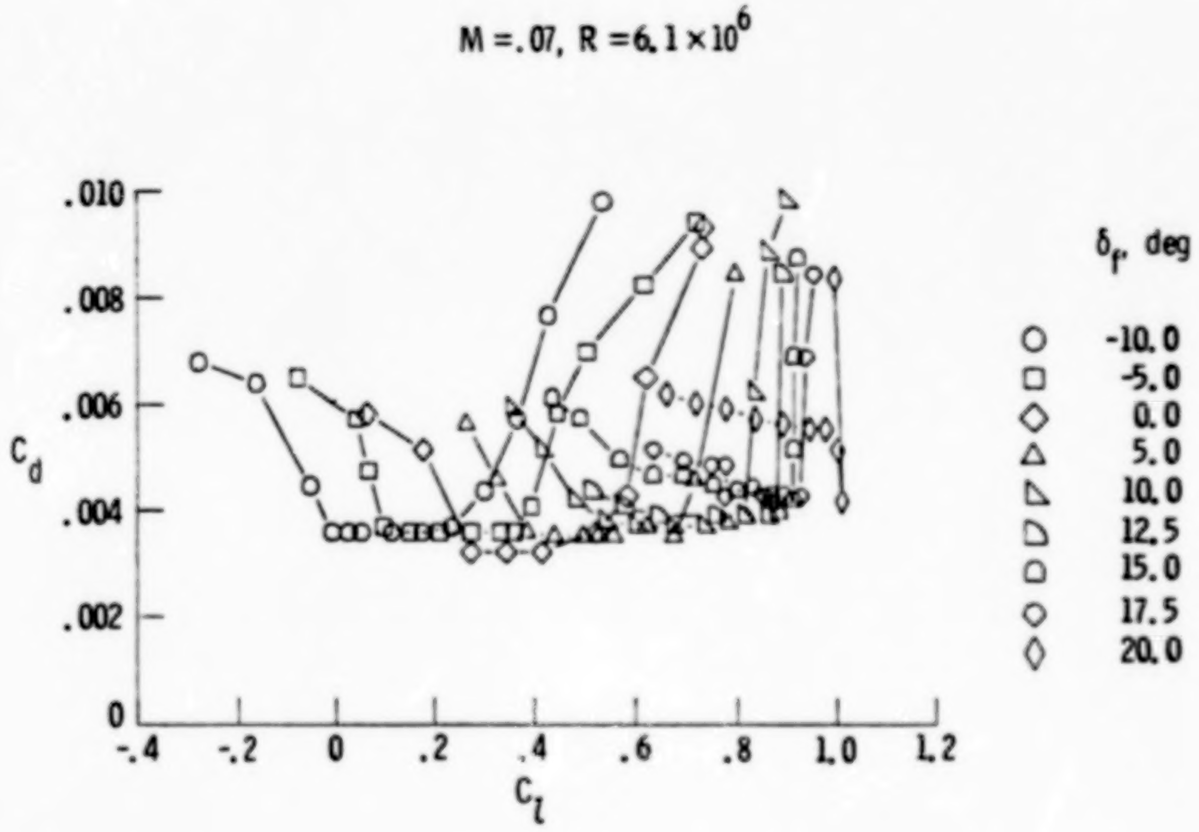

Figure 6

ROUGHNESS EFFECTS

A NLF airfoil has to not only be designed to achieve low profile drag coefficients with extensive laminar flow but must also be able to perform well when the flow is fully turbulent. This can happen when insects or rain cause transition far forward on the airfoil. First, the $c_{l_{max}}$ performance should not be degraded. Second, the airfoil should be designed so that the profile drag at cruise is not usually high, resulting from separation in the far aft pressure recovery. Figure 7 shows that section characteristics of NLF(1)-0414F with transition free and transition fixed near the leading edge at $Re_c = 10 \times 10^6$. The $c_{l_{max}}$ with the flow fully turbulent is 1.81 as compared to 1.83 with free transition. With the flow fully turbulent, the minimum profile drag coefficient is 0.0080, nearly three times that of the extensively laminar value. However, this profile drag coefficient is comparable to that of normal unseparated fully turbulent airfoils.

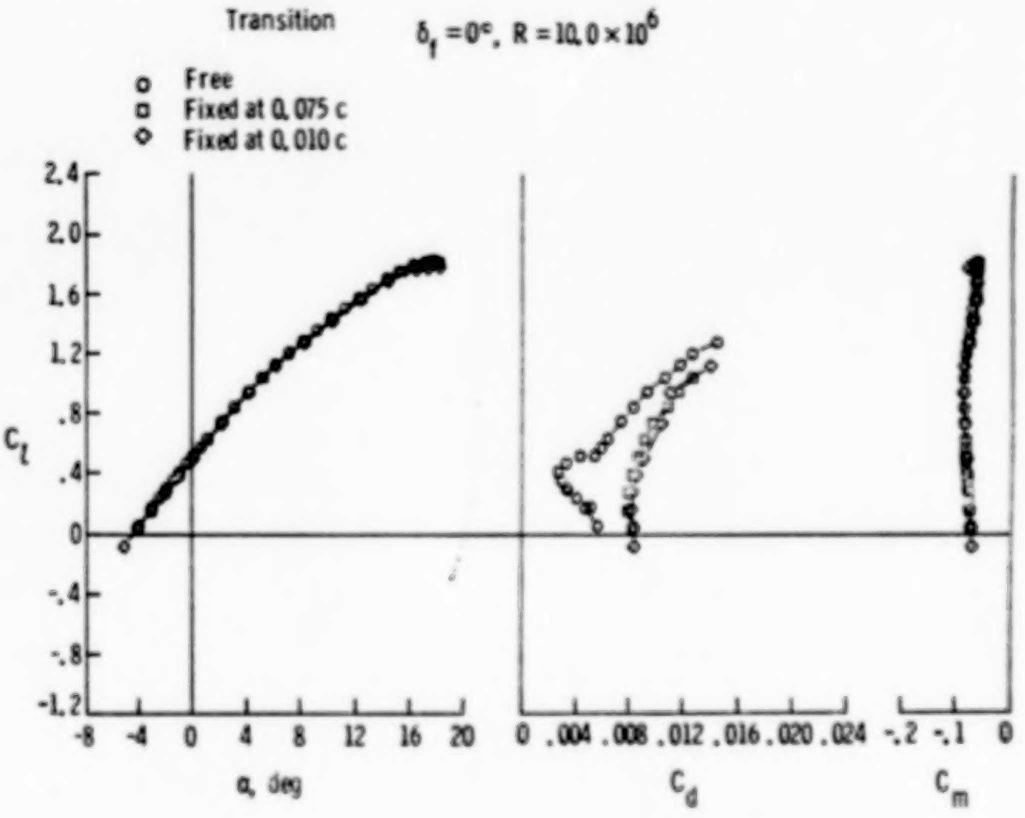

Figure 7

SPLIT FLAP PERFORMANCE

To show the performance of NLF(1)-0414F under the conditions of a high lift system, a split flap was tested in the wind tunnel experiment. A high lift system causes very large negative pressure peaks and will aggravate the leading-edge stall problem if their is one. This split flap was similar to those tested on the NACA 4 and 5 digit and the 6 series airfoils, a 20% chord plate deflected 60° from the lower surface of the model. The section characteristics of NLF(1)-0414F with and without the split flap are shown in figure 8. Drag values were not measured because of the large unsteady wake behind the model. With the split flap installed. $c_{\ell max}$ NLF(1)-0414F was increased to 2.73 at $\alpha = 9.36°$ and $Re_c = 6.1 \times 10^6$. As seen in the plot, the stall is very gently, showing no signs of a leading-edge type stall. At $Re_c = 3 \times 10^6$ with the split flap, $c_{\ell max}$ was 2.66 with the same kind of stall performance.

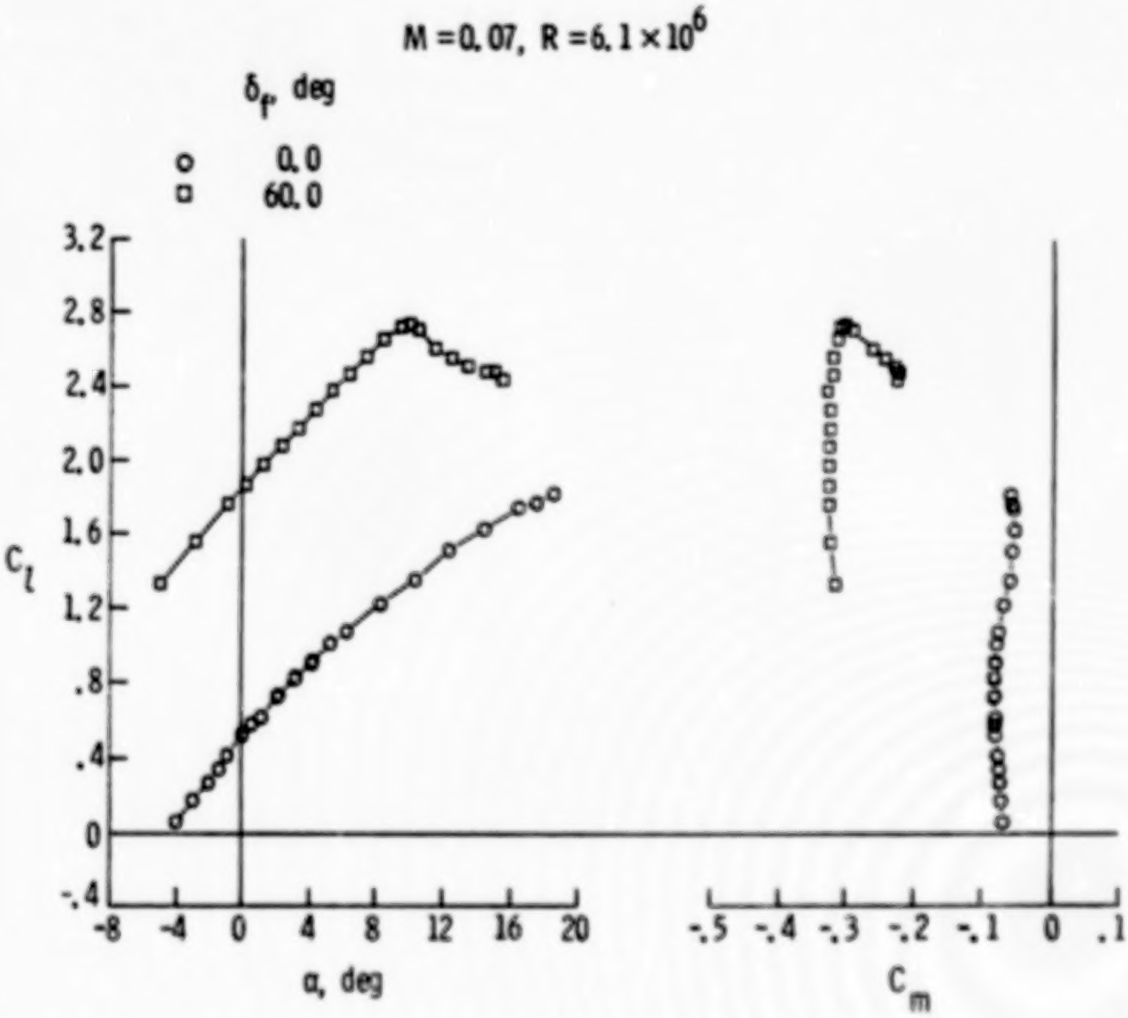

Figure 8

TAPE TURBULATOR EFFECTS

As the Reynolds number is decreased, the boundary layer becomes increasingly stable at the laminar separation point in the beginning of the steep pressure rises on both surfaces. When the highly stable boundary layer reaches the laminar separation point, it separates and takes a considerable distance before transitioning and reattaching back to the airfoil surface. Associated with this separated region are large pressure drag penalties. One method of eliminating this separated region is utilizing turbulators to trip the flow before the laminar separation point is reached. Figure 9 illustrates the drag reduction realized by suppressing these laminar separation regions on NLF(1)-0414F for a range of chord Reynolds numbers from 3 to 10 million. The type of tubulator used in this case was tape of 0.012" thick and 1/4" wide placed at 68% chord on the upper surface and 66% chord on the lower surface. At $c_\ell = 0.4$ and $Re_c = 3 \times 10^6$, with the turbulator tape installed, the profile drag coefficient is 0.0041. This is 20% less than the profile drag coefficient of 0.0051 measured on the clean airfoil. This benefit is reduced as the Reynolds number increases and the boundary layer becomes naturally more unstable. Once the separated region is eliminated naturally, then there is a drag penalty from the tape on the airfoil surface. At $Re_c = 10 \times 10^6$, with turbulator tape installed, the profile drag coefficient is 0.0031, instead of the 0.0027 measured on the clean airfoil.

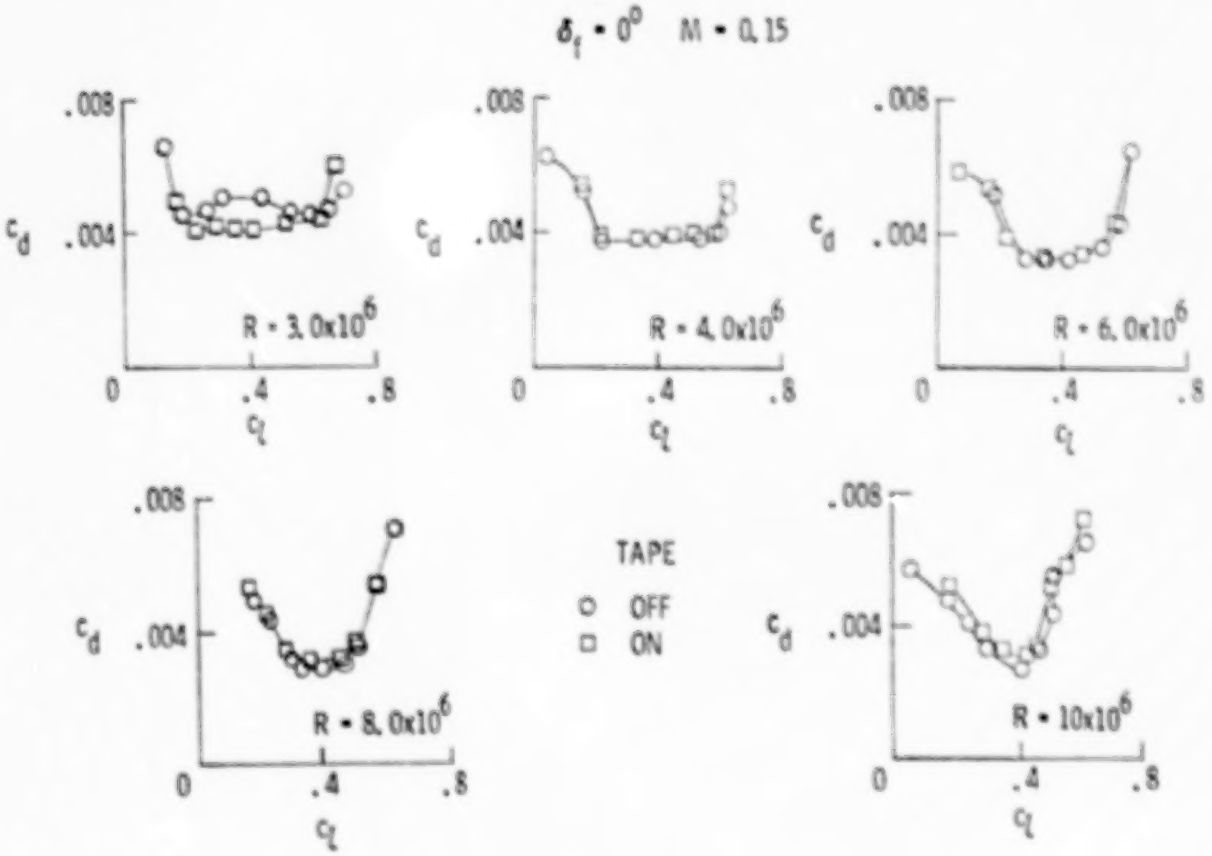

Figure 9

COMPARISON OF AIRFOIL PERFORMANCE

The section characteristics of NLF(1)-0414F are compared with Somers' NASA airfoil section NLF(1)-0215F (ref. 3) figure 10 at $Re_c = 6 \times 10^6$. The NLF(1)-0215F was designed for 40% chord laminar flow on the upper surface and 60% on the lower. With the increased extent of laminar flow for NLF(1)-0414F, 70% of the chord on both surfaces, the minimum profile drag coefficient is 0.0032, where that of NLF(1)-0215F is 0.0045. Even though NLF(1)-0414F has less overall camber, at a chord Reynolds number of 6 million NLF(1)-0414F has a $c_{\ell max}$ of 1.82 at $\alpha = 18.5°$ and NLF(1)-0215F has a $c_{\ell max}$ of 1.74 at $\alpha = 13.2°$.

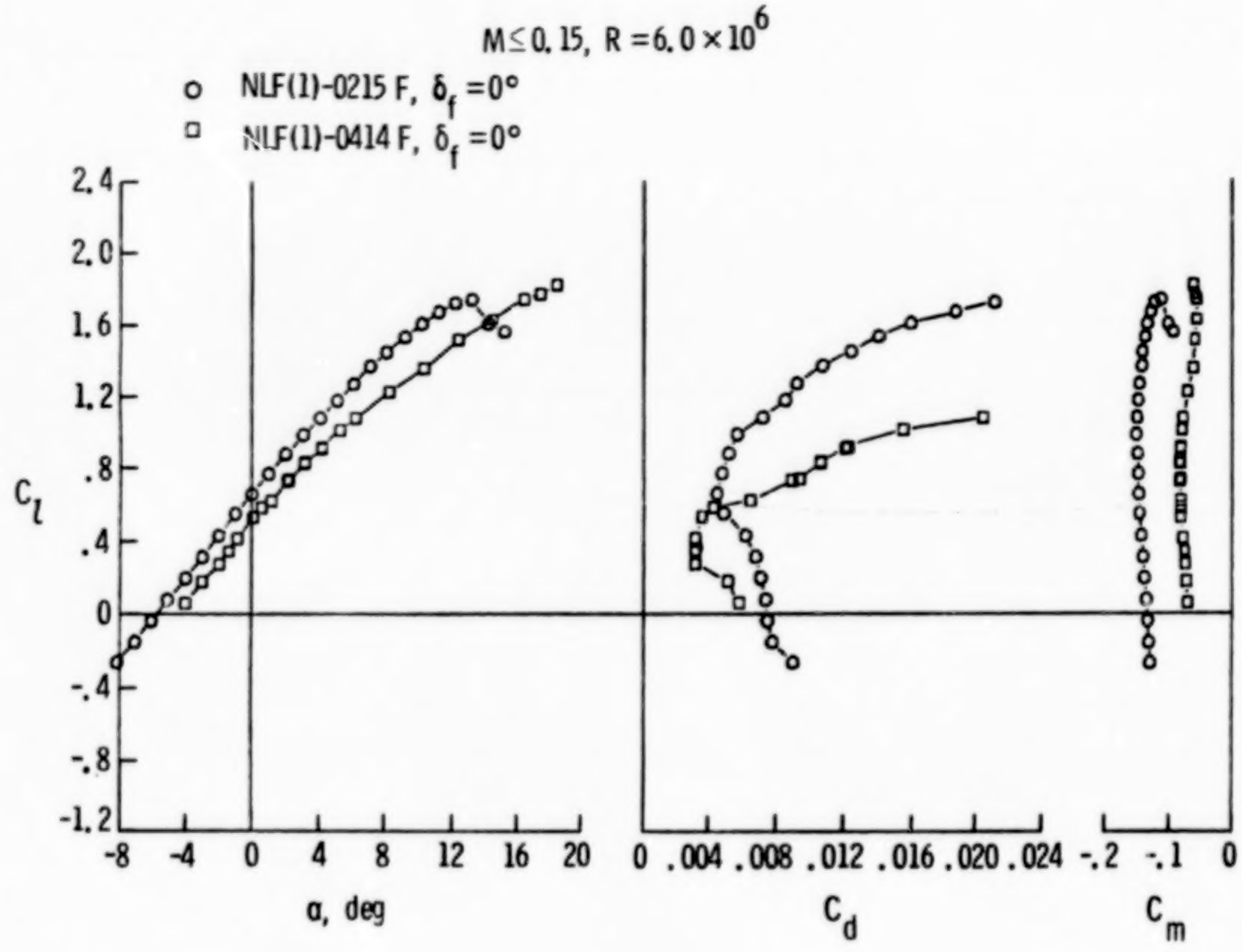

Figure 10

CONCLUSIONS

- 70% CHORD NLF ACHIEVED ON BOTH SURFACES AT $RE_C = 10\text{x}10^6$ IN LTPT ($\tilde{u}/u = 0.04\%$), $C_D = 0.0027$

- WIDE LOW DRAG C_l RANGE ($C_l = 0.0$ TO 0.81) ACHIEVED AT HIGH REYNOLDS NUMBERS BY DEFLECTING A 0.125 CHORD TRAILING-EDGE FLAP, $L/D = 245$ AT $C_l = 0.81$

- $C_{l_{MAX}}$ PERFORMANCE CONSIDERABLY HIGHER THAN EXPECTED, 1.83 WITH $\delta_F = 0°$ AND 2.70 WITH 0.20 CHORD SPLIT FLAP ($\delta_F = 60°$), WITH CORRECT DESIGN OF THE LEADING EDGE AND STEEP PRESSURE RECOVERY

- LOW DRAG PERFORMANCE AT $RE_C = 3\text{x}10^6$ IMPROVED ABOUT 20% BY ELIMINATING LAMINAR SEPARATION BUBBLES ON BOTH SURFACES WITH TAPE TURBULATORS

- ADDITION OF ROUGHNESS NEAR THE LEADING EDGE REDUCED $C_{l_{MAX}}$ BY ONLY 1% AT $RE_C = 10\text{x}10^6$ AND 3% AT $RE_C = 6\text{x}10^6$

REFERENCES

1. Pfenninger , W.: Investigations on Reductions of Friction on Wings, in Particular by Means of Boundary Layer Suction. NACA TM-1181, August 1947.

2. Bauer, F., Garabedian, P., and Korn, D.: A Theory of Supercritical Wind Sections, with Computer Programs and Examples. New York: Springer-Verlag, 1972.

3. Somers, Dan M.: Design and Experimental Results for a Flapped Natural-Laminar Flow Airfoil for General Aviation Applications. NASA TP-1865, June 1981.

D22

N88-14948

COMPUTATIONAL DESIGN OF NATURAL LAMINAR FLOW WINGS FOR TRANSONIC TRANSPORT APPLICATION

S22-02
117246
29P.

Edgar G. Waggoner
Richard L. Campbell
Pamela S. Phillips
Langley Research Center
Hampton, Virginia

Jeffrey K. Viken
ESCON
Grafton, Virginia

[redacted]

ABSTRACT

Two research programs are described which directly relate to the application of natural laminar flow technology to transonic transport-type wing planforms. Each involved using state-of-the-art computational methods to design three-dimensional wing contours which generate significant runs of favorable pressure gradients. The first program supported the Variable Sweep Transition Flight Experiment and involves design of a full-span glove which extends from the leading edge to the spoiler hinge line on the upper surface of an F-14 outer wing panel. Boundary-layer and static-pressure data will be measured on this design during the supporting wind-tunnel and flight tests. These data will then be analyzed and used to infer the relationship between crossflow and Tollmien-Schlichting disturbances on laminar boundary-layer transition. A wing was designed computationally for a corporate transport aircraft in the second program. The resulting wing design generated favorable pressure gradients from the leading edge aft to the mid-chord on both upper and lower surfaces at the cruise design point. Detailed descriptions of the computational design approach are presented along with the various constraints imposed on each of the designs. Wing surface pressure distributions, which support the design objectives and were derived from transonic three-dimensional analyses codes, are also presented. Current status of each of the research programs is included in the summary.

NLF WING DESIGN PROGRAMS

There are two natural laminar flow (NLF) wing design programs in which the Applied Aerodynamics Group has been involved. The Variable Sweep Transition Flight Experiment (VSTFE) was formulated between NASA Ames-Dryden and NASA Langley to establish a data base on the effects of the interaction between crossflow (CF) and Tollmien-Schlichting (TS) instabilities on boundary-layer transition utilizing the F-14 aircraft as a test bed. This involved modifying the F-14 wing outer panel such that favorable pressure gradients could be generated over a wide range of flight conditions. Extensive computations were performed to verify the potential flow methods used in the effort and in the actual design of the wing outer panel.

The second program involved the design of an NLF wing for a proposed high-aspect-ratio, low-sweep, corporate-transport aircraft. Unlike the VSTFE, no data were available on the baseline configuration so the wing design was based totally on computational results. Another unique challenge posed by this design problem was that acceptable aerodynamic characteristics with a fully turbulent boundary layer over the entire wing had to be maintained.

- F–14 OUTER PANEL GLOVE IN SUPPORT OF THE VARIABLE SWEEP TRANSITION FLIGHT EXPERIMENT

- HIGH ASPECT RATIO, LOW SWEEP NLF WING

COMPUTATIONAL METHODS APPLIED TO NLF WING DESIGN

The computational methods that were applied to the NLF wing designs included two two-dimensional codes and three three-dimensional codes.

The New York University airfoil analysis code written by Bauer, Garabedian, and Korn, reference 1, is used extensively by researchers for two-dimensional flow analysis. The inviscid solution solves for steady, isentropic, irrotational flow. Viscous corrections are provided by adding the turbulent boundary layer to the airfoil contour. There is no laminar boundary-layer capability in the code.

The high-lift code, reference 2, is a subsonic panel code with an integral boundary layer. This code is used to evaluate the low-speed, high-lift characteristics of an airfoil.

TAWFIVE, reference 3, solves for the full-potential equation on wing-body configurations using conservative differencing. This code combines FLO-30 with a three-dimensional integral boundary layer. Solutions are obtained on a body-fitting grid which allows for an arbitrary fuselage to be modeled.

WBPPW, reference 4, solves for the flow field around wing, body, pods, pylons, and/or winglets. The code is characterized by a unique grid-embedding technique which provides excellent resolution around various configuration components. Using nonconservative finite-difference approximations, a modified small-disturbance equation is solved in the embedded grid system. Viscous corrections are provided through a two-dimensional strip boundary-layer method which adds displacement thickness slopes to the wing surface slopes.

The FLO-22NM code, reference 5, is the FLO-22 wing-alone code with the following improvements: a quasi-inverse design capability, corrections to the plane of symmetry boundary condition, incorporation of a potential-flow/boundary-layer interaction scheme, simulation of the wing-fuselage interference effect, and an improved drag computation methodology. The full-potential equation is approximated using nonconservative finite-difference techniques. Boundary-layer corrections are based on two-dimensional integral formulations. The quasi-inverse design mode of FLO-22NM is based on an approach by Garabedian and McFadden, reference 6. The wing contour is modified systematically to drive the wing surface pressure distribution toward a specified target pressure distribution.

- TWO – DIMENSIONAL
  - NYU GARABEDIAN AND KORN
  - HIGH LIFT CODE

- THREE – DIMENSIONAL
  - TAWFIVE
  - WBPPW
  - FLO22NM

F-14 VARIABLE-SWEEP TRANSITION FLIGHT EXPERIMENT

An important question that must be answered in order to design wings which effectively utilize NLF relates to boundary-layer transition. It is known that, for boundary layers in a three-dimensional flow environment, there is an interaction between crossflow (CF) and Tollmein-Schlichting (TS) instabilities that can cause transition to occur in an otherwise favorable environment (i.e., favorable pressure gradient, smooth surface, etc.), reference 7. In order to assist in identifying and quantifying the influence of the CF-TS interaction on wing boundary-layer transition, data are needed for various combinations of favorable pressure gradients, Reynolds numbers, and sweep angles. This is the objective of the VSTFE. The F-14 aircraft was selected as the test bed aircraft because of its variable sweep capability, which would allow data to be taken over a wide range of sweep angles.

The approach of this flight experiment is to modify the wing outer panel by gloving on a foam and fiberglass contour so that favorable pressure gradients will be generated over a range of Mach numbers, sweep angles, and Reynolds numbers. Two different gloves were designed which correspond to a M = 0.70 and M = 0.80 design condition. NASA Langley was responsible for the M = 0.70 glove design, and Boeing Aircraft Company was responsible for the M = 0.80 glove design. Both gloves will be flown simultaneously, one on each wing of the F-14, resulting in an asymmetric configuration. Hence, a maximum constraint on the rolling moment because of the asymmetric configuration was imposed on the design.

Objective: Obtain accurate in-flight measurement of boundary layer transition location for wing pressure distributions, sweep angles, and flight conditions representative of future laminar flow transport aircraft.

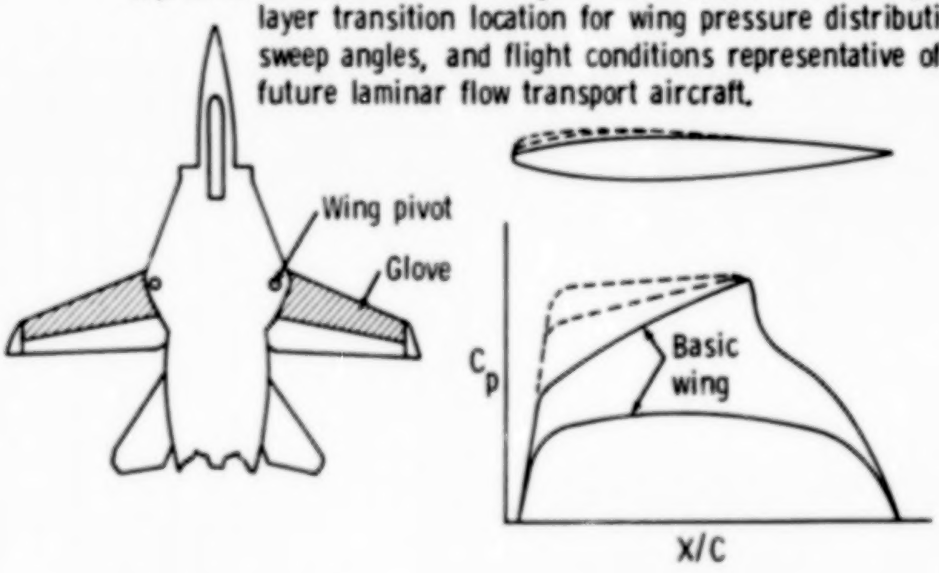

INITIAL QUESTIONS

Extensive computations have been performed using small-disturbance and full-potential flow codes in the design of the NLF glove for the VSTFE. Several questions pertaining to computational modeling of the F-14, the applicability of two-dimensional codes to the design problem, and the ability of three-dimensional codes to accurately predict the flow field on the wing outer panel were addressed. In addition, it was necessary to evaluate the results on the subject configuration from the small-disturbance and full-potential codes.

The F-14 had two geometric characteristics which were the cause for concern with respect to modeling the configuration in the transonic analysis codes. The side-mounted inlet-fuselage combination and the highly-swept strake regions were thought to possibly have significant effects on the outer panel flow field. A sequence of runs was set up to answer these modeling questions using the WBPPW code which has the capability of modeling an arbitrary body. By comparing the results with experimental data the following observations were made (ref. 8):

> The highly-swept strake region has a significant influence on the wing outer panel pressures and therefore should be modeled.
>
> It is not critical to accurately model the inlets or nacelles.
>
> An axisymmetric body with an area distribution equal to the actual aircraft is adequate.

With these observations in hand, it was felt that an accurate configuration model could be developed for the full potential code, TAWFIVE, which would complement the analysis of the small-disturbance code.

Analyses were made on the subject wing in the three-dimensional WBPPW code and compared to results from the two-dimensional Korn-Garabedian code to assess the applicability of the two-dimensional code. From these results, it was seen that the flow field around the outer panel had two-dimensional behavior implying that the Korn-Garabedian code could be used in the design process.

- Which codes could be used?
- How should the strake be represented?
- How should the body/ nacelle be represented?

APPLICATION OF SMALL-DISTURBANCE CODES TO NLF AIRFOILS

There was also concern about applying the small-disturbance code to the natural laminar flow airfoils because of questions relating to the capability of the code to accurately predict leading-edge pressure distributions. This is essential since pressure distributions conducive to NLF have favorable pressure gradients from the leading edge aft to the transition location. If the leading-edge pressures are inaccurate, potential problems with the design could be masked. To gain confidence, an NLF airfoil was analyzed using the two-dimensional option in the WBPPW code and compared to results from the Korn-Garabedian code.

The results showed only minor differences in the pressure distributions, demonstrating that the small-disturbance code could accurately predict the leading-edge pressures of an NLF airfoil.

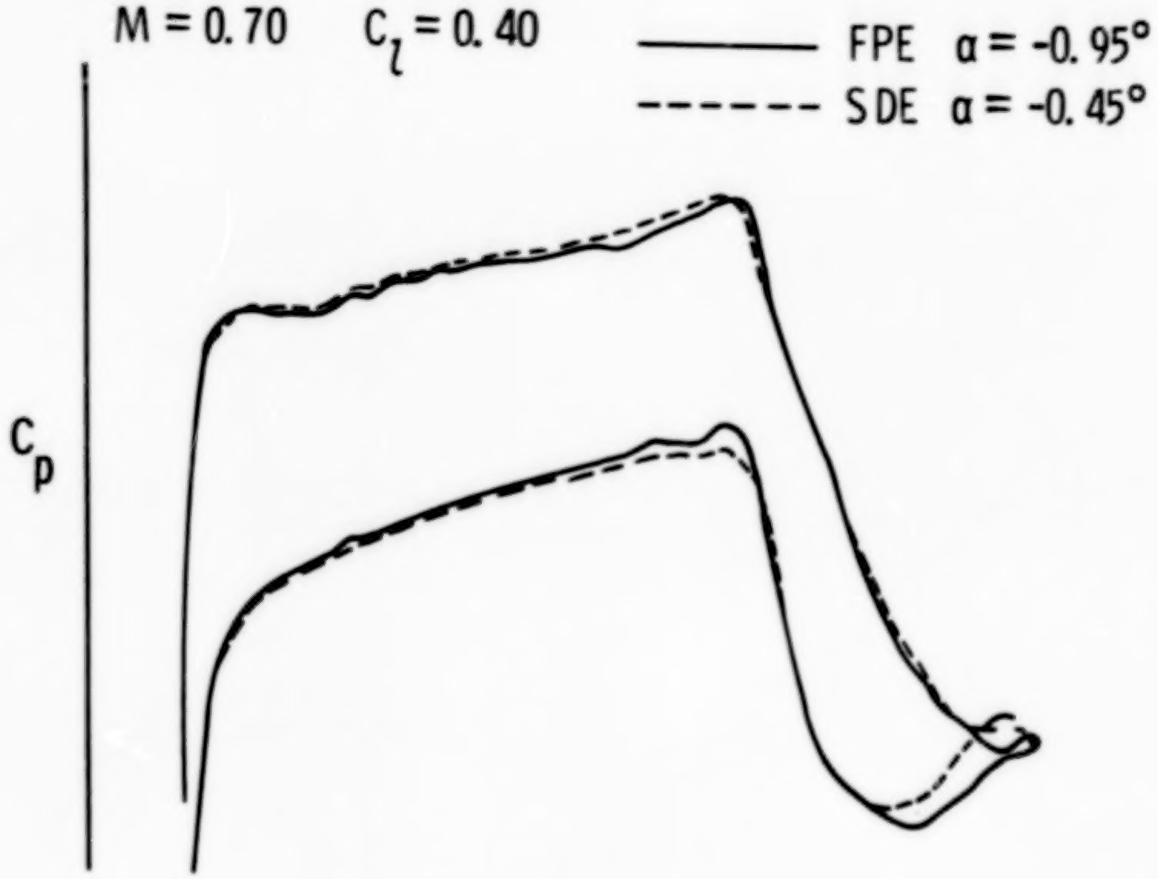

COMPARISON OF FLIGHT TEST AND COMPUTATIONS

A flight test of the F-14 was conducted to explore the test envelope for the VSTFE and to obtain wing pressure data on the basic aircraft (data to be published). From these data, four flight points were designated to be of primary interest. Three of the points correspond to corners of the flight envelope for the VSTFE, and the remaining point is an intermediate flight condition.

Analyses were made in the WBPPW and TAWFIVE codes at the flight Mach number and measured angle of attack. Overall, the comparisons are quite good. Several observations need to be made concerning the comparisons. First, the flight data showed a flow expansion at the leading-edge followed by a compression that neither code predicted. This indicated that possibly the leading-edge slat deflected under load. Static loading corresponding to flight loads confirmed this. The differences seen in leading-edge expansions between the two codes is consistent with the code formulations. Shock resolution is much better in the WBPPW code results because of the denser grid in that region as compared to the TAWFIVE code. Additionally, the TAWFIVE code uses conservative differencing where WBPPW uses nonconservative differencing, which accounts for the discrepancy in shock location.

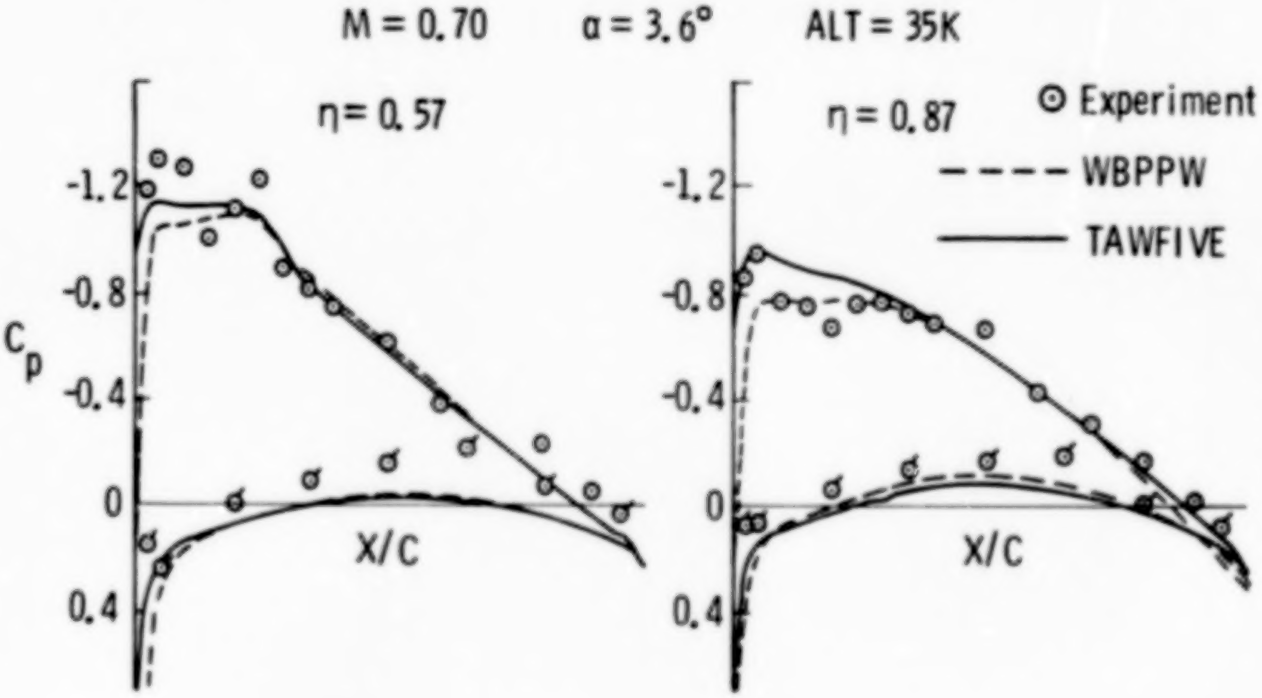

DESIGN APPROACH

Based on the comparisons of the potential flow codes with the flight data and the evaluations of the applicability of the two-dimensional and three-dimensional codes to this design problem, it was felt that an integrated two-dimensional/three-dimensional design process could be formulated. The design process that was used was not formulated a priori but evolved with the program. This loosely defined approach is as follows:

> Equivalent sectional lift coefficients were defined as a function of span for the design point (high altitude, M = 0.70) based on the flight test data. Modifications were made to the sectional contours to yield a slightly favorable gradient from the leading-edge to midchord by using two-dimensional analysis and design procedures followed by a three-dimensional design code (FLO-22NM) to reduce any adverse three-dimensional effects.
>
> The resulting sections were then meticulously refaired, smoothed, and analyzed once again with the two-dimensional analysis codes.
>
> Finally, the outer panel was analyzed at the design and off-design conditions with the TAWFIVE and WBPPW codes as part of the complete F-14 configuration.

DESIGN POINT

$M = 0.7 \qquad C_l = 0.60$

- 2–D DESIGN
- 3–D ANALYSIS AND REDESIGN
- 2–D DESIGN, FAIRING, AND SMOOTHING
- 3–D TAWFIVE ANALYSIS

DESIGN CONSTRAINTS

The physical constraints on the modifications evolved with the design program. The final constraints and supporting rationale are:

> The upper surface could be modified from the leading-edge to the spoiler hinge line ($x/c = 0.60$) in order to utilize the spoilers for roll control. Modifications on the lower surface were limited to the first 10-percent chord.
>
> The thickness of the glove at the spoiler hinge line must be less than 1.0 inch. This constraint was imposed to ensure spoiler effectiveness. For reference, the wing mean chord is 105.66 inches.
>
> The thickness of the glove was required to be a minimum of 0.65 inches. This constraint was required to minimize the possibility of the leading-edge slat deflecting under load.
>
> The rolling moment resulting from the asymmetric configuration was required to be less than 0.01 over the flight test envelope.

- UPPER SURFACE MODIFICATION
  $0.0 < X/C < 0.60$
- LOWER SURFACE MODIFICATION
  $0.0 < X/C < 0.10$
- INCREMENT AT SPOILER HINGE LINE
  LESS THAN 1.0 INCH
- INCREMENT OVER GLOVE REGION A MINIMUM
  OF 0.65 INCHES
- DIFFERENTIAL ROLLING MOMENT LESS THAN 0.01

DESIGN AIRFOIL MEETING FINAL CONSTRAINTS

The design point selected corresponded to a "worst case" condition for the targeted Mach number ($M = 0.70$). This condition corresponded to the highest altitude, hence the largest lift coefficient for 1-g flight. If the sectional contours could be modified such that a slightly favorable gradient could be generated from the leading-edge to the midchord region at this condition, then at lower altitudes there would be an even more favorable pressure gradient. Five defining stations were chosen to be recontoured using linear lofting between defining stations. These corresponded to the inboard and outboard extent of the glove and three intermediate defining stations. With two-dimensional analysis and design procedures, upper surface contours were defined which met the aerodynamic and physical constraints for each defining station. A favorable pressure gradient was observed for a range of lift coefficients on the design airfoil as well as a favorable pressure gradient aft of the leading-edge to the pressure rise.

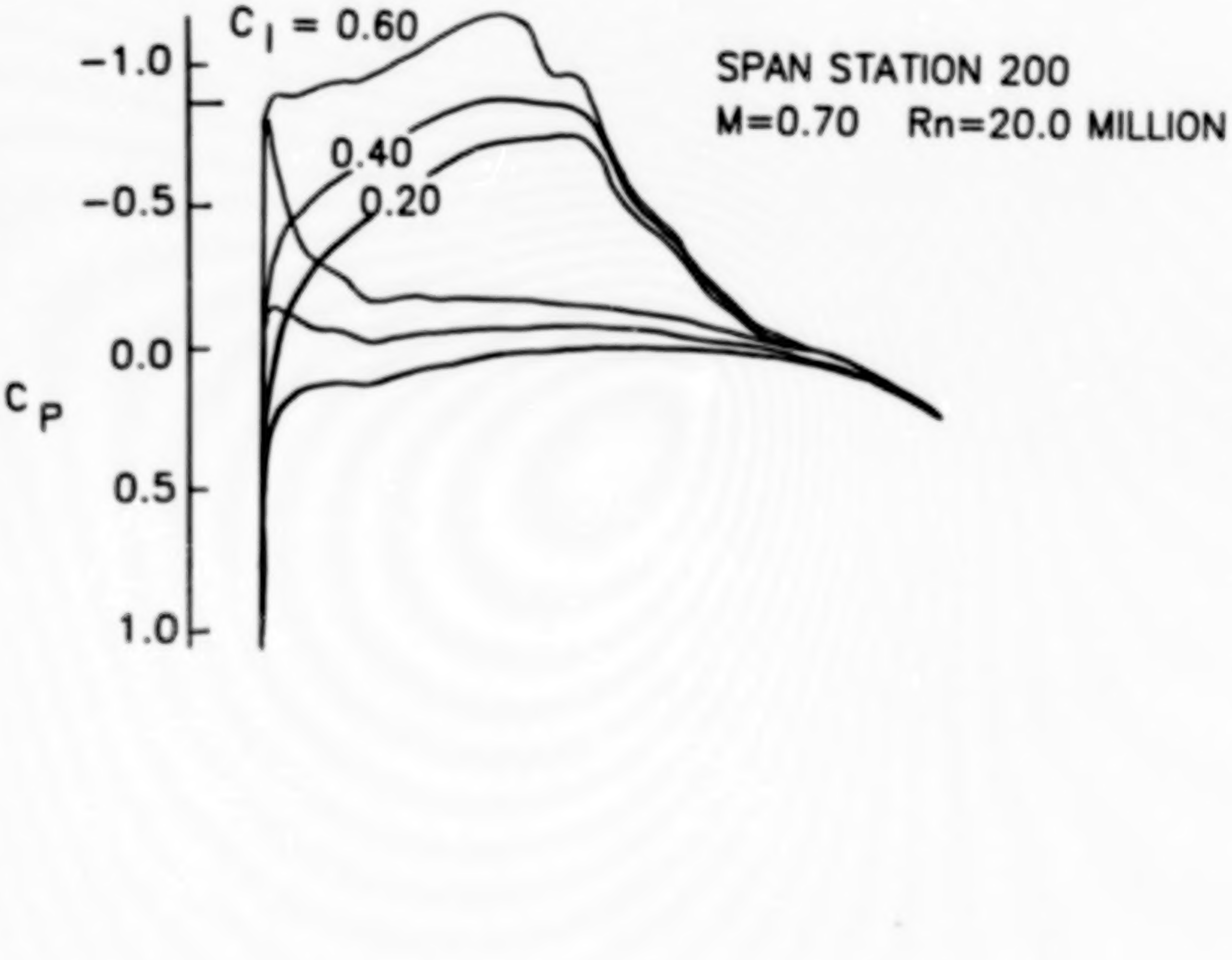

3-D ANALYSIS AND DESIGN

The next step in the design process was to analyze the recontoured outer panel in a three-dimensional environment and further modify the configuration to eliminate any adverse three-dimensional effects. For this phase, a derivative of FLO-22 was used because of its capability to modify a wing contour to yield a desired pressure distribution (ref. 5). The results of a wing-alone analysis revealed two undesirable characteristics in the pressure distributions. A pressure peak at the leading edge appeared as did a flow expansion ahead of the shock. Target pressure distributions were generated to minimize the effects of these two characteristics. A design run was made using the target pressures, which yielded new wing section contours. The design algorithm handled the leading edge quite well; however, the contour changes near the shock caused pressure oscillations. A two-dimensional design code was brought into play that systematically smooths the airfoil curvature while attempting to generate a specified target pressure distribution. Final contours were produced using this code that met the design constraints at each defining station.

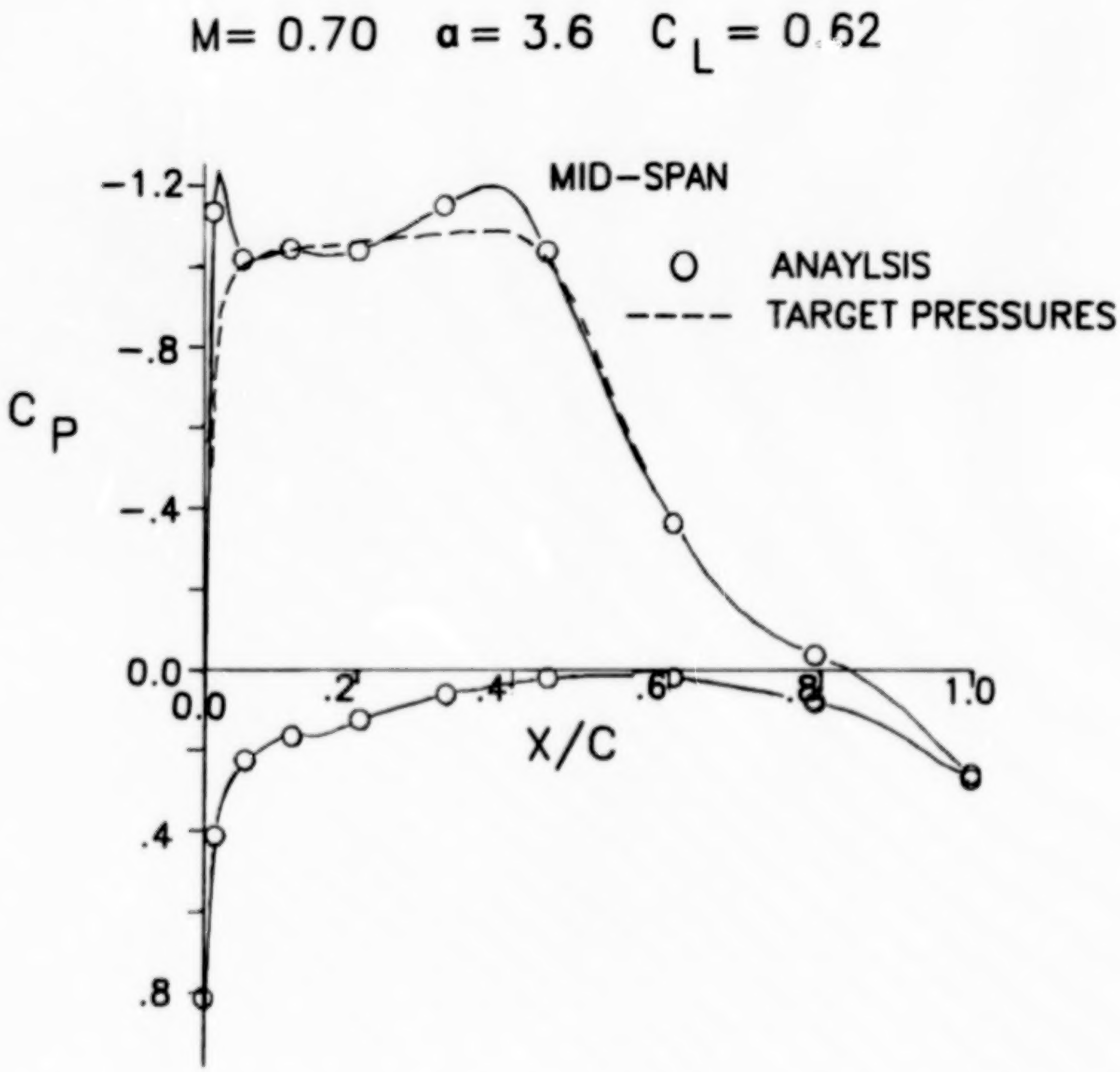

FINAL DESIGN AIRFOIL

The final design airfoils at each defining station met these geometric constraints:

Upper surface modifications were made from the leading-edge to the spoiler hinge line. Lower surface modifications were made on the first 10-percent chord.

Maximum thickness at the spoiler hinge line was less than 1.0 inch. Minimum thickness of the contour over the entire gloved surface was at least 0.65 inches.

An incremental rolling moment between the NASA Langley glove and the Boeing glove was less than 0.01.

Instrumentation leads were to be routed inside the leading edge of the glove, hence it was necessary to extend the glove leading edge 2.0 inches in front of the actual leading-edge of the wing.

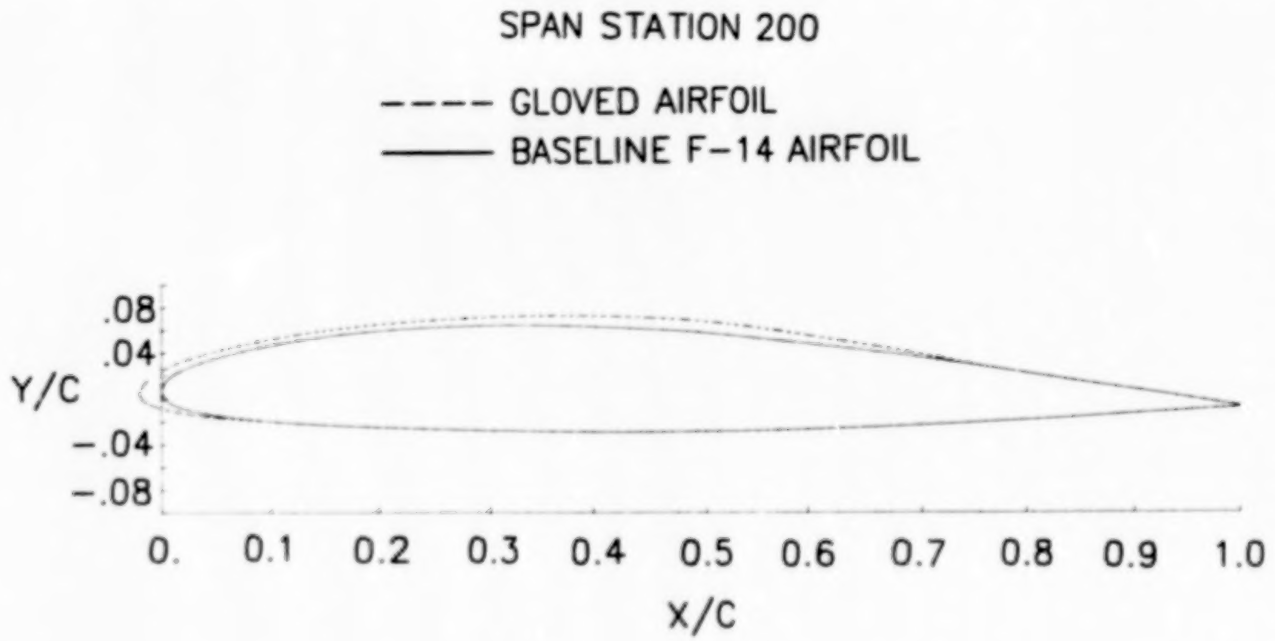
SPAN STATION 200

FINAL NLF F-14 AIRFOIL DESIGN

Two-dimensional analysis of the final airfoil design for each defining station show the desired favorable gradient from the leading-edge to the midchord region over a range of section lift coefficients at M = 0.70. Results gave no evidence of adverse effects from the final section contour modifications. Pressure distributions for the midspan defining station at M = 0.70 for various sectional lift coefficients are shown and are representative of the pressure distributions at the other defining stations.

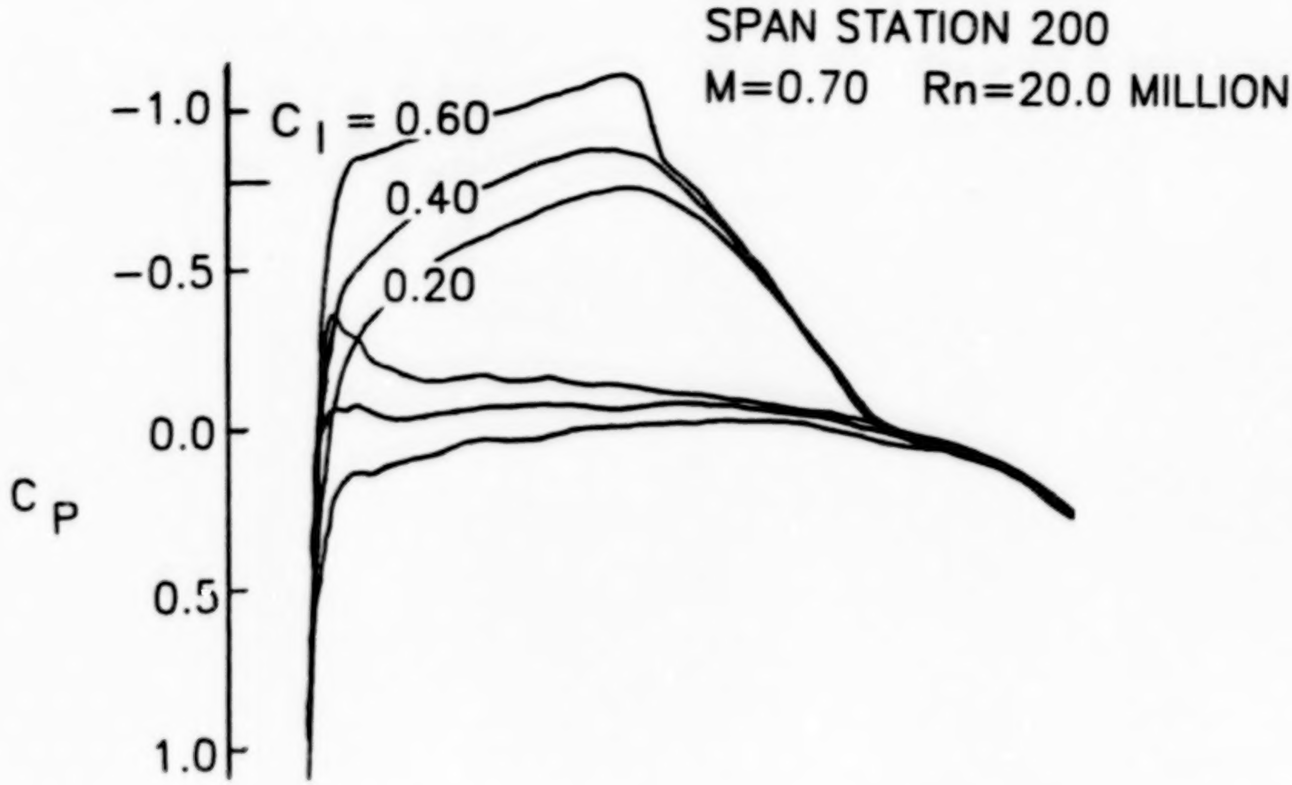

3-D ANALYSIS OF GLOVE DESIGNS

Final computational verification of the design was realized by analyzing the entire configuration (fuselage, nacelles, strake, and outer panel) in the TAWFIVE code. Results show that the design objectives were met over the range of lift coefficients corresponding to the altitudes of interest at M = 0.70. In addition, an analysis solution was obtained at an off-design point which corresponds to Boeing's design point, M = 0.80. The following three figures reflect those results.

The first figure shows the NASA glove design as compared to the Boeing glove design at the low altitude (25,000 feet, $C_L = 0.35$) case at M = 0.70. Note that this condition is an off-design condition for the Boeing design; however, the data for the Boeing glove are included since the designs will be flown simultaneously.

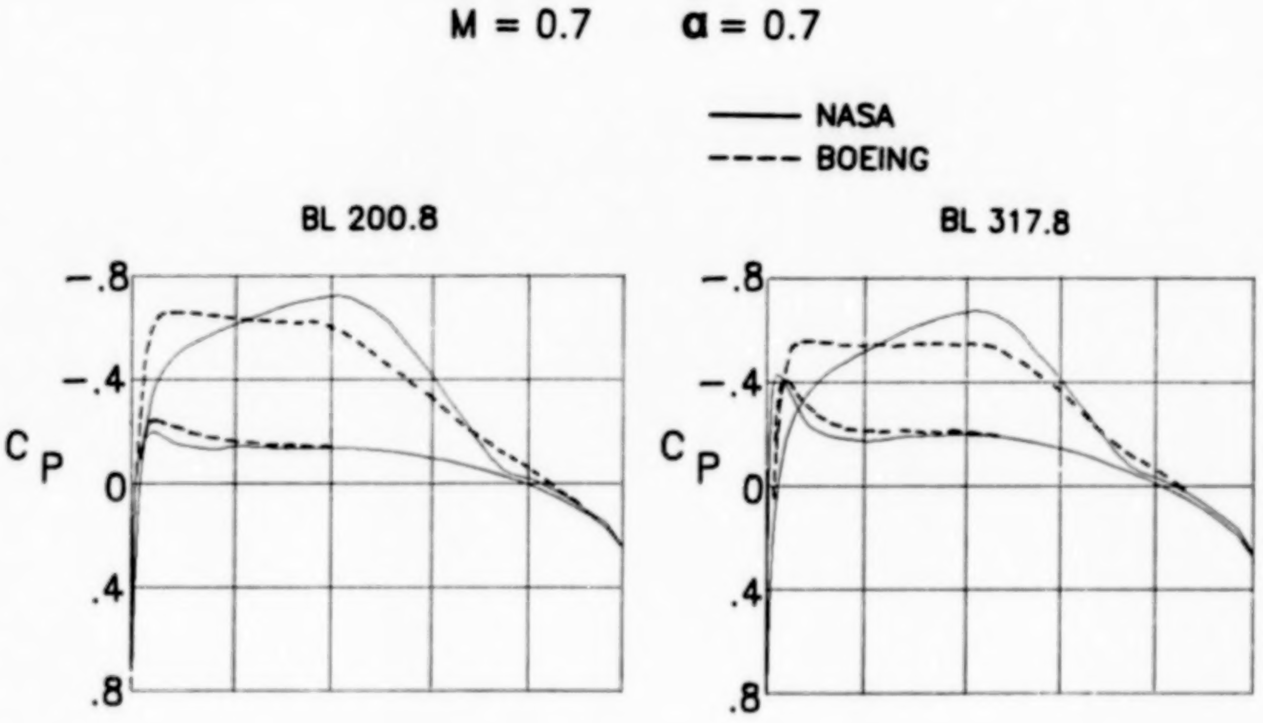

3-D ANALYSIS OF GLOVE DESIGNS

Presented in this figure are the results for the high altitude (35,000 feet, $C_L = 0.52$) case at the targeted Mach number, $M = 0.70$. This condition corresponds to the "worst case" at the targeted Mach number. The results show a slightly favorable gradient from the leading edge aft to the pressure rise. Again, this is an off-design condition for the Boeing glove.

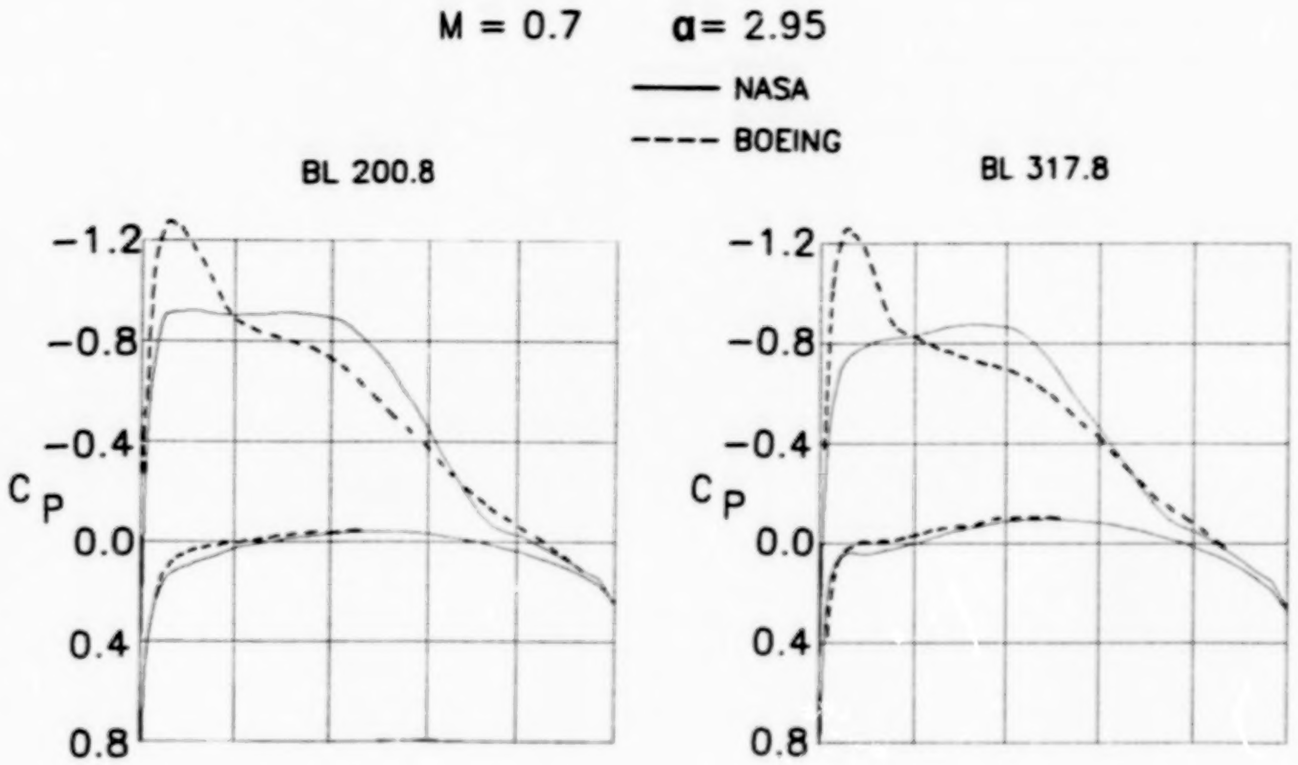

3-D ANALYSIS OF GLOVE DESIGNS

At the high altitude (35,000 feet) off-design Mach number for the NASA glove, M = 0.80, the boundary-layer analysis gave no indication of flow separation. Since the computational analysis predicted acceptable results and the design constraints were met, the glove design was frozen at this point. Note that this off-design point for the NASA glove design is the "worst case" design condition for the Boeing glove design.

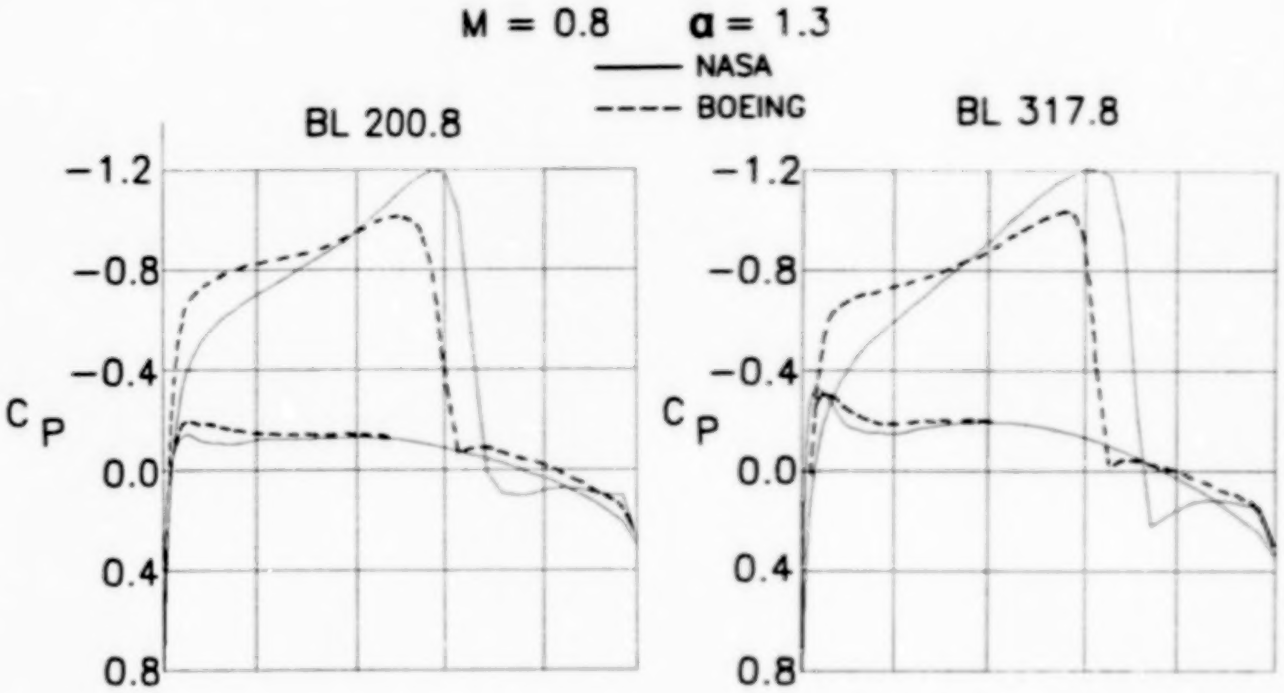

STATUS OF F-14 VSTFE

Glove design has been completed for the VSTFE and model fabrication is underway for a wind-tunnel test to be conducted in the NTF during the early summer 1985. The objectives of the test are to obtain data to verify the glove design and safety-of-flight data for support of the flight-test program. Flight-test instrumentation techniques will be validated in a program which will be flown in late summer or early fall 1985. A "cleanup" glove has been fabricated for the F-14 outer panel which employs the physical constraints described previously and corresponds to the baseline F-14 outer panel contour. Any manufacturing or instrumentation problems uncovered during this program can be addressed before the NLF glove experiment is flown. Manufacture of the NLF glove will commence in the last quarter of 1985 with the flight test following 9 to 12 months later.

- COMPUTATIONAL DESIGN COMPLETED
- WIND TUNNEL TEST FOR DESIGN VERIFICATION AND SAFETY OF FLIGHT – NTF, JUNE 1985
- FLIGHT TEST GLOVE DESIGN – DRYDEN FLIGHT TEST FACILITY, SUMMER 1986

3-D DESIGN OF A HIGH-ASPECT-RATIO NLF TRANSONIC WING

The second design configuration reported in this study is a high-aspect-ratio, natural laminar flow wing for a corporate transport. The objective for this program was to design a wing which would operate efficiently at a transonic cruise point and generate significant runs of laminar flow on both upper and lower surfaces. Because the aircraft had a single jet engine, it had to meet a landing speed requirement of 68 knots. This requirement dictated a relatively large wing area and a maximum lift coefficient of about 3.8. The large wing area, however, meant that at the cruise Mach number of 0.7 the lift coefficient was only 0.25. Other design constraints included: 1) a maximum thickness-to-chord ratio of at least 12.5 percent (for fuel volume and landing gear storage) and 2) good aerodynamic characteristics with a fully turbulent boundary layer.

DESIGN A WING WHICH OPERATES EFFICIENTLY AT A TRANSONIC CRUISE DESIGN POINT AND WHICH GENERATES SIGNIFICANT RUNS OF LAMINAR FLOW ON BOTH UPPER AND LOWER SURFACES

CONSTRAINTS AND DESIGN CONDITIONS :

- CRUISE AT $M=0.70$ AND $C_L = 0.25$
- $T/C > 12.5\%$
- $C_{l_{MAX}} = 3.8$
- GOOD AERODYNAMIC CHARACTERISTICS WITH A FULLY TURBULENT BOUNDARY LAYER

APPROACH

The approach used in the design of this wing was to apply both two-dimensional and three-dimensional transonic potential flow methods which have been validated for transport configurations. The major airfoil design modifications were made using the Garabedian and Korn two-dimensional analysis code. This code has been widely used by industry and is robust and accurate. The two-dimensional subsonic panel code was used to evaluate the low speed, high lift characteristics of the final airfoil. Analyses of the configuration with the airfoils developed from the two-dimensional design methods were made using two of the three-dimensional transonic codes described earlier. The primary code used was TAWFIVE, a full-potential wing/fuselage code which includes a three-dimensional boundary layer calculation to model viscous effects. This code has not been extensively validated with data, but has shown some very encouraging results. A second code, WBPPW, which has been run for many configurations, was also used to add confidence to the TAWFIVE results.

- APPLY RELIABLE 2–D AND 3–D TRANSONIC POTENTIAL FLOW METHODS WHICH HAVE BEEN VALIDATED FOR TRANSPORT APPLICATION.
- TWO–DIMENSIONAL ANALYSIS:
  - **NYU GARABEDIAN AND KORN**
  - **HIGH LIFT CODE**
- THREE–DIMENSIONAL ANALYSIS:
  - **TAWFIVE (FPE/ 3–D BL)**
  - **WBPPW (ESD/ 2–D BL)**

WING PLANFORM

The design variables used in this study were airfoil shape and wing twist. The wing planform was specified a priori and had a span of 252.6 inches, an area of 250.0 square feet, an aspect ratio of 8.0, and a taper ratio of 0.35. The essentially unswept quarter-chord line reduces the chances that crossflow instabilities in the laminar boundary layer would cause premature transition. The low sweep and high aspect ratio of the wing meant that the two-dimensional airfoil design pressures were maintained on the three-dimensional wing except for the regions near the tip and the side of the fuselage.

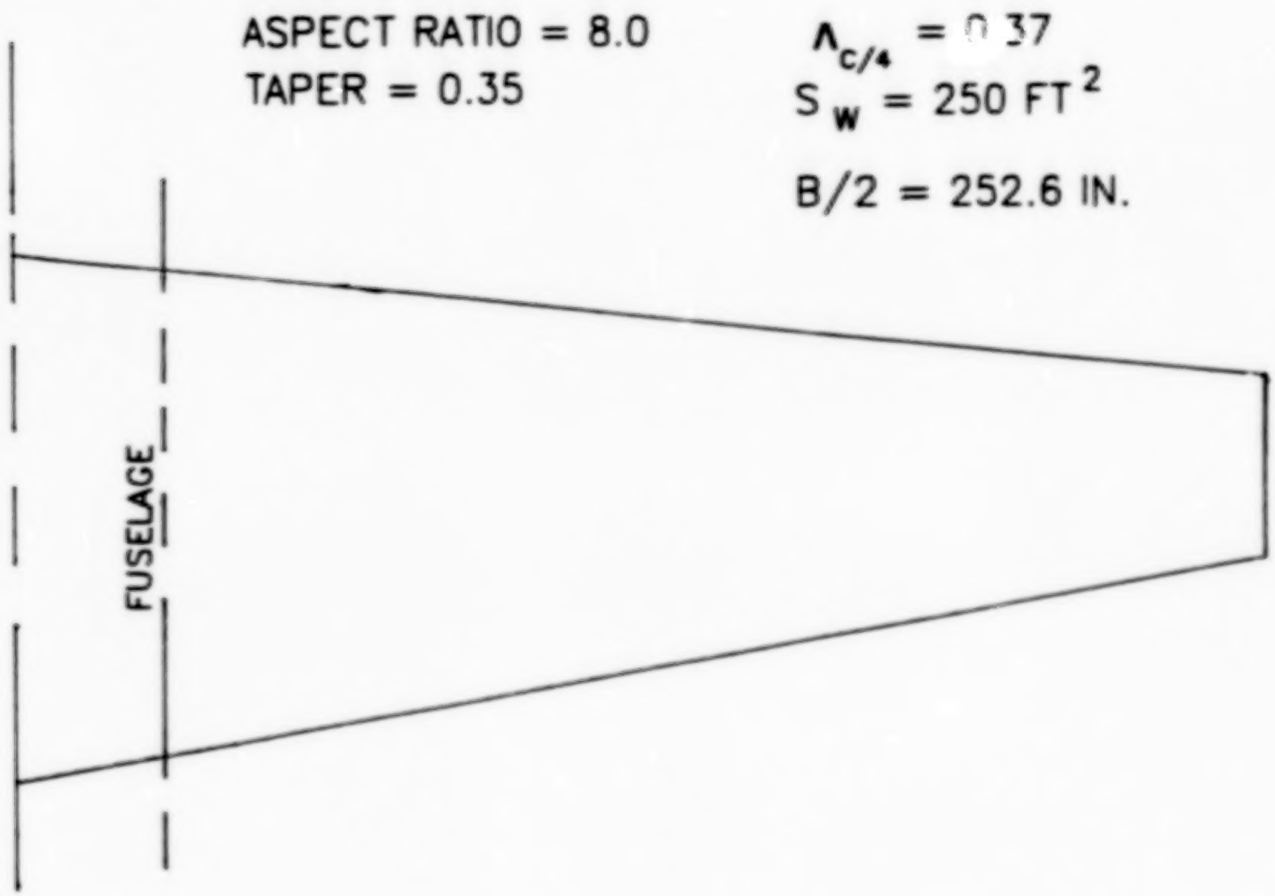
ASPECT RATIO = 8.0
TAPER = 0.35
$\Lambda_{c/4}$ = 0.37
S_W = 250 FT^2
B/2 = 252.6 IN.
FUSELAGE

INITIAL DESIGN

The starting point for the airfoil design was a 14-percent thick medium-speed NLF airfoil developed at NASA Langley by Viken, reference 9. This airfoil maintained laminar flow back to about 70-percent chord on both surfaces at a Mach number of 0.4, a lift coefficient of 0.4, and a Reynolds number of 10 million. The first design modification involved scaling down the airfoil thickness to account for the increase in design Mach number. The trailing edge camber was also reduced to lower the design lift coefficient to 0.25. The pressure distribution at the design Mach number of 0.7 and lift coefficient of 0.25 was calculated using the two-dimensional code and is shown below.

Two undesirable features were present in these results. First, the slight pressure peak at the leading edge of the lower surface could cause the boundary layer on that surface to transition. Second, the adverse gradient that begins at about 70-percent chord on each surface is too steep and would probably cause the flow to separate.

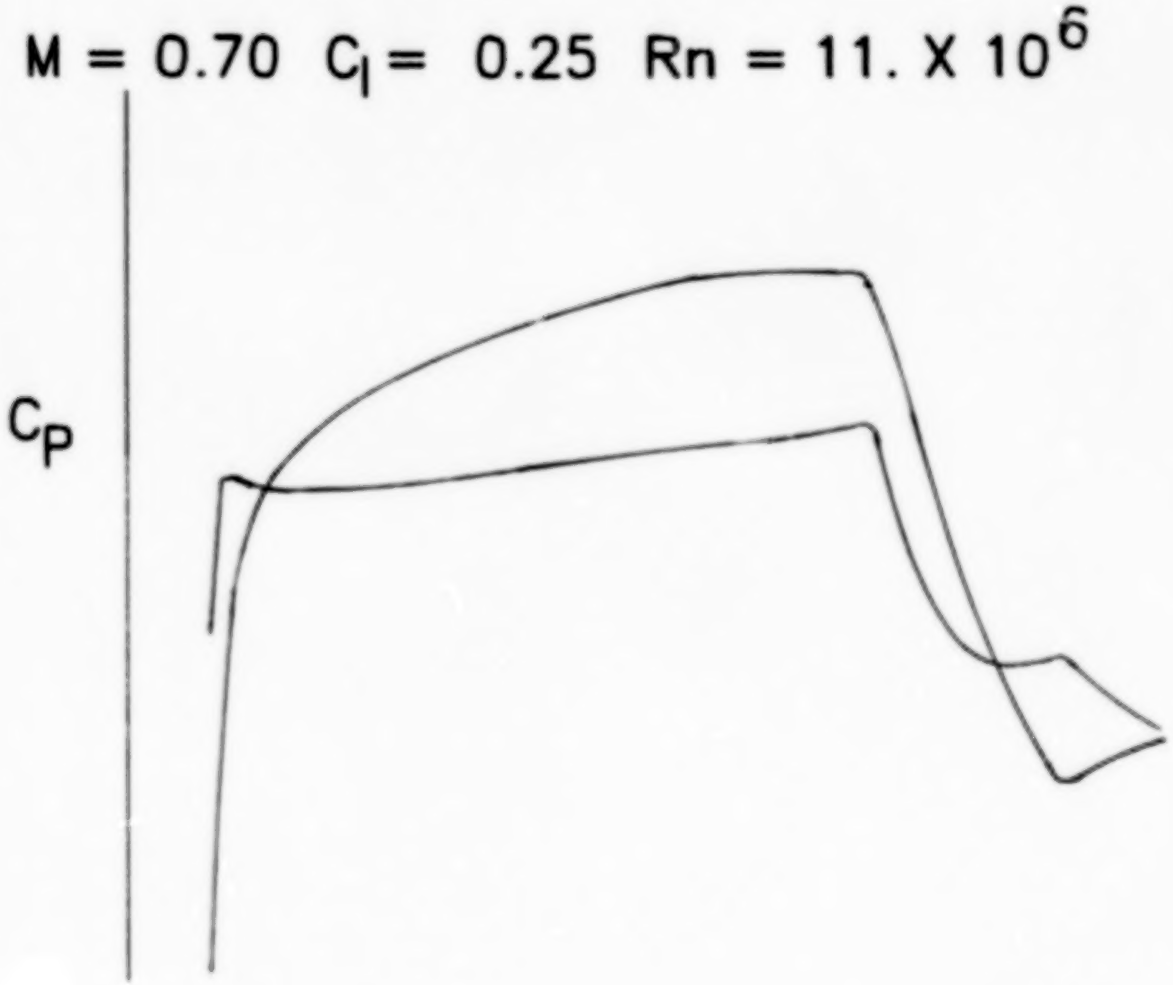

$M = 0.70 \quad C_l = 0.25 \quad Rn = 11. \times 10^6$

COMBINATION AIRFOIL DESIGN

The initial design airfoil was modified to eliminate the undesirable features in its pressure distribution. The modified shape was evaluated using both two-dimensional and three-dimensional analysis codes. The pressure distributions calculated by the two-dimensional Garabedian and Korn code for both the initial and final airfoil designs are shown in the accompanying figure. The leading-edge peak on the lower surface was eliminated and the adverse pressure gradients were softened on both surfaces. This reduction in the adverse gradients eliminated the flow separation on the upper surface; it also, however, limited the extent of laminar flow to about 50-percent chord on that surface. It is interesting to note that almost no load is carried on the last 30-percent of the airfoil.

HYBRID AIRFOIL DEFINED WITH VIKEN DESIGNED UPPER SURFACE AND CAMPBELL DESIGNED LOWER SURFACE LEADING EDGE

$M = 0.70 \quad C_l = 0.25 \quad R_n = 11. \times 10^6$

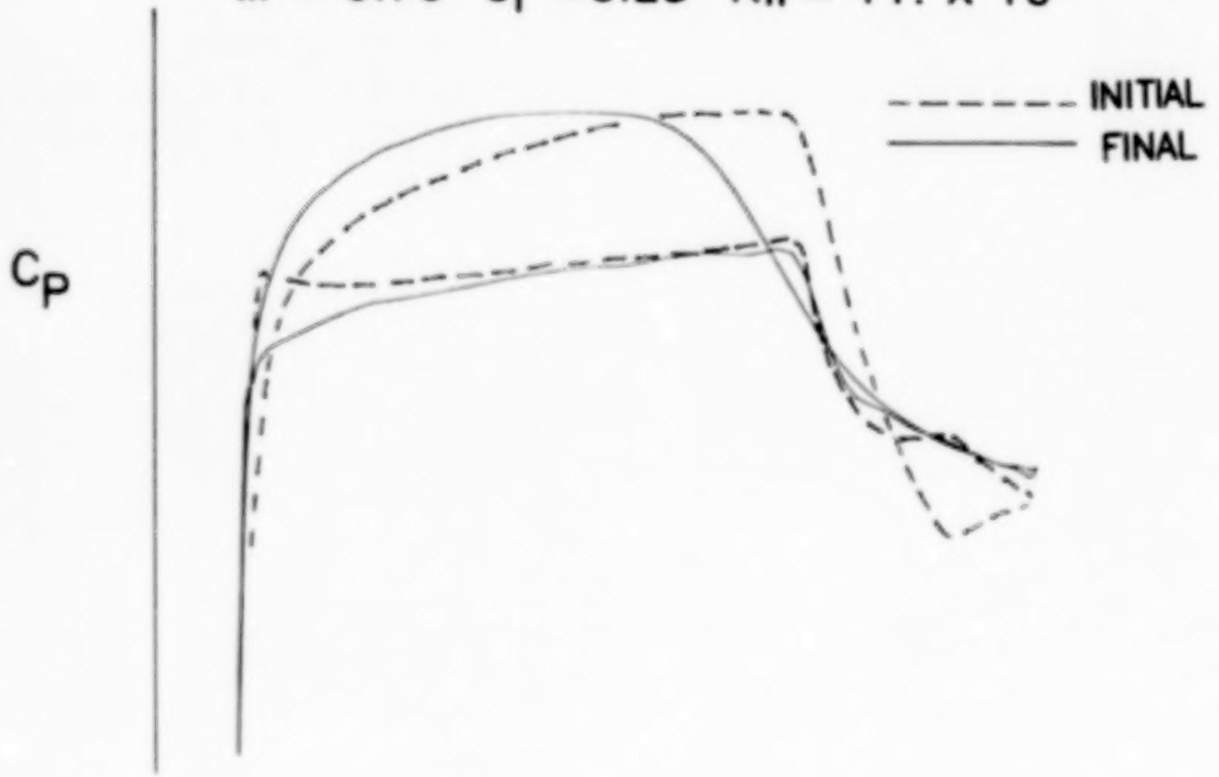

VARIATION OF SKIN FRICTION DRAG COEFFICIENT WITH SECTIONAL LIFT COEFFICIENT

Since the primary reason for using NLF airfoils is a reduction in viscous drag, an estimate of this drag benefit was made using the Garabedian and Korn program. Runs were made at Mach numbers of 0.70 and 0.75 and lift coefficients from about 0.2 to 0.4. Because the code only has a turbulent boundary-layer model, the laminar flow case was simulated by beginning the boundary-layer calculation at an assumed transition location of 50-percent chord. Transition for the turbulent flow case was fixed at 10-percent chord. As seen in this figure, a reduction of about 50 counts of drag is obtained at a Mach number of 0.70 (circles) when going from the turbulent case (solid symbols) to the laminar flow case (open symbols). An even greater reduction of about 80 counts occurs at a Mach number of 0.75. Again, these estimates are a little high since the laminar flow region was modeled as contributing no drag, but should be representative of relative reductions in turbulent boundary layer skin friction drag.

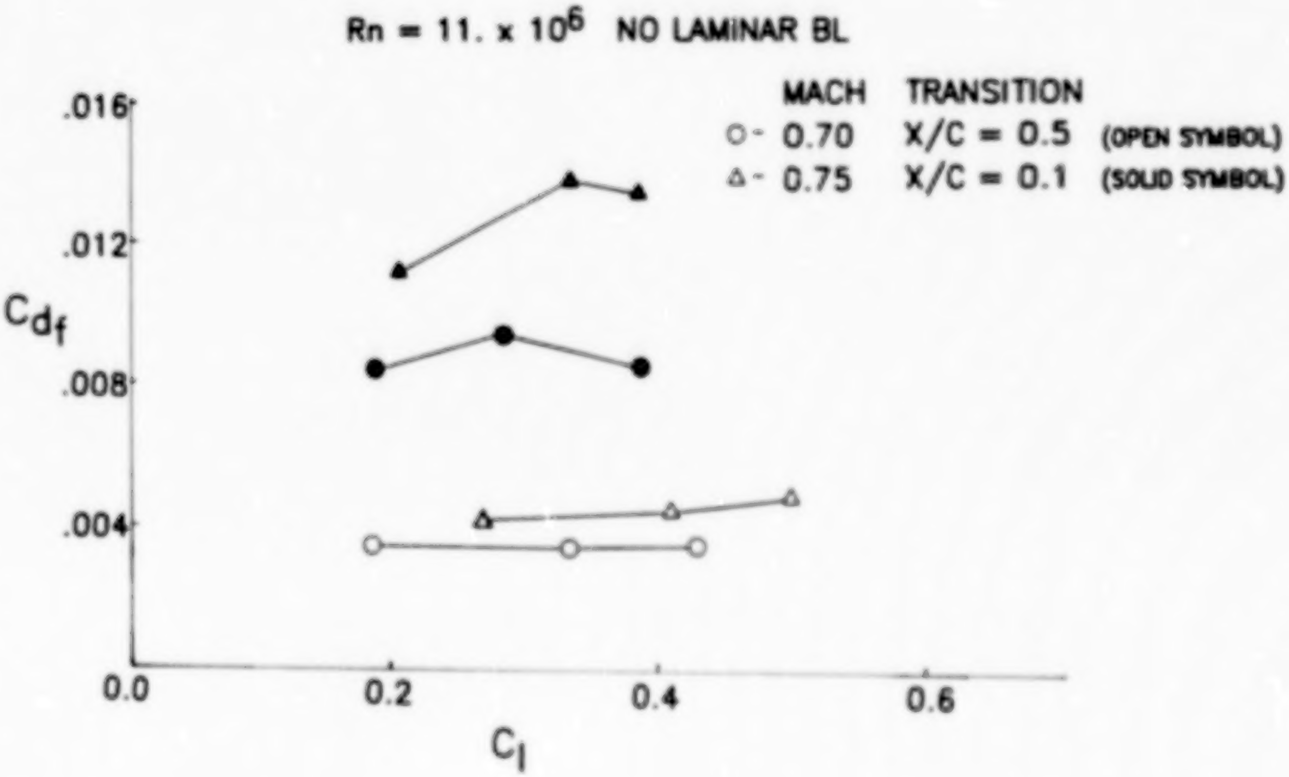

3-D EVALUATION OF COMBINATION AIRFOIL

One of the design requirements for this configuration was that there be no large changes in the aerodynamic characteristics, except for an increase in viscous drag, if laminar flow was lost. In order to examine this condition, the wing/body configuration using the final airfoil design was run in TAWFIVE with transition set at forward and aft positions. For the laminar flow case, transition was set at 50-percent chord on the upper surface and 65-percent chord on the lower surface; the turbulent flow case had transition fixed at the leading edge. The TAWFIVE code, unlike the Garabedian and Korn two-dimensional code, did have a laminar as well as a turbulent boundary-layer model. The pressure distributions calculated for a station near mid-semispan show that transition location has very little effect for these cases. This was not surprising; however, it was important that no separation was predicted for either case. This means that if the wing suddenly lost laminar flow while in a cruise condition, no sudden change in aircraft flying qualities would occur.

PLANFORM 2 NON-LINEAR TWIST

$C_L = 0.25$ $M = 0.7$ $\eta = 0.383$

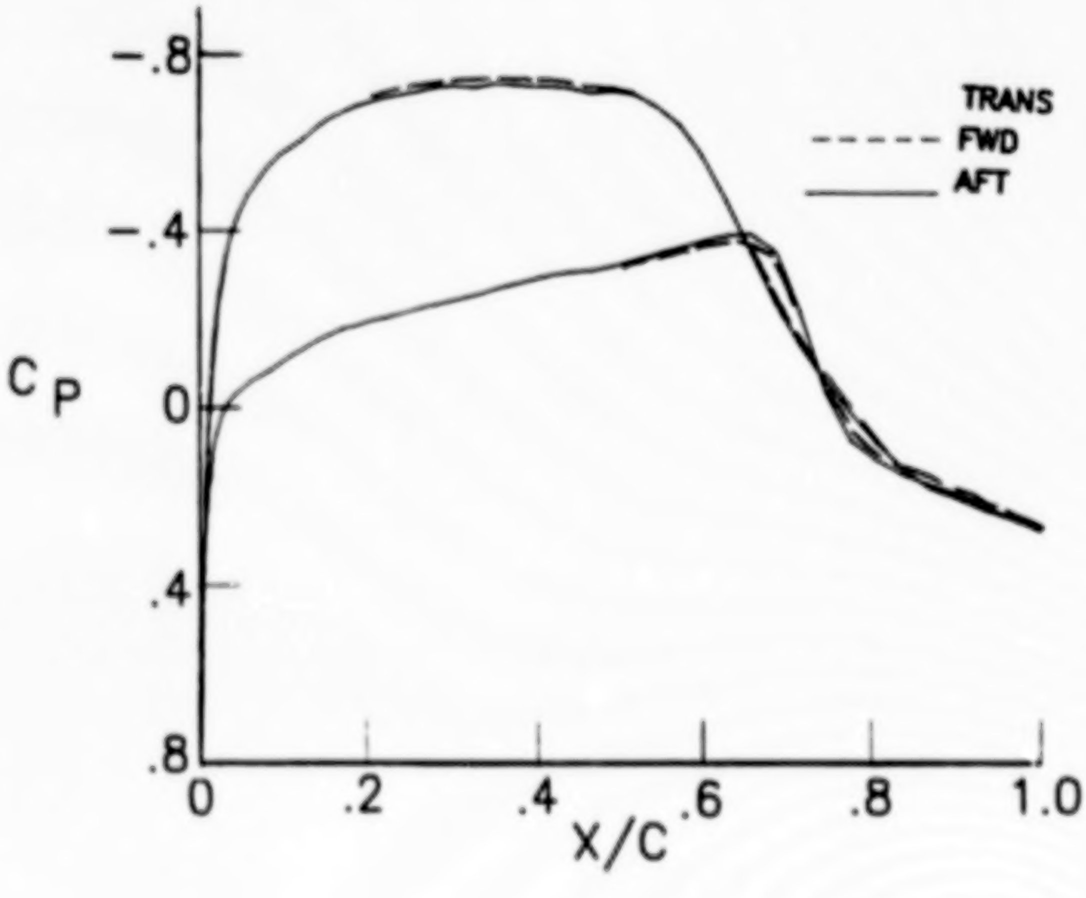

COMPUTATIONAL WING DESIGN EFFORT

This wing design study covered several areas in addition to the design of the airfoil sections which are not described in detail in this report. A summary of the design effort is given in this chart. The study began with the definition of initial airfoil sections. After evaluating them using a two-dimensional airfoil code, an initial three-dimensional analysis was made. This run identified some problem areas and led to two parallel airfoil modification efforts. While the airfoil modifications were being made using two-dimensional codes, the three-dimensional codes were being utilized to predict the effects of a proposed planform modification. Also, an investigation of several linear and non-linear twist distributions was carried out. The two airfoils developed in the parallel efforts were combined to form a hybrid airfoil that retained the good characteristics of each one at the design conditions. This airfoil was then evaluated at numerous off-design conditions using both two-dimensional and three-dimensional analyses.

One additional area of study was the design of a leading-edge extension for the outboard part of the wing. This type of wing modification has been found to be very effective in improving the stall departure and spin resistance characteristics of a general aviation aircraft, reference 10. Two extensions were designed for this aircraft, both extending from about 75-percent semispan to the tip. The leading edges of the airfoils were extended forward 2- and 3-percent chord and drooped for the two cases. Both two-dimensional and three-dimensional transonic codes were used to evaluate the modified airfoils at the cruise condition and the low-speed, high-lift chararcteristics were predicted using the two-dimensional subsonic code.

- INITIAL 3–D ANALYSIS
- PROBLEM IDENTIFICATION AND AIRFOIL MODIFICATION
- PLANFORM MODIFICATION
- NON–LINEAR TWIST INVESTIGATION
- HYBRID AIRFOIL DEFINITION
- OFF–DESIGN ANALYSIS
- LEADING EDGE EXTENSION DESIGN

SUMMARY

In summary, state-of-the-art computational methods were used to design a high aspect ratio NLF wing for a corporate transport. This effort included making a total of about 80 three-dimensional analysis runs and dozens of two-dimensional analysis runs over a period of about two months. The final design was predicted to maintain laminar flow back to 50-percent chord on the upper surface and 60-percent chord on the lower surface at the design conditions (Mach number of 0.7 and lift coefficient of 0.25). The requirement of no boundary-layer separation if transition should occur at the leading edge was also met for the design point. Based on two-dimensional calculations, a drag divergence Mach number of 0.75 was determined, which would give an adequate margin above cruise.

One purpose of this study was to evaluate the use of these codes in a project environment. Strengths and weaknesses of the various codes were identified and new computational tools were developed to complement the two-dimensional and three-dimensional design methods.

- COMPUTATIONAL NLF WING DESIGN COMPLETED
- APPROXIMATELY 65 3-D ANALYSIS RUNS TAWFIVE
  APPROXIMATELY 15 3-D ANALYSIS RUNS WBPPW
  DOZENS OF 2-D ANALYSIS RUNS
- 50%/60% LAMINAR FLOW ON US/LS AT DESIGN POINT
- NO SEPARATION WITH TRANSITION AT LEADING EDGE AT DESIGN POINT
- DRAG DIVERGENCE MACH = 0.75 AT CRUISE
- IDENTIFIED INADEQUACIES AND DEVELOPED METHODS TO COMPLEMENT 2-D AND 3-D DESIGN EFFORTS

CONCLUDING REMARKS

In conclusion, computational wing design methodologies were successfully applied in two unique programs. The two-dimensional and three-dimensional aerodynamic codes used in these studies proved to be robust and reliable in a stringent schedule environment. The automated design procedure available in one of the three-dimensional codes yielded excellent results and the inclusion of that procedure or a similar one in the other aerodynamic codes is being pursued. Some deficiencies in the capabilities of the codes were identified and possible corrections and improved running strategies are being addressed. The final accuracy of the design methods will be evaluated when wind-tunnel tests of both configurations are completed.

- SUCCESSFULLY APPLIED COMPUTATIONAL WING DESIGN METHODOLOGIES IN TWO UNIQUE PROGRAMS

- 2–D AND 3–D CODES WERE ROBUST AND RELIABLE IN STRINGENT SCHEDULE ENVIRONMENT

- AUTOMATED DESIGN PROCEDURES YIELDED EXCELLENT RESULTS

- DEFICIENCIES IN CAPABILITIES WERE IDENTIFIED AND ARE BEING ADDRESSED

- WIND TUNNEL DATA WILL VALIDATE THE COMPUTATIONAL WING DESIGNS

REFERENCES

1. Bauer, F.; et al.: Supercritical Wing Sections II. Lecture Notes in Economics and Mathematical Systems, Vol. 108, 1975.

2. Stevens, W. A.; Goradia, S.M.; and Broden, J.A.: Mathematical Model for Two-Dimensional Multi-Component Airfoils in Viscous Flow. NASA CR-1843, July 1971.

3. Melson, N. D.; and Streett, C.L.: TAWFIVE: A Users' Guide. NASA TM-84619, September 1983.

4. Boppe, C. W.; and Stern, M. A.: Simulated Transonic Flows for Aircraft with Nacelles, Pylons, and Winglets. AIAA Paper 80-0130, January 1980.

5. Raj, P.; and Reaser, J. S.: An Improved Full-Potential Finite-Difference Transonic-Flow Code (FLO22.5) For Wing Analysis and Design. LR 29759, Lockheed-California Company, November 1981.

6. Bauer, F.; Garabedian, P.; and McFadden, G.: The NYU Inverse Swept Wing Code. NASA CR-3662, January 1983.

7. Hanks, G. W.; et al.: F-111 Natural Laminar Flow Glove Flight Test Data Analysis and Boundary Layer Stability Analysis. NASA CR-166051, January 1984.

8. Waggoner, E. G.; Phillips, P. S.; Viken, J. K.; and Davis, W. H.: Potential Flow Calculations and Preliminary Wing Design in Support of an NLF Variable Sweep Transition Flight Experiment. AIAA Paper 85-0426, January 1985.

9. Viken, J. K.: Aerodynamic Design Considerations and Theoretical Results for a High Reynolds Number Natural Laminar Flow Airfoil. Masters Thesis, George Washington University, January 1983.

10. Newsom, W. A., Jr.; Satran, D. R.; and Johnson, J. L., Jr.: Effects of Wing-Leading-Edge Modifications on a Full-Scale, Low-Wing General Aviation Airplane. NASA TP-2011, 1982.

D23

N88-14949

NATURAL LAMINAR FLOW NACELLE FOR TRANSPORT AIRCRAFT

IN-05

117247
16P.

Milton Lamb
William K. Abeyounis
James C. Patterson, Jr.
Richard J. Re
NASA Langley Research Center
Hampton, Virginia

PAGE 444 INTENTIONALLY BLANK

PRECEDING PAGE BLANK NOT FILMED

[redacted] PURPOSE OF TEST

Conceptually, a nacelle designed to have laminar flow over a significant portion of its length should provide a substantial reduction in the installed drag of the engine/nacelle/pylon of transport airplanes. While many factors may make the attainment of laminar flow on nacelles difficult, the magnitude of the reduction in installed drag and the corresponding increase in airplane performance makes research in this area of interest. Therefore, the Propulsion Aerodynamics Branch at the NASA Langley Research Center has undertaken, in cooperation with the General Electric Company, a research program to study the potential of laminar flow nacelles for reducing installed engine/nacelle drag.

The purpose of this research program was twofold: (1) to experimentally verify a method for designing laminar flow nacelles and (2) to determine the effects of installation on the extent of laminar flow on the nacelle and on the nacelle pressure distributions. The procedures used to accomplish these objectives were:

1). Analytical design a nacelle that had a pressure distribution favorable for the maintenance of laminar flow.

2). Verify this nacelle design experimentally by measuring the pressure distributions on an uninstalled flow-through-nacelle model and through flow visualization techniques determine the location of transition.

3). Following successful completion of steps 1 and 2, analytically design a nacelle and pylon installed on a high wing transport configuration. The design criteria was that the installed nacelle have essentially the same pressure distribution as the uninstalled nacelle.

4). Determine experimentally whether the installation of the nacelle on the high wing transport produced the predicted pressure distributions and also determine if the installation causes premature transition.

The analytical designs were developed by the General Electric Company. The experimental investigations were conducted in the Langley 16-Foot Transonic Tunnel. The tests were made at a freestream Mach number of 0.80 and a unit Reynolds number of approximately 4 million per foot. At a freestream Mach number of 0.8, boundary layer transition occurs in this facility on a 10 deg. polished cone at a Reynolds number of 5.4 million. The angle-of-attack was varied from -2.5 deg. to 4 deg.

In order to assess the integration effects on the laminar flow nacelle design, the effects of fixed and free transition, nacelle longitudinal position, and pylon contouring were investigated using a high wing transport model. The results indicated that nacelle/pylon/wing integration did not affect the laminar flow on the nacelle. The increment in installed drag between free and fixed transition for the nacelle on a symmetric pylon was essentially the difference between the calculated turbulent and laminar skin friction drag for the nacelle. Locating the nacelle in a forward position relative to the wing reduced the compressibility effect on the wing lower surface thereby reducing the installed drag. Contouring the pylon resulted in a further reduction in the installed drag.

ORIGINAL PAGE IS
OF POOR QUALITY

ISOLATED NACELLE IN THE 16-FOOT TRANSONIC TUNNEL

The isolated nacelle was designed by General Electric to have a favorable pressure distribution over 70 percent of its length. The nacelle shown was the largest possible model based on the restraints of the existing inlet test rig of the 16-Foot Transonic Tunnel. The nacelle had a maximum diameter of 21 inches with a throat diameter of 15.6 inches and was approximately 22 inches in length. The nacelle was designed to have a maximum length of favorable pressure gradient at a Mach number of 0.78 and design cruise mass flow ratio of 0.88. To help maintain laminar flow, the surface was highly polished.

COMPARISON OF MEASURED AND PREDICTED MACH NUMBER DISTRIBUTION

The theoretical Mach number distribution (solid line) was predicted by the GE Streamtube Curvature Method which solves the Euler equations. Considerable contour tailoring near the velocity peak was required to produce an adverse pressure gradient that would initiate transition and yet not separate the flow. Wind tunnel results show excellent agreement with pre-test calculations.

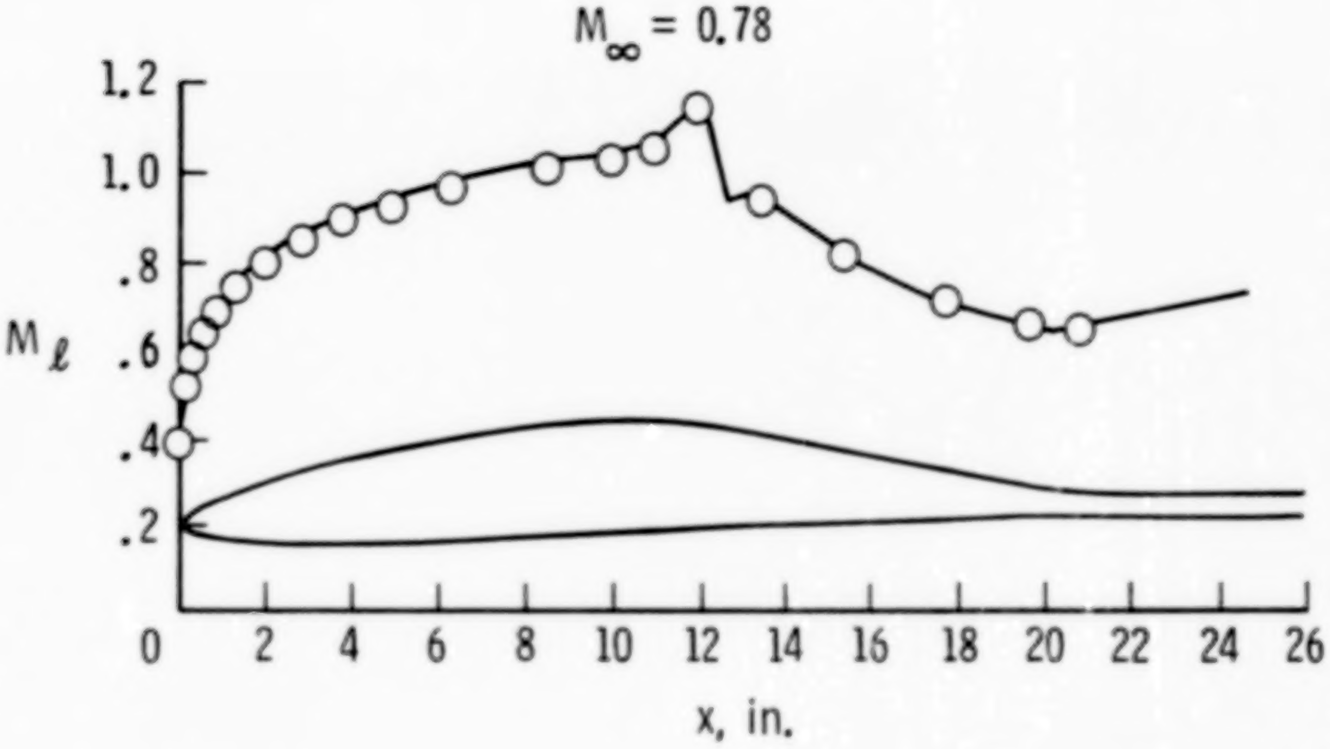

PHOTOGRAPH OF MODEL WITH NACELLES INSTALLED

The model used in this investigation was a 1/24 scale transport model with a supercritical wing designed for a Mach number of 0.8. The high wing transport was considered desirable since it would provide more fuselage outwash than a typical low wing aircraft and therefore represent a more severe test case. The flow-through laminar flow nacelle was designed using a low order panel method in conjunction with a specific compressibility correction technique to solve for the basic installed flow field. The desired nacelle shape was analytically modeled into the wing-body flow field, and the resulting nacelle's pressure gradient was checked for separation as well as for peak surface Mach number. If either the pressure gradient or peak Mach number proved unsatisfactory, the nacelle contour was modified and the entire process repeated until a satisfactory shape was obtained. The final nacelle shape had a favorable pressure gradient over 60 percent of its length. The surfaces of these nacelles were highly polished.

ORIGINAL PAGE IS
OF POOR QUALITY

ORIGINAL PAGE IS
OF POOR QUALITY

ISOLATED NACELLE FLOW VISUALIZATION RESULTS

Acenaphthene was utilized for flow visualization to assess where transition from laminar to turbulent flow occurred. Acenaphthene is a sublimating chemical with a sublimation rate that is proportional to heat transfer rate (faster in turbulent flow). It is a distinct white after it is sprayed on the model and the fully laminar flow region appears a bright white after the wind tunnel run. Some portions of the nacelle produced laminar flow all the way back to the desired transition location, while other portions developed "turbulent wedges" prior to the design transition location. The sources of these premature transitions were attributable to two factors:

1. Surface roughness occurring as a result of non-uniform particle deposits of acenephthene.
2. Leading edge surface contamination due to wind tunnel particles impingement and subsequent nicks and dents.

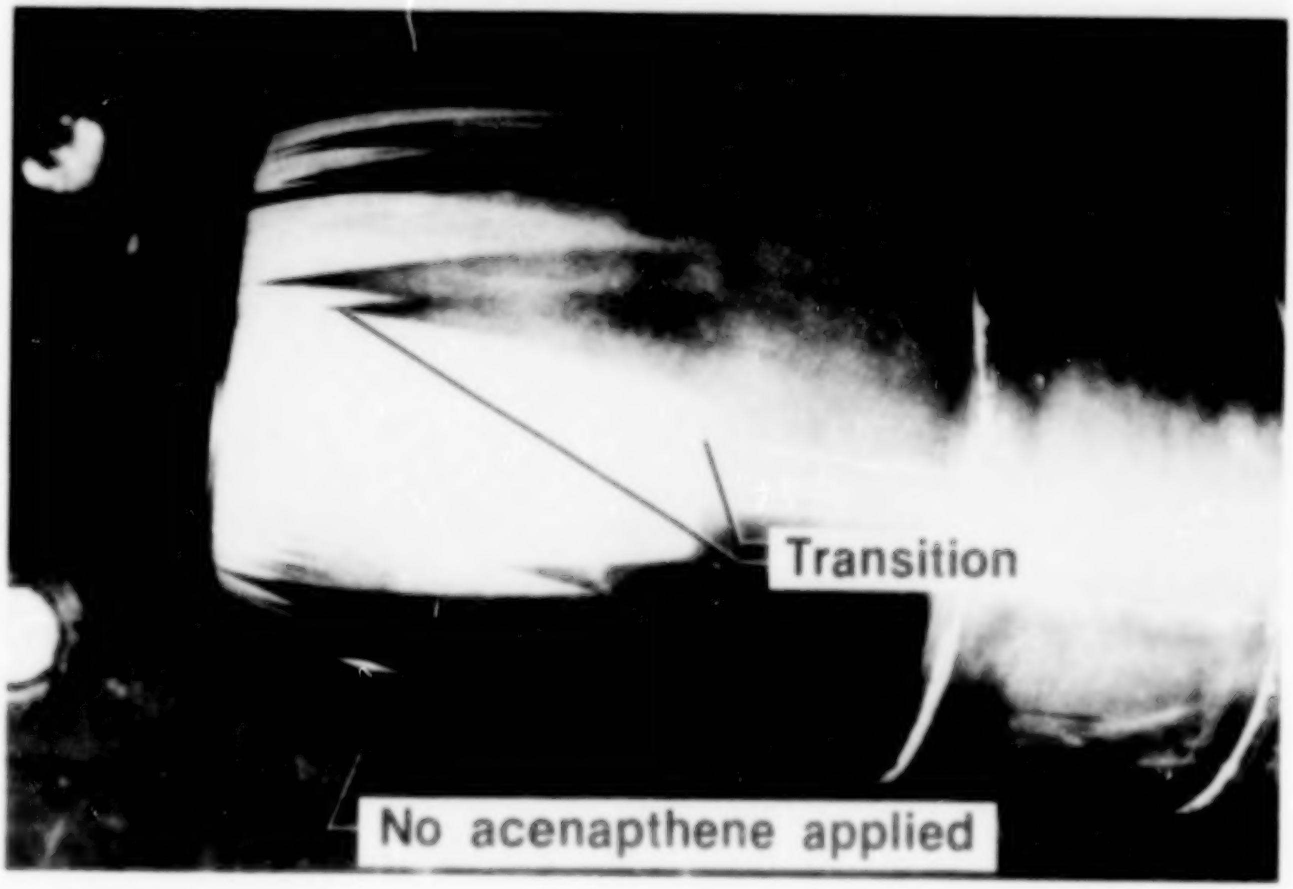

TEST MATRIX

In order to fully assess the integration effect on a nacelle designed to achieve laminar flow, the effects of fixed and free transition, nacelle longitudinal position, and pylon contouring were investigated. The nacelle was tested in a rearward and forward position on a symmetrical pylon and in a forward position on a contoured pylon.

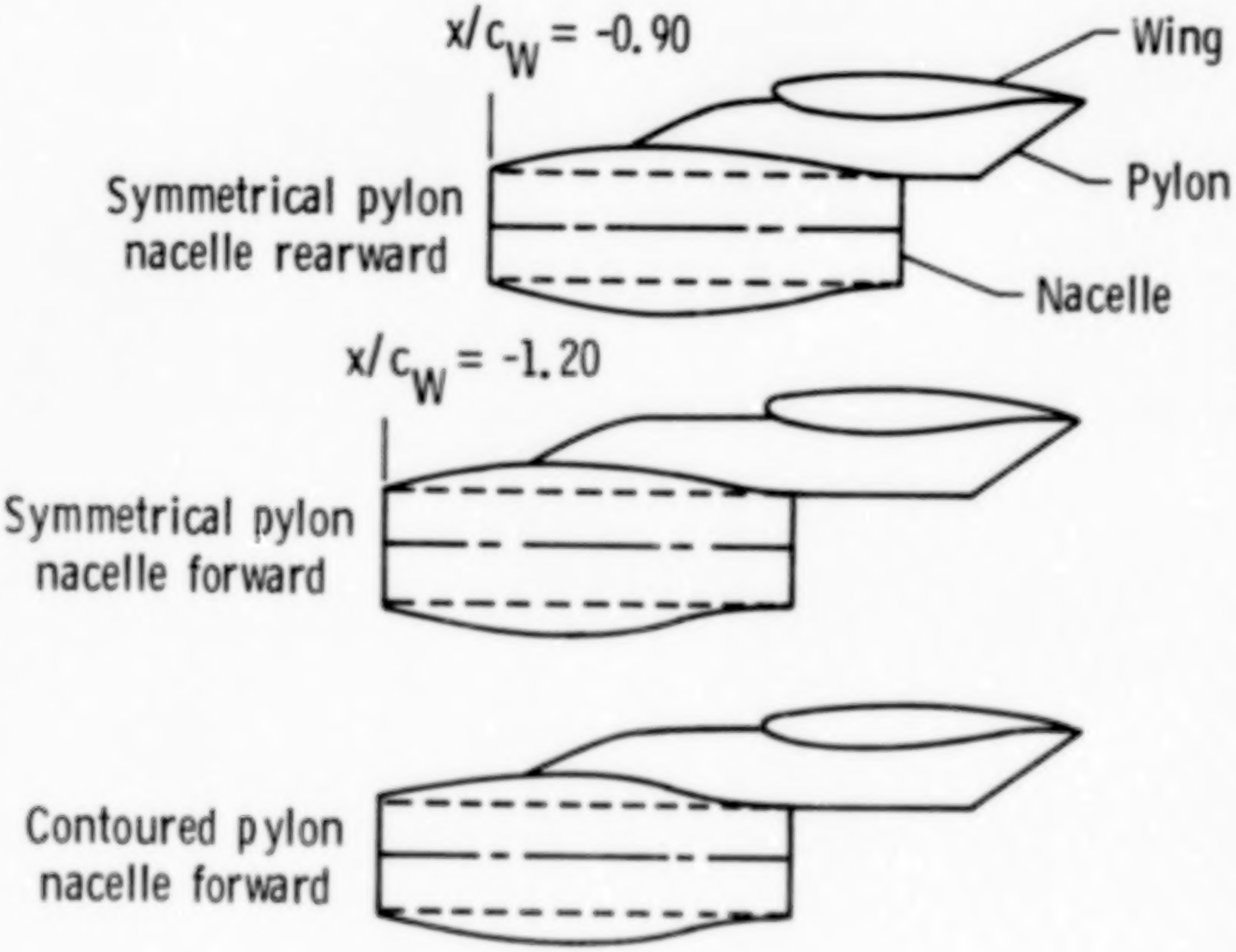
$x/c_W = -0.90$
Wing
Pylon
Symmetrical pylon nacelle rearward
Nacelle
$x/c_W = -1.20$
Symmetrical pylon nacelle forward
Contoured pylon nacelle forward

EFFECT OF NACELLE AND NACELLE TRANSITION ON LIFT

The addition of the nacelle/pylon to the wing-body configuration reduced the lift as would be expected. The addition of grit on the nacelle to trip the flow from a 60 percent laminar flow condition to a fully turbulent condition along the entire length of the nacelle, had no effect on the lift characteristics.

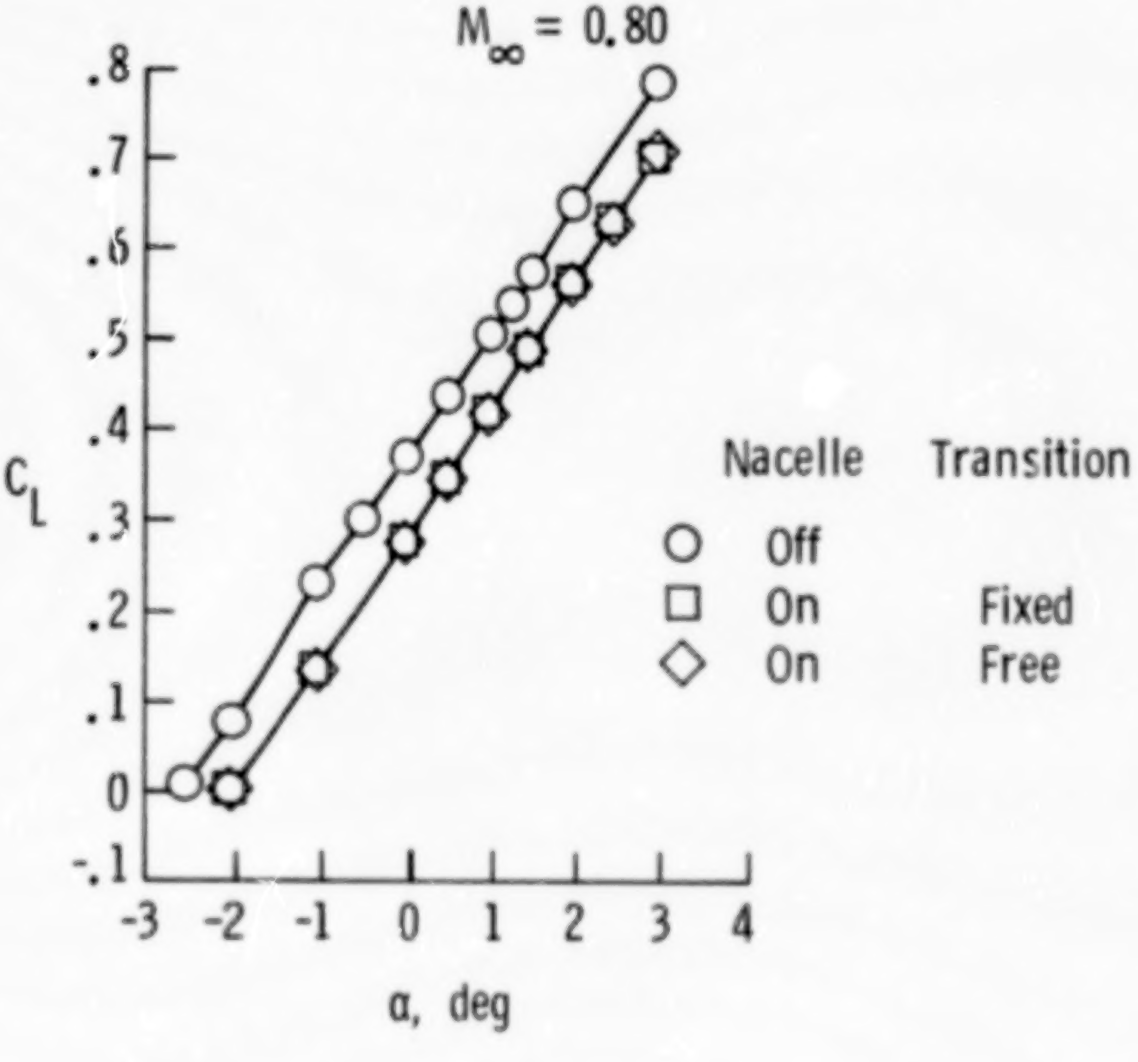

EFFECT OF NACELLE AND NACELLE TRANSITION ON DRAG

The addition of the nacelle/pylon to the wing-body configuration resulted in an increase in drag. The removal of the transition grit from the nacelle resulted in a decrease in total airplane drag (approximately 9 counts at the cruise C_L of 0.45). The increment in the flat plate friction drag for these nacelles and pylons with fixed and free transition on the nacelle indicated that the drag reduction for two nacelles of this size with 60 percent laminar flow are approximately 9 counts. This would indicate that integration effects do not significantly alter the extent of the nacelle laminar flow achieved.

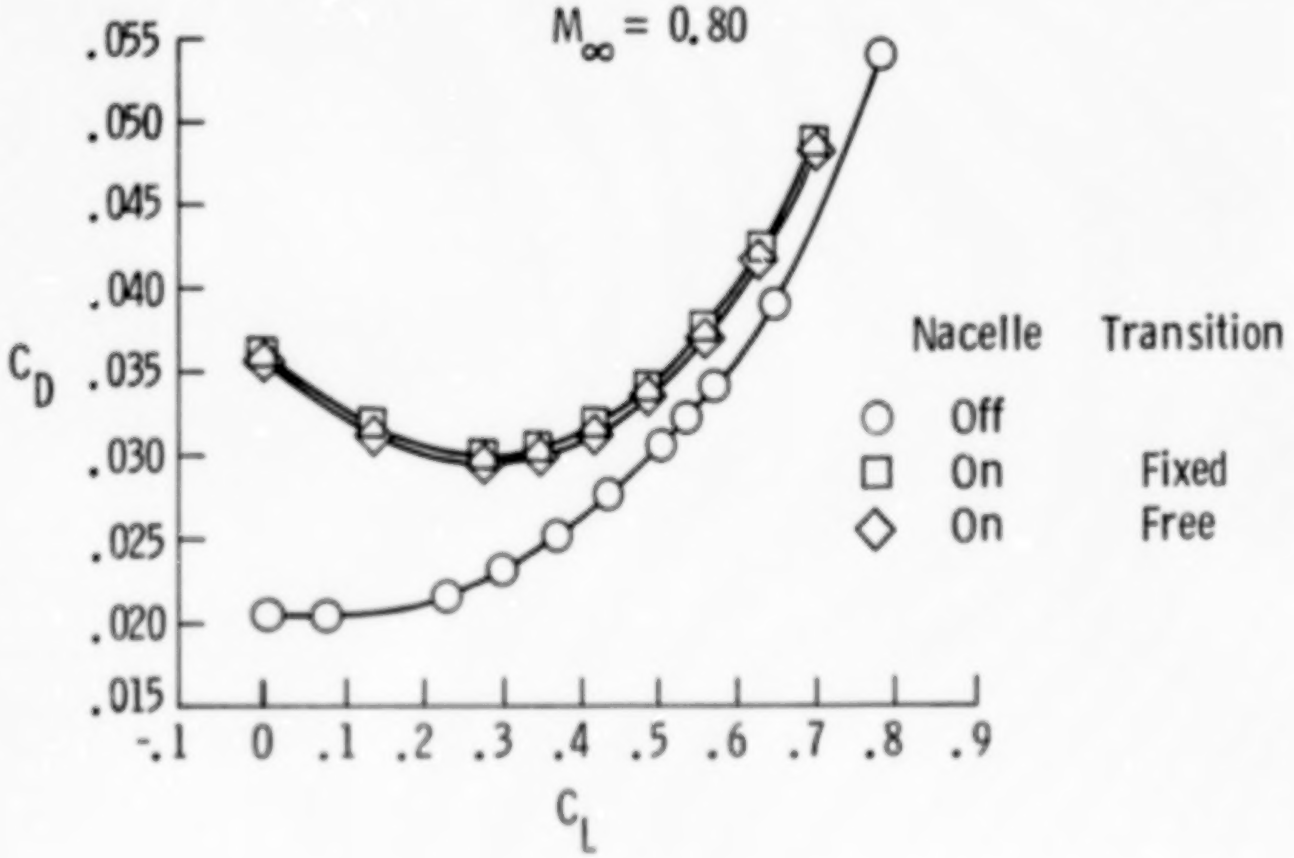

ORIGINAL PAGE IS
OF POOR QUALITY

INSTALLED NACELLE FLOW VISUALIZATION RESULTS

Acenaphthene was again used for the flow visualization. As noted for the isolated nacelle, there are portions of "turbulent wedges;" however, the extent of laminar flow can be clearly seen. The laminar flow on the installed nacelles is approximately 60 percent of the nacelle length.

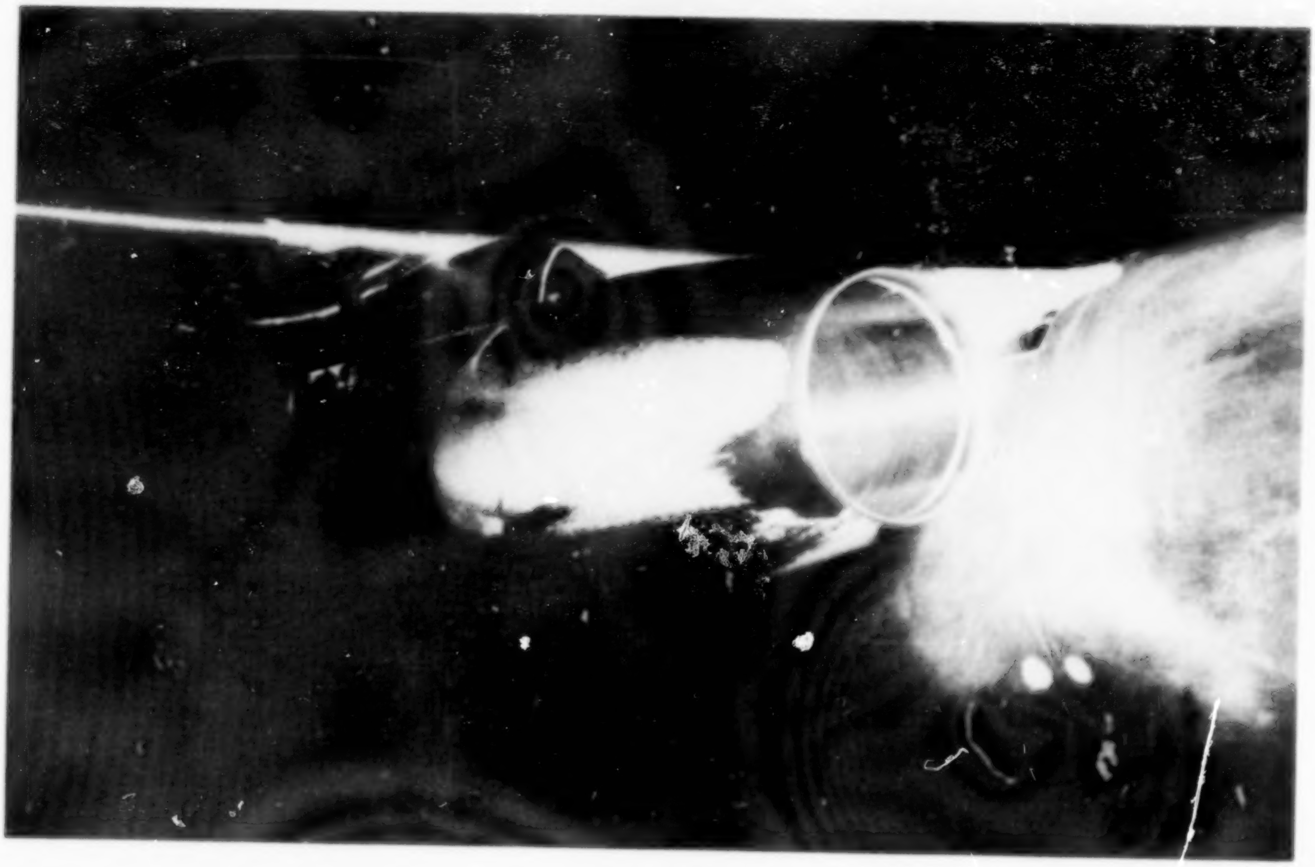

ORIGINAL PAGE IS
OF POOR QUALITY

EFFECT OF NACELLE POSITION ON LIFT

An additional study was conducted in an attempt to reduce the installed drag of the wing-body-nacelle-pylon configuration by proper nacelle positioning. Moving the nacelle forward reduced the compressibility effect on the wing lower surface, thereby resulting in a lower installed lift loss.

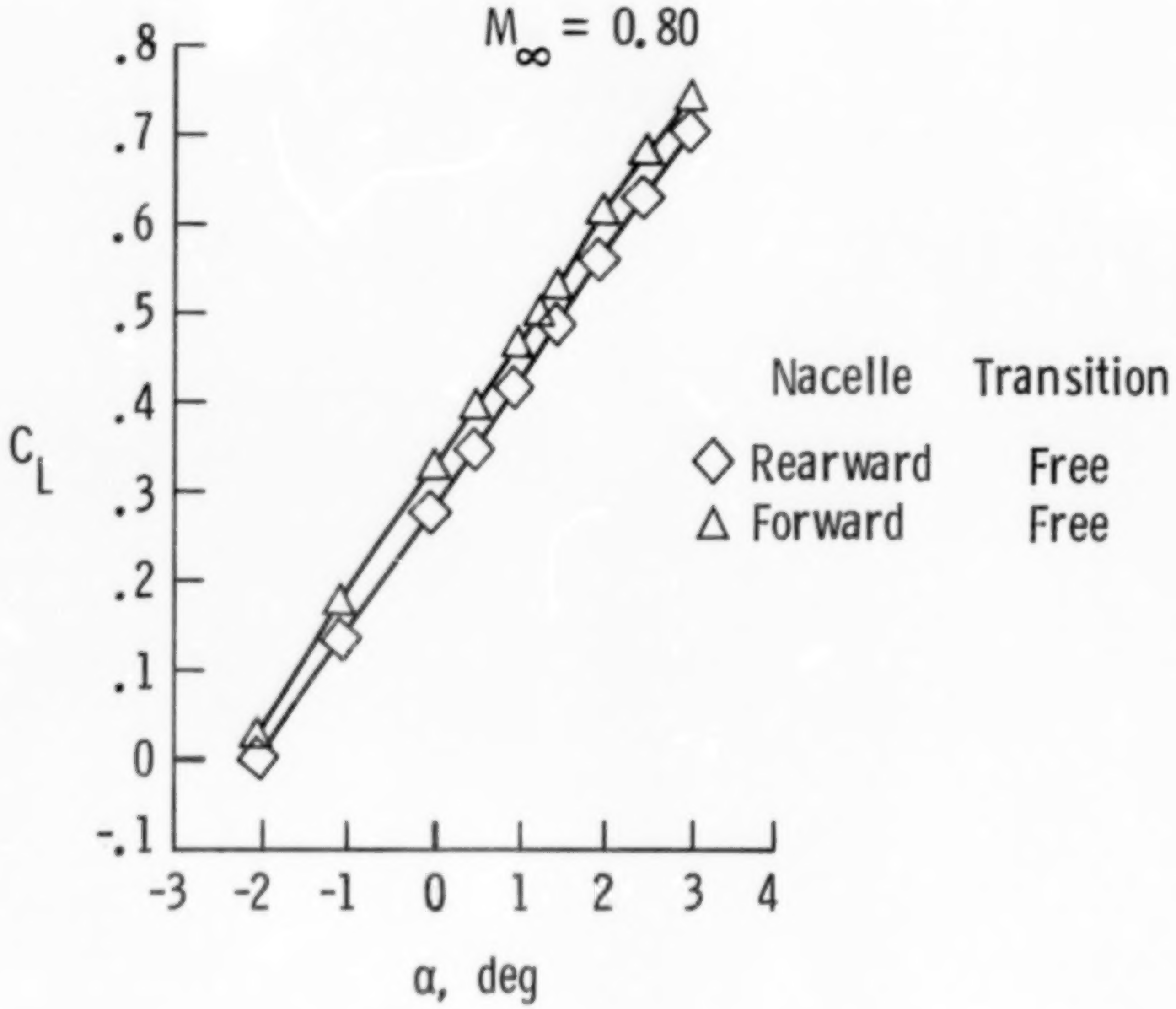

EFFECT OF NACELLE POSITION ON DRAG

Moving the nacelle to a forward position reduces the compressibility and nacelle interference effects on the wing lower surface. This results in a drag reduction of approximately 10 counts at the cruise lift of 0.45.

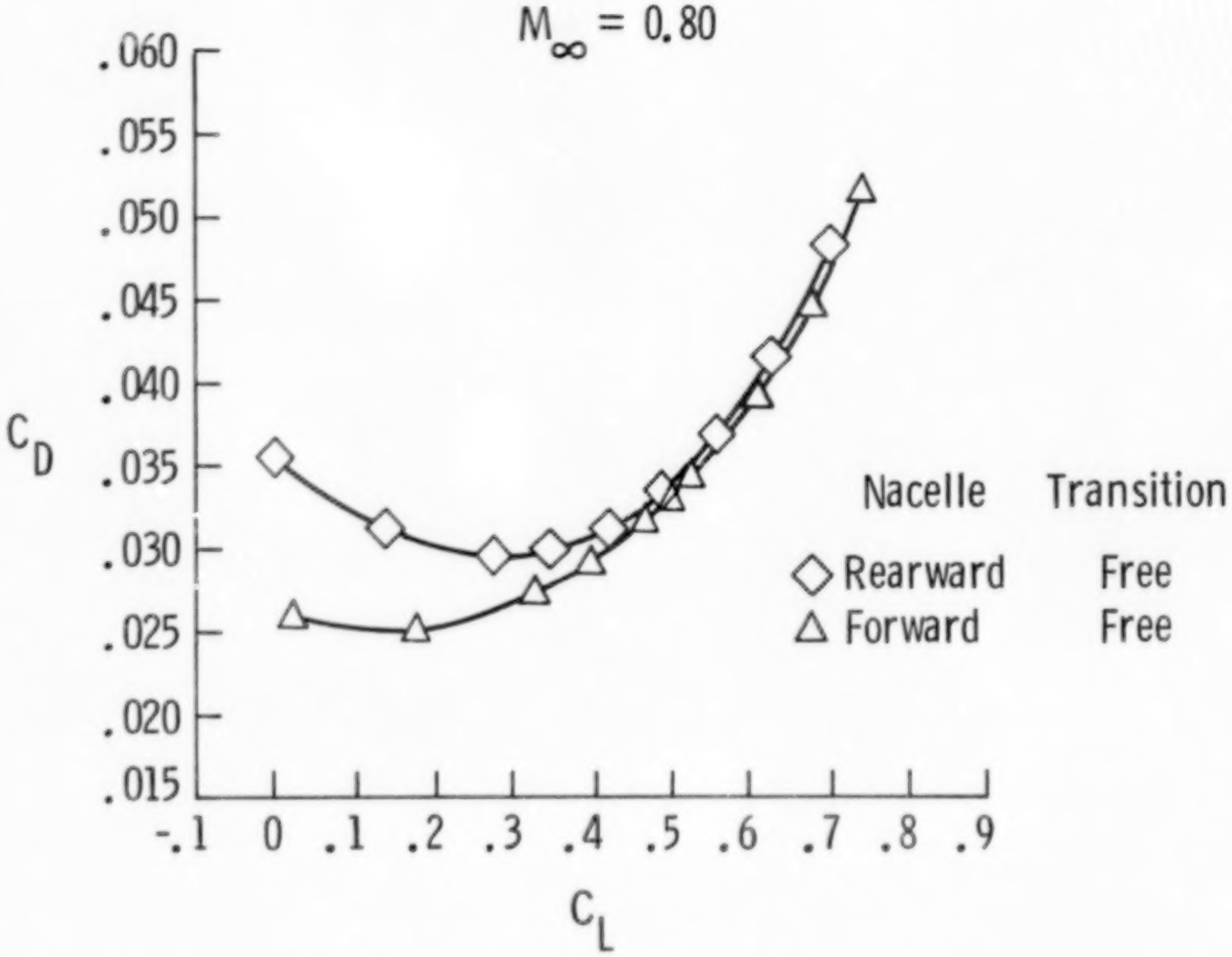

EFFECT OF PYLON CONTOUR ON LIFT

A study was also conducted to determine the reduction in installed drag that might be obtained by contouring the pylon to conform with the local streamlines. The contoured pylon had very little effect on the lift coefficient.

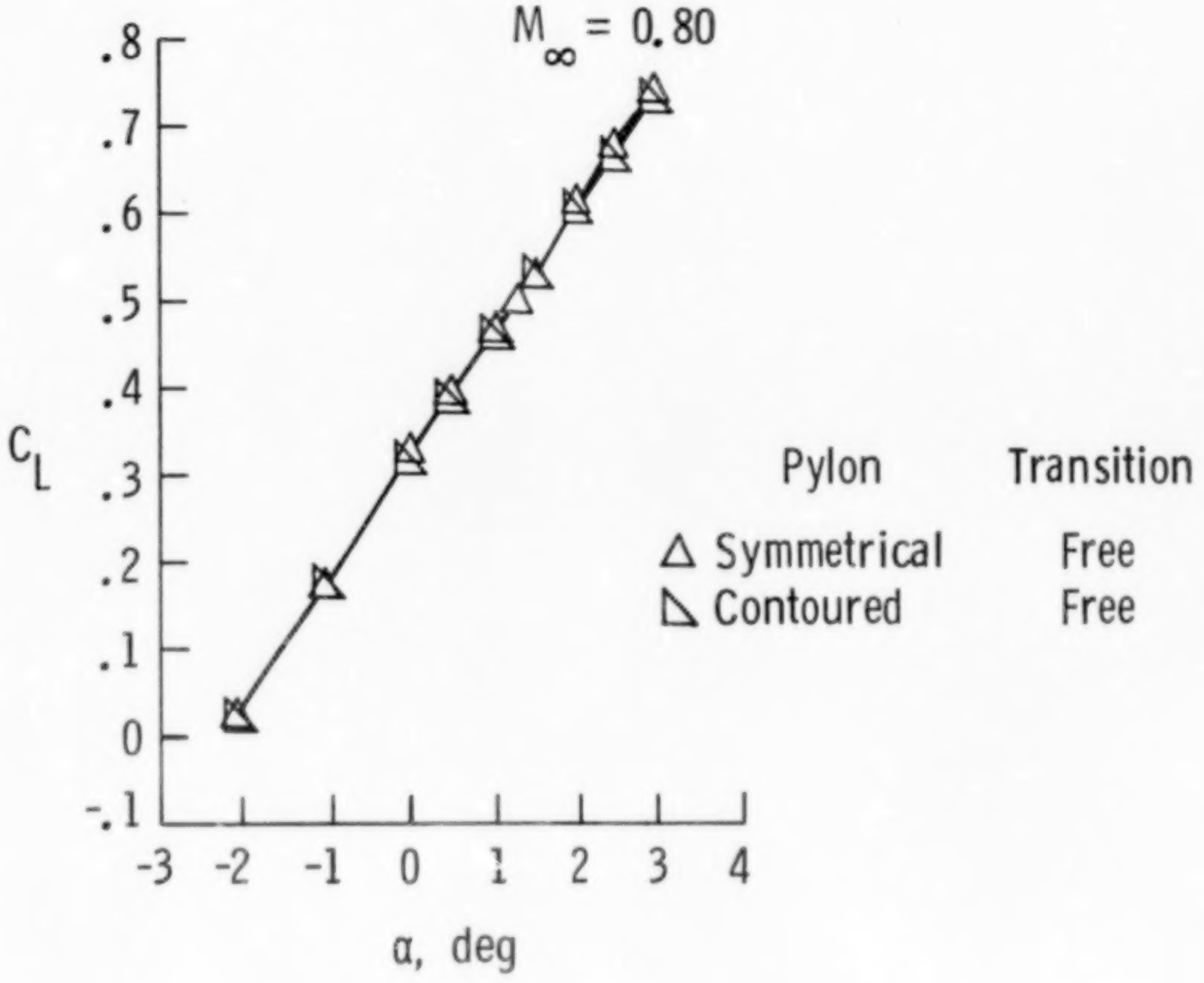

EFFECT OF PYLON CONTOUR ON DRAG

Since flow accelerations caused by pylons are a major contributor to high velocity peaks on the wing lower surface, the pylons were contoured in an attempt to reduce these high velocities. Contouring the pylon resulted in a decrease in drag of approximately 7.5 counts.

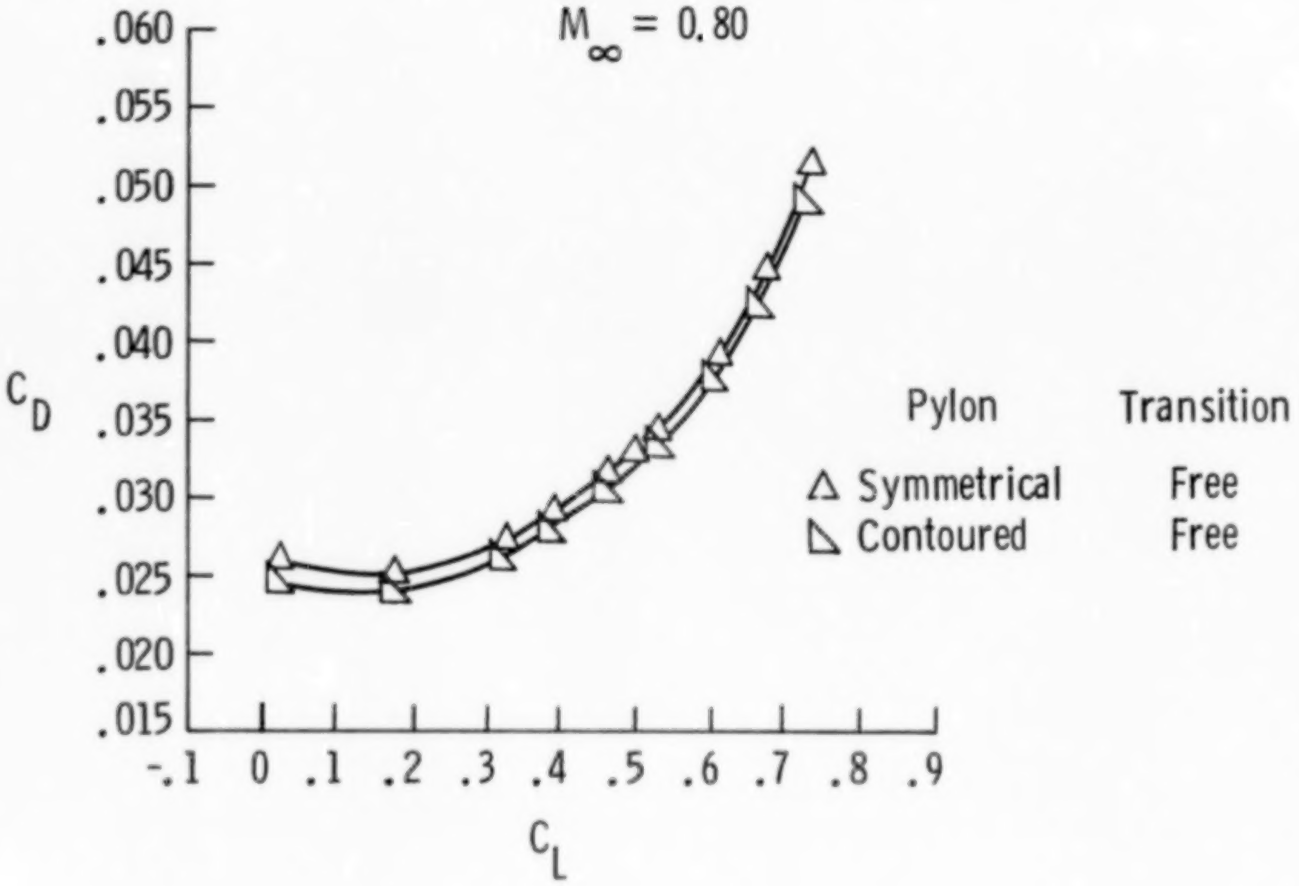

INSTALLED DRAG FOR M = 0.80 AND C_L = 0.45

The incremental drag results obtained from this investigation (wing-body-nacelle/pylon - wing-body) is presented, including the calculated flat plate skin friction drag, for each nacelle/pylon configuration. The difference in installed drag for the nacelles in the rearward position, transition fixed and free, is comparable to the difference in the calculated skin friction drag. An additional reduction in installed drag was obtained by locating the nacelle in the forward position. Pylon contouring further reduced the interference drag (including wave and form drag) to a value just above skin friction.

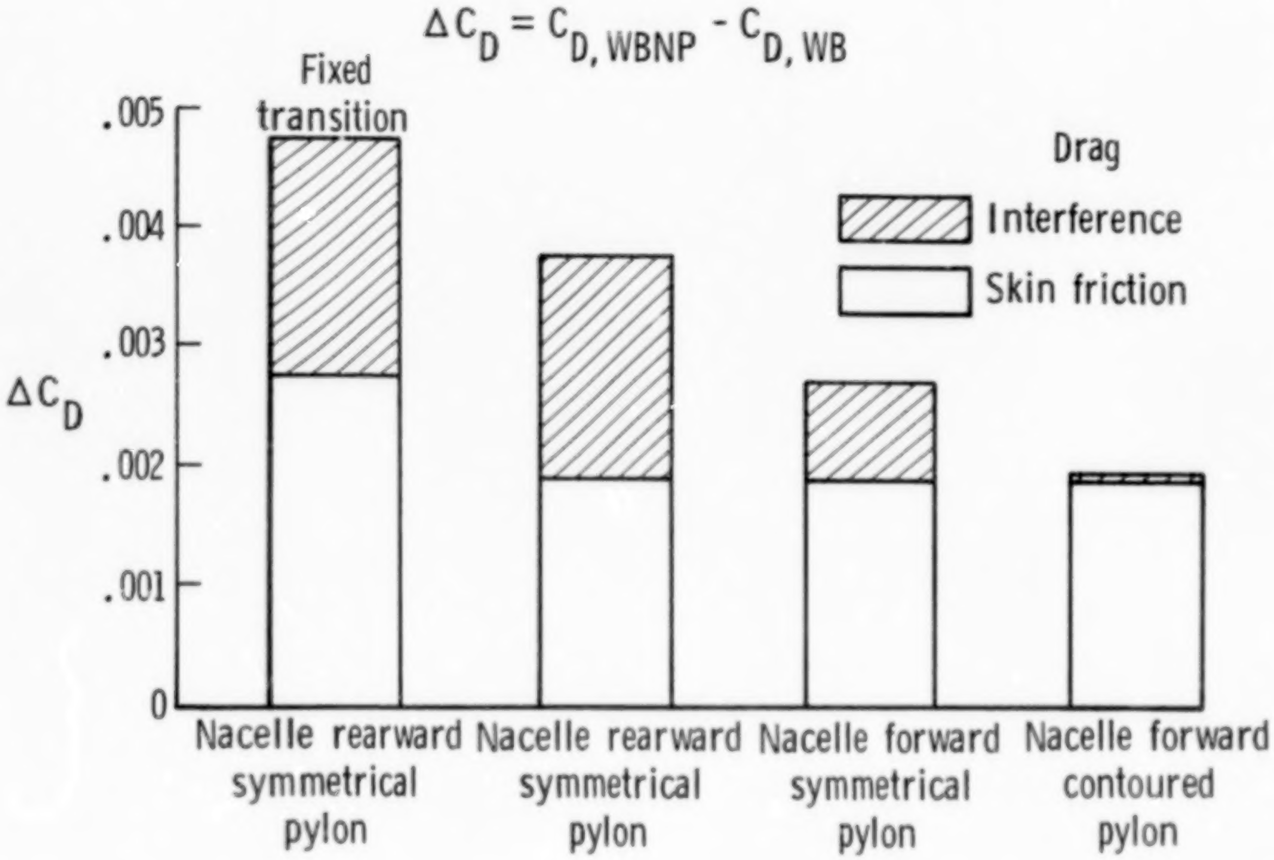

$$\Delta C_D = C_{D,\,WBNP} - C_{D,\,WB}$$

SUMMARY

The results of the isolated nacelle test illustrated that laminar flow could be maintained over the desired length.

Installing the nacelles on wing/pylon did not alter the extent of laminar flow occurring on the nacelle.

The results illustrated that a significant drag reduction was achieved with this laminar flow design.

Further drag reduction could be obtained with proper nacelle location and pylon contouring.

D24

N88-14950

524-34

117248

14P

FLIGHT RESEARCH ON NATURAL LAMINAR FLOW

B. J. Holmes, C. C. Croom, and E. C. Hastings, Jr.
NASA Langley Research Center
Hampton, Virginia

C. J. Obara
Kentron International, Incorporated
Hampton, Virginia

C. P. van Dam
Vigyan Research Associates, Incorporated
Hampton, Virginia

INTRODUCTION

[redacted] experiences with natural laminar flow (NLF) have provided a basis of understanding how this technology can be used for reduction of viscous drag on modern practical airplanes. The classical concerns about the practicality of NLF have related to achievability and maintainability. The earliest efforts to achieve NLF in flight were uniformly successful on specially prepared and gloved airframe surfaces, and unsuccessful on the production metal surfaces of the 1940's and 1950's era. More recent NASA flight experiments have demonstrated the achievability of NLF on modern metal and composite airframe surfaces. These experiments (refs. 1 to 6), more than 30 in total, were conducted over a range of free-stream conditions including Mach numbers up to 0.7, transition Reynolds numbers up to 14×10^6, chord Reynolds numbers up to 30×10^6, and on wings of relatively small leading-edge sweep angles, typically less than 27°.

In contrast to the difficulties encountered on older production airframe surfaces of the 1940's and 1950's, NLF is achievable today because of the small waviness of modern production wings, because of the lower values of unit Reynolds numbers at the higher cruise altitudes of modern airplanes, and because of the favorable influence of subcritical compressibility on two-dimensional laminar stability at the higher cruise Mach numbers of modern airplanes.

The significant implications of the past research are the following:

1. NLF is a practical drag reduction technology on modern metal and composite airframe surfaces for Mach numbers as high as 0.7, chord Reynolds numbers as large as 30×10^6 and wing sweep angles of 17° and 27° depending on length Reynolds number and unit Reynolds number.

2. NLF is more persistent and durable in typical airplane operating environments at high-speed subsonic conditions than previously expected.

While the lessons of the past have been very instructive for current efforts to apply NLF to aircraft designs, research efforts continue to explore the limits of practical applications for NLF. These limits may be thought of in terms of combinations of maximum angles of sweep, Reynolds numbers and Mach numbers for which NLF can be achieved and maintained on practical airplanes in typical operating environments. Beyond these limits for NLF, laminar flow control (LFC) by suction appears as a promising means for achieving laminar viscous drag reduction benefits. This paper concentrates on NLF subjects.

NLF APPLICATIONS

Applications of NLF can include all surfaces of an aircraft. Favorable pressure gradients can be designed onto fuselages, horizontal and vertical tails and nacelles as well as the wings. For a high performance business jet, the potential drag reduction with NLF ranges between about 12 percent (for NLF on the wing only) to about 24 percent (for NLF on the wing, fuselage, empennage, and engine nacelles). These values of drag reduction are calculated as a percent of total airframe drag at a cruise Mach number of 0.7. Individual component benefits are tabulated below:

Component	% of Body Length NLF	% of Drag Reduction
Wing	50	12
Horizontal tail	30	2
Vertical tail	30	1
Fuselage	30	7
Nacelles	30	2
TOTAL:		24

These benefits can amount to large savings in fuel cost as well as increased performance. These drag reductions are calculated for NLF added to an existing configuration; larger benefits would accrue for integrated design calculations.

Drag reduction as percent of total airplane drag

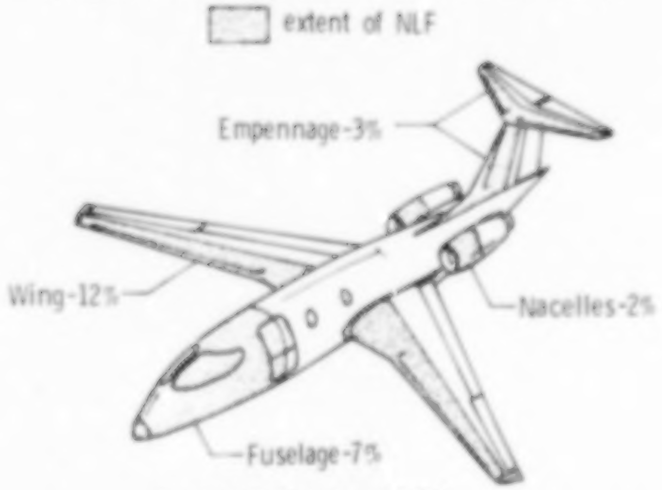

Total NLF drag benefit-24%

FAVORABLE EFFECTS OF CRUISE UNIT REYNOLDS NUMBER ON NLF ACHIEVABILITY AND MAINTAINABILITY

In recent years, two major trends in airplane fabrication methods and in airplane operational conditions have significantly aided laminar-flow achievability. First, modern airframe construction materials and fabrication methods produce aerodynamic surfaces which meet NLF requirements for roughness and waviness. These modern techniques include composites, milled aluminum skins, and bonded aluminum skins, among others. The second modern trend favorable to NLF is the smaller values of unit Reynolds numbers at which current business, commuter, and transport airplanes operate. The figure illustrates the flight conditions for these aircraft. Many modern high-speed airplanes cruise at unit Reynolds numbers less than 1.5×10^6 ft^{-1} (and some at less than 1.0×10^6 ft^{-1}) making the achievement of NLF-compatible airframe surfaces relatively easier than for older airplanes cruising at high speeds and lower altitudes. Early attempts to apply NLF were at unit Reynolds numbers sometimes exceeding 3×10^6 ft^{-1}. The resulting very thin, sensitive boundary layers at these conditions were far less tolerant of the roughness and waviness which existed on the older airframes. These conditions were responsible for the repeated failures of attempts to achieve and maintain NLF on the World War II fighter airplanes.

This realization has important implications for the maintainability of NLF on modern airplanes. Maintainability becomes significantly easier and less costly as unit Reynolds number decreases. Laminar flow has been a practical reality on sailplanes for decades, in large part because of the smaller value of unit Reynolds number experienced by these airplanes. As shown on the figure, unit Reynolds number decreases dramatically as altitude increases at constant Mach number. For example, an airplane flying at Mach = 0.8 at 40,000 ft experiences the same unit Reynolds number as a sailplane flying about 140 knots indicated airspeed at 10,000 ft. This comparison illustrates the relative improvements in achievability and maintainability of NLF resulting from the smaller values of cruise unit Reynolds numbers.

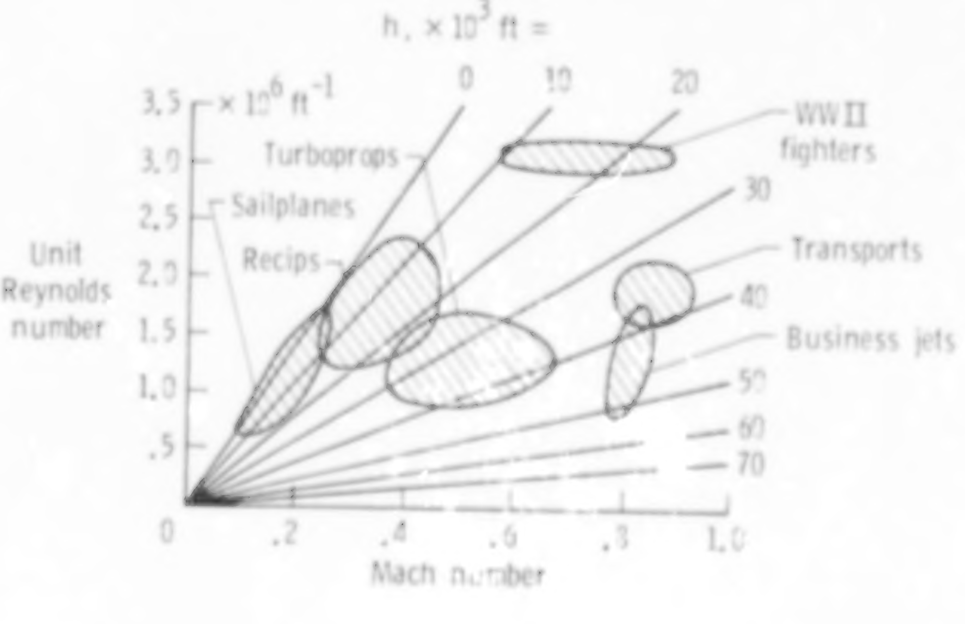

FAVORABLE COMPRESSIBILITY EFFECTS ON TOLLMIEN-SCHLICHTING GROWTH IN NLF

On swept wings, obtaining NLF requires a compromise between the need for damped Tollmien-Schlichting (T-S) growth by favorable pressure gradients and the conflicting requirement for limiting the growth of three-dimensional disturbances (crossflow vortices) by design of less favorable gradients. The growth rate of crossflow vortices is rapid in the region of rapidly falling pressure near the leading edge. Interaction can occur between the crossflow vortices and T-S waves to the detriment of laminar stability. The technical challenge to the successful design of swept NLF wings is to meet both of these conflicting pressure gradient design requirements and to avoid catastrophic growth of either the two- or three-dimensional instabilities. The successful NLF swept-wing design will achieve laminar runs at the design condition back to near the point of minimum pressure on the airfoil sections, with transition occurring either due to laminar separation or due to very rapid amplification of disturbances in the adverse pressure-gradient region.

Fortunately, nature provides assistance in meeting these conflicting design constraints for pressure gradients on swept NLF wings. As Mach number increases for a given pressure gradient, T-S wave growth and crossflow vorticity amplification rates are reduced by compressiblity effects. T-S wave growth, in particular, is significantly reduced by compressibility as illustrated in the figure. T-S amplification ratios, $n_{max} = n(A/A_o)$, were calculated for constant Mach number and increasing chord Reynolds number for the pressure distribution shown in the figure. These data show that n_{max} does not exceed 15 for even the largest value of chord Reynolds number (70×10^6). These predictions indicate that in dominantly two-dimensional compressible flows, transition by T-S instability may not occur prior to the point of minimum pressure on an airfoil even at higher Reynolds numbers. For the conditions analyzed here, even though the length Reynolds number is increasing, very little increase in compressible amplification ratio takes place. This phenomenon provides protection or enhancement of laminar boundary layer stability. Higher design Mach numbers are usually sought at higher altitudes, and since higher altitudes mean smaller unit Reynolds number, these two trends provide favorable influence for making NLF useful even at higher speeds.

C-6

FAVORABLE INFLUENCE OF COMPRESSIBILITY ON 2-D NLF STABILITY

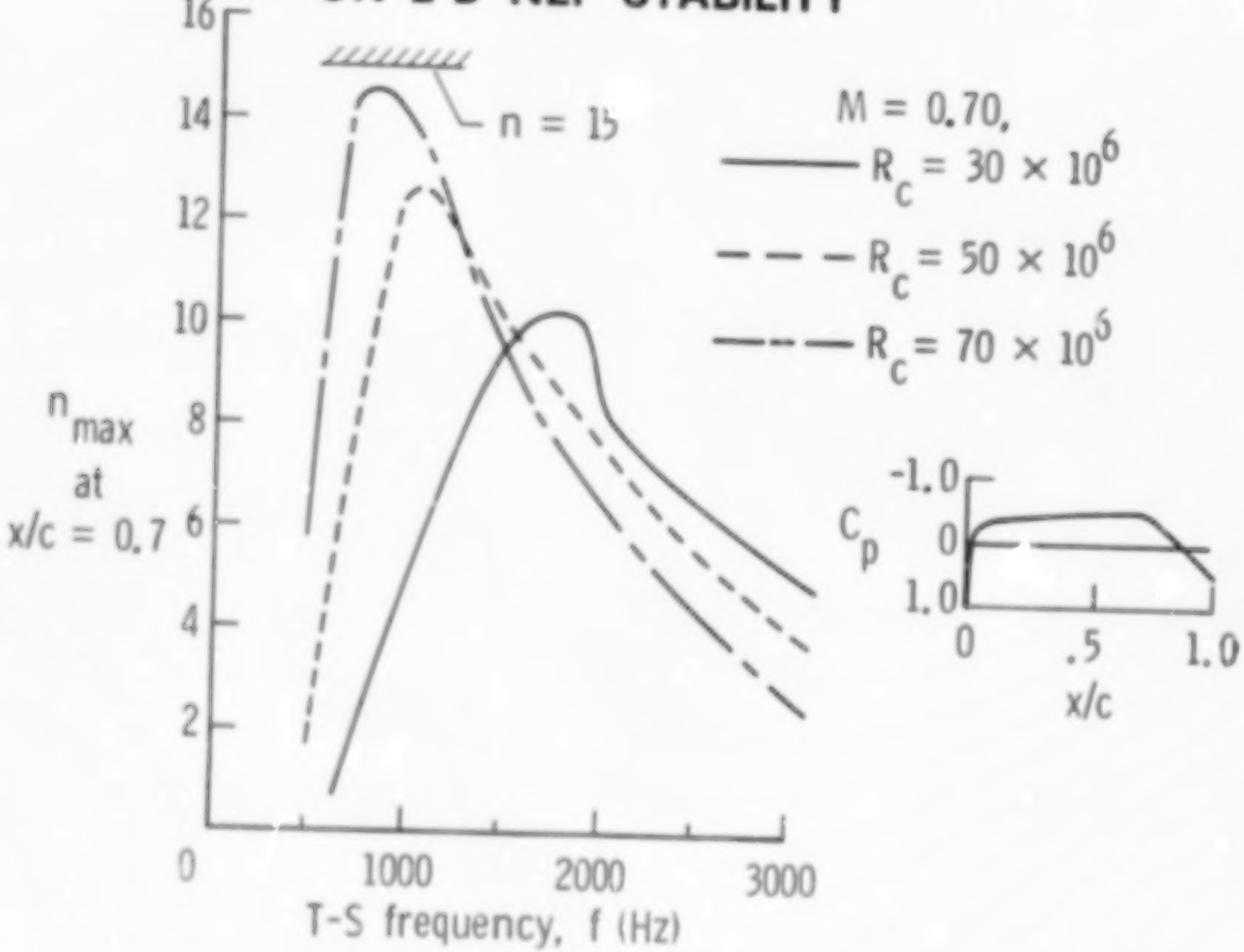

ORIGINAL PAGE IS
OF POOR QUALITY

CITATION III SWEPT-WING NLF FLIGHT EXPERIMENTS

Recent NLF flight experiments on the Cessna Citation III business jet have provided transition data useful for calibration of linear stability codes such as Malik's COSAL (ref. 7). Preliminary results from these 27° swept-wing experiments include two significant transition-location measurements; transition with minimum crossflow effect was observed at the pressure peak at 30-percent chord ($M = 0.7$, $R' = 1.2 \times 10^6\ \text{ft}^{-1}$), and was observed with significant crossflow effect, occurring well forward of the pressure peak at 10-percent chord ($M = 0.3$, $R' = 1.6 \times 10^6\ \text{ft}^{-1}$). It is encouraging that at the higher Mach number, transition occurred at or downstream or the pressure peak, indicating that NLF can be practical for swept wings at the flight conditions for business jet aircraft.

C-6

LEAR 28/29 NLF FLIGHT RESEARCH INSTRUMENTATION

The research instrumentation on the Lear 28/29 has been developed to document both location and mode of the transition on a moderately swept wing in compressible flow. Pressure belts containing 192 ports will be used to document the wing pressure distributions. A multi-element hot-film gage containing 25 hot-film sensors will be used to provide documentation of the locations of attachment line flow and transition. The hot-film data and pressure distribution data will be obtained simultaneously. Flow reversal sensors will be used to detect the presence of laminar separation as a cause of transition. Cross-flow hot-film sensors will be used to sense the presence of crossflow vorticity and transition in the laminar boundary layer. Both the flow-reversal and crossflow sensors are postage-stamp-size stick-on probes. Using these various methods will allow complete documentation of the transition phenomenon. Both the nature of transition and the location where the transition occurs will be determined.

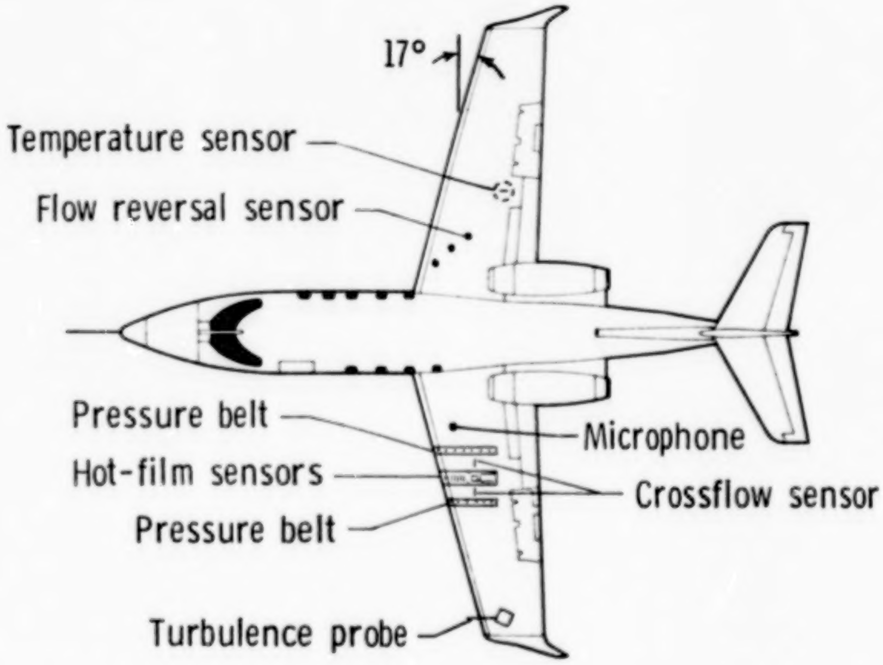
17°
Temperature sensor
Flow reversal sensor
Pressure belt
Hot-film sensors
Pressure belt
Turbulence probe
Microphone
Crossflow sensor

ORIGINAL PAGE IS
OF POOR QUALITY

OV-1 NLF ENGINE NACELLE FLIGHT EXPERIMENTS

A series of flight experiments with NLF nacelles will be conducted using the NASA modified version of the Grumman OV-1 aircraft. The initial experiments will demonstrate the feasibility of NLF on a nacelle in the presence of jet engine noise. For these experiments, a laminar flow glove has been bonded to the existing nacelle. Transition and pressure distribution on the glove will be determined while laminar surface is exposed to acoustic disturbances from the JT-15D jet engine and an external noise source.

OV-1 NLF NACELLE FLIGHT EXPERIMENTAL CONFIGURATION

In the next phase of the laminar flow nacelle flight experiments, the existing JT-15D jet engine and nacelle will be removed, and three, flow-through NLF nacelle configurations (provided by General Electric) will be installed and flown. Both internal and external acoustic disturbance sources will be used to study the sensitivity of various boundary layer conditions to directivity, amplitude, and frequency of acoustic disturbances. The frequencies and sound pressure levels representative of large jet engines will be generated in flight by noise sources inside an underwing pod and in the NLF nacelle illustrated in the figure. For the second test configuration, three NLF nacelles with different pressure distributions will be flown individually to measure the laminar boundary layer stability under exposure to an external noise source. Transition will be documented during these flights using surface-mounted hot-film gages. Correlations with existing empirical transition criteria will provide improved confidence in the use of these criteria for design of larger scale NLF nacelles.

The objectives of these experiments are to demonstrate NLF feasibility in representative engine noise environments and to broaden the base data for prediction of the effects of engine-generated acoustic disturbances on boundary layer transition in the flight environment. The NLF nacelles will be instrumented with microphones for surface noise measurements, hot-film strips to determine transition locations, and pressure ports of measurement of surface pressure distribution.

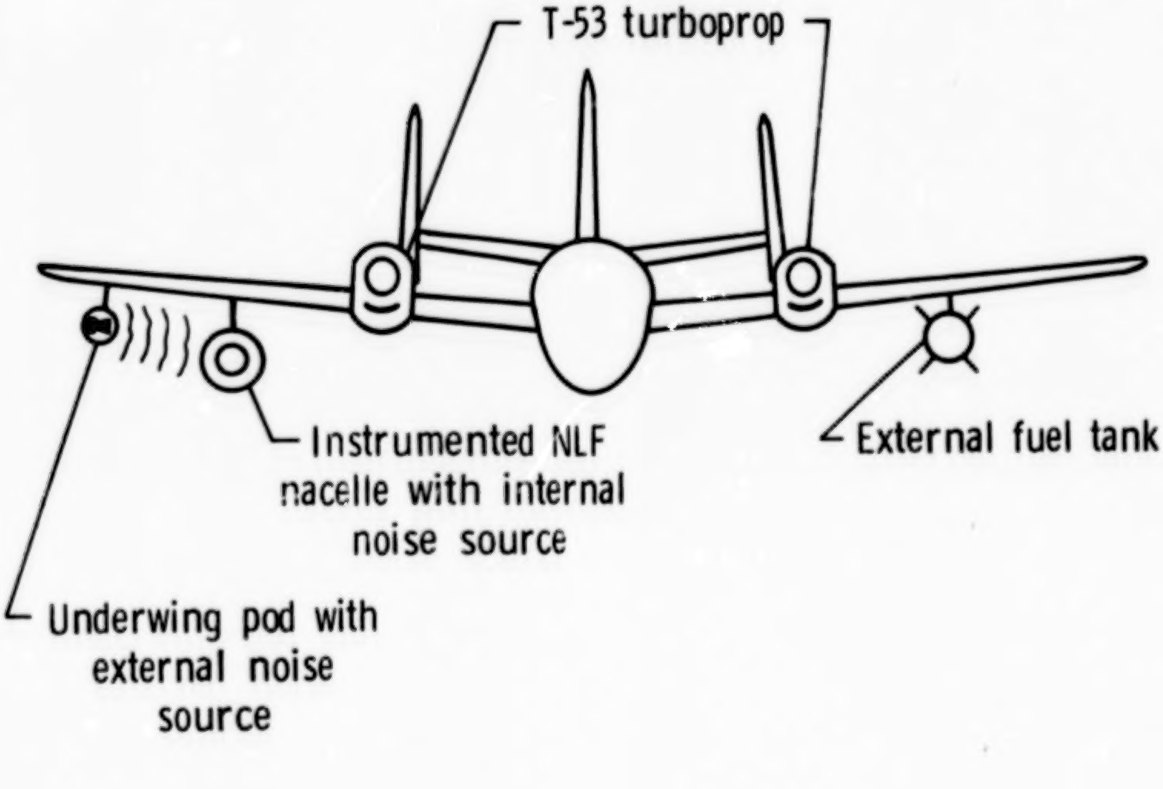
T-53 turboprop
Instrumented NLF nacelle with internal noise source
External fuel tank
Underwing pod with external noise source

ORIGINAL PAGE IS
OF POOR QUALITY

LEAR 28/29 VISCOUS DRAG REDUCTION FLIGHT RESEARCH PROJECT

NLF flight experiments are planned on the Lear 28/29 turbojet business airplane. The Lear 28/29 has extensive laminar flow on its wing and provides free-stream conditions ($M = 0.8$, $h = 51,000$ ft, $R' = 3 \times 10^6$ ft^{-1}) suitable for NLF research applicable to a wide variety of aircraft types. Wing leading-edge sweep is 17°; with an additional 7° of sweep available by side-slipping the airplane, a total of 24° can be tested. For these flight conditions, both the determination of the nature of transition as well as the development of laminar boundary layer transition visualization methods will be attempted. Correlations of measurements with linear compressible stability theory will provide improved calibration for the use of such methods for NLF swept surface designs.

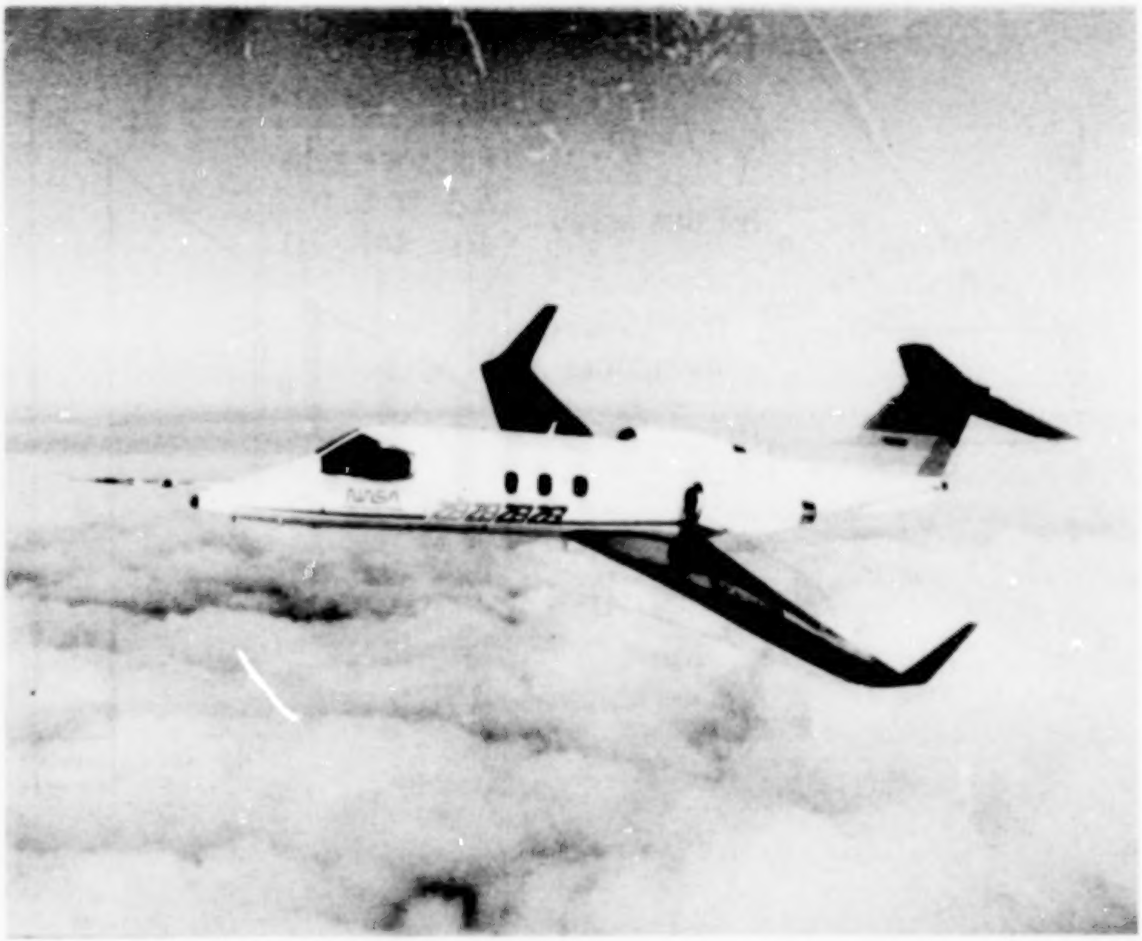

CITATION III NLF SWEPT-WING FLIGHT EXPERIMENTS

Flight experiments were conducted on the Cessna Citation III turbofan business airplane to measure the location and behavior of transition on a smoothed test section of the 27° swept wing. Surface hot-film transition sensors and sublimating chemical transition visualization were used. Surface pressure distributions were measured using pressure belts. Engine noise was monitored with a microphone attached on the upper surface of the test wing. This was done to investigate any possible effects of engine-generated acoustic disturbances on the wing laminar stability. Sideslip conditions were flown to effectively increase and decrease the leading-edge sweep angle and thus affect amplication of crossflow vorticity. Analysis of linear uncoupled stability of the laminar boundary layer has been conducted.

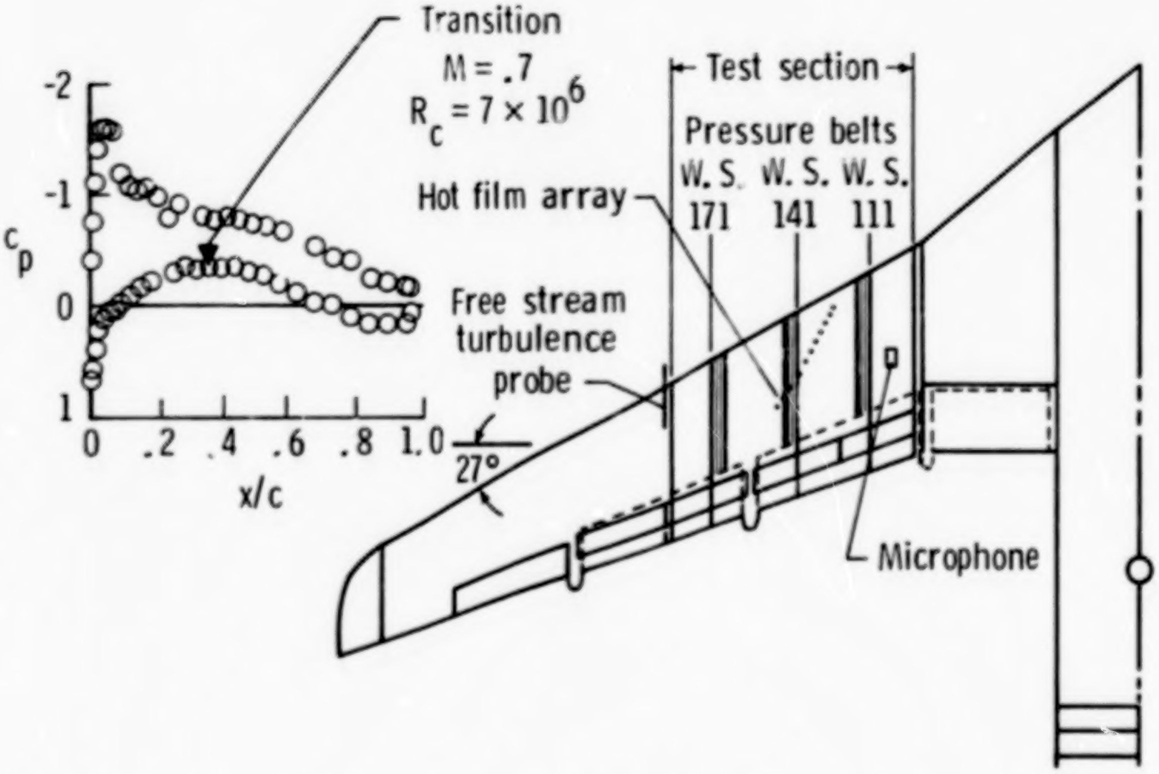
Transition
M = .7
$R_c = 7 \times 10^6$
-2
-1
c_p
0
1
0
.2
.4
.6
.8
1.0
x/c
Test section
Pressure belts
W. S. 171
W. S. 141
W. S. 111
Hot film array
Free stream turbulence probe
27°
Microphone

REFERENCES

1. Holmes, B. J.; Obara, C. J.; Gregorek, G. M.; Hoffman, M. J.; and Freuler, R. J.: Flight Investigation of Natural Laminar Flow on the Bellanca Skyrocket II. SAE Paper 830717, 1983.

2. Holmes, B. J.; and Obara, C. J.: Observations and Implications of Natural Laminar Flow on Practical Airplane Surfaces. J. Aircraft, Survey Paper, vol. 20, no. 12, pp. 993-1006, December 1983.

3. Holmes, Bruce J.; Obara, Clifford J.; and Yip, Long P.: Natural Laminar Flow Experiments on Modern Airplane Surfaces. NASA TP-2256, 1984.

4. Obara, Clifford J.; and Holmes, Bruce J.: Flight Measured Laminar Boundary-Layer Transition Phenomena Including Stability Theory Analysis. NASA TP-2417, 1985.

5. Ward, D. T.; Miley, S. J.; Reininger, T. L.; and Stout, L. J.: Flight Test Techniques for Obtaining Airfoil Pressure Distributions and Boundary Layer Transition. AIAA Paper 83-2689, 1983.

6. Wentz, W. H.; Ahmed, A.; and Nyenhuis, R.: Further Results of Natural Laminar Flow Flight Test Experiments. SAE Paper 850862, April 1985.

7. Malik, Mujeeb R.: COSAL -- A Black-Box Compressible Stability Analysis Code for Transition Prediction in Three-Dimensional Boundary Layers. NASA CR-165925, May 1982.

BIBLIOGRAPHY

1. Bragg, M. B.; and Maresh, J. L.: The Role of Airfoil Geometry in Minimizing the Effect of Insect Contamination of Laminar Flow Sections. AIAA Paper 84-2170, 1984.

2. Croom, C. C.; and Holmes, B. J.: Flight Evaluation of an Insect Contamination Protection System for Natural Laminar Flow Wings. SAE Paper 850860, 1985.

3. Holmes, Bruce J.; Croom, Cynthia C.; Obara, Clifford J.; and Kelliher, Warren C.: Sublimating Chemical Method for Detecting Laminar Boundary Layer Transition. NASA Technical Brief No. 13089, 1983.

4. Holmes, B. J.; Obara, C. J.; Martin, G. L.; and Domack, C. S.: Manufacturing Tolerances for Natural Laminar Flow Airframe Surfaces. SAE Paper 850863, 1984.

5. Holmes, B. J.: Progress in Natural Laminar Flow Research. AIAA Paper 84-2222, 1984.

6. Howard, R. M.; Miley, S. J.; and Holmes, B. J.: An Investigation of the Effects of the Propeller Slipstream on the Laminar Wing Boundary Layer. SAE Paper 850859, April 1985.

7. van Dam, C. P.: Natural Laminar Flow Airfoil Design Considerations for Winglets on Low-Speed Airplanes. NASA CR 3853, 1984.

D25

N88-14951

DESIGN AND EXPERIMENTAL EVALUATION OF A SWEPT SUPERCRITICAL LAMINAR FLOW CONTROL (LFC) AIRFOIL

S25-05

117249

10P.

W. D. Harvey, C. D. Harris, C. W. Brooks,
P. G. Clukey, and J. P. Stack
NASA Langley Research Center
Hampton, VA

[redacted]

ABSTRACT

A large chord swept supercritical laminar flow control (LFC) airfoil has been designed, constructed, and tested in the NASA Langley/8-ft. Transonic Pressure Tunnel (TPT). The LFC airfoil experiment was established to provide basic information concerning the design and compatibility of high-performance supercritical airfoils with suction boundary layer control achieved through discrete fine slots or porous surface concepts. It was aimed at validating prediction techniques and establishing a technology base for future transport designs and drag reduction. Good agreement was obtained between measured and theoretically designed shockless pressure distributions. Suction laminarization was maintained over an extensive supercritical zone up to high Reynolds numbers before transition gradually moved forward. Full-chord laminar flow was maintained on the upper and lower surfaces at $M_\infty = 0.82$ up to $R_c \leq 12\times10^6$. When accounting for both the suction and wake drag, the total drag could be reduced by at least one-half of that for an equivalent turbulent airfoil. Specific objectives for the LFC experiment are given in figure 1.

LFC EXPERIMENT OBJECTIVE

Conduct basic aerodynamic and fluid dynamics research program on a high-performance, swept supercritical, LFC airfoil to determine:

- Ability to laminarize over extensive supercritical region
- Ability of stability theories to predict transition and suction laminarization requirements
- Relative merit of slotted and perforated suction surfaces for LFC and HLFC
- Effects of surface conditions and boundary layer influences on laminarization

Figure 1

TEST SETUP FOR LFC EXPERIMENT IN THE 8-FT. TPT

A schematic of the overall LFC experiment in the Langley 8-ft. tunnel is shown in figure 2 along with tunnel modifications. The major component was a large chord, 23° swept supercritical LFC airfoil of aspect ratio near one which spanned the full tunnel height. Laminar flow control by boundary layer removal was achieved by suction through closely spaced fine slots extending spanwise on the airfoil surface. After passing through the slots, the air passed through metering holes located in plenums beneath each slot and was collected by spanwise ducts with nozzles located at the ends. From the duct/nozzles, the air passed through airflow system evacuation lines, through airflow control boxes which controlled the amount of suction to each individual duct nozzle, and through sonic nozzles to a 10,000 ft^3/min compressor which supplied the suction. All four walls of the tunnel were contoured in order to produce a transonic wind tunnel flow which simulated unbounded free air flow about an infinite yawed wing at model design conditions. The contoured liner was shaped to conform to computed streamlines around the wing and corrected for growth of the wall boundary layer. The success of the LFC experiment depended to a large extent on the environmental disturbance levels in the test section. Isolation of the test section from downstream disturbances was achieved by an adjustable two wall-choke (sonic throat). Reduction of upstream disturbances such as pressure and vorticity fluctuations was achieved by the installation of a honeycomb and five screens in the settling chamber.

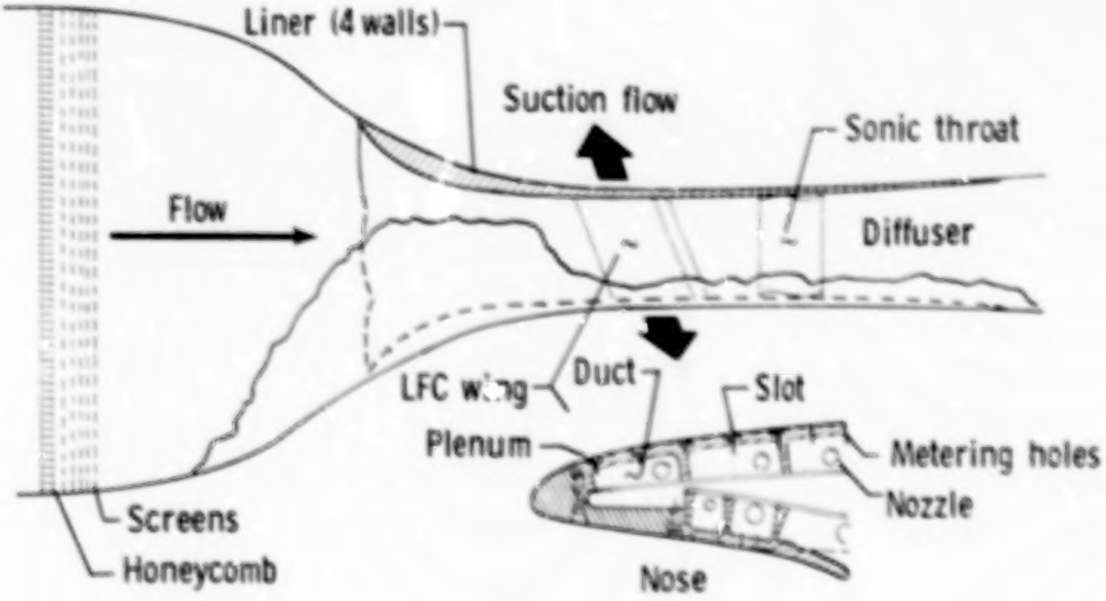

Figure 2

ORIGINAL PAGE IS
OF POOR QUALITY

PHOTOGRAPH OF MODEL INSTALLED IN TUNNEL - UPSTREAM VIEW

Figure 3 is an upstream view of the finished liner and wing trailing edge as seen from the test section diffuser entrance where the liner faired into the original tunnel lines. The LFC model extended from floor to ceiling and blended with the liner. The offset of the wing mean plane from the tunnel centerline may be seen as well as the development of the liner floor and ceiling step which resulted from the differential spanwise flow displacement in the tunnel channels "above" and "below" the wing surfaces. The dark vertical area on the left of the photograph and downstream of model trailing edge is the edge of the test section access door. The dark rectangular area ahead of the model is the tunnel contraction throat region.

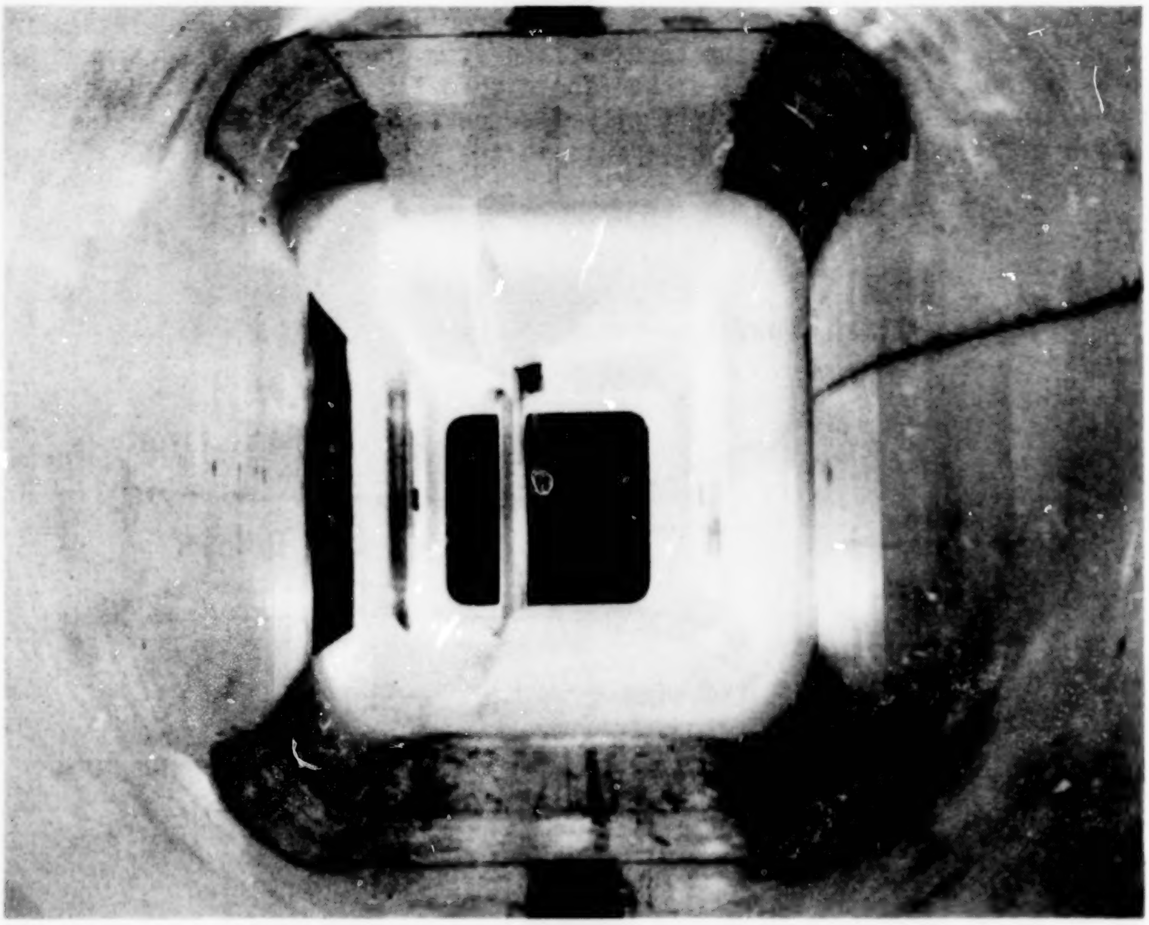

Figure 3

ORIGINAL PAGE IS
OF POOR QUALITY

PHOTOGRAPH OF MODEL INSTALLED IN TUNNEL - DOWNSTREAM VIEW

Figure 4 is a downstream view of the upper surface of the model taken from immediately upstream of the model. This figure illustrates the smooth streamline contour of the liner and how it blended with the model. The dark areas at the top and bottom liner model juncture regions are suction panels in the "collar" around the ends of the model to control the growth of the boundary layer in these regions. The dark area on the left vertical wall and downstream of the model is one of the flexible two-wall chokes (sonic throat). The choke plate on the opposite wall is hidden behind the model. The dark area immediately in back of the model is the tunnel test section access door followed by the downstream high speed diffuser.

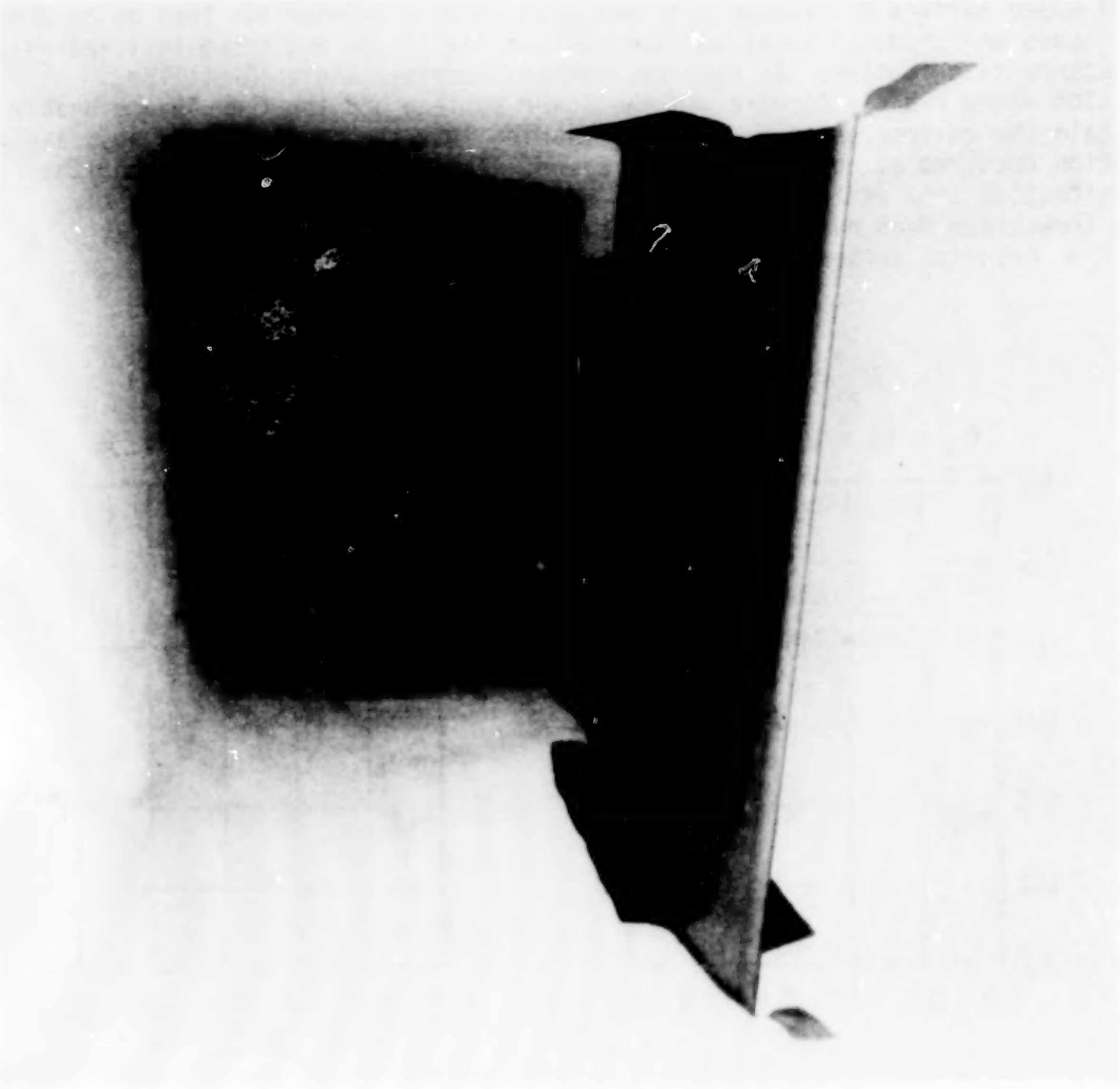

Figure 4

MEASURED AND DESIGN PRESSURE DISTRIBUTIONS

Measured and design chordwise pressure distributions on the upper and lower surfaces of the LFC model are shown in figure 5 for two chord Reynolds numbers at the design Mach number of 0.82. In general, these representative results indicate measured pressure distributions very close to design. Shockfree flow is shown for 10-million Reynolds number and essentially shockfree flow for 20-million. The slightly overall higher velocities on the upper surface and the chordwise deviation from the design pressure distribution were attributed to classical problems associated with wind tunnel testing, wall interference and model deformation under design air loads. The velocity field between the upper surface and tunnel wall (supersonic bubble zone) was slightly higher than predicted due to the liner contour and inability to completely account for boundary layer displacement effects in the design analysis. Coordinate deviations from design over the LFC model forward upper surface at midspan were measured under simulated air load to be about 0.003-inches and produced local surface contour deviations and irregularities in the pressure distribution. As Reynolds number increased above 10-million, transition moved rapidly forward on the lower surface and the flow became unable to sustain the adverse pressure gradient leading into the trailing-edge cusp and separation occurred at about 80-percent chord. This separated flow changed the local effective area distribution of the test section resulting in a slightly higher freestream Mach number and increased upper surface shock strength at 20-million Reynolds number.

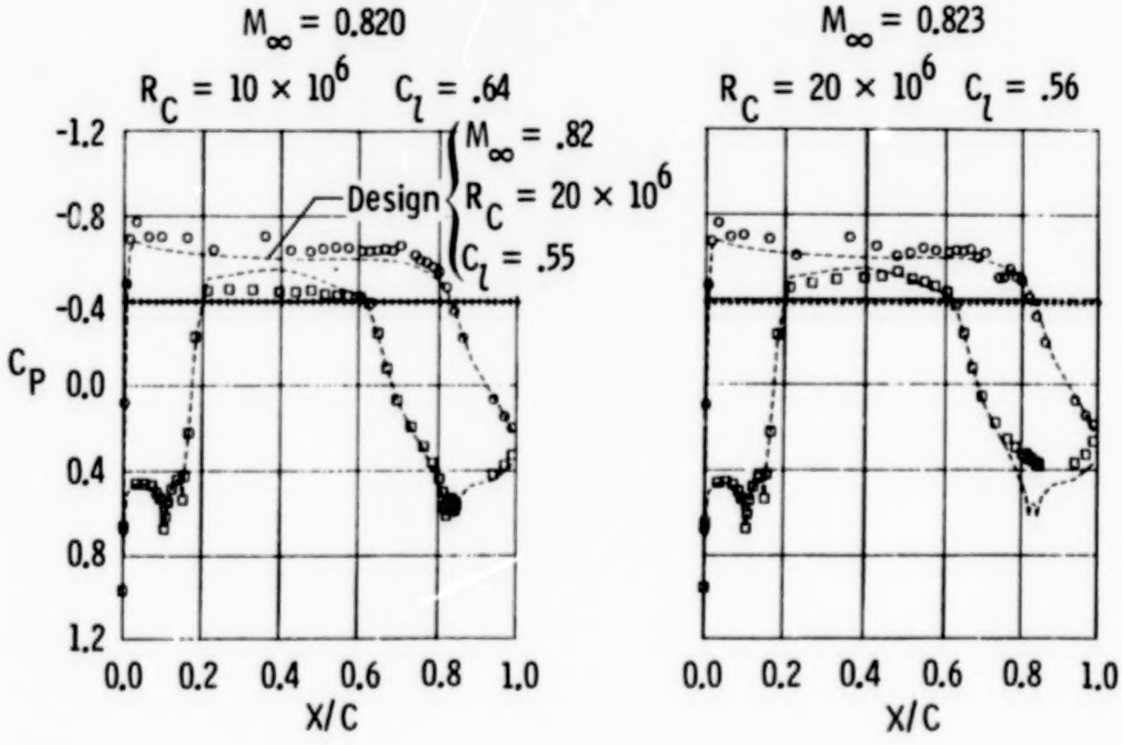

Figure 5

ORIGINAL PAGE IS
OF POOR QUALITY

MEASURED AND THEORETICAL SUCTION DISTRIBUTIONS

The measured chordwise suction coefficient (C_Q) distribution required to maintain full chord laminar flow over both surfaces at the design Mach number of 0.82 and 10-million chord Reynolds number is shown in figure 6 compared to the theoretical suction distribution. The required suction level was higher than the theory over most of the upper and lower surfaces. About two-thirds of the predicted or measured total suction contribution for both surfaces is necessary for control of the lower surface geometry alone. The higher suction requirements were due to the overvelocities and the surface pressure irregularities, as well as higher suction control required to overcome the cross flow instabilities associated with the steep pressure gradients on the upper and lower surfaces and the minimization of centrifugal Taylor-Görtler type boundary layer instabilities and interactions in the concave regions of the lower surface. The overall higher suction levels are also influenced by tunnel disturbance levels which are inherently higher than free-air turbulence levels expected in flight.

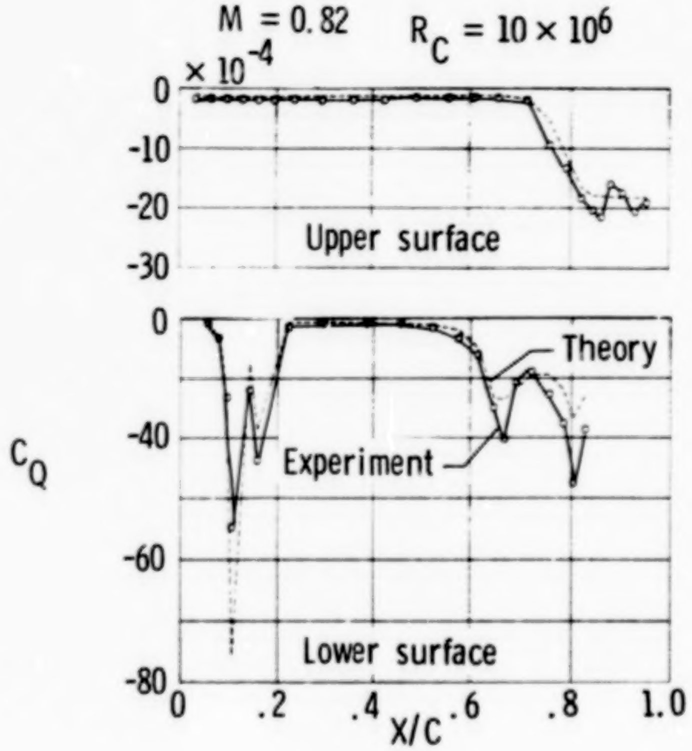

Figure 6

SUMMARY OF TRANSITION VARIATION WITH REYNOLDS NUMBER

The data presented in figure 7 show the chordwise extent of laminar flow achieved on the upper surface for several Mach numbers up to the design Mach number of 0.82, as determined by a grid of flush mounted surface thin film gages. At R_c = 10-million, full chord laminar flow could be maintained over the upper and lower surfaces for all Mach numbers. As Reynolds number was increased for constant Mach number, transition moved gradually forward on the upper surface. The Reynolds number at which this forward movement began was dependent on Mach number and occurred at progressively lower Reynolds numbers as Mach number increased. For the design Mach number of 0.82, the forward movement began between 11- and 12-million and reached about 65-percent chord at R_c = 20-million. Transition on the lower surface moved more rapidly than on the upper surface and occurred near the leading edge for M = 0.82 and R_c = 20-million. It was concluded that suction laminarization over a large supercritical zone is feasible to high chord Reynolds numbers even under non-ideal surface conditions on a swept LFC airfoil at high lift.

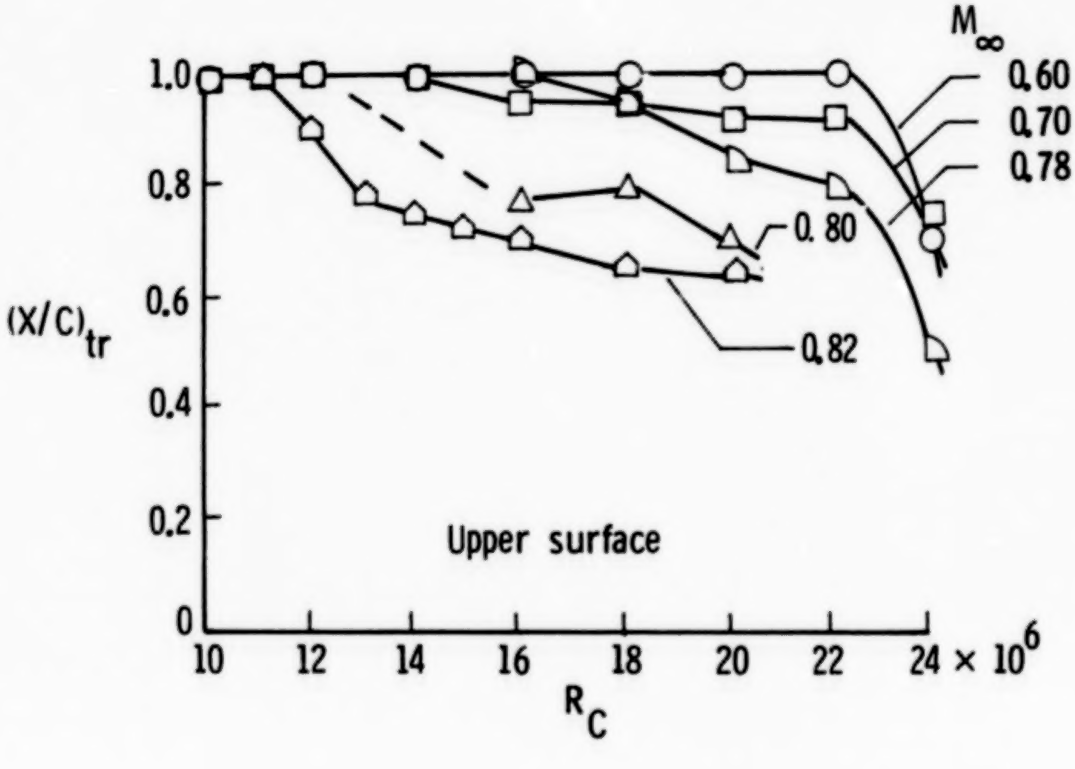

Figure 7

SUMMARY OF DRAG WITH M_∞

The total drag at $M_\infty = 0.40$ and 0.82 and R_c = 10 million with full chord laminar flow is seen in figure 8 to be equal to about 31 counts ($c_d = 0.0031$). This represents an approximate 60-percent drag reduction as compared to an equivalent conventional turbulent airfoil drag level of about 80 counts. Total drag is the sum of measured wake drag from a wake rake at midspan and the suction drag penalty required to maintain full chord laminar flow. The suction required to maintain full chord laminar flow was somewhat higher than anticipated and the contribution to the total suction drag was approximately 40-percent from the upper surface and 60-percent from the lower surface. The increase in wake drag for Mach numbers just below the design Mach number of 0.82 was associated with the formation of a weak shock wave near the leading edge as the supersonic bubble began to develop. As the bubble developed ($0.78 < M_\infty < 0.80$) full chord laminar flow was still present but periodic turbulent bursts occurring over the upper surface caused an increase in the wake drag. As the Mach number increased to 0.82, the supersonic zone spread rearward to approximately the 80-percent chord, the turbulent bursts over the upper surface disappeared, and the wake drag returned to near its subsonic level.

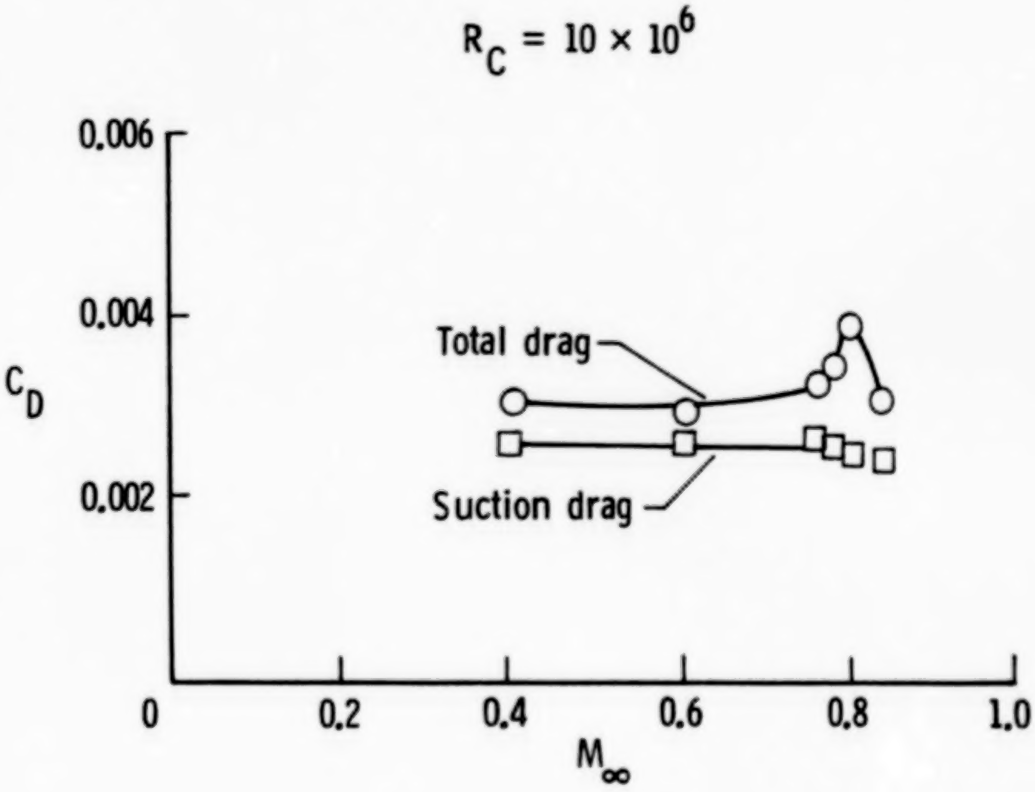

Figure 8

MEASURED DRAG ON AIRFOILS WITH/WITHOUT SUCTION CONTROL

A summary of the measured drag on airfoils with and without suction control, developed by the Airfoil Aerodynamics Branch of the Transonic Aerodynamics Division over the past several years, is shown in figure 9. The most recent design concepts with Natural Laminar Flow (NLF) or Laminar Flow Control (LFC) are identified as NLF(1)-0414F, HSNLF(1)-0213, and SCLFC(1)-0513F. Performance evaluation of all the concepts shown was conducted in NASA Langley facilities that have been rehabilitated or modified for improved flow quality and low drag testing except the 6- × 28-inch Transonic Tunnel (TT) which has not been modified. The total drag of the swept supercritical LFC airfoil with suction slots includes the suction drag penalty required to maintain full chord laminar flow. The solid symbols represent drag levels obtained with the maximum extent of laminar flow at the design lift coefficient and Reynolds number. The open symbols indicate drag levels obtained with the same airfoils with fully turbulent, attached flow tripped at the leading edge. In general, the results indicate about 60% drag reduction achieved with laminar flow over the speed range, with or without suction control or sweep, when compared with a turbulent drag level of about 80 counts. Of further major importance is the fact that both the NLF(1)-0414F and HSNLF(1)-0213 airfoils showed no degradation of lift performance or pitching moment characteristics when fully turbulent.

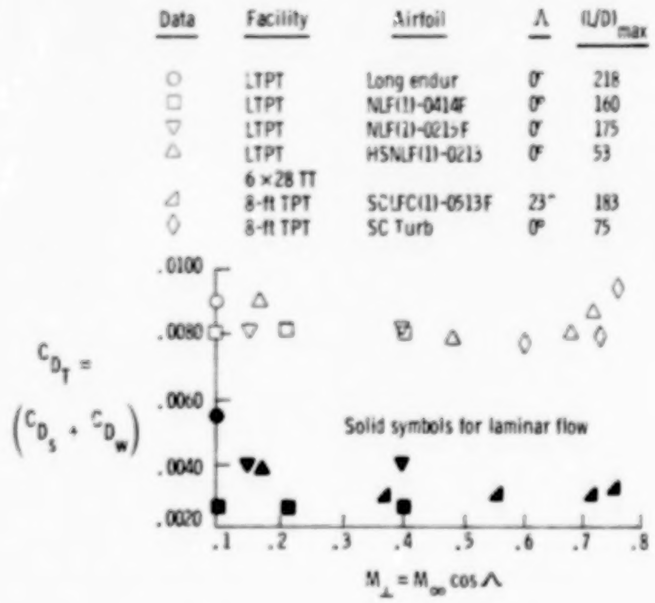

Figure 9

D26

N88-14952

LAMINAR FLOW INTEGRATION - FLIGHT TESTS
STATUS AND PLANS

S26-34

117250

34P.

R. D. Wagner*; D. F. Fisher**; M. C. Fischer*;
D. W. Bartlett*; and R. R. Meyer, Jr.**
*NASA Langley Research Center
Hampton, Virginia

**Ames-Dryden Flight Research Center
Edwards Air Force Base, California

[redacted]INAR FLOW INTEGRATION - FLIGHT TESTS

Under the Aircraft Energy Efficiency - Laminar Flow Control Program in the Projects Directorate at the Langley Research Center, there are currently three flight tests programs under way to address critical issues concerning laminar flow technology application to commercial transports (ref. 1). The Leading-Edge Flight Test (LEFT) with a JetStar aircraft is a cooperative effort with the Ames/Dryden Flight Research Facility to provide operational experience with candidate leading-edge systems representative of those that might be used on a future transport. In the Variable Sweep Transition Flight Experiment (VSTFE), also a cooperative effort between Langley and Ames/Dryden, basic transition data on an F-14 wing with variable sweep will be obtained to provide a data base for laminar flow wing design. Finally, under contract to the Boeing Company, the acoustic environment on the wing of a 757 aircraft will be measured and the influence of engine noise on laminar flow determined with a natural laminar flow glove on the wing. This presentation reports the status and plans for these programs.

- **LEADING EDGE FLIGHT TEST - JETSTAR**
- **VARIABLE SWEEP TRANSITION FLIGHT EXPERIMENT - F-14**
- **WING NOISE SURVEY AND NLF GLOVE FLIGHT TEST - 757**

LAMINAR FLOW CONTROL LEADING-EDGE FLIGHT TEST

The most difficult problems of achieving laminar flow on commercial transports appear to be associated with the leading-edge region. Solutions to these problems will remove many concerns about the ultimate practicality of laminar flow. A flight program is currently under way within NASA to evaluate the effectiveness of integrated LFC leading-edge systems developed by Douglas and Lockheed over the past few years. Under NASA contracts, both companies have designed and fabricated a leading-edge test article to be installed on a JetStar to demonstrate that the required systems can be packaged into a leading-edge section representative of future LFC commercial transport aircraft, and that these systems can operate reliably with minimum maintenance in an airline flight environment.

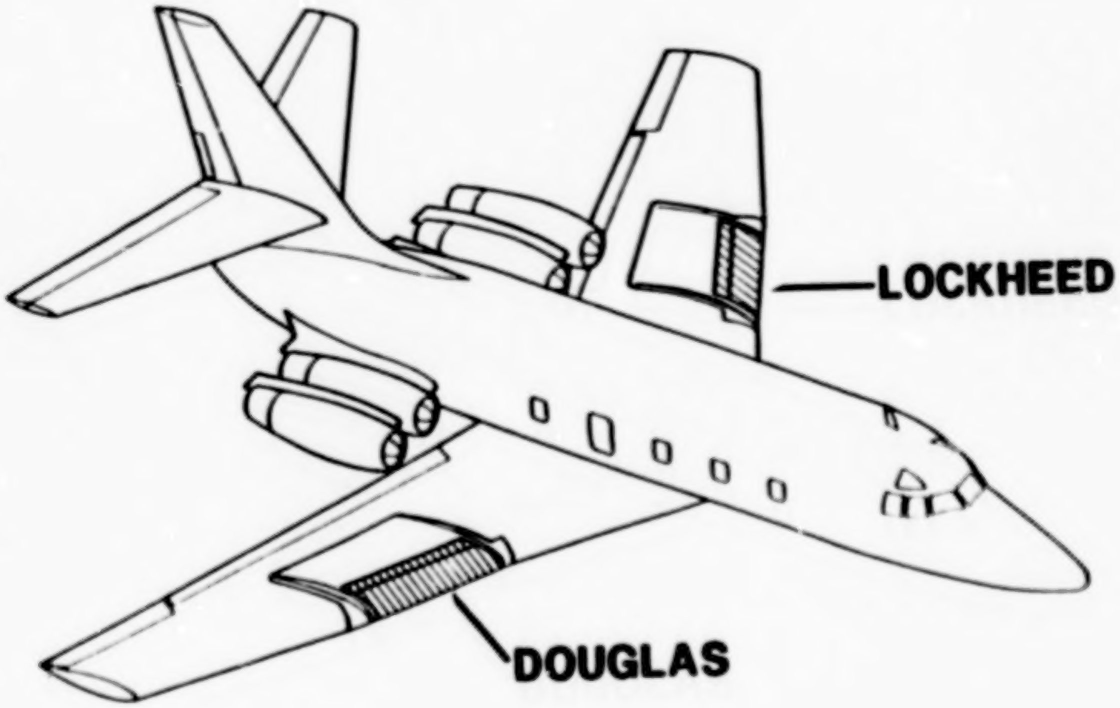

OBJECTIVE: DEMONSTRATE THE EFFECTIVENESS AND PRACTICALITY OF L.E. SYSTEMS IN MAINTAINING LAMINAR FLOW UNDER REPRESENTATIVE FLIGHT CONDITIONS

LEADING-EDGE FLIGHT TEST
LOCKHEED TEST ARTICLE

The Lockheed leading-edge concept (ref. 2) is illustrated in this figure. The leading-edge box structure is a sandwich construction. A 0.016-in. thick titanium outer sheet is bonded to a sandwich substructure of graphite/epoxy face sheets with a Nomex honeycomb core. Suction is accomplished through 27 fine, spanwise slots (0.004 inch in width) distributed chordwise on both the upper and lower surfaces back to the front spar. The suction flow is routed through the structure by a combination of slot ducts, metering holes and collector ducts embedded in the honeycomb. The Lockheed insect protection system is integrated with the anti-icing protection system. It consists of dispensing a cleaning/anti-icing fluid over the surface through slots above and below the attachment line (previous studies (ref. 2) have shown that insects will not adhere to a wet wing). These slots are purged of fluid during climb-out and provide suction to achieve laminar boundary layer flow at cruise conditions.

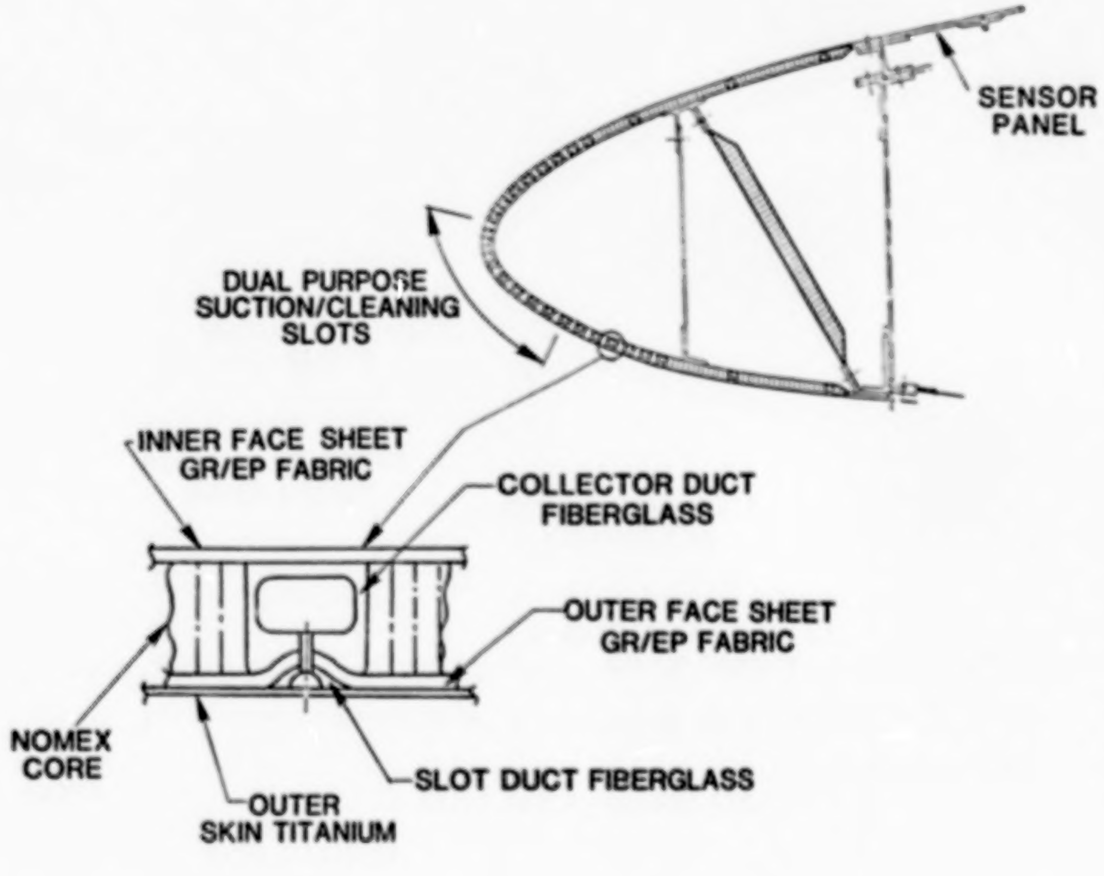
SENSOR PANEL
DUAL PURPOSE SUCTION/CLEANING SLOTS
INNER FACE SHEET GR/EP FABRIC
COLLECTOR DUCT FIBERGLASS
OUTER FACE SHEET GR/EP FABRIC
NOMEX CORE
SLOT DUCT FIBERGLASS
OUTER SKIN TITANIUM

LEADING-EDGE FLIGHT TEST
DOUGLAS TEST ARTICLE

The Douglas leading-edge concept (ref. 3) illustrated in the figure consists of an electron-beam perforated (EBP) titanium sheet bonded to a fiberglass sandwich substructure which forms a suction panel. This removable suction panel is attached to a ribbed supporting substructure. The areas where the EBP skin bonds to the corrugated substructure are impervious to flow; thus, suction is through perforated strips. Alternate substructure flutes are used for suction air collection. Suction is applied only on the upper surface from just below the attachment line to the front spar. A Krueger-type flap serves as a protective shield against insect impact. Spray nozzles on the underside of the Krueger shield provide added insect protection and are a part of the leading-edge anti-icing protection. These nozzles coat the leading-edge with a freezing point depressant fluid to provide protection against lighter insects which might impinge on the wing. In icing conditions, the Krueger serves as the primary anti-icing protection of the leading edge, supplemented as required with the spray nozzle system. The shield leading edge is equipped with a TKS* (commercially available) ice protection system. A system for purging fluid from the suction flutes and surface perforations is provided if required.

*TKS Aircraft Deicing Ltd., England.

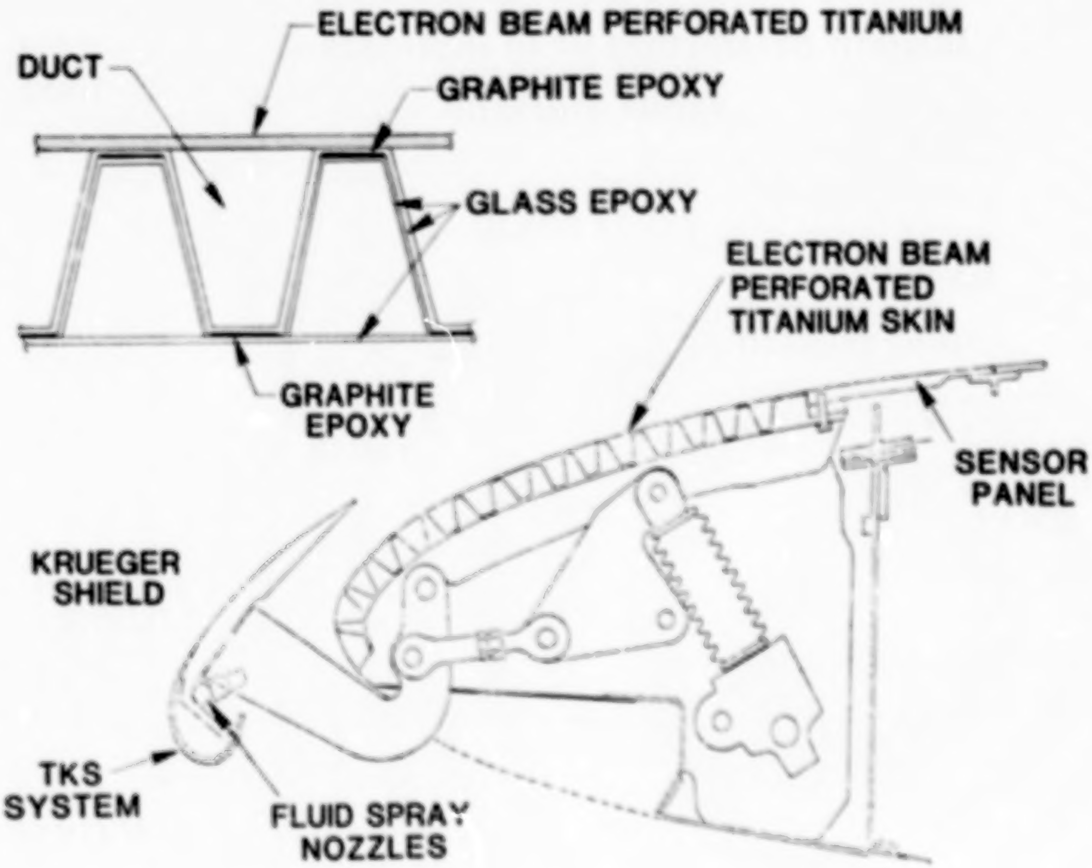
ELECTRON BEAM PERFORATED TITANIUM
DUCT
GRAPHITE EPOXY
GLASS EPOXY
GRAPHITE EPOXY
ELECTRON BEAM PERFORATED TITANIUM SKIN
SENSOR PANEL
KRUEGER SHIELD
TKS SYSTEM
FLUID SPRAY NOZZLES

JETSTAR LEFT CONFIGURATION

A schematic of the JetStar configured for the leading-edge flight test program is presented in this figure. The heart of the suction system is the centrifugal air turbine compressor used as a suction pump. The compressor is mounted in the unpressurized rear fuselage compartment of the JetStar. To enchance the research value of the flight test, to allow the control and measurement of key parameters, and to permit optimization of the systems, each of the 15 suction strips on the Douglas test article and each of the 27 slots on the Lockheed test article have individual flow adjustment control. Individual flow control is accomplished through the use of chamber valves. One chamber valve handles the 15 Douglas suction lines and there are two valves: one chamber valve for the Lockheed upper surface lines and one chamber valve for the Lockheed lower surface lines. Each suction line has its own needle valve within the chamber valve to adjust the suction flow. Control of the chamber valves and data acquisition is accomplished at two operator consoles and one data console in the cabin.

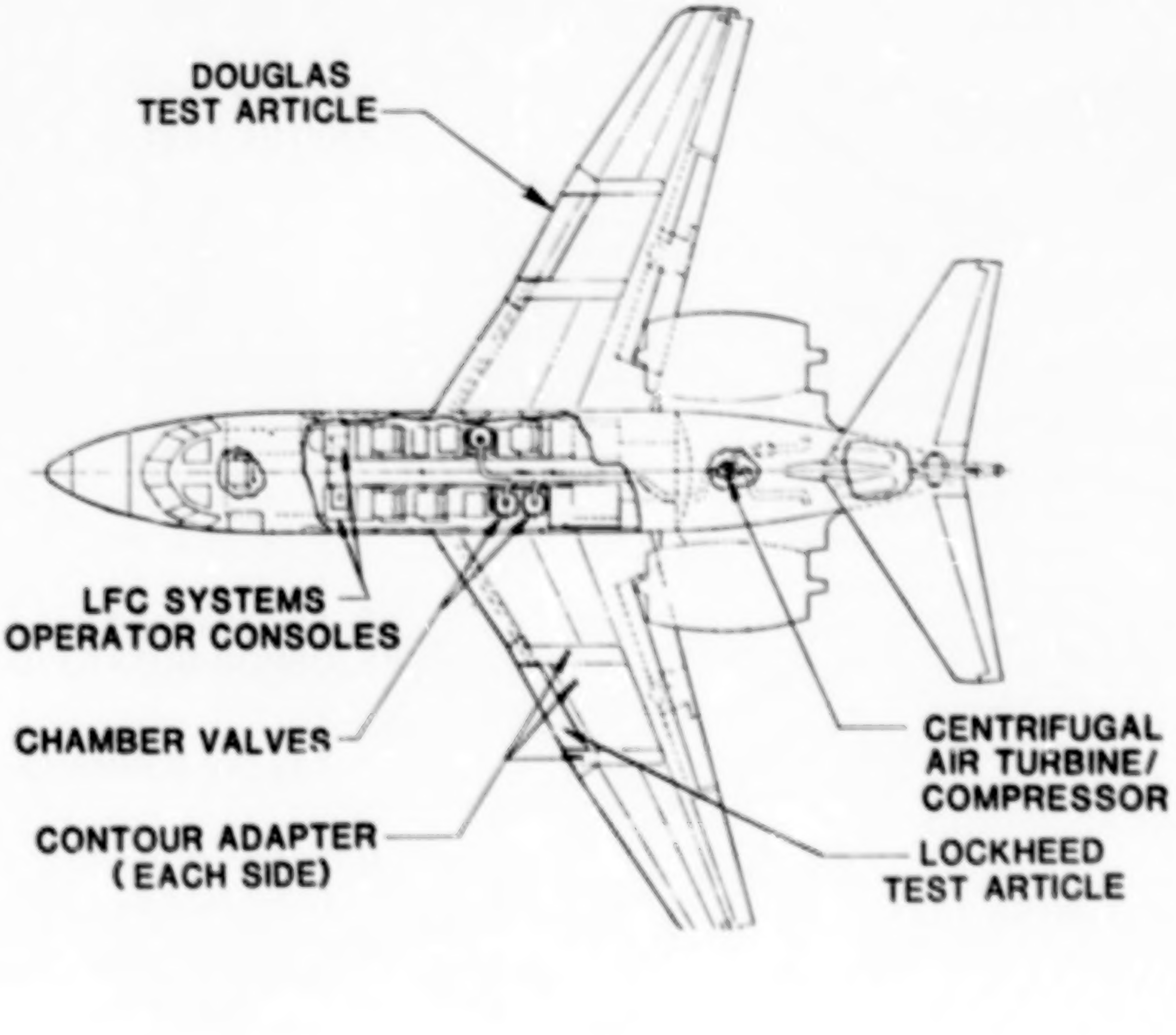
DOUGLAS TEST ARTICLE
LFC SYSTEMS OPERATOR CONSOLES
CHAMBER VALVES
CONTOUR ADAPTER (EACH SIDE)
CENTRIFUGAL AIR TURBINE/ COMPRESSOR
LOCKHEED TEST ARTICLE

ORIGINAL PAGE IS
OF POOR QUALITY

LOCKHEED TEST ARTICLE

The photograph shows the Lockheed test article. Note the instrumentation at the front spar on the upper and lower surfaces. Two reference pitot tubes are shown mounted on struts about two inches above the wing surface. Twenty equally spaced spanwise pitot tubes at the front spar (about 0.060 inches above the wing surface) are used to determine whether the boundary layer is laminar or turbulent.

In the fabrication of the Lockheed test article, a number of difficult fabrication problems were encountered which led to a surface quality that was only marginally acceptable in terms of meeting laminar flow smoothness and waviness criteria. During fabrication, adhesive flow into subsurface plenums also resulted in repairs and residual suction blockage that could affect laminar flow performance. Undoubtedly these flaws in the article are in part responsible for the less successful initial results in achievement of laminar flow compared to the Douglas article which was considerably smoother and more wave-free.

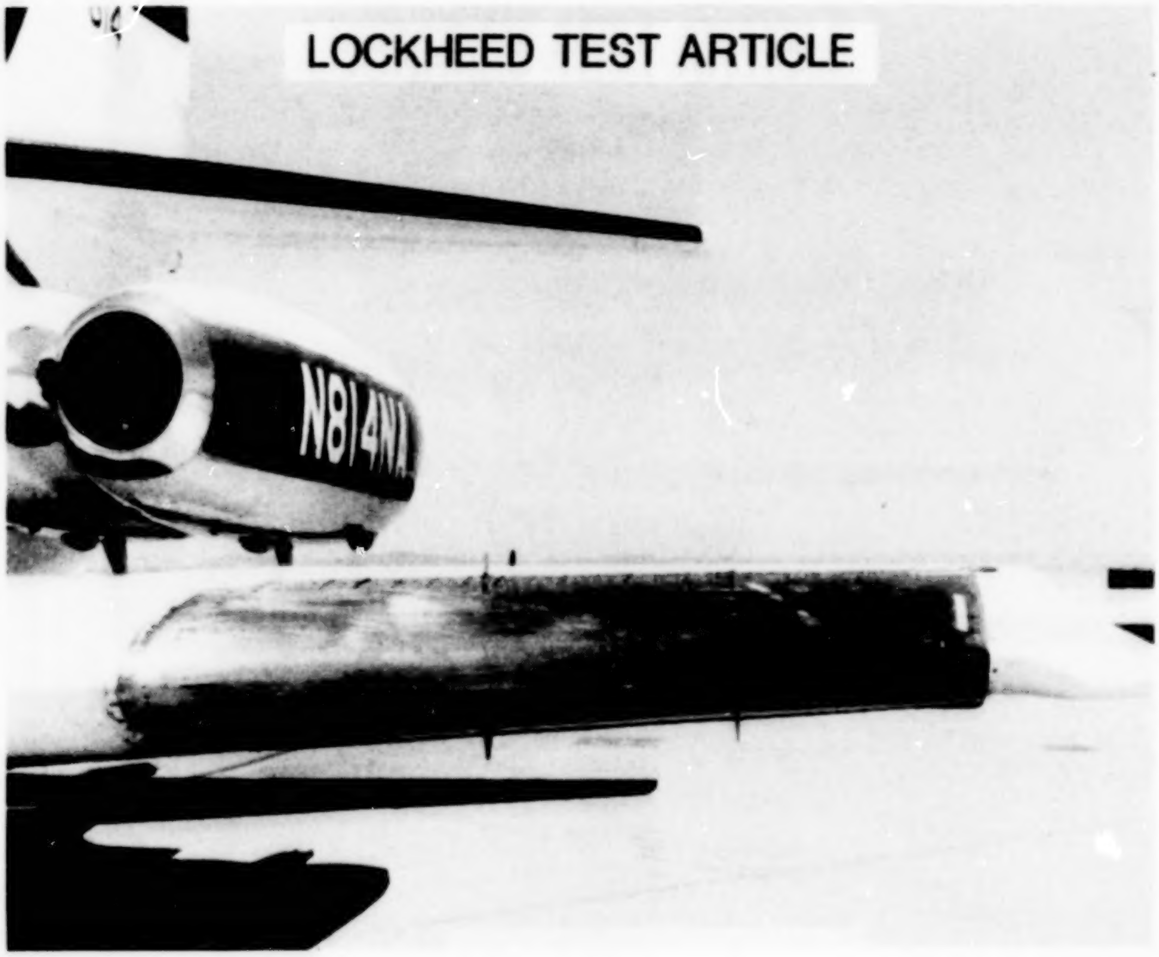

DOUGLAS TEST ARTICLE

The photograph shows the Douglas test article installed on the JetStar. The white areas inboard and outboard of the test article are aerodynamic fairings which fair the test article contour back to the JetStar wing surface. Aft of the front spar, a fairing also extends to the rear spar to close out the wing sections. The step in the outboard fairing is indicative of how much thicker the new wing sections are relative to the basic wing. Back to the front spar the LEFT section on the JetStar is roughly about the same size as the forward wing sections on a DC-9-30 at the mean aerodynamic chord.

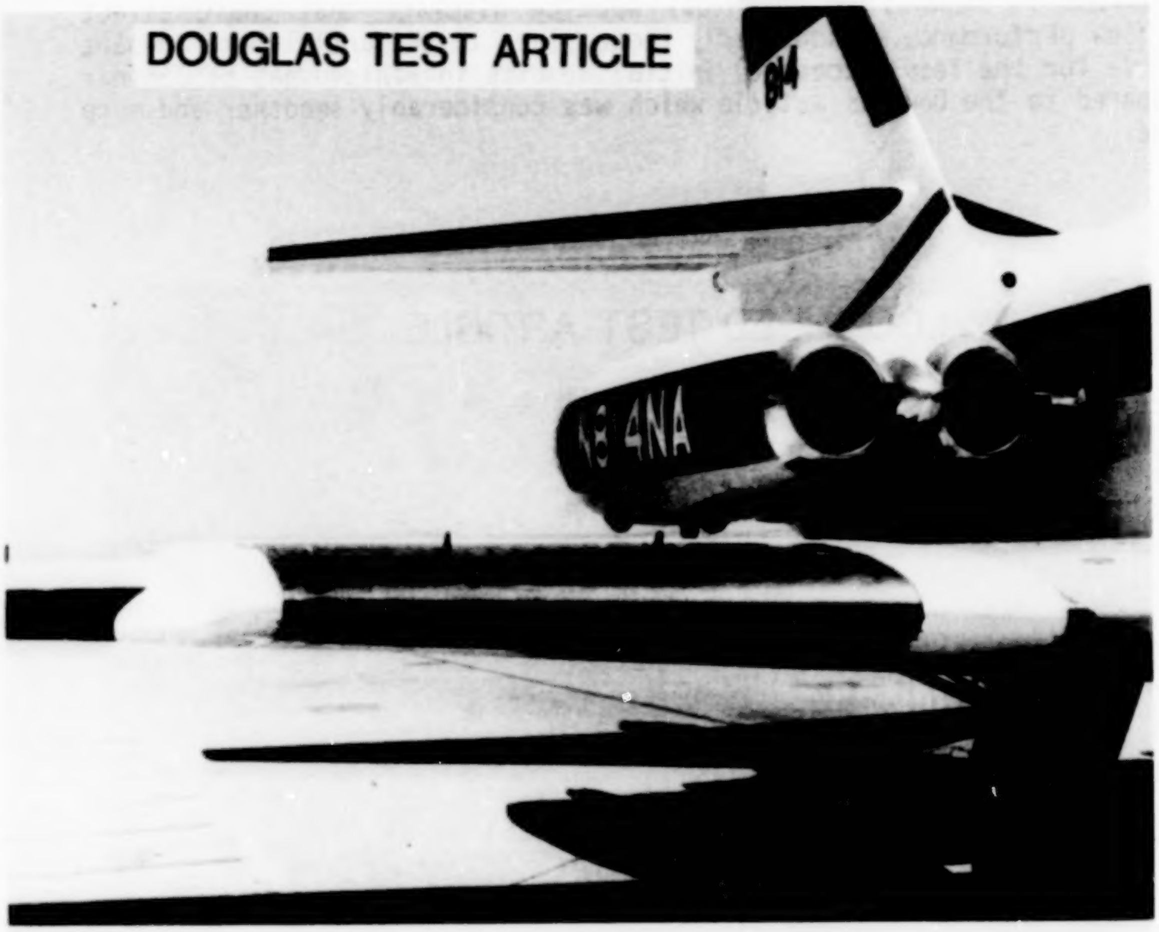

ORIGINAL PAGE IS
OF POOR QUALITY

ORIGINAL PAGE IS
OF POOR QUALITY

DEPLOYED DOUGLAS INSECT SHIELD

This photograph shows the Douglas insect shield deployed. The shield is deployed at takeoff and retracted at about 6000 feet altitude. During descent, the shield is deployed at 6000 feet. In the event of an ice encounter, the aircraft reduces speed to M=0.4 and the shield is then deployed. A freezing point depressant fluid spray system, located on the underside of the Krueger, is used if required for supplemental insect and ice protection.

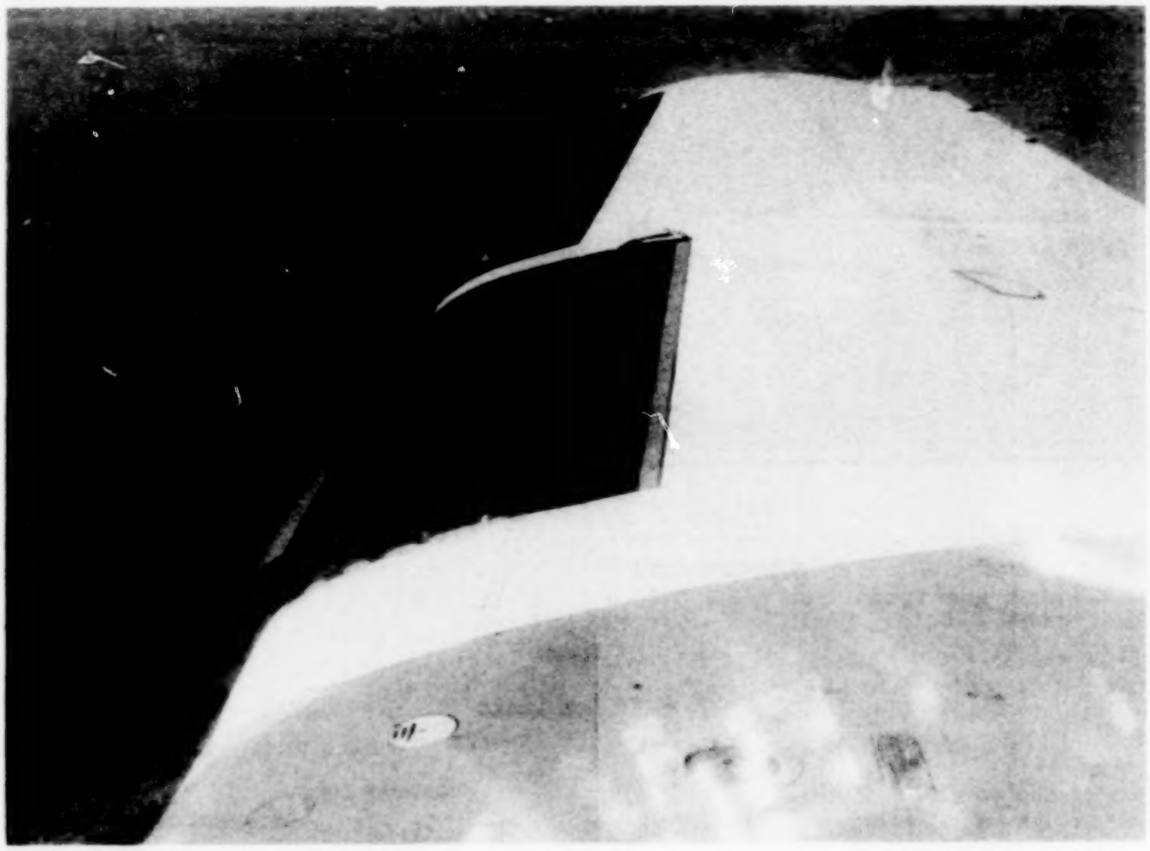

LEFT JETSTAR AND FLIGHT TEST SCHEDULE

The aircraft modifications were completed in FY '84 and the first flight of the aircraft took place in December 1983. Acceptance testing and performance evaluation of the new systems extended through FY '84. During the research flights, the laminar flow performance is to be optimized. Simulated service flights will begin in mid FY 85. These will be structured to gain operational experience with the test articles.

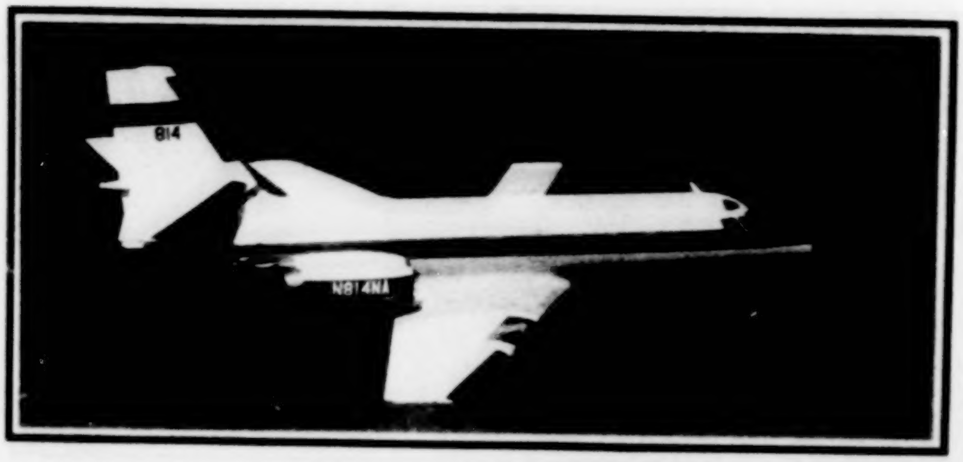

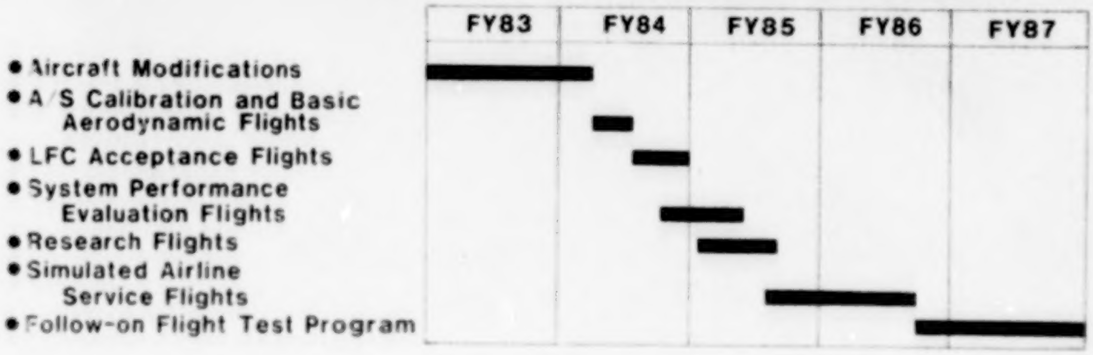

ORIGINAL PAGE IS
OF POOR QUALITY

LEADING-EDGE FLIGHT TEST

At the design point, M = 0.75 at 38,000 feet altitude, the chordwise pressure distribution at three span stations on the Douglas test article and five span stations on the Lockheed test article are shown. The solid line is a data fairing. The flight results are quite close to the desired pressure distribution and have acceptable spanwise gradients.

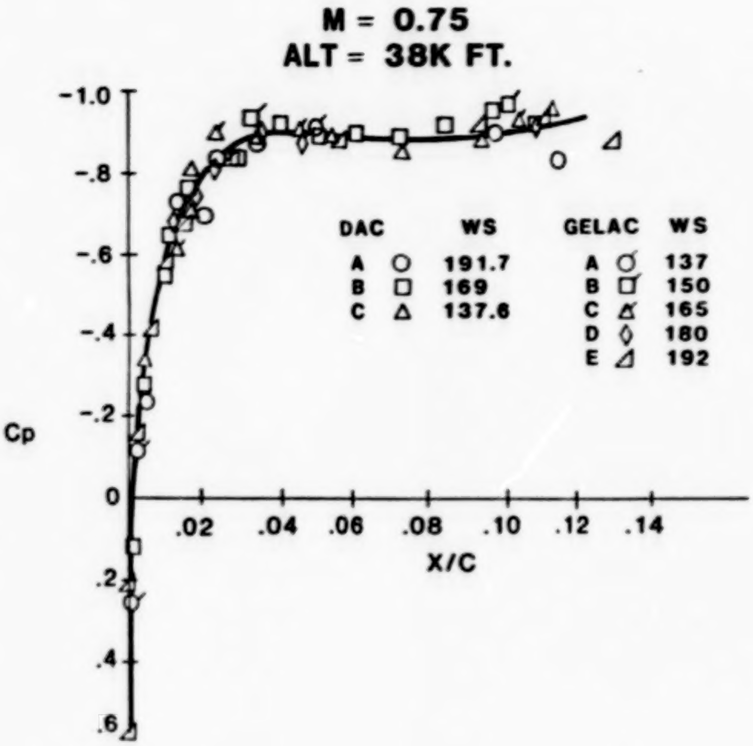

DOUGLAS TEST ARTICLE SURFACE PRESSURES

Extended pressure distributions back to the rear spar are shown. The data consist of only the Douglas test article mid span row of surface pressures at 38,000 feet altitude. The pressure distribution becomes "peaky" at the lower Mach number, and above the design point Mach number .75, a favorable gradient exists to the front spar.

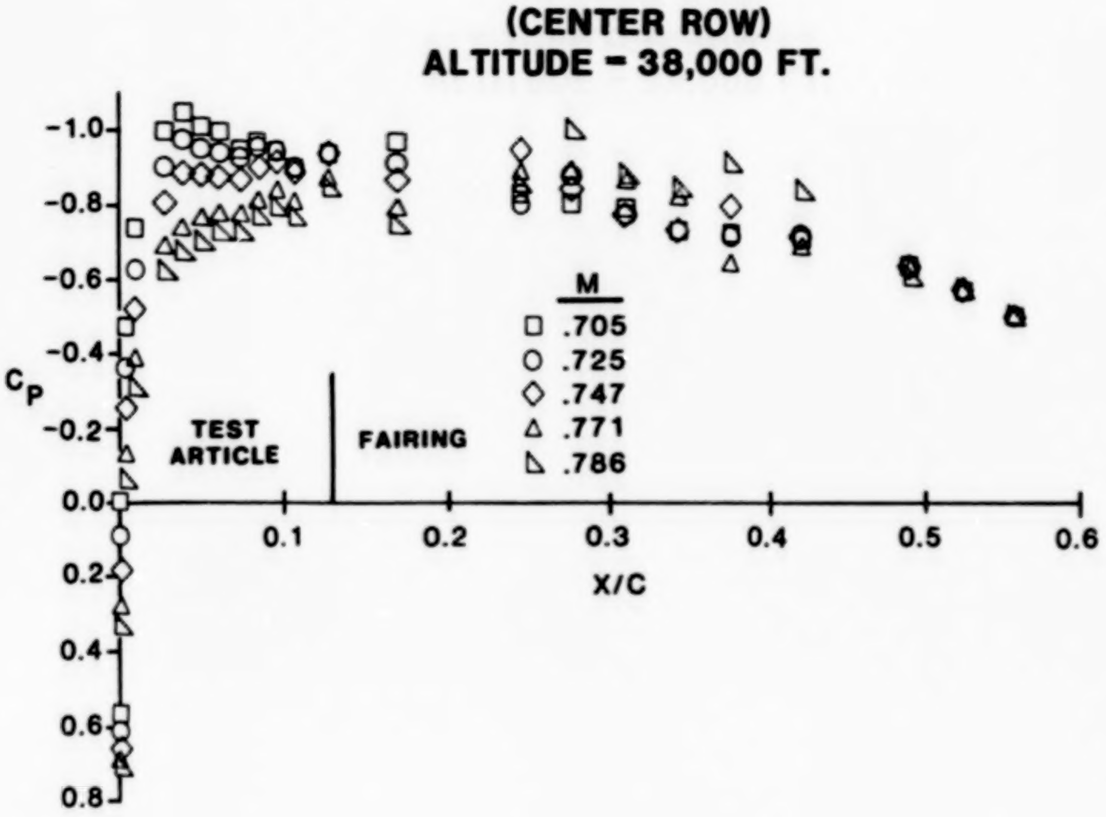

DETERMINATION OF SPANWISE EXTENT OF LAMINAR FLOW AT FRONT SPAR

This figure illustrates how pitot tubes near the surface (about 0.06 inch above the surface) are used to detect the nature of the boundary layer. If laminar flow exists at the pitot tube, the boundary layer will be thin enough to pass under the tube which will then register the same pressure as the reference probe, two inches above the surface. If transition occurs ahead of the near-to-surface pitot tube, it will be emersed in a turbulent boundary layer with much reduced pitot pressure, depending upon where transition occurs.

Data taken in the initial flights on the Douglas test article show the pressure differentials that exist on twenty pitot tubes spaced about two inches apart across the front spar. At the design point, M = .75 at 38,000 feet altitude, the outboard 76% of the test article span is laminar at the front spar. The inboard region is turbulent and the readings near 200 psf differential pressure indicate that transition occurs at or near the attachment line for those inboard span stations. At lower altitudes this turbulent region spreads outboard, until at 34,000 feet the entire span of pitot data indicates that transition occurs on the attachment line.

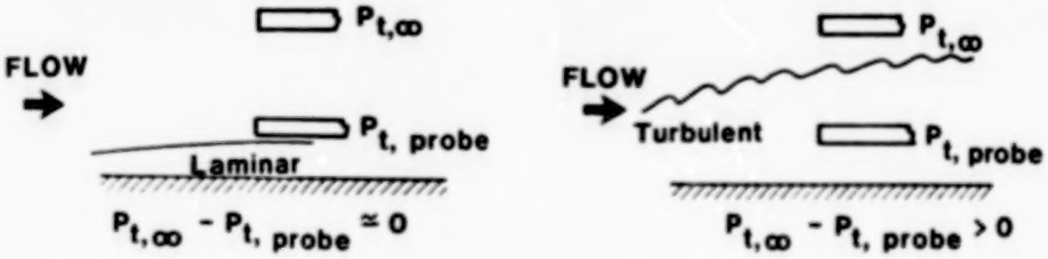

DOUGLAS TEST ARTICLE: M = 0.75

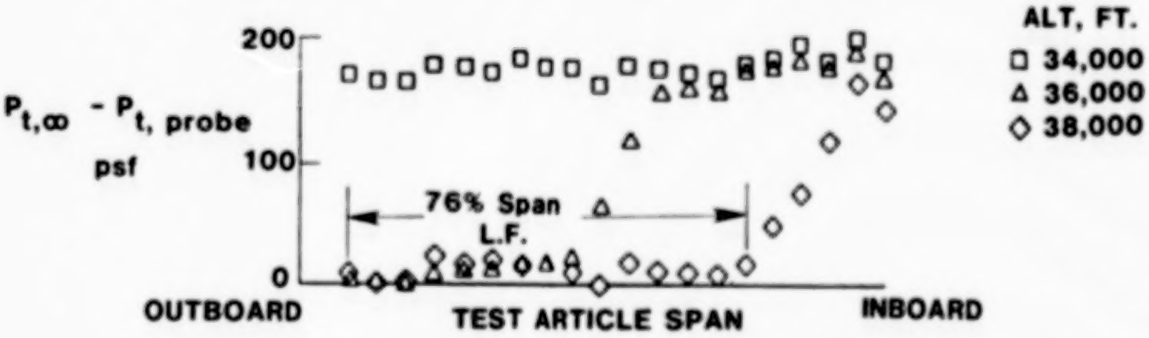

SPANWISE EXTENT OF LAMINAR FLOW AT FRONT SPAR (INITIAL FINDINGS)

These data were obtained from the initial flights to assess the laminar flow performance of the test articles. The spanwise extent of laminar flow, as determined from the twenty pitot tubes, is shown over the cruise altitude and Mach number range of the JetStar. The results were disappointing because turbulence contamination from the inboard region of the wing resulted in only a limited Mach number and altitude range for which full span laminar flow was observed. On the Lockheed test article, no laminar flow at the front spar was observed except when the aircraft was side-slipped to lower the effective sweep of the Lockheed test article leading edge. These data indicated the need to employ some method to suppress the leading-edge turbulence contamination.

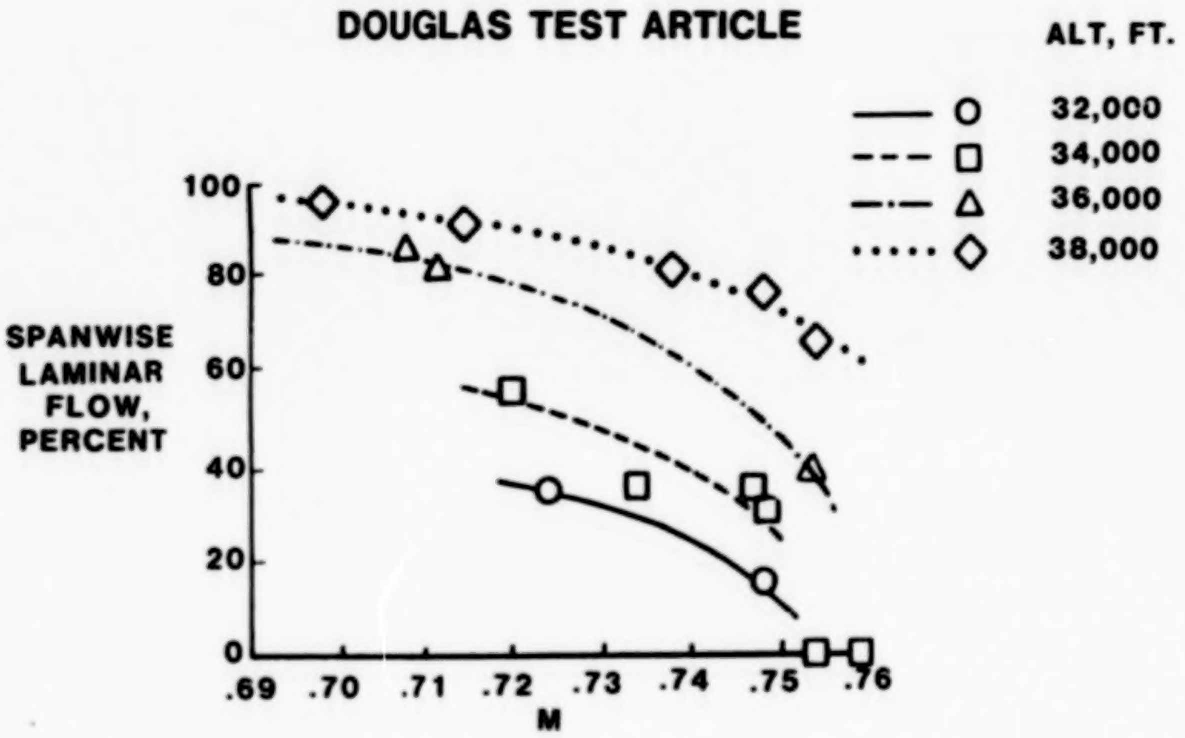

NOMINAL SUCTION DISTRIBUTION
DOUGLAS TEST ARTICLE

The design nominal suction distribution was used for all flights. The higher suction level in the forward region of the test article is required to control crossflow instabilities; the aft, lower level suction controls the growth of Tollmien-Schlichting disturbances.

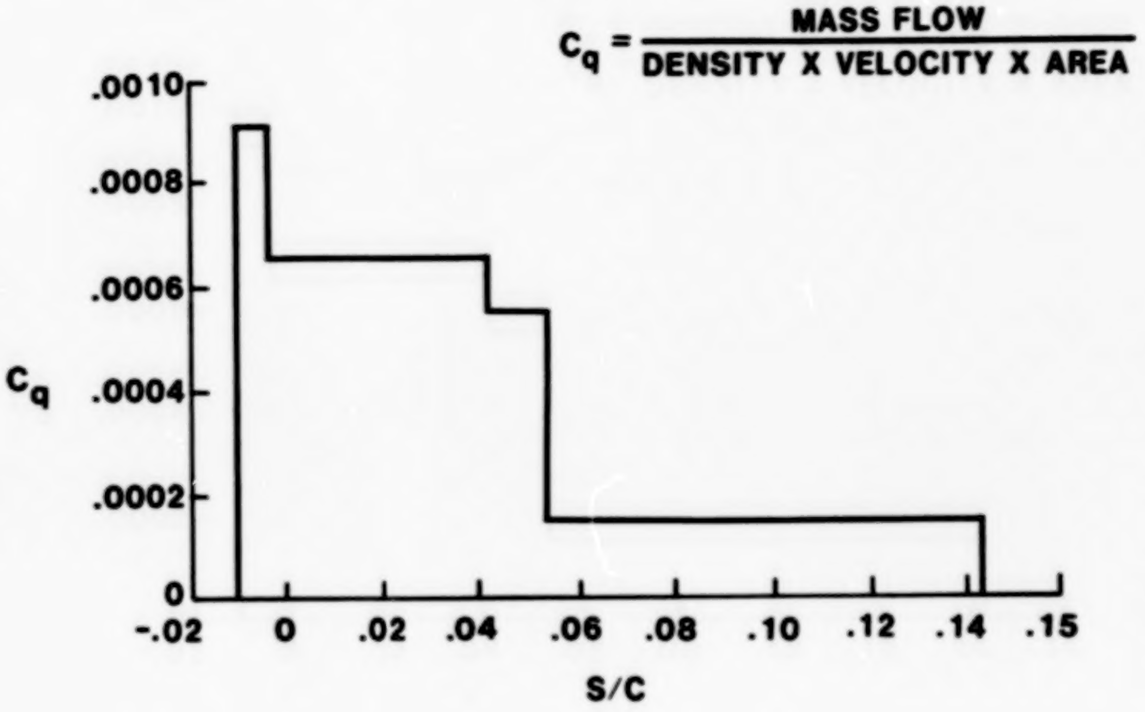

CANDIDATE METHODS TO CONTROL ATTACHMENT LINE CONTAMINATION

Three approaches to control spanwise turbulence contamination at the leading edge were examined. A Gaster bump (ref. 4) and a notch are simple devices placed on the wing inboard of the test article. The intent of these devices is to establish a new laminar attachment line from the stagnation point created by the bump or notch. The Gaster bump was found to be effective over a limited range of angle of attack, but the notch was ineffective. The best results were obtained with a combination notch/bump.

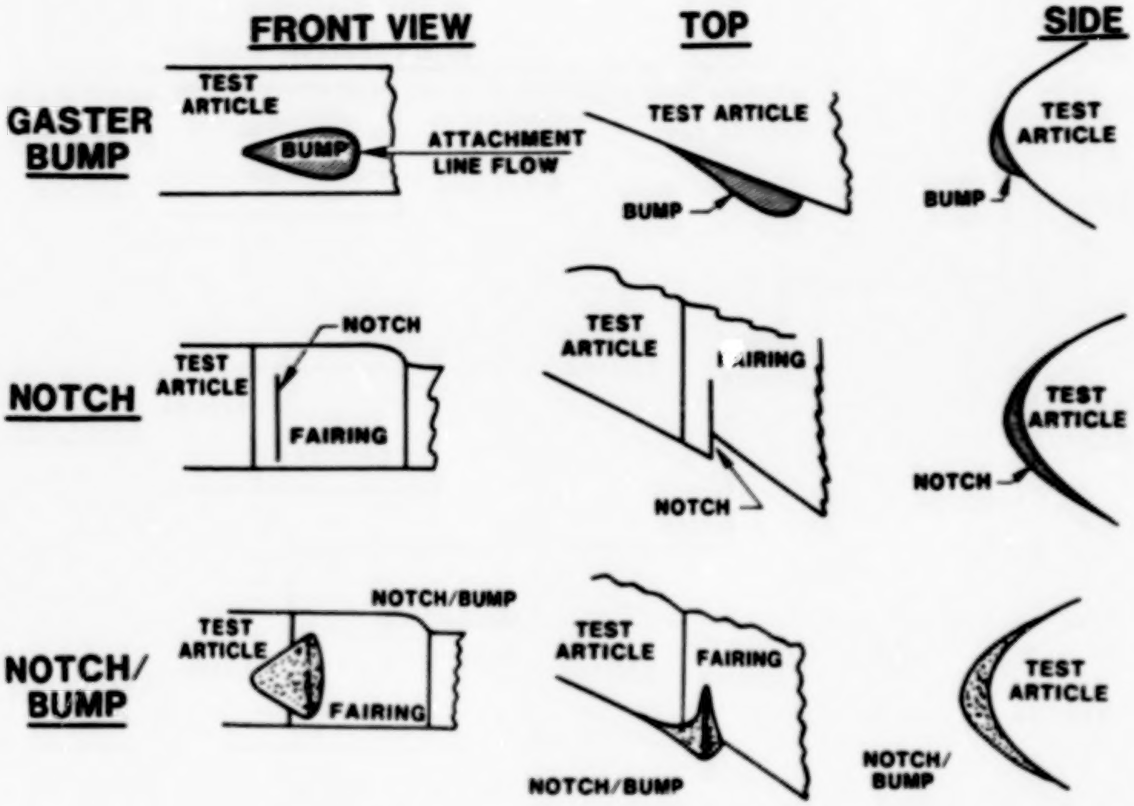
FRONT VIEW
TOP
SIDE
GASTER BUMP
TEST ARTICLE
BUMP
ATTACHMENT LINE FLOW
TEST ARTICLE
BUMP
TEST ARTICLE
BUMP
NOTCH
NOTCH
TEST ARTICLE
FAIRING
TEST ARTICLE
FAIRING
NOTCH
TEST ARTICLE
NOTCH
NOTCH/ BUMP
NOTCH/BUMP
TEST ARTICLE
FAIRING
TEST ARTICLE
FAIRING
NOTCH/BUMP
TEST ARTICLE
NOTCH/ BUMP

ORIGINAL PAGE IS
OF POOR QUALITY

DOUGLAS NOTCH/BUMP

This figure is a three view of the final configuration of the combination notch/bump.

PLANFORM VIEW

SIDE VIEW

FRONT VIEW

SPANWISE EXTENT OF LAMINAR FLOW AT FRONT SPAR
DOUGLAS TEST ARTICLE (WITH NOTCH/BUMP OR GASTER BUMP)

A comparison of the results obtained with the Gaster bump and the notch/bump shows the latter to be the most effective in controlling the turbulence contamination. With increased suction in the aft flutes (see following figure) nearly the entire span of the test article has laminar flow at the front spar over the operational flight envelope.

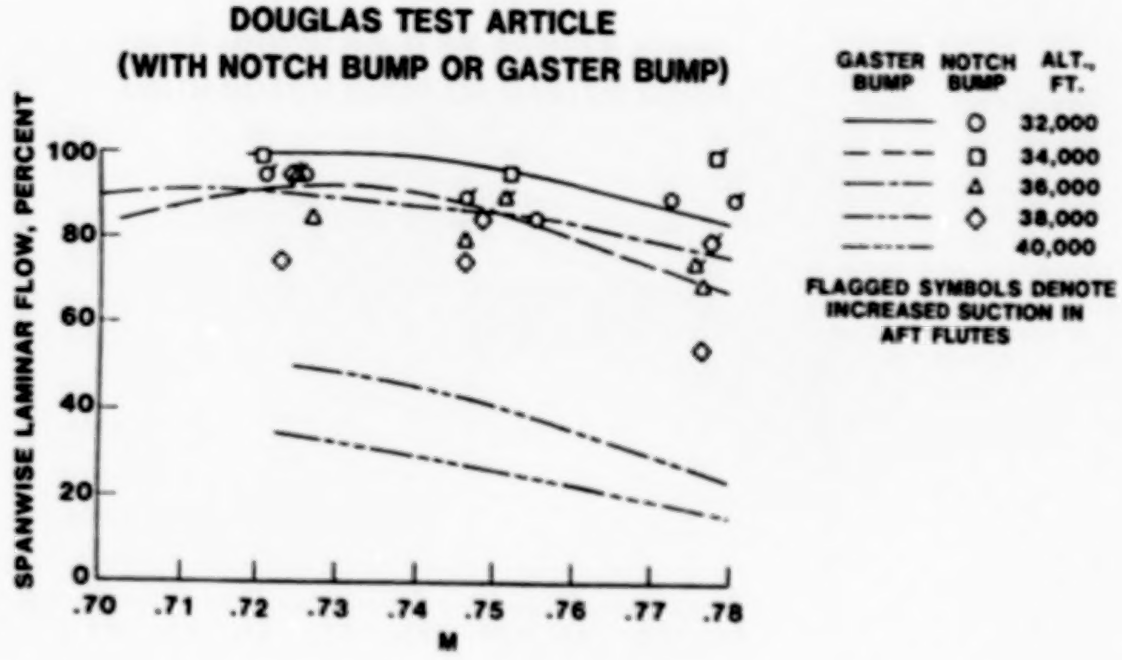

SUCTION DISTRIBUTION

Further improvements in the spanwise extent of laminar flow with the notch/bump were achieved with increased suction in the aft flutes of the Douglas test article. These suction increases were made after data analyses indicated some outflow due to spanwise surface pressure gradients in this area.

DOUGLAS TEST ARTICLE

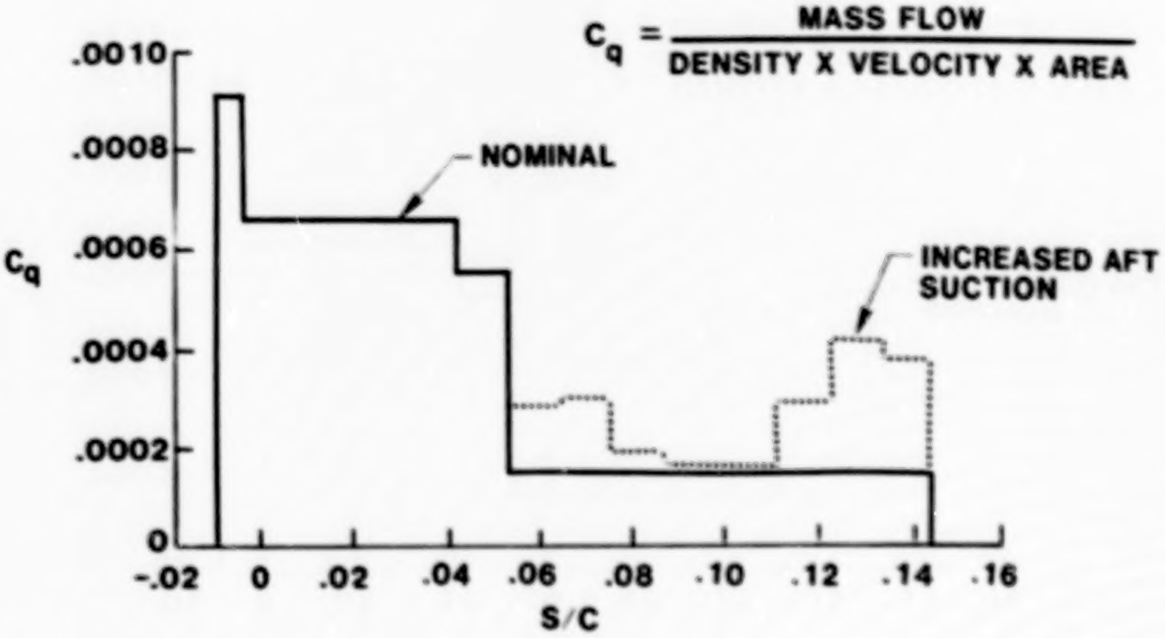

SPANWISE EXTENT OF LAMINAR FLOW AT FRONT SPAR
LOCKHEED TEST ARTICLE (WITH GASTER BUMP) - UPPER SURFACE

The Gaster bump greatly improved the performance of the Lockheed test article; however, the achievement of laminar flow is still quite limited. Our plans are to duplicate the notch/bump configuration used on the Douglas test article and retest the Lockheed article.

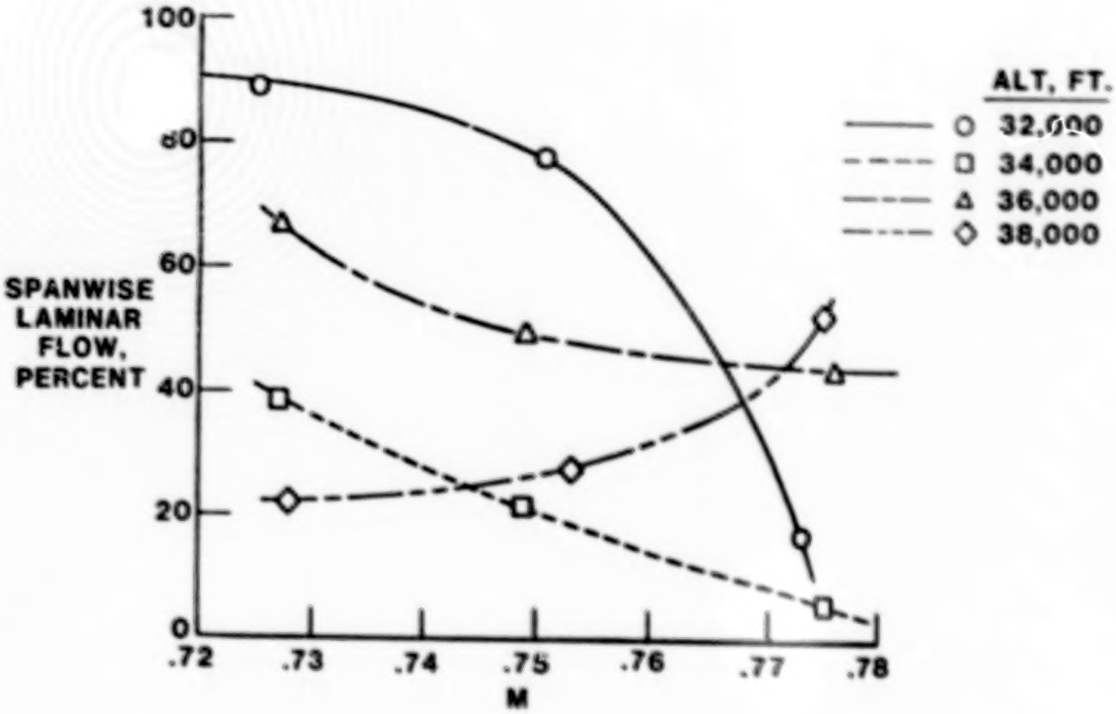

NOMINAL SUCTION DISTRIBUTION
LOCKHEED TEST ARTICLE - UPPER SURFACE

The suction distribution on the Lockheed article is similar to the Douglas suction distribution. Unlike the Douglas test article (which has suction along the attachment line), the first slot on the Lockheed article is located downstream of the attachment line at the cruise design point.

$$C_q = \frac{\text{MASS FLOW}}{\text{DENSITY X VELOCITY X AREA}}$$

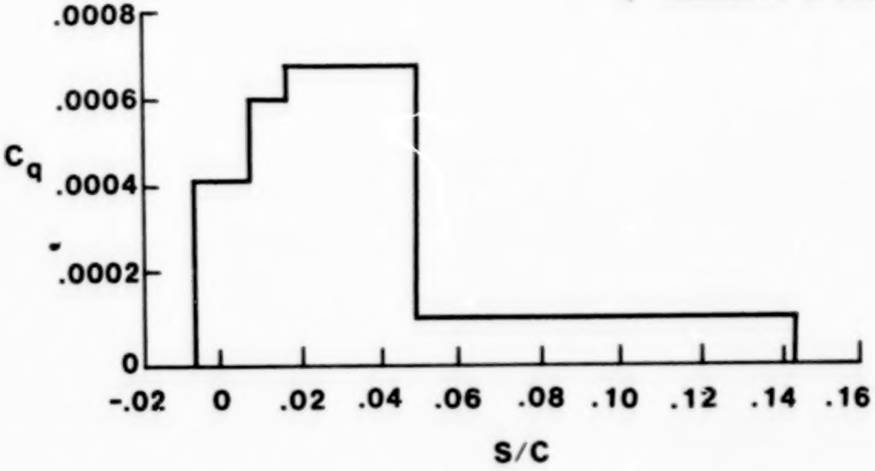

JETSTAR LEFT RESULTS - MARCH 1985

During the past year, good progress has been made in the flight test program. The design pressure distribution goals have been achieved. The in-flight washing and ice protection systems have been operated and function as designed. With the addition of a passive device to suppress leading-edge turbulence contamination, nearly full span laminar flow has been achieved on the Douglas test article over the operational cruise speed and altitude range of the JetStar. A maximum of 85% spanwise extent of laminar flow has been achieved on the Lockheed test article with a Gaster bump at M = 0.725 at 32,000 feet; the prospects for further improvements are believed to be good.

- **Design pressure distribution goals achieved**
- **In-flight washing and ice protection systems function as designed**
- **Douglas test article nearly fully laminar at altitudes up to 38,000 ft. with notch/bump**
- **Lockheed test article laminar for 85 percent of span at M = 0.725, alt = 32,000 ft with Gaster bump**

SIMULATED SERVICE HOME BASES

In the summer of 1985, we intend to initiate a simulation of airline service operations. The aircraft will be operated out of home bases throughout the United States. Operation of the laminar flow systems will rely heavily on the experience accrued in the earlier phases of flight testing. The JetStar will operate for approximately a 2-week period from each home base flying into and out of major commercial airports. Two or more flights will be conducted daily, with each consisting of takeoff, climb-to-cruise altitude, achievement of laminar flow for some minimal period, descent, landing, and inspection of the test articles. The condition of the test articles (possible insect remains, clogged or contaminated suction surfaces, etc.) will be fully documented after each flight. Special measures to clean or otherwise maintain the test article surfaces or systems will be minimal in order to establish a maintenance and reliability data base.

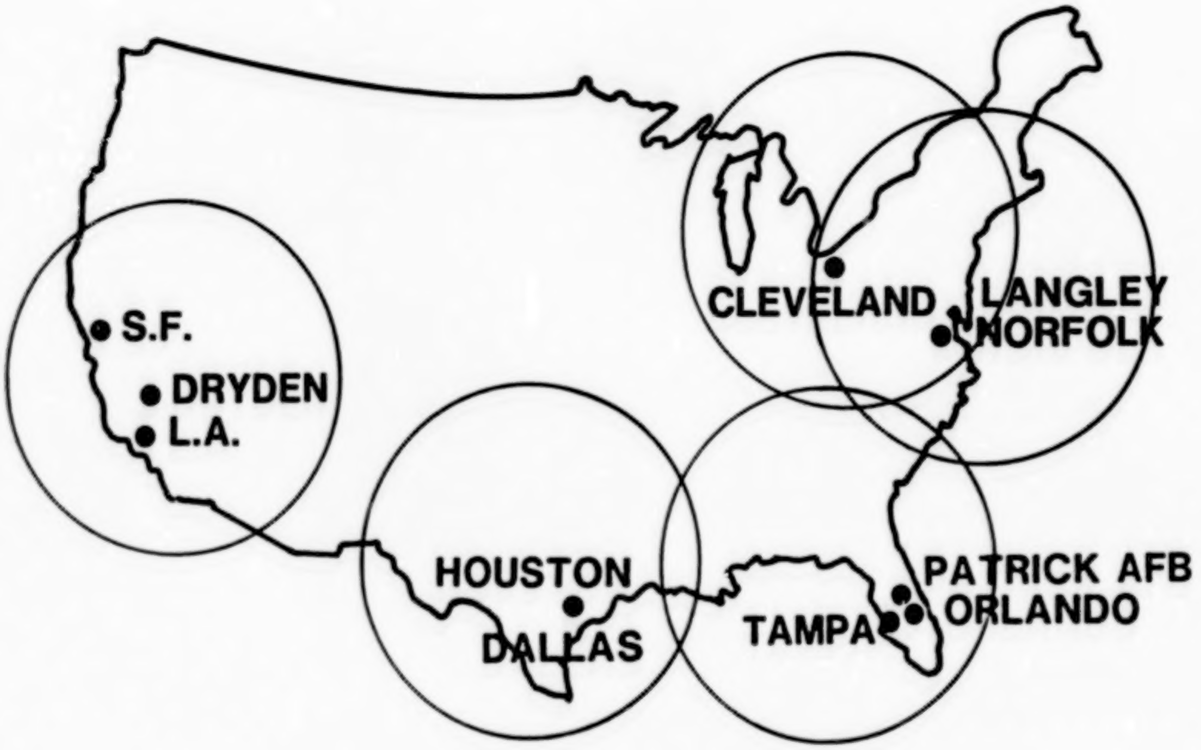

TACT NLF GLOVE AND TEST RESULTS

Recent NASA research is encouraging with regard to the prospects of obtaining significant amounts of laminar flow on small commercial transports with natural laminar flow (NLF) or a hybrid of natural laminar flow and laminar flow control (LFC). In 1980, the TACT (F-111) aircraft at the NASA Ames/Dryden Flight Research Facility was flown with a full chord, partial span glove designed to achieve natural laminar flow. The glove employed a supercritical NLF airfoil. In these flight tests (ref. 5), extensive laminar flow was observed at moderate wing sweeps suggesting that NLF could be a design option provided wing sweep is not excessive. The sweep limitation of natural laminar flow might be overcome by a hybrid laminar flow control (HLFC) concept, which shows attractive gains from combining LFC suction in the leading-edge region with NLF over the wing box. The suction in the leading-edge box controls the strong crossflow disturbances that occur initially on swept wings; over the wing box the pressure distribution is tailored to provide favorable gradients to stabilize the two-dimensional disturbances.

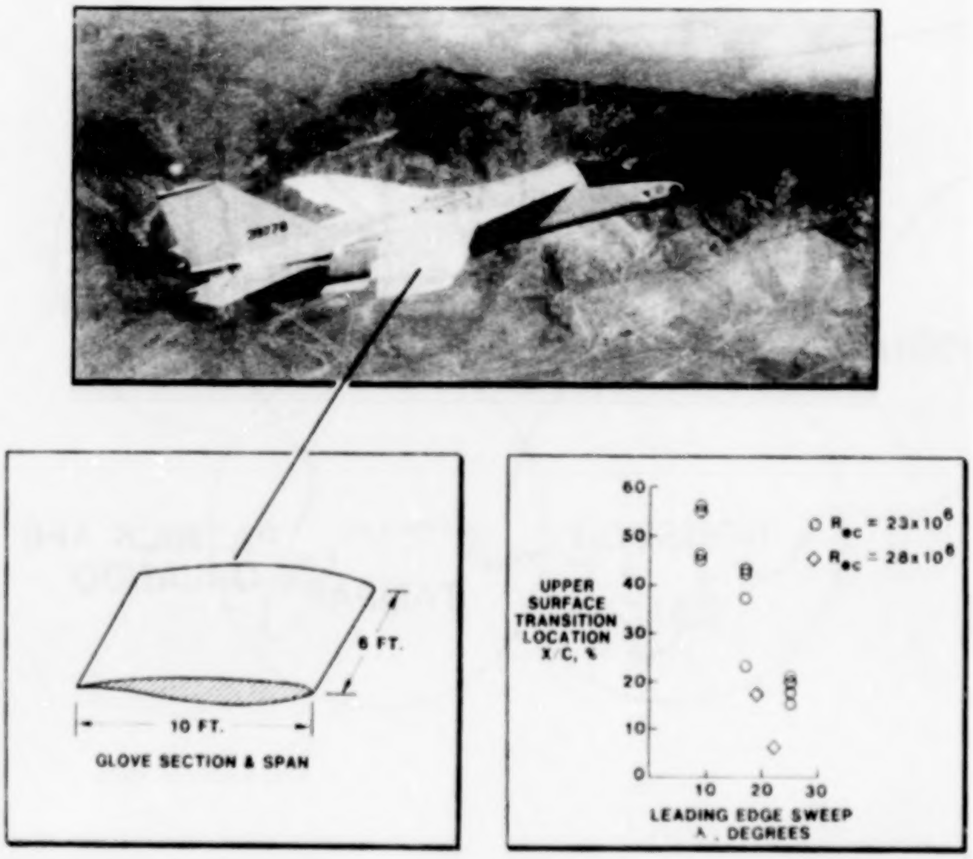

ORIGINAL PAGE IS
OF POOR QUALITY

VARIABLE SWEEP TRANSITION FLIGHT EXPERIMENT

At present, transition data applicable to swept wings with NLF or HLFC pressure distributions are limited and are needed in order to make valid assessments of the potential of NLF or HLFC wings for transports of various sizes and speeds. A flight program has been initiated to provide a transition data base for such wing designs. An F-14 aircraft with variable wing sweep capability will be modified with three full-span gloves to produce a range of upper surface wing pressure distributions. The gloves will be constructed of foam and fiberglass with no provisions for suction and scabbed onto the existing wing surface. The gloves will extend from below the attachment line over the upper surface to the spoiler hinge line (about 60% chord). The first glove will be a simple surface cleanup of the basic wing which has a strong favorable pressure gradient over the wing box. The other two gloves have design Mach numbers of 0.7 and 0.8 and were designed by the Langley Research Center and under contract to the Boeing Company respectively. These gloves have more moderate pressure gradients in the wing box area (ref. 6).

OBJECTIVE

ESTABLISH BOUNDARY LAYER TRANSITION DATA BASE FOR LAMINAR FLOW WING DESIGN

F-14

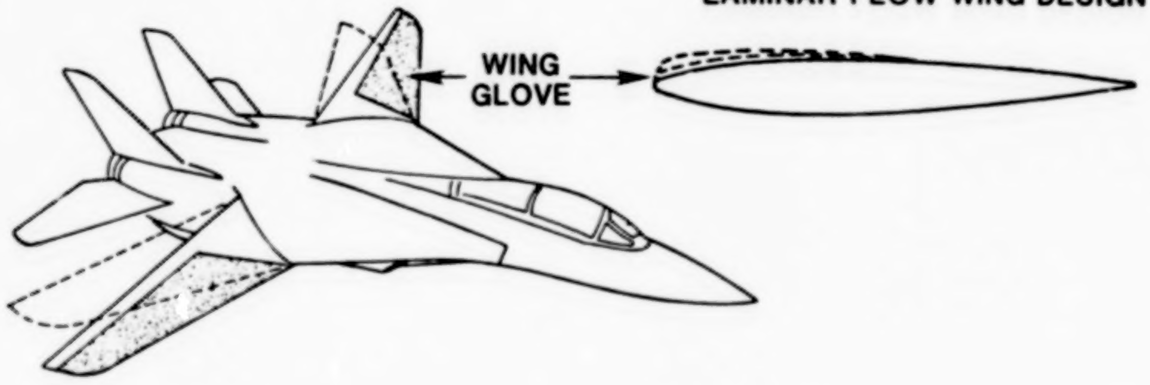

$M_\infty \sim$ 0.7 TO 0.85

SWEEP $\sim$ 15° TO 35°

$R_{\infty c_{max}} \sim 30 \times 10^6$

APPROACH

- USE VARIABLE SWEEP AIRCRAFT
- GLOVE UPPER WING SURFACE FROM ROOT TO TIP
- FLIGHT TEST THREE GLOVES
  - WING CLEAN-UP
  - M = 0.7 DESIGN
  - M = 0.8 DESIGN

VARIABLE SWEEP TRANSITION FLIGHT EXPERIMENT

Current plans are to begin flight testing of the clean-up glove in the fall of 1985. Wind tunnel test verification of the other two glove designs will be made in Langley's NTF Tunnel about the same time. Approximately a year later, these gloves will be installed on the aircraft (the M = 0.7 glove on one wing and the M = 0.8 glove on the other wing) and flight tested.

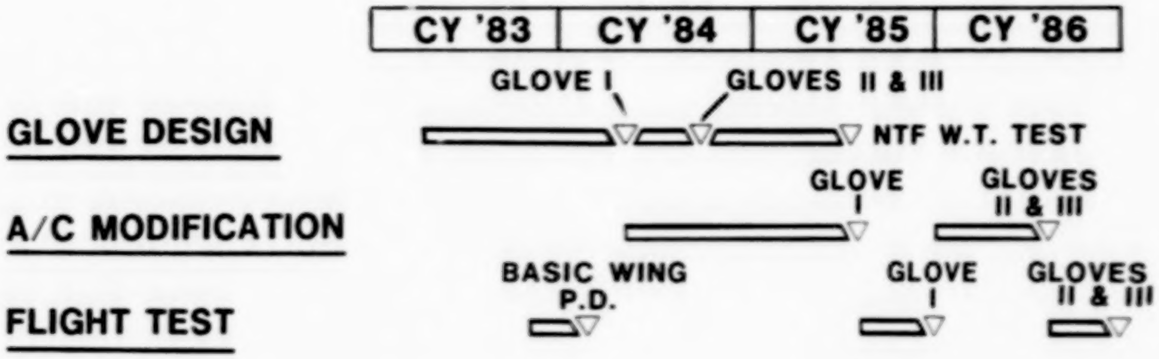

GLOVE I	**WING CLEAN-UP**
GLOVE II	**M = 0.7 DESIGN**
GLOVE III	**M = 0.8 DESIGN**

VARIABLE SWEEP TRANSITION FLIGHT EXPERIMENT
MACH NUMBER EFFECT ON BASIC WING Cp(X/c)

Pressure distributions on the basic F-14 wing are shown for two Mach numbers. The basic wing section is a modified NASA 6 series airfoil. The pressure minimum occurs at 25% and 55% chord for M = 0.7 and 0.8, respectively.

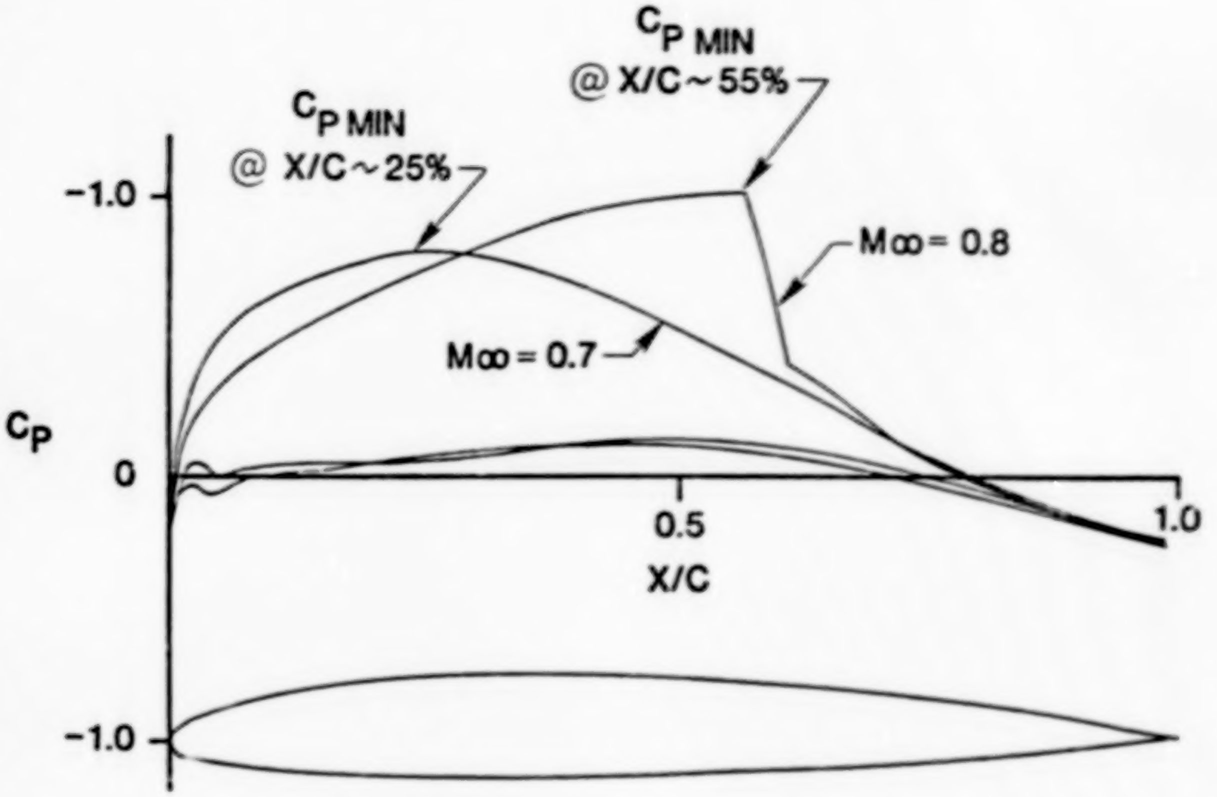

ORIGINAL PAGE IS
OF POOR QUALITY

F-14 CLEAN-UP GLOVE FABRICATION

This photograph shows the F-14 wing in a support fixture with the clean-up glove installed. The glove has a constant thickness of 0.65 inch from x/c = 0.05 on the lower surface, around the leading-edge, to x/c = 0.60 on the upper surface. The glove consists of a layer of fiberglass at the wing surface, 0.5 inches of foam, and six layers of fiberglass with a sailplane surface finish produced by body filler and paint.

F-14 CLEAN UP GLOVE FABRICATION

VARIABLE SWEEP TRANSITION FLIGHT EXPERIMENT
GLOVE AERODYNAMIC ANALYSES

The design pressure distribution at twenty degrees of sweep for the M = 0.7 and 0.8 designs are shown in this figure. Over the wing box the pressure gradient for the two gloves is approximately $dC_p/d(x/c) = -0.75$, somewhat less than the basic wing.

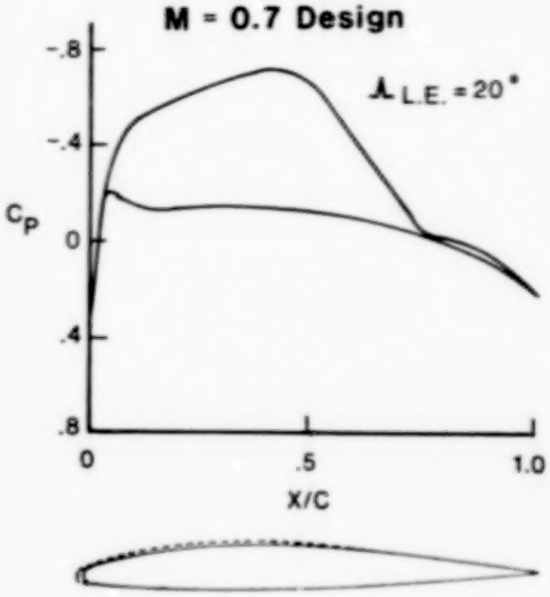

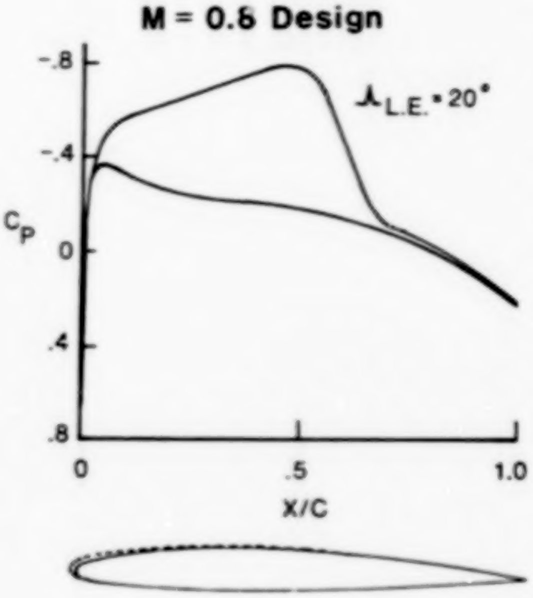

BOUNDARY LAYER STABILITY ANALYSIS

Boeing's analysis of the boundary layer stability for the M = 0.8 glove at Re = 26 x 10 is shown for three wing sweeps. At each sweep the flight Mach number will be chosen to produce the normal Mach number component of M = 0.77. M = 0.77 corresponds to M = 0.8 at 20° leading-edge sweep. Results are shown in terms of the N factor growth of crossflow and Tollmien-Schlichting disturbances. Results of a basic F-14 wing analysis are also shown for one condition. The shaded area is a transition correlation performed by Boeing from the analysis of the limited TACT NLF glove data (ref. 7). The basic wing boundary layer transition should be crossflow dominated over the range of flight conditions. With the variable sweep capability, however, the M = 0.8 design should provide a wide range of interactions between crossflow and Tollmien-Schlichting disturbances.

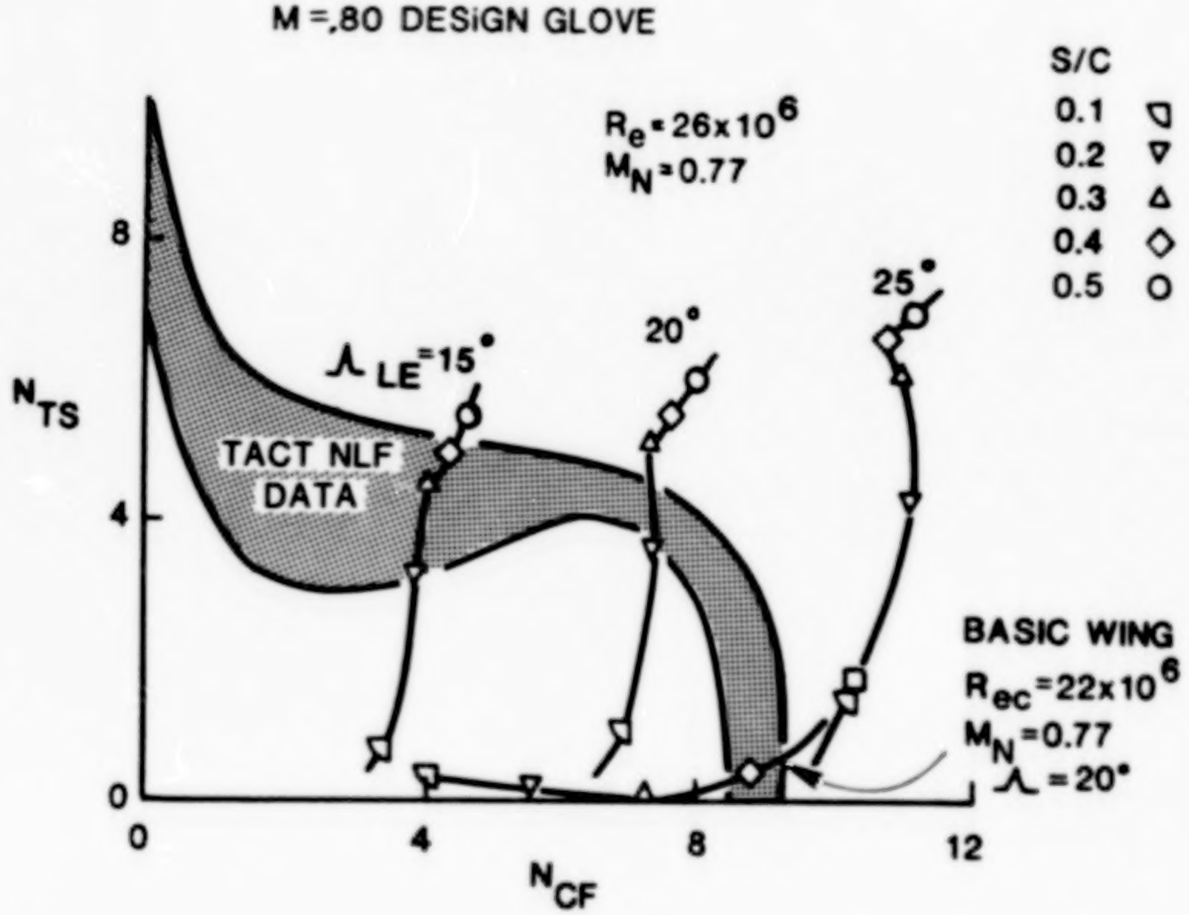

757 WING NOISE SURVEY AND NLF GLOVE FLIGHT TEST

The acoustic pressure field impinging on the surface of a wing with natural or controlled laminar boundary layers can cause transition to turbulent flow if the fluctuating acoustic pressures are of sufficient amplitude and in an unstable frequency range for the laminar boundary layer. Very little acoustic environment data measured on the wing of an aircraft are available. The available data show that the sound pressure levels on the surface of a wing with wing-mounted engines are significantly higher than those on the wing of an aircraft with engines installed on the aft fuselage. However, this does not necessarily preclude the application of laminar flow techniques to configurations with wing-mounted engines. To avoid possible design limitations, NASA has contracted with the Boeing Company to perform a flight test program using the Boeing 757 research aircraft with wing-mounted high-bypass ratio engines to obtain accurate and comprehensive acoustic environment data on the wing surfaces. As part of this effort, a section of the wing will be modified with a natural laminar flow glove to allow direct measurement of the effect of varying engine power setting on the extent of laminar flow.

The objectives of the 757 wing noise survey and the NLF glove flight test are to: (1) measure the engine-generated acoustic environment on the surfaces of a wing of a 757 with a PW 2037 high-bypass ratio engine, and (2) directly measure the effect of engine noise on the extent of natural laminar flow on a portion of the wing near the engine.

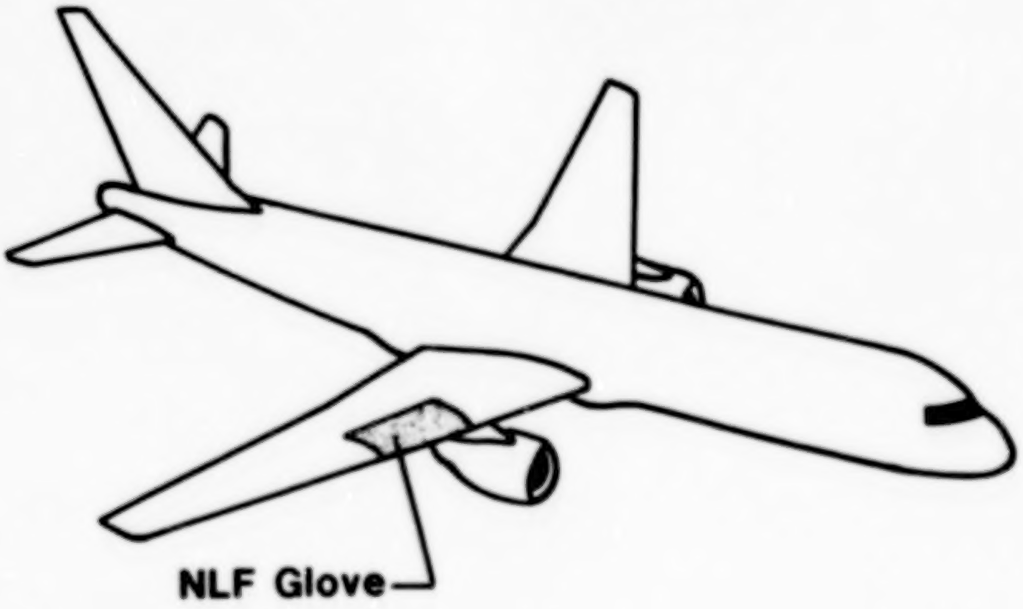

OBJECTIVES:

- **Measure acoustic environment on wing surface**
- **Measure effect of engine noise on extent of NLF**

757 WING NOISE SURVEY AND NLF GLOVE FLIGHT TEST

The NLF glove will be installed on the 757-200 left wing immediately outboard of the number one engine. The slat outboard of this engine will be removed and replaced with a glove which will consist of a dense rigid foam block with a structural supporting beam and ribs, covered with a smooth fiberglass surface. The leading-edge sweep of the glove will be 21 degrees. The glove will be instrumented with surface pressure orifices, hot films for transition detection, and flush microphones. Microphones on the remainder of the wing will be used to survey the wing acoustic environment. Both the upper and lower surface of the wing and glove will be instrumented.

The desired glove pressure distribution near its mid-span location is shown in the figure. An estimated 3-5 feet of chordwise extent of laminar flow will occur in the absence of engine noise. The effect of engine noise on the extent of laminar flow will be determined by varying the engine power setting at given flight conditions.

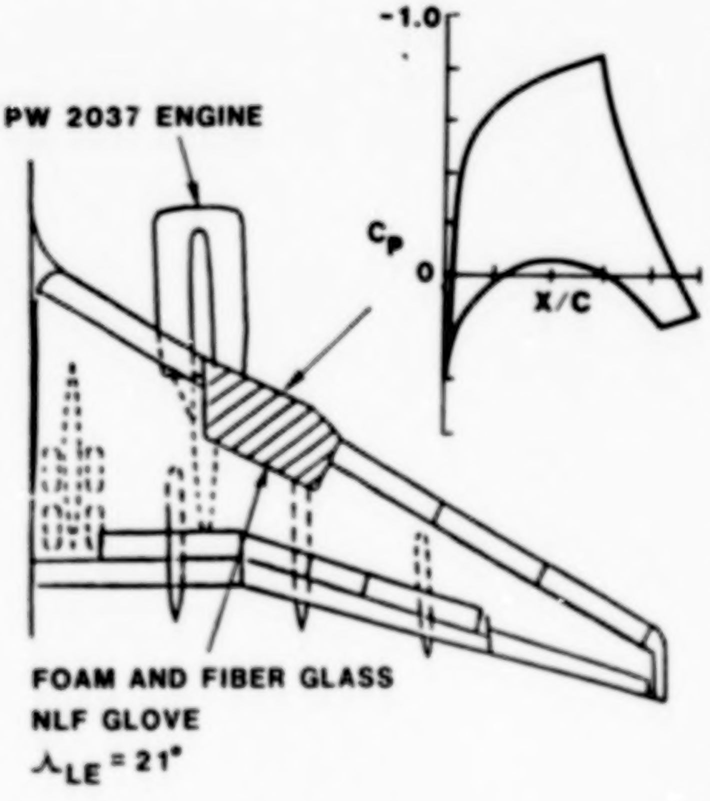

CONTRACTOR

BOEING COMMERCIAL AIRPLANE COMPANY

FLIGHT CONDITIONS

- $0.6 \leq M_\infty \leq 0.84$
- 30K ft. ≤ ALT. ≤ 41K ft.
- 3 TO 5 FT. OF LAMINAR FLOW

MEASUREMENTS

NLF GLOVE:

- SURFACE STATIC PRESSURES
- SURFACE HOT FILMS
- FLUSH MICROPHONES

WING SURFACE:

- FLUSH MICROPHONES
- AERODYNAMIC MICROPHONES

757 WING NOISE SURVEY AND NLF GLOVE FLIGHT TEST SCHEDULE

Contract go-ahead was in November 1984. Parts manufacture will be completed in April, at which time the aircraft will be laid up for modifications. The flight test occurred in June 1985 and we expect a final data report to be issued in 1985.

REFERENCES

1. Wagner, R. D., and Fischer, M. C.: Developments in the NASA Transport Aircraft Laminar Flow Program. AIAA Paper No. 83-0090, Jan. 1983.

2. Etchberger, F. R.: LFC Leading Edge Glove Flight - Aircraft Modification Design, Test Articles Development, and Systems Integration. NASA CR 172136, Nov. 1983.

3. Douglas Aircraft Company: Laminar Flow Control Leading Edge Glove Flight Test Article Development. NASA CR 172137, Nov. 1984.

4. Gaster, M.: A Simple Device for Preventing Turbulent Contamination on Swept Leading Edges. Journal of the Royal Aeronautical Society, Vol. 69, p. 788, 1965.

5. Montoya, L. C.; Steers, L. L.; Christopher, D; and Trujillo, B.: F-111 TACT Natural Laminar Flow Glove Flight Results. NASA Conference Publication 2208, Sept. 1981.

6. Boeing Commercial Airplane Company: Variable Sweep Transition Flight Experiment - Parametric Pressure Distribution Boundary Layer Stability and Wing Glove Design Task. NASA CR 177951, 1985.

7. Boeing Commercial Airplane Company: F-111 Natural Laminar Flow Glove Flight Test Data Analysis and Boundary Layer Stability Analysis. NASA CR 166051, Jan. 1984.

D-27

N88-14953

527-34
117251
19P.

ROUGHNESS AND WAVINESS REQUIREMENTS FOR LAMINAR FLOW SURFACES

Clifford J. Obara
PRC Kentron Incorporated
Hampton, VA

Bruce J. Holmes
NASA Langley Research Center
Hampton, VA

[redacted]

INTRODUCTION

Many modern metal and composite airframe manufacturing techniques can provide surface smoothness which is compatible with natural laminar flow (NLF) requirements. Specifically, this has been shown in flight investigations over a range of free-stream conditions including Mach numbers up to 0.7, chord Reynolds numbers up to about 30 million, and transition Reynolds numbers up to about 14 million. The recent flight experiments were conducted on flush-riveted thin aluminum skins, integrally stiffened milled thick aluminum skins, bonded thin aluminum skins, and composite surfaces. The most important conclusion concerning manufacturing to be drawn from these experiences is that the *waviness* of the surfaces in the tests met the NLF criterion for the free-stream conditions flown. However, in addition to waviness, an equally important consideration is *manufacturing roughness* of the surface in the form of steps and gaps perpendicular to the free stream. While much work has been done in the past, many unknowns still exist concerning the influences of wing sweep, compressibility, and shapes of steps or gaps on manufacturing tolerances for laminar flow surfaces. Even less information is available concerning NLF requirements related to practical three-dimensional roughness elements such as flush screw head slots and incorrectly installed flush rivets.

The principal challenge to the design and manufacture of laminar flow surfaces today appears to be in the installation of leading-edge panels on wing, nacelle, and empennage surfaces. Another similar challenge is in the installation of access panels, doors, windows, and the like on fuselage noses and engine nacelles where laminar flow may be desired. These surface discontinuities appear to be unavoidable for typical current aircraft; the challenge is, "Can laminar flow be maintained over these discontinuities?"

NLF APPLICATIONS

Applications of NLF can include all surfaces of an aircraft. Favorable pressure gradients can be designed onto fuselages, horizontal and vertical tails and nacelles as well as the wings. For a high performance business jet, the potential drag reduction with NLF ranges between about 12 percent (for NLF on the wing only) to about 24 percent (for NLF on the wing, fuselage, empennage, and engine nacelles). These values of drag reduction are calculated as a percent of total airframe drag at a cruise Mach number of 0.7. Individual component benefits are tabulated below:

Component	% of Body Length NLF	% of Drag Reduction
Wing	50	12
Horizontal tail	30	2
Vertical tail	30	1
Fuselage	30	7
Nacelles	30	2
TOTAL:		24

These benefits can amount to large savings in fuel cost as well as increased performance. These drag reductions are calculated for NLF added to an existing configuration; larger benefits would accrue for integrated design calculations.

DRAG REDUCTION AS PERCENT OF TOTAL
EXTENT OF NLF

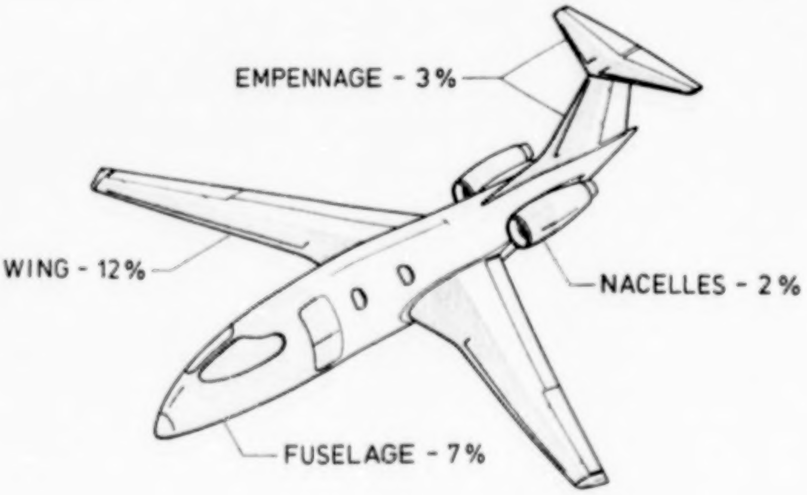

TOTAL NLF DRAG BENEFIT - 24%

NLF MANUFACTURING TOLERANCES

Existing criteria for NLF surfaces deal with waviness and with both two- and three-dimensional roughnesses. Each of these types of surface imperfections can cause transition by different mechanisms in the boundary layer. The definition of critical height for waviness or roughness is related to the mechanism by which transition is affected. The mechanisms of most practical interest include laminar separation, amplification of Tollmien-Schlichting (T-S) waves, amplification of crossflow vorticity, and interactions between any of these mechanisms. In addition, free-stream turbulence and acoustic disturbances may interact with these mechanisms to influence critical waviness and roughness heights. Criteria exist only for critical waviness and roughness which cause either laminar separation or amplification of T-S waves. No criteria exist which fully address surface-imperfection-induced transition related to crossflow amplification on swept wings or interactions between the various transition mechanisms and free-stream disturbances.

The following definitions appear in the literature and are useful for the present discussion. Critical waviness height-to-length ratio (h/λ) and critical step height or gap width can be defined as those which produce transition forward of the location where it would occur in the absence of the surface imperfection. Experimentally, premature transition was identified in past work as the first appearance of turbulent spots downstream of either a waviness or roughness surface imperfection. This is the definition used by Fage (ref. 1) and Carmichael (ref. 2) to establish critical conditions for surface imperfections.

- WAVINESS
  - CHORDWISE
  - SPANWISE
- ROUGHNESS
  - TWO-DIMENSIONAL
  - THREE-DIMENSIONAL
- COUPLING EFFECTS
  - SWEEP
  - ACOUSTICS
  - COMPRESSIBILITY

EFFECTS OF 2-D SURFACE IMPERFECTIONS ON LAMINAR FLOW

For most common applications in two-dimensional flows, the previous definition physically relates to the viscous amplification of T-S waves, or to (Rayleigh's) inflectional instability growth over a laminar separation bubble. This figure illustrates possible effects of a given two-dimensional surface imperfection on transition. A subcritical condition exists when transition is unaffected by the disturbance (top of figure). The middle of the diagram illustrates the critical condition at which transition just begins to be affected by the disturbance. In the extreme, a surface imperfection could cause sufficiently rapid T-S wave amplification for transition to occur very near the wave itself, as illustrated at the bottom of the figure. Another limiting condition of practical interest is the occurrence of transition at the surface imperfection caused by the inflectional instability in the free shear layer over the laminar separation bubble formed there.

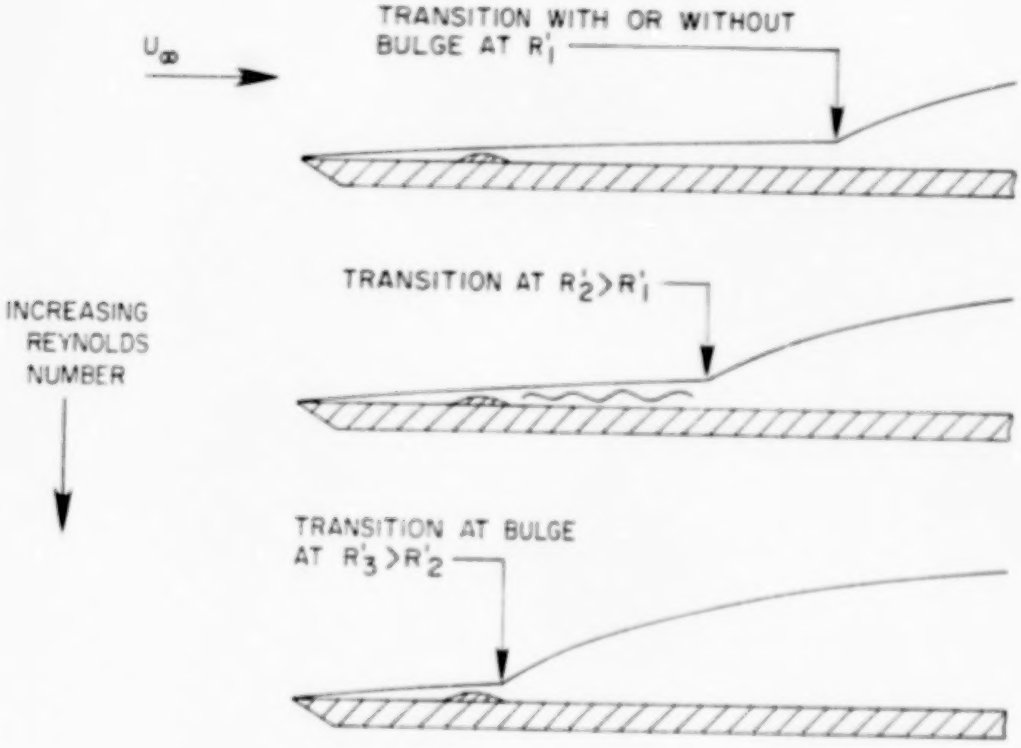
U_∞
TRANSITION WITH OR WITHOUT BULGE AT R'_1
INCREASING REYNOLDS NUMBER
TRANSITION AT $R'_2 > R'_1$
TRANSITION AT BULGE AT $R'_3 > R'_2$

PRESSURE DISTRIBUTION OVER A BULGE

From Schlichting (ref. 3), the laminar boundary layer will separate for $(\theta^2/\nu)\ (du_e/dx) < -0.1567$ where θ is the boundary layer momentum thickness, ν is the local kinematic viscosity, and u_e is the local potential flow velocity. Calculation of values of $(\theta^2/\nu)\ (du_e/dx)$ for both Fage's (ref. 1) and Carmichael's (ref. 4) surface imperfections indicate that the critical value for laminar separation was exceeded at most of the test conditions for those studies. For example, at the conditions shown in the figure (from Fage), $(\theta^2/\nu)\ (du^e/dx) = -0.19$. Similar results occur for analysis of Carmichael's data (ref. 4). Apparently, for many of the critical surface imperfections tested by Fage and Carmichael, laminar separation at the imperfection was present. Thus, the mechanism for forward movement of transition due to a surface imperfection could involve both the effect of local adverse pressure gradient on T-S amplification and the effect of Rayleigh's inflectional instability.

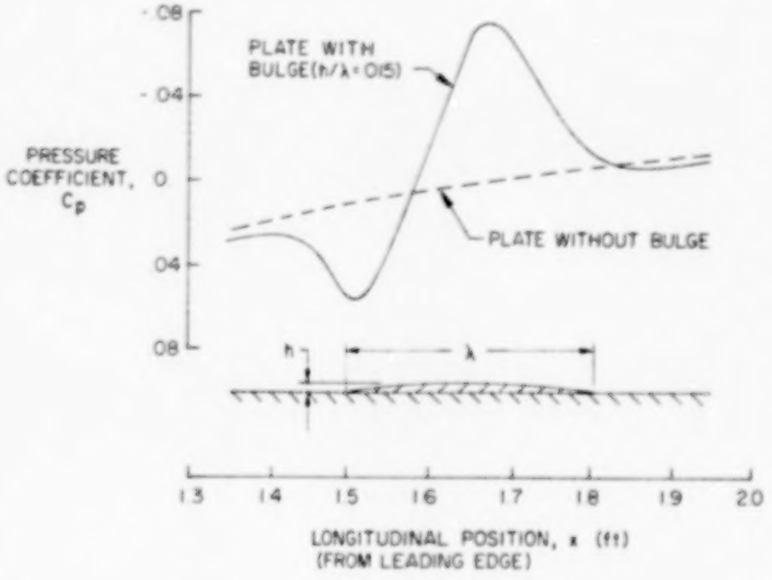

TOLLMIEN-SCHLICHTING INSTABILITY GROWTH IN THE PRESENCE OF A WAVE

Using flight data from Obara and Holmes (ref. 5), this figure illustrates the predicted local increase in growth rate of T-S instability caused by a surface wave. The surface wave tested was 0.010 in. high and had a wave length of 2.5 in. The effects of this wave on the pressure distribution between 10 and 13 percent chord and on maximum T-S amplitude ratios are apparent in the figure. In the adverse pressure gradient of the wave, the logarithmic exponent of T-S wave growth is seen to grow from about 1 to near 4. Elsewhere, in favorable pressure gradients, the rate of growth of the T-S disturbance is damped. For the surface wave and flight conditions tested, the growth rate of T-S instability was not large enough to cause premature transition. The measured location of boundary layer transition was at 40 percent chord which corresponded to the predicted location of laminar separation.

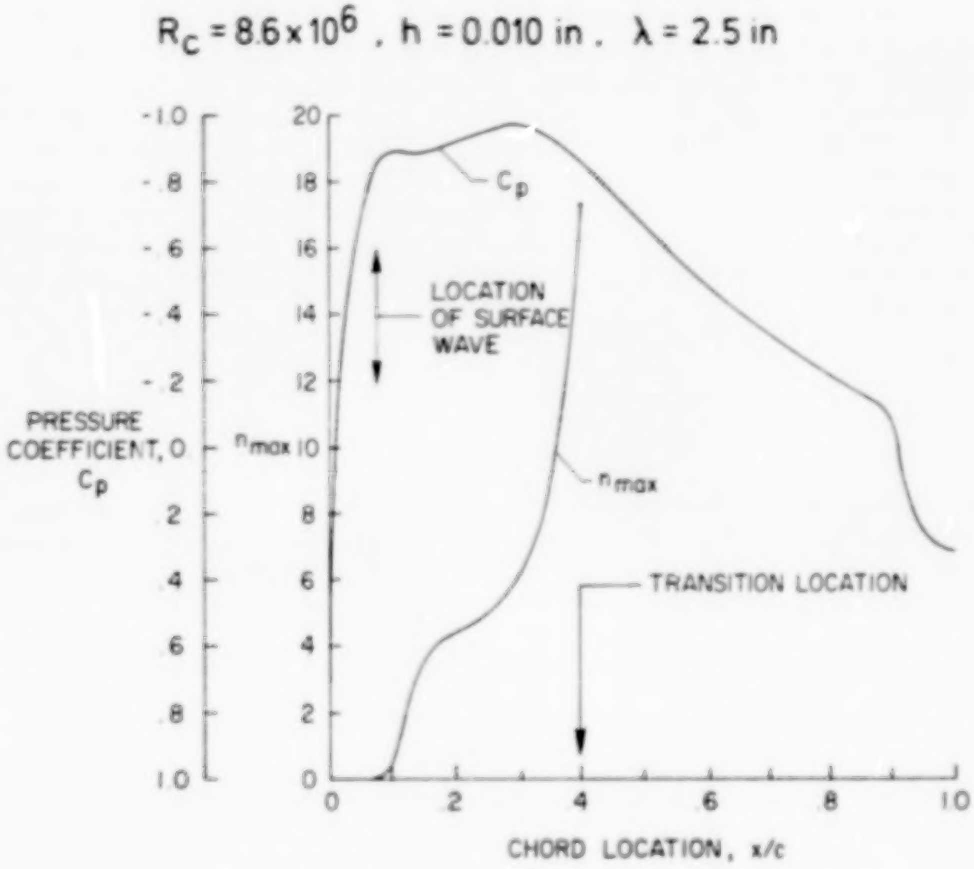

WAVINESS CRITERION (CARMICHAEL)

The research of Carmichael (ref. 2) provided the basis for the existing criterion on allowable waviness for both swept and unswept wing surfaces. Carmichael's investigations at least partially included the influences of compressibility, boundary layer stabilization by suction and pressure gradient, multiple waves, and wing sweep. Compressibility favorably increases the damping of growth rates for T-S waves. A second, unfavorable effect results from the increased pressure peak amplitude over a wave due to compressibility. It is not clear which effect dominates. With wing sweep, Carmichael and Pfenninger (ref. 6) observed a slight reduction in allowable waviness. Furthermore, a slightly greater reduction in allowable wave height to wave length ratio (h/λ) was observed for multiple waves on a swept wing than for multiple waves on an unswept wing. This might be expected to result from the interaction between the T-S instability growth in the deceleration on the backside of the wave and the crossflow instability growth due to the spanwise pressure gradient. Carmichael (ref. 2) defined a critical wave as the minimum (h/λ) which prevents the attainment of laminar flow to the trailing edge under boundary layer stabilization using moderate suction. On a non-suction wing, the criterion applies for waves in regions of boundary layer stabilization using a favorable pressure gradient (flow acceleration). The criterion was based on experimental results for waves located more than 25-percent chord downstream of the leading edge. Thus for waves located in very highly accelerated flows closer to the leading edge, the criterion may under-predict allowable waviness. Conversely, the criterion would over-predict the allowable waviness in a region of unaccelerated flow. Carmichael's waviness criterion is given as:

$$\frac{h}{\lambda} = {\frac{59000\ c\ \cos^2 \Lambda}{\lambda R_c^{1.5}}}^{0.5}$$

where h is the double-amplitude wave height in inches, λ is the wavelength in in., c is the streamwise wing chord in in., Λ is the wing leading-edge sweep and R_c is the chord Reynolds number based on chord length and airspeed in the free-stream direction.

ON MODERN SUBSONIC WINGS WITH
SMALL SWEEP, FAVORABLE PRESSURE
GRADIENTS, USE CARMICHAEL'S (X-21)
CRITERION FOR SINGLE WAVES

$$\frac{h}{\lambda} = \left(\frac{59{,}000 \cdot c \cdot \cos^2 \Lambda}{\lambda \cdot R_c^{\,3/2}} \right)^{1/2}$$

WAVINESS CRITERION (FAGE)

The classical research by Fage (ref. 1) provided criteria for critical height of 2-D bulges, ridges and hollows in incompressible 2-D boundary layers. His shapes do not accurately represent many of the surface imperfections observed on modern airframe surfaces. However, the pressure disturbances over Fage's bulges and hollows do simulate those which will occur over sinusoidal waves. In spite of these limitations, Fage's experiments did provide an understanding of some of the mechanisms associated with transition over these imperfections. Fage's criterion is given by:

$$\frac{h'}{\lambda} = 9 \times 10^6 \; {\frac{u_e s_t}{\nu}}^{-3/2} \; {\frac{s_t}{\lambda}}^{1/2}$$

where h' is the height of a bulge in ft above the nominal surface, λ is the length of the bulge in ft, s_t is the surface length to transition in ft, u_e is the boundary layer edge velocity in ft/sec at the location of the center of the bulge for the undistorted surface, and ν is the kinematic viscosity. Using local C_p and free-stream velocity, u_e can be determined directly for use in the equation. Fage's work covered a range of transition Reynolds numbers from 1×10^6 to 3.5×10^6, and did not include any effects of compressibility or sweep.

ON FLAT PLATES WITH
NO SWEEP, ZERO PRESSURE GRADIENT
AND INCOMPRESSIBLE FLOW
USE FAGE'S CRITERION

$$\frac{h}{\lambda} = 9 \times 10^6 \cdot \left(\frac{u_e \cdot s_t}{\nu}\right)^{-3/2} \cdot \left(\frac{s_t}{\lambda}\right)^{1/2}$$

NLF WAVINESS TOLERANCES FOR A HIGH-PERFORMANCE BUSINESS AIRPLANE

This figure presents examples of allowable waviness for free-stream conditions representative of a high-performance business airplane flying at Mach 0.7 at 41,000 ft. The chart shows allowable waviness using both Fage's (ref. 1) and Carmichael's (ref. 2) equations. Using Carmichael's criterion, the effect of sweep on allowable waviness is seen to be on the order of 10 percent. These calculations show that with a wavelength of 6 in., the allowable wave height is 0.025 in. on a 25° swept wing, with a favorable pressure gradient. Such a manufacturing tolerance for waviness is within the capabilities of modern airframe manufacturing methods. Were this same 6-in. wave in a region of unaccelerated flow, the allowable height would be about 0.010 in. This calculation assumes it is reasonable to relate Carmichael's wave height (h) to Fage's wave height (h') by a factor of 2; that is, an allowable double amplitude wave height may be estimated using 2 x h' in Fage's equation for comparisons with h in Carmichael's equation. The dashed line for Fage's criterion in the figure is presented with the caution that it has never been verified for compressible flows. The figure shows the effect of an unaccelerated flow (Fage's criterion) on reducing the allowable waviness significantly compared to allowable waviness in an accelerated flow (Carmichael's criterion). This result illustrates the dominant effect of pressure gradient on waviness tolerances. The reason for this effect is explained by the dominant effect of pressure gradient on boundary velocity profiles and, hence, on T-S stability.

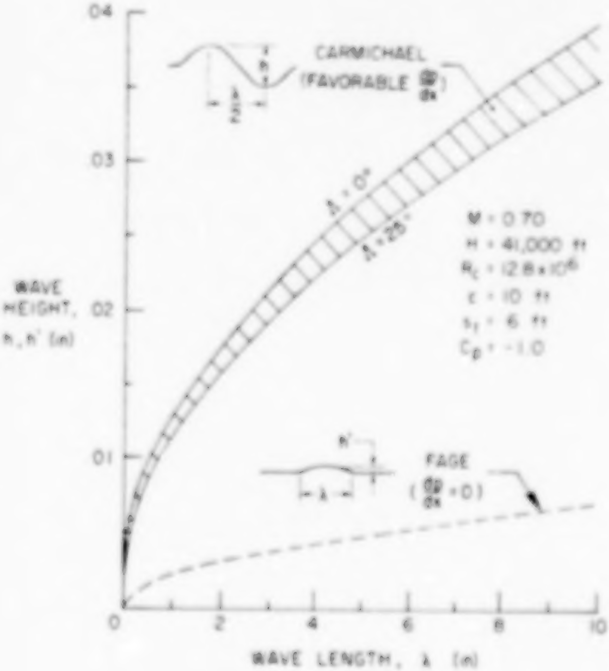

ORIGINAL PAGE IS
OF POOR QUALITY

CHARACTERISTICS OF LAMINAR SEPARATION OVER A STEP

A potentially misleading conclusion from Fage (ref. 1) was that shape did not affect the critical size of the surface imperfection. This conclusion resulted at least in part from the particular shapes tested by Fage. In the case of his ridges, each shape produced a laminar separation region at the front of the ridge and a second laminar separation at the aft facing step on the downstream edge of the ridge. Transition behind Fage's ridges could have been dominated by the inflectional instability growth over these two separated flow regions. For modern airframe surfaces, the simple forward-facing step, aft-facing step, or gap (perpendicular to the free stream) are of more practical interest. This figure shows the characteristics of laminar separation over such a step. Laminar separation bubbles form at the corner and at the top of the step. Depending on the step height Reynolds number, the boundary layer will reattach as turbulent or laminar behind the second separation bubble.

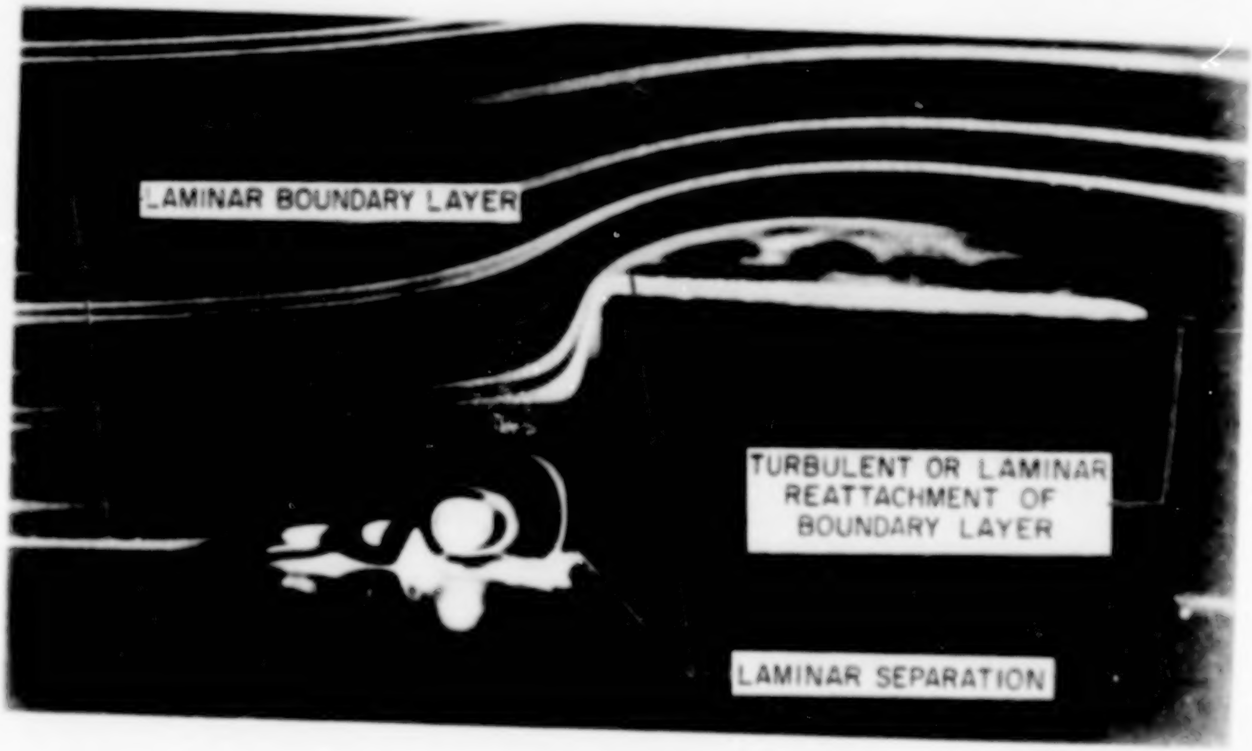

INFLUENCE OF SHAPED STEPS AND GAPS ON LAMINAR SEPARATION

The mechanism by which transition is affected by steps and/or gaps in a laminar surface involves both the viscous Tollmien-Schlichting (T-S) growth and the inflection (Rayleigh's) instability across the free shear layer over regions of laminar separation. Thus, the allowable height of a step or width of a gap will depend in part on the length of the region of laminar separation for a given Reynolds number.

The figure illustrates the significant influence of step and gap shapes on the presence and length of laminar separation regions associated with surface imperfections. The streamlines were calculated by M.D. Gunzburger, R. A. Nicolaides (Carnegie-Mellon, unpublished data), and C. H. Liu (NASA Langley, unpublished data) using a complete finite difference Navier-Stokes solution with a Blasius boundary layer input boundary condition. The streamlines illustrate the reduction in size of the laminar separation regions for the rounded or ramped steps in comparison to the orthogonal sharp steps. These differences in laminar separation explain the differences in flight-measured critical Reynolds numbers for the various shapes.

COMPLETE N-S SOLUTION AT $R_h = 600$
(GUNZBURGER, NICOLAIDES AND LIU)

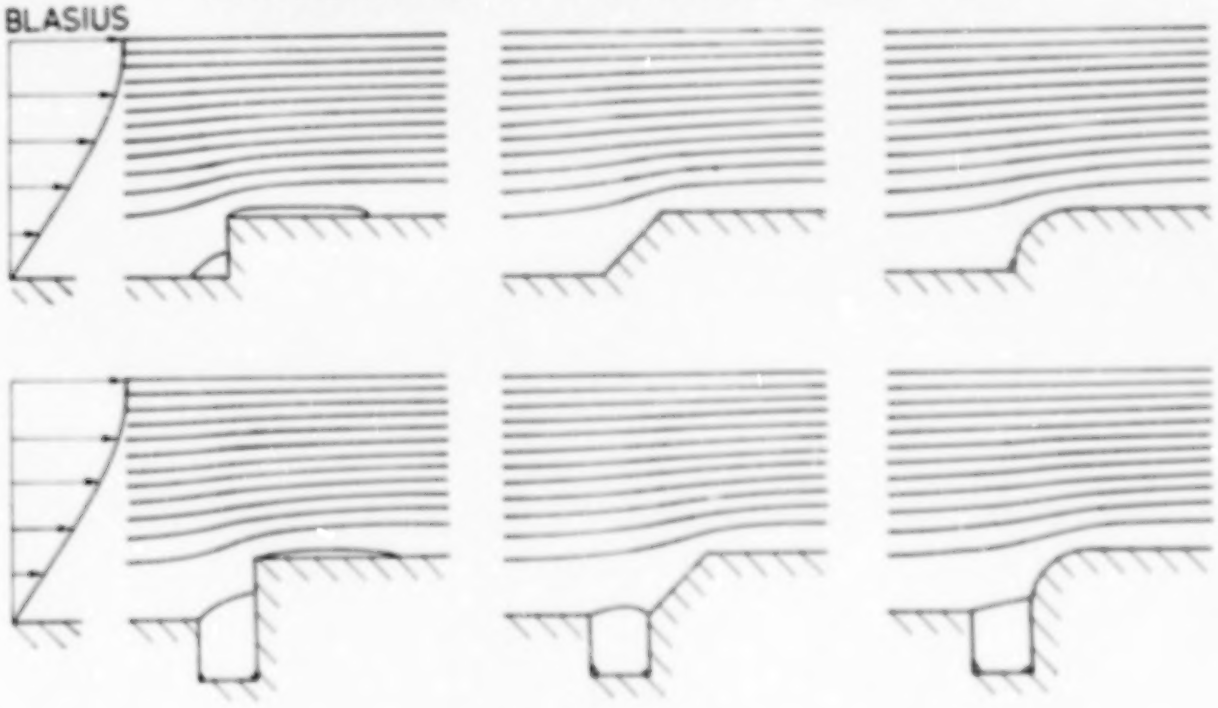

NLF SURFACE IMPERFECTION TOLERANCES

The past work on criteria for step and gap tolerances came from the X-21 experiments (ref. 7). The literature does not state what definition was used to determine critical Reynolds numbers for these surface imperfections. However, according to Dr. Werner Pfenninger (ESCON, Grafton, VA, and C. J. Obara, PRC Kentron, Hampton, VA, private communication) who conducted wind tunnel experiments to develop these criteria, the critical step height Reynolds number was established based on the conditions where the first turbulent spots occurred far downstream from the surface imperfection. Thus, these criteria were developed in a manner consistent with those for the waviness criteria. The critical Reynolds number $R_{h,crit} = (Uh/\nu)$, h is determined based on free-stream airspeed U_∞ and kinematic viscosity and on the height of the step or length of the gap (h). The shapes and critical Reynolds numbers for which tolerances were established in the X-21 experiments are illustrated in the figure. In addition, the figure presents information from recent NASA investigations (ref. 8) on the influence of rounded steps on critical Reynolds numbers. For three of the illustrated surface imperfection shapes (indicated by question marks), no criteria exists.

The NASA flight experiments on shaped steps were conducted on a NLF glove installed on a T-34C airplane. These experiments illustrate (in contrast to Fage's experiments) that shape of the surface imperfection influences the allowable height. The reason for the difference in Fage's conclusions and the recent experiments has to do with sensitivity of the laminar boundary layer to inflectional instability growth over a laminar separation region. In the case of the present experiments, the boundary layer was subjected to smaller regions of laminar separation than in Fage's experiments. This occurred because in the NASA experiments, the rounded shape of the step reduced the length of the region of laminar separation over the step, thus reducing the inflectional instability growth. Critical step heights may be larger for steps with shapes which reduce the length of the region of laminar separation.

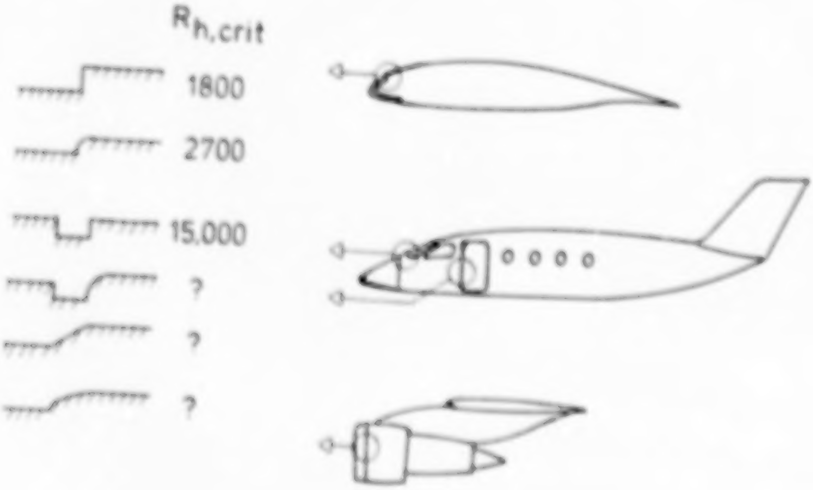

T-34C NLF GLOVE STEP SHAPE FLIGHT EXPERIMENT

This figure illustrates the NASA flight experiments on shaped steps. Previous flight transition experiments on the T-34C NLF glove are described by Obara and Holmes (ref. 5). The steps were located on the lower surface of the NLF glove at the 5-percent chord location. The pressure distribution over the region of the steps was slightly favorable as shown.

Determination of critical step height Reynolds number for the square and rounded steps was made by flying both step shapes of equal height on one flight using sublimating chemicals to detect transition. A flight condition was chosen to provide a step height Reynolds number which would significantly exceed the critical value of 1800 for a square forward-facing step. The condition flown resulted in an R_h of 2720, thus exceeding 1800 by more than 50 percent. At this condition, transition occurred at the square step as expected. For the round step, on the other hand, transition occurred far downstream from the step (about 2 ft downstream). These data establish a conservative value of $R_{h,crit}$ = 2700 for a rounded forward-facing step, close to the leading edge, on an unswept wing, with a radius approximately equal to the step height.

$R' = 1.95 \times 10^6 \text{ ft}^{-1}, c = 7.667$ ft

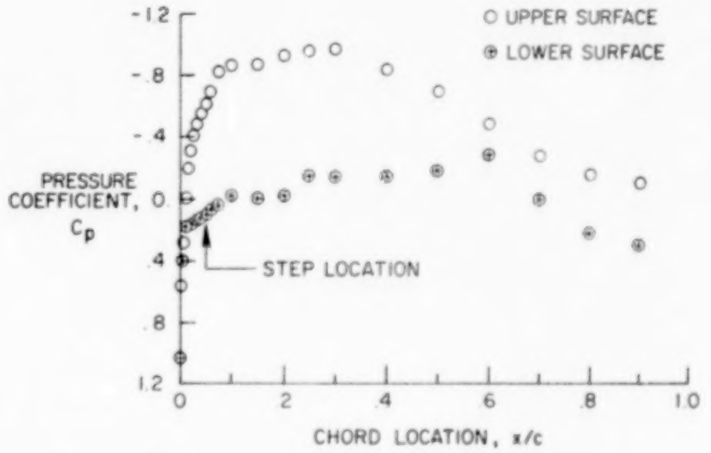

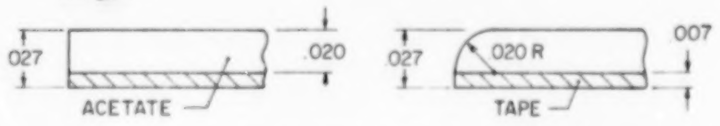

STEP SHAPES TESTED

T-34C NLF GLOVE FLIGHT EXPERIMENTS

Additional flight experiments were conducted to simulate both forward and aft-facing steps at several sweep angles. The sweep angle in this context is the angle between the ridge of the step and the free stream. Acetate sheets were attached to the upper surface of the T-34C glove. The purpose of these experiments was to develop a technique for installation of large thin films carrying flush instrumentation (e.g. hot-film transition sensors) on swept airplane wings for NLF flight experiments. These experiments were designed to crudely simulate the flow which a spanwise facing step would see on a swept wing. On an actual swept lifting surface, the presence of crossflow vorticity would very likely produce smaller critical step sizes. The shape of the steps was varied until the step no longer caused boundary layer transition. At a step height of 0.0215 in. and a sweep angle of 73°, both the forward-facing square step and the aft-facing ramp step caused transition. The figure shows the modified step shapes that did not cause boundary layer transition at step sweep angles (Λ) of 73° and 45°. The step height Reynolds numbers for these two steps were R_h = 4024 and 4110, for the forward ramp step and the aft ramp step, respectively. These values of R_h can be used as a guide to size allowable forward and aft facing steps with up to 45° of step sweep in a region of accelerated two-dimensional flow, with steps shaped as shown in the figure.

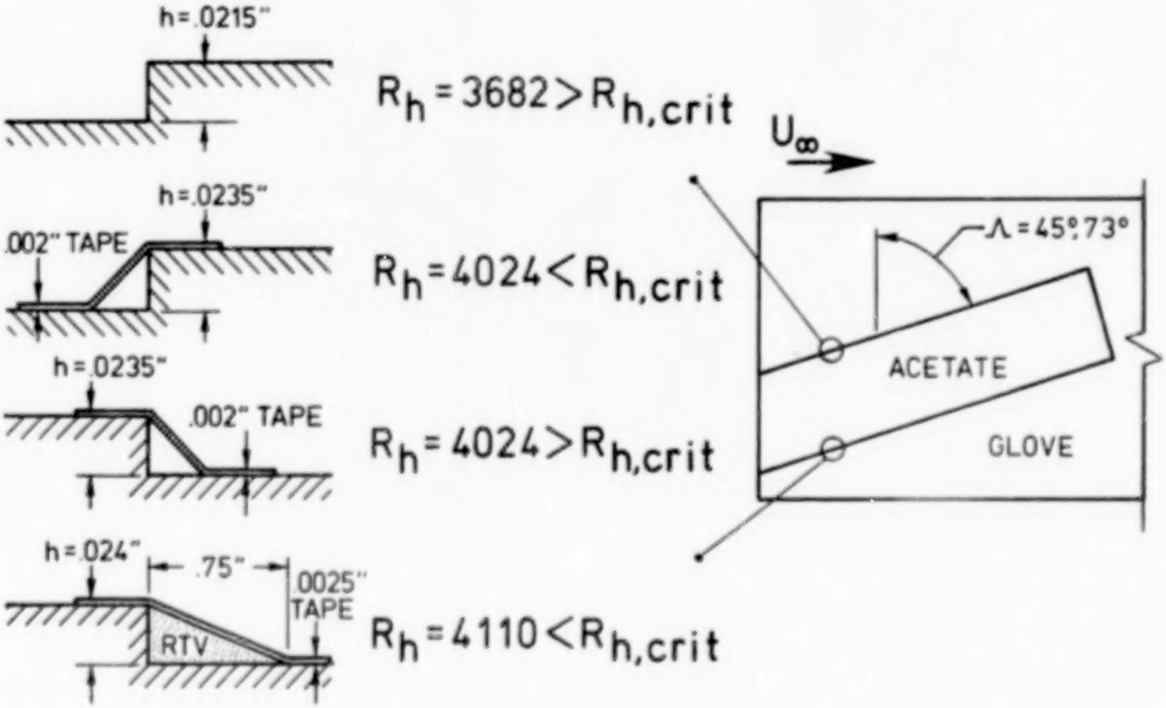

ALLOWABLE STEP HEIGHTS AND GAP WIDTHS FOR NLF AT M = 0.7

For one set of free-stream conditions representative of a high performance business airplane, this figure illustrates allowable step heights and gap widths for a range of cruise altitudes. The strong beneficial effect of higher altitudes on allowable step heights and gap widths is readily apparent. The increases in tolerances with increased altitude results directly from the decrease in unit Reynolds number. As the unit Reynolds number decreases, the length of the laminar separation regions associated with the steps decreases, reducing the growth of the inflectional instability and increasing the allowable step height.

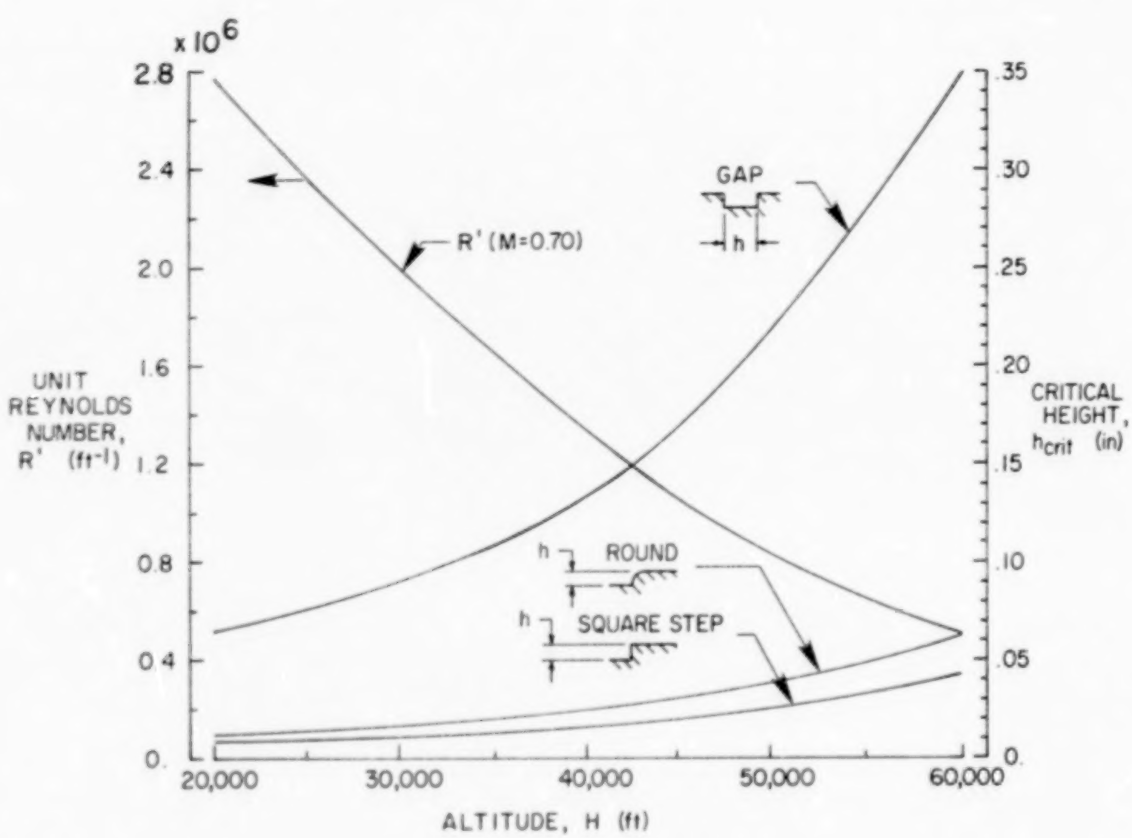

CONCLUSIONS

A review of past work on roughness and waviness manufacturing tolerances and comparisons with more recent experiments provided the following conclusions.

1. On modern airframe surfaces where large waves typically occur only at major structural joints, the assumption of multiple waves for use of Carmichael's waviness criterion (ref. 2) is too conservative. Based on recent flight experiences with modern airframes, it is recommended that Carmichael's criterion be used with the single wave assumption.

2. In contrast to Fage's (ref. 1) conclusion concerning the unimportance of the shape of a two dimensional step in a laminar boundary layer, it has been demonstrated experimentally that shape has a significant effect on critical Reynolds numbers. For a forward-facing rounded step, close to the leading edge, with a radius approximately equal to the step height, a conservative value for the critical step height Reynold's number of 2700 is indicated. This value is more than a 50-percent increase over the critical step height Reynolds number for a forward-facing square step.

3. For steps with up to 45° to 73° of sweep in two-dimensional flows, step height Reynolds numbers of 4000 and 4100 can be used as a guide to size foward- and aft-facing steps, respectively. These values apply to swept forward-facing ramp steps with rounded corners and to swept aft-facing ramp steps.

- USE SINGLE WAVE CRITERION

- SHAPED STEPS AND GAPS INCREASE 2-D ROUGHNESS TOLERANCES

REFERENCES

1. Fage, A.: The Smallest Size of Spanwise Surface Corrugation Which Affects Boundary Layer Transition on an Airfoil. Brit. A.R.C., England. R&M No. 2120, 1943.

2. Carmichael, B. H.: Surface Waviness Criteria for Swept and Unswept Laminar Suction Wings. Northrop Aircraft Inc., Beverly Hills, CA, Norair Rep. No. NOR-59-438 (BLC-123), 1959.

3. Schlichting, H.: Boundary Layer Theory. McGraw-Hill, 7th ed., 1979.

4. Carmichael, B. H.; Whites, R. C.; and Pfenninger, W.: Low-Drag Boundary Layer Suction Experiments in Flight on the Wing Glove of an F-94A Airplane. Northrop Aircraft Inc., Beverly Hills, CA, Rep. No. NAI-57-1163 (BLC-101), 1957.

5. Obara, Clifford J.; and Holmes, Bruce J.: Flight Measured Laminar Boundary-Layer Transition Phenomena Including Stability Theory Analysis. NASA TP 2417, 1985.

6. Carmichael, B. H..; and Pfenninger, W.: Surface Imperfection Experiments on a Swept Laminar Suction Wing. Northrop Aircraft, Inc., Beverly Hills, CA, Norair Rep. No. NOR-59-454 (BLC-124), 1959.

7. Anon: Final Report on Aircraft Design Data Laminar Flow Control Demonstration Program. NOR 67-136 (Contract AF 33(657)-13930), Northrop Aircraft Inc., Beverly Hills, CA, June 1967. (Available from NTIS as AD 819 317).

8. Holmes, B. J.; Obara, C. J.; Martin, G. L.; and Domack, C. S.: Manufacturing Tolerances For Natural Laminar Flow Airframe Surfaces. SAE Paper 850863, April 1985.

BIBLIOGRAPHY

1. Braslow, Albert L.; and Knox, Eugene C.: Simplified Method for Determination of Critical Height of Distributed Roughness Particles for Boundary Layer Transition at Mach Numbers From 0 to 5. NACA TN 4363, 1958.

2. Braslow, Albert L.; Hicks, Raymond M.; and Harris, Roy V., Jr.: Use of Grit-Type Boundary Layer Transition Trips on Wind Tunnel Models. NASA TN D-3579, 1966.

3. Bushnell, Dennis M.; and Tuttle, Marie H.: Survey and Bibliography on Attainment of Laminar Flow Control in Air Using Pressure Gradient and Suction. NASA RP 1035, vol. 1, 1979.

4. Carmichael, B. H.: Prediction of Critical Reynolds Number for Single Three Dimensional Roughness Elements. NAI-58-412 (BLC-109), Northrop Aircraft, Inc., Beverly Hills, CA, May 1958.

5. Carmichael, Bruce H.: Survey of Past Experience in Natural Laminar Flow and Experimental Program for Resilient Leading Edge. NASA CR 152276, 1979.

6. Gyorgyfalvy, D.: Effect of Pressurization of Airplane Fuselage Drag. J. of Aircraft, vol. 2, no. 6, 1965, pp. 531-537.

7. Holmes, Bruce J.; Obara, Clifford J.; and Yip, Long P.: Natural Laminar Flow Flight Experiments on Modern Airplane Surfaces. NASA TP 2256, 1984.

8. Hood, M. J.: The Effects of Some Common Surface Irregularities on Wing Drag. NACA TN 695, 1939.

9. Klebanoff, P. S.; Schubauer, G. B.; and Tidstrom, K. D.: Measurements of the Effect of Two Dimensional and Three Dimensional Roughness Elements on Boundary Layer Transition. J. of Aeron. Sci., Nov. 1955, pp. 803-804.

10. Lachman, G. V., ed: Boundary Layer and Flow Control, Its Principles and Applications. Pergamon Press, 1961.

11. Laine, S. K.: A Theoretical Study of the Effect of a Step in a Flat Plate Upon the Laminar Boundary Layer - Numerical Solutions of the Navier Stokes Equations. Doctor of Technology Thesis, Helisinki University of Technology, 1972.

12. Loftin, Larry K., Jr.: Effects of Specific Types of Surface Roughness on Boundary Layer Transition. NACA WR L-48 (ACR L5J29A), 1946.

13. Nash, J. F.; and Bradshaw, P.: The Magnification of Roughness Drag by Pressure Gradients. J. Royal Aeronautical Sci., vol. 71, pp. 44-49, 1967.

14. Nenni, J. P.; and Gluyas, G. L.: Aerodynamic Design and Analysis of an LFC Surface. Aeronautics and Astronautics, July 1966, pp. 52-57.

15. Pfenninger, W.: Summary of Laminar Boundary Layer Control Research. Wright Aeronautical WADC Development Center, Wright Patterson AFB, OH. Tech. Rep. No. 56-111, 1957.

16. Spence, D.A.; and Randall, D.G.: The Influence of Surface Waves on the Stability of a Laminar Boundary Layer With Uniform Suction. A.R.C., England. C.P. No. 161 (15.916), T.N. No. AERO 2241, 1953.

17. Stall, C. G.; and Pfenninger, W.: Present Status of Production Aircraft Surface Waviness at Norair. Northrop Aircraft, Inc., Beverly Hills, CA, Norair Rep. No. NOR-59-444 (BLC-126), 1959.

18. The Staffs of the S.M.E. and Aero. Departments, R.A.E.: The Design of Smooth Wings. Brit. A.R.C., England. R.A.E. Rep. S.M.E. 3236, Nov. 1942.

D28

N88-14954

INSECT CONTAMINATION PROTECTION FOR LAMINAR FLOW SURFACES

528-05

Cynthia C. Croom and Bruce J. Holmes
NASA Langley Research Center
Hampton, Virginia

117252
18P.

PRECEDING PAGE BLANK NOT FILMED

PAGE 538 INTENTIONALLY BLANK

[redacted]

INTRODUCTION

The ability of modern airplane surfaces to achieve laminar flow has been well-accepted in recent years. Obtaining the maximum benefit of laminar flow for aircraft drag reduction requires maintaining minimum leading-edge contamination. Previously proposed insect contamination prevention methods have proved impractical due to cost, weight, or inconvenience. Past work has shown that insects will not adhere to water-wetted surfaces, but large volumes of water required for protection rendered such a system impractical. This paper presents results of a flight experiment conducted by NASA to evaluate the performance of a porous leading-edge fluid discharge ice protection system operated as an insect contamination protection system. In addition, these flights explored the environmental and atmospheric conditions most suitable for insect accumulation.

SKYROCKET II NLF FLIGHT EXPERIMENTS

ORIGINAL PAGE IS
OF POOR QUALITY

The effect of insect contamination on natural laminar flow (NLF) wings by insect debris is an important consideration in NLF airfoil design as well as in the operation of airplanes with laminar flow wings. In practice, the seriousness of insect debris contamination will likely be dependent on airplane characteristics and mission. During flight tests on the Bellanca Skyrocket (ref. 1), a representative insect debris contamination pattern was accumulated by flying for 2.2 hrs at less than 500 ft above ground level at calibrated airspeed (V_c) equal to 178 knots. Chemical sublimation was used to distinguish between insect strikes that caused transition and those that did not.

NASA
BELLANCA
N14666

INSECT CONTAMINATION ON THE SKYROCKET II NLF WING

This figure depicts the heights and positions of the insects collected along the span of the right wing. Insects that caused transition are denoted as supercritical and those that did not are denoted as subcritical. The figure illustrates that only about 25 percent of the insects collected caused transition at sea level. Analysis shows that at a more typical cruise altitude of 25,000 ft where the boundary layer is thicker, caused by a lower unit Reynolds number, only about 9 percent of the insects would have caused transition. Thus, even though large numbers of insects might be collected on a wing leading edge, relatively few of them can be expected to cause transition at high cruise altitudes. The sample insect contamination data presented here serve to illustrate a certain inherent level of insensitivity of this particular combination of airfoil geometry and operating conditions to insect contamination. It is important to recognize that although sufficient insect contamination can seriously degrade airplane performance, the occurrence of serious contamination levels is infrequent for many combinations of place, time of day, time of year, airfoil geometry, and mission profile.

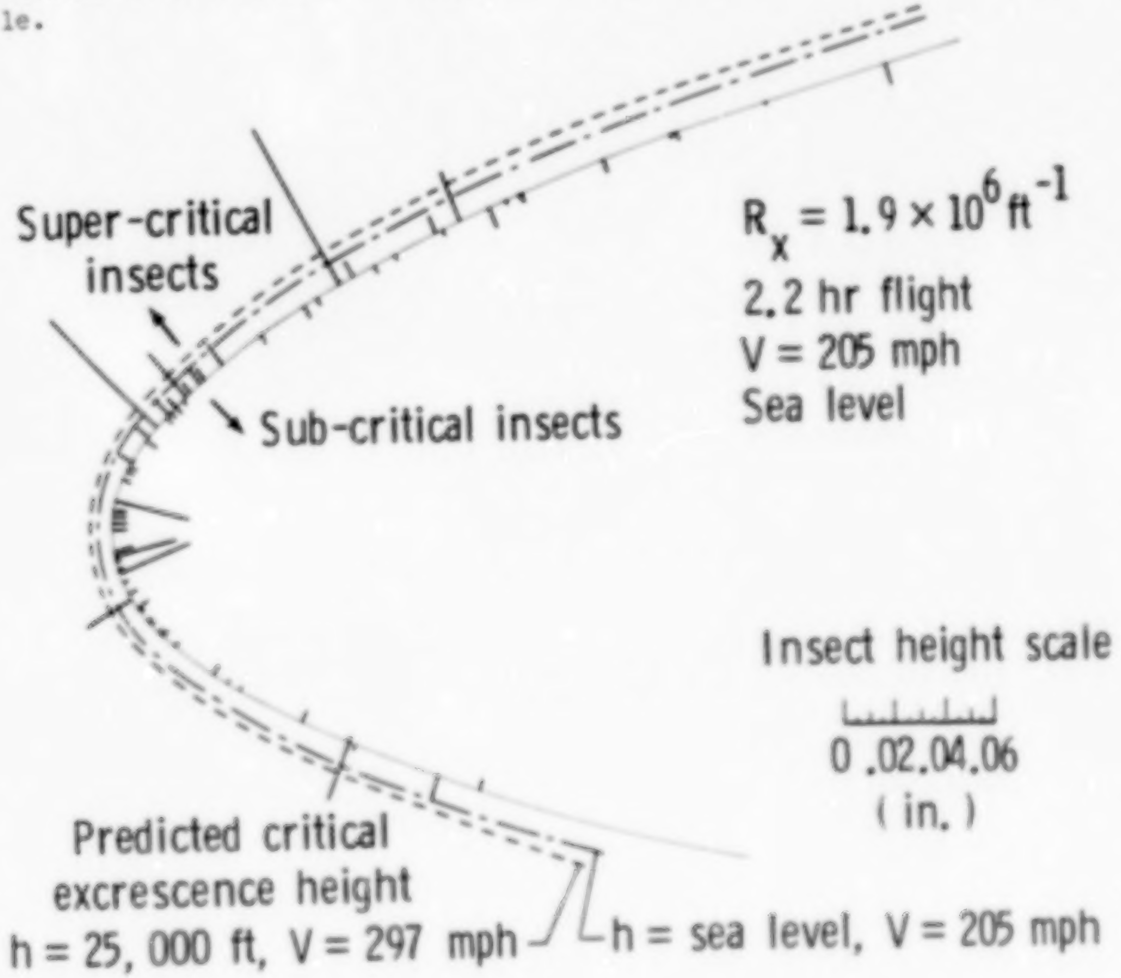
Super-critical insects
Sub-critical insects
$R_x = 1.9 \times 10^6 ft^{-1}$
2.2 hr flight
V = 205 mph
Sea level
Insect height scale
0 .02 .04 .06
(in.)
Predicted critical excrescence height
h = 25, 000 ft, V = 297 mph
h = sea level, V = 205 mph

INSECT CONTAMINATION PROTECTION TECHNIQUES

Previous attempts to develop insect contamination protection systems have included mechanical devices (temporary paper covers, scrapers, deflectors), and surface films (solid or quasi-static films which were washed off, adhesive surface coatings, resilient surface or fluid films discharged onto the surface). The figure lists the previous systems tested for insect contamination protection. All of these systems, to some degree, successfully protected surfaces against insect contamination; however, most of these concepts suffered some shortcoming in practicality. Two of the less practical approaches to contamination protection from the past include jettisoned paper coverings (refs. 2 to 4) and mechanical wiping or scraping devices (refs. 3 and 4) which traveled along the wing leading edge after take off. While such devices do work, the drawbacks for commercial applications are obvious.

Past research on leading-edge films and coatings (ref. 5) included quasi-static films, soluble films, and ice coatings. These soluble films provided very effective insect contamination protection in the wind tunnel experiments by Coleman. The principal shortcomings of these concepts are their mechanical complexity and impracticality for most aircraft operational environments. Also, these approaches only provide protection once per flight; after the protective coating has been removed, the airplane must land to have another protective coating applied on the ground. Passive resilient surfaces were suggested by Wortmann (ref. 6) and supported by Carmichael (ref. 7) for contamination protection. Materials for leading-edge coverings included solid rubber, foam rubber, and solid or foam silicone materials. While Wortmann's exploratory results with resilient surfaces were very promising for low speed airplane applications, the poor rain erosion characteristics for the limited number of materials tested appears as a serious drawback to higher speed aircraft applications. Retractable deflectors have been successfully tested in wind tunnel and flight evaluations (refs. 8 and 9). The systems utilized on the current NASA Jetstar laminar flow control (LFC) flight experiments (ref. 10) incorporate the deflector concept and the liquid spray concept.

Previous work on liquid discharge systems includes injection of water and surfactants (wetting agents) onto the leading edge, thereby preventing insect accumulation on the wet surface. Peterson's flight experiments (ref. 8) illustrated that continuous flow of water over the wing leading edge would prevent insect debris from adhering on a wing. However, the significant shortcoming of previous water discharge approaches was that very large volumes of water were required for successful contamination protection.

Among the various insect protection concepts discussed above, the fluid injection approach appears to hold the most promise, provided the required fluid flow rates can be reduced to practical levels. The present paper discusses results of a flight investigation of a porous surface fluid discharge type of system installed on an unswept wing. These flight experiments demonstrated successful insect contamination protection using very small quantities of an ice protection fluid (glycol/water solution).

PAST INSECT CONTAMINATION PROTECTION TECHNIQUES

- Paper covering
- Scrapers, wipers
- Deflectors
- Soluble films
- Resilent surface
- Liquid spray systems
- Porous leading edges

ICE AND INSECT PROTECTION FOR LAMINAR AIRFOILS

Among the various insect protection concepts tested, the fluid injection approach appears to hold the most promise, provided the required fluid flow rates can be reduced to practical levels. In these systems, fluids are discharged onto the test surface creating thin sheets that wet the surface either through slots or through metal skins made porous by election beam or laser beam drilled holes. The holes are about 0.0025 in. in diameter with a spacing of about 0.0205 in. Porous, woven sintered stainless-steel mesh is also a candidate surface material. These porous metal leading-edge concepts are based on the TKS, Ltd. (British) ice protection system (see ref. 9) which has been certified for ice protection on several aircraft using monoethylene glycol (MEG) and water fluid solutions. One of the interesting properties of MEG observed by TKS personnel is that the fluid acts as a solvent for insect body protein content. The drying of this protein content serves as the glue which causes the adhesion of insect debris to impacted surfaces. Therefore, this solvent property of MEG may serve to enhance its effectiveness in insect contamination protection, thus reducing the fluid required to small, practical quantities.

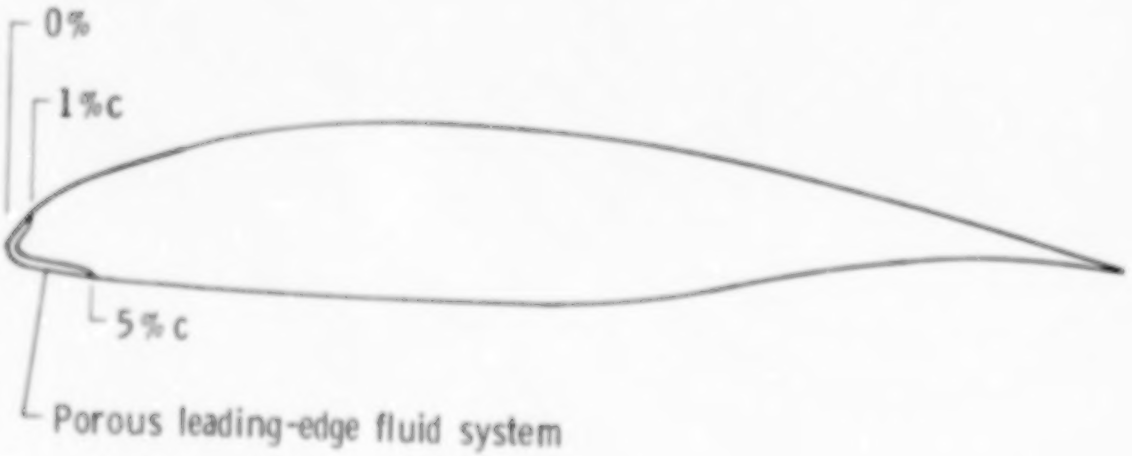

- Electron beam drilled sheet titanium
- Laser beam drilled sheet titanium
- Sintered stainless steel weave

INSECT PROTECTION FLIGHT EXPERIMENTS

ORIGINAL PAGE IS
OF POOR QUALITY

NASA conducted flight experiments to determine insect accumulation rates and protection efficiency under a variety of flight and atmospheric conditions using a Cessna 206 equipped with a TKS porous leading edge as shown in the figure. Test conditions, including location and time of day, were sought which would provide maximum insect population density (insects/million ft^3), thus providing maximum rates of insect accumulation on the test airplane. For these tests, the TKS system was deactivated on all surfaces except the right wing leading edge. The insect protection system effectiveness could then be evaluated by comparing the right, protected wing with the left, unprotected wing, for various flight and atmospheric conditions. Flight durations for these tests ranged from 10 to 50 min.; the airspeed was between 80 and 130 mph and the altitude was 50 ft.

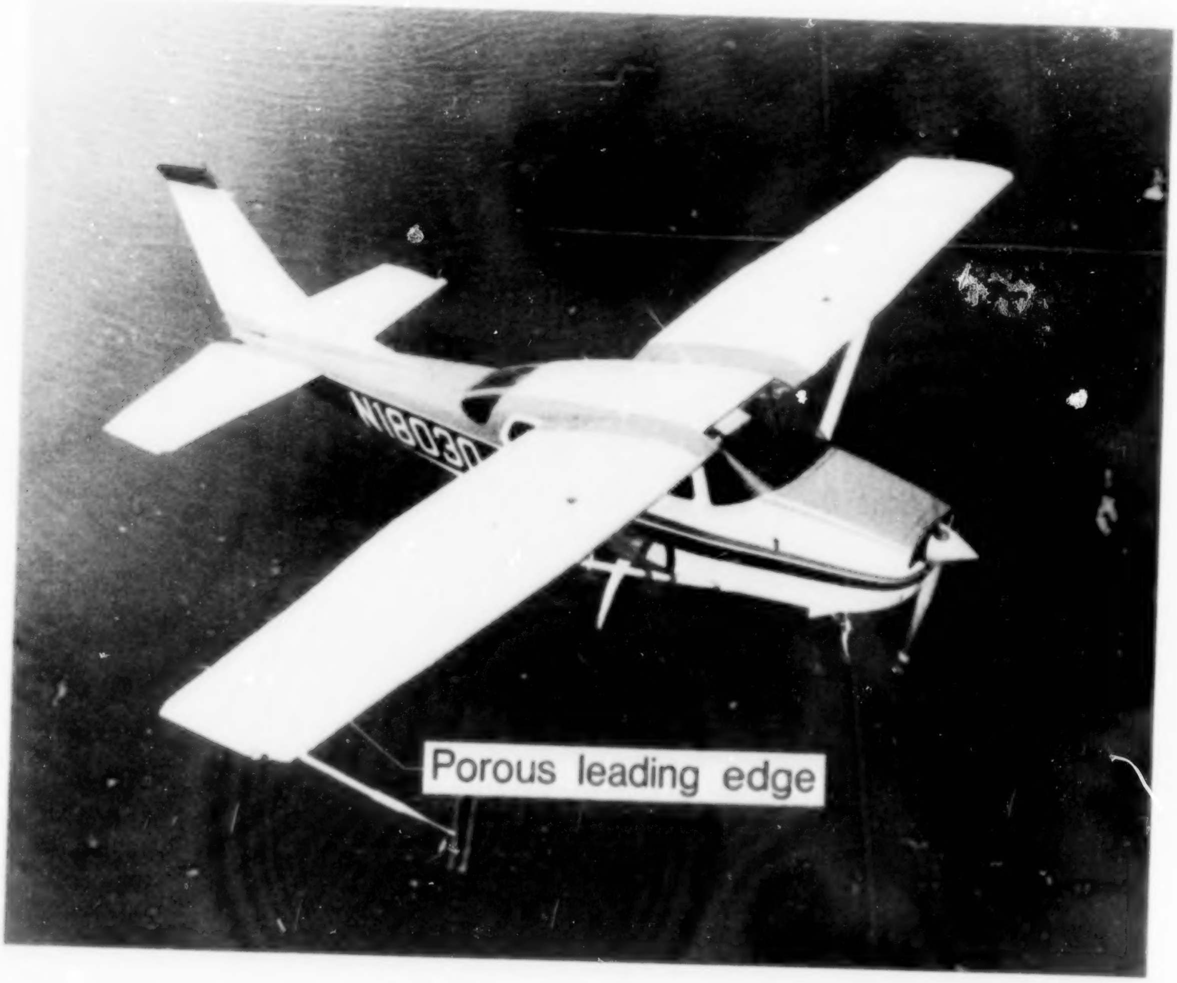

FACTORS AFFECTING RATE OF INSECT ACCUMULATION

This figure lists six factors that affect the rate of insect accumulation. Bragg (ref. 11) showed in recent analytical studies that the insect impact pattern is affected by airfoil section geometry. Past research (refs. 12 to 16) has shown that flight conditions such as altitude and airspeed affect the insect accumulation on aircraft. Certain atmospheric conditions such as temperature, wind speed, and humidity or moisture significantly affect the number of insects present. These atmospheric conditions as well as the effect of altitude will be further discussed in this presentation.

- Airfoil geometry
- Altitude
- Airspeed
- Temperature
- Wind speed
- Humidity/moisture

EFFECT OF TEMPERATURE ON NORMALIZED INSECT POPULATION DENSITY

In this figure, insect accumulation data obtained during the Cessna 206 tests are compared with data from previous insect population studies (refs. 13 to 15). Relative population density is plotted against temperature. The present data were obtained by dividing the number of insects accumulated by the accumulation time, airspeed and exposed frontal area to yield insect population density. The present data are shown in three wind speed categories; data have been normalized to the largest population density value from each category to compare with the previous studies. The data show that insect accumulation rate is strongly dependent on temperature. Accumulation rates steadily increased with increasing temperature up to about 77°F. Above 70°F, the correlation is good between the earlier studies and the present experiments. As the temperature decreases below 70°F, the decrease in relative population density is much less in the earlier studies than for the present tests, but the curves do follow similar trends. The differences may be attributed to variations in the types of insects indigenous to the test areas. Data obtained less than 12 hrs after precipitation show a slight increase in the rate of insect accumulation compared to data points at similar temperatures and wind speeds. Previous researchers concluded that no absolute correlation existed between precipitation and insect accumulation rates. The most important factor is that insect accumulation rates are greatest between 70°F and 80°F with a peak near 77°F.

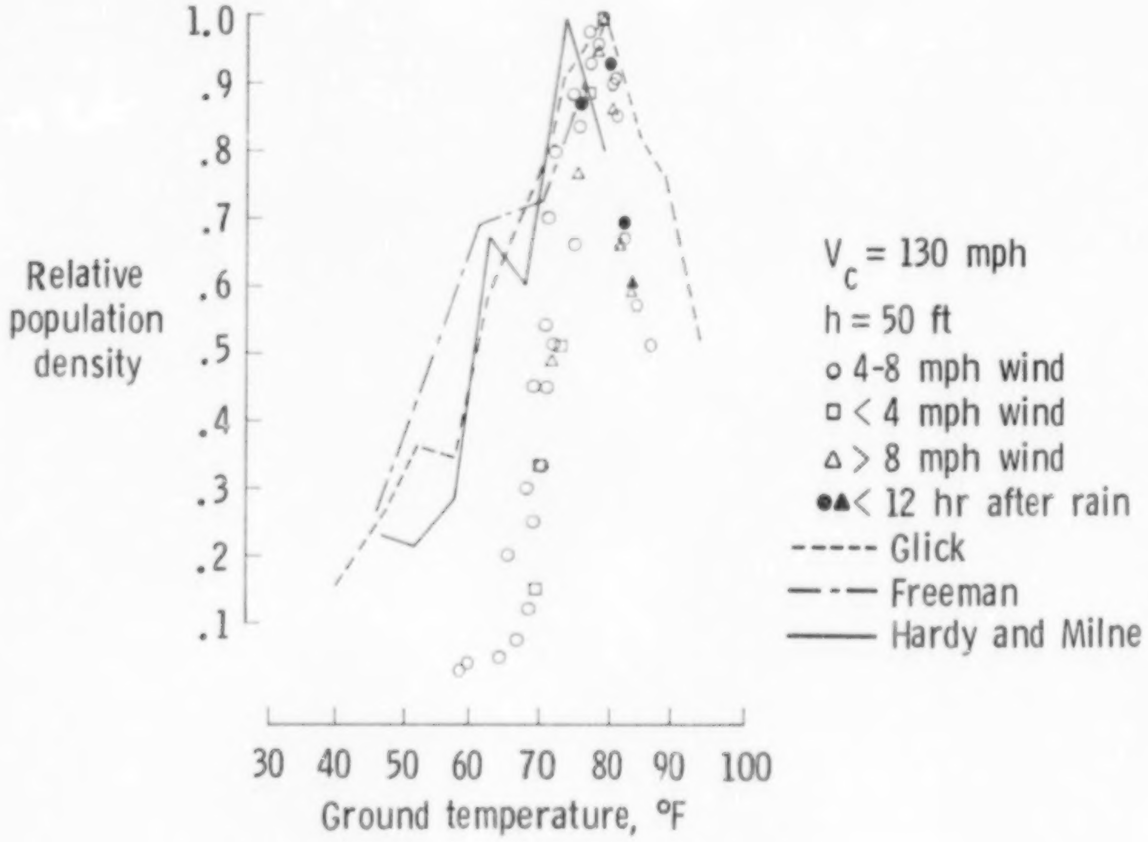

EFFECT OF WIND VELOCITY ON NORMALIZED INSECT POPULATION DENSITY

This figure compares the effect of wind speed on the Cessna 206 insect accumulation data with data from the earlier studies (refs. 13 to 15). The relative population density is plotted against surface wind speed. For the present experiments, only the data obtained where the temperature is above 72°F were plotted so that the effect of temperature on insect accumulation rate data is minimized. All of the data have been normalized to the largest population density value. Wind speeds from 4 to 8 mph yielded the highest relative population densities with slightly reduced population densities for calm winds. Above 8 mph, the earlier studies and the present data indicate large reductions in population density. Although the present tests offer no data for wind conditions over 15 mph, earlier studies show that insect debris accumulations on airplanes will be significantly reduced for wind speeds above 20 mph.

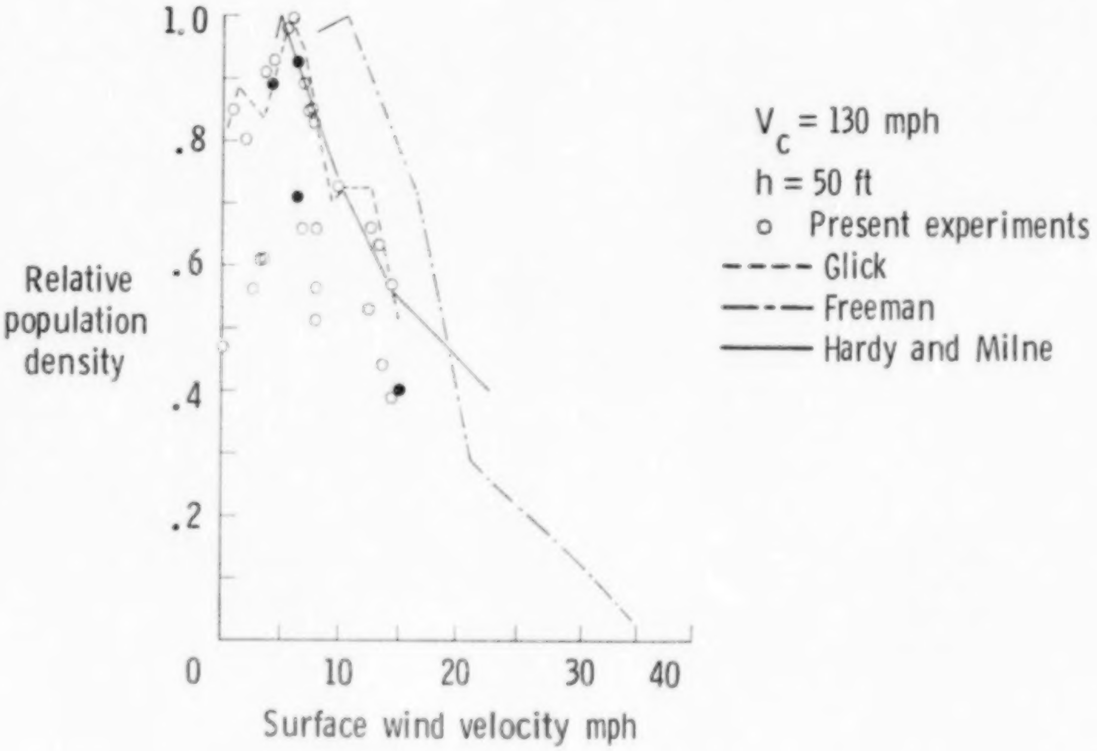

VERTICAL DISTRIBUTION OF POPULATION DENSITY

The vertical distribution of insects has been well documented and summarized by Coleman (ref. 12). The results are curve-fitted and shown in this figure along with averaged population data obtained in the present tests at altitudes from 50 to 1000 ft. For each flight, the airplane made a quick ascent to the test altitude, flew until a large number of insect strikes were accumulated, and then quickly descended and landed. With this flight test procedure, the majority of the insects collected would be obtained at the test altitude condition.

This figure shows five data points; each data point is an average of all the population density data obtained at that test altitude. The distribution of insects rapidly decreases from ground level to 500 ft. The data suggest that insect protection for laminar flow airplanes is probably not necessary above 500 ft.

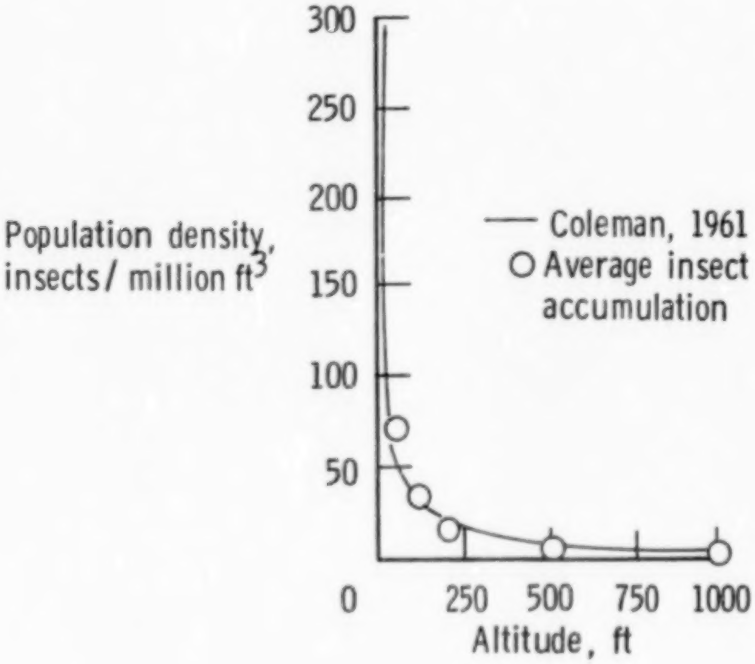

ORIGINAL PAGE IS
OF POOR QUALITY

POROUS STAINLESS-STEEL PANELS FOR INSECT PROTECTION

This figure shows a closeup photograph of the porous stainless-steel panels on the Cessna 206. Although designed for ice protection, the TKS system on the Cessna 206 provided effective insect contamination protection. The test airplane was exposed to a high density of insects much longer than in a typical airplane operation environment. The system was not effective in removing insect debris in flight that had been accumulated on a dry surface prior to activating the TKS system. Altitude and airspeed had no effect on the system's ability to protect against insect contamination.

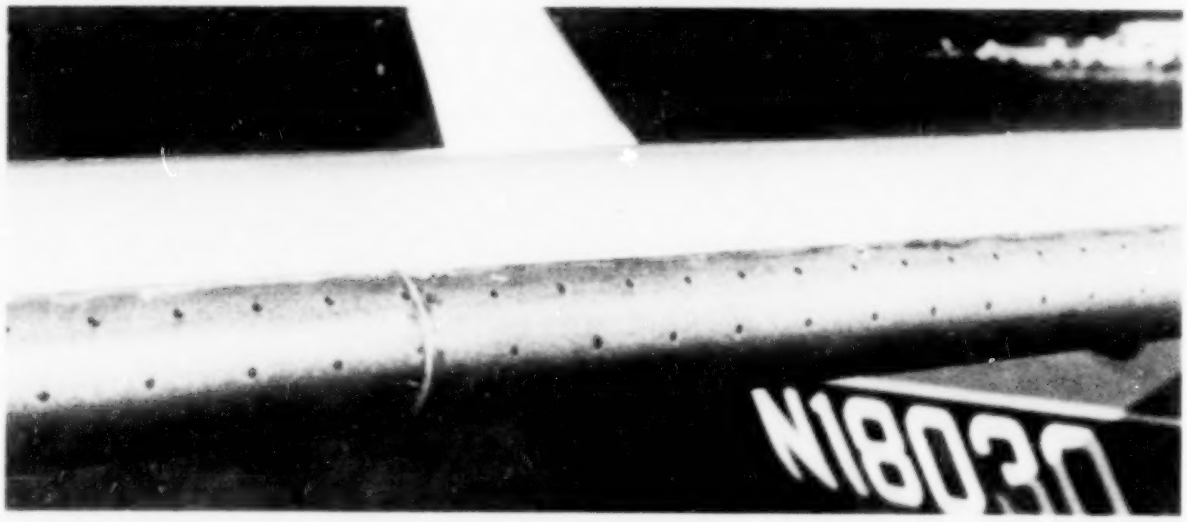

EFFECT OF SOLUTION MIXTURE ON INSECT PROTECTION

The most significant fluid property for successful insect protection was the ratio of water to mono-ethylene glycol (MEG) in the solution. This figure shows insects accumulated versus location on the upper and lower surface shown in percent chord. The shaded region denotes the right wing which had the TKS system activated. Data are shown for solution mixtures of 80 percent water/20 percent MEG and 20 percent water/80 percent MEG. This figure shows that even at the highest flow rate of 0.027 gal/min/ft^2, the system could not effectively prevent insect adhesion with the 20 percent MEG/80 percent water solution; the 80 percent MEG/20 percent water solution, however, was very effective, providing a 75 percent or greater reduction in the number of insect strikes which adhered to the surface. The effective insect protection observed in these tests can be attributed to both the TKS system design and the fluid properties. The porous skin allows a protective film to continually wet the airplane surface using a minimal amount of fluid. Because the MEG fluid acts as a solvent for insect body protein content, the effective insect contamination protection is enhanced, thus reducing the fluid required for protection.

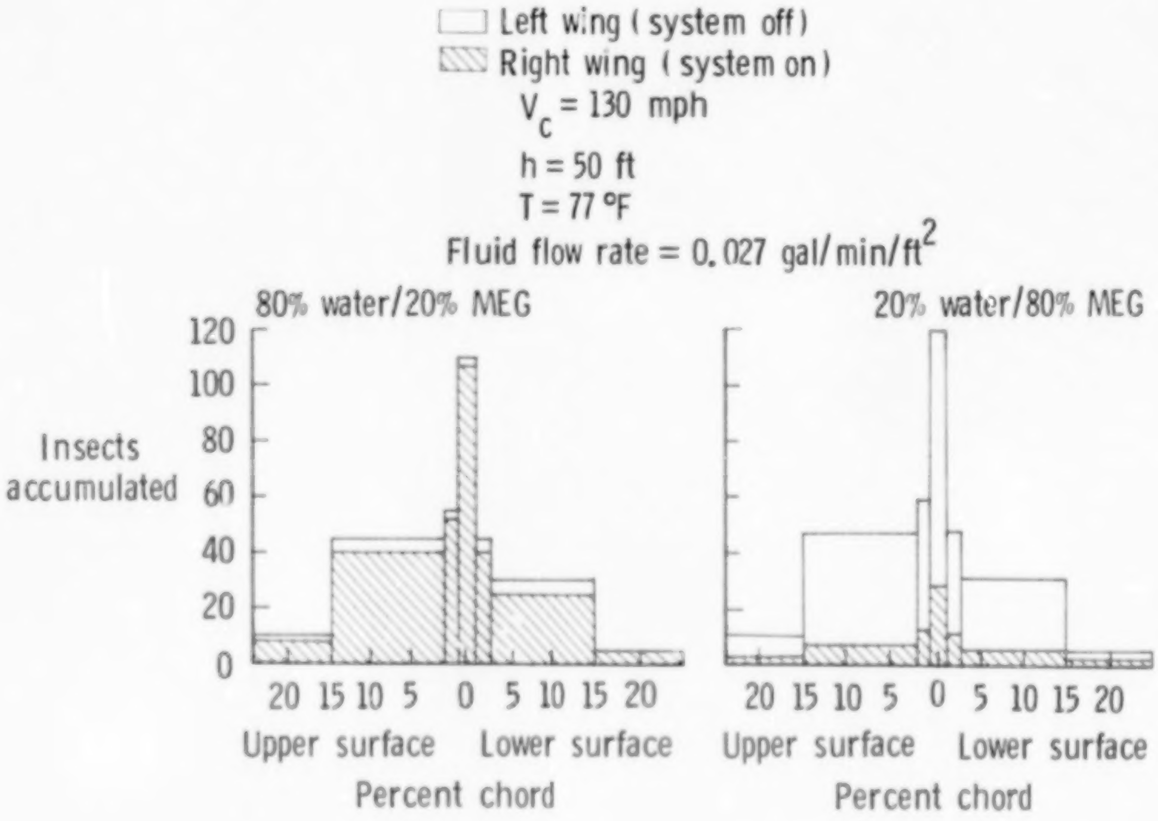

ORIGINAL PAGE IS
OF POOR QUALITY

FLUID REQUIREMENTS FOR INSECT PROTECTION

The flow rates shown to be effective for insect protection in the porous leading-edge flight experiments (ref. 16) were from 0.013 to 0.027 gal/min/(ft^2 of projected leading-edge frontal area). A typical business jet airplane with a 50-ft wing span and 12-percent thickness-to-chord ratio and average chord of 7 ft would require about 3 in. porous region in the panel. A flow rate of 0.16 to 0.33 gal/min would be required for a 68 to 82 percent reduction in insect accumulation. This is a significant improvement (about 100 fold) over the fluid injection approach tested by Peterson (ref. 8) which required about 24 gal/min for insect protection. It may be possible to further reduce the fluid flow rates required for contamination protection with the addition of a surfactant to the solution. A surfactant would reduce the tendency of the glycol fluid to form beads or rivulets and thus improve surface wetting.

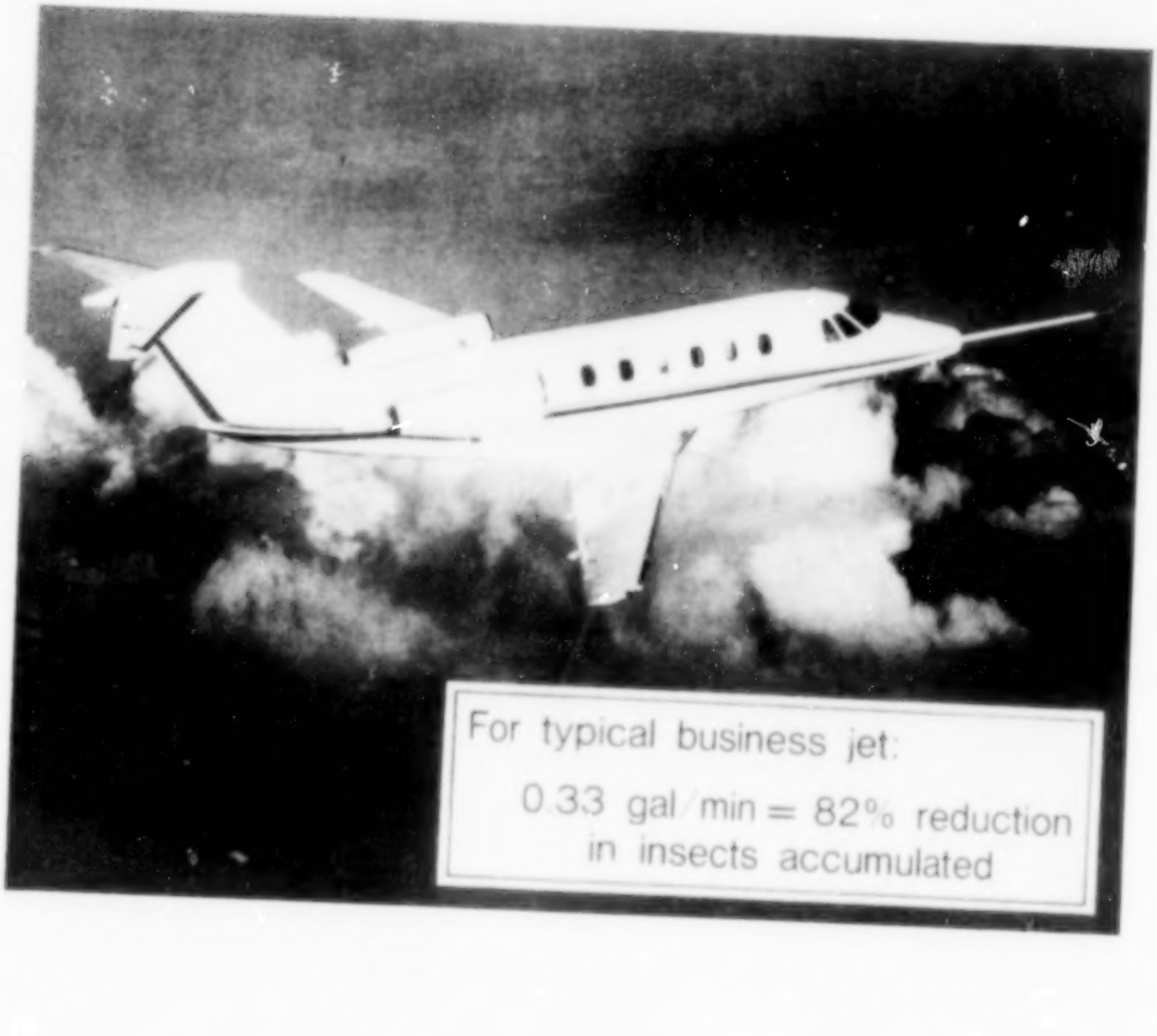

For typical business jet:

0.33 gal/min = 82% reduction in insects accumulated

CONCLUSIONS

Previous studies have shown that the seriousness of insect debris contamination will likely be dependent on aircraft characteristics and mission. In many cases, insect debris may be minimized by minimizing airplane flight time in environmental and atmospheric conditions where insect population densities are at a maximum. Flight tests have shown that temperatures from 70°F to 80°F (with a peak near 77°F), wind speeds from 4 to 8 mph, and altitudes below 500 ft yield the highest insect population densities.

When insect contamination cannot be avoided, the porous leading-edge fluid discharge ice protection system has been shown to be an effective insect contamination protection system. Good insect contamination protection can be achieved using a solution of 80 percent MEG and 20 percent water at flow rates between 0.013 and 0.027 gal/min/ft^2 of projected leading-edge frontal area.

- Maximum insect accumulations for:
    - Temperature - 70°F - 80°F
    - Wind speed - 4 - 8 mph
    - Altitude - < 500 ft
- Porous leading edge insect contamination protection is possible with:
    - Solution - 80% monethylene glycol/ 20% water
    - Flow rate - 0.013 - 0.027 gal/min/ft^2

REFERENCES

1. Holmes, B. J.; Obara, C. J.; Gregorek, G. M.; Hoffman, M. J.; and Freuler, R. J.: Flight Investigation of Natural Laminar Flow on the Bellanca Skyrocket II. SAE Paper 830717, April 1983.

2. Smith, F.; and Higton, D. J.: Flight Tests on a King Cobra FZ440 to Investigate the Practical Requirements for the Achievement of Low Profile Drag Coefficients on a Low Drag Aerofoil. R&M No. 2375, British A.R.C., 1950.

3. Beech, G.; and Nicholas, W. M.: A Mechanical Type of Scraper for Dealing with Insect Contamination of Aircraft Wings. Armstrong Whitworth Rep. No. W.T. 53/18, 1953.

4. Anon: Note on the Blackburn and General Aircraft Wind Tunnel Tests of the Armstrong Whitworth Fly Scraper. BLCC Paper No. B 0142, M.O.S. London, 1953.

5. Coleman, W. S.: Wind Tunnel Experiments on the Prevention of Insect Contamination by Means of Soluble Films and Liquids Over the Surface. Rep. to the Boundary Layer Control Committee, BLCC Note 39, 1952.

6. Wortmann, F. X.: A Method for Avoiding Insect Roughness on Aircraft. NASA TT F-15454, 1974. (Translation of "Eine Moglicnkeitzur Vermeidung der Insect Tenrauhigkeit an Flugzeugen," Luftfahrttechnik, Raumfahrttechnik, vol. 9, no. 9, September 1963, pp. 272-274).

7. Carmichael, Bruce H.: Summary of Past Experience in Natural Laminar Flow and Experimental Program for Resilient Leading Edge. NASA CR 152276, 1979.

8. Peterson, J. B., Jr.; and Fisher, D. F.: Flight Investigation of Insect Contamination and its Alleviation,. NASA CP 2036, 1978.

9. Kohlman, D. L.: Icing Tunnel Tests of a Glycol-Exuding Porous Leading Edge Ice Protection System on a General Aviation Airfoil. NASA CR 165444, 1981.

10. Fischer, M. C.; Wright, A. S., Jr.; and Wagner, R. D.: A Flight Test of Laminar Flow Control Leading Edge Systems. NASA TM 85712, 1983.

11. Bragg, Michael B.; and Maresh, J. L.: The Role of Airfoil Geometry in Minimizing the Effect of Insect Contamination of Laminar Flow Sections. AIAA Paper no. 84-2170, 1984.

12. Coleman, W. S.: Roughness Due to Insects. Boundary Layer and Flow Control, vol. 2, Pergammon Press, 1961.

13. Glick, P. A.: The Distribution of Insects, Spiders, and Mites in the Air. Technical Bulletin No. 673, U.S. Department of Agriculture, 1935.

14. Freeman, J. A.: Studies in the Distribution of Insects by Aerial Currents - The Insect Population in the Air from Ground Level to 300 Ft. Journal of Animal Ecology, vol. 14, 1945, pp. 128-154.

15. Hardy, A. C.; and Milne, P. S.: Studies in the Distribution of Insects by Aerial Currents. Journal of Animal Ecology, vol. 7, 1938, pp. 199-229.

16. Croom, C. C.; and Holmes, B. J.: Flight Evaluation of an Insect Contamination Protection System for Laminar Flow Wings. SAE Paper 850860, April 1985.

5/9

N88-14955

RIBLETS FOR AIRCRAFT SKIN-FRICTION REDUCTION

59-05

117253

15P

Michael J. Walsh
NASA Langley Research Center
Hampton, Virginia

[redacted]

ABSTRACT

Energy conservation and aerodynamic efficiency are the driving forces behind research into methods to reduce turbulent skin friction drag on aircraft fuselages. Fuselage skin friction reductions as small as 10 percent provide the potential for a 250 million dollar per year fuel savings for the commercial airline fleet. One passive drag reduction concept which is relatively simple to implement and retrofit is that of longitudinally grooved surfaces aligned with the stream velocity. These grooves (riblets) have heights and spacings on the order of the turbulent wall streak and burst dimensions. Present paper summarizes riblet performance (8 percent net drag reduction thus far), sensitivity to operational/application considerations such as yaw and Reynolds number variation, an alternative fabrication technique, results of extensive parametric experiments for geometrical optimization, and flight test applications.

C-7

RIBLETS

Local skin friction reductions as large as 8-10 percent have been experimentally measured in the wind tunnels at NASA Langley Research Center. The research has reached a stage where flight applications are near term. The riblets are now available on a thin vinyl film with adhesive backing. This film could be applied to new as well as existing aircraft. Data indicate that the film could be applied to both fuselage and wing surfaces. The 8-percent local skin friction reduction would therefore translate into an 8-percent reduction in the turbulent viscous drag of the aircraft, or approximately 4 percent aircraft drag. An added advantage of the riblet drag reduction technique is that it is passive.

**Bottom line - 8 percent aircraft viscous drag reduction
for CTOL aircraft, retrofittable and passive**

C-7

WHAT ARE RIBLETS?

Riblets are streamwise surface striations that are aligned with the local free-stream velocity. The typical cross section of an optimum riblet is shown on the slide. The optimum and most practical riblet has sharp valleys and sharp peaks. The purpose of the riblets is to modify the near-wall structure of the turbulent boundary layer. The spanwise surface variation down in the cross section imposes a strong spanwise viscous force that creates a wall slip layer.

Riblet $\equiv$ streamwise surface striation

Cross section → 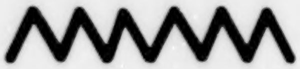

Purpose - Alter turbulence dynamics near the wall by imposing/utilizing strong spanwise viscous forces to create a wall slip layer

APPLICATION ISSUES RESOLVED

The work at Langley Research Center has resolved many of the application issues. The present paper discusses test results on optimum riblet geometry, maximum drag reduction, riblets scaling for drag reduction at flight conditions, yaw sensitivity, and a practical application technique.

- Optimum geometry for maximum drag reduction
- How much drag reduction?
- Scaling (wind tunnel to flight)
- Yaw sensitivity
- Retrofittable application technique

RIBLET MODELS TESTED

Determination of optimum riblet geometry required parametric testing. This slide indicates the range of shapes studied. The test results show that the symmetric v-groove gave the maximum drag reduction performance. The peaks and the valleys of the grooves should be relatively sharp for maximum drag reduction.

Model	Description
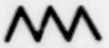	Symmetric V-groove
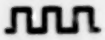	Rectangular
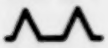	Spaced triangular
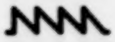	Right angle rib
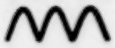	Peak curvature
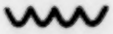	Valley curvature
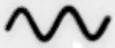	Peak and valley curvature
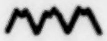	Notched peak
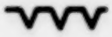	Spaced V-groove
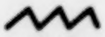	Unsymmetric groove
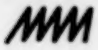	Oblique V-groove

OPTIMUM RIBLET

This slide presents net drag data for an optimum riblet surface that was tested in the low-speed wind tunnel at Langley. The drag data is referenced to the drag of a flat plate reference. The horizontal coordinate is the spacing of the grooves in wall coordinates, s^+. The parameter s^+ is related to the free-stream velocity and skin friction as shown in the equation on the slide. The maximum drag reduction of 8 percent was found to be insensitive to upstream history and free-stream velocity as long as the physical dimensions of the riblet were sized to an h^+ and $s^+ = 15$ at the operating free-stream velocity of interest. The parameter h^+ is the height of the groove in wall coordinates. This scaling of the drag reduction in wall coordinates allows the extrapolation of the low-speed wind tunnel results to a flight environment. The equations for s^+ and $\sqrt{C_f}$ shown on the slide indicate that the physical size of the riblet for drag reduction is only a weak function of Re_x, the Reynolds number based on distance along the aircraft fuselage (1/10 power). Therefore, the riblet dimension could be fixed for a particular aircraft rather than varying drastically along the fuselage.

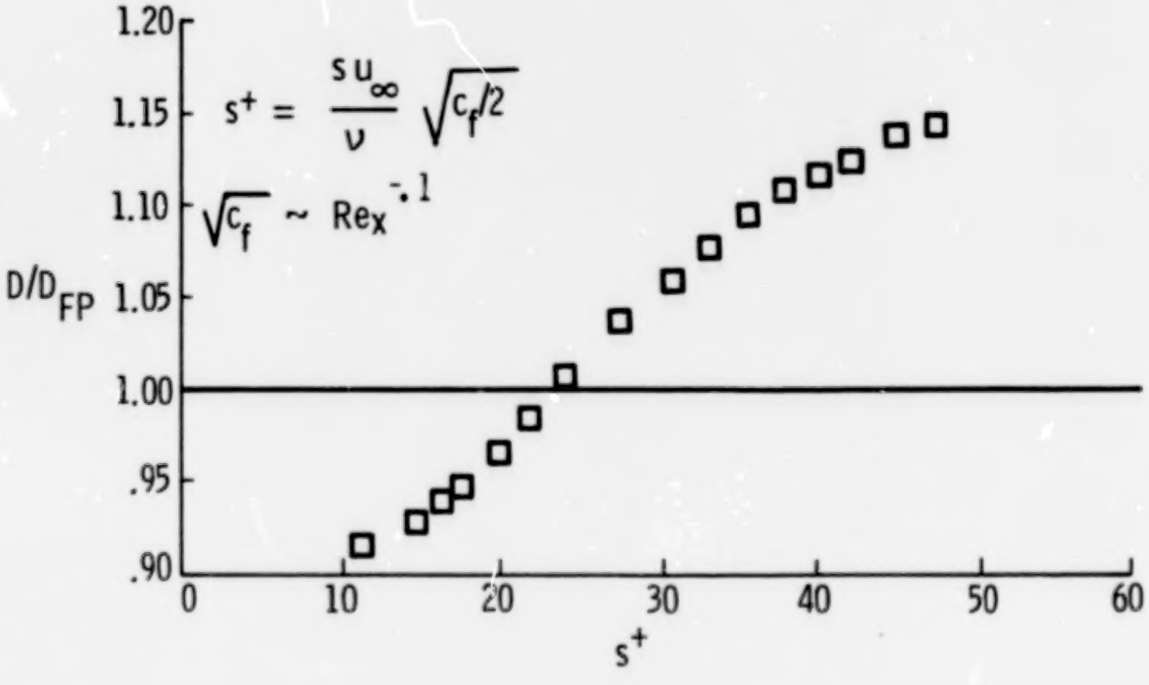

VINYL FILM RIBLET

The previous slide indicated the riblet scaling parameters. The next step to achieving a flight-capable device was to find a practical fabrication technique. The method advocated by 3M Co. was to make the riblets on a vinyl film with an adhesive backing. This slide shows drag data obtained with a vinyl riblet compared to a riblet which had been machined on an aluminum surface. Due to the manufacturing process, the aspect ratio (h/s) for the vinyl riblet was somewhat smaller than that for the aluminum riblet. The reduced aspect ratio of the vinyl riblet resulted in a smaller drag reduction than that obtained with the aluminum riblet. The data are significant in that drag reduction was obtained on a surface suitable for aircraft application.

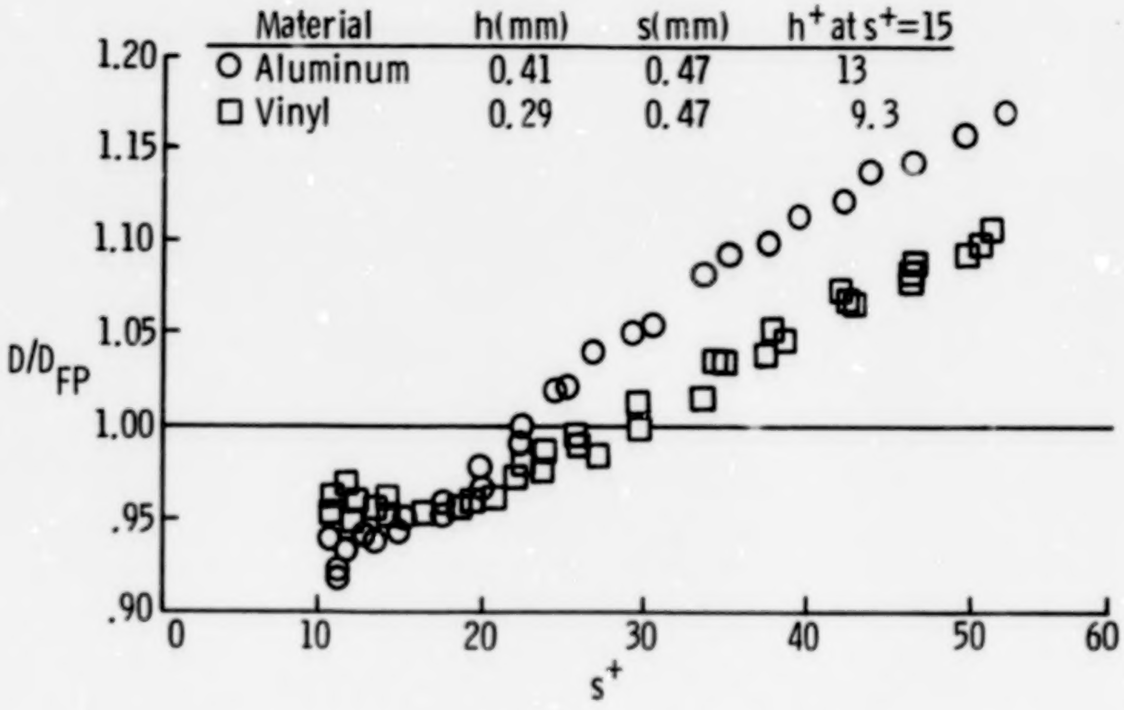

Material	h(mm)	s(mm)	h^+ at $s^+=15$
○ Aluminum	0.41	0.47	13
□ Vinyl	0.29	0.47	9.3

ORIGINAL PAGE IS
OF POOR QUALITY

FLIGHT TEST FILM

The scaling parameters have been used to determine the physical dimensions of a riblet film suitable for drag reduction at flight conditions. The slide shows a micro-photogragh of a riblet film to be flight tested in July 1985. The physical height and spacing of the riblet is 0.0013 inch. Despite the overall physical size the film still has sharp peaks and valleys.

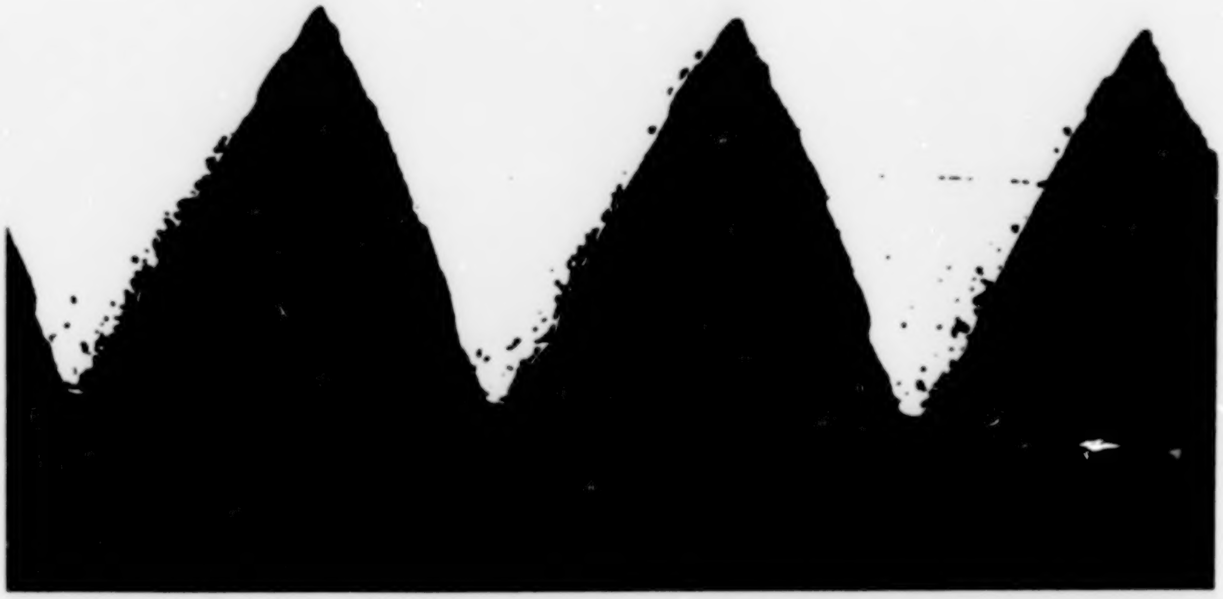

EFFECT OF YAW

Another aspect of a flight application is the yaw sensitivity of the riblets. All data shown previously have been for zero angle of yaw. This slide shows the vinyl film at 0°, 15°, and 30° yaw. There is little change in the maximum drag reduction at 15°; however, all drag reduction is lost at 30° yaw. In a riblet application it would be important to keep the grooves aligned with the flow within 15°. For cruise the near surface streamlines are usually in this less than 15° range for CTOL aircraft.

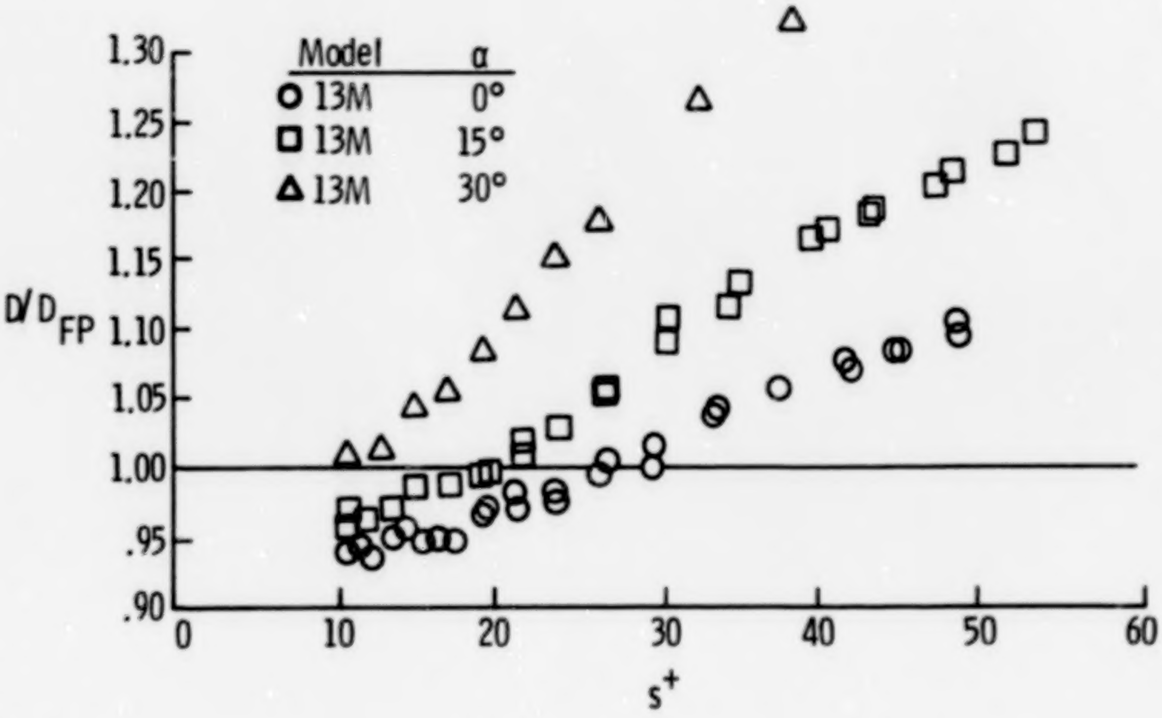

SUMMARY OF RIBLET PERFORMANCE

The riblet drag reduction appears to result from the spanwise velocity gradient $\partial u/\partial z$. There is a thickening of the viscous near wall region that moves the turbulent fluctuations further from the wall. This whole process reduces the turbulent production magnitude. The basic turbulence interaction process is unaltered. A maximum drag reduction of 8 percent is obtained with a sharp peak v-groove having a space and height $0(15^+)$. The drag reduction is present up to 15° angles of yaw; however, by 30° yaw, the drag reduction is lost. Vinyl riblets provide a simple method for application to new aircraft as well as aircraft presently flying.

- Spanwise geometry causes a $\partial U/\partial z$
    - Thickens viscous region near the wall
    - Moves turbulent fluctuations further from the wall and reduces turbulence production magnitude
    - Turbulence interaction/production processes unaltered
    - Basically, provides a "slip layer" at surface
- Maximum drag reduction for riblets 8 percent
    - Optimum geometry is V-groove with "sharp" tips
    - Optimum size is $0(15^+)$
    - Insensitive to yaw angles up to 15°
    - Vinyl riblets make aircraft applications simple and retrofittable

REQUIRED AND ONGOING RESEARCH

Ongoing research at Langley is presently focusing on increasing the riblet drag reduction performance by increasing the aspect ratio (h/s) of the riblet geometry. Present data indicate that the drag reduction increased with aspect ratio with a maximum value of one tested thus far. Further research will attempt to increase the aspect ratio above one. Now that the scaling of the riblet drag reduction has been firmly established, the wind tunnel results can be used to extrapolate to flight conditions. Two sets of flight tests are planned in the near future: a subsonic test at $M = .7$ on the fuselage of a Learjet; and a $M = 2.0$ test on a flight test fixture mounted on the underside of the fuselage of an F-104G aircraft at Dryden Flight Research Facility. Details of these upcoming flight tests will be discussed on the next two slides. Tests are also planned in the 7' x 10' tunnel in 1986. These tunnel tests will be conducted at high U_∞, Q_∞, , and Re_x (100×10^6). Also to get the riblet film ready for fleet application, the following areas will have to be examined: durability, porosity, ultraviolet sensitivity, and clogging. The need for a porous film will be discussed further in a later slide.

- Improved performance (increased H/S)
- Flight tests
    - Learjet fuselage at $M = .7$ (July 1985)
    - Dryden, $M = 2$ (May - June 1985)
- High U_∞, Q_∞, Re_x (100×10^6) tests in 7' × 10' tunnel (1986)
- Long duration flight readiness
    - Durability
    - Porosity
    - Ultraviolet sensitivity
    - Clogging

ORIGINAL PAGE IS
OF POOR QUALITY

TURBULENT DRAG REDUCTION FLIGHT RESEARCH

This slide shows a photograph of a Learjet Model 28/29 aircraft to be used for riblet flight tests in July 1985. The riblet film will be tested at Mach numbers up to 0.8 and Reynolds number per foot up to 3.0×10^6. Drag reduction performance will be measured with a drag balance and a boundary layer rake. Two riblet films will be tested: one with h = s = 0.003" and the other h = s = 0.0013".

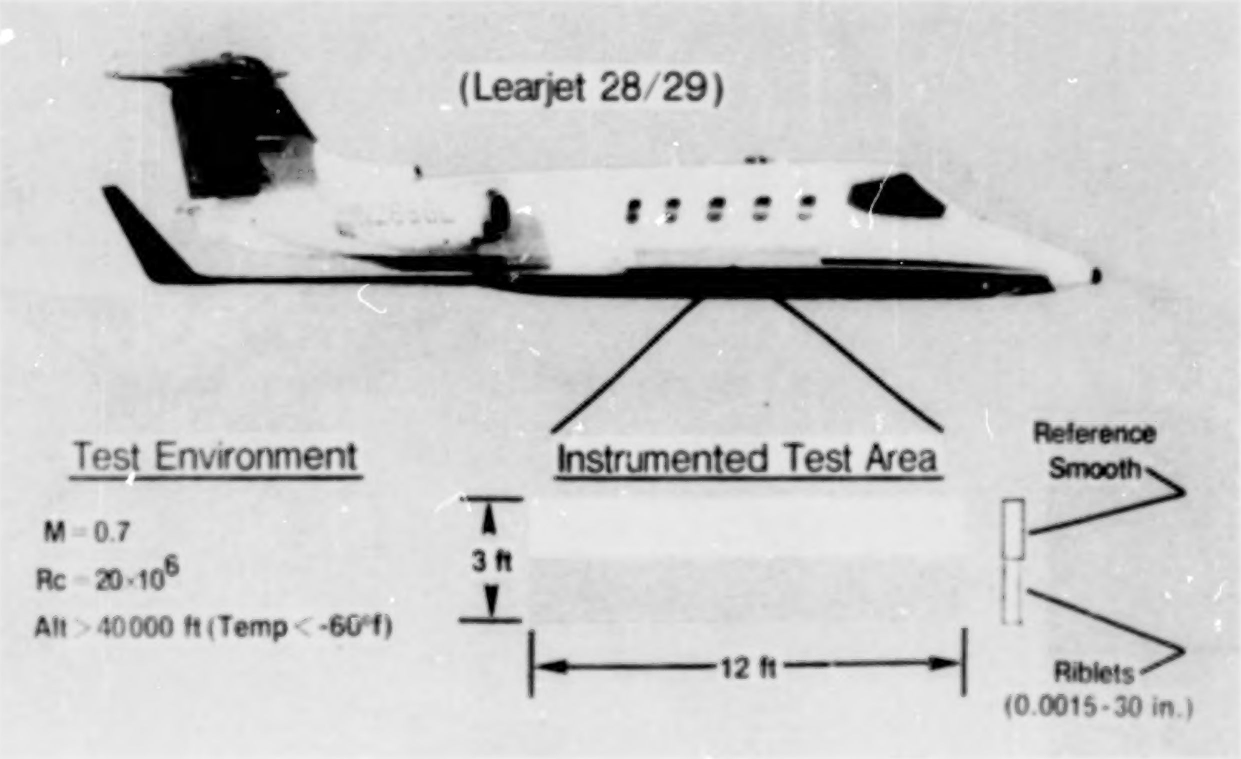

(Learjet 28/29)

Test Environment

M = 0.7

Rc = 20×10^6

Alt > 40000 ft (Temp < -60°f)

Instrumented Test Area

Reference Smooth

Riblets (0.0015-30 in.)

FLIGHT TEST FIXTURE ON F-104G

This slide shows the flight test fixture mounted on the underside of the fuselage of an F-104G aircraft at Dryden Flight Research Facility. The test fixture can provide data for Mach numbers 0.4 to 2.0. A drag balance and a boundary layer rake are mounted on each side of the fixture. This test facility will provide data showing the supersonic drag reduction performance of the riblets. The tests are presently scheduled for May-June 1985.

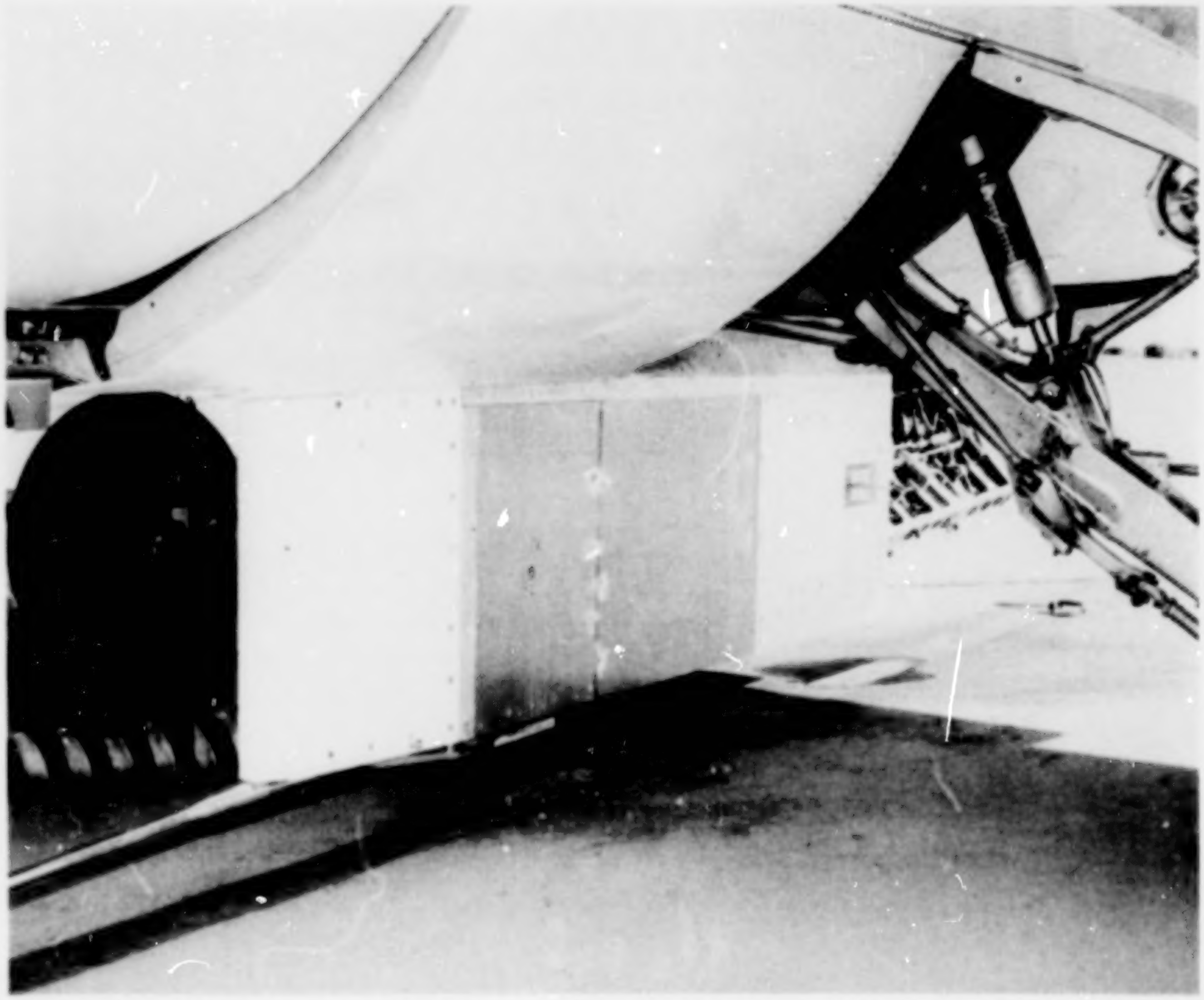

ORIGINAL PAGE IS
OF POOR QUALITY

NET EFFECT OF RIBLET APPLICATION

This slide summarizes the net effect of a riblet application. The riblet film has application to civilian as well as military aircraft. The riblet has the potential to reduce turbulent skin friction on the aircraft fuselage by 8 percent. This skin friction reduction on the fuselage and wing is associated with a displacement thickness reduction (δ^*) that results in a 6 percent reduction of the afterbody form drag. The riblet film itself, if made porous, could reduce the 5 percent of fuselage drag which is due to leakage from the pressurized cabins and the roughness drag of the aircraft by 3 percent. The summation of the riblet drag reduction benefits is a possible 16 percent reduction in fuselage drag or a 4 percent reduction in the net drag of the aircraft. In addition the riblet film would provide corrosion resistance and could be used as a substitute for paint. Many of the markings and decorations on aircraft flying now are made out of a vinyl film. Wing application benefits would be additive to these.

- Civilian
  - CTOL
  - SST
- Military
  - Tanker
  - Transport (C130, C141, C5)
  - Patrol (P3)

	Percent drag reduction for fuselage	Source
	8% direct C_f reduction 6% reduction of afterbody form drag	Control of wall turbulence, δ^* reduction upstream of afterbody region
	5% reduction due to modification of leakage from pressurized cabins	Converting jet leakage into porous injection
	3% roughness drag reduction	Smoothing due to surface film

Total fuselage drag reduction = 16%
Total aircraft drag reduction = 4%

- Additional benefits
  - Corrosion resistance (cost reduction)
  - Substitute for paint (colors molded into film) (cost/wt. reduction)

D30

N88-14956

530-05

117254

13P.

AIRFOIL LARGE EDDY BREAKUP DEVICES FOR TURBULENT DRAG REDUCTION

J. B. Anders
NASA Langley Research Center
Hampton, Virginia

PRECEDING PAGE BLANK NOT FILMED

PAGE 572 INTENTIONALLY BLANK

[redacted] Large Eddy Breakup Devices

Large eddy breakup (LEBU) devices are thin elements (plates or airfoils) placed horizontally in a turbulent boundary layer for the purpose of modifying the turbulent structure to achieve reduced skin friction. While the exact mechanism by which LEBU devices modify the turbulence is not well understood at this time, several proposed mechanisms are currently the subject of study at a number of research institutions in this country. What is known is that these thin-element devices can produce large reductions in turbulent skin friction for extended downstream distances. The most effective LEBU geometry thus far is a tandem arrangement of plates, 6 to 10 chord lengths apart, near the edge of the turbulent boundary layer. Net drag reductions (i.e., accounting for the drag of the thin plates) of the order of 10 percent have been reported from experiments both here at Langley and the Illinois Institute of Technology under a Langley grant. The major issues considered thus far have been concerned with minimizing device drag (through the use of very thin plates) and maximizing the drag reduction performance through parametric geometry changes.

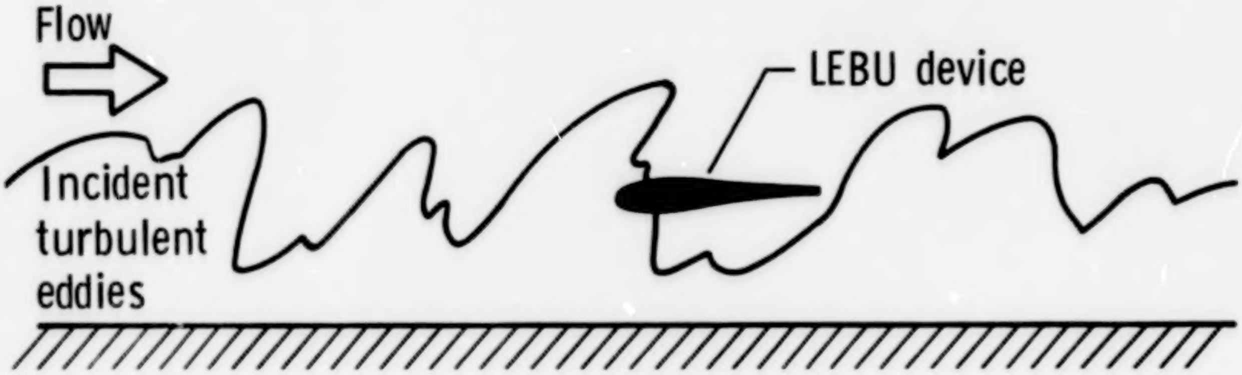

Definition of a LEBU

A device to break up and modify the large outer scales of a turbulent boundary layer for the purposes of turbulence control and drag reduction

Issues

- Device drag
- Drag reduction performance

Key Application Issues for LEBU's

While the use of thin plates to minimize device drag is a viable technique for low-speed wind tunnel experiments, it is not practical for the actual flight environment where significant structural integrity will be required. The present work was initiated to develop LEBU devices sufficiently rugged enough for flight and to determine their drag reduction performance at higher Reynolds numbers.

CTOL aircraft

- Performance at high Reynolds numbers
- Device structural integrity
- Can transonic-capable devices produce net drag reduction?

LEBU Devices

Initial LEBU experiments were conducted using thin, flat ribbons in tandem arrays, as shown here. Second generation devices utilized flat ribbons with tapered trailing edges to reduce device drag. Currently, airfoil-shaped devices are under investigation to utilize their low-drag/higher structural stiffness characteristics.

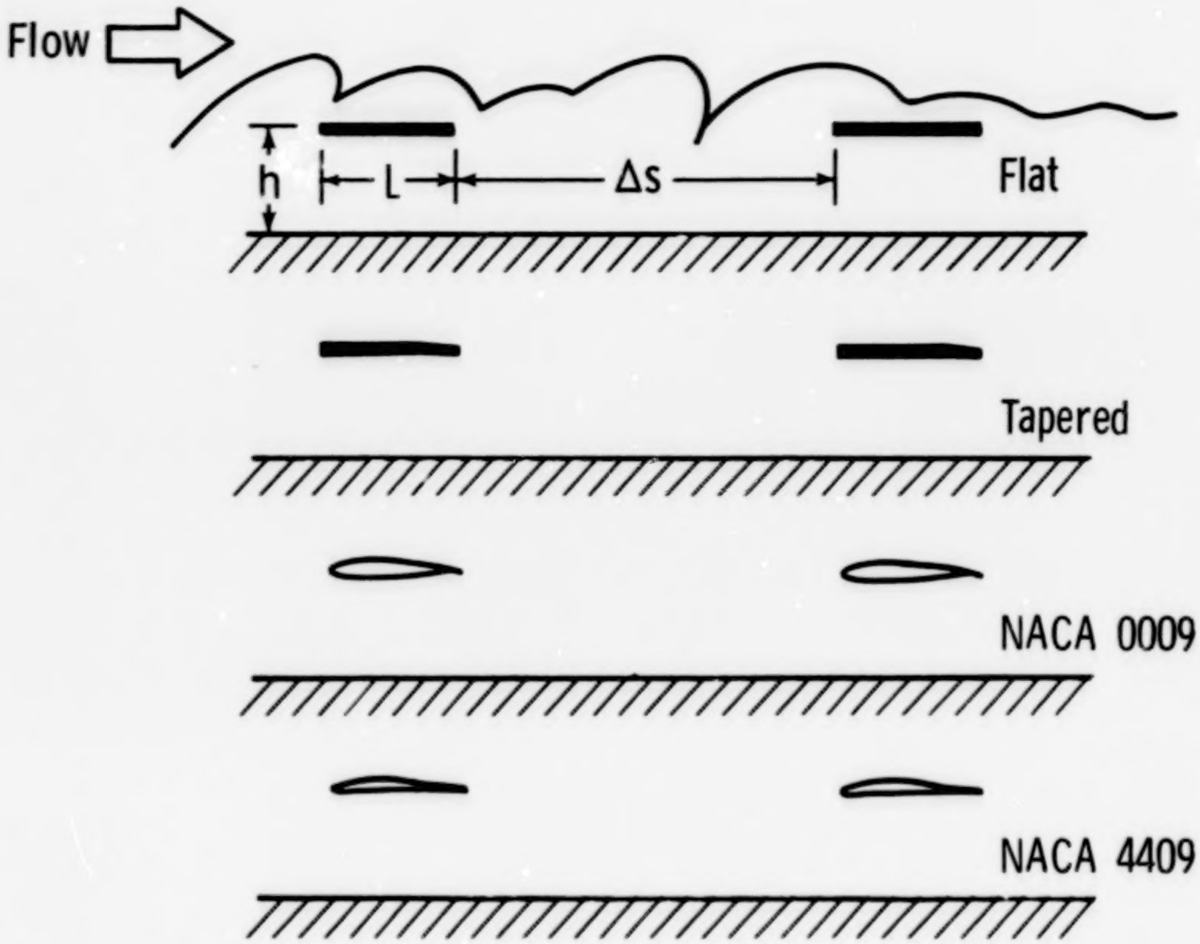
Flow
h
L
Δs
Flat
Tapered
NACA 0009
NACA 4409

Skin Friction Reduction

The effectiveness of LEBU devices is a function of both the magnitude and the extent of the reduced C_f region downstream. This figure shows results obtained at Langley and the Illinois Institute of Technology for thin-plate devices in a tandem arrangement. The downstream extent is shown in terms of boundary layer thicknesses (δ_0) from the device location (x_0). Maximum C_f reductions approaching 50 percent have been measured with recovery lengths greater than 100 boundary layer thicknesses. The parasite drag of the devices themselves is not included in this figure.

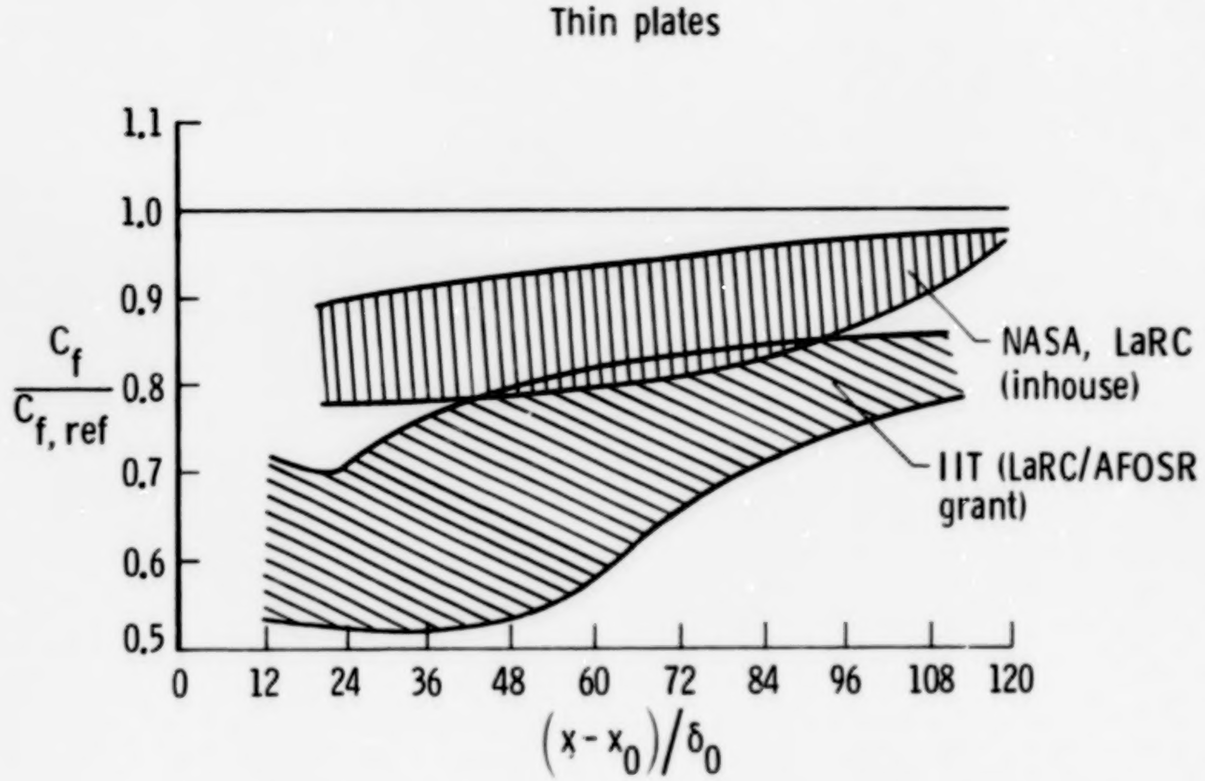

Net Drag Reduction

Net drag reduction is simply the downstream skin-friction drag plus the device drag of the LEBU's nondimensionalized by the reference (no device) skin-friction drag. This figure shows that the reduced skin friction downstream of LEBU devices quickly compensates for the added parasitic device drag and that net reductions $(D/D_{ref} < 1)$ can be obtained within 30 boundary layer thicknesses downstream. Net drag reduction effectiveness is a sensitive function of device thickness, device height in the boundary layer and device chord. The spread of the data shown is a reflection of that sensitivity.

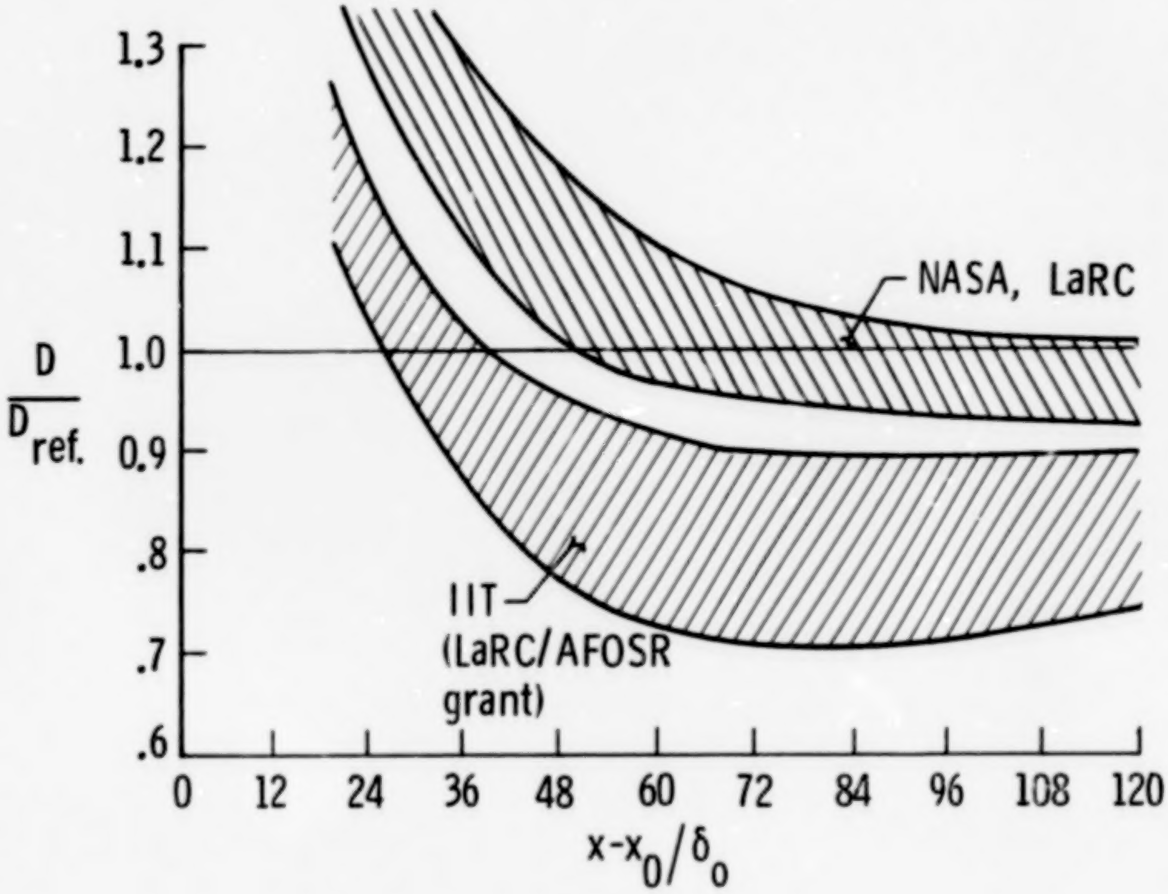

Test Plate

The present experiments were conducted on the test plate shown in this figure. The plate spanned the wind tunnel test section and the tunnel ceiling was adjusted to give a near-zero pressure gradient down the entire plate length. The LEBU devices were positioned approximately one-third of the way back from the plate leading edge where the turbulent boundary layer thickness was 25 mm. The usable test region extended approximately 300 cm downstream (120 boundary layer thicknesses). Data was obtained in the form of velocity profiles and local skin friction was deduced from the longitudinal variation of the integral properties of the boundary layer (momentum balance).

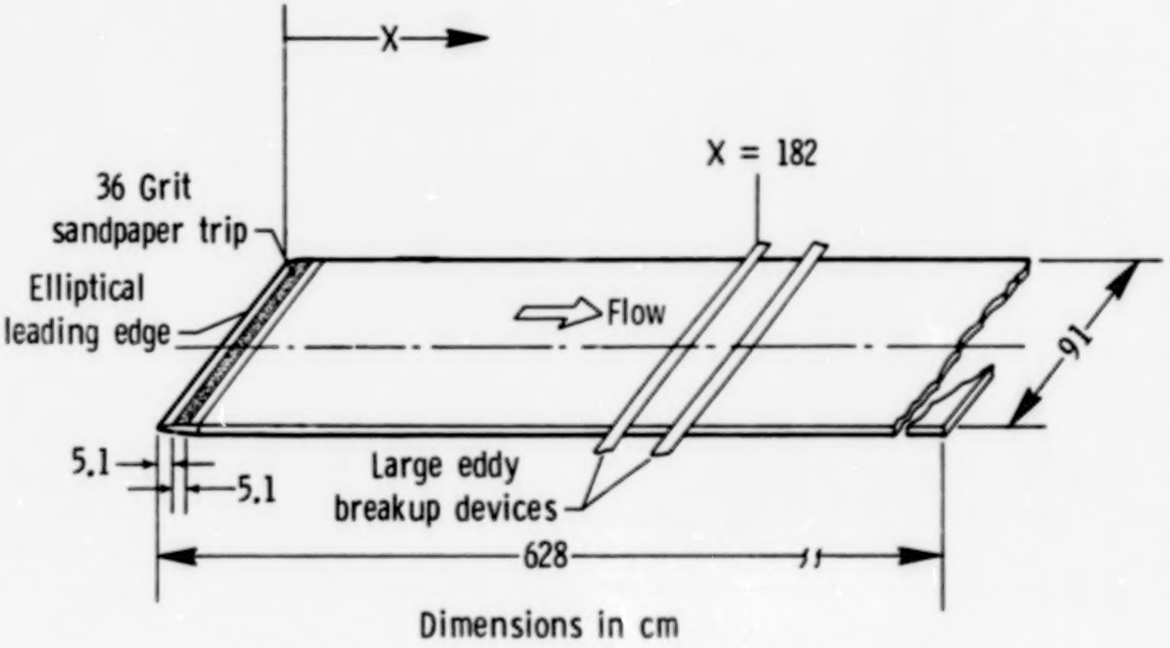
X
X = 182
36 Grit sandpaper trip
Elliptical leading edge
Flow
91
5.1
5.1
Large eddy breakup devices
628
Dimensions in cm

Net Drag Reduction for Thin Plates

Shown in this figure are the net drag reductions obtained downstream of thin plates at both high and low Reynolds numbers. As indicated, the drag reduction performance at high Reynolds numbers is actually somewhat better, although insufficient downstream test length was available to determine the maximum net reduction obtainable for the high Reynolds number case. This gives confidence that previous, low Reynolds number results are conservative and no inherent limitations are present to prevent the application of LEBU technology to the high Reynolds number flight environment.

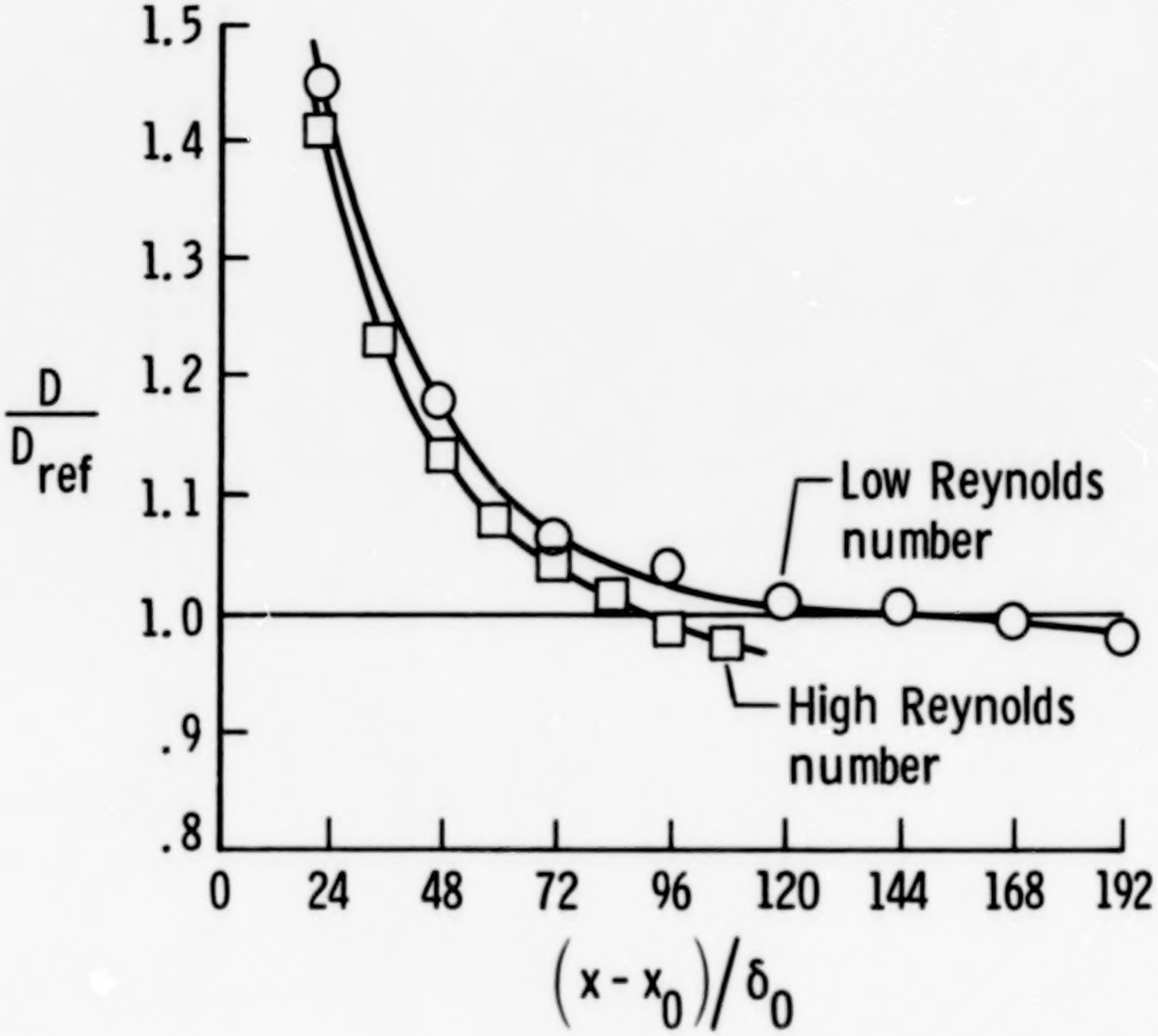

Drag of Single Devices

The device drag of thin plates (thickness/chord = .01) at low Reynolds numbers is shown in this figure to be near that expected for laminar skin friction drag. Laminar skin friction drag is the theoretical minimum device drag obtainable for single elements, and hence represents a lower limit for the LEBU device drag penalty. As velocity is increased (larger R_l) flow-induced vibration of the thin plates becomes important and the plate thickness must be increased to provide greater stiffness. These thicker plates (thickness/chord = .02) significantly increase the device drag (see thick plate data in the figure). Ultra-thin plates (thickness/chord = .008) can reduce this increased device drag but at the higher Reynolds numbers they must have closely spaced vertical supports to suppress the flow-induced vibrations. Since these vertical supports locally destroy the skin friction reduction effectiveness of the LEBU devices it is desirable to minimize the number of supports. The answer to the conflicting requirements of increased device rigidity with minimal device drag lies with airfoil-shaped devices. As shown in the figure, an NACA 0009 airfoil (thickness/chord = .1) has near laminar skin friction drag even though it is 10 times thicker and 1000 times stiffer than the thin plates.

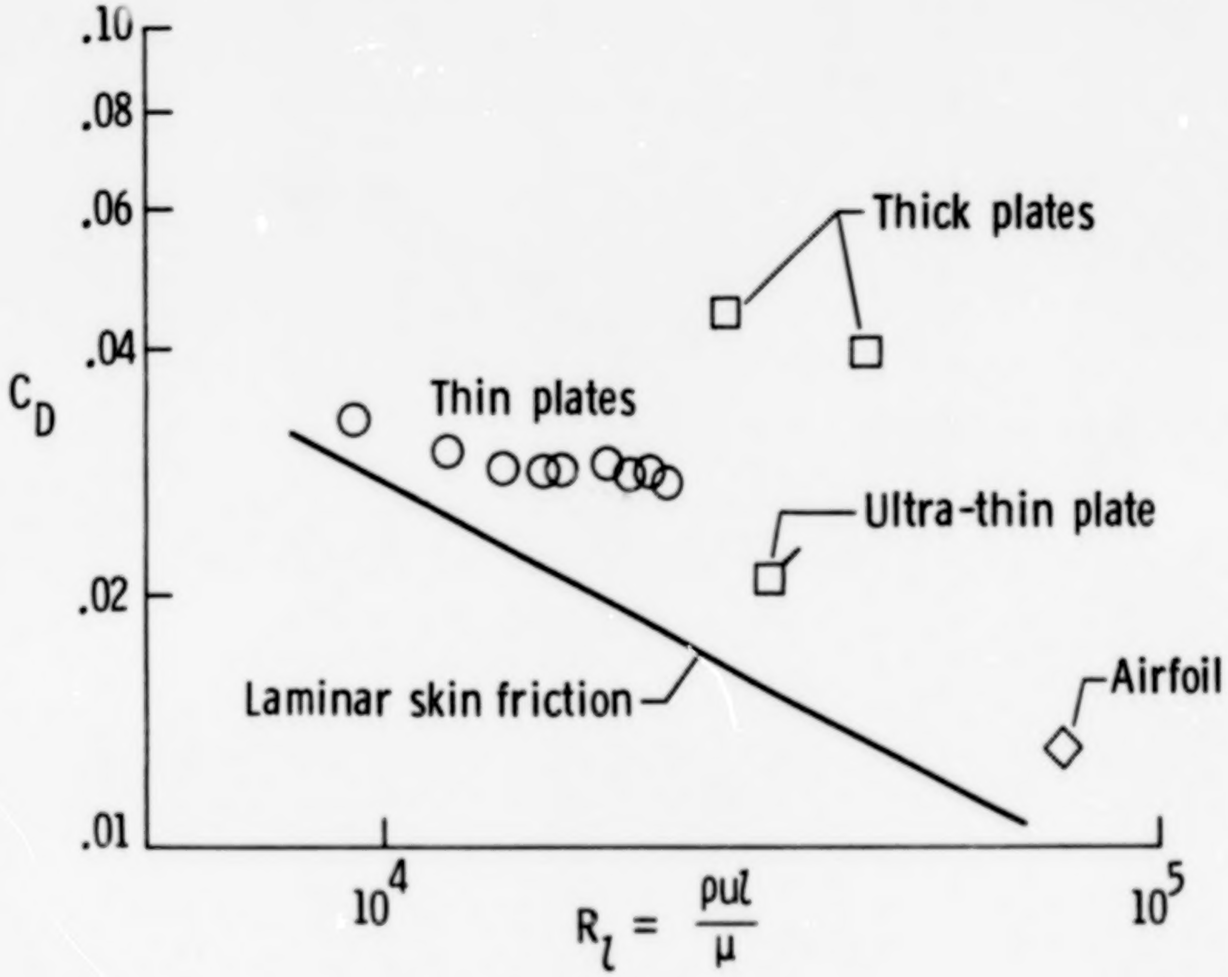

Airfoil LEBU Skin Friction Reduction

The measured, local skin friction downstream of a tandem set of NACA 0009 airfoils is shown in this figure. The maximum skin friction reduction of 30 percent occurs approximately 40 boundary layer thicknesses downstream followed by a return toward flat plate levels over the remaining 60 boundary layer thicknesses of the test region. These results compare favorably with the thin-plate results obtained previously at lower Reynolds numbers. These data indicate that airfoil-shaped devices are at least as effective in reducing skin friction as thin plates.

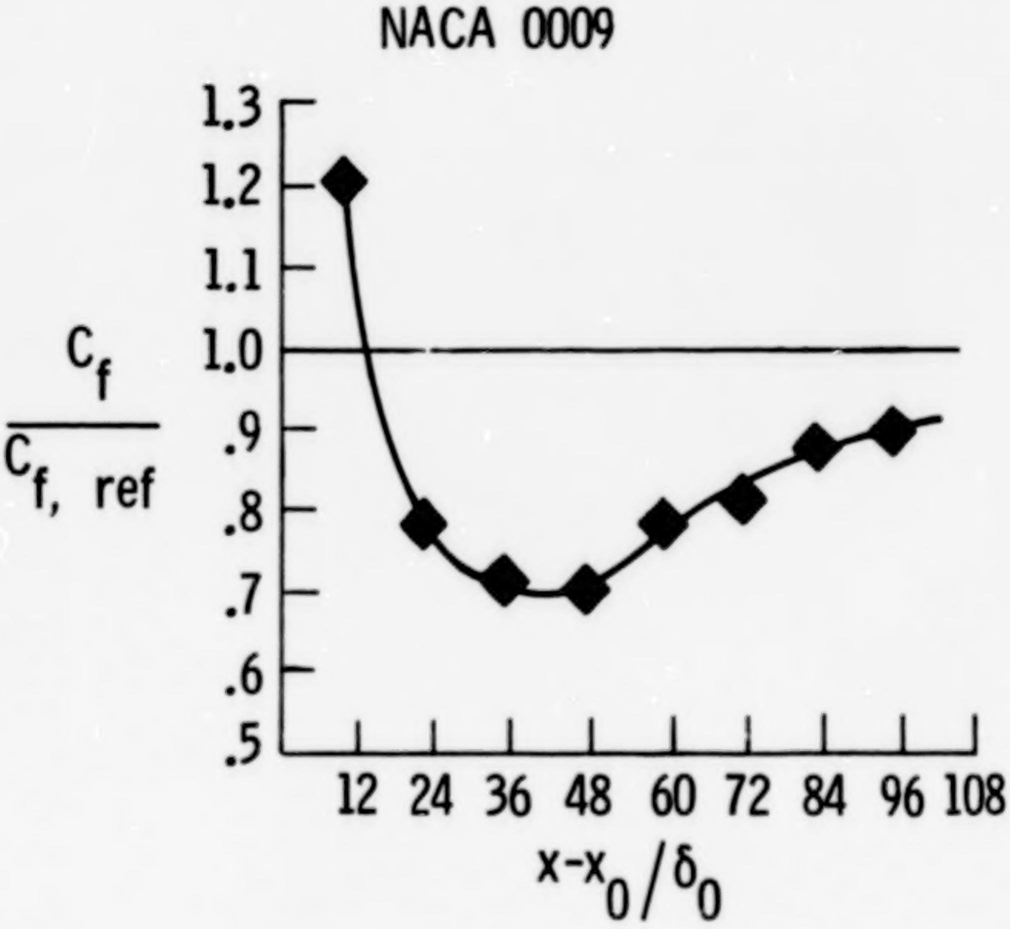

Airfoil LEBU Net Drag Reduction

Net drag reductions obtained with tandem, NACA 0009 airfoils at high Reynolds numbers compare well with the low Reynolds number thin-plate data. The foreshortened test region for the high Reynolds number tests prevented a determination of the maximum net reduction obtainable, but it is clear from this figure that the NACA 0009 airfoils can produce net drag reductions of the order of 10 percent over approximately 100 boundary layer thicknesses.

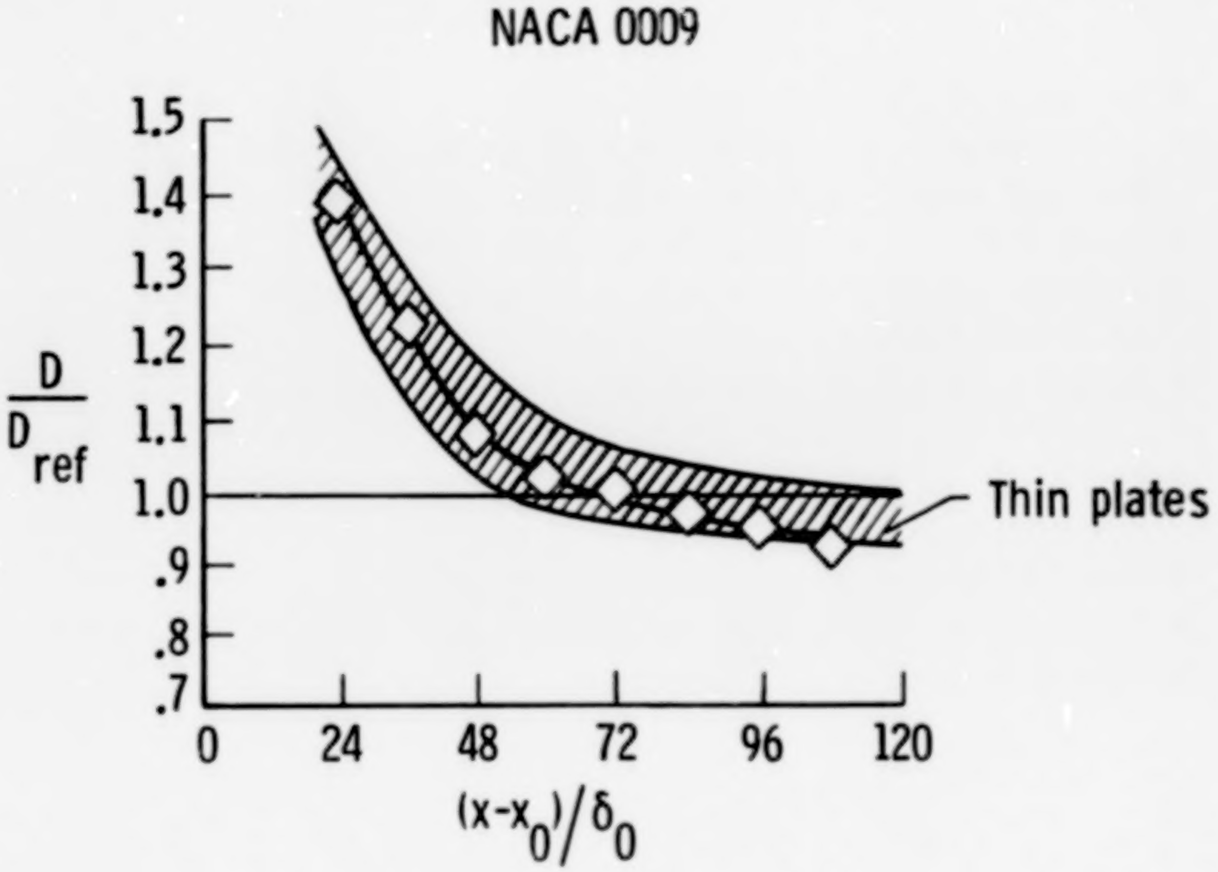

Possible Alternative Uses of LEBU Devices Other Than Turbulent Drag Reduction on Smooth Surfaces

The potential application of these devices to other uses are listed and additional applications will doubtlessly be suggested as research continues. The passive nature of the devices encourages retrofit uses in problems of controlling turbulence.

- Reduce drag on rough surfaces
- Lower radiated turbulent boundary layer noise (possibly less weight of sound insulation in fuselage)
- Lower self-noise on sonar domes/towed arrays
- Increased performance of laser and telescope windows on aircraft fuselages
- Reduce noise signature of torpedoes by reduction of turbulent eddy-propeller interaction
- Reduce size of B. L. diverters on fighter aircraft inlets for lower drag
- Free mixing control (sound/mixing augmen./supp.)
- Combine with riblets (drag reductions add)
- Control of shock-B. L. interaction

Conclusions

It has been determined from the present LaRC experiments that tandem, airfoil-shaped LEBU devices can reduce local skin friction as much as 30 percent with a recovery region extending more than 100 boundary layer thicknesses downstream. These airfoils experience near laminar skin friction device drag and produce net drag reductions of up to 7 percent. In contrast to the thin plates used in previous experiments, these airfoils are more than 1000 times stiffer and hence have the potential to withstand the "real" flight environment (dynamic pressure 36 times larger than in low-speed wind tunnels). In addition, the higher Reynolds numbers of the present tests indicate drag reduction performance is at least as good (or better) as at lower Reynolds numbers.

- Symmetric, airfoil-shaped LEBU devices work as well as flat elements
  - Local C_f reductions up to 30%
  - Reduced C_f region extends more than 100 δ_0
  - Net drag reductions up to 7%
  - Transonic capable devices (10 times thicker, 1000 times stiffer)
  - Near laminar skin friction device drag
- LEBU devices work as well (or even better) at high Reynolds numbers as at low Reynolds numbers

Omit to
end

ATTENDEES
LANGLEY RESEARCH CENTER
SYMPOSIUM ON AERODYNAMICS
APRIL 23-25, 1985

MILITARY:

DARPA:
James N. Allburn

AIR FORCE:
Barry L. Barnes
Edward R. Hartman
Elton R. Thompson (AEDC)
Nicholas G. Vretakis (Liaison/NASA)

AFWAL:
Christopher J. Boison
Richard Dyer (ASD/ENFTA)
James Mace (FIMM)
Ojars Skujins
Charles Suchomel

NAVY:
David W. Coder (DNTSR)
David J. Goodrich (Naval Underwater Systems Center)
Uwe R. Jettmar (Naval Surface Weapons Center)
Melvin A. Luter (Naval Air Systems Command)
Richard Phillips (Naval Underwater Systems Center)
Robert L. Traskos (Naval Air Systems Command)
Lynn A. Trobaugh (Naval Air Systems Command)
Ray Van Aken (Naval Weapons Center)
Andrew B. Wardlaw (Naval Surface Weapons Center)

WRIGHT PATTERSON AFB:
John Chuprin, Jr. (ASD/XRH)
James R. Snyder (ASD/XRHI)

INDUSTRY:

ARNOLD ENGINEERING DC:
William B. Baker, Jr.
Marion L. Laster

BELL HELICOPTER - TEXTRON:
Jing G. Yen

PRECEDING PAGE BLANK NOT FILMED

PAGE 586 INTENTIONALLY BLANK

BOEING:
Ronald L. Bengelink (Boeing Commercial Airplane Co.)
Jeffrey L. Colehour
Winifred Feifel (Boeing Aerospace)
William W. Herling (Boeing Aerospace)
William K. Howell (Boeing Military Aircraft Co.)
Spencer Leader (Wichita)
Fred W. May (Boeing Military Airplane Co.)
Michael A. McVeigh (Boeing VertoL)
A. L. Nagel (Boeing Commercial Airplane Co.)
Emmett M. Omar (Boeing Military Airplane Co.)
John H. Sandvig (Boeing Military)
Frederick F. Tolle (Boeing Military Airplane Co.)
Frank L. Wright (Boeing Commercial Airplane Co.)
Neng John Yu (Boeing Commercial Airplane Co.)

CALSPAN FIELD SERVICES, INC.:
Robert W. Cayse
John W. Davis (AEDC)
Milton Nesbitt (AEDC)
Alfred Ritter (AEDC)

CESSNA AIRCRAFT CORP.:
David R. Ellis

DEI-TECHNOLOGY, INC.:
Anne C. Edwards
Robert T. Taylor
K. B. Walkley
Richard White

DOUGLAS AIRCRAFT CO.:
Preston A. Henne
Robert B. Harris
Frank T. Lynch
John Morris
R. E. Pendley
Robert H. Welge

ESCON:
Gregory Jones
Werner Pfenninger

FAIRCHILD REPUBLIC:
Anthony Casaccio
Dale S. Williams

FLUIDYNE ENGINEERING CORP.:
James S. Holdhusen

GENERAL DYNAMICS CORP.:
R. G. Bradley
William W. Brayman
Charles K. Clark
Harry B. Henderson
R. W. McGuffee
T. F. Paniszczyn
Charles A. Smith

GENERAL ELECTRIC COMPANY:
Bobby R. Delaney
Faust G. Kemp
Paul H. Kutschenreuter

GRUMMAN AEROSPACE CORP.:
Charles W. Boppe
Gianky Daforno
William H. Mason
Robert E. Melnik
Rudolph C. Meyer
Richard R. Price
Michael J. Siclari
Mark Siegel
Guiseppe Volpe

GULFSTREAM AEROSPACE:
Alvin E. Holmes
William Murphy

HIGH TECHNOLOGY CORPORATION:
Malik Mujeeb

KENTRON INTERNATIONAL INC.:
Fred L. Beissner, Jr.
B. F. Downie
Michael J. Hemsch
Michael G. Jones
Dan Neuhart
Ollie J. Rose

LOCKHEED:
Paul M. Bevilaqua (Lockheed Adv. Aeronautics Co.)
Andrew L. Byrnes (California)
Grant E. Carichner (California)
Lyle N. Long (California)
Jerry E. Meyer (California)
Andrew Srokowski (Georgia)
Clive Whitmore (California)

MARTIN MARIETTA:
Robert J. Cavalleri

THE MARQUARDT CO.:
Allen M. Simen
Cum F. Young

MCDONNELL AIRCRAFT CO.:
Jack Abercrombie
Don L. Althen

MCDONNELL DOUGLAS:
Frank W. Spaid
Norbert F. Smith

MCDONNELL DOUGLAS ASTRONAUTICS:
John E. Williams, Jr.

NORTHROP CORPORATION:
Gary E. Erickson
Heinz A. Gearhardt (Aircraft Div.)
W. A. Lusby
Thomas L. Williams
Peter Wooler

OMAC:
Wyatt C. Ingram

PRATT AND WHITNEY:
M. L. Holcomb
Thomas A. Wynosky

ROCKWELL INTERNATIONAL:
Ellwood Bonner

SANDIA NATIONAL LABS.:
Harold R. Spahr

SVERDRUP TECHNOLOGY, INC.:
C. J. Scheuler

TRAYCOR HYDRONAUTICS:
Clinton E. Brown

UNITED TECHNOLOGIES:
Warren E. Anderson
Arthur J. Karanian

VIGYAN RESEARCH ASSOC. INC.:
Sudhir C. Mehrotra
Dhanvada M. Rao

VOUGHT AEROPRODUCTS:
Tom D. Beatty

GOVERNMENT:

AMES RESEARCH CENTER:
James C. Daughtery
Francis J. Kmak
Thomas Snyder

DRYDEN RESEARCH FLIGHT CENTER:
Lisa Jennett
Terry W. Putnam

LEWIS RESEARCH CENTER:
Robert J. Antl
Bernard J. Blaha
Richard R. Burley
Roger Chamberlin
Carl. C. Ciepluch
Thomas F. Gelder
Douglas E. Harrington
Melvin J. Hartmann
Edward J. Mularz
Harvey Neumann
David J. Poferl
Louis Povinelli
Lonnie Reid
Charles Trefny
Joseph E. Wasserbauer

LANGLEY RESEARCH CENTER:

Abeyounis, William K.
Althoff, Susan L.
Anders, John B., Jr.
Andrews, Earl H., Jr.
Applin, Zachary T.

Barnwell, Richard W.
Bartlett, Dennis
Beach, H. L., Jr.
Beasley, William D.
Beckwith, Ivan E.
Bezos, Gaudy M.
Blair, A. B., JR.
Block, P. J. W.
Bobbitt, Percy J.
Bower, Robert E.
Boyden, Richmond P.
Brandon, Jay
Bushnell, Dennis M.

Campbell, James F.
Campbell, Richard L.
Carlton, Tamara
Cary, Aubrey M., JR.
Catherines, John
Corlett, William A.
Chamberlain, James P.
Chestnutt, David
Clukey, Patricia G.
Croom, Cynthia

Darden, Christine M.
Dollyhigh, Sam
Driver, Cornelius
Dunham, Dana K.
Dunham, R. Earl, Jr.
Dwoyer, Douglas C.

Edwards, C. L. W.
Erickson, Wayne D.

Farmer, Moses
Ferris, James C.
Fischer, Michael C.
Foughner, Jerome T., Jr.
Frink, Neal T.

Gentry, Garl L.
Gilbert, William P.
Gloss, Blair
Greene, George C.
Green, Lawrence L.
Guy, Robert W.

Hall, Robert M.
Hansen, Perry W.
Hastings, Earl
Harris, Charles D.
Harris, Roy V., Jr.
Harvey, William D.
Hefner, Jerry N.
Hemsch, Michael J.
Henderson, William P.
Holbrook, M. L.
Honaker, Lawrence
Huston, Robert J.

Igoe, William B.

Jacobs, Peter F.
Jarrett, Olin, Jr.
Johnson, Charles B.
Johnson, Joseph J., Jr.
Johnson, Stewart K.
Johnston, Patrick J.
Jones, Kenneth M.

Keyes, J. Wayne
Kirkham, F. S.
Kumar, Ajay

Letchworth, Robert
Lamb, Milton
Liu, Chen-Huei
Liu, Grace
Londenberg, W. Kelly
Luckring, James M.

Macaraeg, Michele G.
Maddalon, Dal V.
Maestrello, Lucio
Maglieri, Dominic
Mann, Michael J.
Margason, Richard J.
Marcolini, Michael A.
Martin, James A.
McGhee, Robert J.
McKinney, L. Wayne
Mineck, Raymond E.
Miller, David S.
Molloy, John K.
Moul, Thomas M.
Morris, Charles E. K., Jr.
Morris, Shelby J., Jr.

Newman, Perry A.
Nguyen, Luat T.
Northam, G. Burton

Obara, Clifford J.
Ogburn, Marilyn E.

Parrott, T. L.
Patterson, J. C., Jr.
Pellett, Gerald L.
Penland, Jim A. (DRA)
Petersen, Richard
Peterson, John B.
Pinckney, S. Z.

Quinto, P. Frank

Rivera, Jose
Rose, Lester J.
Rumsey, Christopher

Salas, Manuel D.
Satran, Dale
Schoenster, James A.
Schoonover, Elliott
Sellers, William L.
Sewall, William
Shrout, B. L.
Small, W. J.
Sobieskie, J.
Somers, Dan M.
South, Jerry C., Jr.
Stack, John P.
Stack, Sharon H.
Stainback, P. Calvin
Stallings, Robert L.
Stephens, David G.
Stewart, Eric C.
Stickle, Joseph W.
Streett, Craig
Stough, H. Paul, III
Swanson, Charles

Talcott, Noel A. Jr.
Thomas, James L.
Tolson, Robert
Trexler, Carl A.

Vatsa, Veer N.
Viken, Jeffrey K.
Voland, Randall T.

Waggoner, E.
Wagner, Richard D.
Wagner, Timothy C.
Walker, Betty S.
Walsh, Michael J.
Weidner, John
Weston, Robert P.
Whipple, Raymond D.
Whitcomb, Richard (DRA)
Wilkinson, Stephen P.
Williams, Louis J.
Wilmoth, Richard g.
Wilson, John C.
Wood, Richard

Yaros, Steven F.
Young, Jim

Zang, T. A., Jr.

NASA HEADQUARTERS:
Randolph Graves
Gary B. Hicks
Raymond Rose

FAA:
Terence J. Barnes

UNIVERSITIES:

CARNEGIE-MELLON UNIVERSITY:
Max D. Gunzburger

UNIVERSITY OF DELAWARE:
J. E. Danberg

GEORGE WASHINGTON UNIVERSITY:
John Carter
Glenn S. Diskin
Lawrence Huebner
John Whitesides

ICASE:
Stephen F. Davis
Milton E. Rose

IOWA STATE UNIVERSITY:
George R. Inger

JOHNS HOPKINS APL:
L. L. Cronvich
David Van Wie

UNIVERSITY OF MARYLAND:
John D. Anderson, Jr.
Everrett Jones
W. L. Melnick

MASSACHUSETTS INSTITUTE OF TECHNOLOGY:
Baron R. Judson

STATE UNIVERSITY OF NEW YORK:
Ram Banchan Ram

NEW YORK UNIVERSITY:
Lu Ting

NORTH CAROLINA STATE UNIVERSITY:
Keith D. Hoffler
Shawn Woodson

OHIO STATE UNIVERSITY:
Gerald Gregorek
John D. Lee

OLD DOMINION UNIVERSITY:
Debra L. Carraway
Osama A. Kandil
William D. Lakin

PRINCETON:
Seymour Bogdonoff

RENSSELAER POLYTECHNIC INSTITUTE:
Henry T. Nagamatsu

TEXAS A&M:
Leland A. Carlson

UNIVERSITY OF TENNESSEE SPACE INSTITUTE:
John S. Steinhoff
Jimmy Wu

VIRGINIA POLYTECHNIC INSTITUTE:
Bernard Grossman

AUTHOR INDEX

(Keyed to paper numbers)

Abeyounis, William K., 24
Adcock, Jerry B., 16
Anders, John B., Jr, 31
Andrews, Earl H., Jr., 37
Antcliff, Richard R., 15
Applin, Zachary T., 12

Banks, Daniel W., 45
Barnwell, Richard W., 13
Bayliss, Alvin, 17
Beach, H. Lee, Jr., 36
Beckwith, Ivan E., 12
Beeler, George B., 18
Blair, A. B., Jr., 48
Block, Patricia J. W., 35
Bobbitt, Percy J., 2
Bower, Robert E., 1
Boyden, Richmond P. 14
Brandon, Jay M., 38
Brooks, Cuyler W., Jr., 26
Burley, James R., II, 33

Campbell, Bryan A., 43
Campbell, Richard L., 23
Carlson, Harry W., 43
Carraway, Debra, 15
Chamberlain, James P., 9
Clukey, Patricia G., 26
Coe, Paul L., Jr., 34
Covell, Peter F., 46
Croom, Cynthia C., 25, 29
Croom, Mark A., 38

Darden, Christine M., 43
Dicarlo, Daniel J., 40
Doria, Michael L., 3
Dunham, Dana Morris, 34
Dunham, R. Earl, Jr., 19

Frink, Neal T., 42
Fuller, Dennis E., 16

Gatlin, Gregory M., 45
Glover, Kenneth E., 40
Goodman, Wesley L., 18, 19
Green Lawrence L., 3
Greene, George C., 20
Gumbert, Clyde R., 4
Guy, Robert W., 37

Hahne, David E., 39
Hallissy, James B., 42, 44
Harris, Charles D., 26
Harris, Roy V., Jr., 41
Hartwich, Peter-Michael, 9
Harvey, William D., 26
Hastings, Earl C., Jr., 25
Hefner, Jerry N., 21
Henderson, William P., 32
Holmes, Bruce J., 15, 25, 28, 29
Hom, Kam W., 43
Honaker, William C., 15
Howard, Floyd G., 19
Hussaini, M. Yousuff, 8

Jackson, Jeffrey S., 43
Jarrett, Olin, Jr., 15
Johnson, Charles B., 15
Johnson, Mathew E., 43
Johnson, Stuart K., 50
Johnston, Patrick J., 49
Jones, Kenneth M., 5
Jordan, Frank L., Jr., 40

Kemmerly, Guy T., 45
Kemp, William B., Jr., 13
Keyes, J. Wayne, 50
Kubendran, L. R., 20
Kumar, Ajay, 11

Lamar, John E., 20
Lamb, Milton, 24
Lawing, Pierce L., 15
Leavitt, Laurence D., 33
Lindemann, A. Margarethe, 18
Liu, Chen-Huei, 9, 20
Luckring, James M., 10

Maestrello, Lucio, 12, 17
Malik, Mujeeb R., 17
Mangalam, Sivaramarkrish, 17
Mann, Michael J., 44
Marcum, Don C., Jr. 49
Margason, Richard J., 19
McGhee, Robert J., 22
McGinley, Catherine B., 18
McKinney, Linwood W., 16
McMillin, S. Naomi, 47
Mercer, Charles E., 44

PAGE 598 INTENTIONALLY BLANK

PRECEDING PAGE BLANK NOT FILMED

Meyers, James F., 15
Miller, David S., 46
Mineck, Raymond E., 13
Monta, William J., 48
Murri, Daniel G., 39

Newman, Perry A., 13
Nguyen, Luat T., 38, 39

Obara, Clifford J., 15, 25, 28
Ogburn, Marilyn E., 39
Olinger, Frank V., 50

Patterson, James C., Jr., 24, 34
Paulson, John W., Jr., 45
Pfenninger, Werner, 22
Phillips, Pamela S., 23
Pinckney, S. Zane, 37

Quinto, P. Frank, 45

Re, Richard J., 24
Riebe, Gregory D., 43
Rogers, R. Clayton, 15
Rose, O. J., 47
Rudy, David H., 6, 19
Rumsey, Christopher L., 19,

Salas, Manuel D., 4
Sanders, Bobby W., 50
Sawyer, Wallace C., 49
Schoonover, W. Elliot, Jr., 42
Sellers, William L., III, 19
Shrout, Barrett L., 43
Small, William J., 43
South, Jerry C., Jr., 3
Stack, John P., 15, 26
Stainback, P. Calvin, 12, 15
Stallings, Robert L., Jr., 48
Stough, H. Paul, III, 19, 40
Swanson, Roy C., Jr., 6, 7

Talcott, Noel A., 5
Tcheng, Ping, 14
Thomas, James L., 6, 19
Trexler, Carl A., 11
Turkel, Eli, 7

Van Dam, Cornelius P., 25
Vatsa, Veer N., 7
Viken, Jeffrey K., 22, 23

Waggoner, Edgar G., 23
Wagner, Richard D., 27
Walsh, Michael J., 30
Walters, Robert W., 6
Watson, Ralph D., 31
Watts, Joe D., 50
Weidner, John P., 50
Weston, Robert P., 9
Whipple, Raymond D., 38
Wilcox, Floyd J., Jr., 48
Wilkinson, Stephen P., 15, 18
Wood, Richard M., 47

Yip, Long P., 42

Zang, Thomas A., Jr. 8

1. Report No. CP-2397	2. Government Accession No.	3. Recipient's Catalog No.
4. Title and Subtitle Langley Symposium on Aerodynamics Volume I		5. Report Date January 1986 6. Performing Organization Code 505-31-03-02
7. Author(s) Sharon H. Stack, Compiler		8. Performing Organization Report No. L-16031
9. Performing Organization Name and Address NASA Langley Research Center Hampton, VA 23665-5225		10. Work Unit No. 11. Contract or Grant No. 13. Type of Report and Period Covered Conference Publication
12. Sponsoring Agency Name and Address National Aeronautics and Space Administration Washington, DC 20546-0001		14. Sponsoring Agency Code

16. Abstract

This publication is a compilation of the papers presented at the Langley Symposium on Aerodynamics held on April 23-25, 1985, at NASA Langley Research Center, Hampton, Virginia. The purpose of this symposium was to present current work and results of the Langley Aeronautics Directorate covering the areas of computational fluid dynamics, viscous flows, airfoil aerodynamics, propulsion integration, test techniques, and low-speed, high-speed, and transonic aerodynamics. The symposium was organized into the following seven sessions:

I. Theoretical Aerodynamics
II. Test Techniques
III. Fluid Physics
IV. Viscous Drag Reduction
V. Propulsion/Integration
VI. Flight Dynamics
VII. High Performance Vehicles

Papers are grouped by sessions in the order in which they were presented. An author index and a list of attendees are included at the end of each volume.

17. Key Words (Suggested by Author(s)) Configuration aerodynamics Flight dynamics Propulsion/integration Drag reduction High angle of attack Testing techniques Computational fluid dynamics Hypersonics Maneuverability	18. Distribution Statement [redacted] Subject Category 01

19. Security Classif. (of this report) Unclassified	20. Security Classif. (of this page) Unclassified	21. No. of Pages 609	22. Price A99

[redacted]